National Cooperative Highway Research Program

NCHRP REPORT 24-15 (2)

ABUTMENT SCOUR IN COHESIVE MATERIALS

J.-L. Briaud, H.-C. Chen, K.-A Chang, S. J. Oh, X. Chen

October 2009

Transportation Research Board

National Research Council

NOMENCLATURE

#200	Percentage of soil passing No.200 sieve
a	Width of pier
α	Contraction transition angle
α_0	Turning angle between the surface streamline direction and the upstream approaching direction
A_1	Total flow area in the approach section immediately upstream of the abutment
A_2	Total flow area in the contracted section
A_{f1}	Flow area on the floodplain in the approach section immediately upstream of the abutment
A_{f2}	Flow area on the floodplain in the contracted section
β_a	Slope of abutment
β_m	Slope of main channel
C	Chezy's coefficient
$C_{f\_\max}$	Maximum friction coefficient
C_{f_center}	Friction coefficient along the channel center and in the middle of the abutment
C_{f-vw}	Maximum bed friction coefficient around a vertical wall
C_{f-cp}	Maximum bed friction coefficient for circular pier
C_r	Unit discharge ratio $C_r = Q_{total} / (Q_{total} - Q_{blocked})$
d_1	Distance from water surface to the low chord of the bridge at upstream face of the bridge
d_{deck}	Thickness of bridge deck
D	Hydraulic diameter
D_{50}	Median diameter of sediment
D_r	Middleton's dispersion ratio
ε	Average height of the roughness elements
f	Friction factor obtained from Moody chart
Fr	Froude number based on V_1 and y_{f1}
$Fr_{(Pier)}$	Froude number based on V_1 and a
$Fr_{c(Pier)}$	Critical Froude number based on V_c and a
Fr_{f2}	Froude number based on V_{f2} and y_{f1}
Fr_{m2}	Froude number based on V_2 and y_{m1}
Fr_{fc}	Froude number based on V_c and y_{f1}
Fr_{mc}	Critical Froude number based on V_{mc} and y_{m1}

g	Gravitational acceleration
γ	Unit weight of water
Gs	Specific gravity of cohesionless soil
h	Distance from the low chord of the bridge to the river bottom before scour starts
k_α	Correction factor of the contraction transition angle for τ_{max}
k_c	Correction factor of channel conveyance ratio for τ_{max}
k_{Cr}	Correction factor of discharge ratio for τ_{max}
k_{Fr}	Correction factor of Froude number for τ_{max}
k_L	Correction factor of the abutment location for τ_{max}
k_o	Correction factor of overtopping for τ_{max}
k_θ	Correction factor of attack angle for τ_{max}
k_R	Correction factor of contraction ratio for τ_{max}
k_s	Correction factor of abutment shape for τ_{max}
k_{sh}	Correction factor of aspect ratio for τ_{max}
k_{Wa}	Correction factor of the contraction length for τ_{max}
K_1	Correction factor of pier or abutment shape for maximum abutment or pier scour depth
K_2	Correction factor of attack angle for maximum abutment or pier scour depth
K_I	Correction factor for flow intensity
K_f	Correction factor for spiral flow at the abutment toe
K_G	Correction factor for channel geometry
K_L	Correction factor of the abutment location for maximum abutment scour depth
K_{sp}	Correction factor of the pier spacing for maximum pier scour depth
K_p	Correction factor of pressure flow for maximum abutment scour depth
K_v	Ratio of velocity at the abutment toe to the mean velocity in the contracted section
K_w	Correction factor of water depth for maximum abutment or pier scour depth
L'	Length of embankment projected normal to flow
L_1	Width of channel at approach section
L_2	Width of channel at contracted section
L_f	Width of floodplain
L_m	Half width of main channel
M	Discharge contraction ratio $\left(M = \frac{Q_{total} - Q_{block}}{Q_{total}} \right)$
n	Manning's coefficient
ν	Kinematic viscosity of water
θ	Attack angle

PI	Plasticity index (%)
p	Pressure (N/m^2)
q_1	Unit discharge at approach section
q_2	Unit discharge around abutment
Q_{block}	Discharge blocked by bridge embankment defined by approach average velocity on flood-plain times the area extending the bridge to approach section
Q_{total}	Total discharge
Q_{fp1}	Discharge on the floodplain in the approach section immediately upstream of the abutment
ρ	Unit mass of water
R_h	Hydraulic radius
Re	Reynolds number based on a or W_a
S	Spacing of group piers or the energy slope
SAR	Sodium adsorption ratio
S_i	Initial slope at the origin of the erosion function $\left(=d\dot{z}/d\tau\right)_i$
S_u	Undrained shear strength of soil
t	Elapsed time after start of scour
t_e	Equivalent time necessary for the highest velocity in the hydrograph to create the same scour depth as the entire hydrograph
t_{hydro}	Duration of the hydrograph
$\tau_{approach}$	Approach bed shear stress
τ_b	Bed shear stress
τ_c	Critical shear stress
$\tau^*_{\max}$	Shear stress increment due to abutment alone
$\tau_{max(Abut)}$	Maximum shear stress of around abutment
$\tau_{max(Cont)}$	Maximum shear stress of in the middle of channel
$\tau_{max(Pier)}$	Maximum shear stress of around pier
τ_s	Bed shear strength at depth z below initial bed-fluid interface
V_1	Approach average velocity
V_{f1}	Approach average velocity on the floodplain
V_{f2}	Velocity around the toe of the abutment
V_{fc0}	Critical velocity on the floodplain without back water effect
V_{fc}	Critical velocity on the floodplain
V_{max}	Maximum velocity in the hydrograph
V_{mc}	Critical velocity in the main channel
ω	Vorticity at the point

ω_{nose}	Vorticity at the spur dike nose
W	Water content (%)
W_a	Top width of the abutment or length of contraction channel
y_{Cont}	Total flow depth of scour in the contracted section ($y_{m1}+y_{s(Cont)}$)
y_{f0}	Water depth at the approach section on the floodplain without back water effect
y_{f1}	Water depth at the toe of the abutment estimated as the water depth immediately upstream of the toe of the abutment
y_{max}	Total flow depth of abutment scour depth ($y_{f1}+y_{s(Abut)}$)
y_{m1}	Water depth in the main channel at immediately upstream of bridge contraction
$y_{s(Abut)}$	Maximum abutment scour depth adjacent to the toe of the abutment
$y_{s(Cont)}$	Maximum contraction scour depth in the middle of channel
$y_{s(Pier)}$	Maximum pier scour depth
$y_s(t)$	Scour depth at time t
$\dot{z}_f$	Erosion rate when $\tau - \tau_s = 0$
$\dot{z}_i$	Initial rate of scour
$\dot{z}_{i,mean}$	Mean initial rate of scour corresponding to the maximum velocity

TABLE OF CONTENTS

Page

NOMENCLATURE ..... **i**

TABLE OF CONTENTS ..... **v**

LIST OF FIGURES ..... **xi**

LIST OF TABLES ..... **xxiii**

EXCUTIVE SUMMARY ..... **xxvi**

CHAPTER

1 INTRODUCTION **1-1**

1.1 BRIDGE SCOUR **1-1**

1.2 SOILS CLASSIFICATION **1-1**

1.3 THE PROBLEM ADDRESSED **1-1**

1.4 WHY WAS THIS PROBLEM ADDRESSED? **1-3**

1.5 APPROACH SELECTED TO SOLVE THE PROBLEM **1-3**

1.6 ORGANIZATION OF THE REPORT **1-3**

2 ERODIBILITY OF COHESIVE SOILS **2-1**

2.1 ERODIBILITY: A DEFINITION **2-1**

2.2 EROSION PROCESS **2-2**

2.3 EXISTING KNOWLEDGE ON ERODIBILITY OF COHESIVE SOILS **2-2**

2.4 ERODIBILITY AND CORRELATION TO SOIL AND ROCK PROPERTIES? **2-3**

3 THE SRICOS-EFA METHOD **3-1**

3.1 EROSION FUNCTION APPARATUS **3-1**

3.1.1 Concept **3-1**

3.1.2 EFA Test Procedure **3-2**

3.1.3 EFA Test Data Reduction **3-3**

3.1.4 EFA Precision and Typical Results 3-5

3.2 THE SRICOS-EFA METHOD 3-6

3.2.1 SRICOS-EFA Method for Cylindrical Piers in Deep Water 3-6

3.2.2 SRICOS-EFA Method for Maximum Scour Depth at Complex Piers 3-7

3.2.3 SRICOS-EFA Method for Initial Scour Rate at Complex Piers 3-7

3.2.4 SRICOS-EFA Method for Maximum Contraction Scour Depth 3-7

3.2.5 SRICOS-EFA Method for Initial Contraction Scour Rate 3-8

3.2.6 SRICOS-EFA Method for Complex Piers Scour and Contraction Scour in Cohesive soils 3-8

3.2.7 Verification of the SRICOS-EFA Method 3-9

3.2.8 Future Hydrographs and Scour Risk Analysis 3-9

3.2.9 Example Problems 3-10

4 THE SRICOS-EFA METHOD FOR INITIAL RATE OF SCOUR AT ABUTMENT 4-1

4.1 LITERATURE REVIEW 4-1

4.1.1 Bed Shear Stress at the Bridge Crossing 4-1

4.1.2 Issues in the Numerical Simulation of Bridge Scour on Cohesive Soils 4-6

4.1.2.1 Critical Shear Stress of the Cohesive Soils 4-7

4.1.2.2 Erosion Rate of Soils 4-8

4.1.2.3 Effect of Roughness 4-9

4.1.2.4 Effect of Turbulence Intensity 4-10

4.2 GOVERNING EQUATIONS FOR CHEN3D PROGRAM 4-11

4.3 MAXIMUM BED SHEAR STRESS AROUND AN ABUTMENT IN OPEN CHANNEL FLOW 4-20

4.3.1 Methodology 4-20

4.3.2 Reference Case 4-23

4.3.3 Parametric Studies 4-29

4.3.3.1 Influence of Reynolds Number 4-29

4.3.3.2 Influence of water depth 4-33

4.3.3.3 Influence of Channel Unit Discharge Ratio 4-37

4.3.3.4 Influence of the Aspect Ratio of Abutment 4-41

4.3.3.5 Influence of the Abutment Shape 4-45

4.3.3.6 Influence of the skew angle 4-52

4.3.4 Maximum Bed Shear Stress Equation in a Rectangular Channel..... 4-56

4.3.5 Influence of a Compound Channel Configuration..... 4-57

4.3.6 Maximum Bed Shear Stress Equation in Compound Channel..... 4-66

4.3.7 Verification of the Maximum Bed Shear Stress Equation 4-66

4.3.8 Correction of Maximum Bed Shear Stress around Abutment Based on Flume Tests 4-70

4.3.9 Recommended Equation for Maximum Shear Stress around an Abutment..... 4-74

5 MAXIMUM BED SHEAR STRESS AROUND ABUTMENT IN OVERTOPPING FLOW 5-1

5.1 VERIFICATION OF THE OVERTOPPING FLOW SIMULATION..... 5-1

5.2 OVERTOPPING IN RECTANGULAR CHANNELS 5-3

5.3 OVERTOPPING IN COMPOUND CHANNELS 5-10

5.3.1 Overtopping in Symmetric Compound Channels 5-10

5.3.2 Overtopping in Non-Symmetric Compound Channels..... 5-15

5.4 OPEN CHANNEL FLOW IN A CHANNEL BEND 5-18

5.4.1 Influence of R/W..... 5-19

5.4.2 Influence of Abutment Location 5-20

5.4.3 Influence of Abutment Shape..... 5-21

5.5 OVERTOPPING FLOW ON CHANNEL BEND..... 5-30

5.5.1 Comparison of Open Channel Flow and Overtopping Flow in a Channel Bend..... 5-31

5.5.2 Influence of R/W..... 5-31

5.5.3 Influence of abutment location..... 5-32

5.5.4 Influence of abutment shape 5-33

5.6 CONFLUENCE OF TRIBUTARY UPSTREAM OF A BRIDGE..... 5-39

5.7 MAXIMUM SHEAR STRESS FOR OVERTOPPING FLOW 5-40

6 VERIFICATION OF NUMERICAL SIMULATIONS 6-1

6.1 SOIL PROPERTIES 6-1
6.2 SCOUR RATE MODELS IN COHESIVE SOILS 6-3
6.3 SCOUR PREDICTION OF THE FLUME TESTS IN NCHRP 24-15(2) 6-5
6.3.1 Scour Prediction on Compound Channel 6-6
6.3.1.1 Observations from the Flume Tests 6-6
6.3.1.2 Simulation Result and Analysis of Case 9 6-7
6.3.1.3 Simulation Result and Analysis of Case 1 6-11
6.3.1.4 Simulation Result and Analysis of Case 4 6-15
6.3.2 Scour Prediction on Rectangular Channel 6-18
6.3.2.1 Observations from the Flume Tests 6-18
6.3.2.2 Simulation Result and Analysis of Case 14 6-19
6.3.2.3 Simulation Result and Analysis of Case 13 6-22
6.4 SCOUR PREDICTION WITH OVERTOPPING 6-25

7 SRICOS EFA METHOD FOR MAXIMUM SCOUR DEPTH FOR ABUTMENT AND CONTRACTION 7-1

7.1 LITERATURE REVIEW 7-2
7.1.1 Abutment Scour in Sand 7-2
7.1.2 Abutment Scour in Clay 7-14
7.1.3 Contraction scour in sand and in clay 7-15
7.2 EXPERIMENT SETUP 7-17
7.2.1 Soil and Soil Bed Preparation 7-17
7.2.2 Measurement Equipment 7-18
7.2.3 Test Conditions 7-28
7.3 WATER DEPTH AND VELOCITY MEASUREMENT RESULTS 7-31
7.3.1 Water Surface Profiles 7-31
7.3.2 Velocity Distribution 7-35
7.3.3 Comparison with HEC-RAS Results 7-42
7.4 SCOUR DEVELOPMENT 7-51
7.4.1 Pattern of Scour 7-51
7.4.2 Maximum Scour Depth 7-62

7.5 DATA ANALYSIS 7-65

7.5.1 Contraction Scour 7-65

7.5.1.1 Variables and Experiment Results of Contraction Scour 7-65

7.5.1.2 Dimensional Analysis 7-66

7.5.1.3 Prediction of Contraction Scour 7-67

7.5.2 Abutment Scour 7-70

7.5.2.1 Variables and Experimental Results of Abutment Scour 7-70

7.5.2.2 Dimensional Analysis 7-72

7.5.2.3 Prediction Equation 7-74

7.5.2.4 The Effect of Abutment Shape (K_1) 7-75

7.5.2.5 The Effect of Abutment Alignment (K_2) and Abutment Location (K_L) 7-76

7.5.2.6 The Effect of Channel Geometry (K_G) 7-79

7.5.2.7 Preliminary Prediction Equation for Abutment Scour and Reynolds number effect (K_{Re}) 7-80

7.5.2.8 The Correction Factor for Pressure Flow (K_p) 7-85

7.5.2.9 The Prediction Equation for Abutment Scour 7-85

7.6 NEW APPROACH FOR ABUTMENT SCOUR DEPTH CALCULATION 7-88

7.7 NEW APPROACH FOR CONTRACTION SCOUR DEPTH CALCULATION 7-98

8 VERIFICATION OF THE SRICOS-EFA METHOD 8–1

8.1 CONTRACTION SCOUR 8–1

8.2 ABUTMENT SCOUR 8–3

8.2.1 Comparison with Laboratory Test Results 8–3

8.2.2 Comparison with Full Scale Measurement 8–7

8.2.3 Comparison with Previous Equations for Abutment Scour Depth Using Imaginary Condition 8–7

9 SCOUR EXAMPLE PROBLEMS 9–1

REFERENCES..... Refs – 1

APPENDIX A DISTRIBUTION OF VELOCITY AND TURBULENCE INTENSITY A-1

APPENDIX B SCOUR DEVELOPMENT.....B-1

APPENDIX C PHOTOGRAPHS FROM THE FLUME TESTS.....C-1

LIST OF FIGURES

Page

Figure 1.1 Typical bridge with bridge scour. 1–2

Figure 2.1 Erodibility Function for a clay and for a sand. 2–1

Figure 2.2 Critical shear stress versus mean soil grain diameter. 2–5

Figure 2.3 Erosion properties as a function of water content.....2–5

Figure 2.4 Erosion properties as a function of undrained shear strength. 2–6

Figure 2.5 Erosion properties as a function of plasticity index.....2–6

Figure 2.6 Erosion properties as a function of percent passing sieve #200. 2–7

Figure 3.1 Schematic diagram and result of the EFA (Erosion Function Apparatus).....3–1

Figure 3.2 Photographs of the Erosion Function Apparatus (a) General view (b) closeup of the test section. 3–2

Figure 3.3 Moody chart (reprinted with permission from Munson et al. 1990).....3–4

Figure 3.4 Erosion Function for a soil sample taken near Pier 27E of the Existing Woodrow Wilson bridge (2.6 - 3.2 meters depth) : (a) Scour Rate vs. Shear Stress, (b) Scour Rate vs. Velocity. 3–4

Figure 3.5 Proposed erosion categories for soils and rocks based on velocity. 3–5

Figure 3.6 Proposed erosion categories for soils and rocks based on shear stress.....3–6

Figure 4.1 Finite analytic local element. 4–16

Figure 4.2 Definition of the parameters in abutment scour problem. 4–21

Figure 4.3 Definition of the channel unit discharge ratio.....4–22

Figure 4.4 Diagram of the reference case.....4–24

Figure 4.5 Numerical grid for the reference case. 4–26

Figure 4.6 Velocity vectors on water surface (reference case). 4–27

Figure 4.7 Normalized pressure, $\frac{p}{\rho V^2}$ contours around vertical wall abutment. 4–28

Figure 4.8 Bed friction coefficient ($\times 10^2$), $\frac{\tau_b}{\rho V^2}$ contour for Reynolds number 10^5. 4–28

Figure 4.9 Projected velocity vectors on the cross sections around abutment. 4–29

Figure 4.10 Normalized maximum bed shear stresses versus Reynolds number. 4–31

Figure 4.11 Bed friction coefficient ($\times 10^2$), $\frac{\tau_b}{\rho V^2}$ contour for Reynolds number 10^4. 4–32

Figure 4.12 Bed friction coefficient ($\times 10^2$), $\frac{\tau_b}{\rho V^2}$ contour for Reynolds number 10^6. 4–32

Figure 4.13 Bed friction coefficient ($\times 10^2$), $\frac{\tau_b}{\rho V^2}$ contour for Reynolds number 10^7. 4–33

Figure 4.14 Correction factor for water depth. 4–34

Figure 4.15 Bed friction coefficient ($\times 10^2$), $\frac{\tau_b}{\rho V^2}$ contour for y/W_a=0.25.....4–35

Figure 4.16 Bed friction coefficient ($\times 10^2$), $\frac{\tau_b}{\rho V^2}$ contour for y/W_a=0.5.....4–35

Figure 4.17 Bed friction coefficient ($\times 10^2$), $\frac{\tau_b}{\rho V^2}$ contour for y/W_a=1.0.....4–36

Figure 4.18 Geometries for channel unit discharge ratio study. 4–37

Figure 4.19 Correction factor for channel unit discharge ratio.....4–38

Figure 4.20 Bed friction coefficient ($\times 10^2$), $\frac{\tau_b}{\rho V^2}$ contour for C_r =2.5. 4–39

Figure 4.21 Bed friction coefficient ($\times 10^2$), $\frac{\tau_b}{\rho V^2}$ contour for C_r =1.67. 4–39

Figure 4.22 Bed friction coefficient ($\times 10^2$), $\frac{\tau_b}{\rho V^2}$ contour for C_r =1.25. 4–40

Figure 4.23 Geometries for the study of abutment aspect ratio. 4–41

Figure 4.24 Correction factor for abutment aspect ratio. 4–42

Figure 4.25 Friction coefficient ($\times 10^2$), $\frac{\tau_b}{\rho V^2}$ contour for L_a =0.37m. 4–43

Figure 4.26 Bed friction coefficient ($\times 10^2$), $\frac{\tau_b}{\rho V^2}$ contour for L_a =0.73m. 4–43

Figure 4.27 Bed friction coefficient ($\times 10^2$), $\frac{\tau_b}{\rho V^2}$ contour for L_a =1.01m. 4–44

Figure 4.28 Bed friction coefficient ($\times 10^2$), $\frac{\tau_b}{\rho V^2}$ contour for L_a =1.32m. 4–44

Figure 4.29 Definition of abutment shape. 4–45

Figure 4.30 Bed friction coefficient ($\times 10^2$), $\frac{\tau_b}{\rho V^2}$ contour for L_a = 1.01m (WW). 4–46

Figure 4.31 Bed friction coefficient ($\times 10^2$), $\frac{\tau_b}{\rho V^2}$ contour for L_a = 1.21m (WW). 4–47

Figure 4.32 Bed friction coefficient ($\times 10^2$), $\frac{\tau_b}{\rho V^2}$ contour for L_a = 1.62m (WW). 4–48

Figure 4.33 Bed friction coefficient ($\times 10^2$), $\frac{\tau_b}{\rho V^2}$ contour for L_a = 2.23m (WW). 4–48

Figure 4.34 Bed friction coefficient ($\times 10^2$), $\frac{\tau_b}{\rho V^2}$ contour for L_a = 1.01m (ST) 4–50

Figure 4.35 Bed friction coefficient ($\times 10^2$), $\frac{\tau_b}{\rho V^2}$ contour for L_a = 1.32m (ST). 4–50

Figure 4.36 Bed friction coefficient ($\times 10^2$), $\frac{\tau_b}{\rho V^2}$ contour for L_a = 1.62m (ST). 4–51

Figure 4.37 Bed friction coefficient ($\times 10^2$), $\frac{\tau_b}{\rho V^2}$ contour for L_a = 2.23m (ST). 4–51

Figure 4.38 Correction factor for the skew angle of vertical wall abutment. 4–53

Figure 4.39 Bed friction coefficient ($\times 10^2$), $\frac{\tau_b}{\rho V^2}$ contour for 60 degree 4–53

Figure 4.40 Bed friction coefficient ($\times 10^2$), $\frac{\tau_b}{\rho V^2}$ contour for 75 degree 4–54

Figure 4.41 Bed friction coefficient ($\times 10^2$), $\frac{\tau_b}{\rho V^2}$ contour for 105 degree 4–54

Figure 4.42 Bed friction coefficient ($\times 10^2$), $\frac{\tau_b}{\rho V^2}$ contour for 120 degree 4–55

Figure 4.43 Correction factor of abutment location in compound channel. 4–60

Figure 4.44 Bed friction coefficient ($\times 10^2$), $\frac{\tau_b}{\rho V^2}$ contour for L_m = 1.83m. 4–60

Figure 4.45 Bed friction coefficient ($\times 10^2$), $\frac{\tau_b}{\rho V^2}$ contour for Lm = 2.13m. 4–61

Figure 4.46 Bed friction coefficient ($\times 10^2$), $\frac{\tau_b}{\rho V^2}$ contour for Lm = 1.22m. 4–62

Figure 4.47 Bed friction coefficient ($\times 10^2$), $\frac{\tau_b}{\rho V^2}$ contour for L_m = 2.74m. 4–62

Figure 4.48 Bed friction coefficient ($\times 10^2$), $\frac{\tau_b}{\rho V^2}$ contour for L_m = 0.91m. 4–63

Figure 4.49 Bed friction coefficient ($\times 10^2$), $\frac{\tau_b}{\rho V^2}$ contour for L_m = 0.61m. 4–64

Figure 4.50 Bed friction coefficient ($\times 10^2$), $\frac{\tau_b}{\rho V^2}$ contour for L_m = 3.05m. 4–65

Figure 4.51 Bed friction coefficient ($\times 10^2$), $\frac{\tau_b}{\rho V^2}$ contour for L_m = 2.44m. 4–65

Figure 4.52 Comparison of simulated and predicted cases in rectangular channel study. 4–67

Figure 4.53 Comparison of the simulated and predicted cases. 4–70

Figure 4.54 EFA testing results of the porcelain clay used in the flume tests. 4–72

Figure 4.55 Comparison of the $\alpha * \tau_{max\_prediciton}$ and τ_{max_EFA}. 4–73

Figure 5.1 Bridge model for shear stress experiments (after Kerenyi, 2007). 5–1

Figure 5.2 Explanation of notations (after Kerenyi, 2007). 5–2

Figure 5.3 Bed shear stress distribution of h_b = 0.13m 5–2

Figure 5.4 Bed shear stress distribution of h_b = 0.16m 5–3

Figure 5.5 Cross sections at the middle of the abutment for rectangular channels. 5–4

Figure 5.6 Numerical grid for overtopping case. 5–5

Figure 5.7 Bed friction coefficient, $\frac{\tau_b}{\rho V^2}$ ($\times 10^2$) contours for Case (a) 5–7

Figure 5.8 Bed friction coefficient, $\frac{\tau_b}{\rho V^2}$ ($\times 10^2$) contours for Case (b) 5–7

Figure 5.9 Bed friction coefficient, $\frac{\tau_b}{\rho V^2}$ ($\times 10^2$) contours for Case (c) 5–8

Figure 5.10 Bed friction coefficient, $\frac{\tau_b}{\rho V^2}$ ($\times 10^2$) contours for Case (d) 5–8

Figure 5.11 Comparison of the predicted and simulated in overtopping cases. 5–9
Figure 5.12 Cross sections at the middle of the abutment for compound channels 5–10
Figure 5.13 Bed friction coefficient ($\times 10^2$), T1WW. 5–11
Figure 5.14 Bed friction coefficient ($\times 10^2$), Case 09. 5–12
Figure 5.15 Bed friction coefficient ($\times 10^2$), T1ST. 5–12
Figure 5.16 Bed friction coefficient ($\times 10^2$), Case 01. 5–13
Figure 5.17 Comparison of the predicted and simulated $C_{f\_\max}$ in overtopping cases 5–14
Figure 5.18 Cross sections for nonsymmetric compound channels. 5–15
Figure 5.19 Bed friction coefficient ($\times 10^2$), T2WW. 5–16
Figure 5.20 Bed friction coefficient ($\times 10^2$), T2ST. 5–16
Figure 5.21 Comparison of the predicted and simulated $C_{f\_\max}$ in overtopping cases. 5–18
Figure 5.22 Numerical cases for channel bend study in open channel flow. 5–19
Figure 5.23 Cross section of the wingwall abutment cases in channel bend study. 5–19
Figure 5.24 Simulation results of case T3WW_Mid 1:1 5–22
Figure 5.25 Simulation results of case T3WW_Mid 2:1 5–23
Figure 5.26 Simulation results of case T3WW_End 1:1. 5–24
Figure 5.27 Simulation results of T3WW_End 2:1 5–25
Figure 5.28 Simulation results of T3ST_Mid 1:1. 5–26
Figure 5.29 Simulation results of T3ST_Mid 2:1. 5–27
Figure 5.30 Simulation results of T3ST_End 1:1 5–28
Figure 5.31 Simulation results of T3ST_End 2:1 5–29
Figure 5.32 Numerical cases for channel bend study in overtopping flow. 5–30
Figure 5.33 Cross section of the wingwall abutment cases in channel bend study. 5–30

Figure 5.34 Simulation results of T4WW_Mid 1:1. 5–34
Figure 5.35 Simulation results of T4WW_Mid 2:1 5–35
Figure 5.36 Simulation results of T4WW_End 1:1.....5–36
Figure 5.37 Simulation results of T4WW_End 2:1.....5–37
Figure 5.38 Normalized bed shear stress contours of the spillthrough abutment cases 5–38
Figure 5.39 Velocity magnitude contours on the water surface.....5–39
Figure 5.40 Normalized bed shear stress contours.....5–40
Figure 6.1 Correlation between shear stresses and erosion rates (Oh, 2009).....6–2
Figure 6.2 Comparison of erosion functions for porcelain clay.....6–3
Figure 6.3 Geometries of the flume test cases for CHEN3D scour prediction. 6–5
Figure 6.4 Scour patterns for flume test cases on compound channel (After Oh, 2009). 6–7
Figure 6.5 Comparison of measured and predicted scour depths after 10 days (Case 9). 6–8
Figure 6.6 Scour profiles for Case 9 after 10 days at different cross sections. 6–10
Figure 6.7 Time histories of maximum scour depths for Case 9. 6–11
Figure 6.8 Scour profiles for Case 1 after 10 days at different cross sections. 6–13
Figure 6.9 Comparison of measured and predicted scour depths for Case 1 after 10 days. 6–14
Figure 6.10 Time histories of maximum scour depths for Case 1. 6–14
Figure 6.11 Scour profiles for Case 4 after 9 days at different cross sections. 6–16
Figure 6.12 Comparison of measured and predicted scour depths for Case 4 after 9 days. 6–17
Figure 6.13 Time histories of maximum scour depths for Case 4. 6–18
Figure 6.14 Scour patterns for the flume test cases on rectangular channel (After Oh, 2009). 6–18

Figure 6.15 Scour profiles for Case 14 after 10 days at different cross sections. 6–20

Figure 6.16 Comparison of measured and predicted scour depths for Case 14 after 10 days. 6–21

Figure 6.17 Time histories of maximum scour depths for Case 14. 6–22

Figure 6.18 Scour profiles for Case 13 after 10 days at different cross sections. 6–23

Figure 6.19 Comparison of measured and predicted scour depths patterns for Case 13.....6–24

Figure 6.20 Time histories of maximum scour depths for Case 13. 6–24

Figure 6.21 Cross sections and the velocity magnitude contours. 6–26

Figure 6.22 Scour depth contours for overtopping cases. 6–27

Figure 6.23 Time histories of the maximum scour depths for overtopping flow.....6–28

Figure 6.24 Shear stress correction factor for overtopping flow.....6–30

Figure 7.1 Definitions of local bridge scour.....7–1

Figure 7.2 Correction factor of abutment alignment (K_2) (Melville, 1992). 7–5

Figure 7.3 Neill's (1973) critical velocity curve in terms of median diameter of cohesionless soil and water depth. 7–10

Figure 7.4 Abutment shape factor measurement (Maryland SHA bridge scour program (ABSCOUR), 2007). 7–11

Figure 7.5 Boundary of scour condition A and B with the ratio of abutment length to the width of floodplain (Ettema et. al, 2008). 7–12

Figure 7.6 Scour amplification factor versus unit discharge ratio (replotted using data from Ettema et al., 2008).....7–13

Figure 7.7 Sketch of the flume and experimental setup (not to scale). 7–19

Figure 7.8 Channel configurations. 7–20

Figure 7.9 Abutment shapes (all dimensions are in mm). 7–21

Figure 7.10 Grain size distribution of the Porcelain clay. 7–21

Figure 7.11 Results of 11 EFA tests. 7–23

Figure 7.12 Clay installation. 7–23
Figure 7.13 Test section after clay installation....7–24
Figure 7.14 View of ADVs. 7–24
Figure 7.15 Velocity measurement points....7–25
Figure 7.16 Water depth measurement positions. 7–25
Figure 7.17 Diagram of bed profiler (unit: mm). 7–26
Figure 7.18 Points of scour measurement using the bed profiler. 7–26
Figure 7.19 View of carriage and measurement scene. 7–27
Figure 7.20 Definition of variables and coordinate system....7–30
Figure 7.21 Water surface profile in compound channel. 7–31
Figure 7.22 Change of water surface profile with scour development. 7–34
Figure 7.23 Streamwise velocity distribution at approach section....7–36
Figure 7.24 Streamwise velocity distribution in the contracted section along the abutment centerline. 7–37
Figure 7.25 Pattern of velocity distribution (Case 1II). 7–40
Figure 7.26 Pattern of turbulence intensity distribution (Case 1II). 7–41
Figure 7.27 View of flume after setup (Case 7). 7–43
Figure 7.28 Channel geometry for HEC-RAS calculation (Case 7). 7–43
Figure 7.29 HEC-RAS water level comparison to measurement with different Manning's n values (Case 7)....7–44
Figure 7.30 Measured and HEC-RAS calculated water surface profiles. "ST" indicates spillthrough abutment. 7–45
Figure 7.31 Comparison of velocity distribution at approach section between measurement and HEC-RAS calculation. 7–47
Figure 7.32 Comparison of velocity distribution at bridge section between measurement and HECRAS calculation. 7–48

Figure 7.33 Comparison of average streamwise velocity at approach section (at y = -9.1m) on the floodplain and in the main channel between measurement and HEC-RAS calculation (V_{f1} is the velocity on the floodplain and V_{m1} is the velocity in the main channel). 7–50

Figure 7.34 Evolution of channel bottom topography (Case 1II). 7–51

Figure 7.35 Evolution of channel bottom topography (Case 6).....7–52

Figure 7.36 Evolution of channel bottom topography (Case 7).....7–52

Figure 7.37 View of test section (Case 1II, $L'/L_f = 0.75$). 7–53

Figure 7.38 View of test section (Case 6, $L'/L_f = 0.5$). 7–54

Figure 7.39 View of test section (Case 7, $L'/L_f = 1.0$). 7–55

Figure 7.40 Comparisons of scour pattern and velocity pattern (Case 1II). 7–56

Figure 7.41 Turbulence intensity (upper panels) and channel bottom bathymetry (lower panels) for different abutment shape. 7–58

Figure 7.42 Turbulence intensity (upper panels) and channel bottom bathymetry (lower panels) for different abutment alignment for spillthrough abutment (2(H):1(V)).....7–59

Figure 7.43 Evolution of crosssectional abutment scour hole profile in the rectangular channel (L'/L =0.45). 7–60

Figure 7.44 Evolution of crosssectional abutment scour hole profile in the compound channel (L'/L_f = 0.5).....7–61

Figure 7.45 Evolution of crosssectional abutment scour hole profile in the compound channel (L'/L_f = 0.75).....7–61

Figure 7.46 Development of abutment scour depth. 7–62

Figure 7.47 Data fitting of hyperbolic model (Case 17). 7–64

Figure 7.48 Comparison between measurement and hyperbolic model (Case 17). 7–64

Figure 7.49 Geometry of symmetrical channel in Li (2002).....7–65

Figure 7.50 Contraction Scour in Rectangular Channel: Measurement versus Prediction. 7–68

Figure 7.51 Contraction scour in rectangular channel and compound channel: measurement versus prediction. 7–69

Figure 7.52 Channel configurations (all dimensions are in meters)....7–71

Figure 7.53 Abutment shapes. 7–71

Figure 7.54 Abutment alignment....7–71

Figure 7.55 Definition of degree of setback. 7–73

Figure 7.56 Normalized abutment scour depth versus Froude number. 7–75

Figure 7.57 Normalized maximum abutment scour depth with different abutment shape. 7–76

Figure 7.58 Variation of turbulence intensity with different attack angles at the initial test condition. 7–77

Figure 7.59 Pattern of (a) turbulence, and (b) a downstream view of scour hole after 257 hours of experiment for $L'/L_f = 1.0$....7–78

Figure 7.60 Normalized maximum abutment scour depth versus prediction with abutment shape being accounted for. 7–79

Figure 7.61 The effect of channel geometry 7–80

Figure 7.62 Normalized maximum abutment scour depth: Test results versus prediction by preliminary equation. 7–81

Figure 7.63 Comparison between prediction by equation (7.50) and Froehlich's database (1989). 7–82

Figure 7.64 Comparison between prediction by equation (7.50) and Sturm's database (2004). 7–83

Figure 7.65 Comparison between prediction by equation (7.50) and Benedict's database (2006). 7–83

Figure 7.66 The effect of Reynolds number in maximum abutment scour. 7–84

Figure 7.67 Correction factor for pressure flow versus ratio of water depth (d_1/d_{deck}). 7–85

Figure 7.68 Normalized Maximum Abutment Scour Depth: Test Results versus Prediction. 7–87

Figure 7.69 Definitions for open channel flow near a bridge abutment....7–88

Figure 7.70 Definitions for pressure flow near a bridge abutment. 7–88

Figure 7.71 Proposed erosion categories for soils and rocks based on velocity. 7–89

Figure 7.72 Proposed erosion categories for soils and rocks based on shear stress.....7–90

Figure 7.73 Correction factor for pressure flow for abutment scour depth calculation. ...7–94

Figure 7.74 Correction factor of overtopping flow for shear stress calculation.....7–96

Figure 7.75 Definition for the open channel flow at bridge section.....7-98

Figure 7.76 Proposed erosion categories for soils and rocks based on velocity. 7-99

Figure 7.77 Proposed erosion categories for soils and rocks based on shear stress.....7-99

Figure 8.1 NCHRP 2415(2) predictions versus Gill (1981) database.....8–2

Figure 8.2 HEC18 method versus Gill (1981) database (cited from Briaud et al. (2004))....8–2

Figure 8.3 Comparison with Sturm's (2004) data.....8–3

Figure 8.4 Comparison with Froehlich's (1989) data. 8–4

Figure 8.5 Comparison between prediction by present study and measurement results in NCHRP 2420 (2008).....8–5

Figure 8.6 Comparison with NCHRP 2420 (2008).....8–6

Figure 8.7 Comparison with Benedict and et al.'s (2006) data.....8–7

Figure 8.8 Schematic diagram of imaginary full scale channel. 8–8

Figure 8.9 Comparisons with other prediction equations for full scale bridge. 8–10

LIST OF TABLES

Page

Table 2.1 Factors influencing the erodibility of cohesive soils. 2-2

Table 2.2 Database of EFA tests. 2-4

Table 4.1 Manning's n coefficients for open channel flow. 4-1

Table 4.2 Numerical simulation results for Reynolds number study. 4-31

Table 4.3 Numerical simulation results for water depth study. 4-34

Table 4.4 Numerical simulation results for channel contraction study 4-38

Table 4.5 Physical parameters and the correction factors in aspect ratio study 4-42

Table 4.6 Shape correction factors of wing-wall abutment. 4-45

Table 4.7 Shape correction factors of spill-through abutment (w/o correction). 4-49

Table 4.8 Shape correction factors of spill-through abutment (with correction). 4-49

Table 4.9 Proposed Shape correction factors. 4-52

Table 4.10 Numerical simulation results for skew angle study. 4-52

Table 4.11 Correction factors of compound channel effect. 4-58

Table 4.12 Cases used to derive the maximum bed shear stress equation around abutment 4-67

Table 4.13 Numerical simulations initially proposed in this study 4-68

Table 4.14 Prediction of the numerical cases. 4-69

Table 4.15 Flume test cases. 4-71

Table 4.16 Maximum bed shear stresses based on EFA results. 4-71

Table 5.1 Simulation results of overtopping in rectangular channel cases. 5-5

Table 5.2 Prediction of C_{f_max} in rectangluar channel cases with overtoppping. 5-9

Table 5.3 Simulation results of overtopping in symmetric compound channel cases. 5-13

Table 5.4 Prediction of C_{f_max} in compound channel cases with overtoppping. 5-13

Table 5.5 Simulation results of overtopping in non-symmetric compound channel cases. 5-17

Table 5.6 Prediction of C_{f_max} in non-symmetric compound channel cases (overtoppping)..... 5-17

Table 5.7 Influence of abutment shape on channel bend. 5-22

Table 5.8 Results under overtopping and open channel conditions..... 5-31

Table 5.9 Results of wing-wall abutment and spill-through abutment. 5-33

Table 6.1 Soil properties of the clay used in NCHRP 24-15(2) (After Oh, 2009). 6-1

Table 6.2 Dimensional parameters for the cases selected for scour prediction. 6-5

Table 6.3 Simulation results for overtopping cases. 6-30

Table 7.1 Factor of abutment shape (K_1) (Melville, 1992). 7-5

Table 7.2 Equations for uniform contraction scour under live-bed condition. 7-16

Table 7.3 Equations for uniform contraction scour under clear-water condition. 7-16

Table 7.4 Geotechnical properties of the Porcelain clay. 7-21

Table 7.5 Geotechnical properties of the porcelain clay used in Li (2003). 7-22

Table 7.6 Geotechnical properties of the porcelain clay used in Gudavalli (1997). 7-22

Table 7.7 Test matrix in dimensionless form..... 7-28

Table 7.8 Test conditions in dimensional form..... 7-29

Table 7.9 Summary of hyperbolic model and maximum scour depth. 7-64

Table 7.10 Variables and results of contraction scour in Li (2002)..... 7-65

Table 7.11 Variables and results of contraction scour in the present study. 7-66

Table 7.12 Variables and test results. 7-72

Table 7.13 Range of Reynolds numbers (Re_{f2}) in each study..... 7-84

Table 8.1 Summary of the imaginary test conditions for comparisons with different prediction equations. 8–9

EXCUTIVE SUMMARY

The following definitions are used in this presentation for open channel flow near a bridge (Fig. 1) and for pressure flow near a bridge abutment (Fig. 2).

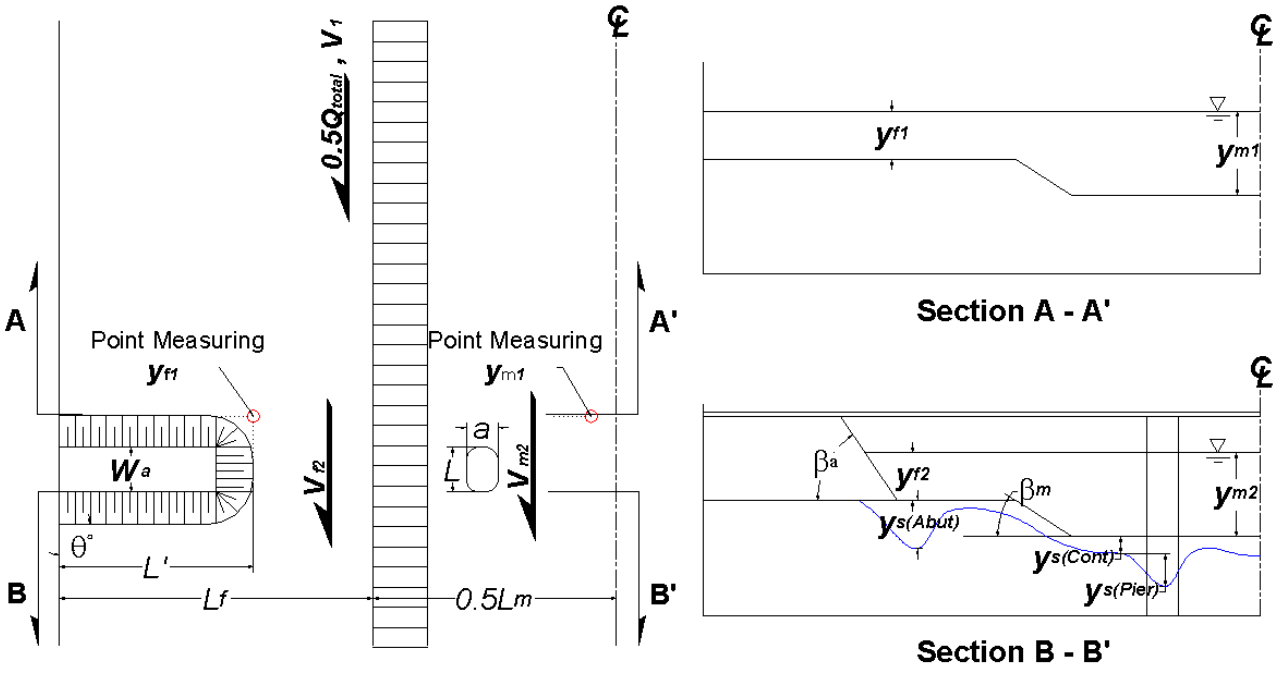

Fig. 1 – Definitions for open channel flow near a bridge abutment

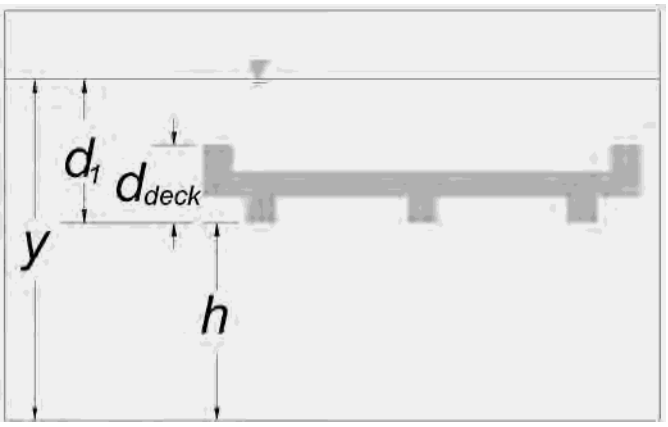

Fig. 2 – Definitions for pressure flow near a bridge abutment

The new approach is established for calculating the depth of the scour hole near an abutment and in the main channel constructed on a soil characterized by EFA curves or equivalent and subjected to a velocity hydrograph. This depth is called the final depth of scour (at the end of the hydrograph) not to be confused with the maximum depth of scour which is the depth reached for a chosen velocity sustained for an infinite time. This approach will be automated by a computer program (SRICOS-EFA). Note that the equations proposed are not limited to cohesive soils since they include a soil parameter able to represent any soil.

The proposed method makes use of samples collected at the site to obtain, as a minimum, the classification characteristics of the soil. One can either use the EFA to obtain the erodibility curves (preferred approach for final design) or the proposed charts (one for velocity and one for shear stress) below to obtain an estimate of the erodibility curve (acceptable for preliminary design). Note that with these recommended charts, the engineer can obtain the critical velocity of the soil by simply classifying the soil and reading the chart at an erosion rate of 0.1 mm/hr set as the threshold for erosion. Note also that some caution needs to be exercised as the velocity also depends on the water depth.

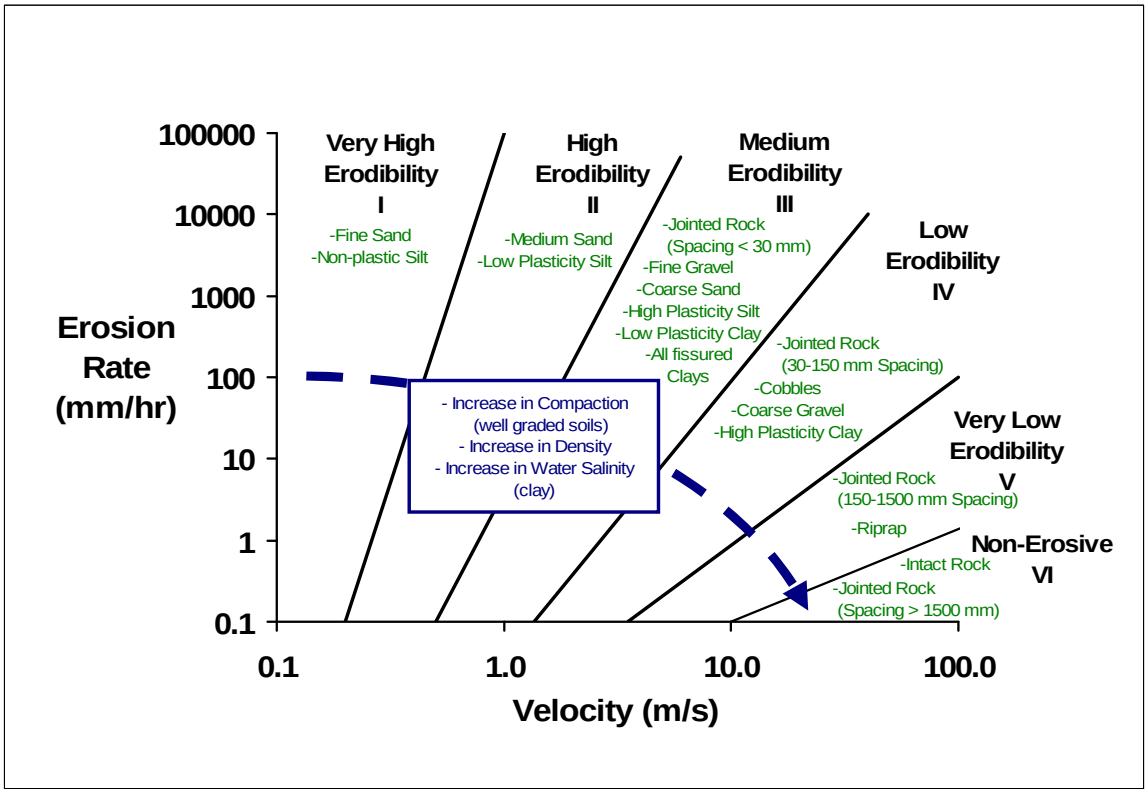

Fig. 3 – Proposed erosion categories for soils and rocks based on velocity

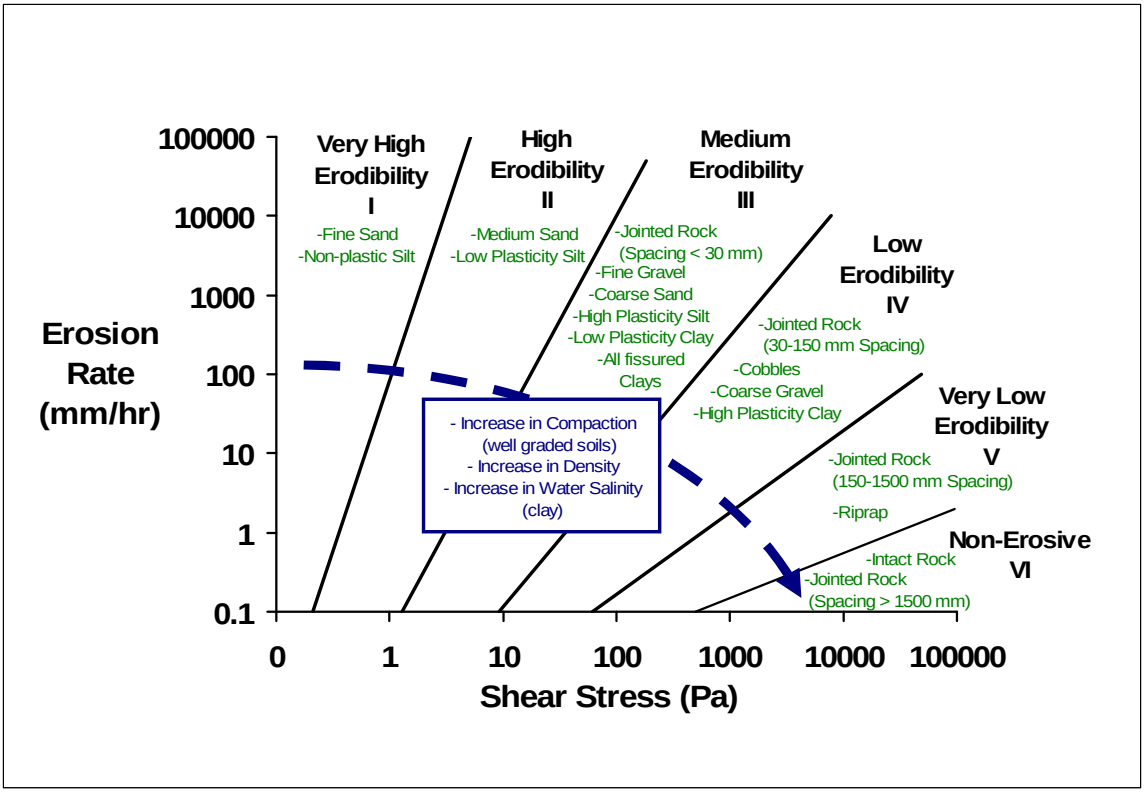

Fig. 4 – Proposed erosion categories for soils and rocks based on shear stress

Once the soil erodibility is classified, HEC-RAS is used to obtain hydraulic information including the unit discharge, the velocity, and the water depth near the abutment. Knowing the soil erosion function and the velocity, one can proceed with equations generated from the flume tests and the numerical simulations that we conducted. The equations give two parameters: the maximum depth of abutment scour (abutment scour depth plus contraction scour depth) and contraction scour depth at the center of channel, and the initial maximum shear stress around abutment and the center of channel on the river bottom before the scour starts. If only the maximum depth of scour is needed, one just uses the maximum depth of scour equation (Method A). To take advantage of the slow erosion process of an erosion resistant soil, one can use the time rate of erosion method proposed (HEC-18 Clay or Method B). This method consists of calculating the scour depth accumulated each day during the design life or remaining life of the bridge. This requires a hydrograph or the knowledge of Q100 and Q500, whichever is available at the site. A short cut to that method is to use a time compression concept to regroup the effect of the whole hydrograph into one time step called the final equivalent time (Method C). The final equivalent time is the time necessary for the highest velocity in the hydrograph to create the same scour depth as the entire hydrograph. In this case, the time rate calculations are significantly reduced and can be done on the back of an envelope.

The steps for Methods A, B, and C are shown below. The SRICOS-EFA computer program which is available free of charge on the web automates the steps of Method B. It will be updated to include abutment scour.

ABUTMENT SCOUR CALCULATION

Method A

1. ***Collect samples at the site.***
2. ***Test the samples in the EFA to get the erodibility curves or use the proposed soil erosion charts.***
3. ***Describe the geometry of the abutment (length, width, shape and skew angle).***
4. ***Describe the geometry of the river (main channel width, flood plain width left, flood plain width right, main channel to flood plain transition slope, flood plain bank slope, Manning coefficient and longitudinal slope of the river.***
5. ***Run HEC-RAS to obtain the water depth immediately upstream of the toe of the abutment and the velocity at bridge section corresponding to the design flood.***
6. ***Use the maximum abutment scour equation (Eq. 1) to calculate the maximum scour depth*** $y_{s(Abut)}$ ***.***

Method B

1. ***Collect samples at the site.***
2. ***Test the samples in the EFA to get the erodibility curves or use the proposed soil erosion charts.***
3. ***Describe the geometry of the abutment (length, width, shape and skew angle) .***
4. ***Describe the geometry of the river (main channel width, flood plain width left, flood plain width right, main channel to flood plain transition slope, flood plain bank slope, Manning coefficient and longitudinal slope of the river)***
5. ***Input the flow hydrograph.***
6. ***Run HEC-RAS to obtain the relationship between the flow and velocity at bridge section, and the flow and water depth immediately upstream of the toe of the abutment.***
7. ***Transform the flow hydrograph into a bridge section velocity hydrograph and a water depth hydrograph for immediately upstream of the toe of the abutment.***
8. ***Calculate the maximum scour depth*** $y_{s(Abut)}$ ***for the*** i^{th} ***velocity on the hydrograph (Eq. 1).***
9. ***Calculate the initial maximum shear stress*** $\tau_{\max}$ ***around the abutment for the*** i^{th} ***velocity (before the scour hole development) (Eq. 2) .***
10. ***Read the initial scour rate corresponding to the initial maximum shear stress*** $\tau_{\max}$ ***on the appropriate EFA curve.***
11. ***Use the results of steps 8 and 10 to construct the scour depth versus time curve for the*** i^{th} ***velocity.***
12. ***Calculate the equivalent time for the*** i^{th} ***velocity and the curve of step 11. The equivalent time for the*** i^{th} ***velocity is the time necessary for the highest velocity in the hydrograph up to the*** i^{th} ***time step to create the same scour depth as the hydrograph from start to the*** i^{th} ***time step.***
13. ***Read the additional scour depth contributed by the*** i^{th} ***velocity during the*** i^{th} ***time step.***
14. ***Repeat steps 8 to 13 for the entire hydrograph.***
15. ***Output the scour depth versus time and read the final scour depth at the end of the***

hydrograph period.

Method C

1. ***Collect samples at the site.***
2. ***Test the samples in the EFA to get the erodibility curves or use the proposed soil erosion charts.***
3. ***Describe the geometry of the abutment (length, width, shape and skew angle).***
4. ***Describe the geometry of the river (main channel width, flood plain width left, flood plain width right, main channel to flood plain transition slope, flood plain bank slope, Manning coefficient and longitudinal slope of the river.***
5. ***Obtain the flow hydrograph.***
6. ***Run HEC-RAS to determine the relationship between the flow and velocity at bridge section, and the flow and water depth immediately upstream of the toe of the abutment.***
7. ***Transform the flow hydrograph into a bridge section velocity hydrograph and a water depth hydrograph for immediately upstream of the toe of the abutment.***
8. ***Obtain the maximum velocity and corresponding water depth in the hydrograph.***
9. ***Calculate the initial maximum shear stress $\tau_{\max}$ around the abutment (before the scour hole develops) (Eq. 2) for the maximum velocity in the hydrograph***
10. ***Read the initial scour rate corresponding to the initial maximum shear stress $\tau_{\max}$ on the EFA curve for the soil.***
11. ***Calculate the maximum scour depth $y_{s(Abut)}$ around the abutment (Eq. 1) for the maximum velocity in the hydrograph***
12. ***Use the results of steps 10 and 11 to construct the scour depth versus time curve for the maximum velocity in the hydrograph (Eq. 3)***
13. ***Calculate the final equivalent time for the entire hydrograph. The final equivalent time for the entire hydrograph is the time necessary for the highest velocity in the hydrograph to create the same scour depth as the entire hydrograph.***
14. ***Read the final scour depth corresponding to the final equivalent time on the scour depth versus time curve of step12***

Abutment maximum scour depth equation

The equation is presented below

$$\frac{y_{s(Abut)}}{y_{f1}} = K_1 \cdot K_2 \cdot K_L \cdot K_G \cdot K_p \cdot 243 \cdot \mathrm{Re}_{f2}^{-0.28} \cdot \left(1.65 \cdot Fr_{f2} - Fr_{fc}\right) \qquad (1)$$

where $y_{s(Abut)}$ = the maximum abutment scour depth adjacent to the toe of the abutment

y_{f1} = water depth at the toe of the abutment estimated as the water depth immediately upstream of the toe of the abutment (the reason the water depth immediately upstream of the toe of the abutment in the uncontracted section is the best estimate of the water depth at the toe of the abutment for scour depth calculations is as follows: at the beginning of the scour hole development the water depth at the toe of the abutment is quite different from the water depth at the end of the scour hole development process. In the long term

the water depth at the toe of the abutment is equal to the water depth immediately upstream of the toe of the abutment in the uncontracted section plus the abutment scour depth). In the case of pressure flow, $y_{f1} = h$ which is the distance between the low chord of the bridge deck and the bottom of the channel before scour develops (clearance under the bridge).

K_1 = correction factor for the abutment shape

$$K_1 = \begin{cases} 1.22 & \text{for Vertical-wall abutment} \\ 1.0 & \text{for Wing-wall abutment} \\ 0.73 & \text{for Spill-through abutment with 2:1 Slope} \\ 0.59 & \text{for Spill-through abutment with 3:1 Slope} \end{cases}$$

K_2 = correction factor for the abutment skew

$$K_2 = \begin{cases} 1.0 - 0.005\left|\theta - 90°\right| & \textit{for } 60° \le \theta \le 120° \\ 0.85 & \textit{otherwise} \end{cases}$$

K_G = correction factor for the channel geometry

$$K_G = \begin{cases} 1.0 & \text{for compound channel} \\ 0.42 & \text{for rectangular channel} \end{cases}$$

K_L = correction factor for the abutment location

$$K_L = \begin{cases} -0.23\dfrac{L_f - L'}{y_{f1}} + 1.35 & \text{for } \dfrac{L_f - L'}{y_{f1}} < 1.5 \\ 1.0 & \text{otherwise} \end{cases}$$

K_p = correction factor for pressure flow

$$K_p = \begin{cases} 0.92 \cdot \left(d_1 / d_{deck}\right) + 1.0 & \text{for } d_1 / d_{deck} < 1.0 \\ 0.21\left(d_1 / d_{deck}\right)^2 - 1.27\left(d_1 / d_{deck}\right) + 2.97 & \text{for } 1.0 \le d_1 / d_{deck} \le 3.0 \\ 1.0 & \text{for } 3.0 < d_1 / d_{deck} \end{cases}$$

d_1 = distance from water surface to the low chord of the bridge at upstream face of the bridge

h = distance from the low chord of the bridge to the river bottom before scour starts

$Fr_{2(Abut)}$ = Froude number around the toe of abutment, defined as

$$Fr_{2(Abut)} = \frac{V_{f2}}{\sqrt{g \cdot y_{f1}}}$$

Fr_{fc} = critical Froude number around the toe of abutment, defined as

$$Fr_{fc} = \frac{V_c}{\sqrt{g \cdot y_{f1}}}$$

Re_{f2} = Reynolds number around the toe of abutment, defined as

$$\mathrm{Re}_{f2} = \frac{V_{f2} \cdot y_{f1}}{\nu}$$

V_{f2} = velocity around the toe of the abutment, defined as

$$V_{f2} = \begin{cases} \frac{Q_{total}}{A_2} & \text{for short setback } \left((L_f - L') \le 5y_{m1}\right) \\ \frac{Q_{fp1}}{A_{f2}} & \text{for long setback } \left(L' \le 0.25L_f\right) \\ \text{otherwise use a linearly interpolated velocity between} & \\ \frac{Q_{total}}{A_2} & \text{for } (L_f - L') = 5y_{m2} \text{ and } \frac{Q_{fp1}}{A_{f2}} \text{ for } L' = 0.25L_f \end{cases}$$

Q_{total} = the total discharge,

Q_{fp1} = the discharge on the floodplain in the approach section immediately upstream of the abutment

A_1 = total flow area in the approach section immediately upstream of the abutment,

A_2 = total flow area in the contracted section

A_{f1} = flow area on the floodplain in the approach section immediately upstream of the abutment

A_{f2} = flow area on the floodplain in the contracted section

$L_f - L'$ = width of floodplain at contracted section (abutment setback from main channel)

V_{fc} = critical velocity for the material around the toe of the abutment, defined as

$$V_{fc} = \frac{\left(y_{f1}\right)^{1/6}}{n} \cdot \sqrt{\frac{\tau_c}{\rho \cdot g}}$$

Abutment maximum shear stress equation

The equation is presented below

$$\frac{\tau_{\max}}{\rho V_1^2} = k_{Cr} k_{sh} k_{Fr} k_s k_{sk} k_L k_o \cdot 12.45 \,\mathrm{Re}^{-0.45} \qquad (2)$$

where $\tau_{\max}$ = the maximum bed shear stress at the interface between the water and the river bottom near the abutment toe.

k_{Cr} = correction factor for channel conveyance ratio

k_{sh} = correction factor for the aspect ratio of the approach embankment

k_{Fr} = correction factor for Froude number

k_s = correction factor for abutment shape

k_{sk} = correction factor for skew angle

k_o = correction factor for overtopping

ρ = mass density of water

V_1 = upstream mean depth velocity in line with abutment edge

R_e = Reynolds number, defined as $R_e = VW_a / \nu$

ν = kinematic viscosity

W_a = top width of the abutment

F_r = Froude number, defined as $F_r = V / \sqrt{gy}$

g = acceleration due to gravity

y = upstream water depth in line with abutment edge

L' = projected abutment length normal to the flow direction

q_1 = unit discharge at approach section

q_2 = unit discharge around abutment

L_f = width of the flood plain

d_1 = distance from the water surface to the low chord of the bridge at upstream face of the bridge

h = distance from the low chord of the bridge to the river bottom before scour starts

$$k_{Cr} = 3.65\frac{q_2}{q_1} - 2.91$$

$$k_{sh} = 0.85 \times \left(\frac{L'}{W_a}\right)^{-0.24}$$

$$k_{Fr} = \begin{cases} 2.07Fr + 0.8, & \text{Fr} > 0.1 \\ 1.0, & \text{Fr} \le 0.1 \end{cases}$$

$$k_s = \begin{cases} 1, & \text{vertical-wall abutment} \\ 0.65, & \text{wing-wall abutment} \\ 0.58, & \text{spill-through abutment} \end{cases}$$

$$k_{sk} = 1.0$$

$$k_L = \begin{cases} 1.0 & \text{for } \left(L_f - L'\right) / y_f \le -2 \\ 0.6(L_f - L') / y_f + 1.2 & \text{for } -2 < (L_f - L') / y_f \le 0 \\ -1.2(L_f - L') / y_f + 1.2 & \text{for } 0 < (L_f - L') / y_f \le 1 \\ 1.0 & \text{for } 1 \le (L_f - L') / y_f \end{cases}$$

$$k_o = \begin{cases} 0.92 \cdot \left(d_1 / d_{deck}\right) + 1.0 & \text{for } d_1 / d_{deck} < 1.0 \\ 0.21\left(d_1 / d_{deck}\right)^2 - 1.27\left(d_1 / d_{deck}\right) + 2.97 & \text{for } 1.0 \le d_1 / d_{deck} \le 3.0 \\ 1.0 & \text{for } 3.0 < d_1 / d_{deck} \end{cases}$$

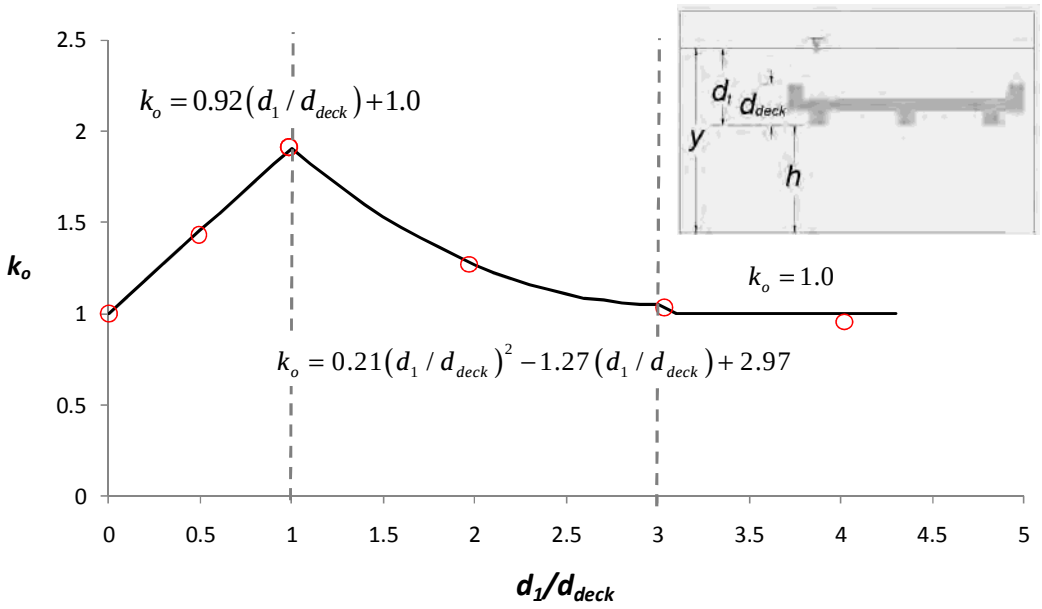

Fig. 5 – Correction factor of overtopping flow

Scour depth versus time curve equation

This equation describes the scour depth versus time curve:

$$y_{s(Abut)}(t) = \frac{t}{\frac{1}{\dot{z}_i} + \frac{t}{y_{s\,(Abut)}}} \tag{3}$$

where $y_{s(Abut)}(t)$ = abutment scour depth (abutment scour depth plus contraction scour depth) at time t

t = elapsed time after start of scour

$\dot{z}_i$ = initial rate of scour

$y_{s\,(Abut)}$ = maximum depth of scour near toe of abutment

CONTRACTION SCOUR CALCULATION

Method A

1. ***Collect samples at the site***
2. ***Test the samples in the EFA to get the erodibility curves or use the proposed soil erosion charts.***
3. ***Describe the geometry of the abutment (length, width, shape, skew angle).***
4. ***Describe the geometry of the river (main channel width, flood plain width left, flood plain width right, main channel to flood plain transition slope, flood plain bank slope, Manning coefficient, and longitudinal slope of the rive***
5. ***Run HEC-RAS to obtain the velocity and water depth corresponding to the design flood.***
6. ***Use the maximum abutment scour equation (Equation (4)) to calculate the maximum scour depth*** $y_{s(Cont)}$.

Method B

1. ***Collect samples at the site***
2. ***Test the samples in the EFA to get the erodibility curves or use the proposed soil erosion charts.***
3. ***Describe the geometry of the abutment (length, width, shape, skew angle).***
4. ***Describe the geometry of the river (main channel width, flood plain width left, flood plain width right, main channel to flood plain transition slope, flood plain bank slope, Manning coefficient, and longitudinal slope of the river)***
5. ***Input the flow hydrograph.***
6. ***Run HEC-RAS to obtain the relationship between the flow and velocity, and the flow and water depth***
7. ***Transform the flow hydrograph into a velocity hydrograph and a water depth hydrograph***
8. ***Calculate the maximum scour depth*** $y_{s(Cont)}$ ***for the*** i^{th} ***velocity on the hydrograph (Equation (4))***
9. ***Calculate the initial maximum shear stress*** $\tau_{\max(Cont)}$ ***at the center line of channel for the*** i^{th} ***velocity (before the scour hole develops) (Equation (5))***
10. ***Read the initial scour rate corresponding to the initial maximum shear stress*** $\tau_{\max(Cont)}$ ***on the appropriate EFA curve***
11. ***Use the results of steps 8 and 10 to construct the scour depth versus time curve for the*** i^{th} ***velocity***

12. ***Calculate the equivalent time for the i^{th} velocity and the curve of step 11. The equivalent time for the i^{th} velocity is the time necessary for the highest velocity in the hydrograph up to the i^{th} time step to create the same scour depth as the hydrograph from start to the i^{th} time step.***
13. ***Read the additional scour depth contributed by the i^{th} velocity during the i^{th} time step***
14. ***Repeat steps 8 to 13 for the entire hydrograph***
15. ***Output the scour depth versus time and read the final scour depth at the end of the hydrograph period.***

Method C

1. ***Collect samples at the site***
2. ***Test the samples in the EFA to get the erodibility curves or use the proposed soil erosion charts.***
3. ***Describe the geometry of the abutment (length, width, shape, skew angle)***
4. ***Describe the geometry of the river (main channel width, flood plain width left, flood plain width right, main channel to flood plain transition slope, flood plain bank slope, Manning coefficient, and longitudinal slope of the river.***
5. ***Obtain the flow hydrograph.***
6. ***Run HEC-RAS to determine the relationship between the flow and velocity, and the flow and water depth***
7. ***Transform the flow hydrograph into a velocity hydrograph and a water depth hydrograph***
8. ***Obtain the maximum velocity and corresponding water depth in the hydrograph***
9. ***Calculate the initial maximum shear stress $\tau_{\max(Cont)}$ at the center line of channel (before the scour hole develops) (Equation (5)) for the maximum velocity in the hydrograph***
10. ***Read the initial scour rate corresponding to the initial maximum shear stress $\tau_{\max(Cont)}$ on the EFA curve for the soil.***
11. ***Calculate the maximum contraction scour depth $y_{s(Cont)}$ in the main channel (Equation (4)) for the maximum velocity in the hydrograph.***
12. ***Use the results of steps 10 and 11 to construct the scour depth versus time curve for the maximum velocity in the hydrograph (Equation (7))***
13. ***Calculate the final equivalent time for the entire hydrograph. The final equivalent time for the entire hydrograph is the time necessary for the highest velocity in the hydrograph to create the same scour depth as the entire hydrograph (Equation (6).***
14. ***Read the final scour depth corresponding to the final equivalent time on the scour depth versus time curve of step12***

Contraction maximum scour depth equation

$$\frac{y_{s(Cont)}}{y_{m1}} = 2.21\left(1.31Fr_{m2} - Fr_{mc}\right) \tag{4}$$

where $y_{s(Cont)}$ is the maximum contraction scour depth, y_{m1} is the main channel depth at the approach section, $Fr_{m2}\left(=\frac{V_2}{\sqrt{gy_{m1}}}\right)$ is the Froude number of the main-channel at the bridge section, $Fr_{mc}\left(=\frac{V_{mc}}{\sqrt{gy_{m1}}}=\frac{\sqrt{\tau_c/\rho}}{gny_{m1}^{1/3}}\right)$ is the critical Froude number of the main-channel, V_2 is the average velocity at the contracted section obtained by HEC-RAS, V_{mc} is the critical velocity in the main channel, τ_c is the critical shear stress, n is Manning's roughness coefficient, and ρ is the water density.

Contraction maximum shear stress equation

$$\tau_{\max(Cont)} = k_R k_\theta k_L \gamma n^2 V_1^2 R_h^{-\frac{1}{3}} \tag{5}$$

where $\tau_{\max(Cont)}$ =contraction maximum shear stress at the center line of channel

γ = unit weight of water

n = Manning's coefficient

R_h = hydraulic radius of approach section

V_1 = average approach velocity

A_1 = the approach channel area

A_2 = the channel area at the bridge section

W_a = top width of bridge abutment

α = the contraction transition angle

$$k_R = 0.62 + 0.38\left(\frac{A_1}{A_2}\right)^{1.75}$$

$$k_\theta = 1 + 0.9\left(\frac{\alpha}{90}\right)^{1.5}$$

$$k_L = \begin{cases} 1 & , for \quad k_L \geq 0.35 \\ 0.77 + 1.36\left(\frac{W_a}{L'_{(Left)} + L'_{(Right)}}\right) - 1.98\left(\frac{W_a}{L'_{(Left)} + L'_{(Right)}}\right)^2 & , for \quad k_L < 0.35 \end{cases}$$

Final equivalent time equation

The final equivalent time t_e refers to the entire hydrograph; it is the time necessary for the highest velocity in the hydrograph to create the same scour depth as the entire hydrograph.

Contraction Scour

$$t_e(\text{hrs}) = 644.32 \cdot \left(t_{hydr}(\text{years})\right)^{0.4242} \cdot \left(V_{\max}\left(\text{m}/\text{s}\right)\right)^{1.648} \cdot \left(\dot{z}_{i,mean}\left(\text{mm}/\text{hr}\right)\right)^{-0.605} \quad (6)$$

where $t_e(\text{hrs})$ = equivalent time necessary for the highest velocity in the hydrograph to create the same scour depth as the entire hydrograph

$t_{hydro}(\text{years})$ = the duration of the hydrograph

$V_{\max}(\text{m/s})$ = maximum velocity in the hydrograph

$\dot{z}_i(\text{mm/hr})$ = initial rate of scour corresponding to the maximum velocity

$\dot{z}_{i,mean}(\text{mm/hr})$ = mean initial rate of scour corresponding to the maximum velocity

Scour depth versus time curve equation

This equation describes the scour depth versus time curve:

$$y_{s(Cont)}(t) = \frac{t}{\frac{1}{\dot{z}_i} + \frac{t}{y_{s\,(Cont)}}} \quad (7)$$

where $y_{s(Cont)}(t)$ = contraction scour depth at time t

t = elapsed time after start of scour

$\dot{z}_i$ = initial rate of scour

$y_{s\,(Cont)}$ = maximum depth of scour near toe of abutment

The abutment scour depth prediction methodology is the third step in the development of scour depth predictions at bridges which have been developed at Texas A&M University over the last 20 years including pier scour, contraction scour, and now abutment scour (flow chart in next page)

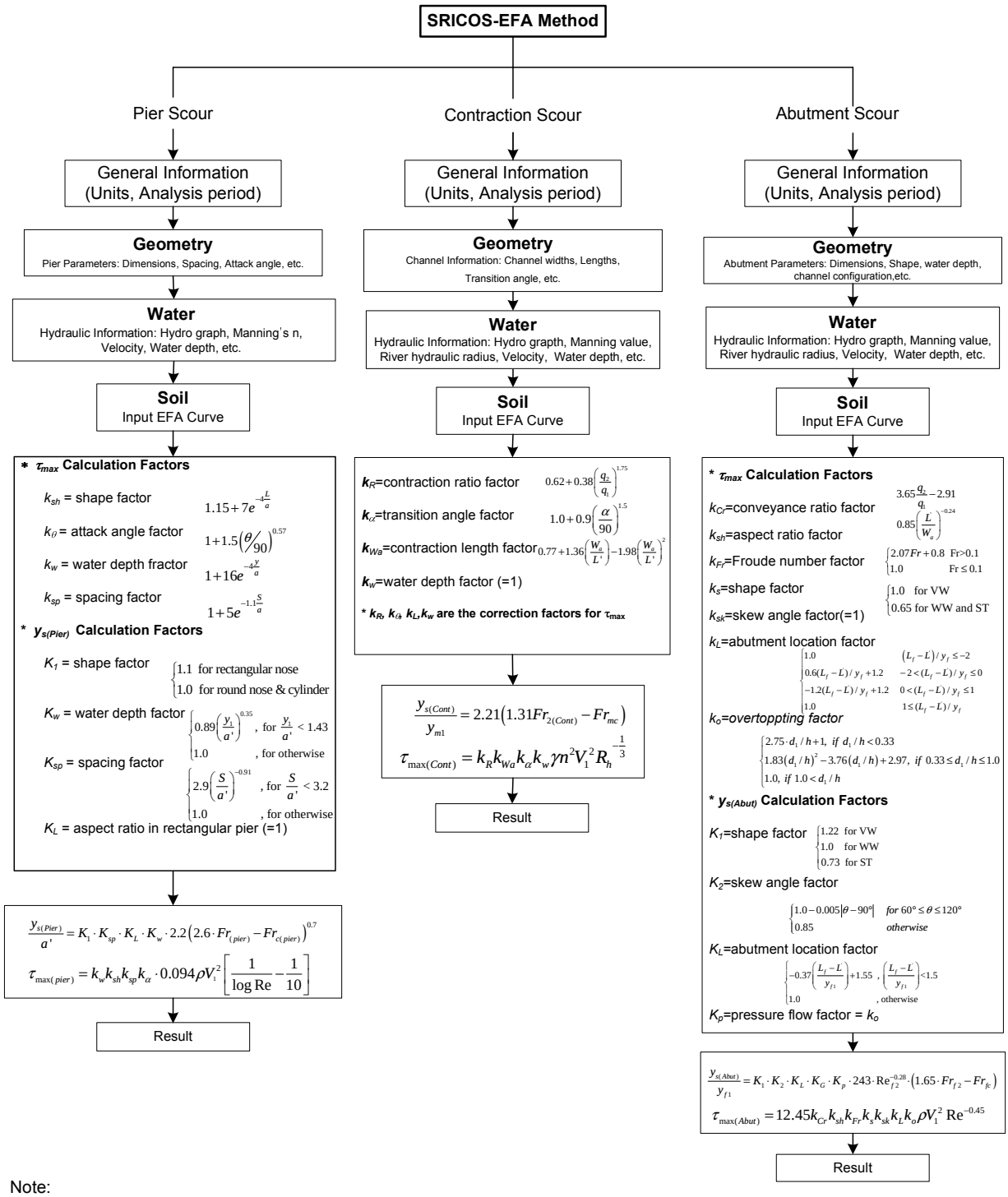

Note:

a: width of pier a': projected pier width α: contraction transition angle d_1: distance from water surface to low chord of bridge deck Fr: Froude number (based on V_1 and y_{f1}) $Fr_{(pier)}$: Froude number (based on V_1 and a') $Fr_{c(pier)}$: Froude number (based on V_c and a') $Fr_{2(Cont)}$: Froude number (based on V_2 and y_{m1}) Fr_{mc}: Froude number (based on V_{mc} and y_{m1}) $Fr_{2(Abut)}$: Froude number (based on V_{f2} and y_{f1}) Fr_{fc}: Froude number (based on V_{fc} and y_{f1}) h: distance from low chord of bridge deck to toe of abutment L: length of pier L': length of abutment projected to normal to flow L_f: width of floodplain n: Manning's coefficient θ: Attack angle q_1: approach unit discharge q_2: unit discharge around the abutment ρ: unit mass of water at 20°C R_h: Hydraulic radius Re: Reynolds number (based on a or W_a) S: spacing of group pier V_1: approach average velocity W_a: width of bridge crest or length of channel contraction y_{f1}: floodplain water depth before contractionfor open channel or h for pressure flow y_{m1}: main channel water depth before contraction $y_{s(Pier)}$: maximum pier scour depth $y_{s(Cont)}$: maximum contraction scour depth $y_{s(Abut)}$: maximum abutment scour depth

CHAPTER 1

INTRODUCTION

1.1 BRIDGE SCOUR

Bridge scour is the loss of soil by erosion due to flowing water around bridge supports. Bridge scour includes general scour and local scour. General scour is the aggradation or degradation of the riverbed not related to the presence of local obstacles. Aggradation is the gradual and general accumulation of sediments on the river bottom; one possible scenario is the existence of slope failures upstream leading to the formation of spoils in the river, the erosion of these spoils under higher velocities, followed by transport and deposition under lower velocities at the aggrading location. Degradation is the gradual and general removal of sediments from the riverbed; one possible scenario is the man-made straightening of a river course, a resulting increase in the water velocity and the associated increase in erosion. Local scour is the scour around obstacles to the water flow; it includes pier scour, abutment scour, and contraction scour. Pier scour is the removal of the soil around the foundation of the pier; abutment scour is the removal of the soil around the abutment at the junction between the bridge and the embankment; contraction scour is the removal of the soil from the bottom of the river due to narrowing of the river channel created by the approach embankments for the bridge.

1.2 SOILS CLASSIFICATION

Soils can be defined as loosely bound to unbound naturally occurring materials which cover the top few hundred meters of the Earth. By opposition, rock is a strongly bound naturally occurring material found within similar depths or deeper. At the boundary between soils and rocks are intermediate geomaterials. Classification tests and mechanical properties help to distinguish between those three types of naturally occurring materials and between different categories of soils. For soils, the classification tests consist of grain size analysis and Atterberg limits (Das, 1997). The D_{50} grain size is the grain size corresponding to 50% of the soil weight passing a sieve of opening equal to D_{50}. The first major division in soils classification is between large-grained soils and fine-grain soils; large-grained soils have D_{50} larger than 0.075mm while fine-grained soils have D_{50} smaller than 0.75mm. Large-grained soils include gravels and sands which are identified on the basis of their grain size. Fine grained soils include silts and clays which are identified on the basis of Atterberg Limits. Large grained soils are typically referred to as non-cohesive soils while silts and clays are typically referred to as cohesive soils.

1.3 THE PROBLEM ADDRESSED

This project deals with pier abutment scour and contraction scour in cohesive soils (Figure 1.1). A previous project performed by the same team of researchers was started in 1990 and was sponsored by the Texas Department of Transportation (Briaud et al., 1999a, 1999b, 2001a and 2001b); it dealt with pier scour in cohesive soils. In the TxDOT project the piers were cylindrical and the water depth was more than two times the pier diameter (deep water case). In the TxDOT project also, a new apparatus called the EFA (Erosion Function Apparatus) was conceived, built,

patented, and commercialized to measure the erodibility of soils. The EFA test gives the erosion function for a soil which became an integral part of the SRICOS method (Scour Rate In COhesive Soils) to predict the scour depth as a function of time when a cylindrical pier founded in a layered soil is subjected to a long-term deep water flow-velocity hydrograph. In a following NCHRP project (Briaud et al., 2004), the SRICOS-EFA method was extended to the case of complex piers and contraction scour. Complex piers refer to piers with various shapes, various flow attack angles, various spacing between piers, and any water depth. Contraction refers to a narrowing of the flow channel by an embankment with a given encroachment length, a given embankment width, and a given transition angle. The input to the SRICOS-EFA method is the geometry of the piers and of the contraction, the water velocity and the water depth as a function of time over the life of the bridge, and the soil erosion functions for the layers involved in the soil stratigraphy. The output is the scour depth as a function of time during the life of the bridge. In this NCHRP project, the SRISCOS-EFA method was extended to the problem of abutment scour, and the contraction scour equation was extended from the single case of a rectangular channel to the general case of a floodplain plus a main channel.

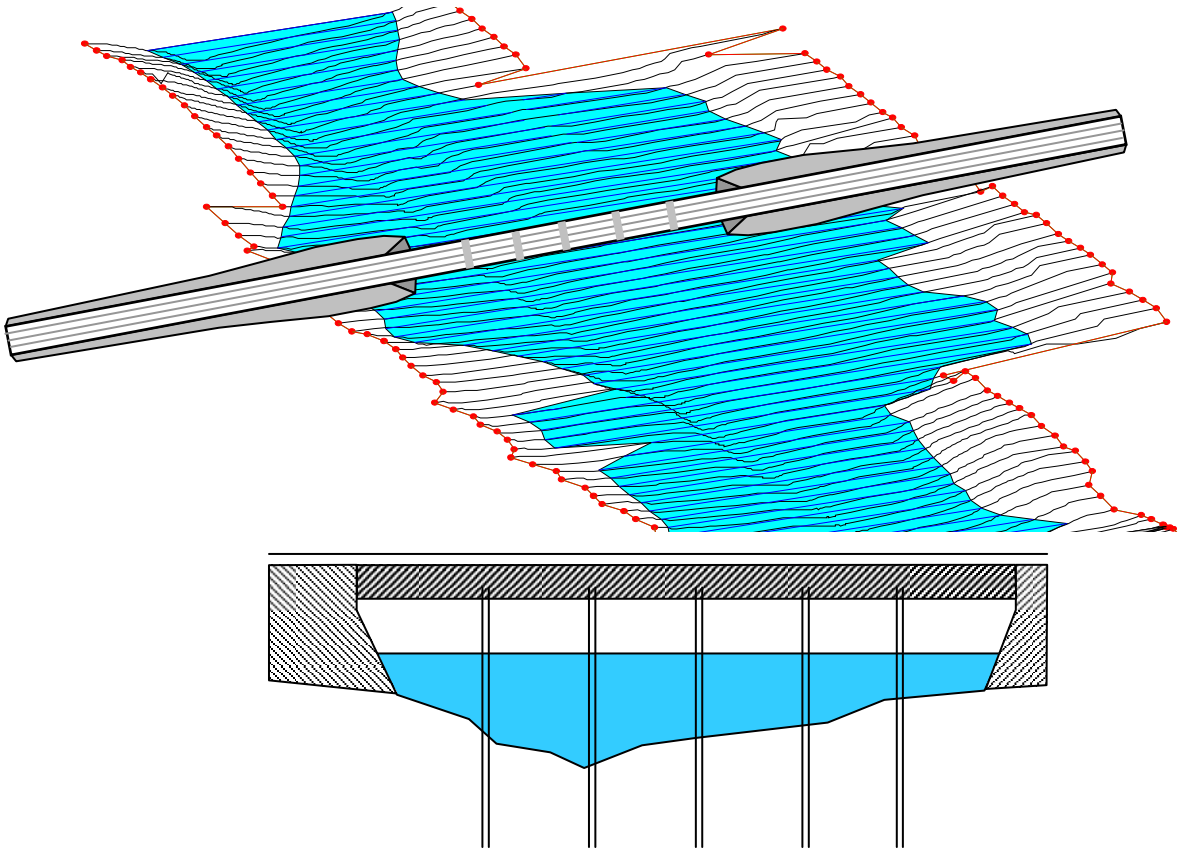

Figure 1.1 - Typical bridge with bridge scour.

1.4 WHY WAS THIS PROBLEM ADDRESSED?

The reason for solving this problem is that a solution did not exists, that in the absence of a solution the calculations were based on the solution developed for cohesionless soils, and that there was a sense that such an approach was sometimes very conservative and therefore costly. Indeed, overly conservative scour depths lead to foundations which were considered to be deeper than necessary. The major difference between cohesionless soils and cohesive soils is the following. Floods create peak velocities that last a few days. A few days is a length of time which is usually sufficient to generate the maximum scour depth in cohesionless soils. This means that only the peak velocity needs to be used in the calculations of scour depth for cohesionless soils and that such a scour depth is the maximum scour depth for that velocity. The velocities used are typically the 100 year flood velocity and the 500 year flood velocity. In cohesive soils, scour and erosion rates can be 1000 times slower than in cohesionless soils and a few days may generate only a small fraction of the maximum scour depth. Therefore, for cohesive soils, it becomes necessary to consider the rate of erosion and accumulate the effect of multiple floods. This complicates the problem significantly but this necessary complication is the price one has to pay to get closer to reality.

1.5 APPROACH SELECTED TO SOLVE THE PROBLEM

The approach selected to solve the problem of predicting the scour depth vs. time for abutment scour in a contracted channel and for a given velocity hydrograph was based on a combination of review of existing knowledge, flume tests, numerical simulations, fundamental principles in method development, and verification of the method against available data. The review of the existing knowledge avoided duplication of effort and helped in establishing a solid foundation. The flume tests gave the equations for the maximum scour depth and the influence of various factors. The flume tests also gave a calibration basis for the numerical simulations. These numerical simulations were used to generate the equations for the maximum initial shear stress at the initiation of scour. The method was assembled by linking the calculated initial conditions (given by the numerical simulation results) to the calculated maximum scour depth (given by the flume tests results) by a hyperbolic model. The multiflood hydrograph and multilayer soil was included through simple accumulation algorithms. Verification was based on comparison to existing databases as well as performing calculations for example cases and evaluating the reasonableness of the results based on experience.

1.6 ORGANIZATION OF THE REPORT

After a review of the existing knowledge in the beginning chapters, Chapter 4 deals with numerical simulations for abutment scour in the open channel. Chapter 5 deals with numerical simulations for abutment scour during overtopping flow. Chapter 6 deals with the comparison of scour development predicted by numerical simulation for cohesive soil to laboratory measurement. Chapter 7 deals with maximum abutment scour and maximum contraction scour including the flume tests and the development of equations. In Chapter 8, the SRICOS-EFA method for contraction and abutment scour is verified using previous laboratory test results and full scale channel data. Examples are worked out in Chapter 9.

CHAPTER 2

ERODIBILITY OF COHESIVE SOILS

2.1 ERODIBILITY: A DEFINITION

Erodibility is a term often used in scour and erosion studies. Erodibility may be thought of as one number which characterizes the rate at which a soil is eroded by the flowing water. With this concept erosion resistant soils would have a low erodibility index and erosion sensitive soils would have a high erodibility index. This concept is not appropriate; indeed the water velocity can vary drastically in rivers from 0 m/s to 5 m/s or more and therefore the erodibility is a not a single number but a relationship between the velocity applied and the corresponding erosion rate experienced by the soils. While this is an improved definition of erodibility, it still presents some problems because water velocity is a vector quantity which varies in direction and magnitude everywhere in the flow. It is much preferable to quantify the action of the water on the soil by using the shear stress applied by the water on the soil at the water-soil interface. Erodibility is therefore defined here as the relationship between the erosion rate $\dot{z}$ and the hydraulic shear stress applied τ (Figure 2.1). This relationship is called the erosion function $\dot{z}(\tau)$. The erodibility of a soil or a rock is represented by the erosion function of that soil or rock.

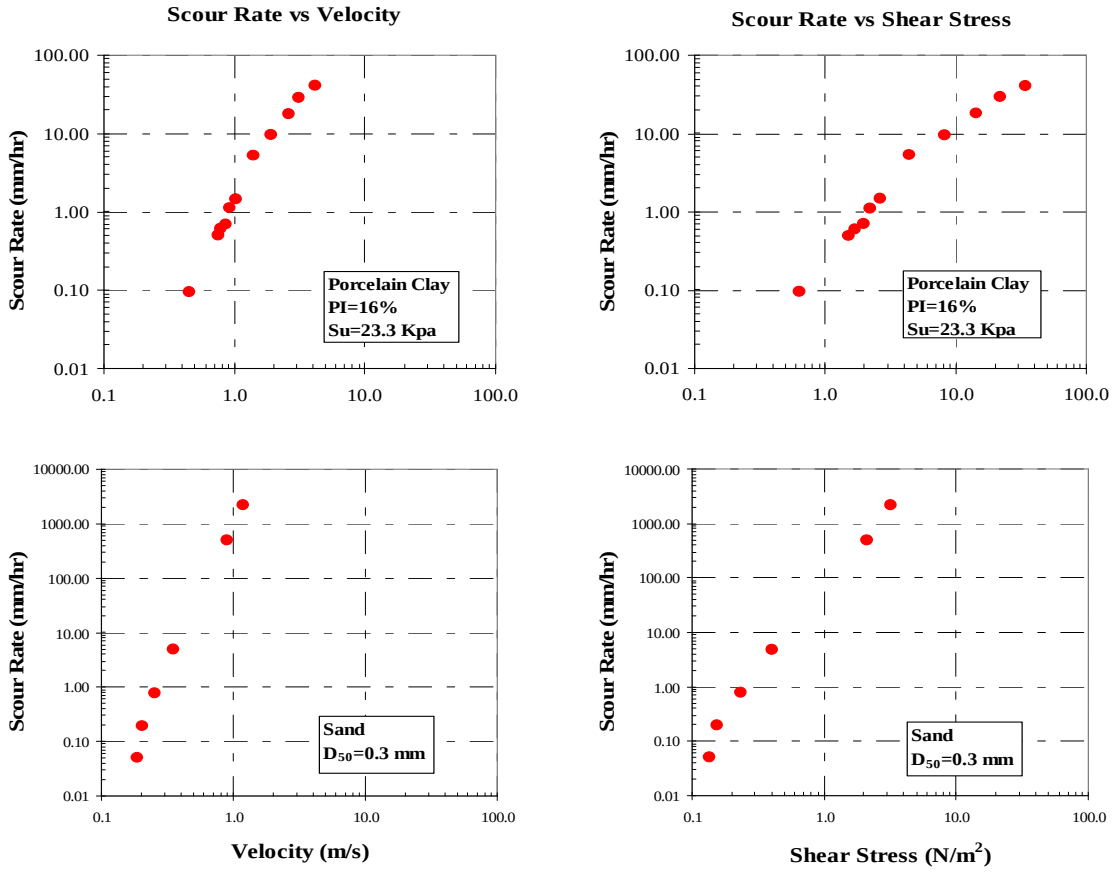

Figure 2.1 - Erodibility Function for a clay and for a sand.

2.2 EROSION PROCESS

Soils are eroded particle by particle in the case of coarse-grained soils (cohesionless soils). In the case of fine-grained soils (cohesive soils), erosion can take place particle by particle or also block of particles by block of particles. The boundaries of these blocks are formed naturally in the soils matrix by micro-fissures due to various phenomena including compression and extension.

The resistance to erosion is influenced by the weight of the particles for coarse grained soils and by a combination of weight and electromagnetic and electrostatic interparticle forces for fine grained soils. Observations at the soil water interface on slow motion videotapes indicates that the removal of particle or blocks of particles is by a combination of rolling and plucking action of the water on the soil.

2.3 EXISTING KNOWLEDGE ON ERODIBILITY OF COHESIVE SOILS

A complete discussion on the erodibility of cohesive soils and a literature review on that topic can be found in Briaud et al. (1999a, and 1999b). The following is a summary of that part of Briaud et al. (1999a, and 1999b). The factors influencing the erodibility of cohesive soils according to the literature survey are listed in Table 2.1. Although there are sometimes conflicting findings, the general trends on the impact of one factor on the erodibility is shown in the table when possible.

Table 2.1 - Factors influencing the erodibility of cohesive soils.

When this parameter increases	Erodibility
Soil water content	
Soil unit weight	decreases
Soil plasticity Index	decreases
Soil undrained shear strength	decreases
Soil void ratio	increases
Soil swell	increases
Soil mean grain size	
Soil percent passing sieve #200	decreases
Soil clay minerals	
Soil dispersion ratio	increases
Soil cation exchange capacity	
Soil sodium absorption ratio	increases
Soil pH	
Soil temperature	increases

Water temperature	increases
Water chemical composition	

The critical shear stress of cohesionless soils is tied to the size of the particles and usually ranges from 0.1 N/m^2 to 5 N/m^2. The rate of erosion of cohesionless soils above the critical shear stress increases rapidly and can reach tens of thousands of millimeters per hour. The most erodible soils are fine sands and silts with mean grain sizes in the 0.1 mm range (Figure 2.2). The critical shear stress of cohesive soils is not tied to the particle size but rather to a number of factors as listed in Table 2.1. The critical shear stress of cohesive soils however varies within the same range as cohesionless soils (0.1 N/m^2 to 5 N/m^2) for the most common cases. Since the critical shear stress controls the maximum depth of scour as will be seen later, it is likely that the final depth of scour will be approximately the same in sands and in clays. One major difference between cohesionless and cohesive soils is the rate of erosion beyond the critical shear stress. In cohesive soils, this rate increases slowly and is measured in millimeters per hour. This slow rate makes it advantageous to consider that scour problems are time dependent and to find ways to accumulate the effect of the complete hydrograph rather than to consider a design flood alone.

2.4 ERODIBILITY AND CORRELATION TO SOIL AND ROCK PROPERTIES?

As can be seen on Figure 2.1, there is a critical shear stress τ_c below which no erosion occurs and above which erosion starts. The critical shear stress is associated with the critical velocity v_c. One can also define an initial slope S_i for the erosion function as shown on Figure 2.1. Both τ_c and S_i are parameters which help describe the erosion function and therefore the erodibility of a material. In cohesionless soils (sands and gravels), the critical shear stress has been related to the mean grain size D_{50} (Briaud et al., 2001a).

$$\tau_c \text{ (N/m}^2\text{)} = D_{50} \text{ (mm)} \tag{2.1}$$

For such soils, the erosion rate beyond the critical shear stress is very rapid and one flood is long enough to reach the maximum scour depth. Therefore there is a need to be able to predict the critical shear stress to know if there will be scour or no scour but there is little need to define the erosion function beyond that point because the erosion rate is not sufficiently slow to warrant a time dependent analysis.

In cohesive soils (silts, clays, and rocks) equation 2.1 is not applicable (Figure 2.2) and the erosion rate is sufficiently slow that a time rate analysis is warranted. Therefore it is necessary to obtain the complete erosion function. An attempt was made to correlate those parameters to common soil properties in hope that simple equations could be developed for everyday use. The process consisted of measuring the erosion function on one hand and common soil properties on the other (water content, unit weight, plasticity index, percent passing sieve no. 200, undrained shear strength). This lead to a database of 91 EFA tests (Table 2.2) which was used to perform

regression analyses and obtain correlation equations (Figure 2.3 to Figure 2.6). All attempts failed to reach a reasonable R^2 value.

Table 2.2 - Database of EFA tests.

Woodrow Wilson Bridge (Washington)	Tests 1 to 12
South Carolina Bridge	Tests 13 to 16
National Geotechnical Experimentation Site (Texas)	Tests 17 to 26
Arizona Bridge (NTSB)	Test 27
Indonesia samples	Tests 28 to 33
Porcelain clay (man-made)	Tests 34 to 72
Bedias Creek Bridge (Texas)	Tests 73 to 77
Sims Bayou (Texas)	Tests 78 to 80
Brazos River Bridge (Texas)	Test 81
Navasota River Bridge (Texas)	Tests 82 and 83
San Marcos River Bridge (Texas)	Tests 84 to 86
San Jacinto River Bridge (Texas)	Tests 87 to 89
Trinity River Bridge (Texas)	Tests 90 and 91

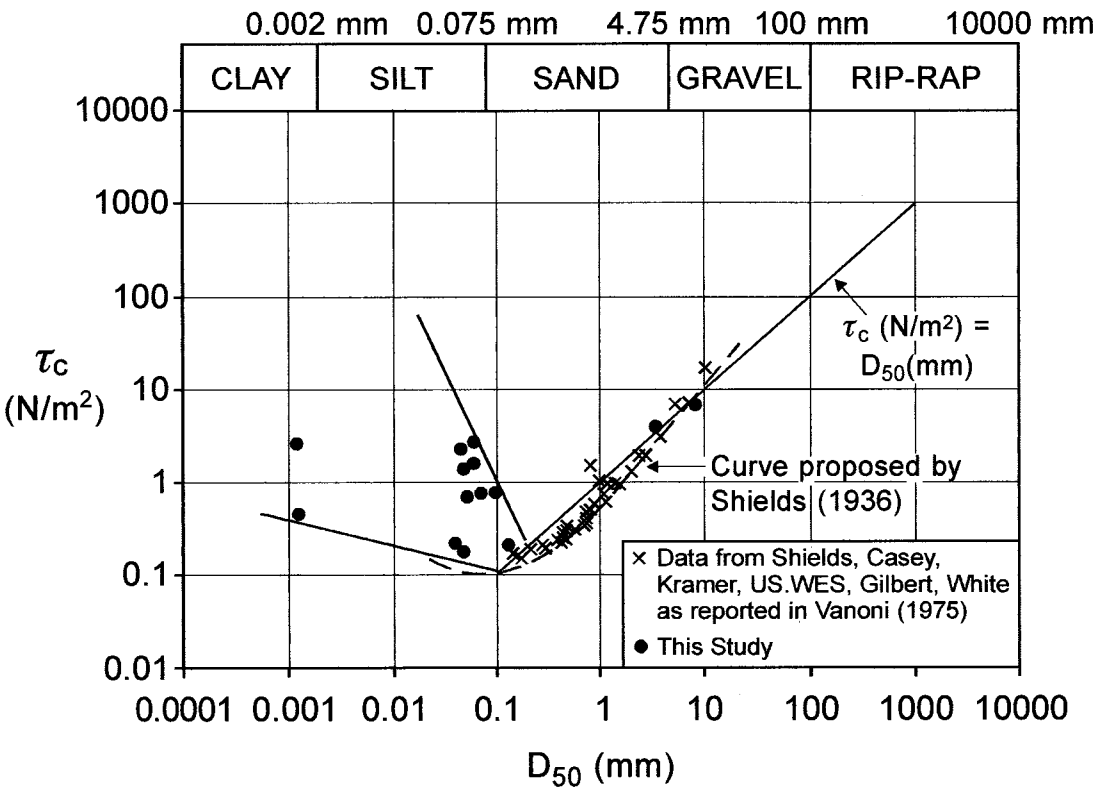

Figure 2.2 - Critical shear stress versus mean soil grain diameter.

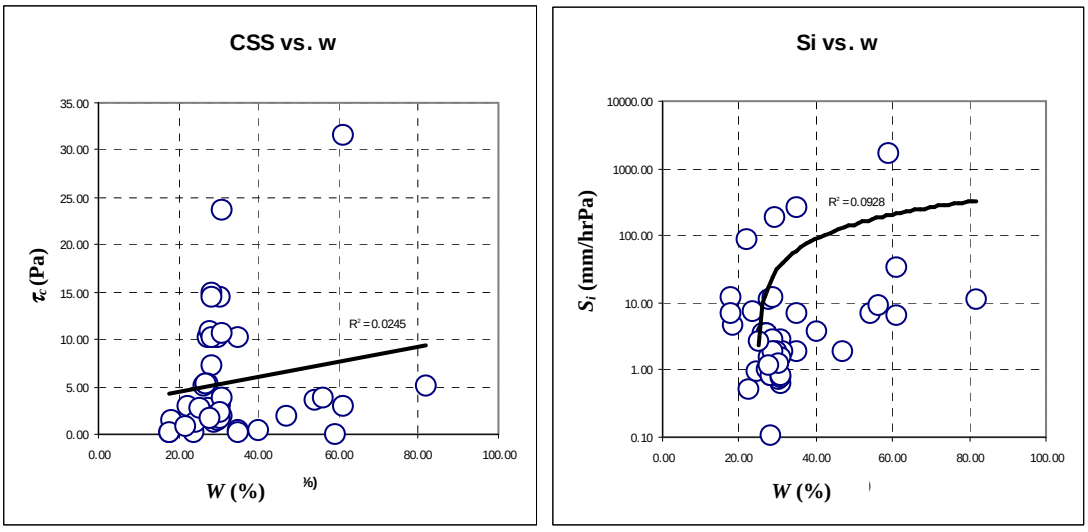

Figure 2.3 - Erosion properties as a function of water content.

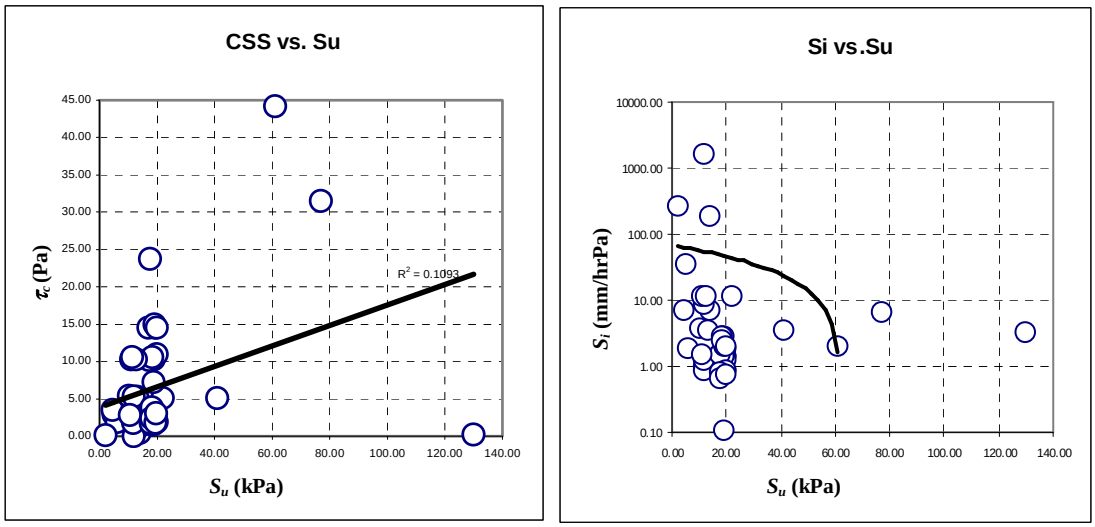

Figure 2.4 - Erosion properties as a function of undrained shear strength.

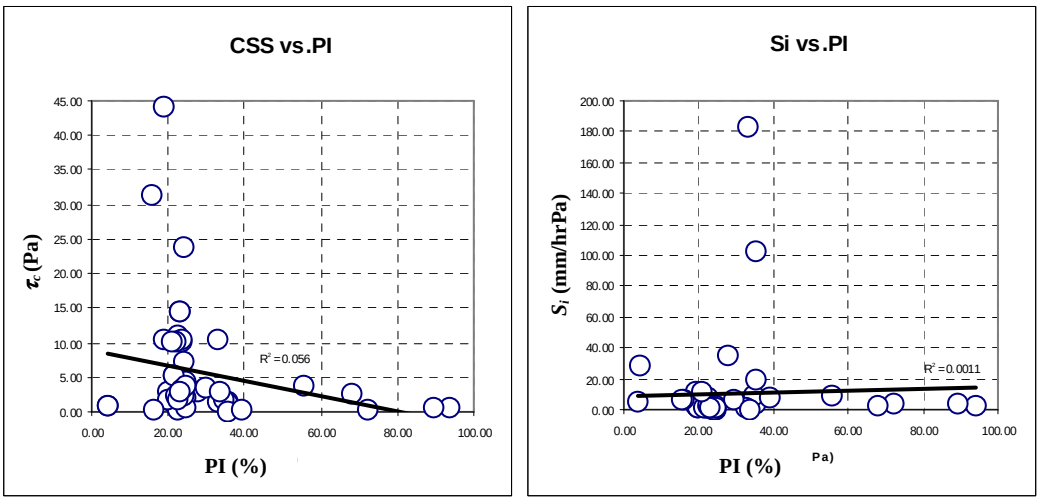

Figure 2.5 - Erosion properties as a function of plasticity index.

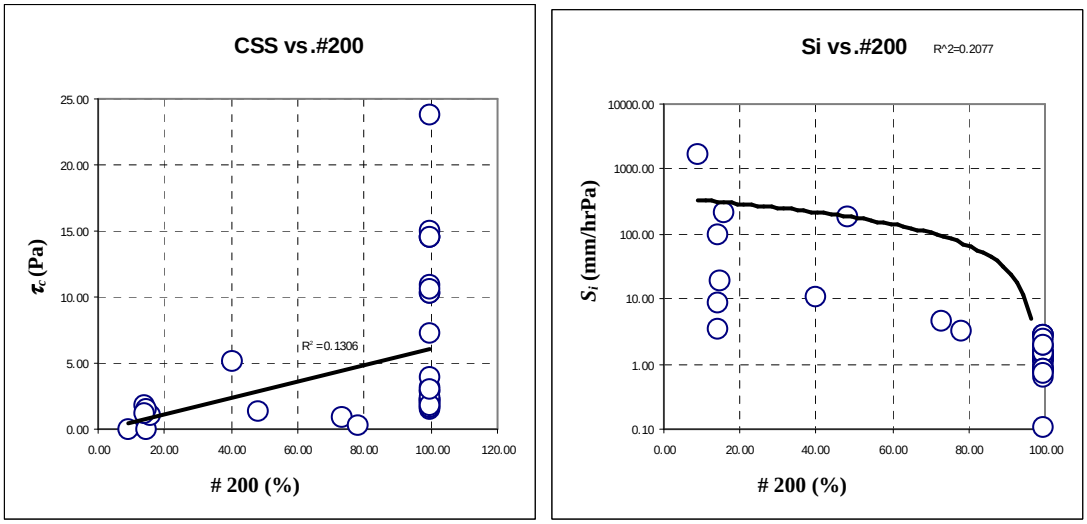

Figure 2.6 - Erosion properties as a function of percent passing sieve #200.

The fact that no relationship could be found in this project between the critical shear stress or the initial slope of the erosion function on one hand and common soil properties on the other seems to be at odds with the accepted idea that different cohesive soils erode at different rates. Indeed if different clays erode at different rates then the erosion function and therefore its parameters should be functions of the soils properties. The likely explanation is that there is a relationship between erodibility and soils properties but that this relationship is quite complicated, involves advanced soil properties, and could not be found within the budget and time of this project. Instead, it was found much easier to develop an apparatus which could measure the erosion function on any sample of cohesive soil from a site. This apparatus was called the Erosion Function Apparatus or EFA.

CHAPTER 3

THE SRICOS-EFA METHOD

3.1 EROSION FUNCTION APPARATUS

3.1.1 Concept

The EFA or Erosion Function Apparatus (Figure 3.1 and Figure 3.2) (Briaud et al. 1999a, 2001a) (http://www.humboldtmfg.com/pdf2/hm4000ds.pdf, http://tti.tamu.edu/geotech/scour) was conceived in 1991, designed in 1992, and built in 1993. The sample of soil, fine-grained or not, is taken in the field by pushing an ASTM standard Shelby tube with a 76.2 mm outside diameter (ASTM D1587). One end of the Shelby tube full of soil is placed through a circular opening in the bottom of a rectangular cross section conduit. A snug fit and an O-ring establish a leak proof connection. The cross section of the rectangular conduit is 101.6 mm by 50.8 mm. The conduit is 1.22 m long and has a flow straightener at one end. The water is driven through the conduit by a pump. A valve regulates the flow and a flow meter is used to measure the flow rate. The range of mean flow velocities is 0.1 m/s to 6 m/s. The end of the Shelby tube is held flush with the bottom of the rectangular conduit. A piston at the bottom end of the sampling tube pushes the soil until it flush with the bottom of the rectangular conduit at the top end. The soil is eroded by the water flowing over it. The erosion rate is the rate at which the piston has to be pushed to maintain the soil surface flush with the bottom of the conduit. The piston is typically 0.5 mm increment.

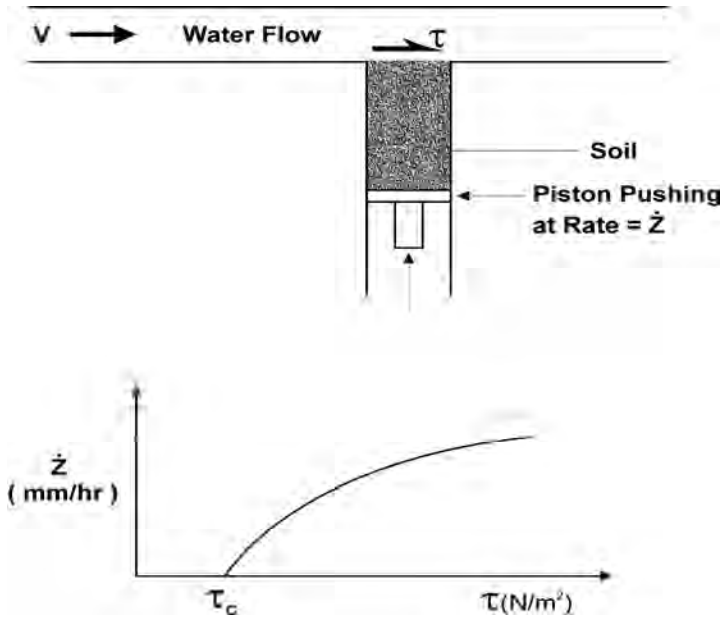

Figure 3.1 - Schematic diagram and result of the EFA (Erosion Function Apparatus) .

(a)

(b)

Figure 3.2 - Photographs of the Erosion Function Apparatus (a) General view (b) close-up of the test section.

3.1.2 EFA Test Procedure

The typical procedure for the EFA test is as follows.

1. Place the sample in the EFA, fill the conduit with water, and wait one hour.
2. Set the velocity to 0.3 m/s.
3. Push the soil in the sampling tube so it is flush with the bottom of the conduit
4. Advance the piston as fast as the soil is being eroded by the water flow (visual inspection through the plexiglass window).
5. Record the time *t* it takes for *h* mm of soil to be eroded.
6. When a few millimeters of soil have been eroded or after 1 hour of flow whichever comes first, increase the velocity to 0.6 m/s.

7. Repeat step 4 5, and 6 for velocities equal to 1 m/s, 1.5 m/s, 2 m/s , 3 m/s, 4.5 m/s, and 6 m/s.

3.1.3 EFA Test Data Reduction

The test result consists of the erosion rate $\dot{z}$ versus shear stress τ curve (Figure 3.1). For each flow velocity V, the erosion rate $\dot{z}$ (mm/hr) is simply obtained by dividing the length of sample eroded by the time required to do so.

$$\dot{z} = \frac{h}{t} \tag{3.1}$$

where h is the length of soil sample eroded in a time t.

After several attempts at measuring the shear stress τ in the apparatus it was found that the best way to obtain τ was by using the Moody Chart (Moody, 1944) for pipe flows.

$$\tau = \frac{1}{8} f \rho V^2 \tag{3.2}$$

where τ is the shear stress on the wall of the pipe, f is the friction factor obtained from Moody Chart (Figure 3.3), ρ is the mass density of water (1000 kg/m3), and V is the mean flow velocity in the pipe. The friction factor f is a function of the pipe Reynold's number Re and the pipe roughness ε/D. The Reynold's number is VD/ν where D is the pipe diameter and ν is the kinematic viscocity of water $\left(10^{-6} m^2/s \; at \; 20^\circ C\right)$. Since the pipe in the EFA has a rectangular cross section, D is taken as the hydraulic diameter $D = 4A/P$ where A is the cross sectional flow area, P is the wetted perimeter, and the factor 4 is used to ensure that the hydraulic diameter is equal to the diameter for a circular pipe. For a rectangular cross section pipe:

$$D = 2ab/(a+b) \tag{3.3}$$

where a and b are the dimensions of the sides of the rectangle. The relative roughness ε/D is the ratio of the average height of the roughness elements on the pipe surface over the pipe diameter D. The average height of the roughness elements ε is taken equal to $0.5D_{50}$ where D_{50} is the mean particle diameter for the soil. The factor 0.5 is used because it is assumed that the top half of the particle protrudes into the flow while the bottom half is buried into the soil mass. In some cases, the surface is rougher than $0.5D_{50}$; in these cases, the height of roughness ε is taken as the estimated mean depression height on the surface of the sample.

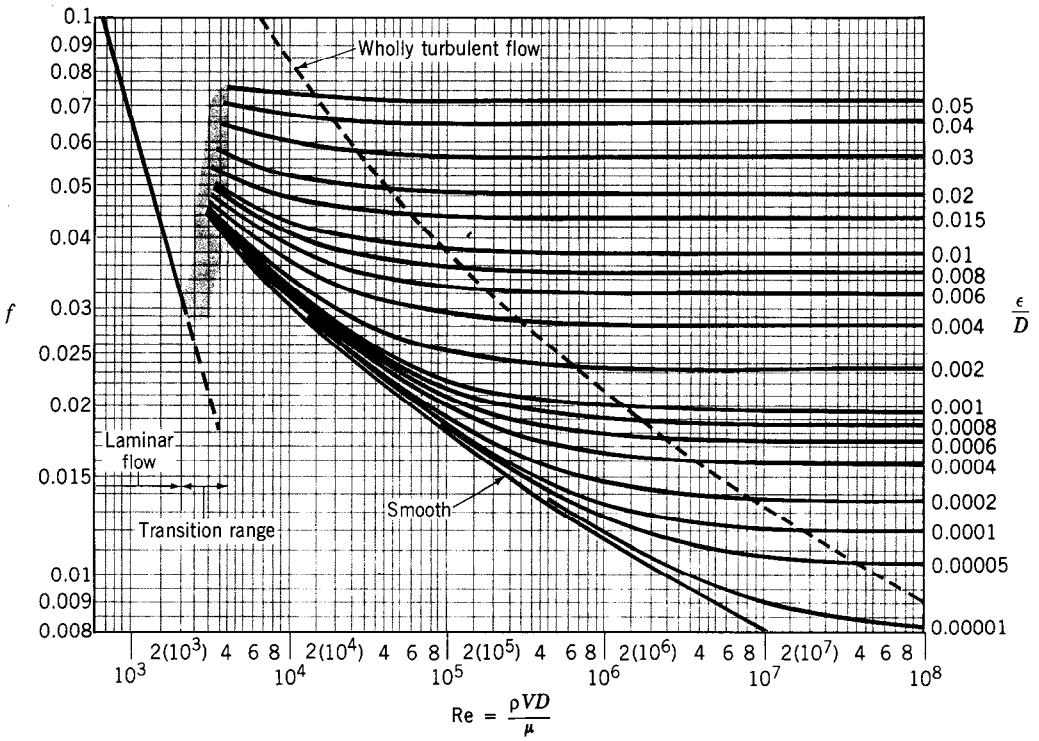

Figure 3.3 - Moody chart (reprinted with permission from Munson et al. 1990).

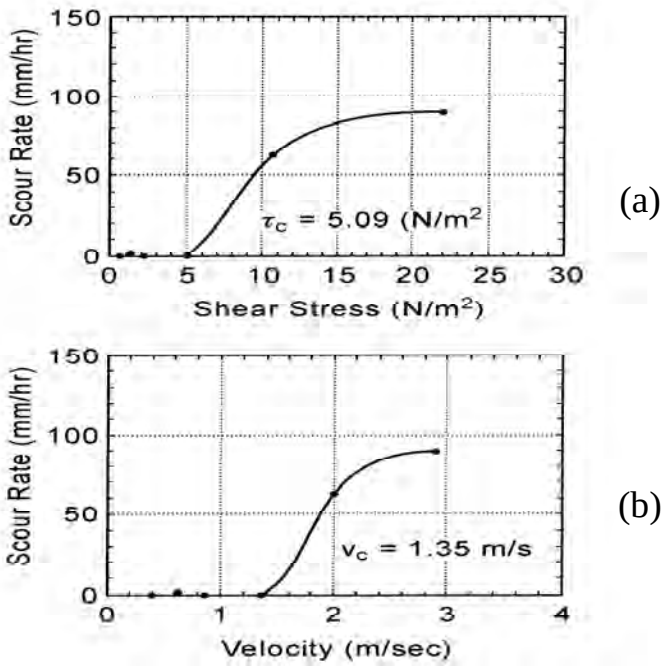

Figure 3.4 - Erosion Function for a soil sample taken near Pier 27E of the Existing Woodrow Wilson bridge (2.6 - 3.2 meters depth) : (a) Scour Rate vs. Shear Stress, (b) Scour Rate vs. Velocity.

3.1.4 EFA Precision and Typical Results

If the erosion rate is slow (less that 10 mm/hr) the error on $\dot{z}$ is estimated at 0.5 mm/hr. If the erosion rate is fast (more than 100 mm/hr) the error on $\dot{z}$ is estimated at 2 mm/hr. Therefore the relative error on $\dot{z}$ is estimated to be less than 10%. Comparison between the τ_c results for the sand and the gravel tested in this study and shown on figure 3 with Shields data indicates a difference of about 10%. Therefore it is estimated that both $\dot{z}$ and τ are measured with a relative error of about 10%.

The $\dot{z}$ vs. τ curve is the result of a series of tests each of which is performed at a constant velocity. A typical series of 6 velocity tests lasts one working day. Figure 2.1 and Figure 3.4 show examples of EFA tests results. Erosion categories are proposed on 15 years of erosion testing experience in order to bring erodibility down in complexity from an erosion rate vs shear function to category number in Figure 3.5. Such a classification system is presented in terms of shear stress in Figure 3.6.

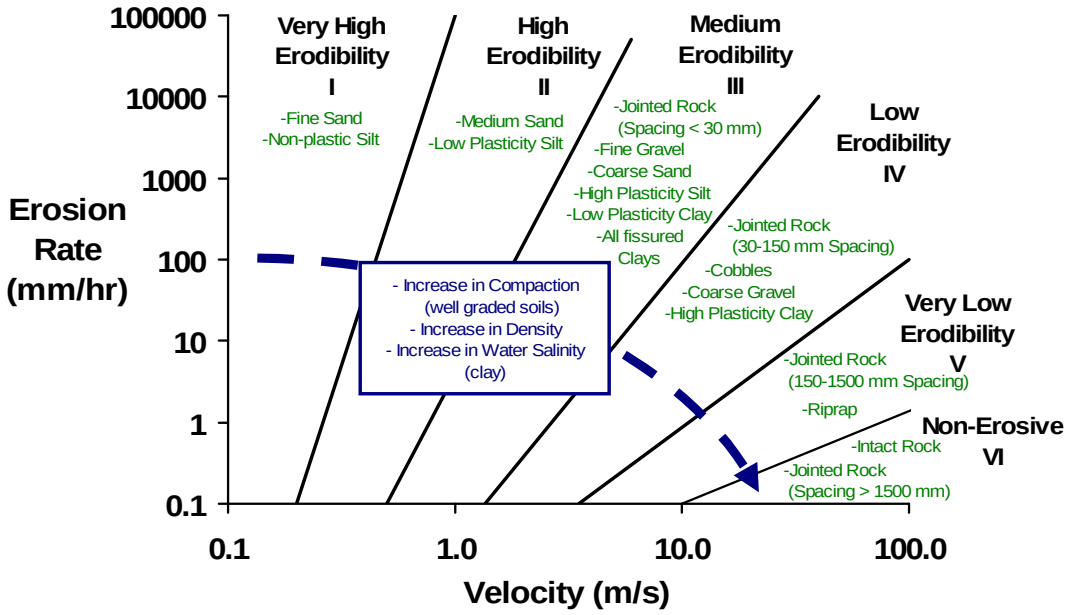

Figure 3.5 - Proposed erosion categories for soils and rocks based on velocity.

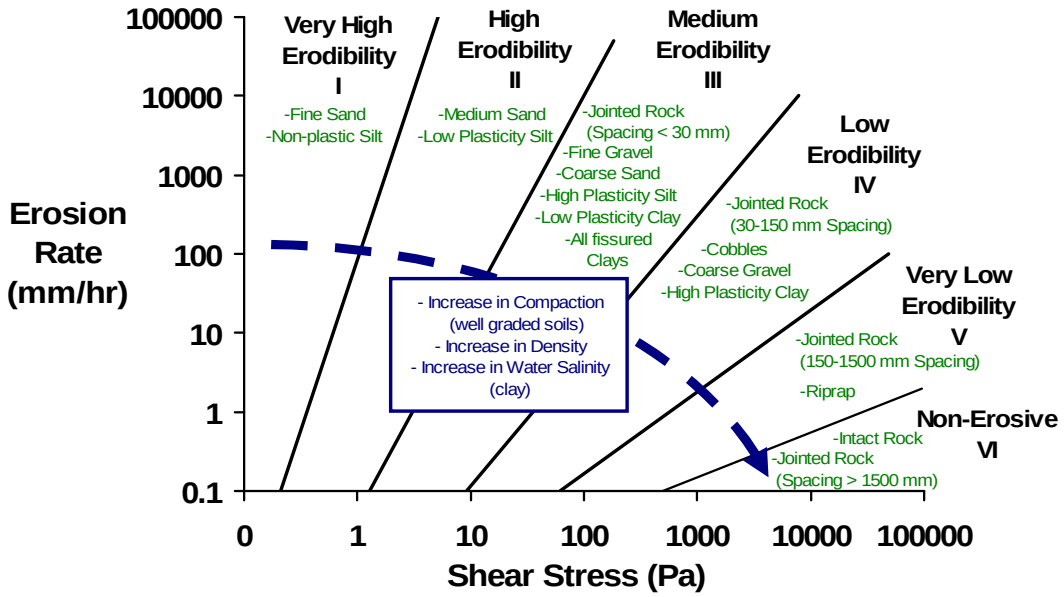

Figure 3.6 - Proposed erosion categories for soils and rocks based on shear stress.

3.2 THE SRICOS-EFA METHOD

The following sections summarize the work already done over the last 20 years to develop the SRICOS-EFA method for pier scour predictions and advance contraction scour predictions. The details of the previous work done can be found in two major publications: a TxDOT report no. 2937-1 (Briaud et al, 1999a) and NCHRP report 516 (Briaud et al, 2004).

3.2.1 SRICOS-EFA Method for Cylindrical Piers in Deep Water

SRICOS stands for Scour Rate In Cohesive Soils. Since the method makes use of the erosion function measured in the EFA, the method is referred to as the SRICOS-EFA method. For a given velocity hydrograph at a bridge, for a given soil exhibiting a multilayered stratigraphy with an erosion function defined for each layer, and for a given cylindrical pier in deep water (water depth larger than 1.6 times the pier diameter), the SRICOS-EFA method (program) gives the scour depth as a function of time for the period covered by the hydrograph.

The method is based on the calculation of two basic parameters: the maximum depth of pier scour and the initial rate of scour. The maximum depth of scour is based on an equation obtained from flume tests and the initial rate is based on an equation giving the initial shear stress obtained from numerical simulations. The initial rate of scour is read on the EFA erosion function at the corresponding value of the calculated initial shear stress. A hyperbola is used to connect the initial scour rate to the maximum or asymptotic scour depth and describes the complete scour depth vs. time curve. Robust algorithms are used to incorpo-

rate the effect of varying velocities and multilayered soil systems. This earlier method was developed by the authors under TxDOT sponsorship (Briaud et al., 1999a) and was verified by satisfactory comparison between predicted scour and measured scour at 8 bridges in Texas.

3.2.2 SRICOS-EFA Method for Maximum Scour Depth at Complex Piers

A set of flume experiments were conducted (Briaud et al., 2004) to study the maximum depth of scour for a pier including the effect of shallow water depth, the effect of rectangular shapes, the effect of the angle of attack on rectangular shapes, and the effect of spacing between piers positioned in a row perpendicular to the flow. The proposed equation for the maximum depth of scour is in the form of the equation for the cylindrical pier in deep water with correction factors based on the results of the flume tests.

$$y_{s(Pier)} = K_w K_{sp} K_1 \left(0.18\,\mathrm{Re}^{0.635}\right) \tag{3.4}$$

where $y_{s(Pier)}$ is the maximum depth of pier scour in millimeters, Re is the Reynolds number equal to VB'/ν, V being the mean depth velocity at the location of the pier if the bridge was not there, ν the water viscosity, the K factors take the shallow water depth, the spacing, and the shape into account, the angle of attack being considered through the use of the projected width B' in the calculation of the Reynolds number.

3.2.3 SRICOS-EFA Method for Initial Scour Rate at Complex Piers

A set of numerical simulations were performed (Briaud et al., 2004) to study the maximum shear stress around a pier including the effect of shallow water depth, the effect of rectangular shapes, the effect of the angle of attack on rectangular shapes, and the effect of spacing between piers positioned in a row perpendicular to the flow. The proposed equation for the maximum shear stress is in the form of the equation for the cylindrical pier in deep water with correction factors based on the results of the numerical simulations.

$$\tau_{\max(Pier)} = k_w k_{sh} k_{sp} k_\theta \left(0.094 \rho V^2 \left[\frac{1}{\log R_e} - \frac{1}{10} \right] \right) \tag{3.5}$$

where $\tau_{max(Pier)}$ is the maximum shear stress around the pier, Re is the Reynolds number equal to VB/ν, V being the mean depth velocity at the location of the pier if the bridge was not there, ν is the water viscosity, B is the pier diameter or pier width, the k factors take shallow water depth, pier shape, pier spacing, and attack angle into account.

3.2.4 SRICOS-EFA Method for Maximum Contraction Scour Depth

A set of flume experiments were conducted (Briaud et al., 2004) to study the depth of scour associated with the contraction of a channel including the effects of the ratio of the contracted channel width over the approach channel width, the contracted channel length, and the transition angle. The proposed equation for the maximum depth of contraction scour is

$$y_{s(Cont)} = K_{\alpha} K_{Wa} 1.90\, y_1 \left(\frac{1.49 V_{hec}}{\sqrt{g y_1}} - \frac{\left(\frac{\tau_c}{\rho} \right)^{0.5}}{g n y_1^{1/3}} \right) \geq 0 \qquad (3.5)$$

where $y_{s(Cont)}$ is the maximum depth of contraction scour, y_1 the water depth along the center line of the uncontracted channel after scour has occurred, V_{hec} the mean depth water velocity at the location of the pier in the contracted channel, τ_c the critical shear stress of the soil, ρ the mass density of water, g the acceleration due to gravity, n the Manning's coefficient, and the K factors take the transition and the contracted channel length into account. Note that the parenthesis in the equation is a factored difference between the Froude number and the critical Froude number. Equations are also proposed for the uniform contraction scour depth as well as the location of the scour depths.

3.2.5 SRICOS-EFA Method for Initial Contraction Scour Rate

A set of numerical simulations were performed (Briaud et al., 2004) to study the maximum shear stress around the contraction of a channel including the effects of the ratio of the contracted channel width over the approach channel width, the transition angle, the water depth, and the contracted channel length. The proposed equation for the maximum shear stress is in the form of the equation for the shear stress at the bottom of an open and uncontracted channel with correction factors based on the results of the numerical simulations.

$$\tau_{\max(Cont)} = k_R k_{\alpha} k_w k_{Wa} \left(\gamma n^2 V^2 R_h^{-\frac{1}{3}} \right) \qquad (3.6)$$

where $\tau_{max(Cont)}$ is the maximum shear stress along the centerline of the contracted channel, γ is the unit weight of water, n is the Manning's coefficient, V is the upstream mean depth velocity, R_h is the hydraulic radius defined as the cross section area of the flow divided by the wetted perimeter, and the k factors take the contraction ratio, the transition angle, the water depth effect, and the contracted length into account. Equations are also proposed for the location of the maximum shear stress.

3.2.6 SRICOS-EFA Method for Complex Piers Scour and Contraction Scour in Cohesive soils

Once the equations were established, the SRICOS-EFA method was assembled. Care was taken not to simply add complex pier scour and contraction scour to get total pier scour. Instead, advantage was taken of the fact that at the end of the maximum contraction scour, the velocity is at the critical velocity and the maximum pier scour should be calculated using the critical velocity of the soil and not the initial velocity in the contracted channel. In addition, the rules of accumulation due to the hydrograph, and due to the multilayer system developed for the simple pier scour method were adapted for the complex pier and contraction scour method. The superposition and accumulation reasoning lead to the following steps for the SRICOS-EFA method for

predicting the scour depth at a complex pier in a contracted channel. This step by step procedure has been automated in a computer program.

1. Collect the input data: velocity and water depth hydrograph, geometry of the pier and of the contracted channel, erosion functions of the soil layers.
2. Calculate the maximum contraction scour depth for the i^{th} velocity in the hydrograph.
3. Calculate the maximum complex pier scour depth using the i^{th} velocity in the hydrograph at the pier location if there is no contraction scour in step 2, or the critical velocity for the soil if there is contraction scour in step 2.
4. Calculate the total pier scour depth as the total of step 2 and step 3.
5. Calculate the initial maximum shear stress for pier scour using the i^{th} velocity in the hydrograph.
6. Read the initial scour rate corresponding to the initial maximum shear stress of step 5 on the erosion function of the soil layer corresponding to the current scour depth.
7. Use the results of steps 4 and 6 to construct the hyperbola describing the scour depth vs time curve for the pier.
8. Calculate the equivalent time for the given curve of step 7. The equivalent time is the time required for the i^{th} velocity on the hydrograph to scour the soil to a depth equal to the depth scoured by all the velocities occurring prior to the i^{th} velocity.
9. Read the additional scour generated by the i^{th} velocity starting at the equivalent time and ending at the equivalent time plus the time increment.
10. Repeat steps 2 to 9 for the (i+1)th velocity and so on until the entire hydrograph is consumed.

These steps are automated through a computer program called SRICOS-EFA available free of charge on the internet at http://ceprofs.tamu.edu/briaud/

3.2.7 Verification of the SRICOS-EFA Method

Several full case histories were identified for verification but none could satisfy the requirements necessary to verify the method developed. Some did not have enough details on the observed scour depth, some turned out not to be made of cohesive soil after drilling, some did not have a gauge station nearby. It was decided to compare the maximum scour depth for pier and contraction to existing databases (Briaud et al., 2004). These databases were mostly in sand however and included those collected by Mueller (pier scour), Froelich (pier scour) and Gill (contraction scour). The comparisons between the predicted and measured scour depths are very satisfactory, although it is not clear whether they should be since the soils were not primarily cohesive. Nevertheless, these comparisons give an indication that the SRICOS-EFA method may not be limited to cohesive soils. Indeed, the fact that the method is based on site specific testing of the erosion function permits incorporating the soil behavior directly into the predictions.

3.2.8 Future Hydrographs and Scour Risk Analysis

A novel technique was presented on generating future hydrographs (Briaud et al., 2004). Indeed, since the SRICOS-EFA method predicts the scour depth as a function of time, it is necessary to input into the program the hydrograph over the design life of the bridge. The proposed technique consists of using a past hydrograph (from a gauge station for example), preparing the frequency distribution plot for the floods within that hydrograph, sampling the distribution ran-

domly and preparing a future hydrograph. This future hydrograph is for the required period and has the same mean and standard deviation as the measured hydrograph. This process is repeated 10,000 times and, for each hydrograph, a final scour depth (the depth reached at the end of the design life of the bridge) is generated. These 10,000 final depths of scour are organized in a frequency distribution plot with a mean and a standard deviation. That plot can be used to quote a scour depth with a corresponding probability of occurrence, or better, to choose a risk level and quote the corresponding final depth of scour. If a hydrograph is not available, this approach can be developed on the basis of the 100 year flood and the 500 year flood only. This is automated in the SRICOS-EFA program available free of charge at http://ceprofs.tamu.edu/briaud/

3.2.9 Example Problems

A set of example problems are presented in chapter 12 of the NCHRP report 516 (Briaud et al., 2004) to help the reader become more familiar with the SRICOS-EFA method. Some examples are done by hand calculations, some of them are done by using the SRICOS-EFA computer program.

CHAPTER 4

THE SRICOS-EFA METHOD FOR INITIAL RATE OF SCOUR AT ABUTMENT

4.1 LITERATURE REVIEW

4.1.1 Bed Shear Stress at the Bridge Crossing

The force resisting the flow in a constant depth channel has been studied many years ago. Under the assumption of steady uniform flow, the bed shear stress is a function of the unit weight of water γ, the hydraulic radius R_h, and the energy slope S as follows (Munson et al., 1998):

$$\tau = \gamma R_h S \tag{4.1}$$

Manning's equation (in SI unit) gives the average channel velocity V as a function of the hydraulic radius R_h and the energy slope S,

$$V = \frac{R_h^{2/3} S^{1/2}}{n} \tag{4.2}$$

The parameter n is the Manning's resistance coefficient. Its value (table 4.1) is dependent on the surface material of the channels' wetted perimeter and is obtained from experiments, having the unit of $s/m^{1/3}$.Hence, the bed shear stress equation in open channel flow can be derived by substituting equation (4.2) into equation (4.1),

$$\tau = \gamma n^2 V^2 R_h^{-1/3} \tag{4.3}$$

Table 4.1 - Manning's n coefficients for open channel flow.

Natural Streams	n value	Floodplains	n value
Clean and Straight	0.030	Pasture, Farmland	0.035
Major Rivers	0.035	Light Brush	0.050
Sluggish with Deep Pools	0.040	Heavy Brush	0.075
		Trees	0.15

For contraction scour, the scour depth at the center of the channel is usually chosen to be the representative value. The bed shear stress at the center of the contracted channel still follows the same rule as the rule of the open channel flow and the influence of the viscous force can be ignored. The influence of the bridge foundation can be incorporated in the correction of the average velocity in equation (4.3).

Nurtjahyo (2003) numerically studied the maximum bed shear stress at the center of the channel under long contraction. The equation is generated by correcting the open channel flow

equation (4.3), including the effect of the contraction ratio k_{c-R}, the effect of the contraction transition angle $k_{c-\theta}$, the effect of the contraction length k_{c-L}.

$$\tau_{\max(Cont)} = k_R k_\theta k_L \gamma n^2 V^2 R_h^{-\frac{1}{3}} \tag{4.4}$$

$$k_R = 0.62 + 0.38\left(\frac{L_1}{L_2}\right)^{1.75}$$

$$k_\theta = 1 + 0.9\left(\frac{\alpha}{90}\right)^{1.5}$$

$$k_L = \begin{cases} 1 & , for \quad k_L \geq 0.35 \\ 0.77 + 1.36\left(\frac{W_a}{L_1 - L_2}\right) - 1.98\left(\frac{W_a}{L_1 - L_2}\right)^2 & , for \quad k_L < 0.35 \end{cases}$$

where γ is the unit weight of water, n is the Manning's coefficient, R_h is hydraulic radius, V is the upstream averaged velocity, L_1 is the upstream channel width, L_2 is the channel width at the contracted zone, W_a is the length of the contracted zone, α is the contraction transition angle.

For local bridge scour, like pier scour and abutment scour, the location of the scour hole is right around the structure. The bed shear stress features will be quite different from the preceding open channel bed shear stress. The bridge foundation will affect the magnitude and the distribution of the bed shear stress. Besides the factors affecting open channel flow, the geometry and the setting of the bridge foundation will also strongly affect the local bed shear stress. In the analysis of the open channel flow, the viscous force (represented by Reynolds number) is ignored. However, for local scour, it is going to be the dominant factor. Many researchers have studied the flow structure at bridge foundations and found a similarity of the flow in and around the scour hole at a pier and at an abutment, especially when the abutment is relatively short compared with the water depth (Melville, 1997). This implies that the bed shear stress should have similar trends around a bridge pier and an abutment.

Hjorth (1975) investigated the bed shear stress around circular pier. Two circular piers of 0.05m and 0.075m diameter were used in the flume test, combined with two different velocities of 0.15m/s and 0.30m/s and two different approach water depths of 0.1m and 0.2m. A hot-film probe was used to measure bed shear stress on the rigid flume bed. Hjorth tried to correlate the local maximum bed shear stress around the pier with the approach bed shear stress and found an amplification factor, $\tau_{\max(Pier)} / \tau_1$, ranging from 5 to 11 for a circular pier.

Wei (1997) studied the maximum bed shear stress around a circular pier in a constant water depth channel by 3D numerical simulation. The maximum bed shear stress equation he proposed was based on pier Reynolds number rather than the commonly used approach bed shear stress in an open channel. The maximum bed shear stress was also found to be independent of the water depth when the upstream flow is deeper than twice the pier diameter.

$$\tau_{\max(Pier)} = 0.094\rho V^2 \left[\frac{1}{\log \mathrm{Re}} - \frac{1}{10} \right] \tag{4.5}$$

where $\mathrm{Re} = \frac{Va}{\nu}$, ρ is the flow density, V is the upstream averaged velocity, a is the diameter of the pier, ν is the kinematic viscosity of water.

Nurtjahyo (2003) further extended Wei's equation to the case of complex pier conditions, including the effect of water depth k_w, the effect of pier spacing k_{sp}, the effect of shape k_{sh}, and the effect of attack angle k_α.

$$\tau_{\max(Pier)} = k_w k_{sp} k_{sh} k_\alpha \times 0.094\rho V^2 \left[\frac{1}{\log \mathrm{Re}} - \frac{1}{10} \right] \tag{4.6}$$

$$k_w = 1 + 16e^{-4\frac{y_1}{a}}$$

$$k_{sp} = 1 + 5e^{-1.1\frac{S}{a}}$$

$$k_{sh} = 1.15 + 7e^{-4\frac{L}{a}}$$

$$k_\alpha = 1 + 1.5\left(\frac{\theta}{90} \right)^{0.57}$$

where $\mathrm{Re} = \frac{Va}{\nu}$, ρ is the flow density, V is the upstream averaged velocity, y_1 is upstream water depth, B is the pier diameter, S is the pier spacing, L is the length of the pier in the flow direction, θ is the flow attack angle.

Awazu (1967) proposed an equation for estimating the maximum bed shear stress around a thin rectangular plate on the basis of 12 flume tests. Froude number was varied between 0.488 and 0.526 and the contraction ratio of channel was changed between 2.5 and 10. Awazu found that the contraction ratio affects the bed shear stress around spur dikes significantly, while the effect of the Froude number is negligible. The maximum amplification, $\tau_{\max}/\tau_1$, was about 3.8 in his experiments. He gave the maximum bed shear stress amplification around spur dikes as,

$$\log_{10}\left[\frac{\tau_{\max}}{\tau_1} \right] = 1.4\left(1 - \frac{L'}{L} \right) - 0.021 \tag{4.7}$$

where $\tau_{\max}$ is maximum bed shear stress around spur dike, τ_1 is approach bed shear stress, *L'* is spur dike protrusion length, *L* is the channel width.

Zaghloul (1974) related bed shear stress around a spur dike to the local velocity and vorticity. He proposed an empirical equation as

$$\tau = \frac{\gamma}{C^2} V \left(1 + K_1 \frac{\omega}{\omega_{nose}} + K_2 \right) \tag{4.8}$$

where τ is bed shear stress, γ is the unit weight of water, V is the local velocity, ω is the vorticity at the point, ω_{nose} is the vorticity at the spur dike nose, C is the Chezy's coefficient, K_1 and K_2 are the empirical constants. K_1 = 0.5 and K_2 is from 0 to 0.2 depending on the distance from the dike.

Rajaratman & Nwachuku (1983) reported 13 measurements of bed shear stress around groin-like structures. The amplification factor $\tau_{\max} / \tau_1$ was found to increase significantly from 3.0 to 4.5 when the blockage ratio varied from 0.08 to 0.16, whereas the influence of Froude number was negligible. The cylindrical pier was found to have slightly smaller amplification factor than that of the thin plate. However, the disturbed area was much smaller for the cylindrical pier compared to the thin plate.

Tingsanchali & Maheswaran (1990) proposed an equation to calculate the bed shear stress around a groin according to the depth averaged velocity. A 2-D numerical simulation of depth-averaged $k-\varepsilon$ turbulence model was used to study the effect of streamline curvature and establish a correction factor near the groin.

$$\tau_b = \gamma n^2 V^2 y^{-1/3} \left[1 + \tan^2 \left(2\alpha_0 \right) \right]^{0.5} \tag{4.9}$$

where τ_b is the bed shear stress, γ is the unit weight of water, n is Manning's coefficient V is the depth averaged velocity , y is the flow depth , α_0 is the turning angle between the surface streamline direction and the upstream approaching direction.

Molinas et al. (1998) proposed a maximum bed shear stress equation around an abutment based on 15 experiments with vertical wall abutment in a rectangular channel. The maximum bed shear stress around the abutment $\tau_{\max(Abut)}$ is taken as the summation of the shear stress at the contraction zone $\tau_{\max(Cont)}$ and the shear stress increment due to abutment alone $\tau^*_{\max}$. From the testing, the contribution from channel contraction is negligible when the length of the abutment is relatively short compared with the channel width. The equation is given below:

$$\tau_{\max(Abut)} = \tau_{\max(cont)} + \tau^*_{\max} \tag{4.10}$$

$$\frac{\tau_{\max(cont)}}{\tau_1} = \left(\frac{1}{R} \right) \left[1 + 5.46 R^{-3.89} Fr_1^{1.74} \left(\frac{L_a}{y_1} \right)^{2.5} \right]$$

$$\frac{\tau^*_{\max}}{\tau_1} = \frac{1}{R^2} \sqrt{1 + \tan^2 \alpha_\omega} - 1$$

$$\alpha_{\omega} = \left[1.485 Fr_1^{0.13} \left(\frac{L_a}{y} \right)^{0.06} \right]$$

where τ_1 is approach averaged bed shear stress, $R = 1 - L_a / L$, L_a is the length of the abutment, L is the half width of the channel, Fr_1 is the approached Froude number, y is the upstream water depth.

Nurtjahyo (2003) proposed an equation for the prediction of the maximum bed shear stress around abutment based on the correction of the open channel flow equation. The effect of the contraction and the effect of the contraction transition angle are considered. He stated that the effect of the water depth has been included in the open channel flow equation; and the contraction length of the channel has little influence on the maximum bed shear stress around the abutment.

$$\tau_{\max\_abut} = k_{a-R} k_{a-\theta} k_{a-y} k_{a-L} \gamma n^2 V^2 R_h^{-\frac{1}{3}} \tag{4.11}$$

$$k_{a-R} = 1.5 \frac{L_1}{L_2} - 0.5$$

$$k_{a-\theta} = 1 + 1.9 \left(\frac{\alpha}{90} \right) - \left(\frac{\alpha}{90} \right)^2$$

$$k_{a-L} \approx 1$$

$$k_{c-H} \approx 1$$

where, γ is the unit weight of the flow, V is the upstream averaged velocity, n is Manning's coefficient, R_h is hydraulic radius, L_1 is the upstream channel width, L_2 is the channel width at the contracted zone, L is the length of the contracted zone, α is the contraction transition angle.

When flooding, the bridge deck may become partially or entirely submerged. Pressure flow occurs when the water surface reaches or exceeds the low chord of the bridge deck, and the floodwater is forced under the bridge deck. The blockage ratio of the channel keeps increasing until the water surface begins to overtop the bridge deck. When the bridge deck is totally submerged, the deck behaves like a broad crested weir. The flow changes from exclusively pressure flow to a combined weir and pressure flow. Pressure flow causes an increase in velocity under the bridge deck and further increases the bed shear stress and the bridge scour. Studies of scour in pressure flow are still in the early stages. Abed (1991) studied the clear water pier scour under pressure flow conditions and found the scour depth to be 2.3-10 times greater than the free surface pier scour; Jones et al (1993) extended Abed's study to isolate the scour due to the deck from the scour due to the pier. One important finding was that the magnitude of the pier scour component under pressure flow was the same as the one under a free surface flow condition. Jones suggested that the scour component due to the pressure flow vertical deck contraction and

to the pressure flow pier scour be added. Umbrell et al (1998) analyzed the data in Jones' study and further improved the vertical deck contraction equation in pressure flow. Arneson (1997) proposed an equation for vertical deck contraction scour based on a similar flume tests study to Jones. Maryland SHA Bridge Scour Program (ABSCOUR) (2007) suggests 10% increase of the abutment scour depth when the approach water depth is equal to or greater than 1.2 times the height of the low chord above the riverbed. Most published work is about scour depth studies. The variation of the bed shear stress around bridge foundation under pressure flow is still unknown.

Laboratory studies of bridge scour have been extensively conducted on constant depth channel (rectangular channel) for simplicity while this is rare in the real world. Typical cross sections in rivers consist of a deep main channel and one or both sides of relatively shallow floodplain. Flood plain is often rougher than main channel. Consequently, velocities tend to be significantly greater in the main channel than on the floodplain. The velocity discrepancy between the main channel and flood plain causes the lateral momentum transfer and a secondary circulation. The flood plain and main channel flow interaction have been studied by many researchers: Rajaratnam & Ahmadi (1979), Knight & Demetriou (1983), Myers & Brennan (1990), Wormleaton & Merrett (1990) and Naot et al. (1993). However, the influence of the complex flow in the compound channel on the local bed shear stress around abutment is still unknown.

4.1.2 Issues in the Numerical Simulation of Bridge Scour on Cohesive Soils

3D numerical simulation of bridge scour is a very young topic in the history of bridge scour study. It is a promising tool for the study of the interaction between the water and the soil. Its development depends on both the computational fluid dynamics model and the soil erosion model. Bridge scour in cohesive soils, is usually associated with clear water scour. Therefore, the sediment transport equation will not be solved together with the fluid calculation. The erosion rate model for the cohesive soils is the shear stress model. The parameters appearing in the model are the bed shear stress, the critical shear stress of the soils, and the slope of the erosion rate vs. shear stress curve.

Wei et al. (1997) numerically studied the pier scour process in cohesive soils. The scour rate was assumed to be a linear function of the streambed shear stress. The important flow features, such as horseshoe vortex in front of the pier and the wake vortices behind the pier, were observed in the simulation. Simulations showed a reasonable prediction of the time history of scour depth with the tuned erosion rate function.

Chen (2002) conducted bridge scour simulations for a model scale complex rectangular pier configuration and for a prototype complex circular pier configuration. The erosion rate was assumed to vary linearly with the bed shear stress. Both the global and local pier scour were observed in the simulations. This shows the applicability of the three-dimensional numerical simulation to solve the really complicated engineering problems.

4.1.2.1 Critical Shear Stress of the Cohesive Soils

The critical shear stress τ_c for cohesionless soils has been studied extensively by researchers and many equations have been proposed and applied in practice. It depends mainly on the size of the soil particles. The critical shear stress for cohesive soils however relates more to the cohesive force existing between the fine particles. Research indicates that the critical shear stress in cohesive soils is influenced by the following parameters: Cation Exchange Capacity (CEC), Salinity, Sodium Adsorption Ratio (SAR), PH-level of pore water, temperature, w%, PI, Su, e, swell, D50, %200, clay mineral, dispersion ratio, turbulence, water chemical component, etc. (Winterwerp 1989, Cao 2001,).

Mirtskhoulava (1988) founded that there were two steps of the erosion of clay: (1) Initially, loosened particles with weak bonds are removed in a short period. This process is very similar to the erosion of cohesionless soils and leads to a rougher surface. (2) The bonds between aggregates of particles are destroyed gradually by the pulsating drag and lift forces caused by the turbulent flow and the aggregate is carried away simultaneously when the holding cohesion force disappears.

Dunn (1959) studied the correlation between the critical shear stress of soils and the vane shear strength experimentally. He concluded that the critical shear stress increases with an increase in clay content and proposed the critical shear stress equation as following,

$$\tau_c = \left(S_v + 8.62\right)\tan\theta \tag{4.12}$$

where τ_c is the critical shear stress (Pa), S_v is the vane shear strength (kPa), and θ is the slope of the linear relation between critical shear stress and vane shear strength.

Smerdon and Beasley (1959) investigated the influence of plasticity index, dispersion ratio, and mean particle size of clay on the critical shear stress by conducting flume tests. The relation between the critical shear stress, τ_c, and the plasticity index, PI, and Middleton's dispersion ratio, D_r, were given by

$$\tau_c = 0.0034\left(PI\right)^{0.84} \tag{4.13}$$

$$\tau_c = 0.213\left(D_r\right)^{-0.63} \tag{4.14}$$

where τ_c is the critical shear stress ($\mathrm{lbs/ft^2}$), PI is the plasticity index (%), Dr is Middleton's dispersion ratio.

Ivarson (1999) proposed a relation between critical shear stress τ_c, unconfined compressive strength of clay soils S_u, and mean average velocity V, based on the stream stability criteria for cohesive soils by Flaxman as:

$$\tau_c = \frac{12.11\log S_u - 28.67}{V} \tag{4.15}$$

where τ_c is the critical shear stress (lbs/ft^2), S_u is the unconfined compressive strength of clay soils (lbs/ft^2), and V is the mean average velocity (ft/sec).

Briaud et al (1999a, and 1999b) argued that the critical shear stress does not theoretically exist. However, they believe that the concept of critical shear stress is practically useful and suggest that τ_c should be defined based on a standardized small scour rate. This threshold scour rate is proposed as 0.1 mm/hr in the application of EFA (erosion function apparatus). The research also shows that large variations exist in the predicted τ_c among different researchers, from 0.02 to 100 Pa. Hence, they recommended to measure τ_c directly by EFA testing.

4.1.2.2 Erosion Rate of Soils

The scour around a bridge foundation can reach the equilibrium scour depth in cohesionless soils for just one flood since gravity is the main factor. By comparison, it may take several floods to reach the final scour depth in cohesive soils and take about tens or hundreds of years.

Arulanandan (1975) proposed an erosion rate equation for cohesive soils based on tests in the rotating cylinder apparatus with a number of different types of remolded clay. The erosion rate was found to be linearly proportional to the applied hydraulic shear stress. The following relationship is given as:

$$\begin{aligned} \dot{z} &= M\left(\frac{\tau}{\tau_c}-1\right) \qquad \tau \geq \tau_c \\ \dot{z} &= 0 \qquad\qquad\qquad\quad \tau < \tau_c \end{aligned} \tag{4.16}$$

where M is an erosion rate constant which varies from soil to soil.

Parchure and Mehta (1985) conducted a series of laboratory studies on the erosion of soft cohesive estuarial sediments. They developed an experimental procedure involving layer-by-layer erosion under a successively increasing bed shear stress for a certain range. An erosion rate equation for these estuarial soft clay sediments was proposed as follows,

$$\ln\frac{\dot{z}}{\dot{z}_f} = \alpha(\tau-\tau_s)^{1/2} \tag{4.17}$$

where $\dot{z}$ is erosion rate, $g/cm^2-\min$; $\dot{z}_f$ is erosion rate when $\tau-\tau_s=0$, $g/cm^2-\min$; α is a factor which is inversely proportional to the absolute temperature, $m/N^{1/2}$; τ is bed shear stress, N/m^2 ; τ_s is bed shear strength at depth z below initial bed-fluid interface, N/m^2 .

Shaikh et al. (1988) studied the erosion rate of unsaturated compacted sodium and calcium montmorillonite clay. The erosion rate was found to vary linearly with the shear stress and presented as

$$\dot{z} = C\tau \tag{4.18}$$

$$C = 4.41(SAR)^{-1.34}$$

where $\dot{z}$ is the erosion rate, $N/m^2/\min$;τ is the shear stress, N/m^2 ; C is an erosion rate coefficient, $\min^{-1}$; SAR is Sodium Adsorption Ratio.

Briaud et al. (1999a, 1999b, 2001a, 2001b, and, 2008) used the EFA (Erosion Function Apparatus) to measure the erosion rate of soils directly. The water flows over the soil in the Shelby tube and the soil is pushed out by a piston into the conduit as fast as the water erodes the soil. The erosion rate is the length of soil eroded per unit of time for a given flow velocity. The shear stress is calculated by using Moody Chart.

4.1.2.3 Effect of Roughness

The influence of river bed roughness on the flow field can be separated into (1) particle roughness accounting for the interaction between the flow and the individual particles and (2) form roughness due to bedform configurations. The influence of the particle roughness has been studied decades ago. The most well known result is due to Nikuradse (1933) (see, Cebeci and Bradshaw, 1977) for flow in pipe with a sand-roughened surface. The principal result from the data of Nikuradse is that the velocity distribution near a rough wall has the same slope (giving the same Karman constant, κ) as a smooth wall, but has a different intercept, ΔB:

$$u^+ = \frac{1}{\kappa}\ln y^+ + B - \Delta B \tag{4.19}$$

where $u^+ = U/u_\tau$, $y^+ = u_\tau y/\nu$, y is the distance from the wall, U is the velocity at y location, u_τ is the friction velocity, υ is kinematic viscosity, κ=0.418, B is the additive constant (for pipe, B=5.45 and for open channel, B=5.2), ΔB is a function of $k_s^+ (= k_s u_\tau/\nu)$, k_s is the surface roughness.

Ioselevich and Pilipenko (1974) (see, Cebeci and Bradshaw, 1977) gave the analytic fit to the data of Nikuradse:

$$\Delta B = \begin{cases} 0, \ k_s^+ < 2.25 \\ \left[B - 8.5 + \frac{1}{\kappa}\ln k_s^+ \right] \sin\left[0.4258\left(\ln k_s^+ - 0.811\right)\right], \ 2.25 \le k_s^+ < 90 \\ B - 8.5 + \frac{1}{\kappa}\ln k_s^+, \ k_s^+ > 90 \end{cases} \tag{4.20}$$

In a natural river channel, the river bed is rarely flat. Extensive studies on bed form configuration and geometry have been performed for river beds with cohesionless soils. Simons and Richardson (1963, 1966) classified bedforms into lower and upper flow regimes. Bridge scour happens in the lower regime, namely when the flow is subcritical (Fr <1). The typical types of bedforms are ripples and dunes; ripple shapes vary from nearly triangular to almost sinusoidal,

dunes are larger than ripples, and often triangular with fairly gentle upstream and downstream slopes. Liu (1957), Chabert and Chauvin (1963), Simons and Richardson (1963, 1966), Yalin (1964) and van Rijn (1984a, 1984b, 1984c) proposed many techniques to predict the formation and size of ripples and dunes. For these types of bedforms, the form roughness is dominant instead of particle roughness. Hence the roughness k_s in ΔB should include the contribution not only from particles, but also from the bedforms. For a cohesive river bed, the soil particles are extremely fine. Hence, the bed form roughness is the dominant factor.

In order to cover surface roughness, many researchers tried to modify the existing turbulence models for hydraulically smooth boundary conditions, such as Patel & Yoon (1995), Zhang et al (1996), and Durbin et al. (2001). Zhang et al (1996) stated that rough surface models can be classified into two categories: 1) equivalent sand grain roughness models;2) topographic form-drag models. Patel (1998) pointed out that the turbulence model for surface roughness should consider two factors: (a) the model has the capability to classify three roughness regions, i.e. hydraulic smooth, transitional, and fully-rough surfaces, and (b) the model has the capability to describe separated flow.

Patel & Yoon (1995) proposed a roughness turbulence model based on modifying mixing length in two layer $k-\varepsilon$ model. The roughness effect can also be included easily by changing the boundary conditions in the $k-\omega$ model. By comparing these two models, they concluded that the $k-\omega$ model of Wilcox is better than the modified $k-\varepsilon$ model and that the modified $k-\varepsilon$ model needed further tuning of the constants and damping functions in the length-scale equations.

Zhang et al. (1996) built a new-low-Reynolds-number $k-\varepsilon$ model to simulate turbulence flow over smooth and rough surfaces. They continued to adopt the equivalent sand grain roughness concept and modified reduction factors in the low Reynolds number models. They showed that the model is capable of predicting the log-law velocity profile, friction factors, turbulent kinetic energy and dissipation rate by comparing them with experiments.

Durbin et al. (2001) presented a modified two-layer $k-\varepsilon$ model. The new model modified the mixing length formula by adding a hydrodynamic roughness length into the wall distance and also modified the boundary condition for turbulence kinetic energy.

4.1.2.4 Effect of Turbulence Intensity

Nurtjahyo (2003) stated that bridge scour simulations with the mean shear stress model could not predict the scour pattern correctly, even if the scour depth was reasonable compared with the flume tests. The mean bed shear stress on the downstream side of the pier is small while the turbulent intensity is significant. This implies that the flow turbulence can contribute to an increase in the erosion. Nurtjahyo (2003) added a turbulence kinetic energy term into the erosion rate equation and improved the scour pattern prediction in clear water pier scour simulations.

Dufresne et al. (2007) investigated the influence of both the bed shear stress (BSS) and bed turbulent kinetic energy (BTKE) on the sedimentation and mass separation in storm-water tank. The authors found that BSS can only be used for no overflow cases; while BTKE should be cho-

sen for overflow cases. Neither of them taken independently can predict the measurement well for both conditions.

The study of the effect of turbulence on the scour process is still in the early stages. It is believed that the turbulence affects the whole scour process and contributes to both the final scour depth and scour pattern.

4.2 GOVERNING EQUATIONS FOR CHEN3D PROGRAM

CHEN3D (**C**omputerized **H**ydraulic **EN**gineering program for **3D** flow) has been employed in conjunction with a chimera domain decomposition approach for time-domain simulation of flow around complex hydraulic configurations. The turbulent flow is simulated using the Reynolds-Averaged form of the Navier-Stokes equations. The entire computational domain can be divided into two regions in order to facilitate the implementation of the two-layer turbulent model approach. One is the thin layer region around the solid boundary, where one-equation turbulence model is applied to account for the wall-damping effects; and the other one is the fully turbulent region away from the wall, employing the standard $k-\varepsilon$ two equation model to resolve the fully turbulent flow. The formulation has been described in detail in Chen and Patel (1988) and Chen and Korpus (1993). The CHEN3D program has been further developed to include the roughness and scour model in current research to simulate clear water scour. The approach by Patel and Yoon (1995) is used to capture the effect of roughness; and the method proposed by Nurtjahyo (2003) is implemented to perform the scour development. A summary of the approach is given below.

Governing Equations for Hydrodynamics

The non-dimensional Reynolds-Averaged Navier-Stokes equations for incompressible, viscous flow in Cartesian coordinates $(x_i,t)=(x,y,z,t)$ are as follows:

$$\sum_{i=1}^{3}\frac{\partial U_i}{\partial x_i}=0 \tag{4.21}$$

$$\frac{\partial U_i}{\partial t}+\sum_{j=1}^{3}\left(U_j\frac{\partial U_i}{\partial x_j}+\frac{\partial \overline{u_i u_j}}{\partial x_j}\right)+\frac{\partial p}{\partial x_i}-\frac{1}{\mathrm{Re}}\nabla^2 U_i=0 \tag{4.22}$$

Equation (4.21) represents the continuity equation and equation (4.22) represents the momentum equations. $U_i=(U,V,W)$ and $u_i=(u,v,w)$ represent Cartesian components of the mean and the fluctuating velocities respectively, t is time, p is pressure, $\mathrm{Re}=U_0B/\nu$ is the Reynolds number based on the characteristic length B, the reference velocity U_0, and the kinematic viscosity ν. All quantities in the above equations, and those which follow, are made dimensionless by U_0, B and fluid density ρ, and the body force is ignored here. For open channel flow, the influence of gravity can be considered as free surface boundary conditions.

In equation (4.22), the six additional Reynolds stresses terms $-\overline{u_i u_j}$ make the equations unsolvable without additional equations. Based on the assumption of Boussinesq, the Reynolds stresses can be expressed in terms of an isotropic eddy viscosity ν_t and the mean rate of strain, which is analogous to the molecular viscosity. The Reynolds stresses can then be written as:

$$-\overline{u_i u_j} = \nu_t \left(\frac{\partial U_i}{\partial x^j} + \frac{\partial U_j}{\partial x^i} \right) - \frac{2}{3} \delta_{ij} k \tag{4.23}$$

where $k = \left(\overline{uu} + \overline{vv} + \overline{ww}\right)/2$ is the turbulent kinetic energy and δ_{ij} is the Kronecker delta. Substituting into (4.22) yields:

$$\frac{\partial U_i}{\partial t} + \sum_{j=1}^{3} \left(\left(U_j - \frac{\partial \nu_t}{\partial x_j} \right) \frac{\partial U_i}{\partial x_j} - \frac{\partial \nu_t}{\partial x_j} \frac{\partial U_j}{\partial x_i} \right) + \frac{\partial}{\partial x_i} \left(p + \frac{2}{3} k \right) - \frac{1}{R_U} \nabla^2 U_i = 0 \tag{4.24}$$

The quantity $1/R_U = 1/\mathrm{Re} + \nu_t/\sigma_U$ represents the effective turbulent viscosity. The eddy viscosity can be computed from the turbulent kinetic energy k and its dissipation rate ε:

$$\nu_t = C_\mu \frac{k^2}{\varepsilon} \tag{4.25}$$

where $C_\mu = 0.09$ and the turbulent quantities of k and ε can be determined from the corresponding transport equations:

$$\frac{\partial k}{\partial t} + \sum_{j=1}^{3} \left(U_j - \frac{1}{\sigma_k} \frac{\partial \nu_t}{\partial x_j} \right) \frac{\partial k}{\partial x_j} - \frac{1}{R_k} \nabla^2 k - G + \varepsilon = 0 \tag{4.26}$$

$$\frac{\partial \varepsilon}{\partial t} + \sum_{j=1}^{3} \left(U_j - \frac{1}{\sigma_\varepsilon} \frac{\partial \nu_t}{\partial x_j} \right) \frac{\partial \varepsilon}{\partial x_j} - \frac{1}{R_\varepsilon} \nabla^2 \varepsilon - C_{\varepsilon 1} \frac{\varepsilon}{k} G + C_{\varepsilon 2} \frac{\varepsilon^2}{k} = 0 \tag{4.27}$$

$$G = \nu_t \sum_{j=1}^{3} \sum_{i=1}^{3} \left(\frac{\partial U_i}{\partial x_j} + \frac{\partial U_j}{\partial x_i} \right)^2 \tag{4.28}$$

the coefficients $C_{\varepsilon 1} = 1.44$, $C_{\varepsilon 2} = 1.92$ $\sigma_u = \sigma_k = 1.0$ $\sigma_\varepsilon = 1.3$ are given in Chen and Patel (1988). The effective viscosities in equation (4.26) and (4.27) are taken as $1/R_k = 1/\mathrm{Re} + \nu_t/\sigma_k$, and $1/R_\varepsilon = 1/\mathrm{Re} + \nu_t/\sigma_\varepsilon$, respectively.

The standard $k-\varepsilon$ two equations model mentioned above is only applied in the fully turbulent regions. In the two-layer approach of Chen and Patel (1988), the one-equation of Wolfstein (1969) is employed in the near wall region. Close to the wall, the dissipation rate is determined from the turbulent production and the dissipation length scale, rather than being solved from equation (4.27):

$$\varepsilon = \frac{k^{3/2}}{l_\varepsilon} \tag{4.29}$$

$$l_\varepsilon = C_l y\left[1 - \exp\left(-R_y / A_\varepsilon\right)\right]; R_y = \mathrm{Re}\sqrt{k}\, y \tag{4.30}$$

The inner layer is specified when the parameter $y^+ = U_\tau y/\nu \le 300 - 1000$, where y is the dimensionless normal distance from the wall and $U_\tau = \sqrt{\tau_w / \rho}$ is the friction or shear velocity. Using this relationship, the turbulent production can be determined from equation (4.26). The eddy viscosity is then found from:

$$v_t = C_\mu \sqrt{k} l_\mu \tag{4.31}$$

$$l_\mu = C_l y\left[1 - \exp\left(-R_y / A_\mu\right)\right] \tag{4.32}$$

The constants $C_l = \kappa C_\mu^{-0.75}$, $A_\mu = 70$, $A_\varepsilon = 2C_l$ and $\kappa = 0.418$ are given in Chen and Patel (1988) and chosen to yield a smooth transition of eddy viscosity between the two regions.

The above one equation model for the inner layer is based on the assumption of a hydrodynamic smooth wall. Patel and Yoon (1995) extended the model to a rough wall by modifying the two length scales:

$$l_\mu = C_l (y + \Delta y)\left[1 - \exp\left(-\frac{\left(R_y + \Delta R_y\right)}{A_\mu}\right)\right] \tag{4.33}$$

$$l_\varepsilon = C_l (y + \Delta y)\left[1 - \exp\left(-\frac{\left(R_y + \Delta R_y\right)}{A_\varepsilon}\right)\right] \tag{4.34}$$

$$\Delta R_y = \mathrm{Re}\sqrt{k}\,\Delta y \tag{4.35}$$

The Δy is normalized by the shear velocity U_τ and the kinematic viscosity ν to yield $\Delta y^+ = U_\tau \Delta y / \nu$, and Δy^+ is related to the roughness of the wall and expressed by:

$$\Delta y^+ = 0.9\left[\sqrt{k_s^+} - k_s^+ \exp\left(-\frac{k_s^+}{6}\right)\right] \tag{4.36}$$

where $k_s^+ = \mathrm{Re}\, k_s U_\tau$, and k_s is the normalized height of the sand grain. In case of non-uniform sand, the median diameter D_{50} is usually chosen.

To facilitate the coding of the program, the transport equations for U_i, k and ε are rewritten in the general form:

$$\nabla^2\phi = R_\phi\left[\left(U_j - \frac{1}{\sigma_\phi}\frac{\partial \nu_t}{\partial x_j}\right)\frac{\partial \phi}{\partial x_j} + \frac{\partial \phi}{\partial t}\right] + s_\phi \tag{4.37}$$

where ϕ represents any of the transport quantities U_i k and ε. The source functions s_ϕ are:

$$s_{U_i} = R_U\left[\frac{\partial}{\partial x_i}\left(p + \frac{2}{3}k\right) - \sum_{j=1}^{3}\frac{\partial \nu_t}{\partial x_j}\frac{\partial U_j}{\partial x_i}\right] \tag{4.38}$$

$$s_k = -R_k(G - \varepsilon) \tag{4.39}$$

$$s_\varepsilon = -R_\varepsilon\frac{\varepsilon}{k}(C_{e1}G - C_{\varepsilon 2}\varepsilon) \tag{4.40}$$

To accurately solve the flow around the boundary of complex geometries, the boundary fitted coordinate system is used in CHEN3D. Hence, the Cartesian coordinate $(x_i, t) = (x, y, z, t)$employed in the physical space, has to be transformed to a general curvilinear coordinate system $(\xi^1, \xi^2, \xi^3, \tau) = (\xi, \eta, \zeta, \tau)$. The vector operations in the transformed coordinates are:

$$(\nabla\phi)_i = \frac{\partial \phi}{\partial x_i} = \frac{1}{J}\sum_{j=1}^{3} b_i^j \frac{\partial \phi}{\partial \xi^j} \tag{4.41}$$

$$\nabla^2\phi = \sum_{i=1}^{3}\sum_{j=1}^{3}(g^{ij}\frac{\partial^2\phi}{\partial\xi^i\xi^j} + \sum_{l=1}^{3}\Gamma_{ij}^l\frac{\partial\phi}{\partial\xi^l}) = \sum_{i=1}^{3}\sum_{j=1}^{3}g^{ij}\frac{\partial^2\phi}{\partial\xi^i\xi^j} + \sum_{j=1}^{3}f^j\frac{\partial\phi}{\partial\xi^j} \tag{4.42}$$

$$\frac{\partial \phi}{\partial t} = \frac{\partial \phi}{\partial \tau} - \frac{1}{J}\sum_{i=1}^{3}\sum_{j=1}^{3} b_i^j \frac{\partial x_i}{\partial \tau}\frac{\partial \phi}{\partial \xi^j} \tag{4.43}$$

$$b_i^l = J\frac{\partial \xi^l}{\partial x_i} = \left(\frac{\partial x_j}{\partial \xi^m}\frac{\partial x_k}{\partial \xi^n} - \frac{\partial x_k}{\partial \xi^m}\frac{\partial x_j}{\partial \xi^n}\right) \tag{4.44}$$

$$g^{li} = \sum_{p=1}^{3} b_p^l b_p^i = \frac{1}{J^2}\left(g_{mj}g_{nk} - g_{mk}g_{nj}\right) \tag{4.45}$$

$$f^i = \nabla^2\xi^i = -\sum_{m=1}^{3}\sum_{n=1}^{3} g^{mn}\Gamma_{mn}^i = \frac{1}{J}\sum_{j=1}^{3}\frac{\partial}{\partial \xi^j}\left(Jg^{ij}\right) \tag{4.46}$$

$$g_{ij} = \sum_{m=1}^{3}\frac{\partial x_m}{\partial \xi^i}\frac{\partial x_m}{\partial \xi^j} \tag{4.47}$$

$$J^2 = \det(g_{ij}) = g_{11}g_{22}g_{33} + 2g_{12}g_{13}g_{23} - g_{11}(g_{23})^2 - g_{22}(g_{13})^2 - g_{33}(g_{12})^2 \tag{4.48}$$

where b_i^l, g^{li}, and f^i are the geometric coefficients. Using these relationships, equations (4.21)

and (4.37) are transformed into:

$$\sum_{i=1}^{3}\frac{\partial U_i}{\partial x_i}=\sum_{i=1}^{3}\sum_{j=1}^{3}\frac{\partial \xi^j}{\partial x_i}\frac{\partial U_i}{\partial \xi^j}=\frac{1}{J}\sum_{i=1}^{3}\sum_{j=1}^{3}\frac{\partial}{\partial \xi^j}(b_i^j U_i)=0 \tag{4.49}$$

$$\sum_{j=1}^{3}\left(g^{jj}\frac{\partial^2\phi}{\partial\xi^j\partial\xi^j}-2a_\phi^j\frac{\partial\phi}{\partial\xi^j}\right)=R_\phi\frac{\partial\phi}{\partial\tau}+S_\phi \tag{4.50}$$

where

$$2a_\phi^j=\frac{R_\phi}{J}\sum_{n=1}^{3}b_n^j\left(U_n-\frac{\partial x_n}{\partial\tau}-\frac{1}{J\sigma_\phi}\sum_{m=1}^{3}b_j^m\frac{\partial\nu_t}{\partial\xi_m}\right)-f^j \tag{4.51}$$

$$S_\phi=s_\phi-2\left(g^{12}\frac{\partial^2\phi}{\partial\xi^1\partial\xi^2}+g^{13}\frac{\partial^2\phi}{\partial\xi^1\partial\xi^3}+g^{23}\frac{\partial^2\phi}{\partial\xi^2\partial\xi^3}\right) \tag{4.52}$$

$$G=\frac{1}{2}\nu_t\sum_{j=1}^{3}\sum_{i=1}^{3}\left(\frac{1}{J}\sum_{l=1}^{3}\left(b_j^l\frac{\partial U_i}{\partial\xi^l}+b_i^l\frac{\partial U_j}{\partial\xi^l}\right)\right)^2 \tag{4.53}$$

$$s_{U_i}=\frac{R_U}{J}\sum_{l=1}^{3}b_i^l\frac{\partial}{\partial\xi^l}\left(p+\frac{2}{3}k\right)-R_U\sum_{j=1}^{3}\left(\frac{1}{J}\sum_{l=1}^{3}b_j^l\frac{\partial\nu_t}{\partial\xi^l}\right)\left(\frac{1}{J}\sum_{l=1}^{3}b_i^l\frac{\partial U_j}{\partial\xi^l}\right) \tag{4.54}$$

$$s_k=-R_k(G-\varepsilon) \tag{4.55}$$

$$s_\varepsilon=-R_\varepsilon\frac{\varepsilon}{k}(C_{e1}G-C_{\varepsilon 2}\varepsilon) \tag{4.56}$$

Finite analytic method (FAM)

In CHEN3D, the governing equation is locally linearized in each rectangular numerical element, $\Delta\xi=\Delta\eta=\Delta\zeta=2$, by calculating the coefficients at the interior node (P) of each local element. The second order accuracy time domain discretization scheme was proposed by Liu (2002). Based on Chen et al. (1990), the following is the final 13-point FAM formula for the equation as described in Figure 4.1.

$$\begin{aligned}\phi_p^n=&\frac{1}{1+C_p\left[C_U+C_D+1.5R_\phi/\Delta\tau\right]}\\&\left\{\sum_1^8 C_{nb}\phi_{nb}+C_p\left[C_U\phi_U+C_D\phi_D+\frac{R_\phi}{\Delta\tau}\left(2\phi_p^{n-1}-0.5\phi_p^{n-2}\right)\right]-C_p\left(S_\phi\right)_p\right\}\end{aligned} \tag{4.57}$$

The subscript nb denotes neighboring nodes (NE: northeast, NW: northwest, etc).

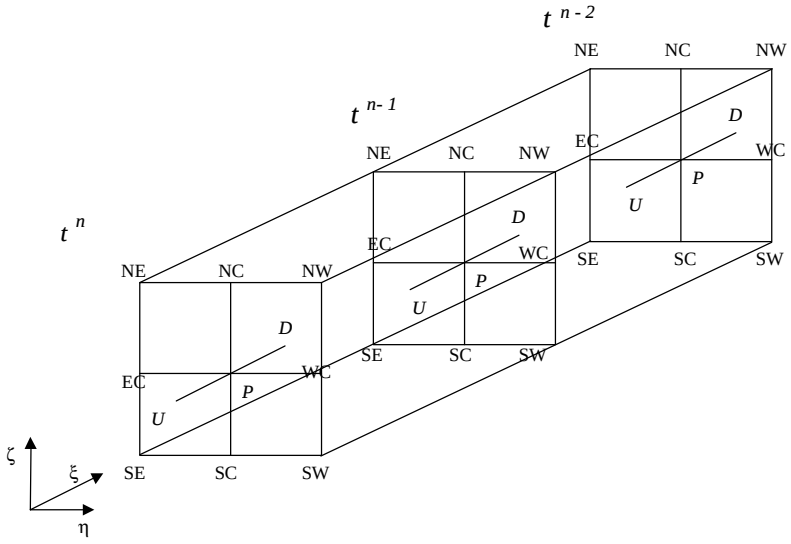

Figure 4.1 - Finite analytic local element.

The finite analytic coefficients C_{nb}, C_P, C_U, C_D have been explained in detail by Chen and Chen (1982,1984). Equation (4.57) indicates that ϕ_P^n depends on all eight neighboring nodal values in the $\eta\zeta$ plane as well as the values of the upstream node U, the downstream node D, and the value at the previous time step (n-1) and (n-2). This equation is implicit in both space and time.

Continuity equation: velocity-pressure coupling

In most practical applications, the pressure is unknown and must be determined by requiring the velocity field to satisfy the continuity equation. Since a direct method for the simultaneous solution of all six equations is not feasible with present computer capacity, it is necessary to convert the continuity equation into an algorithm for the calculation of the pressure field appearing in the momentum equation. Chen and Patel (1989) have proposed the hybrid SIMPLER/PISO algorithm for velocity-pressure coupling. In the SIMPLER/PISO algorithm, it is convenient to use contravariant components $\left(U^1, U^2, U^3\right)$ of the velocity vector in the body-fitted coordinates $\left(\xi^1, \xi^2, \xi^3, \tau\right)$. Hence, the continuity equation can be expressed as:

$$\sum_{i=1}^{3} \frac{\partial U^i}{\partial \xi^i} = 0 \tag{4.58}$$

Furthermore, the contravariant components of the velocity vector can be specified into a pressure dependent term and a pseudo-velocity term as below:

$$U^i = \hat{U}^i - E^{ii} \frac{\partial p}{\partial \xi^i} \tag{4.59}$$

where

$$\hat{U}^i = \sum_{n=1}^{3} b_n^i \hat{U}^n - E^{ij} \frac{\partial p}{\partial \xi^j} - E^{ik} \frac{\partial p}{\xi^k} \tag{4.60}$$

$$E^{ij} = \frac{R_\phi C_p}{J\left[1 + C_p\left(C_U + C_D + 1.5R_\phi / \Delta\tau\right)\right]} \sum_{m=1}^{3} b_m^i b_m^j \tag{4.61}$$

A relationship for pressure can now be derived by requiring the contravariant velocity field, U^i, to satisfy the equation of continuity. Approximating equation (4.58) with central differences and substituting equation (4.59) for each point in the stencil gives:

$$\begin{aligned} &\left(E_d^{11} + E_u^{11} + E_n^{22} + E_s^{22} + E_e^{33} + E_w^{33}\right)P_p \\ &= E_d^{11}P_D + E_u^{11}P_U + E_n^{22}P_{NC} + E_s^{22}P_{SC} + E_e^{33}P_{EC} + E_w^{33}P_{WC} - \hat{D} \end{aligned} \tag{4.62}$$

where

$$\begin{aligned} \hat{D} &= \hat{U}_d^1 - \hat{U}_u^1 + \hat{U}_n^2 - \hat{U}_s^2 + \hat{U}_e^3 - \hat{U}_w^3 \\ &= \frac{1}{2}\left(\hat{U}_D^1 - \hat{U}_U^1 + \hat{U}_{NC}^2 - \hat{U}_{SC}^2 + \hat{U}_{EC}^3 - \hat{U}_{WC}^3\right) \end{aligned} \tag{4.63}$$

Boundary Conditions

Boundary conditions describe the interface between the surroundings and the system that is modeled. The boundary conditions for the system can be classified into no-slip boundary, inlet boundary, outlet boundary and free surface boundary conditions.

(1) No slip boundary condition

At the abutment surface or riverbed surface, a no slip boundary applies in all directions, i.e.:

$$U_i = 0 \tag{4.64}$$

Extrapolation points near the solid boundary are used to determine the pressure at the solid boundary surface.

$$\frac{\partial p}{\partial n} = 0 \tag{4.65}$$

(2) Outlet boundary condition

In the viscous flow, a zero gradient boundary condition is used in the far field, which can be expressed as:

$$\frac{\partial U_i}{\partial n} = \frac{\partial p}{\partial n} = 0 \tag{4.66}$$

(3) Inlet boundary condition

On the inlet, the velocity and the pressure are prescribed. It is assumed:

$$U_1 = 1, U_2 = U_3 = p = 0 \tag{4.67}$$

(4) Free surface boundary condition

The free surface elevation δ is a function of two other space directions and time, i.e., $\delta = z - z_{surf} = \delta(x, y, t)$, z_{surf} is the initial water surface elevation taken as the datum for the hydrostatic force. Based on the chain rule, the kinematic boundary conditions on the free surface are expressed as:

$$U_3 = \frac{d\delta}{dt} = \frac{\partial \delta}{\partial t} + U_1 \frac{\partial \delta}{\partial x} + U_2 \frac{\partial \delta}{\partial y} \tag{4.68}$$

Equation (4.68) ensures that the fluid particles on the free surface remain on the free surface and can be solved by simply extrapolating the velocities from the inner fluid domain. For an open channel problem, gravity plays an important role, which has not been included in the momentum equation (4.22). By ignoring the surface tension and free surface turbulent boundary layer, the effect of the gravity can be considered in the pressure term. Conservation of momentum for a viscous fluid flow with a gravitational acceleration in the vertical direction can be written as:

$$\frac{\partial U_i}{\partial t} + \sum_{j=1}^{3} \left(U_j \frac{\partial U_i}{\partial x_j} + \frac{\partial \overline{u_i u_j}}{\partial x_j} \right) + \frac{\partial p}{\partial x_i} - \frac{1}{\mathrm{Re}} \nabla^2 U_i + \frac{\delta_{i3}}{Fr^2} = 0 \tag{4.69}$$

Fr is the Froude number, $Fr = \frac{U_0}{\sqrt{gB}}$, where g is the gravitational acceleration.

By introducing a new variable for the pressure, which includes both the hydrostatic and static component of the pressure $\psi = p + \frac{x_3}{Fr^2}$, the equation of the momentum can be rewritten as:

$$\frac{\partial U_i}{\partial t} + \sum_{j=1}^{3} \left(U_j \frac{\partial U_i}{\partial x_j} + \frac{\partial \overline{u_i u_j}}{\partial x_j} \right) + \frac{\partial \psi}{\partial x_i} - \frac{1}{\mathrm{Re}} \nabla^2 U_i = 0 \tag{4.70}$$

The Froude number now enters explicitly in the boundary condition instead of the governing equation. The procedure mentioned in the previous section can still be used to solve the open channel flow with a suitable boundary condition.

A dynamic condition has also to be fulfilled at the surface. If the surface tension is neglected and the flow is considered non viscous on the surface, the dynamic boundary conditions can be simplified to be $p = p_{atm}$, p_{atm} is the atmospheric pressure. The corresponding boundary condition for ψ becomes

$$\psi = p_{atm} + \frac{\delta}{Fr^2} \tag{4.71}$$

If we say $p_{atm} = 0$, then

$$\psi = \frac{\delta}{Fr^2} \tag{4.72}$$

Clear Water Scour

Clear water scour means that no deposition takes place. Once the soil is eroded, it is gone. Clear water scour usually exists for cohesive riverbed. The initiation of the scour process is determined by the critical shear stress, the smallest streambed shear stress to start the erosion process. Based on this understanding, the scour rate can be expressed as a function of the streambed shear stress and the critical shear stress. The scour rate equation can be written in the following dimensional form:

$$\dot{z} = \dot{z}(\tau_b, \tau_c) \tag{4.73}$$

where $\dot{z}$ is the scour rate, τ_b is the streambed shear stress, and τ_c is the critical shear stress. τ_b is evaluated using the Newtonian stress-strain law:

$$\tau_b = \left| \rho \nu \frac{\partial q}{\partial z_n^*} \right| \tag{4.74}$$

where q is the velocity, z_n^* is the normal distance from the streambed. In the numerical computations, after the flow field is computed at each time step, the scour rate at each point of the stream bed is determined by the scour rate equation and τ_b. The increase in scour depth is then evaluated by multiplying the scour rate by the time increment.

Overall Solution Algorithm

For the scour problem involving the grid movement on the river bed and free surface variation, the solution procedure can be summarized as follows:

1. Construct the grid for each component of the configuration.
2. Construct a boundary condition table specifying appropriate boundary conditions for each face.
3. Specify the initial condition for velocity, pressure, and turbulence fields.
4. Determine interpolation information to link the grids together using the PEGSUS program.
5. Calculate the geometric coefficients.
6. Calculate the finite analytic coefficients and source functions.

7. Solve the momentum equations (U_i) and turbulence equations (k, ε) using the iterative ADI scheme.
8. Calculate the pseudo velocities (V^i) and calculate pressure (p) using the iterative ADI scheme.
9. Repeat step 7 and 8 for several internal iterations to get the converged result.
10. Calculate the new free surface elevation using kinematics free surface boundary conditions.
11. For clear water scour, calculate the new bed surface elevation using the scour rate equation.
12. Adjust the volume grid to conform to free surface and riverbed elevations in z-direction.
13. Return to step 4 for next time step.

4.3 MAXIMUM BED SHEAR STRESS AROUND AN ABUTMENT IN OPEN CHANNEL FLOW

The maximum bed shear stress around an abutment, one of the two basic parameters in the SRICOS method, is studied in this chapter. All the simulation results given in this chapter are for open channel flow. The maximum bed shear stress around an abutment is studied first for the simple rectangular channel. After establishing the maximum bed shear stress equation for a rectangular channel, compound channel correction factors are proposed so that the equation can be extended to include compound channel situations. The CHEN3D program introduced in chapter III is used for all numerical simulations. The flume test cases performed in this study are simulated numerically and used to verify the proposed equation. The final equation for the maximum bed shear stress around an abutment is recommended based on the results of flume tests and the erosion function of the soils from EFA testing.

4.3.1 Methodology

A typical river channel including the abutment and approach embankment is presented in Figure 4.2. In the real world, the elevation of the river bed may change gradually from the center of the main channel to the flood plain and have no clear main channel slope. The main channel slope β_m may vary over a large range, depending on the soil type, from a small number in cohesionless soils to almost vertical in cohesive soils. However, β_m is believed to be a minor factor in the current study so that a constant main channel slope (1V:1H) is used in all compound channel simulations.

To simplify the problem, the rectangular channel is studied first, with $\beta_m = 0$, $y_m = y_f = y$ and $L = L_m + L_f$ (Figure 4.2). The maximum bed shear stress around an abutment in a rectangular channel is believed to be dependent on the abutment geometry, channel width, water depth,

approach velocity, water density, fluid viscosity and gravitational acceleration. The relationship is of the form:

$$\tau_{\max(Abut)} = f\left[\rho, V, \nu, y, g, L_a, L, W_a, \beta_a, \theta\right] \tag{4.75}$$

where $\tau_{\max(Abut)}$ = maximum bed shear stress around abutment, ρ = water density, V = upstream mean velocity, ν = kinematic viscosity of the fluid , y = upstream water depth, g = gravitational acceleration, L_a = length of abutment and the approach embankment(to the toe of the abutment), L = half width of the channel, W_a = top width of the abutment, β_a = slope of the abutment, and θ = skew angle of approach embankment.

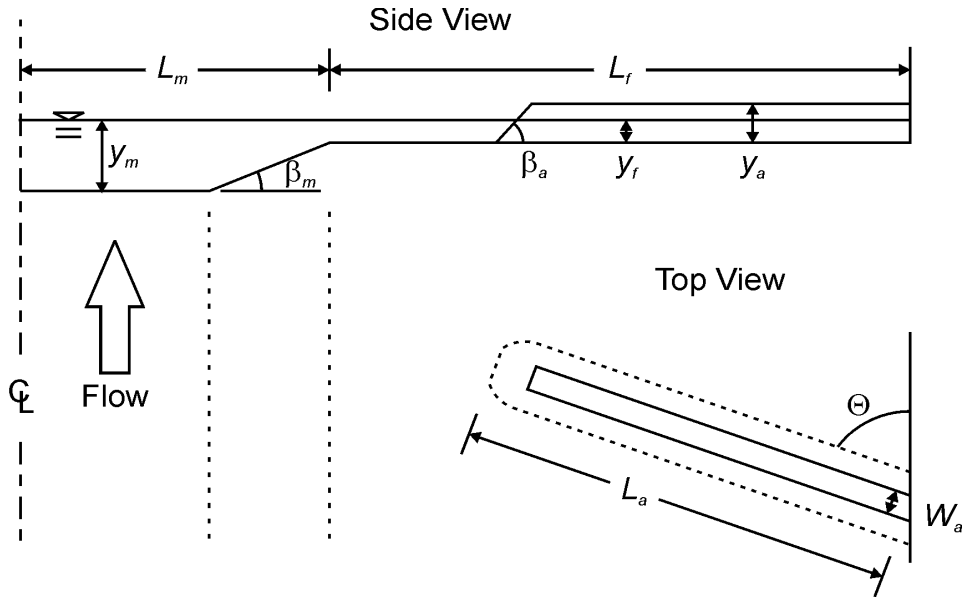

L: half width of channel	L_m: half width of main channel
y_m: water depth on main channel	L_a: Length of approach embankment
tan(β_a): slope of abutment (V:H)	V: upstream mean velocity
L_f: width of flood plain	Θ (°)skew angle of approach embankment
y_f: water depth on flood plain	W_a: top width of abutment
y: water depth for constant depth channel ($y = y_f = y_m$)	

Figure 4.2 - Definition of the parameters in abutment scour problem.

Dimensional analysis of equation (4.75) results in:

$$\frac{\tau_{\max}}{\rho V^2} = f\left[\frac{VW_a}{\nu}, \frac{V}{\sqrt{gy}}, \frac{L_a}{W_a}, \frac{L_a}{L}, \frac{y}{W_a}, \beta_a, \Theta\right] \tag{4.76}$$

It is desirable to use the top width of the abutment W_a as the characteristic length because W_a is typically fixed for a given bridge (close to the width of the bridge deck). $\mathrm{Re} = \frac{VW_a}{\nu}$ is the abutment size based Reynolds number; $\frac{V}{\sqrt{gy}}$ is the upstream Froude number; $\frac{L_a}{W_a}$ is the aspect ratio of the abutment and approach embankment, but $\frac{L'}{W_a}$ will be used in the following study (L' is the projected abutment length normal to the flow direction); $\frac{y}{W_a}$ is the relative flow depth. For a rectangular channel, the upstream mean velocity is assumed to be uniform across the entire channel. The channel unit discharge ratio C_r defined in terms of flow rate from upstream as $\frac{Q_{total}}{Q_{total} - Q_{blocked}}$ is identical to the area ratio $\frac{A_{total}}{A_{total} - A_{blocked}}$. It is also worthwhile to note that C_r is equal to $\frac{L}{L - L'}$ for the vertical wall and wing-wall abutments. For convenience, C_r based on the area ratio $\frac{A_{total}}{A_{total} - A_{blocked}}$ will be used to replace the blockage ratio in the dimensional analysis and the following study.

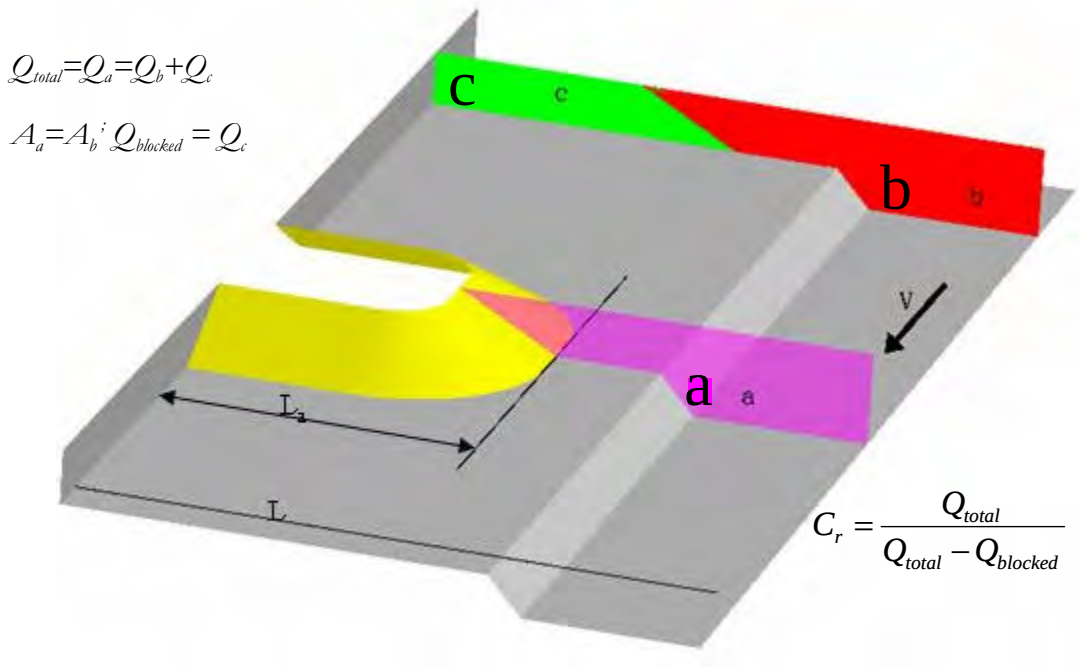

Figure 4.3 - Definition of the channel unit discharge ratio.

The methodology to study the influence of various parameters makes use of a reference case and the parametric studies of the dimensionless parameters given in the dimensional analysis. According to previous studies (Briaud et al. 1999a, 2004), it is believed that the Reynolds number is the determinant factor for the maximum bed shear stress around the abutment when the relative water depth is greater than two. In the parametric study, only one dimensionless parameter is varied at a time while all others are kept identical to the reference case. The relationship between the varying dimensionless parameter and the maximum bed shear stress can then be determined through data regression. By assuming that these dimensionless parameters are independent, the equation of maximum bed shear stress around an abutment in a rectangular channel can be derived by multiplying the influence factors together. The influence of the compound channel geometry will be investigated by comparing the results of a series of cases simulated with different compound channel configurations.

4.3.2 Reference Case

The flow pattern around an abutment is considered to be similar to that around a pier of shape equivalent to the abutment and its mirror image with respect to the channel wall. The maximum bed shear stress at the abutment, however, should be less than that around the equivalent pier due to the retarding effects of channel wall on the flow (Melville, 1997). Based on previous research (NCHRP 24-15, Briaud et al., 2004), the influence of water depth on the maximum bed shear stress around a bridge pier can be ignored when the water depth is deeper than two times the pier diameter, which is called the deep water condition. Actually, this indicates that the influence of Froude number is negligible as long as the relative flow depth is large enough. Therefore, it is convenient to define the reference case as a vertical wall abutment in a rectangular channel as shown in Figure 4.2. The abutment length is chosen to be one-half of the abutment width such that the abutment together with its mirror image forms a square pier. The orientation of the abutment is perpendicular to the flow direction and the water depth is twice the abutment width to ensure that the influence of Froude number is negligible. The dimensions of the reference case can be determined after the flume tests performed in this study. The width of the flume is 3.66m, which is equal to the half width of the channel L since only half of the river is simulated in the flume tests. The top width of the abutment W_a is 0.46m. So the water depth is 0.91m. As seen in **Error! Reference source not found.**, the half width of the channel L is 8 times of the abutment width W_a, which gives a rather small unit discharge ratio of 1.07.

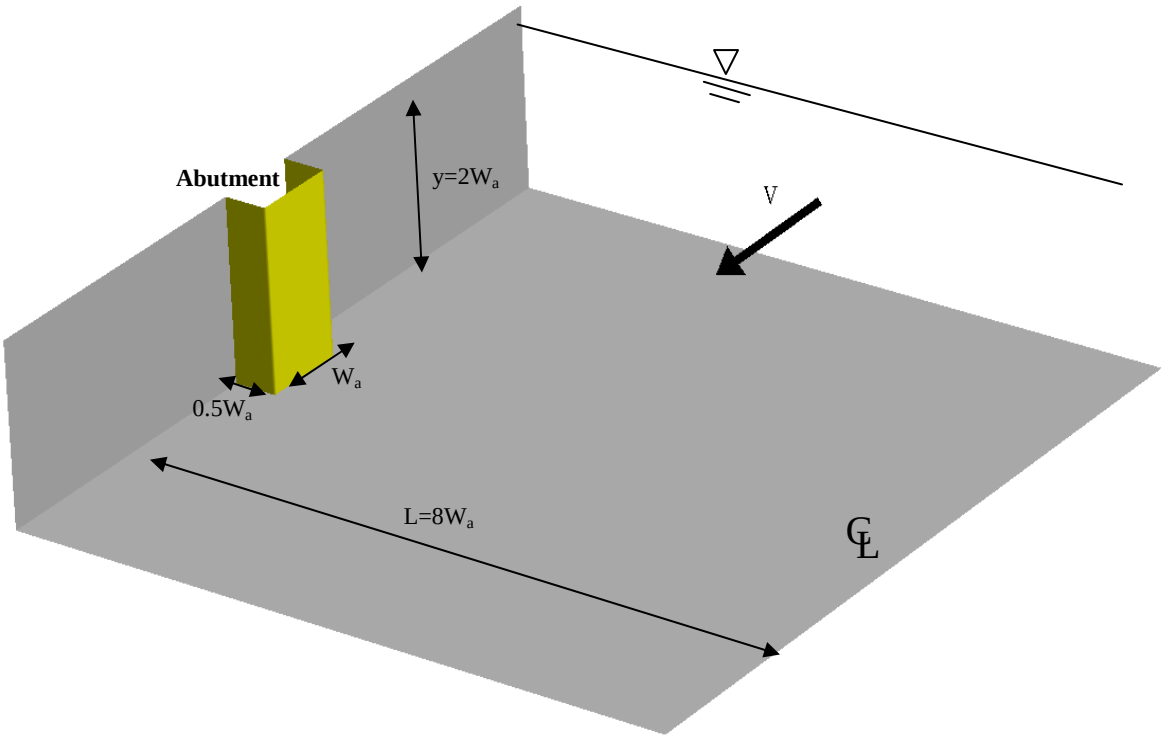

Figure 4.4 - Diagram of the reference case.

A dimensionless (normalized by the abutment top width W_a) Cartesian coordinate system (x,y,z) = (X/Wa, Y/Wa, Z/Wa) is used in the numerical simulations. The xy plane is fixed as the horizontal river bottom; the z coordinate is pointed upward from the riverbed to the water surface; the x coordinate is pointed from upstream to downstream along the straight channel.

An orthogonal grid system is desirable in the numerical simulations. Hence, the entire computation domain is decomposed into several blocks to facilitate the generation of the rectangular grids. As shown in Figure 4.5, a fully-connected body-fitted grid system is used with one cell overlap between neighboring blocks. The numerical grid of the reference case consists of four blocks. The number of the grid points from Block1 to Block 4 are 40×75×31, 29×54×31, 69×26×31, and 80×75×31, respectively, for a total of 383,160 grid points. A multi-block grid is a special condition of the Chimera grid and the data communication between difference blocks is performed through the PEGSUS program (Suhs &Tramel, 1991).

In the CHEN3D program, the two layer method is implemented to solve the flow field all the way to the solid surface. A one equation model is used for the near-wall region and the standard $k-\varepsilon$ model is used in the outer region away from the wall. To accurately solve the near wall flow including the laminar sublayer and buffer layer, the first grid point near the solid surface is placed within the viscous sublayer and satisfies the requirement of $y^+ < 1$, where $y^+ = \mathrm{Re} u_\tau y_n$, y_n = the normalized distance to the wall and u_τ = normalized friction velocity. Therefore, the grid in the near wall region must be extremely fine so that the velocity gradient

can be resolved correctly. To reduce the CPU time and the memory requirement, the channel is assumed to be symmetrical and only one-half of the channel is studied.

As mentioned in the dimensional analysis, the Reynolds number Re=VW_a/ν is defined based on the upstream mean velocity V, the abutment top width W_a and the kinematic viscosity ν (20°C). For the reference case, a Reynolds number of 10^5 is chosen. It is a typical magnitude in most flume tests, which is equivalent to 0.22m/s upstream velocity and 0.46m of abutment top width. A no-slip boundary condition is applied on the river bottom and abutment face. A rigid lid is applied on the free surface since the influence of the water surface is negligible. A dimensionless time increment of 0.2 is chosen in the simulation. The result is found to converge after about 5000 iterations.

Figure 4.6 shows the flow pattern around the abutment on the free surface. The abutment causes complicated flow features, including vortex shedding, wake vortices and large recirculation behind the abutment. Upstream of the abutment, the affected area is very small, about one time the abutment length. Downstream of the abutment, the affected area is very large. The area of recirculation can be as large as several times the abutment length. This large recirculation continues to congest the flow and forces the flow to move toward the channel center. This is why the velocity magnitude along the channel center is higher downstream of the abutment instead of at the mid point of the abutment. At the upstream corner of the abutment, the flow is accelerated and forced around the abutment. The maximum velocity appears around the upstream corner. However, only in the region very close to the abutment, is the velocity increased significantly. In the transverse direction, the flow is disturbed significantly only in a narrow zone in front of the abutment face. Outside of that zone, the velocity vectors remain uniform. A flow separation appears right on the abutment face.

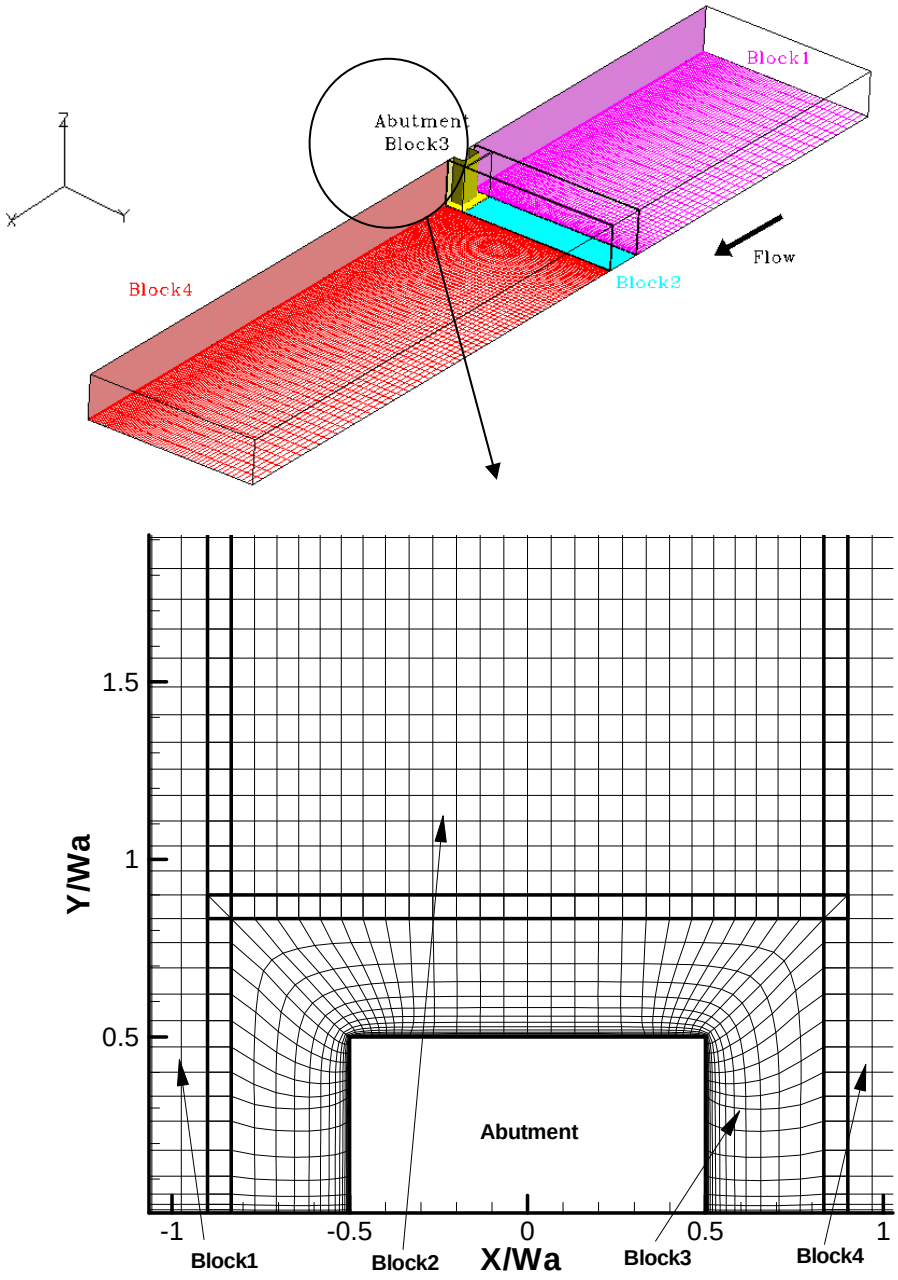

Figure 4.5 - Numerical grid for the reference case.

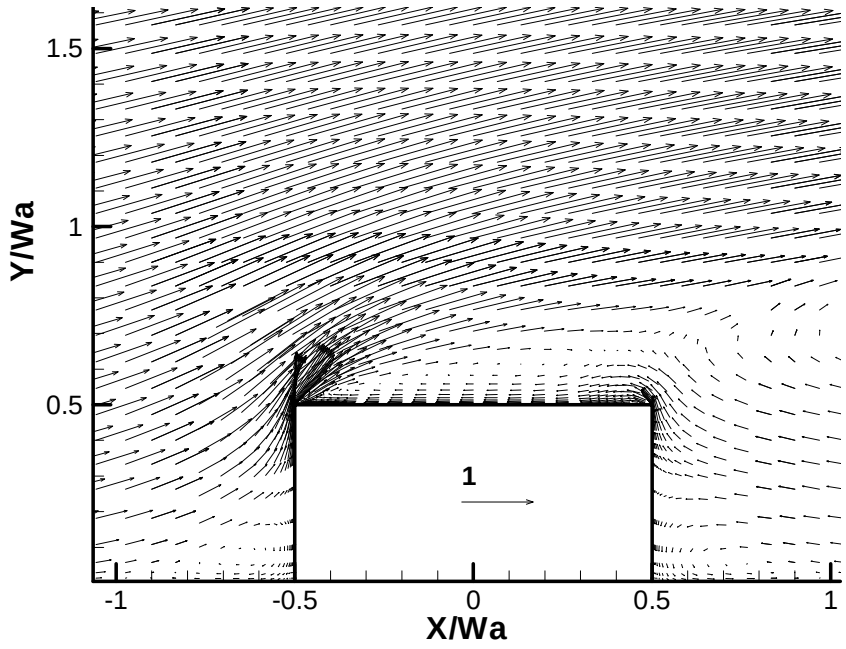

Figure 4.6 - Velocity vectors on water surface (reference case).

Figure 4.7 shows the normalized pressure contours around the abutment. The higher pressures occur on the upstream side due to the abutment obstacle. The pressure drops sharply at the upstream corner; this is consistent with the local velocity acceleration.

Figure 4.8 presents the bed shear stress distribution. The maximum bed shear stress is about 0.5 Pa at the upstream corner of the abutment. This is the initial bed shear stress contour before scour occurs. The shear stress will decrease progressively as the scour hole develops. The scour process stops when the bed shear stress reaches the critical shear stress of the soil.

To study the influence of the water surface boundary condition, cases with a rigid lid and free surface boundary conditions were simulated. The results show little influence of the surface boundary condition on the maximum bed shear stress around the abutment. The difference is within 5%.

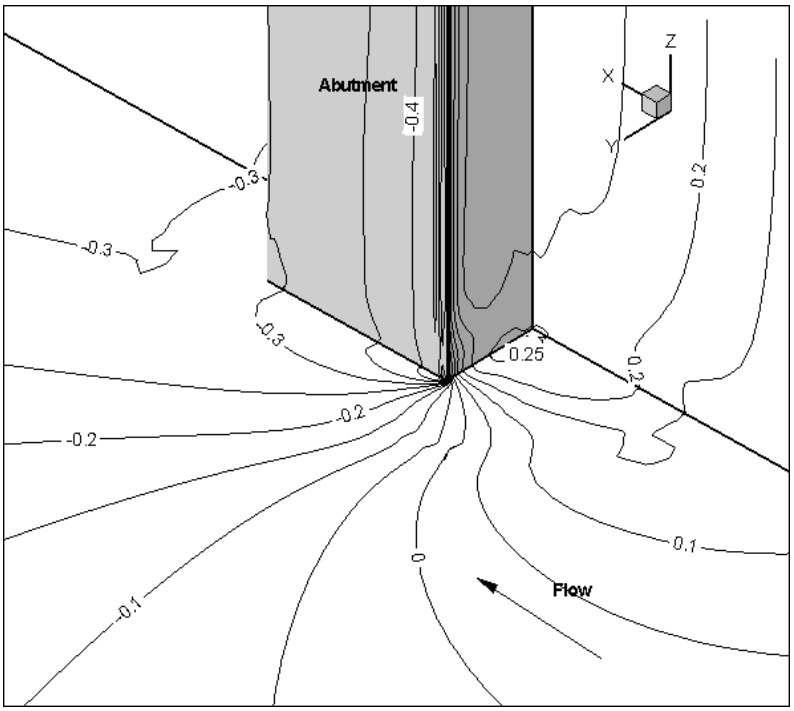

Figure 4.7 - Normalized pressure, $\frac{p}{\rho V^2}$ contours around vertical wall abutment.

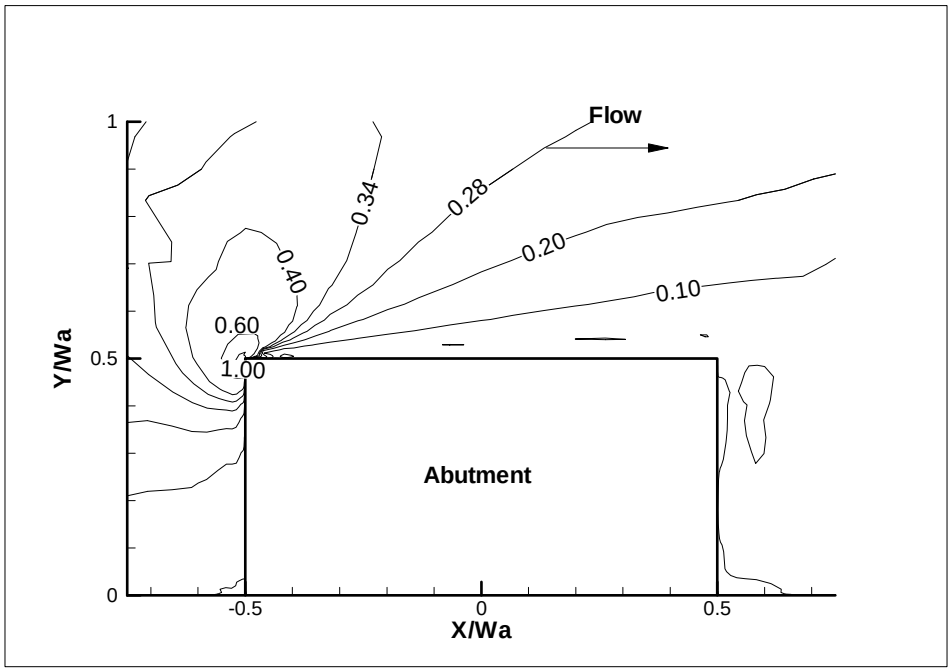

Figure 4.8 - Bed friction coefficient ($\times 10^2$), $\frac{\tau_b}{\rho V^2}$ contour for Reynolds number 10^5.

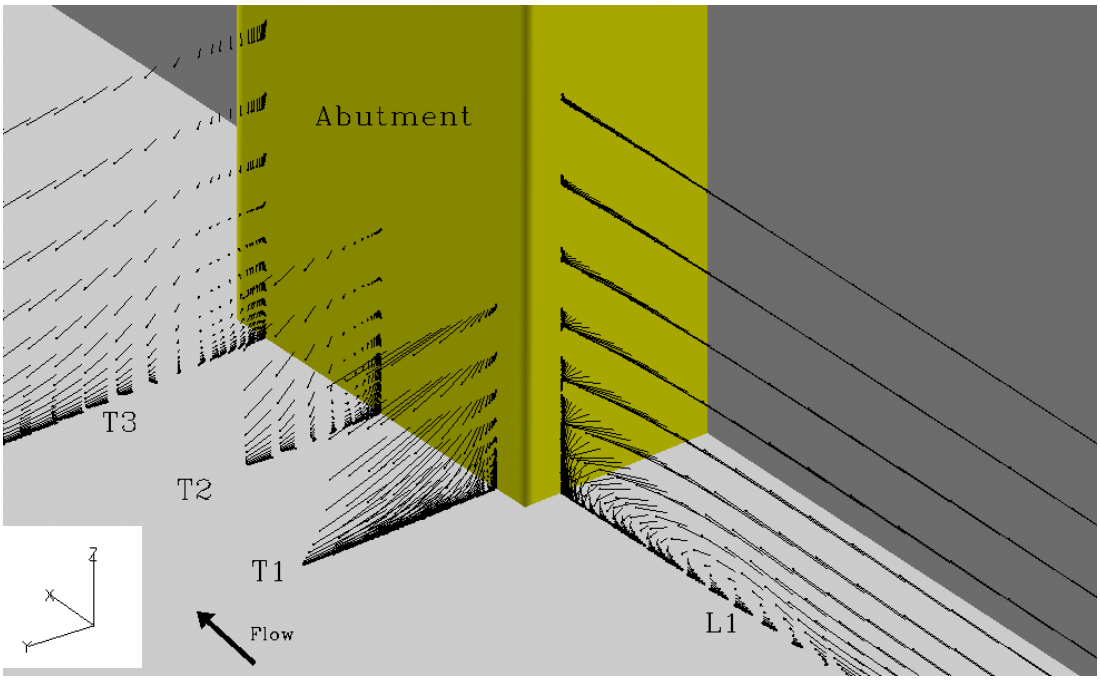

Figure 4.9 - Projected velocity vectors on the cross sections around abutment.

Figure 4.9 shows the variation of the velocity field around the abutment. These four cross sections show the projected velocity components on each plane respectively. Cross sections T1, T2, and T3 are showing the secondary flow in front of the abutment face. Longitudinal cross section L1 clearly shows the horse shoe vortex. The downflow along the abutment upstream face hits the riverbed directly, which contributes to the scour process. The velocity magnitude is extremely high on cross section T1 since the flow direction changes significantly at the upstream corner. On cross sections T2 and T3, the velocity magnitude adjacent to the abutment is not large. But the flow is extremely complicated in this area with very high turbulence intensity. According to the flume tests, the scour depth is still significant in this area. This implies that both the velocity magnitude and the turbulence intensity can contribute to the scour development.

4.3.3 Parametric Studies

4.3.3.1 Influence of Reynolds Number

For the pier scour study in NCHRP report 516 (Briaud et al., 2004), only half of the domain was simulated with a symmetric line passing the center of the circular pier. A symmetric boundary condition was applied on both the symmetric line and the lateral computation boundary. In the current study, a symmetric assumption is also adopted and the symmetric line is along the center of the channel. A no-slip boundary is applied on the side wall of the abutment. The only difference between the previous pier scour study and the current abutment scour study is the boundary condition on the lateral computation boundary along the hydraulic structure. To investigate the influence of the boundary conditions, the same grid was tested for these two settings of

pier and abutment (half of the circular pier). The maximum bed shear stress around the abutment was found to be about 2/3 of that around the pier. This indicates that the influence of the Reynolds number on the maximum bed shear stress around the abutment is not identical to the proposed pier equation in the previous report of NCHRP 24-15. Hence, there is a need to study the influence of Reynolds number on the maximum bed shear stress around the abutment. Another reason is that the typical abutment shape is different from that of a pier. The influence of shape could be significant.

As discussed before, the maximum bed shear stress around an abutment is believed to be a function of Reynolds number. The influence of Froude number is negligible as long as the relative flow depth is large enough. If it is assumed that the correction factors due to all other dimensionless parameters are the ones for the reference case, then equation (4.76) can be simplified as,

$$\frac{\tau_{\max}}{\rho V^2} = f\left[\frac{VW_a}{\nu}\right] \tag{4.77}$$

Numerical simulations were conducted for eight different Reynolds numbers ($Re=VW_a/\nu$): 1×10^4, 2×10^4, 5×10^4, 1×10^5, 5×10^5, 1×10^6, 5×10^6 and 1×10^7. All cases had the same geometry as the reference case. Figure 4.10 shows the variation of the computed maximum bed friction coefficient, $C_{f-vw} = \frac{\tau_b}{\rho V^2}$ around a vertical wall abutment as a function of Reynolds number. For comparison, the maximum bed friction coefficient, $C_{f-cp} = \frac{\tau_b}{\rho V^2}$ equation for circular pier by Briaud et al. (1999a) is also shown in the same figure. Both curves show that the normalized maximum bed shear stress decreases with an increase of Reynolds number. It should be noted that this does not mean that the dimensional bed shear stress also decreases with Reynolds number because it depends also on the upstream velocity. The discrepancy, shown in Figure 4.10, between the previous pier study and the current abutment study is due to the hydraulic structure shape and the side boundary conditions. Generally, the bed shear stress is higher around the vertical wall abutment than around a circular pier. The separation point around a vertical abutment is always at the sharp upstream corner regardless of the magnitude of the Reynolds number. By comparison, the separation point around a circular pier changes with Reynolds number. In Figure 4.10, the curve for the circular pier is much flatter than the one for vertical wall. C_{f_vw} is higher than C_{f_cp} when Reynolds number is smaller than 3×10^5. But when the Reynolds number is higher than 3×10^5, the curve for vertical wall flattens out and the magnitude is lower than that for a circular pier. According to the simulation results, the equation for the circular pier is not suitable for the abutment. Another interesting observation is that the difference between these two curves tends to be small when Reynolds number is very high. As shown in Figure 4.10, these two curves are almost parallel in the high Reynolds region. Figure 4.11, Figure 4.12, and Figure 4.13 present the simulated bed friction coefficient contours for different Reynolds numbers.

Table 4.2 - Numerical simulation results for Reynolds number study.

Re	$C_{f\_pier\_Equ}$	$C_{f\_vw\_CHEN3D}$	Regression
----	----	----	----
1.0E+04	0.0141	0.0333	0.0327
2.0E+04	0.0125	0.0235	0.0239
5.0E+04	0.0106	0.0148	0.0158
1.0E+05	0.0094	0.0103	0.0115
5.0E+05	0.0071	0.0064	0.0056
1.0E+06	0.0063	0.0048	0.0041
5.0E+06	0.0046	0.0034	0.0020
1.0E+07	0.0040	0.0025	0.0014

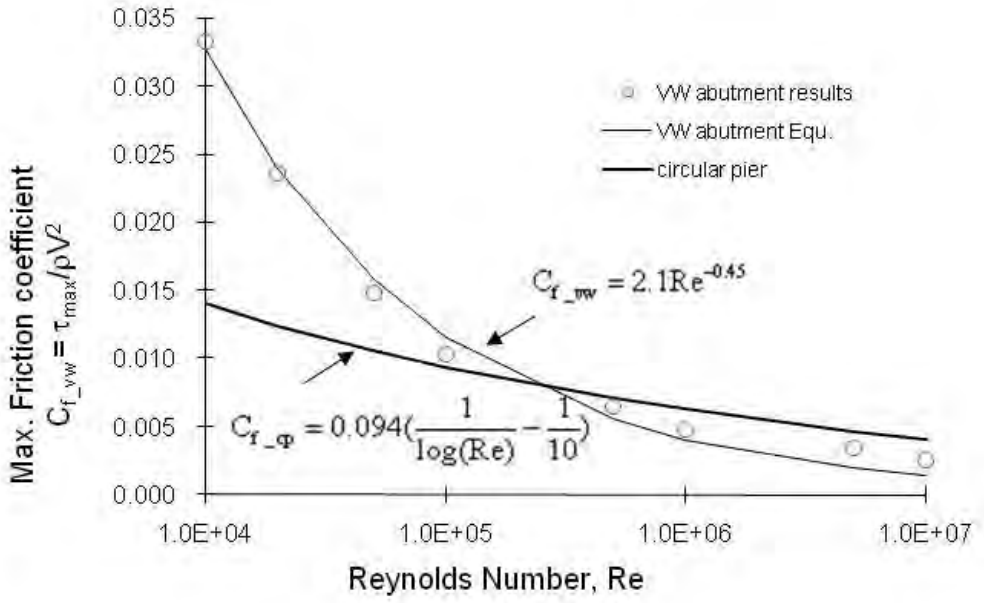

Figure 4.10 - Normalized maximum bed shear stresses versus Reynolds number.

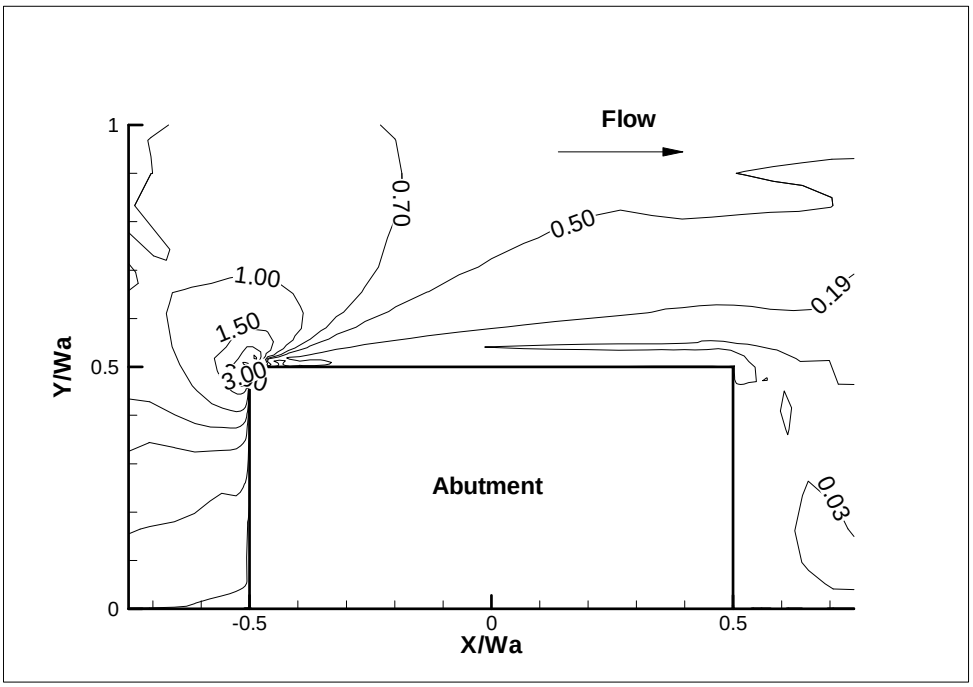

Figure 4.11 - Bed friction coefficient ($\times 10^2$), $\frac{\tau_b}{\rho V^2}$ contour for Reynolds number 10^4.

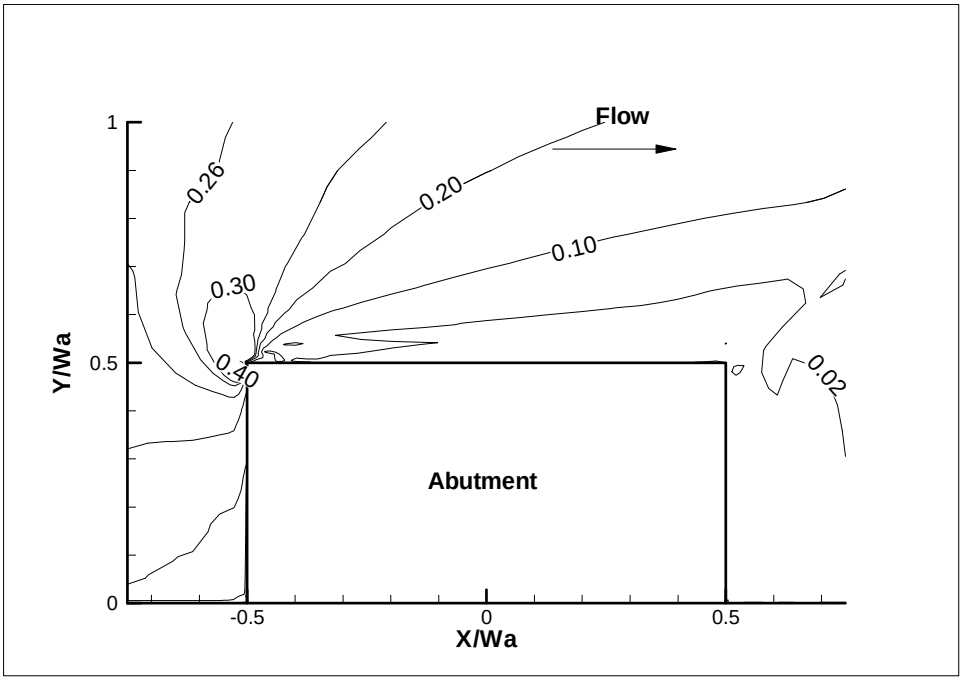

Figure 4.12- Bed friction coefficient ($\times 10^2$), $\frac{\tau_b}{\rho V^2}$ contour for Reynolds number 10^6.

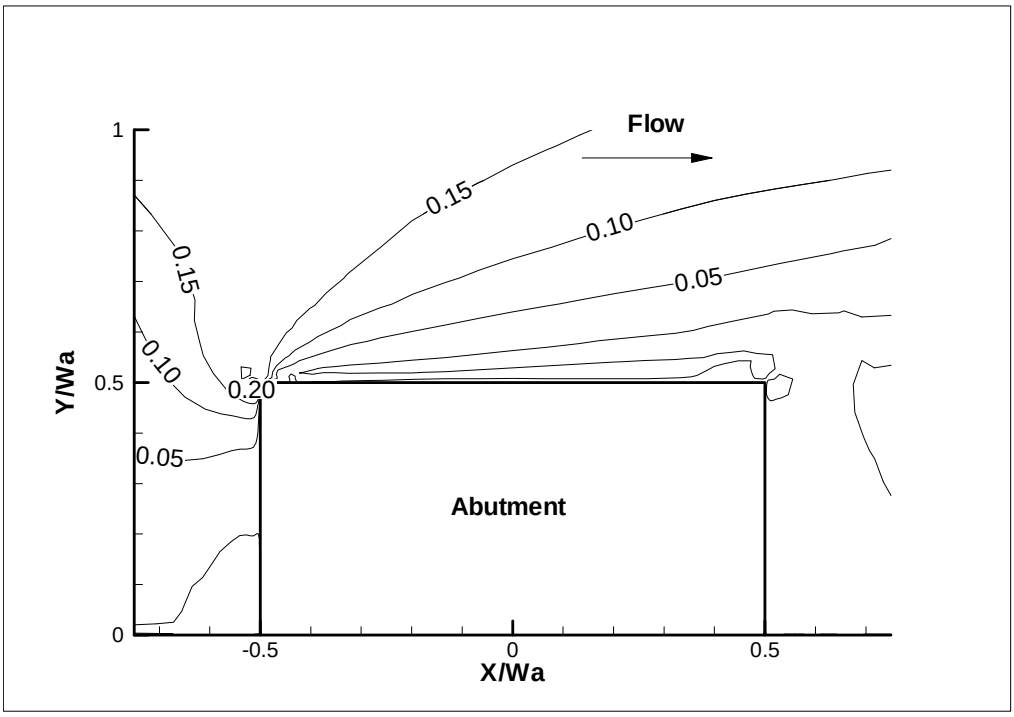

Figure 4.13- Bed friction coefficient ($\times 10^2$), $\frac{\tau_b}{\rho V^2}$ contour for Reynolds number 10^7.

4.3.3.2 Influence of water depth

The grid of the reference case was adjusted vertically to simulate different relative water depth y/W_a. The vertical distribution of the grid points changed with y/W_a but the vertical wall abutment together with the grid system keep the same scale. The Reynolds number was kept the same as the reference case and so were the boundary conditions. Five cases were performed with the CHEN3D program to study the water depth variation, including y/W_a equal 0.125, 0.25, 0.5, 1.0, and 2.0. Actually, the Froude number is changing with the relative water depth y/W_a with values of 0.29, 0.21, 0.15, 0.10, and 0.07. This cannot be avoided since the Reynolds number is kept constant. It is believed that both the Fr and y/W_a represent the influence of the water depth on $\tau_{\max}$ around the abutment and the Froude number is used in the regression. One way to present the results is to plot $\tau_{\max}/\tau_{\max\_reference}$ as a function of Fr. The shallow water correction factor, k_w is the ratio of $\tau_{\max}/\tau_{\max\_reference}$. Figure 4.14 presents the result of the five simulations. When the Froude number is smaller than 0.10, the influence of the water depth is negligible. Figure 4.15, Figure 4.16, and Figure 4.17 show the results of the bed friction coefficient contours for different water depth. Water depth variation has little influence on the bed shear stresses away from the abutment.

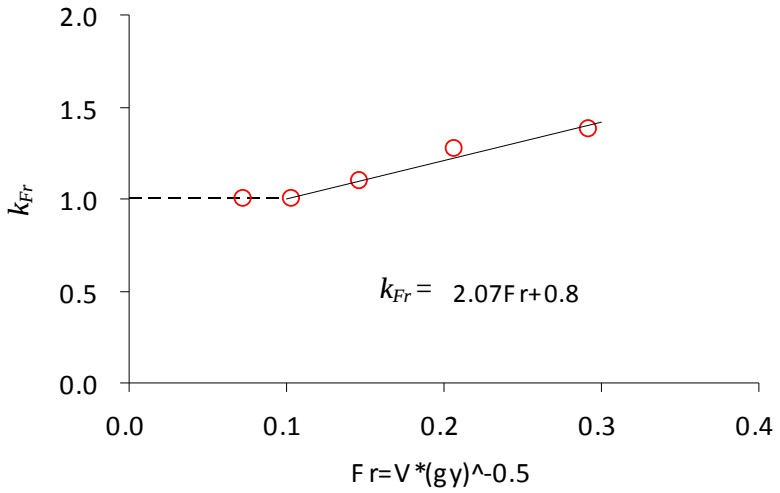

Figure 4.14 - Correction factor for water depth.

Table 4.3- Numerical simulation results for water depth study.

Re	Fr	C_{f_vw}	k_w
1.0E+05	0.07	0.0115	1.00
1.0E+05	0.10	0.0115	1.00
1.0E+05	0.15	0.0126	1.09
1.0E+05	0.21	0.0147	1.28
1.0E+05	0.29	0.0159	1.38

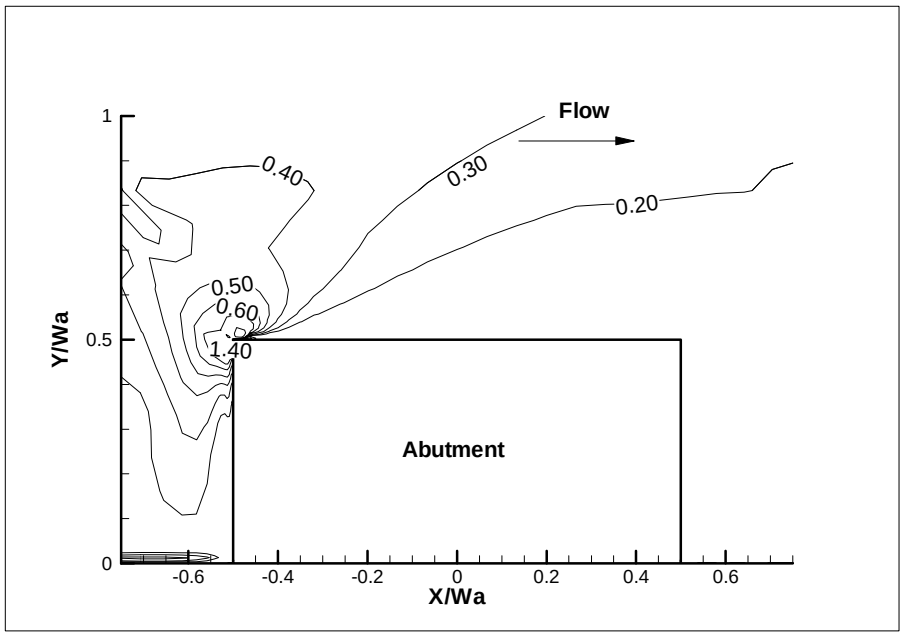

Figure 4.15- Bed friction coefficient ($\times 10^2$), $\frac{\tau_b}{\rho V^2}$ contour for y/W_a=0.25.

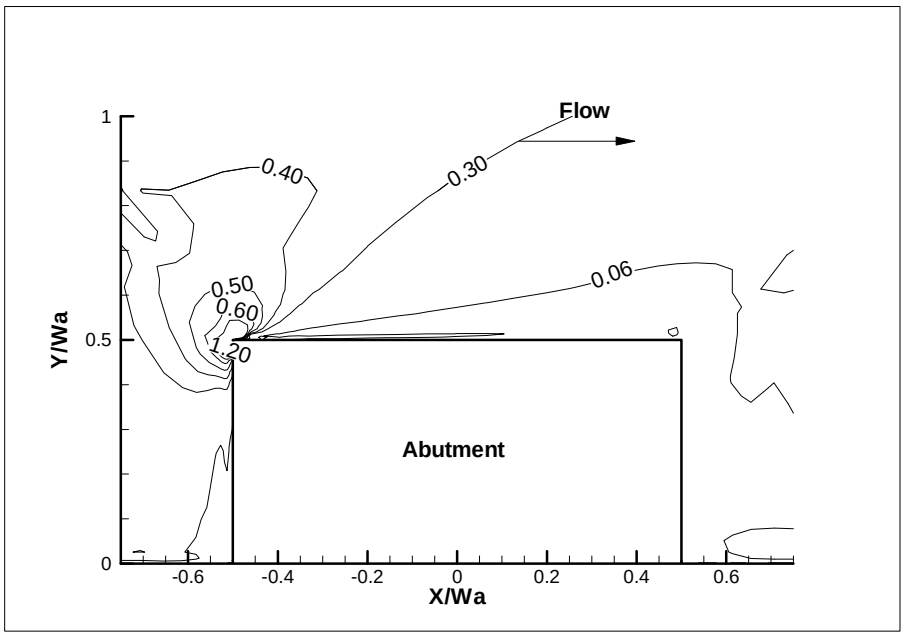

Figure 4.16 - Bed friction coefficient ($\times 10^2$), $\frac{\tau_b}{\rho V^2}$ contour for y/W_a=0.5.

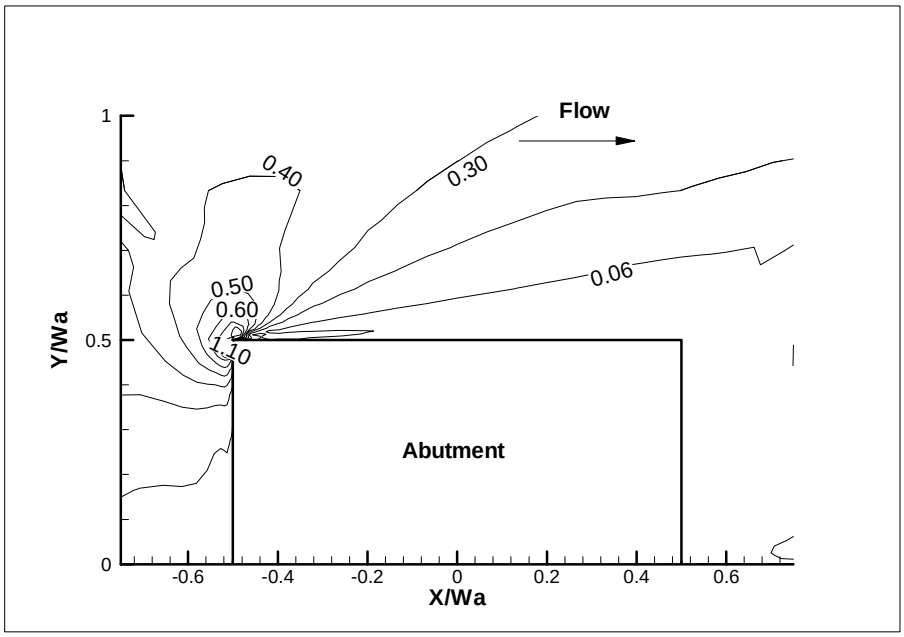

Figure 4.17- Bed friction coefficient ($\times 10^2$), $\frac{\tau_b}{\rho V^2}$ contour for y/W_a=1.0.

4.3.3.3 Influence of Channel Unit Discharge Ratio

The objective of this parametric study is to obtain the relationship between the maximum bed shear stress τ_{max} and the channel unit discharge ratio C_r. The grid of the reference case is modified to have L equal to $0.83W_a$, $1.25W_a$, and $2.5W_a$. All other parameters remain the same as the reference case. Figure 4.18 presents the variation of the channel width. Figure 4.20, Figure 4.21, and Figure 4.22 show the contours of the normalized bed shear stress for different unit discharge ratios. The velocity and the bed shear stress increase with an increase of unit discharge ratio. The maximum bed shear stress τ_{max} is the maximum shear stress that exists on the river bed just before the scour hole develops. One way to present the data is to plot $\tau_{max} / \tau_{max\_reference}$ as a function of the unit discharge ratio C_r shown in Figure 4.19. The unit discharge ratio correction factor k_{Cr} is the ratio of $\tau_{max} / \tau_{max\_reference}$. The data points on Figure 4.19 correspond to the results of the three simulations and the reference case. By data regression, the correction factor k_{Cr} is found to be linearly proportional to the unit discharge ratio C_r. A high unit discharge ratio means that the channel is narrowing significantly. It should be noted that the unit discharge ratio C_r for the reference case is 1.07 and the corresponding correction factor k_{Cr} is equal to 1.0. For the limiting case of a very wide channel with $C_r \rightarrow 1$, it is anticipated that the maximum shear stress around the abutment will be approximately 20% lower (i.e., k_{Cr} = 0.8) than the corresponding value for the reference case.

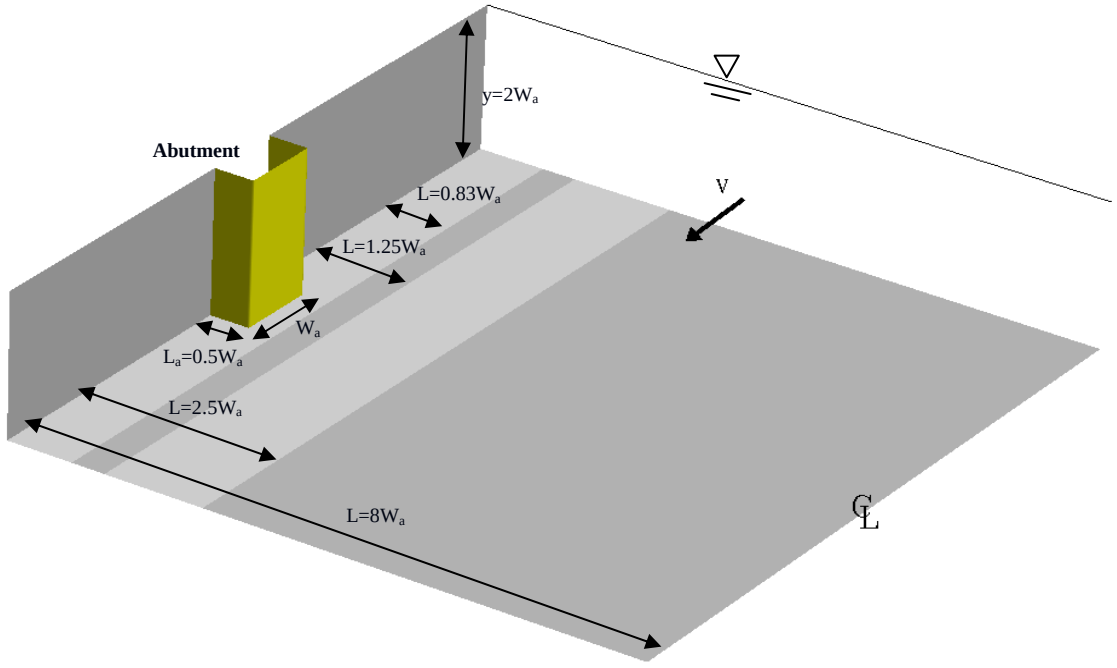

Figure 4.18 - Geometries for channel unit discharge ratio study.

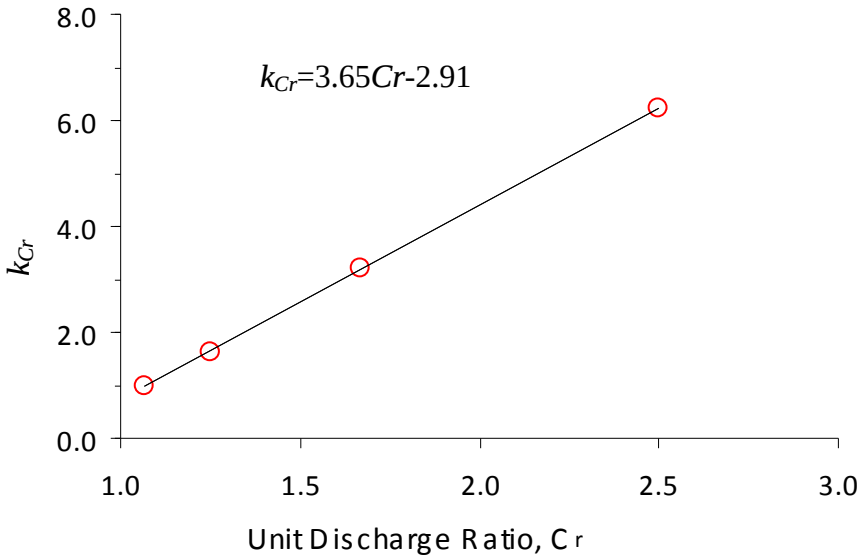

Figure 4.19- Correction factor for channel unit discharge ratio.

Table 4.4- Numerical simulation results for channel contraction study.

C_r	$C_{f\_vw\_CHEN3D}$	k_{Cr}	Regression
1.07	0.0115	1.00	1.00
1.25	0.0189	1.64	1.76
1.67	0.0369	3.19	3.49
2.50	0.0718	6.23	6.96

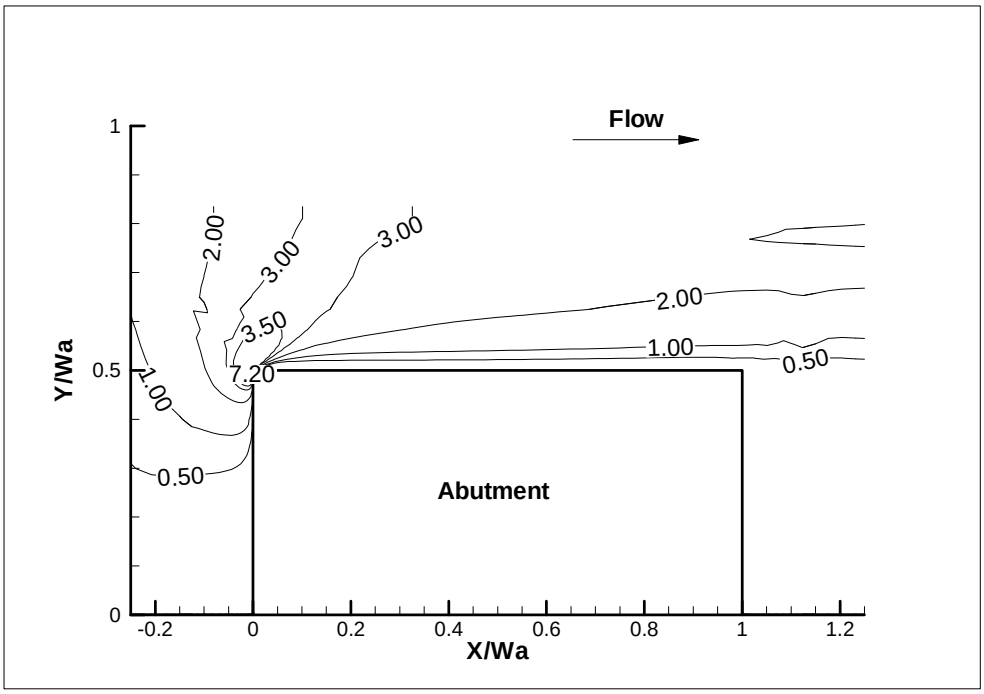

Figure 4.20- Bed friction coefficient ($\times 10^2$), $\frac{\tau_b}{\rho V^2}$ contour for C_r =2.5.

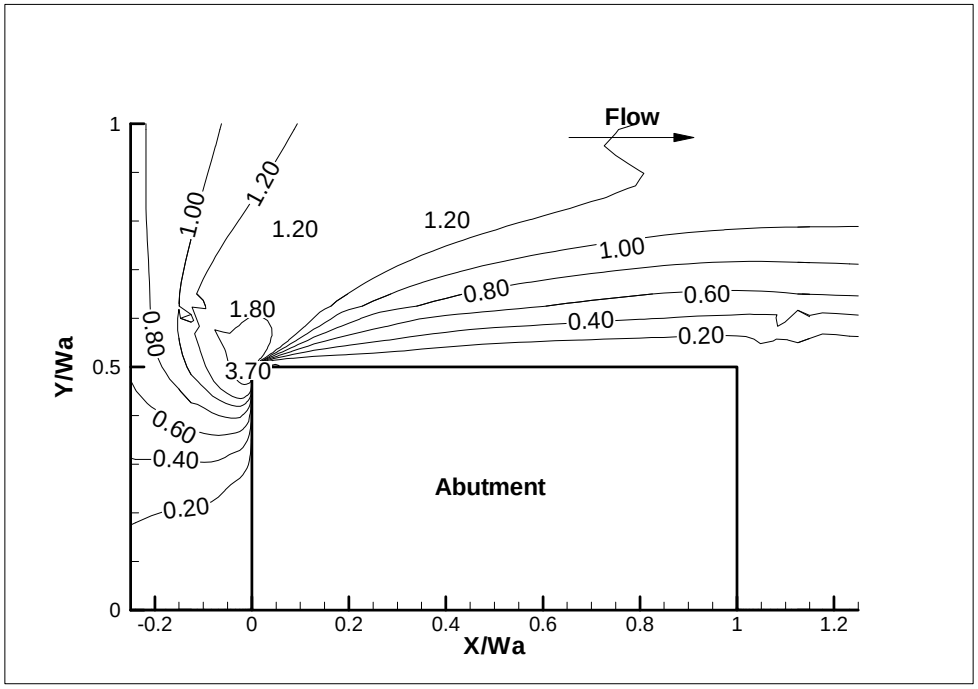

Figure 4.21- Bed friction coefficient ($\times 10^2$), $\frac{\tau_b}{\rho V^2}$ contour for C_r =1.67.

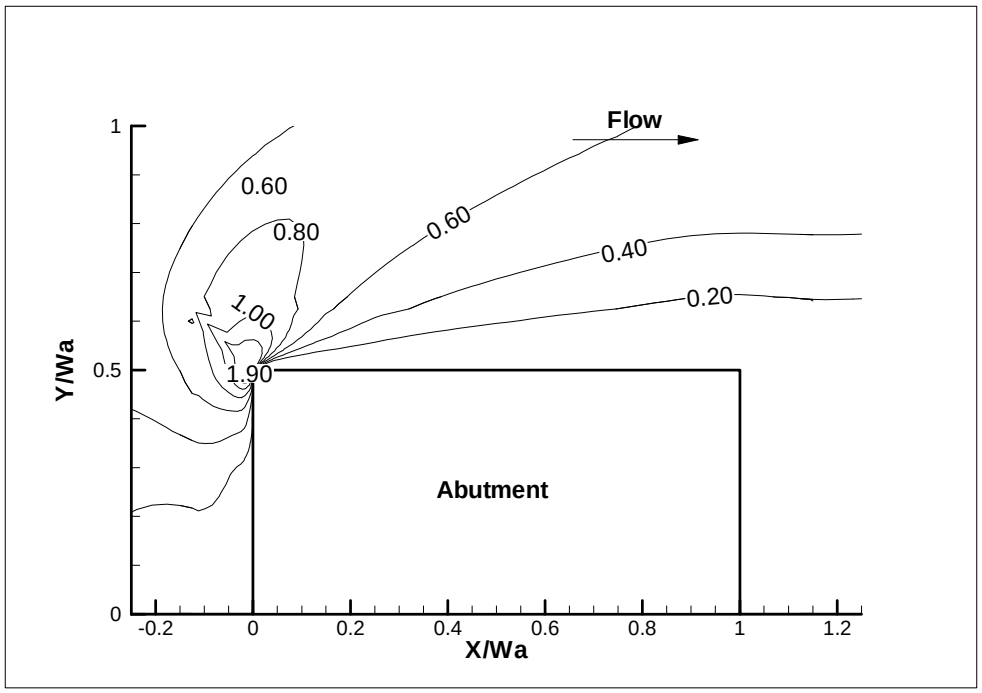

Figure 4.22 - Bed friction coefficient ($\times 10^2$), $\frac{\tau_b}{\rho V^2}$ contour for C_r =1.25.

4.3.3.4 Influence of the Aspect Ratio of Abutment

The objective of this section is to obtain the relationship between the maximum bed shear stress $\tau_{\max}$ and the aspect ratio $L^{'}/W_a$ of the abutment and approach embankment. The length of the abutment in the reference case is modified to generate six new cases with different aspect ratio $L^{'}/W_a$. It should be noted that all the abutments are normal to the flow with $L_a = L^{'}$. These six new cases have the same abutment top width W_a, half channel width L, water depth y and upstream mean velocity V as the reference case. Figure 4.23 shows the variation of the abutment length. One way to present the result is to plot $\tau_{\max}/\tau_{\max\_reference}$ as a function of $L^{'}/W_a$. It should be noted that both aspect ratio $L^{'}/W_a$ and unit discharge ratio C_r vary with the abutment length L_a because the channel width is fixed. Therefore, the variation of $\tau_{\max}$ with the abutment length has two contributors. It is necessary to exclude the influence of the unit discharge ratio in the data analysis in order to isolate the influence of the aspect ratio. The aspect ratio correction factor k_{sh} is equal to $\tau_{\max}/\left(\tau_{\max\_reference}\cdot k_{Cr}\right)$. Table 4.5 lists the parameters need to obtain the aspect ratio correction factor k_{sh} (six cases and the reference case). The correction factor k_{sh} is plotted in Figure 4.24 as a function of the abutment aspect ratio $L^{'}/W_a$. k_{sh} is found to decrease with an increase in $L^{'}/W_a$. The aspect ratio correction factor drops rapidly when $L^{'}/W_a$ increases from 1 to 3. When $L^{'}/W_a$ is larger than 3, the correction factor tends to be steady. The influence of the aspect ratio is not as significant as the unit discharge ratio. Figure 4.25, Figure 4.26, Figure 4.27, and Figure 4.28 give some of the normalized bed shear stress contours for the aspect ratio study.

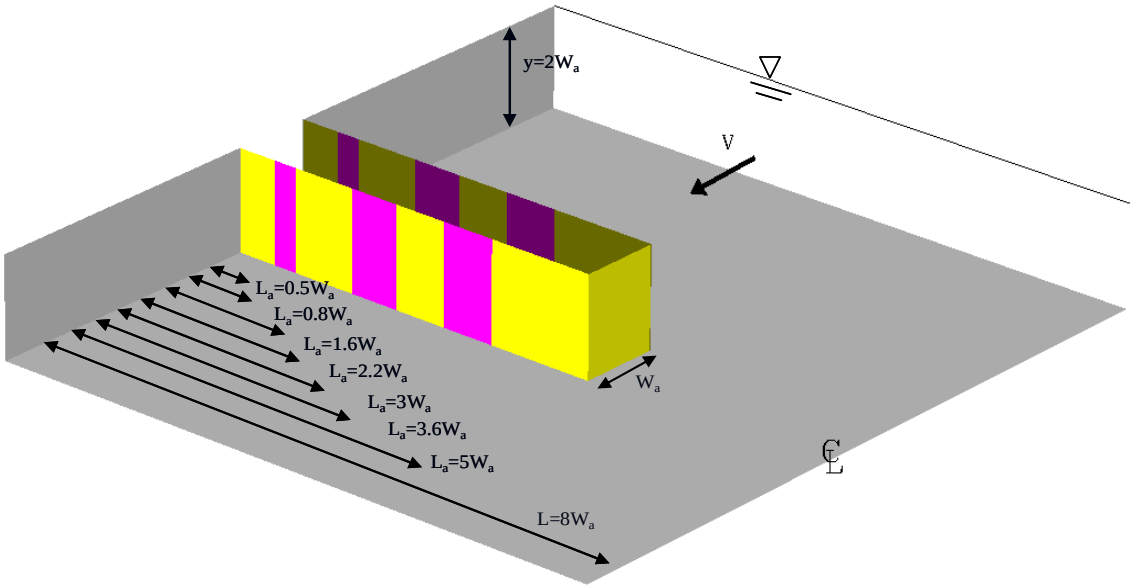

Figure 4.23 - Geometries for the study of abutment aspect ratio.

Table 4.5 - Physical parameters and the correction factors in aspect ratio study.

L'	y	V	W_a	C_{f_max}	Re	Cr	k_{Cr}	L_a/W_a	k_{sh}
m	m	m/s	m	----	----	----	----	----	----
0.23	0.91	0.22	0.46	0.0115	1.00E+05	1.07	1.00	0.50	1.00
0.37	0.91	0.22	0.46	0.0119	1.00E+05	1.11	1.15	0.80	0.89
0.73	0.91	0.22	0.46	0.0146	1.00E+05	1.25	1.66	1.60	0.76
1.01	0.91	0.22	0.46	0.0169	1.00E+05	1.38	2.15	2.22	0.68
1.32	0.91	0.22	0.46	0.0221	1.00E+05	1.56	2.81	2.89	0.68
1.62	0.91	0.22	0.46	0.0283	1.00E+05	1.80	3.67	3.55	0.67
2.23	0.91	0.22	0.46	0.0412	1.00E+05	2.57	6.48	4.89	0.55

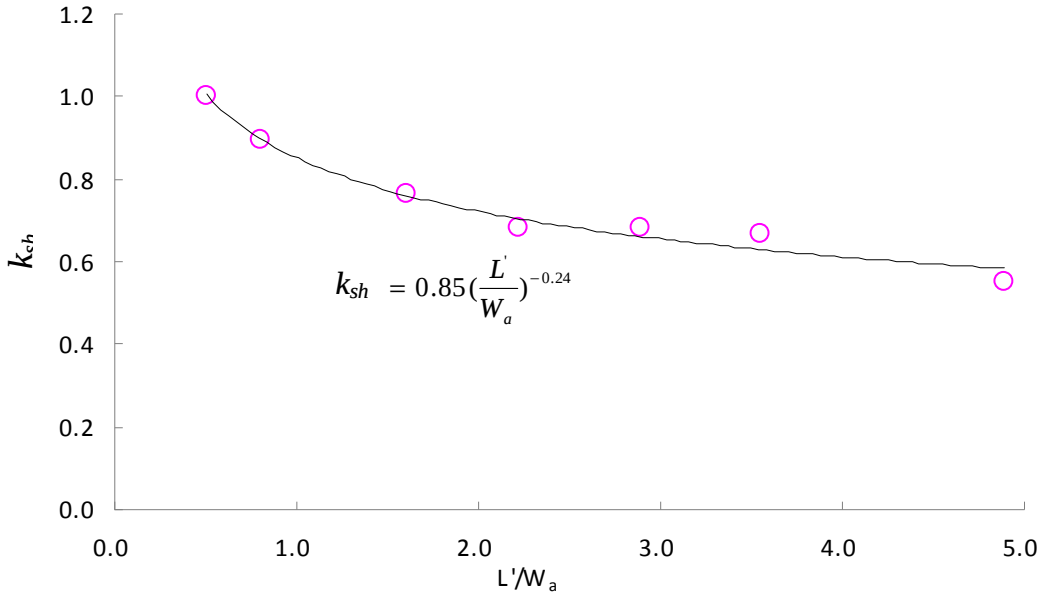

Figure 4.24 - Correction factor for abutment aspect ratio.

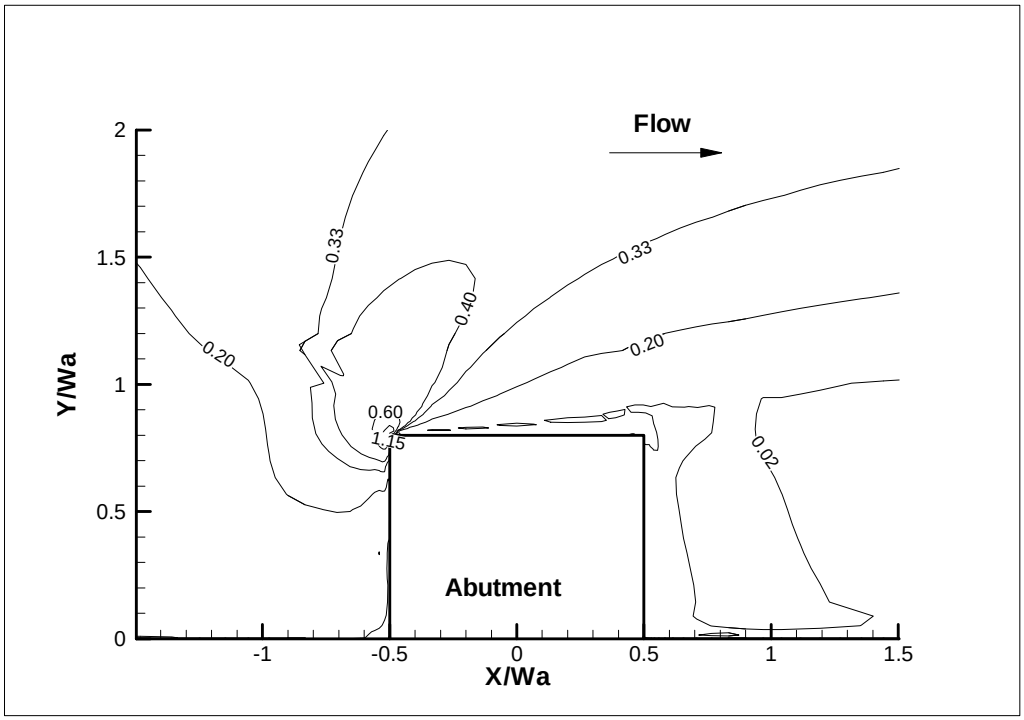

Figure 4.25 - Friction coefficient ($\times 10^2$), $\frac{\tau_b}{\rho V^2}$ contour for L_a=0.37m.

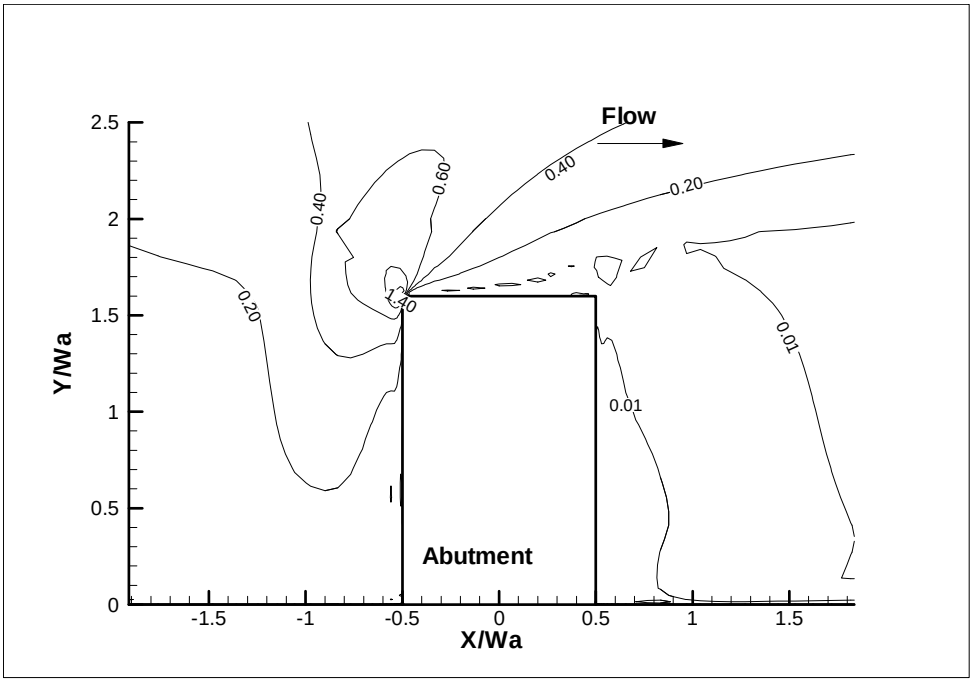

Figure 4.26 - Bed friction coefficient ($\times 10^2$), $\frac{\tau_b}{\rho V^2}$ contour for L_a=0.73m.

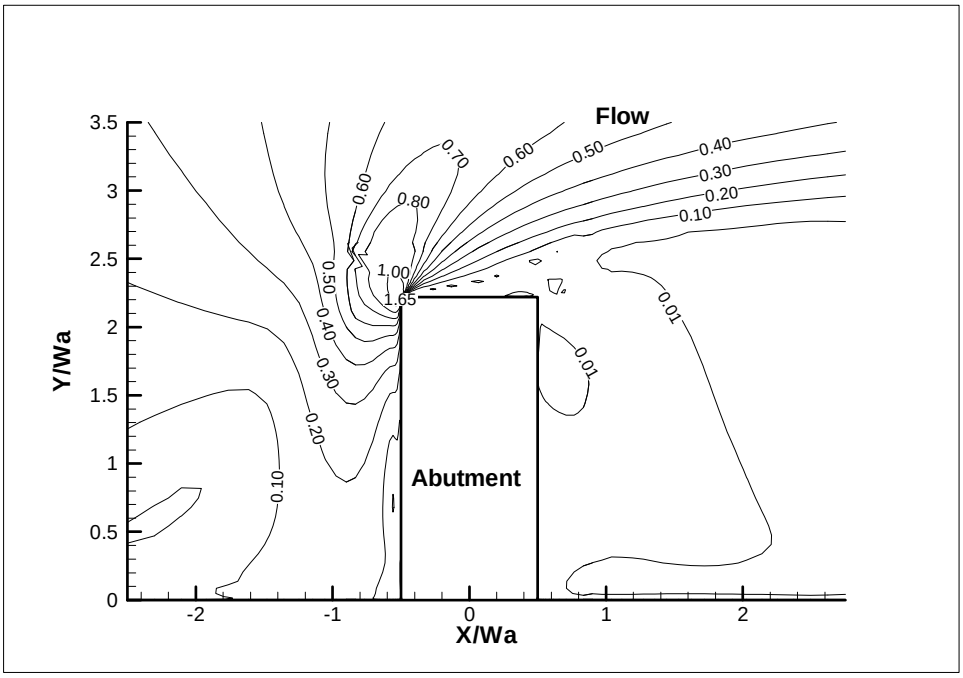

Figure 4.27 - Bed friction coefficient ($\times 10^2$), $\frac{\tau_b}{\rho V^2}$ contour for L_a=1.01m.

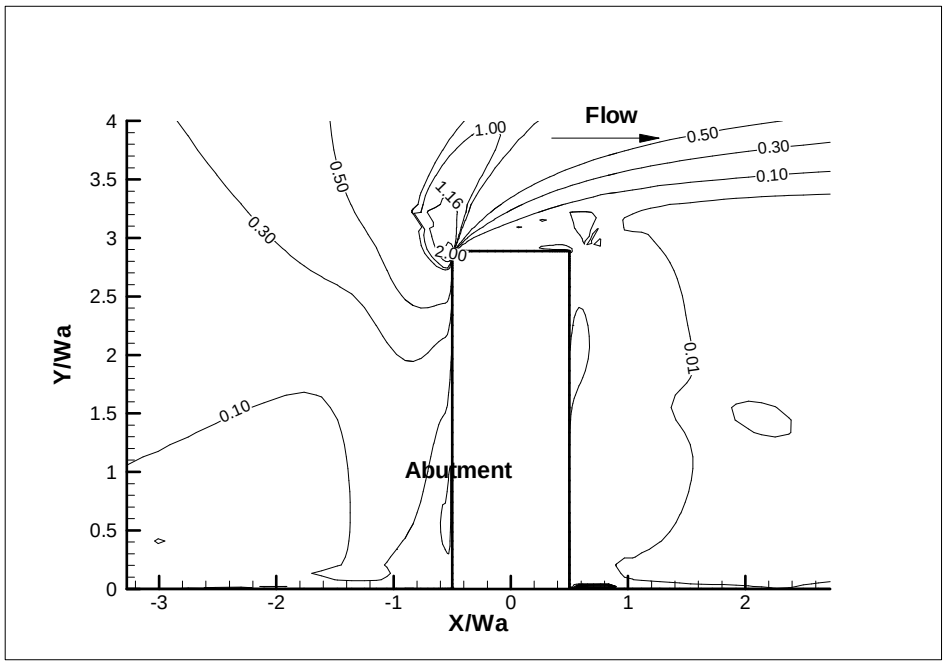

Figure 4.28 - Bed friction coefficient ($\times 10^2$), $\frac{\tau_b}{\rho V^2}$ contour for L_a=1.32m.

4.3.3.5 Influence of the Abutment Shape

The objective of this section is to obtain the relationship between the maximum bed shear stress and the abutment shape (as shown in Figure 4.29). Four flume tests with a wing-wall abutment in a rectangular channel are simulated. They all have the same approach velocity, water depth, channel width but different abutment length in order to study the influence the abutment length on shape factor. All the abutments are normal to the flow direction with $L_a = L^{'}$. Another two sets of simulations are performed with the wing-wall abutment being replaced by a vertical wall and then by a spill-through shape. For the pair of cases with the same abutment length, the unit discharge ratios are identical for wing-wall and vertical wall shape. The shape correction factor k_s for a wing-wall abutment is therefore the ratio of $\tau_{\max\_ww} / \tau_{\max\_vw}$, as tabulated in Table 4.6. The vertical wall abutment is adopted as the reference case and k_s for a vertical wall abutment is one. The influence of abutment length on the shape factor can also be investigated in Table 4.6. The shape correction factors for wing-wall abutments are nearly constant, though the value tends to be smaller with an increase in abutment length. Based on Table 4.6, a constant correction factor of 0.65 is proposed for the wing-wall abutment for simplicity. Figure 4.30 to Figure 4.33 show the normalized bed shear stress contours of these four cases for a wing wall abutment.

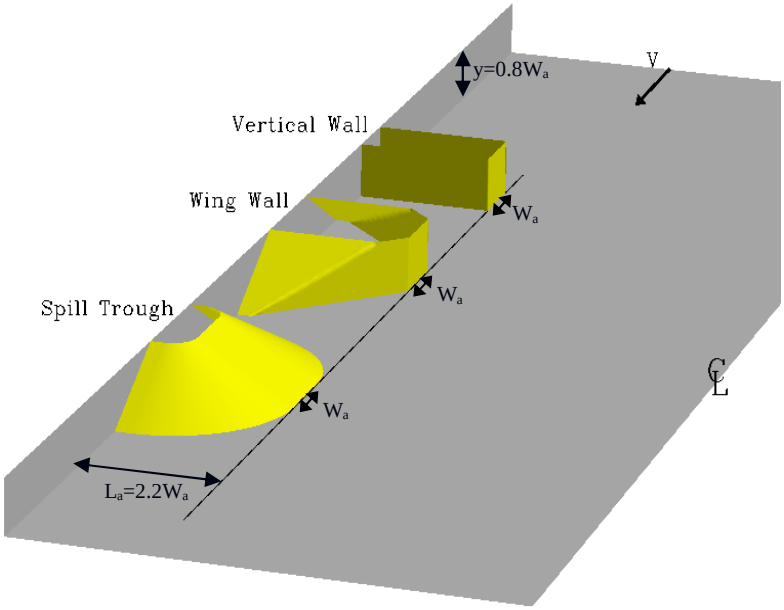

Figure 4.29- Definition of abutment shape.

Table 4.6 - Shape correction factors of wing-wall abutment.

	k_s

y	V	L_a	W_a	$C_{f\_max\_WW}$	$C_{f\_max\_VW}$	
m	m/s	m	m	----	----	----
0.37	0.33	1.01	0.46	0.0107	0.0165	0.65
0.37	0.33	1.32	0.46	0.0138	0.0211	0.65
0.37	0.33	1.62	0.46	0.0161	0.0257	0.63
0.37	0.33	2.23	0.46	0.0260	0.0450	0.58

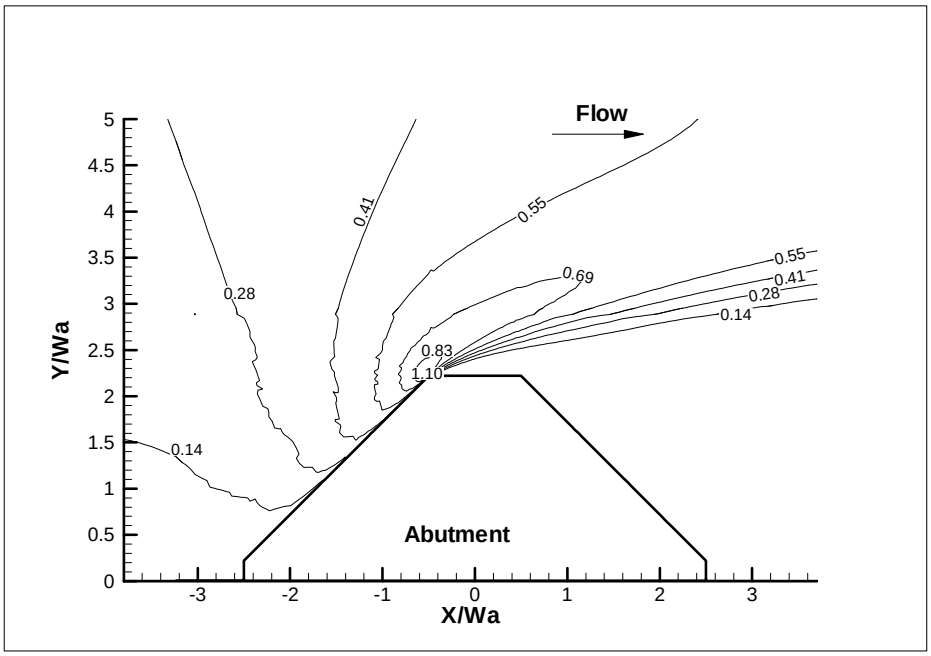

Figure 4.30 - Bed friction coefficient ($\times 10^2$), $\frac{\tau_b}{\rho V^2}$ contour for L_a = 1.01m (WW).

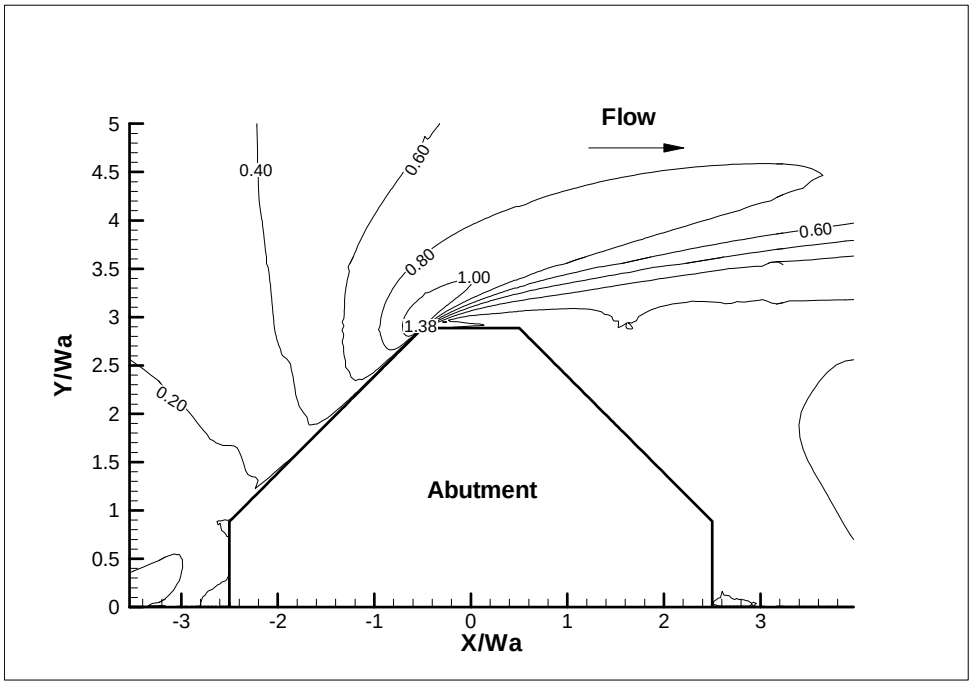

Figure 4.31 - Bed friction coefficient ($\times 10^2$), $\frac{\tau_b}{\rho V^2}$ contour for L_a = 1.21m (WW).

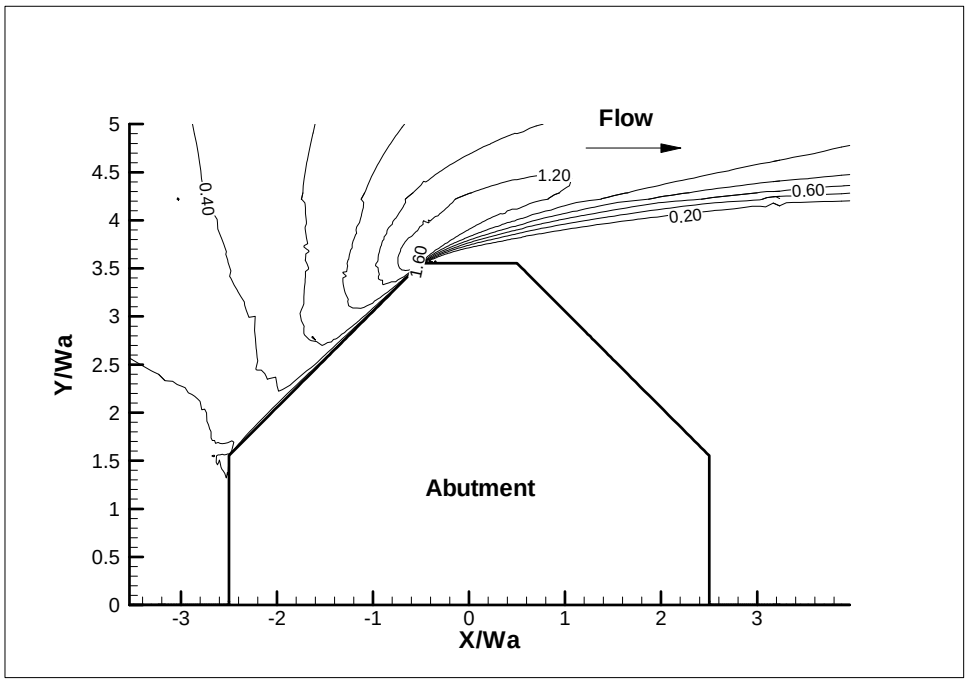

Figure 4.32 - Bed friction coefficient ($\times 10^2$), $\frac{\tau_b}{\rho V^2}$ contour for L_a = 1.62m (WW).

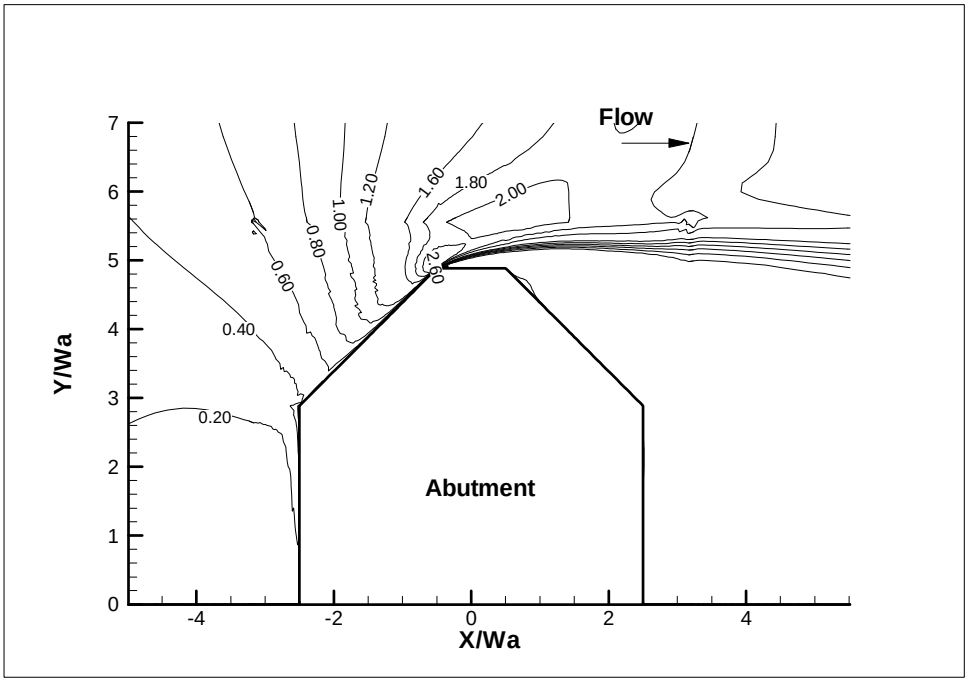

Figure 4.33 - Bed friction coefficient ($\times 10^2$), $\frac{\tau_b}{\rho V^2}$ contour for L_a = 2.23m (WW).

The same approach can be applied to study the spill-through abutment. The case of the spill-through abutment, however, has a lower unit discharge ratio C_r compared to the case of a vertical wall abutment with same length. Hence, the k_s values ($\tau_{max\_ST} / \tau_{max\_VW}$) listed in Table 4.7 include the contribution of the unit discharge ratio. It is necessary to exclude the influence of the unit discharge ratio and get $k_s = (\tau_{max\_ST} / k_{Cr\_ST}) / (\tau_{max\_VW} / k_{Cr\_VW})$. As shown in Table 4.8, k_s for a spill-through abutment decreases with an increase in C_r. The same observation appears for the wing wall abutment. When the contraction is low, the spill through abutment and the wing-wall abutment have almost the same k_s. However, the k_s for the spill though abutment drops faster when the contraction is large. For simplicity, an average correction factor of 0.58 is proposed for the spill-through abutment. Figure 4.33 to Figure 4.37 shows the contours of normalized bed shear stress for these four cases with spill-through abutment. Table 4.9 presents the proposed shape correction factors.

Table 4.7 – Shape correction factors of spill-through abutment (w/o correction).

L_a	y	V	W_a	$C_{f\_max\_ST}$	$C_{f\_max\_VW}$	k_s
m	m	m/s	m	----	----	----
1.01	0.37	0.33	0.46	0.0076	0.0165	0.46
1.32	0.37	0.33	0.46	0.0097	0.0211	0.46
1.62	0.37	0.33	0.46	0.0107	0.0257	0.42
2.23	0.37	0.33	0.46	0.0152	0.0450	0.34

Table 4.8 - Shape correction factors of spill-through abutment (with correction).

L_a	y	W_a	C_{r_ST}	C_{r_VW}	k_{Cr_ST}	k_{Cr_WW}	k_s
m	m	m	----	----	----	----	----
1.01	0.37	0.46	1.2158	1.3841	1.53	2.14	0.65
1.32	0.37	0.46	1.3529	1.5645	2.03	2.80	0.63
1.62	0.37	0.46	1.5248	1.7991	2.66	3.66	0.57
2.23	0.37	0.46	2.0443	2.5696	4.55	6.47	0.48

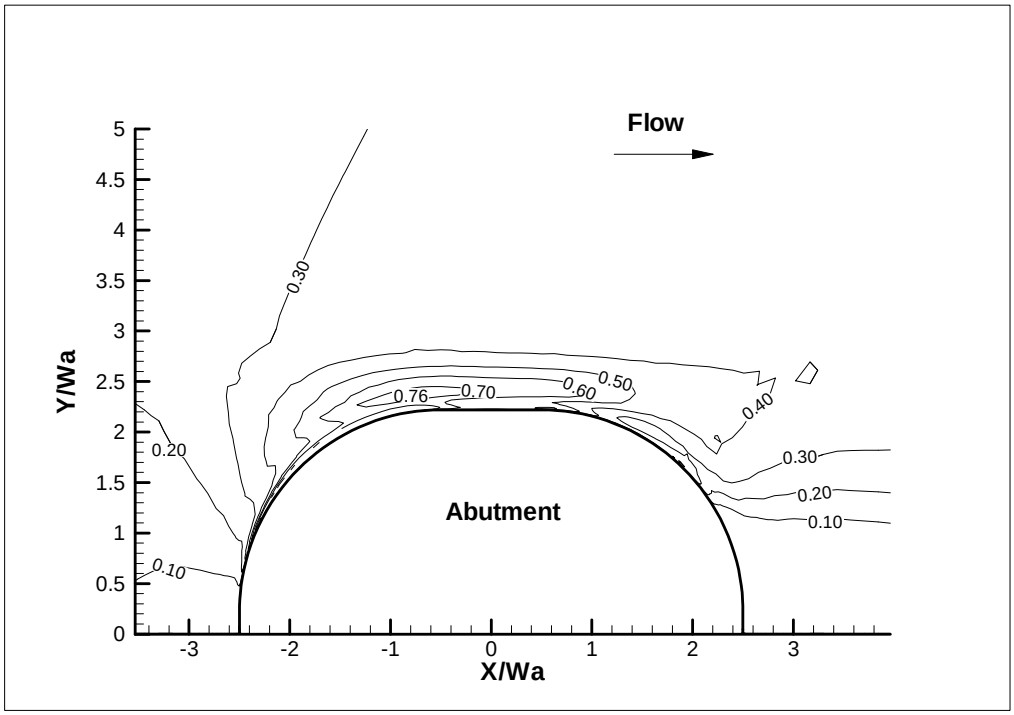

Figure 4.34 - Bed friction coefficient ($\times 10^2$), $\frac{\tau_b}{\rho V^2}$ contour for L_a = 1.01m (ST).

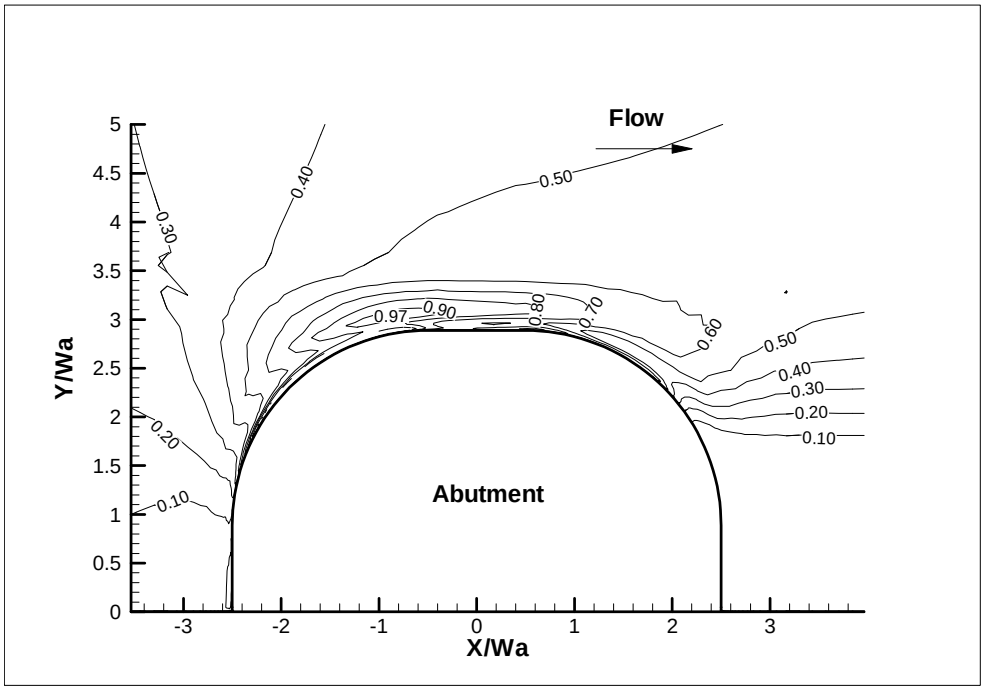

Figure 4.35 - Bed friction coefficient ($\times 10^2$), $\frac{\tau_b}{\rho V^2}$ contour for L_a = 1.32m (ST).

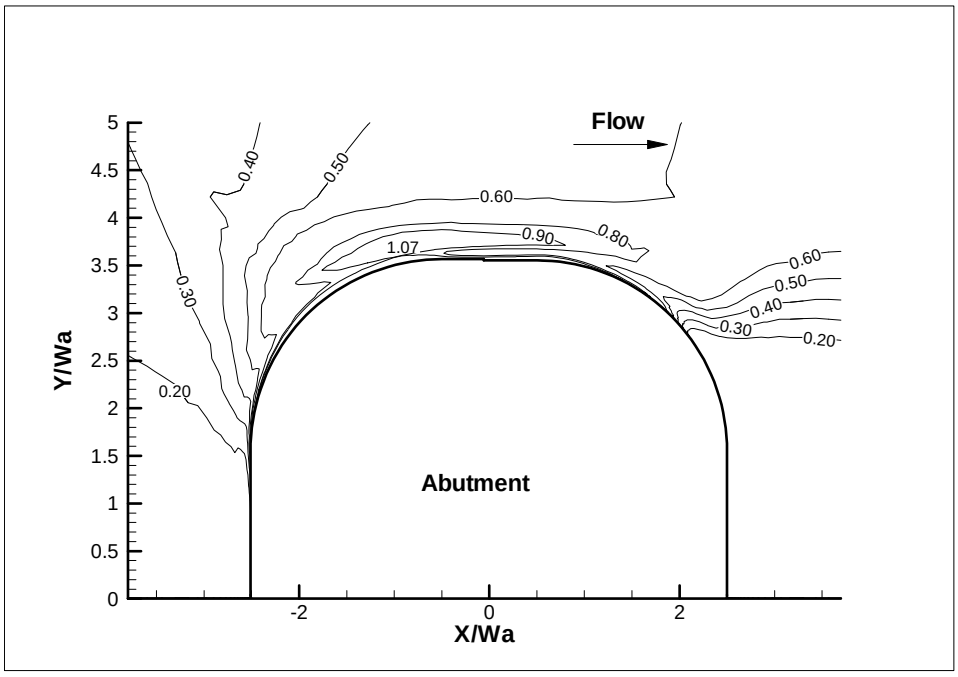

Figure 4.36 - Bed friction coefficient ($\times 10^2$), $\frac{\tau_b}{\rho V^2}$ contour for L_a = 1.62m (ST).

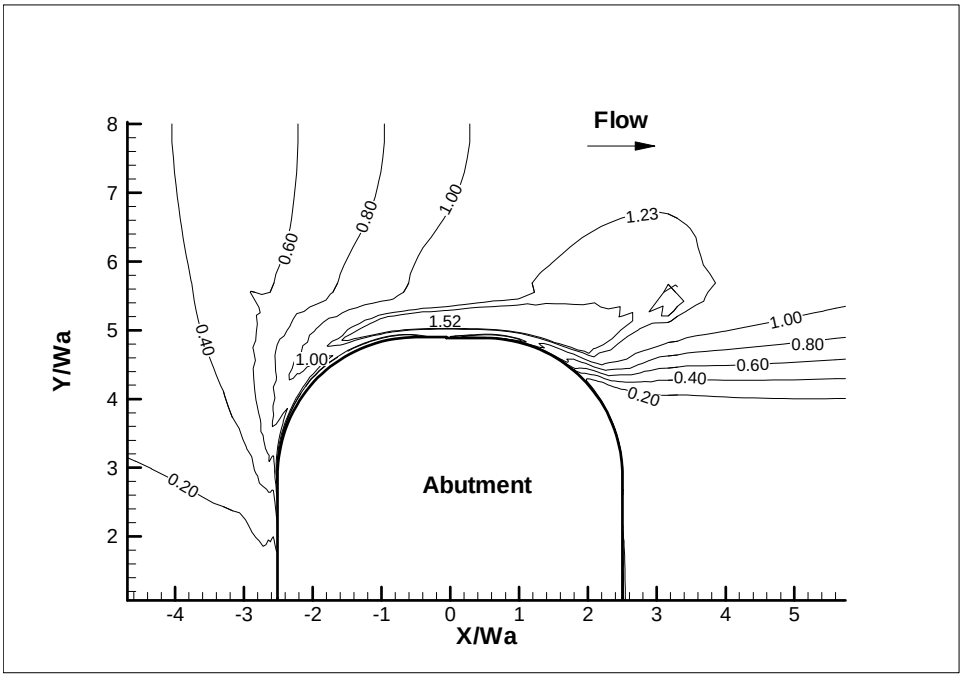

Figure 4.37 - Bed friction coefficient ($\times 10^2$), $\frac{\tau_b}{\rho V^2}$ contour for L_a = 2.23m (ST).

Table 4.9 - Proposed Shape correction factors.

Abutment Shape	Vertical wall	Wing wall	Spill through
k_s	1.0	0.65	0.58

4.3.3.6 Influence of the skew angle

The objective of this section is to obtain the relationship between the maximum bed shear stress τ_{max} and the skew angle θ of abutment (defined in Figure 4.1). Five cases are simulated with the same projected abutment length L' of 1.01m normal to the flow direction for a half river width of 3.66m. The abutment has a vertical wall shape and the skew angle varies from 60 to 120 degree (Figure 4.2). The approach velocity is 0.33m/s and the water depth is 0.37m. The results are shown in Figure 4.39 to Figure 4.42. One way to present the results is to plot $\tau_{max}/\tau_{max(90)}$ as a function of the skew angle θ. The parameter $\tau_{max(90)}$ is the value of τ_{max} for the case with 90 degree skew angle or the most general case of an abutment perpendicular to the flow direction. The skew angle correction factor, k_{sk}, is the ratio of $\tau_{max}/\tau_{max(90)}$. The data points in Figure 4.35 correspond to the results of the five simulations. The case with the 90 degree skew angle has the highest maximum bed shear stress. The maximum bed shear stress decreases when the abutment is skewed towards either the upstream or downstream directions. For the same angle with the normal to the flow, the maximum bed shear stress is higher when the abutment skews toward upstream. Considering that the bridge is usually designed to be normal to the flow direction, the correction factor for skewed angle is proposed to be one in order to provide a conservative prediction of the maximum bed shear stress.

Table 4.10- Numerical simulation results for skew angle study.

V	y	Skewed Angle	C_{f_max}	k_{sk}
m/s	m	degree	----	----
0.33	0.37	60	0.0102	0.62
0.33	0.37	75	0.0111	0.67
0.33	0.37	90	0.0165	1.00
0.33	0.37	105	0.0128	0.78
0.33	0.37	120	0.0122	0.74

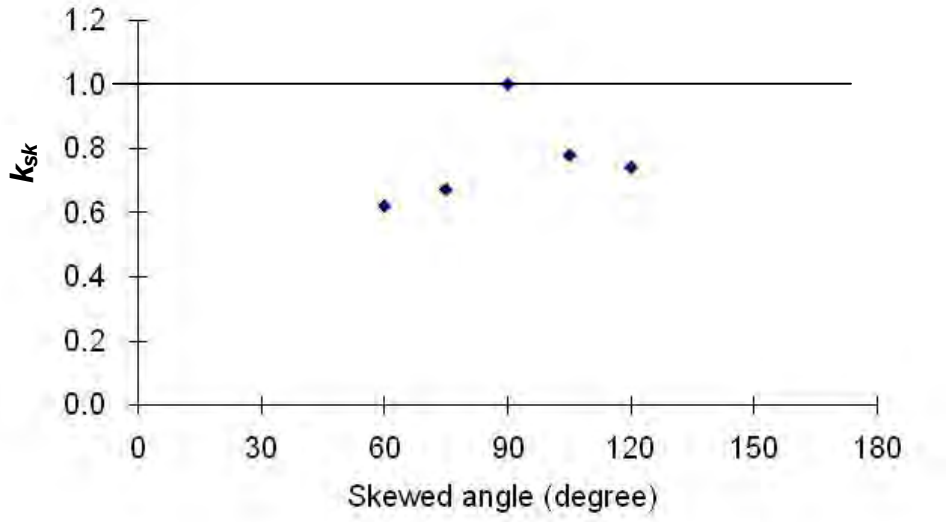

Figure 4.38 - Correction factor for the skew angle of vertical wall abutment.

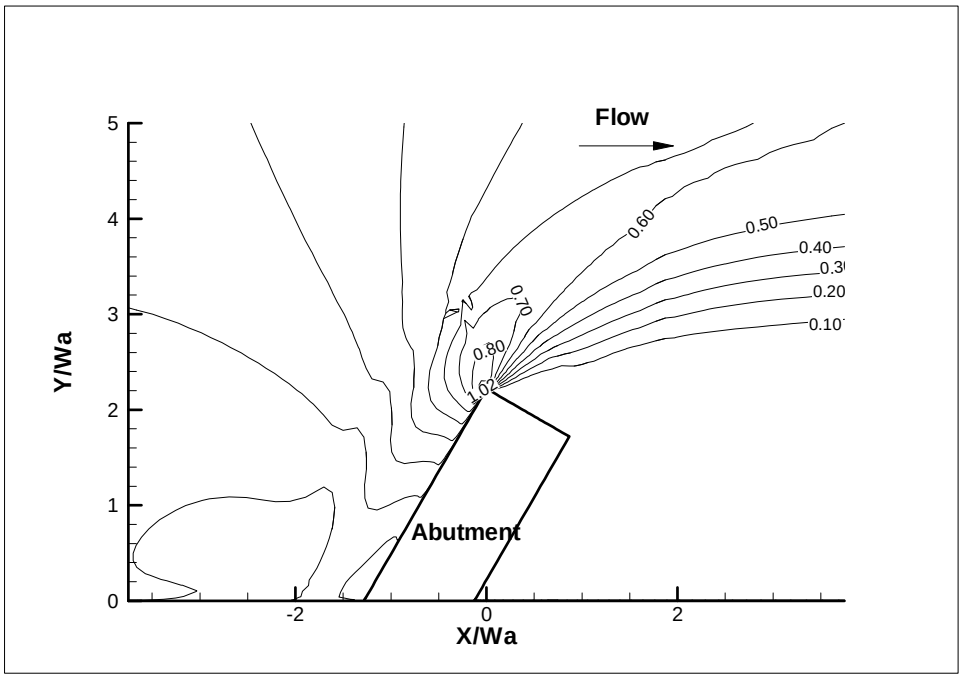

Figure 4.39 - Bed friction coefficient ($\times 10^2$), $\frac{\tau_b}{\rho V^2}$ contour for 60 degree.

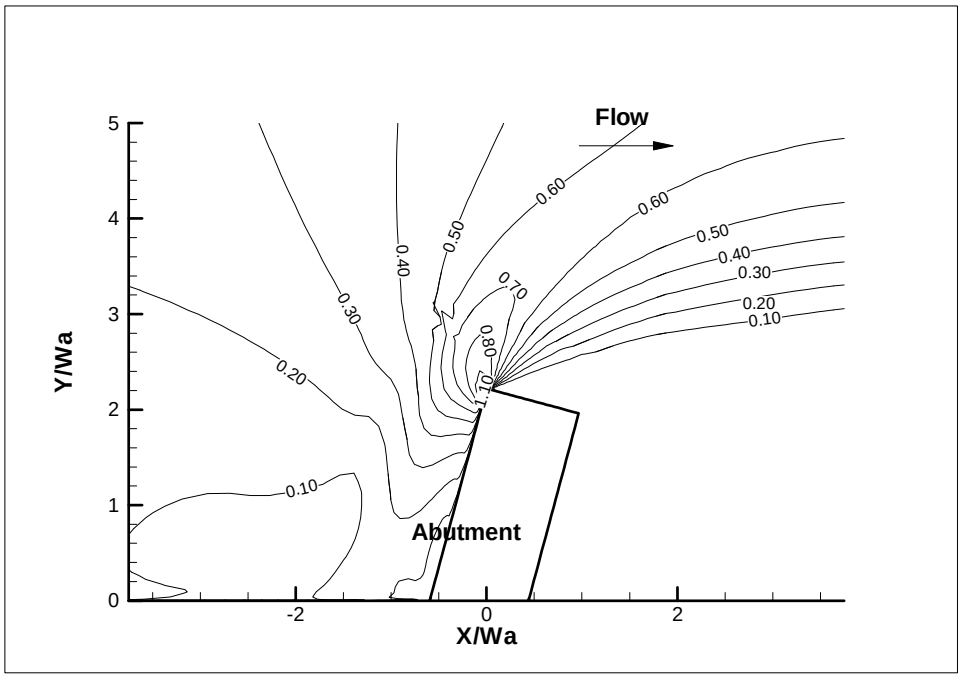

Figure 4.40 - Bed friction coefficient ($\times 10^2$), $\frac{\tau_b}{\rho V^2}$ contour for 75 degree.

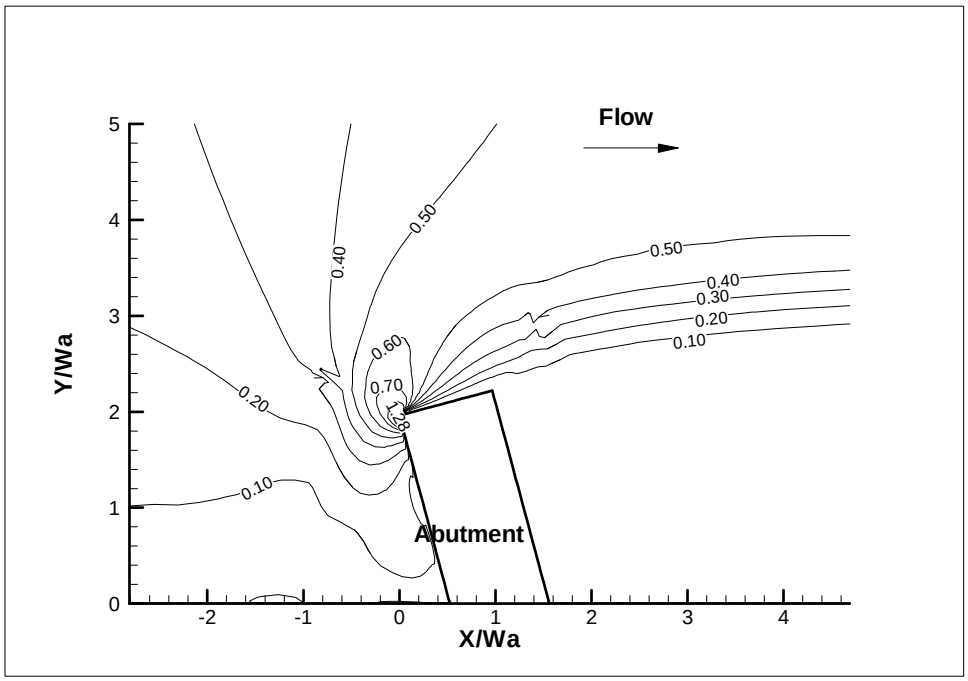

Figure 4.41 - Bed friction coefficient ($\times 10^2$), $\frac{\tau_b}{\rho V^2}$ contour for 105 degree.

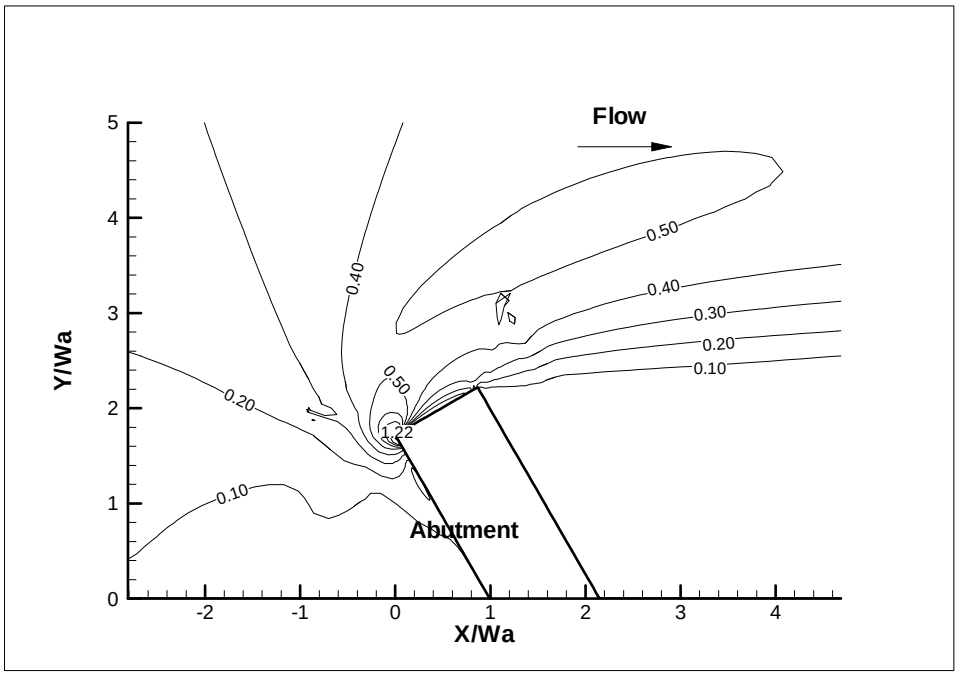

Figure 4.42 - Bed friction coefficient ($\times 10^2$), $\frac{\tau_b}{\rho V^2}$ contour for 120 degree.

4.3.4 Maximum Bed Shear Stress Equation in a Rectangular Channel

The basic equation gives $\tau_{\max}$ for the half square pier in a deep water condition. After the correction factors for the channel unit discharge ratio, abutment aspect ratio, skew angle, water depth and abutment shape are determined, the maximum bed shear stress equation around the abutment in a rectangular channel can be generated as follows:

$$\frac{\tau_{\max}}{\rho V^2} = C_{f\_vw} \cdot k_{Cr} \cdot k_{sh} \cdot k_{Fr} \cdot k_s \cdot k_{sk} \tag{4.78}$$

where $\tau_{\max}$ = the maximum bed shear stress at the interface between the water and the river bottom near the abutment toe.

ρ = mass density of water

V = upstream mean depth velocity

y = upstream water depth

W_a = top width of the abutment

$L^{'}$ = projected abutment length normal to the flow direction

C_r = unit discharge ratio; defined as $C_r = Q_{total} / (Q_{total} - Q_{blocked})$

Q_{total} =total discharge

$Q_{blocked}$ =discharge blocked by the abutment in the upstream

Re = Reynolds number, defined as $\mathrm{Re} = VW_a / \nu$

ν = kinematic viscosity

C_{f_VW} = maximum bed friction coefficient near the toe of vertical wall abutment under deep water conditions

k_{Cr} = correction factor for channel unit discharge ratio

k_{sh} = correction factor for the aspect ratio of the approach embankment

k_{Fr} = correction factor for water depth

k_s = correction factor for abutment shape

k_{sk} = correction factor for skew angle

$$C_{f\_vw} = 2.1\mathrm{Re}^{-0.45} \qquad k_{Cr} = 3.65C_r - 2.91$$

$$k_{sh} = 0.85\left(\frac{L'}{W_a}\right)^{-0.24} \qquad k_{sk} = 1.0$$

$$k_{Fr} = \begin{cases} 2.07\mathrm{Fr} + 0.8, & \mathrm{Fr} > 0.1 \\ 1.0, & \mathrm{Fr} \le 0.1 \end{cases} \qquad k_s = \begin{cases} 1, & \text{vertical-wall abutment} \\ 0.65, & \text{wing-wall abutment} \\ 0.58, & \text{spill-through abutment} \end{cases}$$

4.3.5 Influence of a Compound Channel Configuration

Natural rivers commonly have compound channels that consist of a main channel and flood plains. The channel can typically be taken as rectangular when the flow exists only in the main channel. Then the preceding equation can be applied if the abutment is in the main channel. When flooding occurs, the flood plain is usually submerged; it is then necessary to consider the influence of the compound channel configuration on the maximum bed shear stress around the abutment whether it is in the main channel or in the flood plain. The main channel usually conveys more flow and the unit discharge is generally higher in the main channel than in the flood plain. The flow pattern around the main channel slope can be quite complex because of the lateral momentum exchange between the main channel and the flood plain. This may have a significant influence on the bed shear stress around the abutment when the abutment is close to the edge of the main channel.

The unit discharge ratio is used to describe the blockage effect of the abutment and the approach embankment in a compound channel. As defined in the methodology section, the unit discharge ratio is equal to $\frac{Q_{total}}{Q_{total} - Q_{blocked}}$ (defined in section 4.1.1) and the definition based on discharge is the only one used. The definition based on the width ratio is not precise, yet it can. However, the contraction reflects the averaged blockage effect. The location of the abutment in the compound channel is important when the abutment is close to the edge of the main channel. As mentioned above, the flow field can be very complex when the abutment toe is very close to the main channel slope. Hence, it may be necessary to include another correction for the abutment location in the compound channel. Obviously, this is not necessary in the rectangular channel. This correction factor is believed to be negligible when the abutment toe is far away from the main channel slope.

In the flume tests performed, the clay surface is very smooth before scouring. And the difference of water depth between the main channel and flood plain is not large. Also, the velocity measurements show that the depth averaged velocity is very uniform in the compound channel in the upstream section. Hence, a uniform upstream velocity field is applied at the inlet in the numerical studies of compound channel cases. A hydraulically smooth boundary is applied on the entire river bottom. This makes it reasonable to interchange the discharge based unit discharge

ratio or the area ratio of $\frac{A_{total}}{A_{total} - A_{blocked}}$ (defined in section 4.1.1) in the data analysis. And this can make it possible to apply the maximum bed shear stress equation for rectangular channel in the compound channel conditions with suitable correction factors.

The objective of this section is to study the relation between the abutment location on compound channel and the maximum bed shear stress. One of the flume test cases performed in NCHRP 24-15(2) is selected to initiate the numerical simulation and the spill-through abutment in the flume test is replaced by the vertical wall abutment to avoid the influence of abutment shape. The channel is assumed to be symmetrical and only half is simulated. The 1.83m long vertical wall abutment is sitting in the 3.7m wide flume with main channel water depth y_m of 0.5m and a flood plain water depth y_f of 0.29m. The approach velocity is 0.43m/s. Eight cases with different flood plain width L_f are simulated with CHEN3D program. The width of flood plain L_f is varied from 0.61m to 3.05m. Table 4.11 lists the parameters and the simulation results of the eight compound channel cases. The contours of friction coefficient are given in Figure 4.44 to Figure 4.51. The location of the maximum bed shear stress usually appears at the up-stream corner of the abutment whether the abutment is in the flood plain or in the main channel. If the abutment is in the flood plain, the main channel slope in front of the abutment will suffer higher bed shear stress. But the bed shear stress on the main channel slope will be very low if the abutment protrudes into main channel.

Table 4.11- Correction factors of compound channel effect.

y_f (m)	0.29	0.29	0.29	0.29	0.29	0.29	0.29	0.29
L' (m)	1.83	1.83	1.83	1.83	1.83	1.83	1.83	1.83
L_f (m)	3.05	2.74	2.44	2.13	1.83	1.22	0.91	0.61
$(L_f\text{-}L')/y_f$	4.17	3.13	2.08	1.04	0.00	-2.08	-3.13	-4.17
C_{f_max}	0.02	0.02	0.02	0.02	0.02	0.02	0.02	0.02
C_r	1.84	1.76	1.70	1.65	1.60	1.70	1.77	1.84
k_{Cr}	3.81	3.54	3.31	3.12	2.95	3.32	3.57	3.82
C_{f_max}/k_{Cr}	0.01	0.01	0.01	0.01	0.01	0.01	0.01	0.01
k_L	1.00	1.06	1.01	1.02	1.20	1.02	1.01	1.00

As mentioned above, the abutment length, water depth and the flume width are all kept constant, shown in table 4.11. The unit discharge ratios C_r for these eight cases are not the same. The smallest unit discharge ratio C_r appears when the toe of the abutment lies at the edge of the main channel slope $L' = L_f$. Then the unit discharge ratio will always increase compared to this case whether the flood plain width increases or decreases. The upper limit of the unit discharge ratio is achieved when the flood plain width goes to either zero or the width of the flume. In both extreme cases the compound channel becomes a rectangular channel but the water depth will be different under these two limiting conditions. Based on the study of unit discharge ratio in rectangular channel, the maximum bed friction coefficient C_{f_max} is linearly proportional with the unit discharge ratio C_r. Then the case with the smallest unit discharge ratio (when $L' = L_f$)

should have the lowest $C_{f\_\max}$. To investigate the influence of the abutment location, the influence of the unit discharge ratio must be excluded by correcting $C_{f\_\max}$ with the correction factor k_{Cr} derived from the rectangular channel study. When the abutment toe is far away from the main channel slope, the influence of the lateral momentum exchange between the main channel and the flood plain on the abutment shear stress vanishes. Actually, this can be observed clearly on Figure 4.43 after the correction $C_{f\_\max} / k_{Cr}$ is performed. It should be noted that the influence of water depth is not constant for these eight cases. It can fall into two categories, abutment on flood plain and abutment on main channel. The case where the abutment toe is right at the edge of main channel slope should be put in the category of flood plain because the main channel slope is 1 to 1 and the water depth at the toe is the same as the water depth on the flood plain. The results of $C_{f\_\max} / k_{Cr}$ indicate that the big difference among $C_{f\_\max}$ for these eight cases results mainly from the difference in unit discharge ratio. To eliminate the contribution from the water depth and other parameters, it is desirable to normalize the values of $C_{f\_\max} / k_{Cr}$ with the one far away from the main channel slope $C_{f\_\max\_reference} / k_{Cr\_reference}$. The case of $L_f = 3.05m$ is chosen to normalize the cases with the abutment on the flood plain. The case of $L_f = 0.61m$ is chosen to normalize the cases with the abutment on the main channel. The value of $(C_{f\_\max} / k_{Cr}) / (C_{f\_\max\_reference} / k_{Cr\_reference})$ is called abutment location correction factor k_L. $\frac{L_f - L^{'}}{y_f}$ is preferred to represent the abutment location because it shows the relative distance of the abutment toe to the main channel slope. Figure 4.40 shows the relationship between k_L and $\frac{L_f - L^{'}}{y_f}$. The bed shear stress is about 20% higher when the abutment toe is right at the edge of the main channel slope, and this influence will exist only within a horizontal distance equal to about one time water depth on either side of the main channel slope.

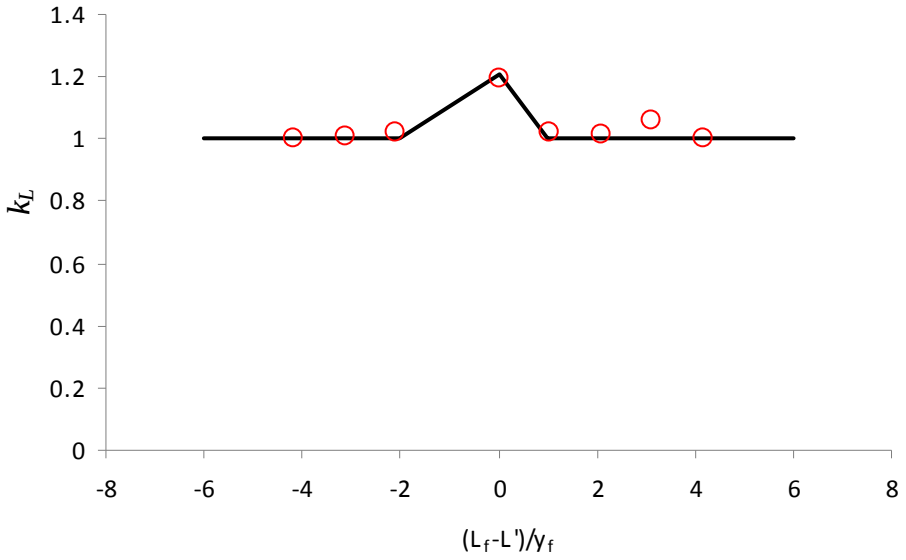

Figure 4.43- Correction factor of abutment location in compound channel.

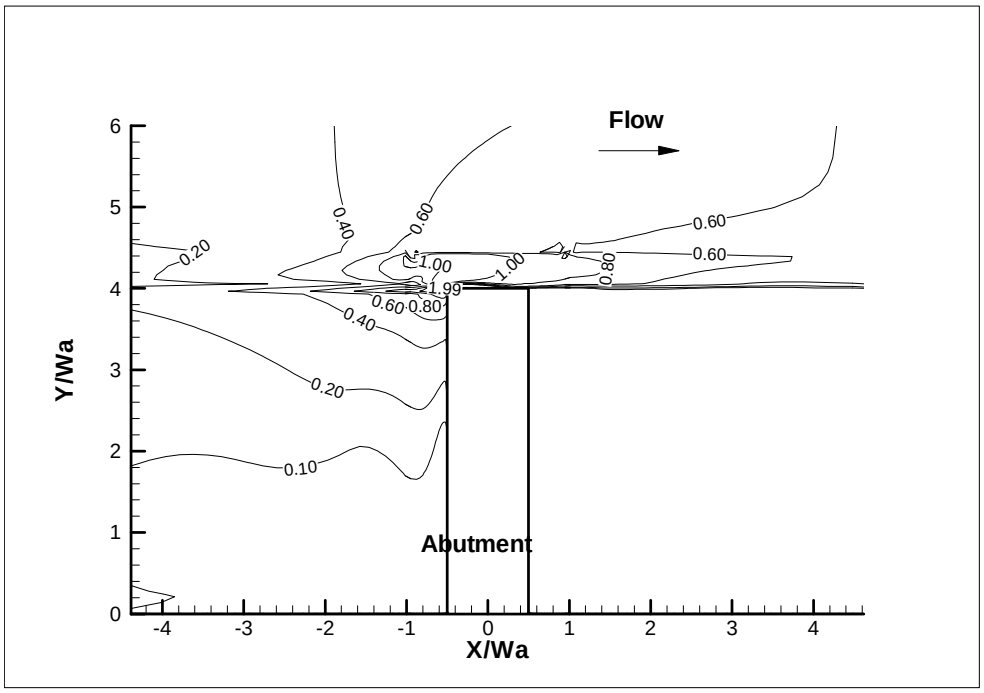

Figure 4.44 - Bed friction coefficient ($\times 10^2$), $\frac{\tau_b}{\rho V^2}$ contour for L_m = 1.83m.

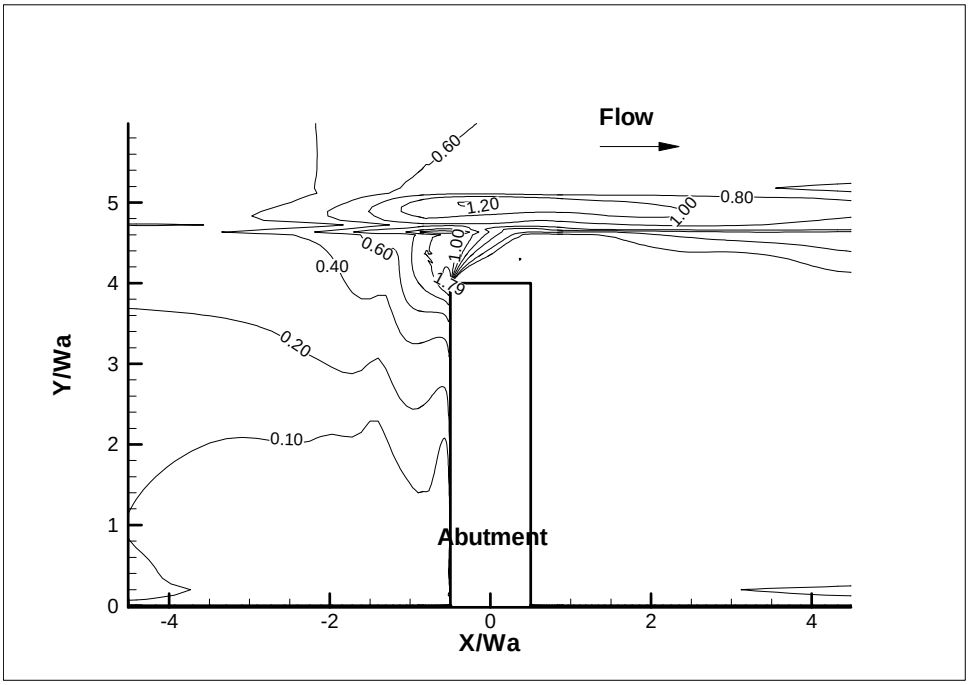

Figure 4.45 - Bed friction coefficient ($\times 10^2$), $\frac{\tau_b}{\rho V^2}$ contour for *Lm* = 2.13m.

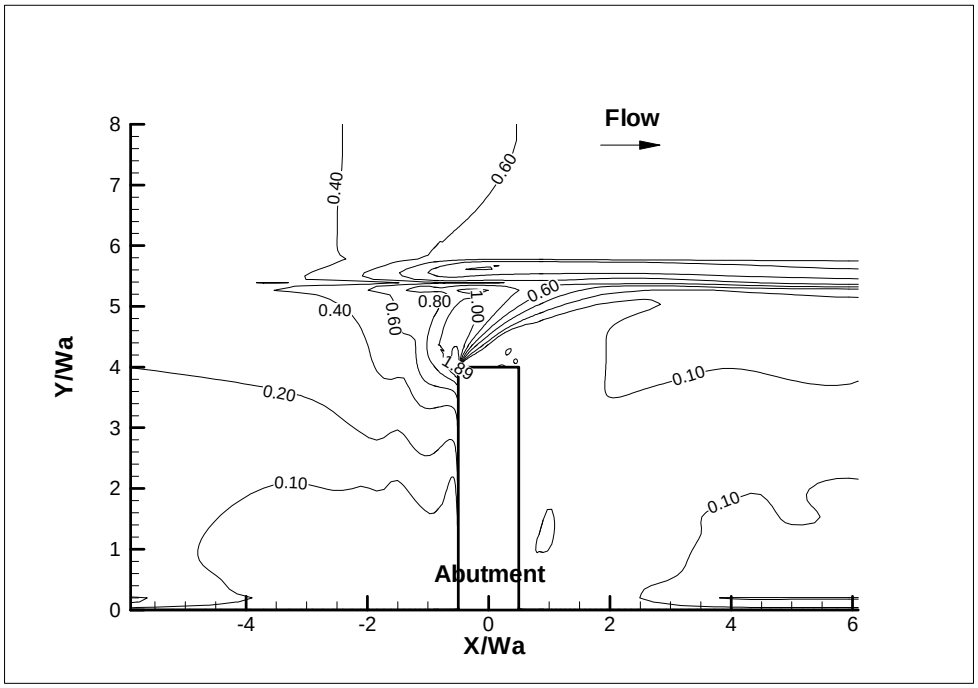

Figure 4.46 - Bed friction coefficient ($\times 10^2$), $\frac{\tau_b}{\rho V^2}$ contour for Lm = 1.22m.

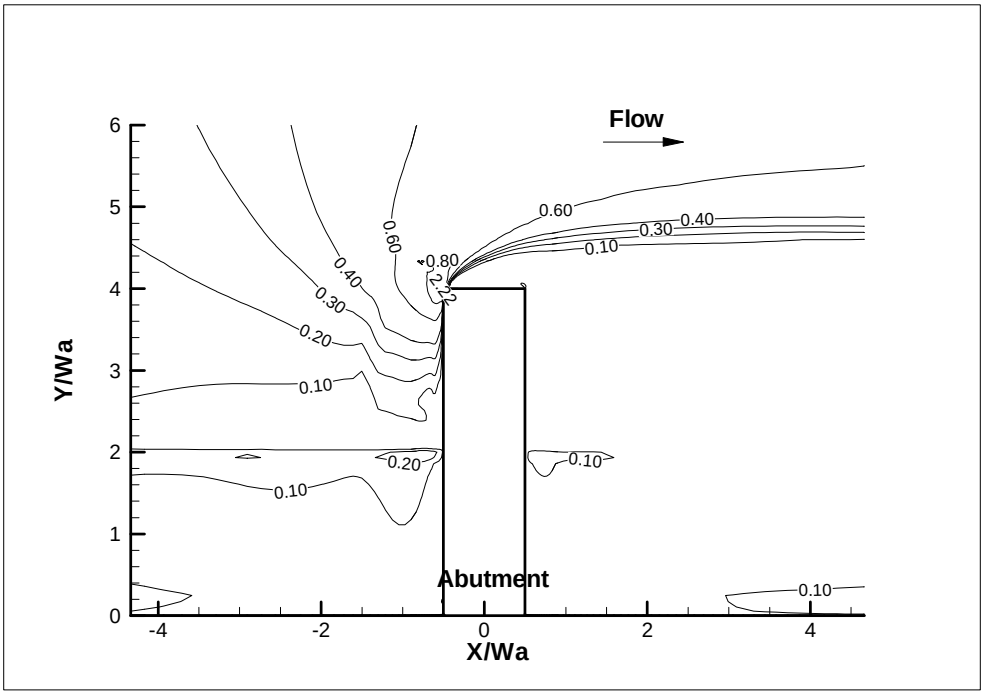

Figure 4.47 - Bed friction coefficient ($\times 10^2$), $\frac{\tau_b}{\rho V^2}$ contour for L_m = 2.74m.

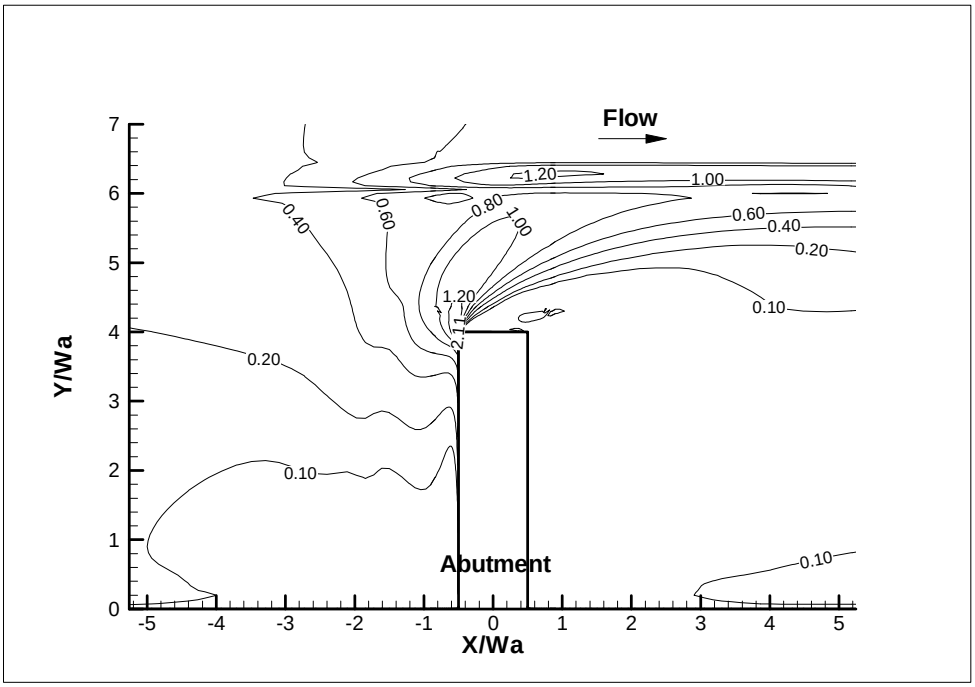

Figure 4.48 - Bed friction coefficient ($\times 10^2$), $\frac{\tau_b}{\rho V^2}$ contour for L_m = 0.91m.

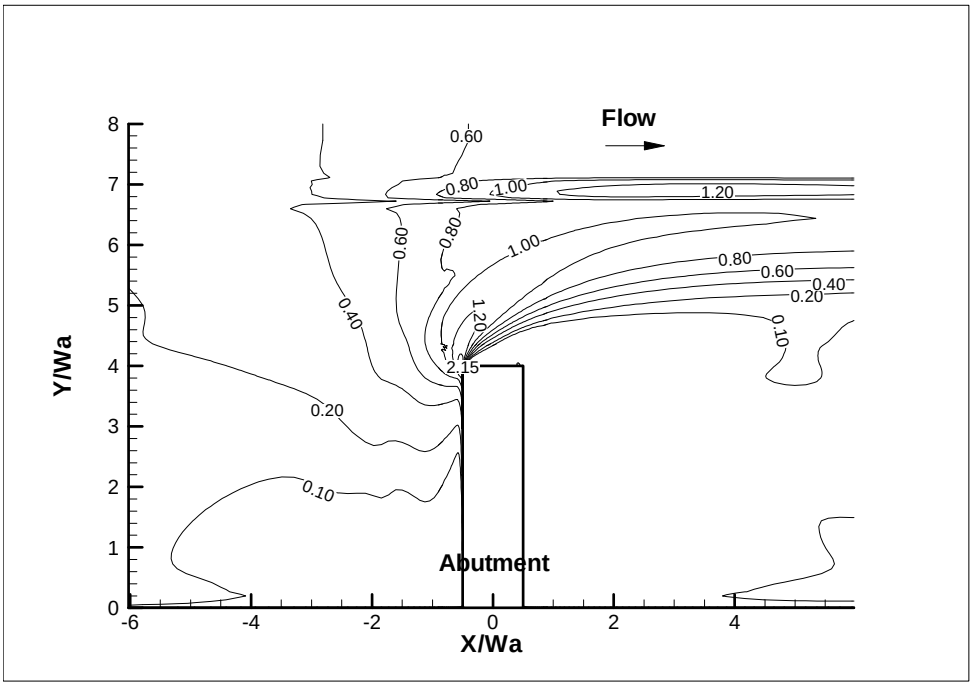

Figure 4.49 - Bed friction coefficient ($\times 10^2$), $\frac{\tau_b}{\rho V^2}$ contour for L_m = 0.61m.

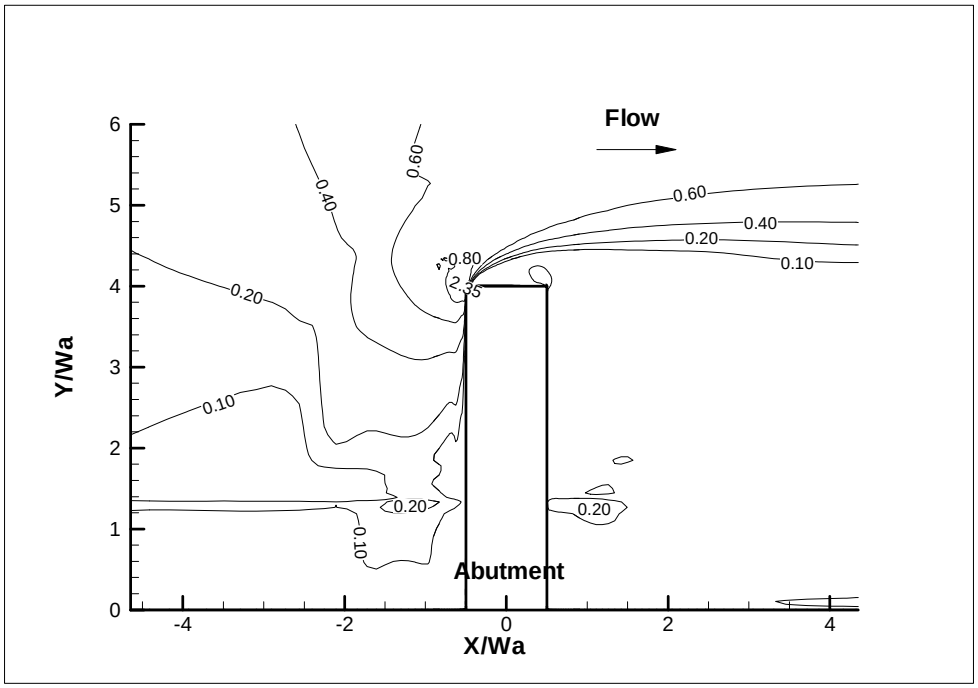

Figure 4.50 - Bed friction coefficient ($\times 10^2$), $\frac{\tau_b}{\rho V^2}$ contour for L_m = 3.05m.

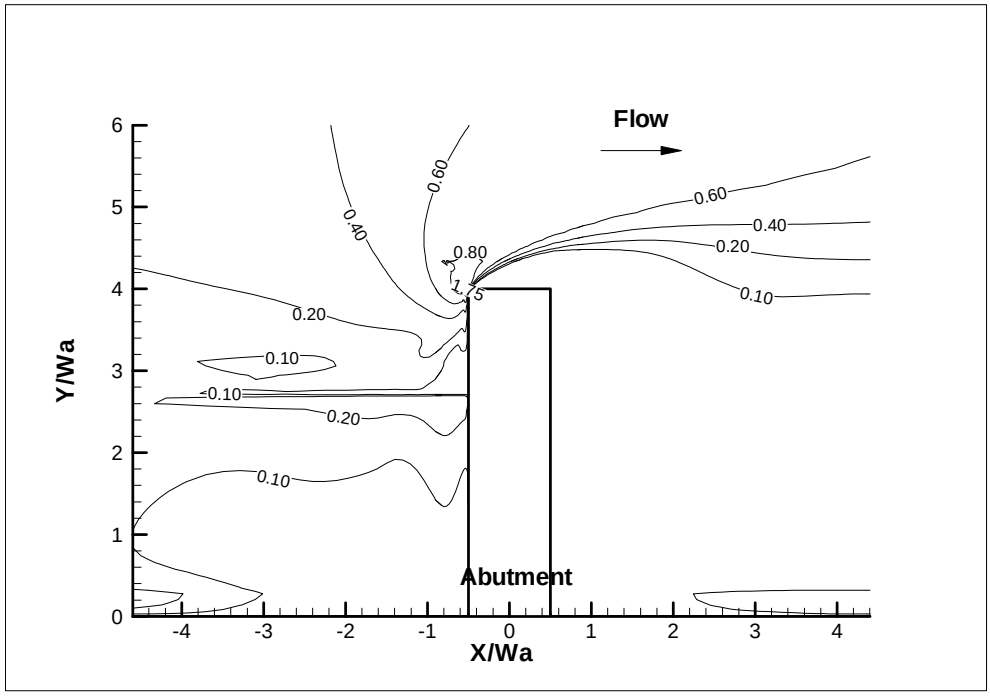

Figure 4.51- Bed friction coefficient ($\times 10^2$), $\frac{\tau_b}{\rho V^2}$ contour for L_m = 2.44m.

4.3.6 Maximum Bed Shear Stress Equation in Compound Channel

The correction needed for the abutment location in the compound channel can be used to generate an equation for maximum bed shear stressing a compound channel:

$$\frac{\tau_{\max}}{\rho V^2} = C_{f\_vw} \cdot k_{Cr} \cdot k_{sh} \cdot k_{Fr} \cdot k_s \cdot k_{sk} \cdot k_L \tag{4.79}$$

where C_{f_vw}, k_{Cr},, k_{sh},, k_{Fr}, k_s, k_{sk} are the same as in the case of the rectangular channel. (Eq. 4.78) and k_L = correction factor for abutment location in compound channel.

$$k_L = \begin{cases} 1 & \text{for } \left(L_f - L^{'}\right)/y_f \le -2 \\ 0.6(L_f - L^{'})/y_f + 1.2 & \text{for } -2 < (L_f - L^{'})/y_f \le 0 \\ -1.2(L_f - L^{'})/y_f + 1.2 & \text{for } 0 < (L_f - L^{'})/y_f \le 1 \\ 1 & \text{for } 1 \le (L_f - L^{'})/y_f \end{cases}$$

It should be noted that the proposed equations in this chapter are based on the channel unit discharge ratio defined by the channel cross section area ratio. The reason is that the water is relatively deep in these simulations and the bed surface roughness is the same in the flood plain and in the main channel. The upstream velocity far from the abutment is found to be uniformly distributed in the numerical simulations and this is also true in the flume tests. Hence the channel conveyance ratio is the same as the area ratio. In engineering practice, the area ratio may not represent the conveyance ratio very well. So in practice the unit discharge ratio should be determined based on the actual conveyance ratio to get a more representative prediction.

4.3.7 Verification of the Maximum Bed Shear Stress Equation

The proposed equation consists of several correction factors. The assumption is that these dimensionless parameters are independent and they can be superposed simply. A verification needs to be conducted to check the performance of this method. The simple product of these parameters could accumulate these errors. This is going to be studied in this section.

One way to check the performance of the equation is to predict the database used in the equation development. All the cases have been tabulated in Table 4.12. The six dimensionless parameters have been marked. In the parametric studies, only one parameter was changed at one time in theory. The predicted maximum bed friction coefficients are also listed in the table. The overall performance of the equation is shown in Figure 4.52. A good agreement is observed for most of the cases. It proves that the method has been well conducted during the data regressions.

Table 4.12 - Cases used to derive the maximum bed shear stress equation around abutment.

Re	C_r	L'/W_a	y/W_a	Abutment Shape	Skew Angle (^{o})	C_{f_vw}	k_{Cr}	k_{sh}	k_{Fr}	k_s	k_{sk}	C_{f_max} CHEN3D	C_{f_max} Prediction
1.00E+04	1.07	0.50	2	VW	90	0.0345	1.00	1.04	1.00	1	1	0.0333	0.0357
2.00E+04	1.07	0.50	2	VW	90	0.0239	1.00	1.04	1.00	1	1	0.0235	0.0248
5.00E+04	1.07	0.50	2	VW	90	0.0158	1.00	1.04	1.00	1	1	0.0148	0.0164
1.00E+05	1.07	0.50	2	VW	90	0.0115	1.00	1.04	1.00	1	1	0.0103	0.0120
5.00E+05	1.07	0.50	2	VW	90	0.0056	1.00	1.04	1.00	1	1	0.0064	0.0058
1.00E+06	1.07	0.50	2	VW	90	0.0041	1.00	1.04	1.00	1	1	0.0048	0.0042
5.00E+06	1.07	0.50	2	VW	90	0.0020	1.00	1.04	1.00	1	1	0.0034	0.0020
1.00E+07	1.07	0.50	2	VW	90	0.0014	1.00	1.04	1.00	1	1	0.0025	0.0015
1.00E+05	1.25	0.50	2	VW	90	0.0115	1.76	1.04	1.02	1	1	0.0189	0.0215
1.00E+05	1.67	0.50	2	VW	90	0.0115	3.51	1.04	1.02	1	1	0.0369	0.0428
1.00E+05	2.50	0.50	2	VW	90	0.0115	6.96	1.04	1.02	1	1	0.0718	0.0850
1.00E+05	1.11	0.80	2	VW	90	0.0115	1.18	0.93	1.02	1	1	0.0119	0.0128
1.00E+05	1.25	1.60	2	VW	90	0.0115	1.76	0.79	1.02	1	1	0.0146	0.0163
1.00E+05	1.38	2.22	2	VW	90	0.0115	2.30	0.73	1.02	1	1	0.0169	0.0196
1.00E+05	1.56	2.89	2	VW	90	0.0115	3.05	0.68	1.02	1	1	0.0221	0.0244
1.00E+05	1.80	3.55	2	VW	90	0.0115	4.05	0.65	1.02	1	1	0.0283	0.0309
1.00E+05	2.57	4.89	2	VW	90	0.0115	7.25	0.60	1.02	1	1	0.0412	0.0512
1.00E+05	1.07	0.50	1	VW	90	0.0115	1.00	1.04	1.10	1	1	0.0111	0.0132
1.00E+05	1.07	0.50	0.75	VW	90	0.0115	1.00	1.04	1.21	1	1	0.0126	0.0151
1.00E+05	1.07	0.50	0.375	VW	90	0.0115	1.00	1.04	1.37	1	1	0.0147	0.0169
1.00E+05	1.07	0.50	0.1875	VW	90	0.0115	1.00	1.04	1.59	1	1	0.0159	0.0182
1.67E+05	1.38	2.22	0.8	WW	90	0.0091	2.32	0.73	1.29	0.65	1	0.0107	0.0116
1.67E+05	1.56	2.89	0.8	WW	90	0.0091	3.07	0.68	1.29	0.65	1	0.0138	0.0144
1.67E+05	1.80	3.55	0.8	WW	90	0.0091	4.04	0.65	1.29	0.65	1	0.0161	0.0180
1.67E+05	2.57	4.89	0.8	WW	90	0.0091	7.25	0.60	1.29	0.65	1	0.0260	0.0299
1.67E+05	1.22	2.22	0.8	ST (2:1)	90	0.0091	1.62	0.73	1.29	0.59	1	0.0076	0.0073
1.67E+05	1.35	2.89	0.8	ST (2:1)	90	0.0091	2.19	0.68	1.29	0.59	1	0.0097	0.0093
1.67E+05	1.52	3.55	0.8	ST (2:1)	90	0.0091	2.90	0.65	1.29	0.59	1	0.0107	0.0117
1.67E+05	2.04	4.89	0.8	ST (2:1)	90	0.0091	5.06	0.60	1.29	0.59	1	0.0152	0.0190
1.67E+05	1.38	2.22	0.8	VW	60	0.0091	2.32	0.73	1.29	1	1	0.0102	0.0178
1.67E+05	1.38	2.22	0.8	VW	75	0.0091	2.32	0.73	1.29	1	1	0.0111	0.0178
1.67E+05	1.38	2.22	0.8	VW	90	0.0091	2.32	0.73	1.29	1	1	0.0165	0.0178
1.67E+05	1.38	2.22	0.8	VW	105	0.0091	2.32	0.73	1.29	1	1	0.0128	0.0178
1.67E+05	1.38	2.22	0.8	VW	120	0.0091	2.32	0.73	1.29	1	1	0.0122	0.0178

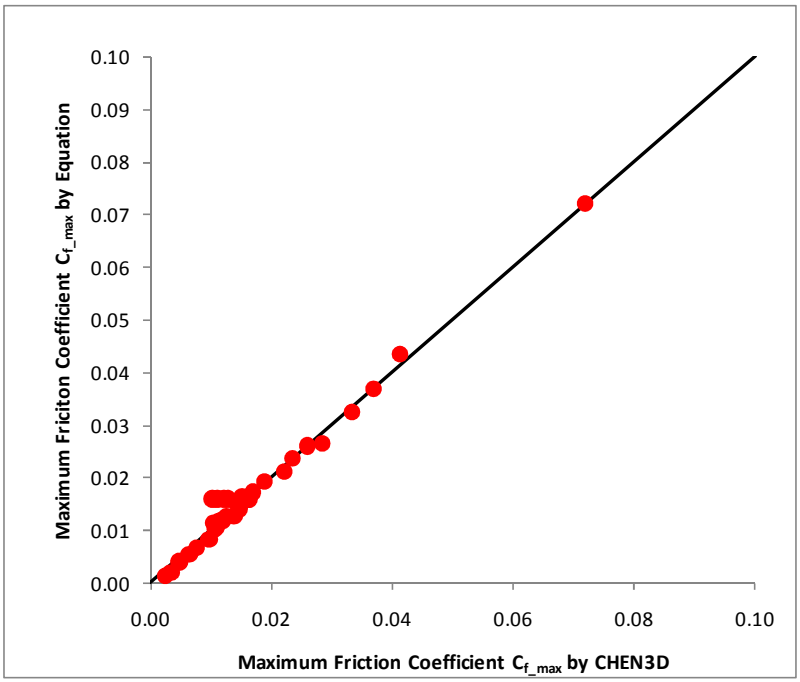

Figure 4.52 - Comparison of simulated and predicted cases in rectangular channel study.

Forty one additional and independent CHEN3D simulations were performed as shown in Table 4.13. It should be noted that most of these cases include a compound channel. It is a good chance to check the consistency of the CHEN3D and the performance of the proposed equation with a new data base. The prediction of these 41 cases and the correction factors are tabulated in Table 4.14. The comparison of the agreement is presented in Figure 4.53.

It should be noted that Case 1, Case 10, Case 11, Case 23, and Case 24 in Table 4.14 have different skew angles, but the maximum bed friction coefficient, $C_{f\_\max} = \frac{\tau_{\max}}{\rho V^2}$ are almost the same. Therefore, the correction factor of 1.0 for the skew angle proposed in the section 4.3.3.6 is reasonable for spill-through abutment.

Table 4.13 - Numerical simulations initially proposed in this study.

Case #	Abutment Shape	Channel Type	L (m)	y_m (m)	y_f (m)	L_f (m)	L' (m)	V_{avg} (m/s)	W_a (m)	Skew Angle (^{o})	C_{f_max} CHEN3D	CHEN3D (Pa)
Case1	ST (2:1)	Comp.	3.658	0.497	0.293	2.438	1.829	0.430	0.457	90	0.0087	1.6
Case2	ST (2:1)	Comp.	3.658	0.387	0.183	2.438	1.829	0.357	0.457	90	0.0076	0.97
Case3	ST (2:1)	Comp.	3.658	0.607	0.402	2.438	1.829	0.491	0.457	90	0.0098	2.37
Case4	ST (2:1)	Comp.	3.658	0.497	0.293	2.438	1.829	0.335	0.457	90	0.0094	1.06
Case5	ST (2:1)	Comp.	3.658	0.497	0.293	2.438	1.829	0.521	0.457	90	0.0072	1.96
Case6	ST (2:1)	Comp.	3.658	0.497	0.293	2.438	1.219	0.366	0.457	90	0.0057	0.76
Case7	ST (2:1)	Comp.	3.658	0.497	0.293	2.438	2.438	0.485	0.457	90	0.0149	3.5
Case8	ST (3:1)	Comp.	3.658	0.497	0.293	2.438	1.829	0.430	0.457	90	0.0084	1.56
Case9	WW	Comp.	3.658	0.497	0.293	2.438	1.829	0.430	0.457	90	0.0117	2.16
Case10	ST (2:1)	Comp.	3.658	0.497	0.293	2.438	1.829	0.430	0.457	60	0.0086	1.59
Case11	ST (2:1)	Comp.	3.658	0.497	0.293	2.438	1.829	0.430	0.457	120	0.0081	1.49
Case12	WW	Comp.	3.658	0.497	0.293	2.438	1.829	0.335	0.457	90	0.0120	1.35
Case13	WW	Rect.	3.658	0.366	0.366	2.438	1.015	0.332	0.457	90	0.0108	1.19
Case14	WW	Rect.	3.658	0.366	0.366	2.438	1.625	0.332	0.457	90	0.0161	1.78
Case15	WW	Rect.	3.658	0.366	0.366	2.438	2.234	0.332	0.457	90	0.0260	2.87
Case16	WW	Rect.	3.658	0.366	0.366	2.438	2.743	0.332	0.457	90	0.0138	1.52
Case17	WW	Rect.	3.658	0.366	0.366	2.438	1.320	0.332	0.457	90	0.0138	1.52
Case18	ST (2:1)	Comp.	3.658	0.497	0.293	2.438	1.829	0.244	0.457	90	0.0111	0.66
Case19	ST (2:1)	Comp.	3.658	0.497	0.293	2.438	1.829	0.616	0.457	90	0.0062	2.35
Case20	ST (2:1)	Comp.	3.658	0.497	0.293	2.438	1.829	0.710	0.457	90	0.0059	3
Case21	ST (2:1)	Comp.	3.658	0.442	0.238	2.438	1.829	0.393	0.457	90	0.0081	1.25
Case22	ST (2:1)	Comp.	3.658	0.552	0.347	2.438	1.829	0.460	0.457	90	0.0086	1.82
Case23	ST (2:1)	Comp.	3.658	0.497	0.293	2.438	1.829	0.430	0.457	75	0.0087	1.61
Case24	ST (2:1)	Comp.	3.658	0.497	0.293	2.438	1.829	0.430	0.457	105	0.0086	1.59
Case25	ST (2:1)	Comp.	3.658	0.448	0.244	2.438	1.524	0.399	0.457	90	0.0078	1.24
Case26	ST (2:1)	Comp.	3.658	0.546	0.341	2.438	2.134	0.457	0.457	90	0.0108	2.26
Case27	ST (2:1)	Comp.	3.658	0.497	0.293	0.914	1.829	0.479	0.457	90	0.0084	1.92
Case28	ST (2:1)	Comp.	3.658	0.497	0.293	2.743	1.829	0.418	0.457	90	0.0096	1.67
Case29	ST (2:1)	Comp.	3.658	0.497	0.293	3.048	1.829	0.408	0.457	90	0.0101	1.69
Case30	ST (2:1)	Comp.	3.658	0.497	0.293	1.219	1.829	0.469	0.457	90	0.0080	1.76
Case31	ST (2:1)	Comp.	3.658	0.497	0.293	0.610	1.829	0.488	0.457	90	0.0081	1.93
Case32	ST (2:1)	Comp.	7.315	0.994	0.585	4.877	3.658	0.607	0.914	90	0.0055	2.03
Case33	ST (2:1)	Comp.	14.630	1.987	1.170	9.754	7.315	0.858	1.829	90	0.0037	2.75
Case34	ST (2:1)	Comp.	21.946	2.981	1.756	14.630	10.973	1.051	2.743	90	0.0023	2.56
Case35	ST (2:1)	Comp.	29.261	3.975	2.341	19.507	14.630	1.213	3.658	90	0.0019	2.84
Case36	ST (2:1)	Comp.	36.576	4.968	2.926	24.384	18.288	1.357	4.572	90	0.0017	3.13
Case37	WW	Comp.	7.315	0.994	0.585	4.877	3.658	0.607	0.914	90	0.0070	2.56
Case38	WW	Comp.	14.630	1.987	1.170	9.754	7.315	0.858	1.829	90	0.0036	2.64
Case39	WW	Comp.	21.946	2.981	1.756	14.630	10.973	1.051	2.743	90	0.0031	3.47
Case40	WW	Comp.	29.261	3.975	2.341	19.507	14.630	1.213	3.658	90	0.0026	3.89
Case41	WW	Comp.	36.576	4.968	2.926	24.384	18.288	1.357	4.572	90	0.0025	4.62

Table 4.14 - Prediction of the numerical cases.

Case #	C_r	Re	C_{f_vw}	k_{Cr}	k_{sh}	k_{Fr}	k_{sk}	k_s	k_m	C_{f_max} Prediction	Prediction (Pa)
Case1	1.530	1.96E+05	0.0085	2.68	0.61	1.33	1.00	0.58	1.00	0.0107	1.97
Case2	1.505	1.63E+05	0.0093	2.59	0.61	1.35	1.00	0.58	1.00	0.0115	1.46
Case3	1.510	2.24E+05	0.0080	2.61	0.61	1.31	1.00	0.58	1.00	0.0097	2.33
Case4	1.530	1.53E+05	0.0095	2.68	0.61	1.21	1.00	0.58	1.00	0.0109	1.23
Case5	1.530	2.38E+05	0.0078	2.68	0.61	1.44	1.00	0.58	1.00	0.0106	2.88
Case6	1.269	1.67E+05	0.0091	1.73	0.67	1.25	1.00	0.58	1.00	0.0077	1.03
Case7	1.934	2.22E+05	0.0081	4.16	0.57	1.39	1.00	0.58	1.20	0.0185	4.34
Case8	1.456	1.96E+05	0.0085	2.41	0.61	1.33	1.00	0.58	1.00	0.0096	1.78
Case9	1.701	1.96E+05	0.0085	3.31	0.61	1.33	1.00	0.58	1.00	0.0132	2.43
Case10	1.530	1.96E+05	0.0085	2.68	0.61	1.33	1.00	0.58	1.00	0.0107	1.97
Case11	1.530	1.96E+05	0.0085	2.68	0.61	1.33	1.00	0.58	1.00	0.0107	1.97
Case12	1.530	1.53E+05	0.0095	2.68	0.61	1.21	1.00	0.65	1.00	0.0122	1.37
Case13	1.384	1.52E+05	0.0096	2.15	0.70	1.16	1.00	0.65	1.00	0.0109	1.20
Case14	1.799	1.52E+05	0.0096	3.67	0.63	1.16	1.00	0.65	1.00	0.0166	1.83
Case15	2.570	1.52E+05	0.0096	6.48	0.58	1.16	1.00	0.65	1.00	0.0272	3.00
Case16	4.000	1.52E+05	0.0096	11.71	0.55	1.16	1.00	0.65	1.00	0.0468	5.16
Case17	1.565	1.52E+05	0.0096	2.81	0.66	1.16	1.00	0.65	1.00	0.0134	1.48
Case18	1.530	1.11E+05	0.0110	2.68	0.61	1.10	1.00	0.58	1.00	0.0114	0.68
Case19	1.530	2.81E+05	0.0072	2.68	0.61	1.55	1.00	0.58	1.00	0.0106	4.03
Case20	1.530	3.25E+05	0.0068	2.68	0.61	1.67	1.00	0.58	1.00	0.0107	5.40
Case21	1.526	1.80E+05	0.0089	2.67	0.61	1.33	1.00	0.58	1.00	0.0111	1.72
Case22	1.523	2.10E+05	0.0082	2.66	0.61	1.32	1.00	0.58	1.00	0.0102	2.16
Case23	1.530	1.96E+05	0.0085	2.68	0.61	1.33	1.00	0.58	1.00	0.0107	1.97
Case24	1.530	1.96E+05	0.0085	2.68	0.61	1.33	1.00	0.58	1.00	0.0107	1.97
Case25	1.386	1.83E+05	0.0088	2.16	0.64	1.33	1.00	0.58	1.00	0.0094	1.49
Case26	1.707	2.09E+05	0.0083	3.33	0.59	1.32	1.00	0.58	1.00	0.0124	2.58
Case27	1.619	2.19E+05	0.0081	3.01	0.61	1.25	1.00	0.58	1.00	0.0108	2.47
Case28	1.571	1.91E+05	0.0086	2.83	0.61	1.31	1.00	0.58	1.00	0.0113	1.97
Case29	1.621	1.87E+05	0.0087	3.01	0.61	1.30	1.00	0.58	1.00	0.0120	2.01
Case30	1.556	2.15E+05	0.0082	2.78	0.61	1.24	1.00	0.58	1.00	0.0100	2.19
Case31	1.682	2.23E+05	0.0080	3.24	0.61	1.26	1.00	0.58	1.00	0.0116	2.75
Case32	1.530	5.55E+05	0.0053	2.68	0.61	1.32	1.00	0.58	1.00	0.0067	2.46
Case33	1.530	1.57E+06	0.0033	2.68	0.61	1.32	1.00	0.58	1.00	0.0042	3.07
Case34	1.530	2.88E+06	0.0025	2.68	0.61	1.32	1.00	0.58	1.00	0.0032	3.50
Case35	1.530	4.44E+06	0.0021	2.68	0.61	1.32	1.00	0.58	1.00	0.0026	3.84
Case36	1.530	6.20E+06	0.0018	2.68	0.61	1.32	1.00	0.58	1.00	0.0022	4.13
Case37	1.701	5.55E+05	0.0053	3.31	0.61	1.32	1.00	0.65	1.00	0.0092	3.40
Case38	1.701	1.57E+06	0.0033	3.31	0.61	1.32	1.00	0.65	1.00	0.0058	4.25
Case39	1.701	2.88E+06	0.0025	3.31	0.61	1.32	1.00	0.65	1.00	0.0044	4.84
Case40	1.701	4.44E+06	0.0021	3.31	0.61	1.32	1.00	0.65	1.00	0.0036	5.31
Case41	1.701	6.20E+06	0.0018	3.31	0.61	1.32	1.00	0.65	1.00	0.0031	5.71

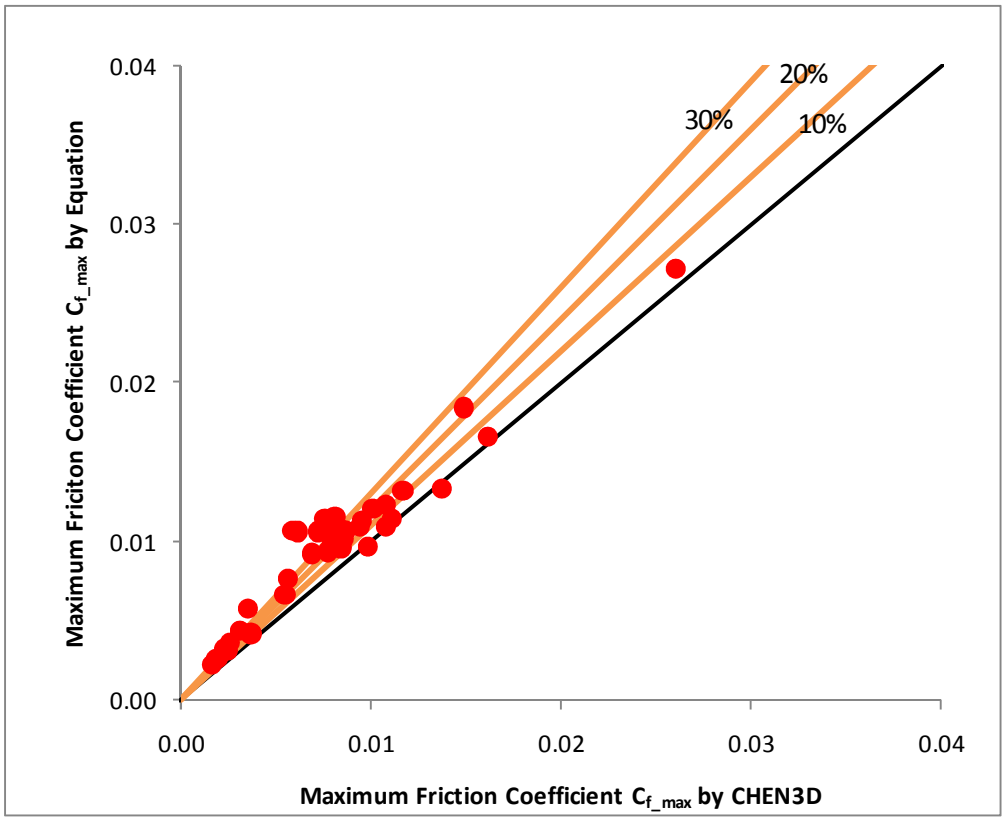

Figure 4.53 - Comparison of the simulated and predicted cases.

As shown in Figure 4.53, the prediction by equation can match the CHEN3D simulation reasonably. For some cases, the predicted values can be about 20% to 30% higher than the simulated values. This is conservative as a higher shear stress will lead to a higher erosion rate. Also, the comparison shown on Figure 4.53 indicates that multiplying the *k* factors is conservative.

4.3.8 Correction of Maximum Bed Shear Stress around Abutment Based on Flume Tests

Eighteen flume test cases have been conducted as shown in Table 4.15. In the original design, these cases were identical to the corresponding cases in the numerical study. During the testing, the flow conditions were changed in several cases for convenience. The detail parameters of these 17 cases are provided in Table 4.15 together with the predicted maximum bed shear stresses. The values of τ_{max} are calculated according to the actual parameters and the proposed equation. The proposed maximum bed shear stresses equation is based on the assumption of a hydraulically smooth boundary condition (roughness is not included in the prediction).

Table 4.15 - Flume test cases.

case #	V_{avg}(m/s)	y_f(m)	y_m(m)	L (m)	L_f (m)	L_a (m)	Q (m^3/s)	C_R	W_a (m)	C_{f_vw}	k_{Cr}	k_{sh}	k_{Fr}	k_{sk}	k_s	k_m	$\tau_{\_max}$(Pa) Prediciton
case1	0.442	0.293	0.496	3.658	2.438	1.829	0.573	1.53	0.457	0.0084	2.69	0.61	1.34	0.58	1	1	2.09
case1II	0.432	0.293	0.497	3.658	2.438	1.829	0.562	1.53	0.457	0.0085	2.69	0.61	1.33	0.58	1	1	2.00
case2	0.357	0.183	0.386	3.658	2.438	1.829	0.32	1.50	0.457	0.0092	2.59	0.61	1.35	0.58	1	1	1.46
case3	0.481	0.4	0.603	3.658	2.438	1.829	0.813	1.50	0.457	0.0081	2.58	0.61	1.30	0.58	1	1	2.22
case4	0.342	0.291	0.494	3.658	2.438	1.829	0.442	1.52	0.457	0.0094	2.66	0.61	1.22	0.58	1	1	1.27
case5	0.51	0.293	0.496	3.658	2.438	1.829	0.662	1.52	0.457	0.0079	2.65	0.61	1.42	0.58	1	1	2.72
case6	0.432	0.293	0.496	3.658	2.438	1.219	0.561	1.25	0.457	0.0085	1.65	0.67	1.33	0.58	1	1	1.35
case7	0.437	0.291	0.494	3.658	2.438	2.438	0.564	1.86	0.457	0.0084	3.87	0.57	1.34	0.58	1	1.2	3.30
case8	0.442	0.29	0.493	3.658	2.438	1.829	0.57	1.43	0.457	0.0084	2.31	0.61	1.34	0.58	1	1	1.80
case9	0.436	0.294	0.497	3.658	2.438	1.829	0.568	1.64	0.457	0.0084	3.08	0.61	1.33	0.65	1	1	2.61
case10																	
case11																	
case12	0.333	0.293	0.497	3.658	2.438	1.829	0.433	1.68	0.457	0.0095	3.23	0.61	1.21	0.65	1	1	1.64
case12B	0.583	0.294	0.497	3.658	2.438	1.829	0.759	1.69	0.457	0.0074	3.29	0.61	1.51	0.65	1	1	4.95
case13	0.322	0.365	0.365	3.658	3.658	1.015	0.43	1.38	0.457	0.0097	2.15	0.70	1.15	0.65	1	1	1.13
case14	0.32	0.371	0.371	3.658	3.658	1.625	0.433	1.80	0.457	0.0097	3.66	0.63	1.15	0.65	1	1	1.70
case15	0.302	0.377	0.377	3.658	3.658	2.234	0.416	2.57	0.457	0.0100	6.49	0.58	1.13	0.65	1	1	2.51
case16	0.208	0.373	0.373	3.658	3.658	2.743	0.285	4.00	0.457	0.0118	11.71	0.55	1.03	0.65	1	1	2.20
case17	0.364	0.364	0.364	3.658	3.658	1.32	0.484	1.56	0.457	0.0092	2.81	0.66	1.20	0.65	1	1	1.75

Based on the measurements in the flume tests, the initial erosion rate at the beginning of the flume test and the maximum scour depth can be estimated by fitting the scour depth history with a hyperbola function. Table 4.16 lists all the initial erosion rates $\dot{z}_{ini}$ and the ultimate scour depths $y_{s(Abut)}$ obtained in such a fashion from the flume tests.

Table 4.16 - Maximum bed shear stresses based on EFA results.

Case #	$\dot{z}_{ini}$ (mm/hr)	$y_{s(Abut)}$ (mm)	$\tau_{\max\_\max}$ (Pa) EFA	$\tau_{\max\_\min}$ (Pa) EFA	$\tau_{\max\_EFA}$ (Pa) EFA	$\tau_{\max\_prediciton}$ (Pa)	$\frac{\tau_{\max\_EFA}}{\tau_{\max\_prediction}}$
Case1	5.37	439	22	8	13.59	2.09	6.50
Case1 II	6.16	490	22	8	14.79	2.00	7.40
Case2	0.74	282	9	1.5	6.54	1.46	4.48
Case3	1.05	589	10	2	7.01	2.22	3.16
Case4	1.14	300	10	2	7.15	1.27	5.63
Case5	1.66	808	10	2	7.94	2.72	2.92
Case6	1.25	351	10	2	7.32	1.35	5.42
Case7	4.55	1190	20	5	12.34	3.30	3.74
Case8	2.20	413	11	3	8.76	1.80	4.87
Case9	1.80	667	10	2	8.15	2.61	3.12
Case12	0.24	155	4	0.7	5.78	1.64	3.52
Case12B	1.47	1429	10	2	7.65	4.95	1.55
Case13	0.54	66	7	1.1	6.24	1.13	5.52
Case14	2.37	304	11	3	9.02	1.70	5.31
Case15	1.73	334	10	2	8.05	2.51	3.21
Case16	3.21	448	20	3	10.3	2.20	4.68
Case17	1.96	262	11	3	8.40	1.75	4.80

A porcelain clay was used in the flume tests. Eleven samples of the clay were tested during the entire flume test period from 2005 to 2008 to monitor the change in erosion property of this manufactured clay. The EFA results are shown in Figure 4.54 and found to scatter in a wide range. This shows the difficulty in the erosion problem. Even for a well controlled lab testing, the erosion property of the same type of soil from the same company could have such a big difference. The regression curve is given in Figure 4.54 and indicates the range of variation. This range shows that soil properties can vary significantly even for a man made material. Natural soils would be expected to have a larger range. Based on that regression, the critical shear stress of the porcelain clay is 5.57 Pa, which is the shear stress defined at 0.1mm/hr in the EFA.

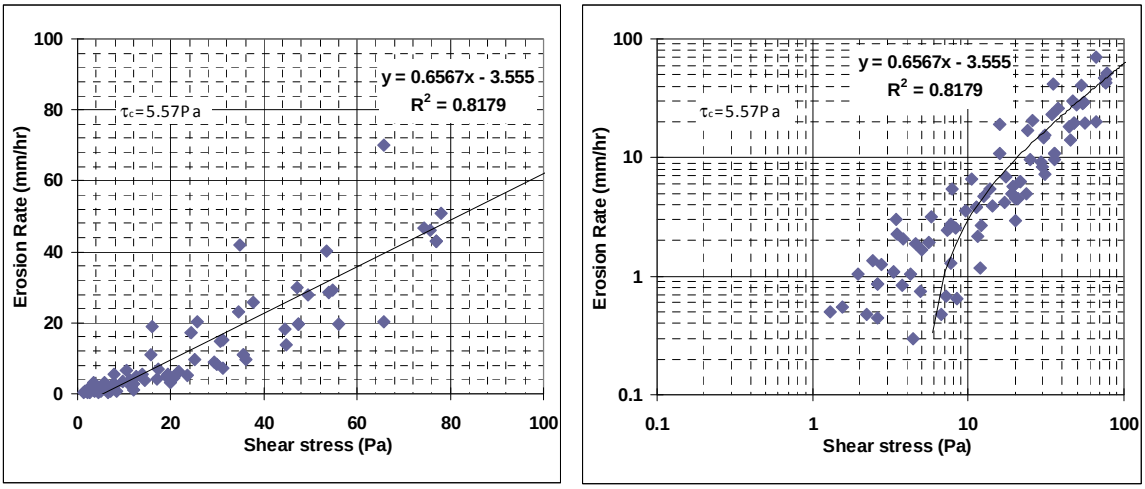

Figure 4.54 - EFA testing results of the porcelain clay used in the flume tests.

In the SRICOS method, the maximum bed shear stress is used to read the initial erosion rate from the erosion function of the soil. Based on the estimated initial erosion rate from Table 4.16, the corresponding bed shear stress can be read from Figure 4.54. The readings are listed in Table 4.16. The highest initial erosion rate appears in Case 1 and the lowest erosion rate appears in Case 12. The deepest scour depth is in Case 7 and the lowest scour depth is in Case 12B. Obviously, a higher initial erosion rate does not necessarily mean a deeper ultimate scour depth and vice versa. For a certain initial erosion rate, the corresponding bed shear stress varies in a wide range and the maximum and minimum values (τ_{max_max} and τ_{max_min}) from Figure 4.54 are listed in Table 4.16. The representative value τ_{max_EFA} is given by the regression curve. Compared with the predicted maximum bed shear stress $\tau_{max\_prediciton}$, the EFA readings are much higher. The average of the ratios of $\tau_{max\_EFA} / \tau_{max\_prediction}$ is 4.46 and the standard deviation is 1.47. The difference in the maximum bed shear stresses between the actual flume test and the prediction is believed to come from two sources. The first one is that τ_{max_EFA} is based on the initial slope of the scour depth history and therefore the initial erosion rate is attributed entirely to the mean shear stress. Generally speaking, the bed shear stress is not the only contributor to the scour development. Many researchers have found that turbulence can be a major contributor to the scour hole development. The second one is the bed roughness. In the flume test, the initial bed channel is very smooth. This is close to the hydraulically smooth boundary condition assumed in the nu-

merical study. However, the surface of the bed is getting rougher and rougher with the scour development. This is not same as the particle roughness in a sand bed. It is more similar to the sand dunes but not as regular. These factors make the prediction of the initial erosion rate difficult. To represent the real scour development in the SRICOS method, the influence of turbulence and of the bed roughness has to be carried by the maximum bed shear stress $\tau_{\max}$. It may be more appropriate to call that maximum bed shear stress in SRICOS method the apparent maximum bed shear stress. The simplest way to account for these factors is to multiply the maximum bed shear stress from the numerical simulation by a correction factor α to get the initial erosion rate reading from the EFA result, which will match to measured behavior in the flume test. The correction factor α is proposed as the summation of the average value and the standard deviation of $\tau_{\max\_EFA} / \tau_{\max\_prediction}$, which will be 5.93. Figure 4.55 shows the comparison of $\tau_{\max\_EFA}$ and $\alpha \cdot \tau_{\max\_prediction}$.

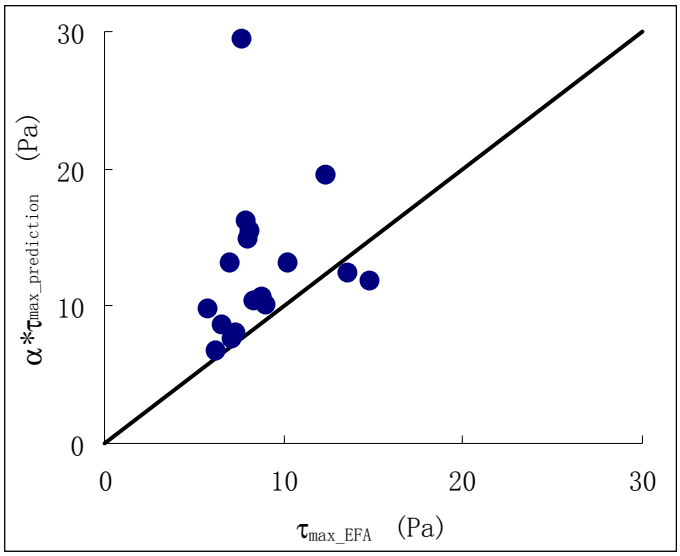

Figure 4.55 - Comparison of the $\alpha * \tau_{\max\_prediciton}$ and $\tau_{\max\_EFA}$.

4.3.9 Recommended Equation for Maximum Shear Stress around an Abutment

$$\frac{\tau_{\max}}{\rho V^2} = \alpha \cdot C_{f\_vw} \cdot k_{Cr} \cdot k_{sh} \cdot k_{Fr} \cdot k_s \cdot k_{sk} \cdot k_L \qquad (4.80)$$

where $\tau_{\max}$ = the maximum bed shear stress at the interface between the water and the river bottom near the abutment toe

ρ = mass density of water

V = upstream mean depth velocity

y = upstream water depth

W_a = top width of the abutment

L' = projected abutment length normal to the flow direction

α = correction factor based on flume tests

C_r = unit discharge ratio; defined as $C_r = Q_{total} / (Q_{total} - Q_{blocked})$

Re = Reynolds number, defined as $\mathrm{Re} = VW_a / \nu$

ν = kinematic viscosity

C_{f_VW} = maximum bed friction coefficient near the toe of vertical wall abutment under deep water conditions

k_{Cr} = correction factor for channel unit discharge ratio

k_{sh} = correction factor for the aspect ratio of the approach embankment

k_{Fr} = correction factor for water depth

k_s = correction factor for abutment shape

k_{sk} = correction factor for skew angle

k_L = correction factor for abutment location in compound channel

$$\alpha = 5.93$$

$$k_{Cr} = 3.65C_r - 2.91$$

$$k_{Fr} = \begin{cases} 2.07\mathrm{Fr} + 0.8, & \mathrm{Fr} > 0.1 \\ 1.0, & \mathrm{Fr} \le 0.1 \end{cases}$$

$$k_{sk} = 1.0$$

$$C_{f\_vw} = 2.1\mathrm{Re}^{-0.45}$$

$$k_{sh} = 0.85\left(\frac{L'}{W_a}\right)^{-0.24}$$

$$k_s = \begin{cases} 1, & \text{vertical-wall abutment} \\ 0.65, & \text{wing-wall abutment} \\ 0.58, & \text{spill-through abutment} \end{cases}$$

$$k_L = \begin{cases} 1.0 & \text{for } \left(L_f - L'\right)/y_f \le -2 \\ 0.6(L_f - L')/y_f + 1.2 & \text{for } -2 < (L_f - L')/y_f \le 0 \\ -1.2(L_f - L')/y_f + 1.2 & \text{for } 0 < (L_f - L')/y_f \le 1 \\ 1.0 & \text{for } 1 \le (L_f - L')/y_f \end{cases}$$

CHAPTER 5

MAXIMUM BED SHEAR STRESS AROUND ABUTMENT IN OVERTOPPING FLOW

The bed shear stress around abutments in overtopping flow is studied in this section. Overtopping is usually defined as the situation when the flow of water is over a dam or on embankment. Here, overtopping means the situation where the water level reaches the bridge deck or higher. The question addressed is: what is the bed shear stress around an abutment when overtopping occurs. Overtopping leads to a flow which is pressurized and to higher bed shear stress. To look into the overtopping problem, different channel configurations are studied, including overtopping in a rectangular channel, overtopping in a compound channel, overtopping in a nonsymetric channel, and overtopping in a channel bend. Finally, the flow at the confluence of two river channels is studied.

5.1 VERIFICATION OF THE OVERTOPPING FLOW SIMULATION

Kerenyi (personal communication, December, 2007) investigated the bed shear stress distribution at the bottom of a simulated river equipped with a shear stress sensor under an overtopped bridge deck. The experiment was conducted at the FHWA lab in Washington, DC. The bridge model is shown in Figure 5.1 and the notations are explained in Figure 5.2. The bed surface was roughened with sand grains with a d_{50} equal to 1mm. The approach velocity was 0.44 m/s; the water depth h_u 0.25m; the Froude number 0.28. The vertical distance h_b between the bridge deck and the river bottom could be adjusted during the test. The experiments focused on the influence of the bridge deck elevation on the bed shear stress distribution. Kerenyi provided four experiment results with h_b equal to 0.13m, 0.16m, 0.19m, and 0.22m (h_u is constant 0.25m). Two simulations with CHEN3D were performed for the cases of h_b=0.13m and h_b=0.16m (h_u is constant 0.25m). The free surface was simulated with a rigid lid, which is believed to be reasonable for these two cases.

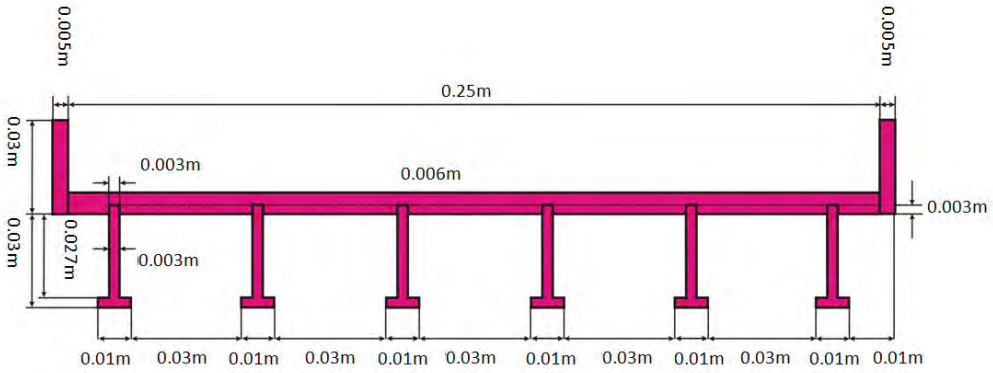

Figure 5.1 - Bridge model for shear stress experiments (after Kerenyi, 2007).

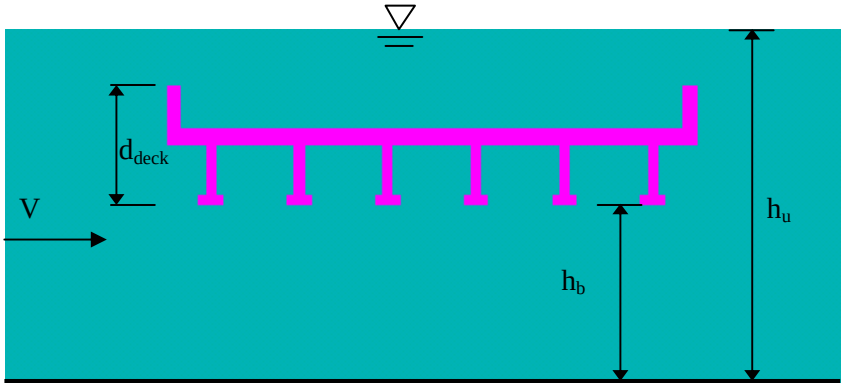

Figure 5.2 - Explanation of notations (after Kerenyi, 2007).

The roughness model of Patel (1995) was implemented in CHEN3D to simulate the effect of the river bottom roughness. A no slip boundary condition was applied on the river bottom when applying the roughness model. To check the performance of the roughness model, three different roughness conditions were considered, including D_{50} = 0mm, D_{50} = 1mm, and D_{50} = 2mm. Figure 5.3 and Figure 5.4 show the comparison of the simulated shear stress with the measurements. All the simulation results provide the correct trend. The shear stress will increase significantly under the bridge deck and be lower upstream and downstream. An X position of 0 mm corresponds to the upstream edge of the deck and the width of the deck is 0.26 m. The τ_{max} occurs under the deck within the upstream half. The smooth boudary condition underestimates the maximum bed shear stress under the bridge deck. When the k_s value (the height of the sandgrain) in the roughness model is taken as the value corresponding to D_{50} = 1mm, the bed shear stress is still underestimated but closer. The prediciton are in good agreement for D_{50} = 2mm. These two simulations of overtopping cases show the significant influence of bed roughness and deck location on the bed shear stress. It appears that the current roughness model needs further refinement because the roughness had to be exaggerated to match the measurements.

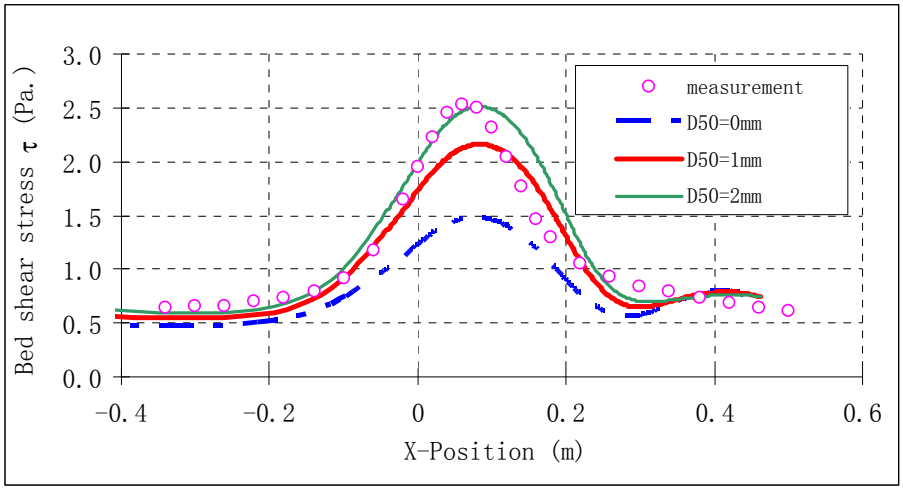

Figure 5.3 - Bed shear stress distribution of h_b = 0.13m.

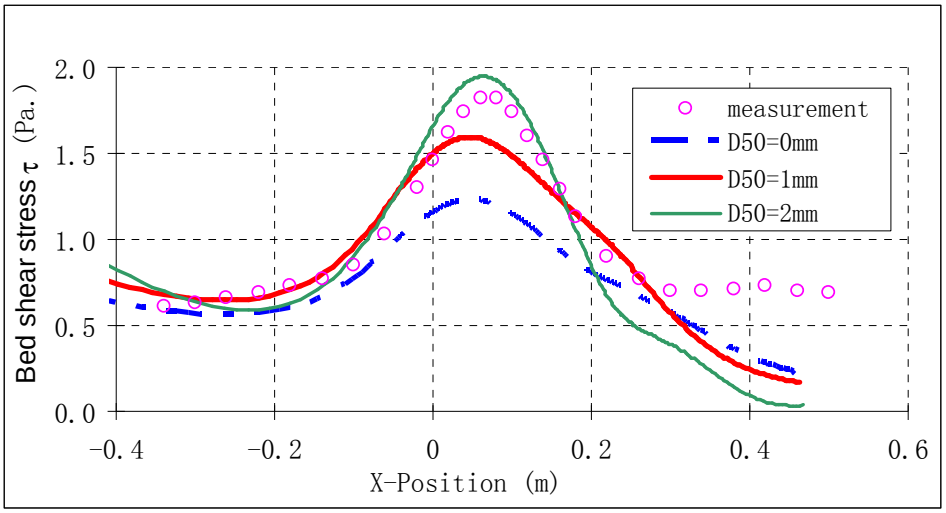

Figure 5.4 - Bed shear stress distribution of h_b = 0.16m.

5.2 OVERTOPPING IN RECTANGULAR CHANNELS

If the water surface is lower than the low chord of the bridge deck, it is a open channel flow condition as studied in Chapter 4. Hence, it is desirable to start from the case with the water surface elevation flush with the low chord of the bridge deck. The overtopping study consisted of increasing the water depth to investigate the change in bed shear stress for different levels of overtopping. The four cases simulated are shown on Figure 5.5.

The bridge is across a rectangular channel with a 1.01m long vertical wall abutment normal to the flow direction ($L_a = L'$), the deck is 0.12m thick and 0.46m wide. The clearance of the deck is 0.37m. The approach velocity is 0.33m/s. The channel is 7.32m wide. Four cases are performed with different water depth (figure 5.5). Case (a) has a 0.37m water depth and the water surface is just below the low chord. This is the limiting case of overtopping flow. Case (b) has the same water depth as Case (a) except that the water surface is in contact with the low chord. The only difference between these two cases is the water surface boundary condition under the deck. Case (c) has a water depth of 0.49m and water surface is flush with the deck surface. In this case, the flow is not overtopping the deck. Case (d) has a water depth of 0.61m. The water surface is 0.12m higher than the deck surface. The diagrams in Figure 5.5 are the transverse cross sections at the middle of the abutment. The channel is symmetrical and only half is shown.

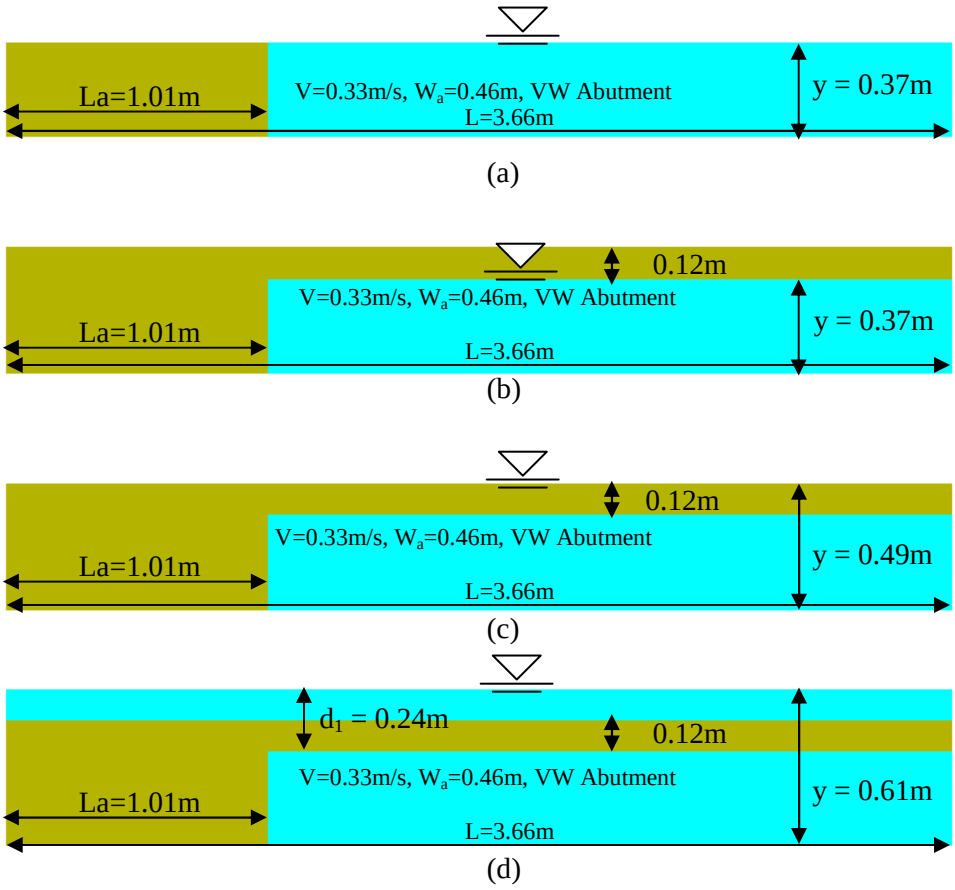

Figure 5.5 - Cross sections at the middle of the abutment for rectangular channels.

The grid of Case (d) used in the overtopping simulations is shown in Figure 5.6. The entire computation domain is divided into 10 blocks. Actually, this grid can be simplified for the simulation of the other three cases. Case (a) consists of block1 to block4. These four blocks are fully connected. The grid of Case (a) with block7 embedded in block2 and block3, can be used for the simulation of Case (b). The purpose of block7 is to provide the no-slip boundary condition on the deck bottom surface. Case (c) is made up of the grid of Cases (b), block 5, and block9. The Chimera technique is applied for the data communication between blocks.

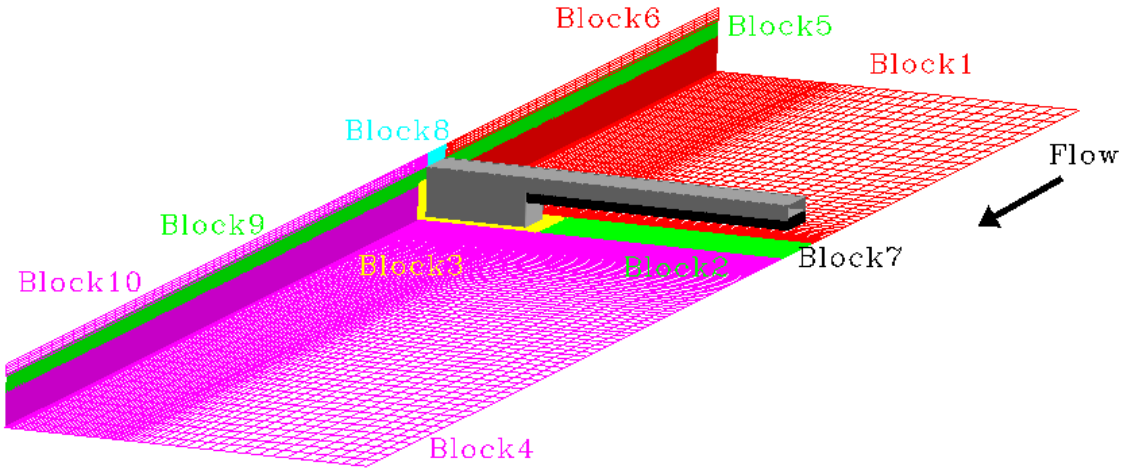

Figure 5.6 - Numerical grid for overtopping case.

Table 5.1 - Simulation results of overtopping in rectangular channel cases.

Case No.	V (m/s)	y (m)	h (m)	d_{deck} (m)	L_a (m)	W_a (m)	Shape	Cr	C_{f_max}	C_{f_center}	C_{f_max}/C_{f_center}	Comment
(a)	0.33	0.37	0.37	0.12	1.01	0.46	VW	1.38	0.0165	0.0060	2.74	No pressure flow
(b)	0.33	0.37	0.37	0.12	1.01	0.46	VW	1.38	0.0158	0.0060	2.64	No pressure flow
(c)	0.33	0.49	0.37	0.12	1.01	0.46	VW	1.85	0.0316	0.0180	1.75	Water at top deck
(d)	0.33	0.61	0.37	0.12	1.01	0.46	VW	1.58	0.0210	0.0100	2.1	Water above deck

As listed in Table 5.1, for Case (a) and Case (b), the unit discharge ratio is the same ($C_r = L/(L-L_a) = 1.38$). The channel is blocked only by the abutment. The bridge deck does not affect the channel blockage since no flow is blocked by the deck. The flow changes from open channel flow to overtopping flow once the water surface reaches the low chord. When the water surface is betweeen the low chord and deck surface, the flow is referred to as pressurized flow since there is no flow over the deck. The unit discharge ratio due to the blockage of the deck will keep increasing until the water surface goes above the deck surface. Case (c) is the condition of pressurized flow corresponding to the largest unit discharge ratio for a given bridge. The unit discharge ratio will decrease once the flow overtops the deck surface. Even thought the flow under the deck is still pressurized. The calculation of the unit discharge ratio for overtopping condition is based on the same definition as shown in the section 4.3.1 methodology The unit discharge ratio of Case (c) is $C_r = Ly/((L-L_a)(y-d_{deck})) = 1.85$. Case (d) is such a condition with a unit discharge ratio of 1.58 ($C_r = Ly/((L-L_a)(y-d_1)+(d_1-d_{deck})L)$), which is smaller than Case (c).

Table 5.1 presents the maximum friction coefficients $C_{f\_\max} = \frac{\tau_{\max}}{\rho V^2}$ and the friction coefficients along the channel center and in the middle of the abutment $C_{f\_center} = \frac{\tau_{center}}{\rho V^2}$. The bed friction coefficient contours are presented in Figure 5.7 to Figure 5.10. The friction coefficient contours for Case (a) and Case (b) are almost identical (Figure 5.7 and Figure 5.8). The values of C_{f_max} are about 0.016. It shows that the change of water surface boundary condition has little influence on the bottom bed shear stress. At the middle of the abutment, C_{f_center} is about 0.006 for both cases. The ratio of the C_{f_max} to C_{f_center} is 2.74.

It is expected that the bed shear stress of Case (c) is the highest among all these cases because of its highest unit discharge ratio. As shown in table 5-1, C_{f_max} is 0.03 for Case (c), almost twice of the values for Case (a) and Case (b); C_{f_center} is 0.018 for Case (c), three times of the results for Case (a) and Case (b). The ratio of the C_{f_max} to C_{f_center} is 1.75 for Case (c). It is worthwile to note that the increasing of bed shear stress is much faster at the center of the channel than around the abutment. Hence, for the same blockage ratio, the influence of the bridge deck on the channel center will be greater than around the abutment.

The unit discharge ratio of Case (d) is the second largest in these four cases. Accordingly, C_{f_max} and C_{f_center} of Case (d) are the second highest among them. Part of the flow blocked by the bridge deck goes over the bridge deck and makes the flow rate under the bridge deck for Case (d) lower than that of Case (c). This proves that the worst condition is when the water surface is up to the top of deck surface. Based on the these simulations, the magnitude of the friction coefficient is highly dependent on the channel contraction. The higher the unit discharge ratio, the higher the friction coefficient.

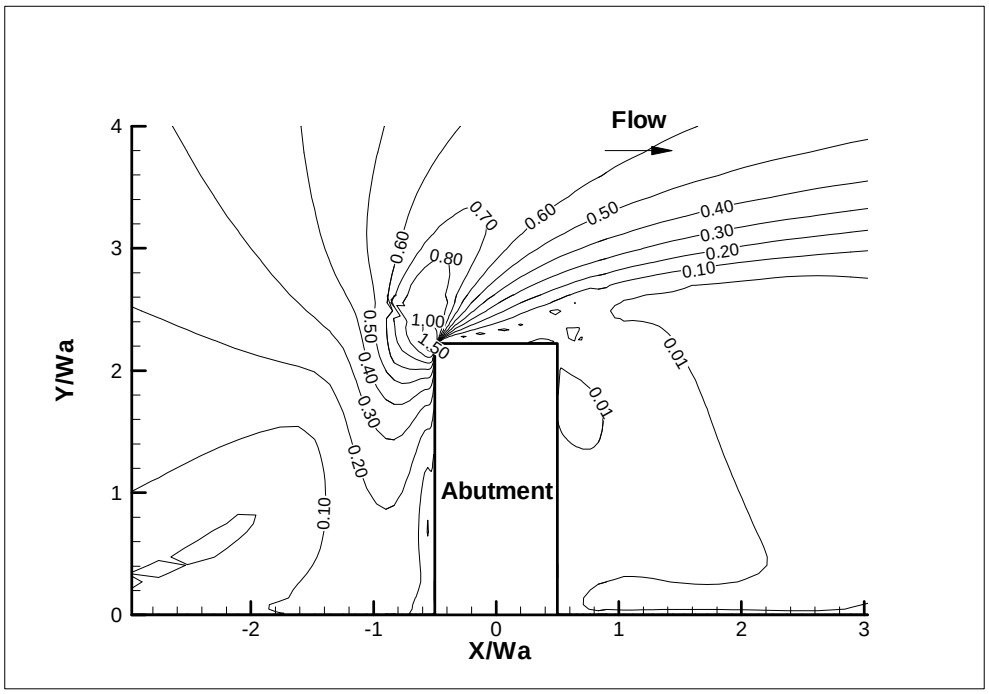

Figure 5.7 - Bed friction coefficient, $\frac{\tau_b}{\rho V^2}$ ($\times 10^2$) contours for Case (a).

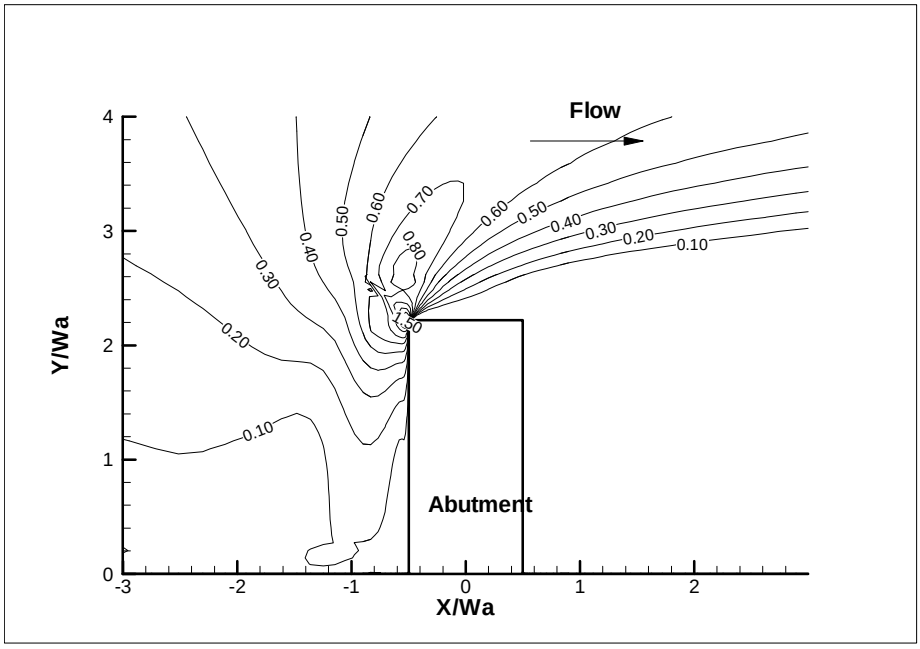

Figure 5.8 - Bed friction coefficient, $\frac{\tau_b}{\rho V^2}$ ($\times 10^2$) contours for Case (b).

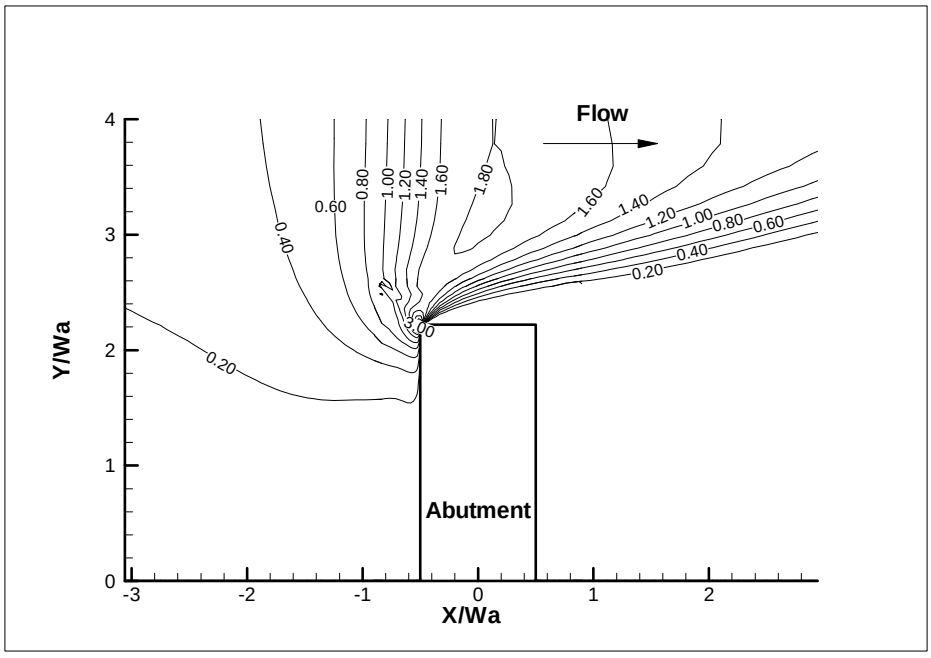

Figure 5.9 - Bed friction coefficient, $\frac{\tau_b}{\rho V^2}$ ($\times 10^2$) contours for Case (c).

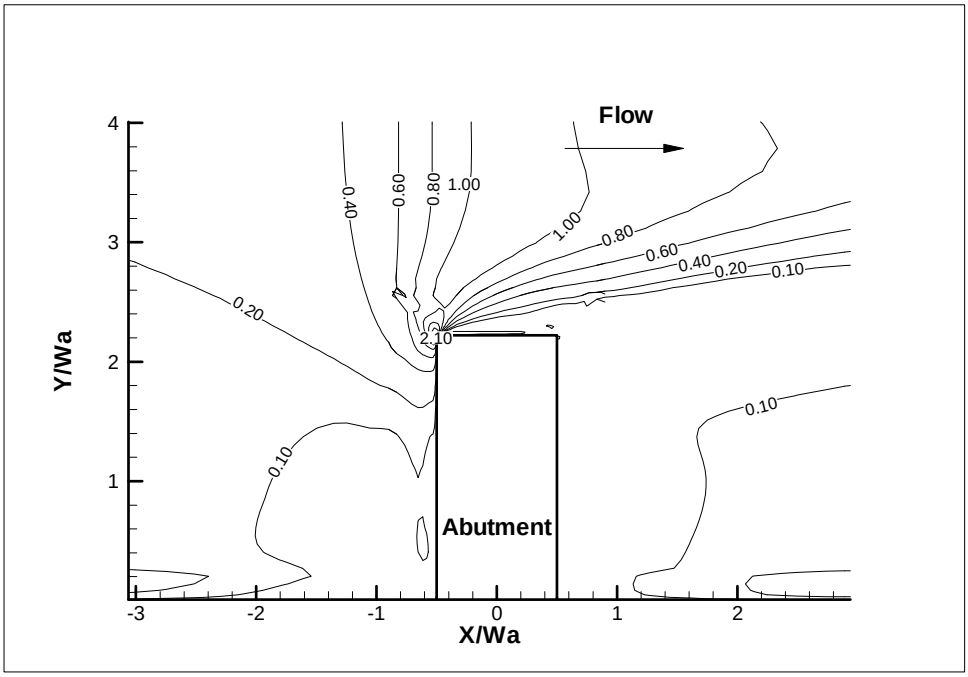

Figure 5.10 - Bed friction coefficient, $\frac{\tau_b}{\rho V^2}$ ($\times 10^2$) contours for Case (d).

Table 5.2- Prediction of C_{f_max} in rectangluar channel cases with overtoppping.

Case #	Re	Cr	C_{f_vw}	k_{Cr}	k_{sh}	k_{Fr}	k_s	k_{sk}	C_{f_max}
	----	----	----	----	----	----	----	----	----
(a)	1.52E+05	1.38	0.0098	2.15	0.70	1.16	1.00	1.00	0.0172
(b)	1.52E+05	1.38	0.0098	2.15	0.70	1.16	1.00	1.00	0.0172
(c)	1.52E+05	1.85	0.0098	3.84	0.70	1.11	1.00	1.00	0.0294
(d)	1.52E+05	1.58	0.0098	2.86	0.70	1.08	1.00	1.00	0.0212

To predict the maximum bed shear stress around the abutment under overtopping conditions, the equation proposed in Chapter 4 is applied. The basic idea is to assume that the overtopping condition is equivalent to an open channel flow condition with the same unit discharge ratio. The detailed calculation is presented in Table 5.2. The predicted maximum friction coefficients are close to the simulated results. The comparison is given in Figure 5.11. It shows that the overtopping situations may be predicted by the existing method within 10% difference in rectangular channel.

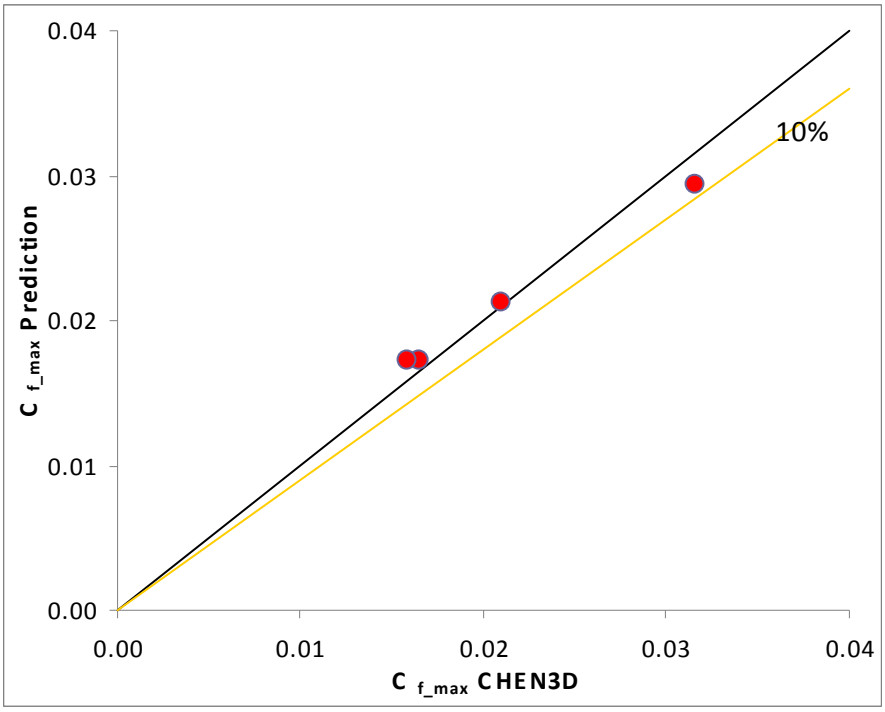

Figure 5.11 - Comparison of the predicted and simulated C_{f_max} in overtopping cases.

5.3 OVERTOPPING IN COMPOUND CHANNELS

5.3.1 Overtopping in Symmetric Compound Channels

Two overtopping cases, T1WW (wing-wall abutment) and T1ST (spill-through abutment), were conducted to investigate the bed shear stress on the river bed in a compound channel. Grid systems similar to the ones as shown in Figure 5.6 were used except that the rectangular channel was replaced by the compound channel. Figure 5.12 shows the detail parameters. For convenience, these two cases are designed based on the flume test Case 01 and Case 09, which are not overtopped. The bridge deck is 0.12 m thick and 0.46 m wide. The water surface is 0.12 m higher than the deck surface. The abutment is normal to the flow direciton with $L_a = L'$.

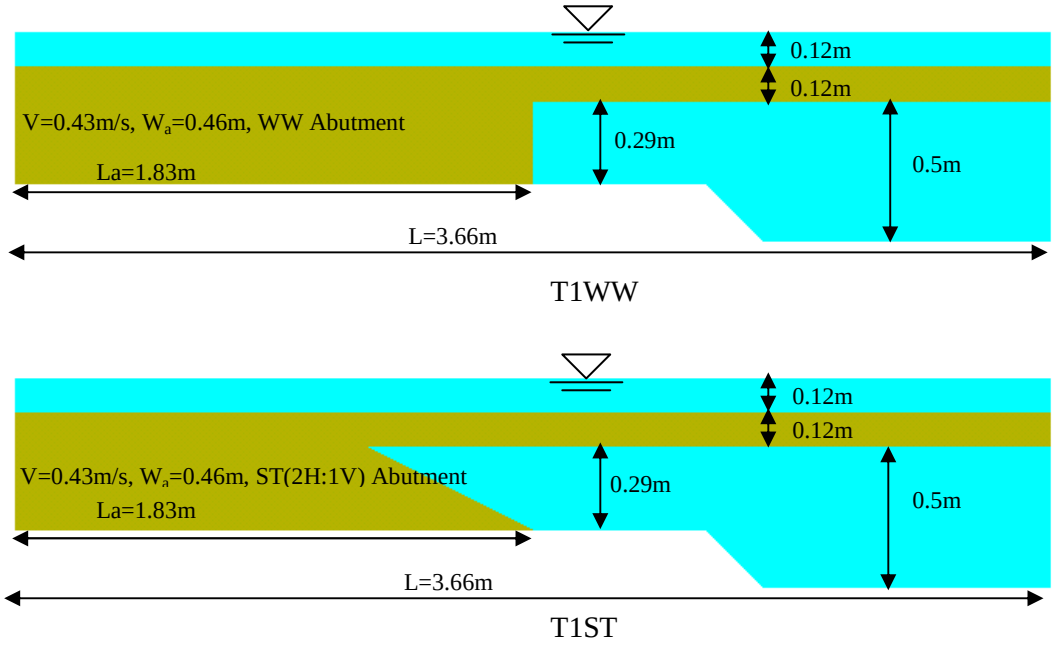

Figure 5.12 - Cross sections at the middle of the abutment for compound channels.

Figure 5.13 to Figure 5.16 present the bed shear stress contours for T1WW, Case 09, T1ST, and Case 01. The bed shear stresses around the abutment increase significantly between the open channel flow and the overtopping flow. For the wing-wall abutment, $C_{f\_\max}$ increases from Case 09 (0.0117) to T1WW (0.018); for the spill-through abutment, $C_{f\_\max}$ increases from Case 01 (0.0097) to T1ST (0.016). At the center of the channel, however, the change of bed shear stress on the main channel is not as large. C_{f_center} increases from about 0.0045 for Case 09 and Case 01 to around 0.006 for T1WW and T1ST.

Overtopping affects the distribution of bed shear stress around the toe of the abutment. For open channel flow cases, the bed shear stress increases gradually when getting closer to the abutment from the upstream side. After reaching the maximum bed shear stress right at the toe of

the abutment, the bed shear stress decresses quickly towards dowstream. For the overtopping cases, the trend is totally opposite. For the same location on the upstream side, the bed shear stress is smaller than that in the open channel case. It is believed that the existence of the bridge deck has little influence on the upstream behavior. The bed shear stress will decrease with an increase in water depth. When getting very close to the bridge deck, the contraction effect of the deck results in a quick increase in bed shear stress. On the downstream side, the highly contracted flow remains intense and makes the bed shear stresse decrease gradually.

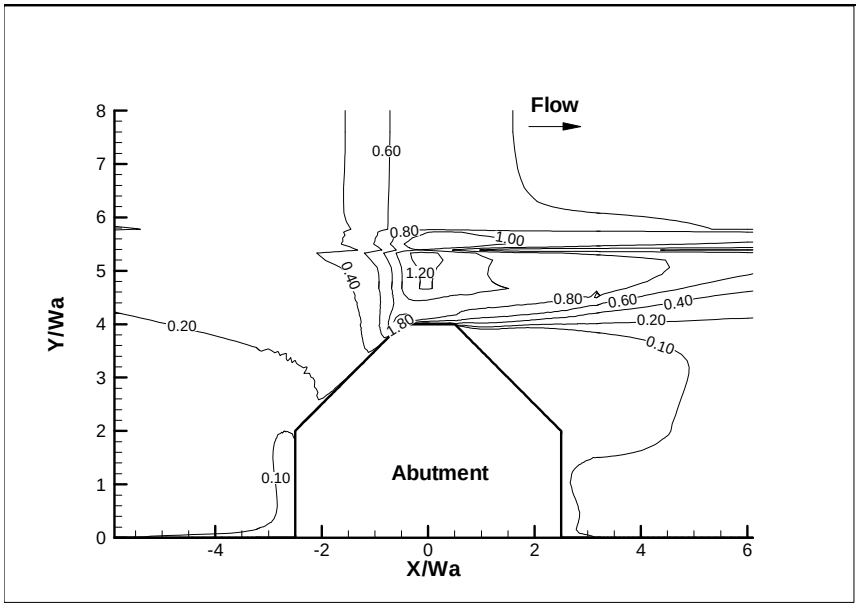

Figure 5.13 - Bed friction coefficient ($\times 10^2$), T1WW.

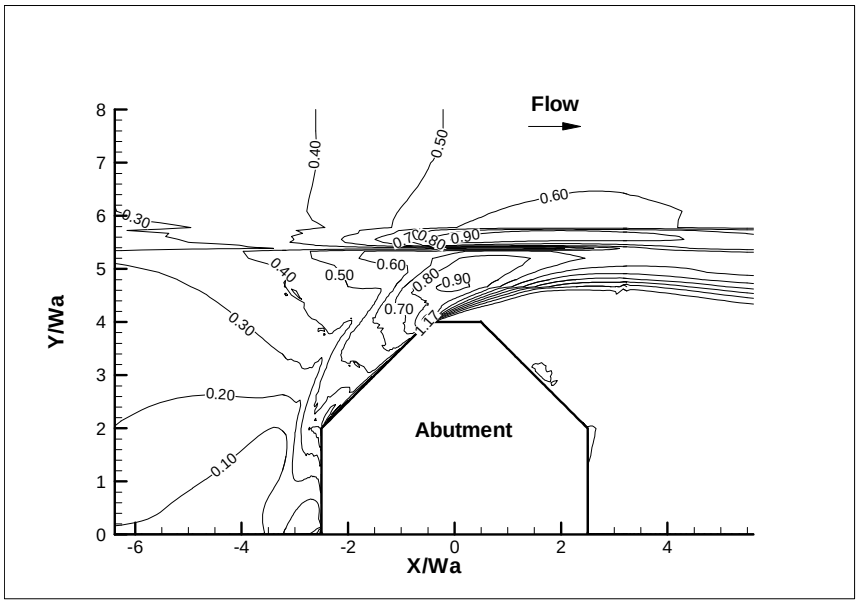

Figure 5.14 - Bed friction coefficient ($\times 10^2$), Case 09.

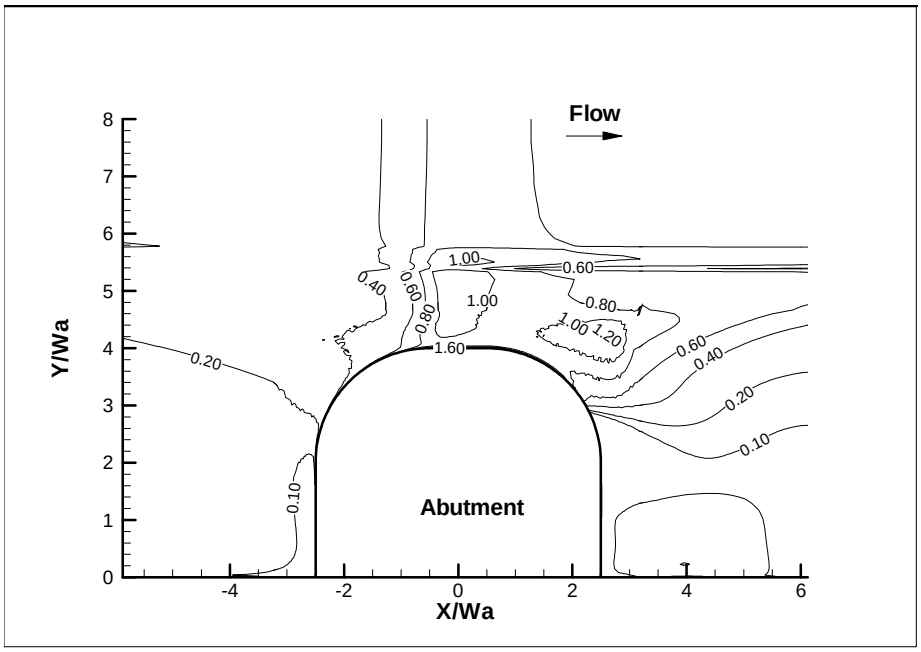

Figure 5.15 - Bed friction coefficient ($\times 10^2$), T1ST.

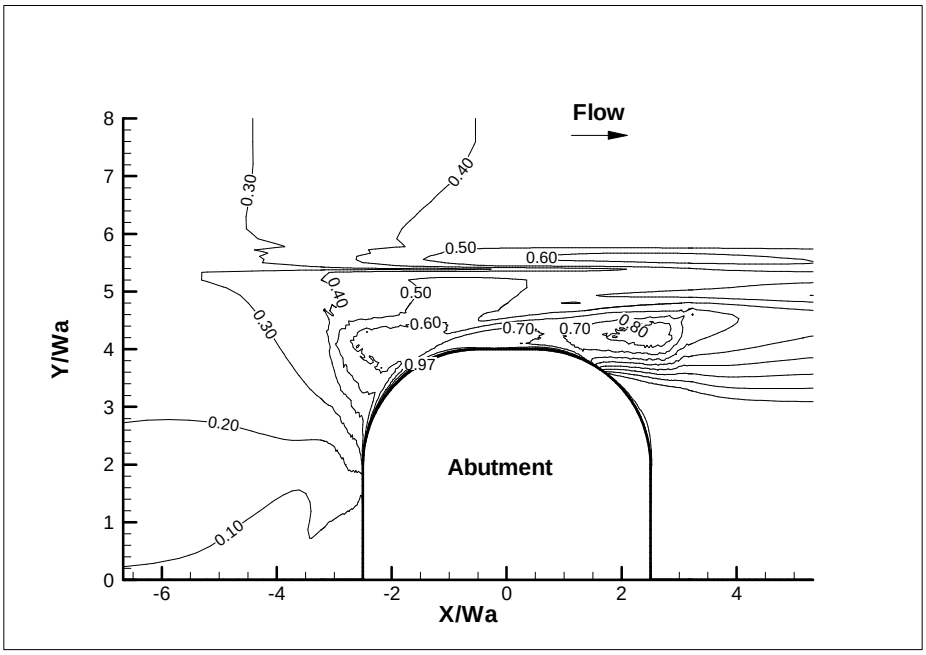

Figure 5.16 - Bed friction coefficient ($\times 10^2$), Case 01.

Table 5.3 - Simulation results of overtopping in symmetric compound channel cases.

Case #	V	y	L_a	W_a	Shape	C_r	C_{f_max}	C_{f_center}	C_{f_max}/ C_{f_center}
	m/s	m	m	m	----	----	----	----	----
T1WW	0.43	0.54	1.829	0.457	WW	1.81	0.0194	0.0060	3.24
Case09	0.43	0.29	1.829	0.457	WW	1.70	0.0117	0.0050	2.34
T1ST	0.43	0.54	1.829	0.457	ST	1.69	0.0163	0.0060	2.71
Case01	0.43	0.29	1.829	0.457	ST	1.53	0.0097	0.0040	2.43

Table 5.4 - Prediction of C_{f_max} in compound channel cases with overtoppping.

Case #	Re	Cr	C_{f_vw}	k_{Cr}	k_{sh}	k_{Fr}	k_s	k_{sk}	C_{f_max}
	----	----	----	----	----	----	----	----	----
T1WW	1.96E+05	1.81	0.0087	3.71	0.61	1.19	0.65	1.00	0.0152
Case09	1.96E+05	1.70	0.0087	3.31	0.61	1.33	0.65	1.00	0.0151
T1ST	1.96E+05	1.69	0.0087	3.27	0.61	1.19	0.58	1.00	0.0120
Case01	1.96E+05	1.53	0.0087	2.68	0.61	1.33	0.58	1.00	0.0109

The maximum bed shear stress equation proposed in chapter IV is tried for these two overtopping cases (T1WW and T1ST) in compound channel. The blockage of the bridge deck is considered through the unit discharge ratio as defined in the methodology section in chapter 4. These two results are listed in table 5.4. For comparison, the results of Case 09 and Case 01(not overtopped) are also given in table 5.4 and figure 5.17. The predicted values in overtopping are

lower than the simulated results with about 30% difference as shown in Figure 5.17. It is opposite to the prediction of open channel flow.

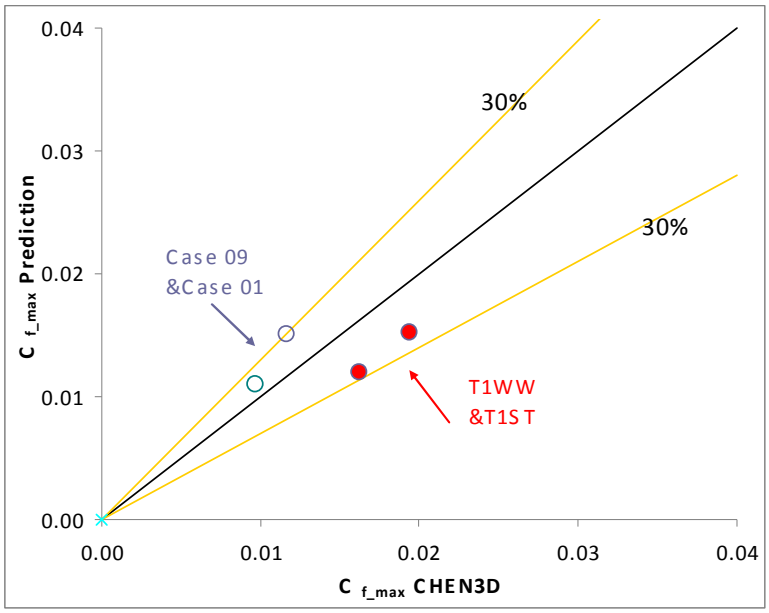

Figure 5.17 - Comparison of the predicted and simulated C_{f_max} in overtopping cases.

5.3.2 Overtopping in Non-Symmetric Compound Channels

All the overtopping simulations presented so far assumed that channel is symmetrical. In real rivers, channels are very likely to be non-symmetrical. So it is helpful to investigate the bed shear stress distribution in non-symmetric channel. For convenience, half of the channel is kept identical to the one in the symmetric compound channel study. The other half is designed to have a shallower water depth on the flood plain. The top width of the abutment is the same on both sides since the bridge deck will not change. Both a spill-through and a wing-wall abutment are studied and are called case T2ST and case T2WW respectively. The parameters are given on Figure 5.18, showing the cross sections in the middle of the abutment. The abutment is normal to the flow direciton with $L_a = L^{'}$. Figure 5.18 is looking upstream. The grid system is similar to the one used for the rectangular channel shown in Figure 5.6 except that the full channel width is simulated. A rigid lid is still applied on the water surface. A no slip boundary condition is applied at the solid surface.

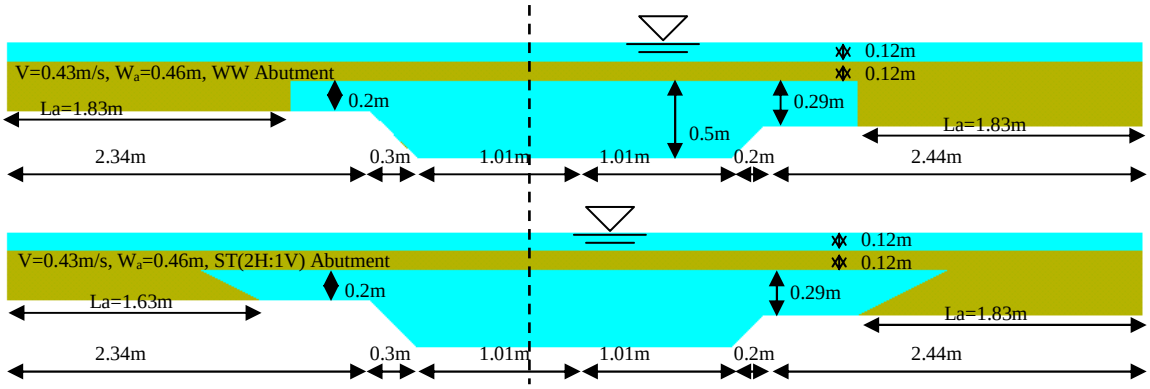

Figure 5.18 - Cross sections for non-symmetric compound channels.

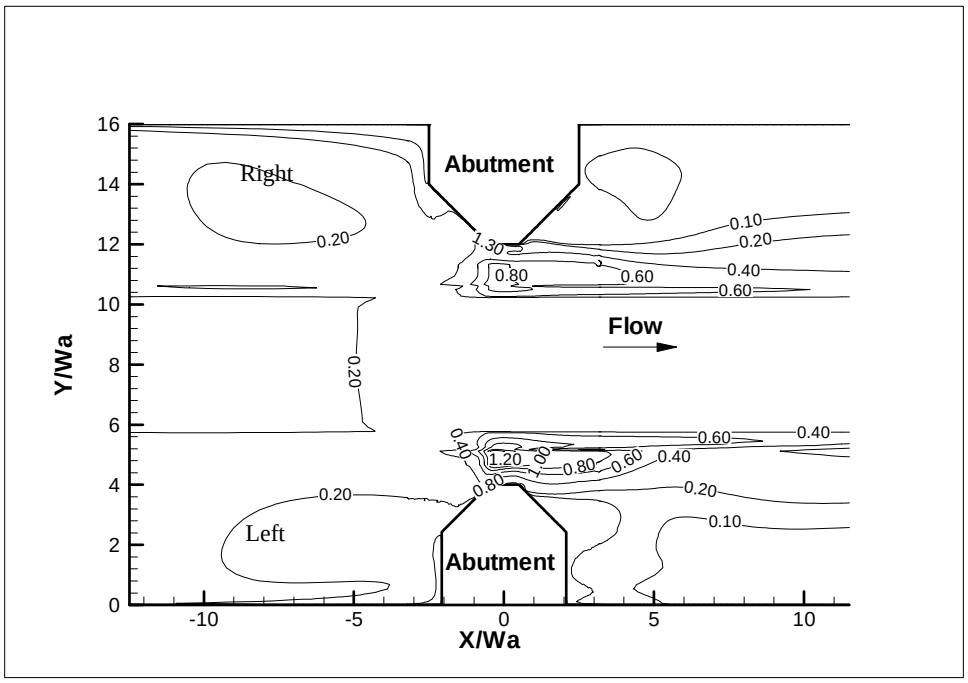

Figure 5.19 - Bed friction coefficient ($\times 10^2$), T2WW.

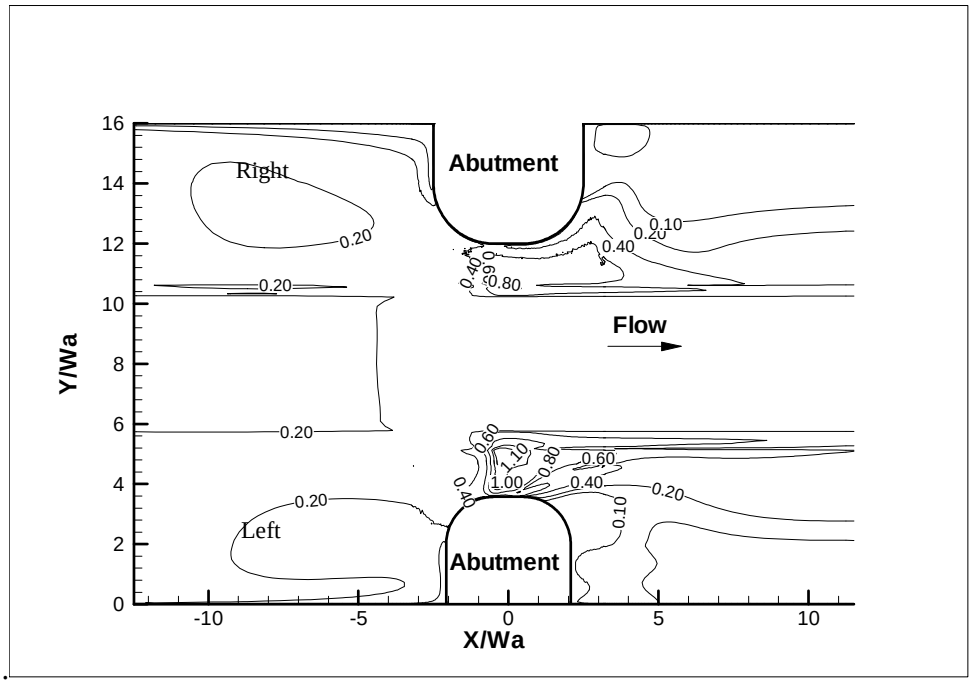

Figure 5.20 - Bed friction coefficient ($\times 10^2$), T2ST.

Figure 5.19 and Figure 5.20 show the bed friction coefficient contours for case T2WW and case T2ST. The left side has a shallower water depth on the flood plain and a higher unit discharge ratio. As a result, the bed friction coefficient on the left flood plain has a higher value than on the right flood plain. This can be seen on Figure 5.19 and Figure 5.20. The geometry of the right side of the compound channels is identical to the symmetric compound channels of case T1WW and case T1ST, respectively. But the bed friction coefficient values, $C_f = \frac{\tau_b}{\rho V^2}$ are lower than those on the corresponding symmetric cases. As shown in Figure 5.19, C_f in front of the right abutment face on the flood plain is about 0.008, while in the symmetric channel, the value is 0.012 for case T1WW. The C_f at the center of the main channel for case T2WW is 0.0032, which is about half of the value at the same location in case T1WW. A similar trend can be observed between case T2ST and case T1ST. These comparisons show that the prediction of the bed shear stress based on half of the channel under symmetric channel assumption could cause discrepencies for non symmetric channel.

Table 5.5 - Simulation results of overtopping in non-symmetric compound channel cases.

Case #		V	y	L_a	W_a	Shape	C_r	C_{f_max}	C_{f_center}	C_{f_max}/ C_{f_center}
		m/s	m	m	m	----	----	----	----	----
T2WW	right	0.43	0.54	1.83	0.46	WW	1.81	0.0131	0.0032	4.09
	left	0.43	0.44	1.83	0.46	WW	2.00	0.0128	0.0032	3.99
T2ST	right	0.43	0.54	1.83	0.46	ST	1.69	0.0077	0.0032	2.42
	left	0.43	0.44	1.83	0.46	ST	1.94	0.0116	0.0032	3.62

Table 5.6- Prediction of C_{f_max} in non-symmetric compound channel cases (overtoppping).

Case #		Re	Cr	C_{f_vw}	k_{Cr}	k_{shh}	k_{Fr}	k_s	k_{sk}	C_{f_max}
		----	----	----	----	----	----	----	----	----
T2WW	right	1.96E+05	1.81	0.0087	3.71	0.61	1.19	0.65	1.00	0.0152
	left	1.96E+05	2.00	0.0087	4.42	0.61	1.23	0.65	1.00	0.0187
T2ST	right	1.96E+05	1.69	0.0087	3.27	0.61	1.19	0.58	1.00	0.0120
	left	1.96E+05	1.94	0.0087	4.18	0.61	1.23	0.58	1.00	0.0158

Table 5.5 presents the simulated maximum bed shear stress around the abutment and the bed shear stress at the channel center in the middle of the abutment. The former is about 2.5 to 4 times the latter. Wing-wall abuments tend to generate slightly higher bed shear stress than Spill-through abutment. The maximum bed shear stress equation (Eq.4.79) has also been tried for the non-symmetric channel based on the asumption that the left and right part of the channel are independent. It means that the channel is divided into two parts from the centerline of the channel and the unit discharge ratio is calculated based on the geometry of the half channel. The detailed calculation are given in Table 5.6. Figure 5.21 presents a direct comparison of the predictions with the measurements. The predicitons can be 50% higher than the simulated results. This is contrary to the findings in the previous study of ovetopping in rectangular channel and in symmetric compound channel. The possible reason is that the asymmetrical channel geometry

causes the redistribution of the flow and makes the real contraction effect different from estimation based on the area ratio $\frac{A_{total}}{A_{total} - A_{blocked}}$.

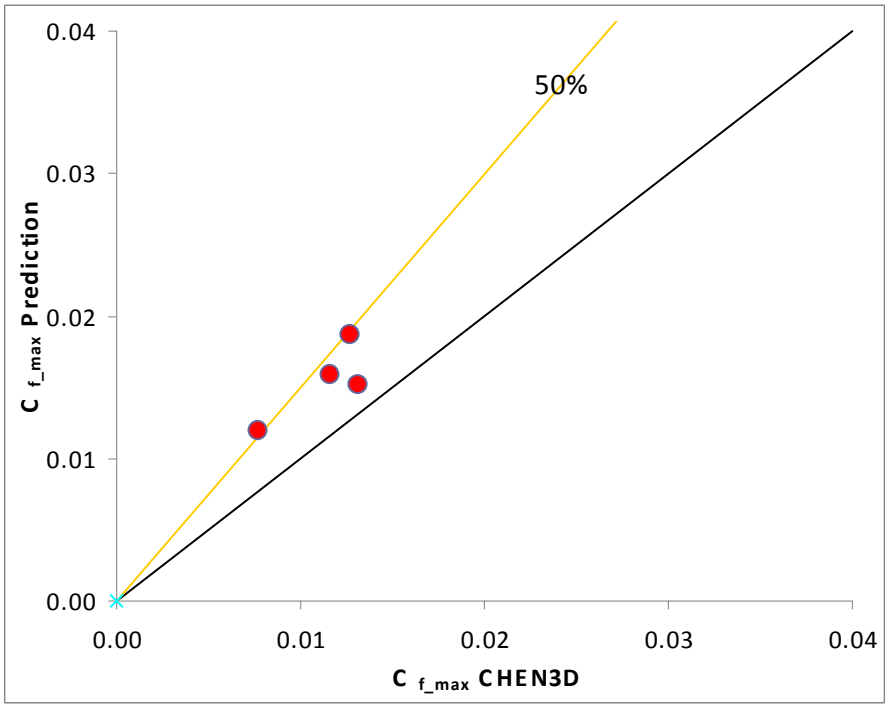

Figure 5.21 - Comparison of the predicted and simulated C_{f_max} in overtopping cases.

5.4 OPEN CHANNEL FLOW IN A CHANNEL BEND

A channel bend can redistribute the flow along the cross section and further change the bed shear stress distribution. It is interesting to look into the influence of channel bend on the bed shear stress around the abutment. The geometry of the channel bend is usually characterized by the ratio of R/W along the center of the channel bend. R is the radius of the bend and W is the width of the channel. Two types of bend are studied with R/W equal to 1 and 2. The bend is fixed with an angle of 90 degree from the inlet to the outlet. The location of the abutment on the channel bend is also studied. Two representive locations, middle of the bend and downstream end of the bend, are considered. To study the influence of the abutment shape, spill-through and wing-wall abutments are included. Overall, eight cases are designed, as listed in Figure 5.22. The grid system is similar to Figure 5.6 and fully connected grids are used. The parameters , such as approach velocity, water depth, abutment length, compound channel configuration are exactly the same as Case 09 and Case 01 so that the effect of the channel bend can be isolated. Figure 5.23 shows the cross section at the middle of the abutment for the wing-wall abutment. Case T1WW with overtopping in a straight channel is also shown.

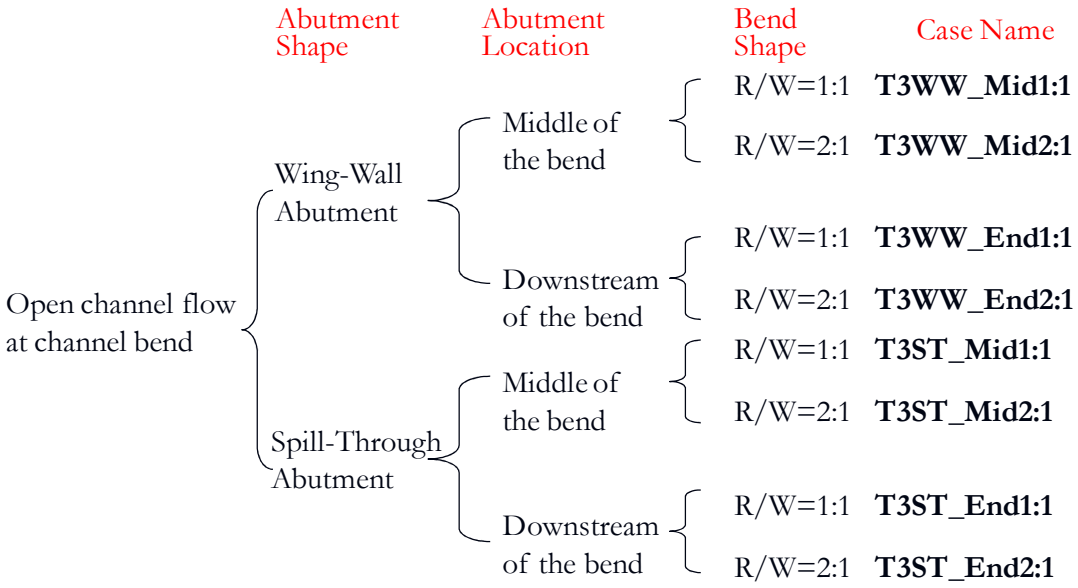

Figure 5.22 - Numerical cases for channel bend study in open channel flow.

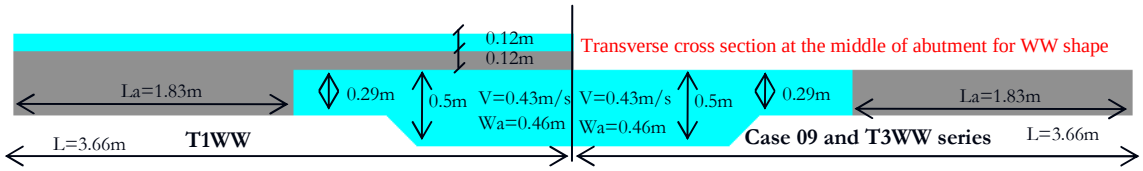

Figure 5.23 - Cross section of the wing-wall abutment cases in channel bend study.

Figure 5.24 to Figure 5.31 show the simulation results for all eight cases. The results are analyzed for the influence of R/W, abutment location, and abutment shape.

5.4.1 Influence of R/W

As shown in Figure 5.22, four groups with different abutment shape and location can be used to study the influence of R/W. Among them, the cases with a wing-wall abutment at the middle of the bend, will be discussed in detail, namely case T3WW_Mid 2:1 and case T3WW_Mid 1:1.

The maximum bed friction coefficient C_{f_max} is 0.013 for case T3WW_Mid 1:1 and 0.011 for case T3WW_Mid 2:1. Both of them have C_{f_max} located at the downstream inner main channel slope. In a straight channel, C_{f_max} ususally occurs at the upstream corner of the wing-wall abutment, such as Case 09 where C_{f_max} is equal to 0.017. On the other hand, the bed shear stress contours are highly non-symmetric when R/W equal to 1. The inner flood plain has a much higher bed shear stress than the outer part of the right bank downstream of the abutment. Further downstream, the outer main channel slope suffers much higher shear stress than the inner part. When R/W is equal to 2, the difference between the inner and outer flood plains is not significant

and the entire bed shear stress level is a lot lower than in the case of R/W equal to 1. Far downstream, the outer main channel slope still suffers high bed shear stresses. These observations indicate that the channel with the lower R/W is subjected to higher bed shear stresses and exhibits shear stress contours which are more non-symmetric.

The influence of the bend geometry can also be observed on the flow field either on the plan view of the water suface or on the cross section plots. For the straight channel, the ratio of R/W is equal to infinity. The flow distribution in the transverse direction will be symmetrical as long as the channel and the abutment are symmetrical. However, the symmetric flow will be disturbed when passing the channel bend. At the beginning of the bend, the inner part of the channel will have a higher velocity. Then the higher velocity region will move to the outer side of the bend. This can be observed in case T3WW_Mid 1:1. The unit flow rate in the inner half of the channel is higher than in the outer half. However, for case T3WW_Mid 2:1, the flow distribution is still symmetrical even close to the abutment. This indicates that the sharp bend can cause a more asymmetric flow, which is consistant with the finding in bed shear stress distribution.

The velocity plan view of case T3WW_Mid 1:1 shows a highly non-symmetric pattern downstream of the bridge. The highest velocity appears on the inner side of the main channel and close to the main channel slope. The higher velocity region is large and extends from the main channel to the outside flood plain.

For case T3WW_Mid 2:1, the flow on the downstream side is close to being symmetrical. The highest velocity appears in the middle of the main channel with the contours skewed slightly towards the inner abutment. The higher velocity region basically remains in the main channel on the downstream side. These observations show that the influence of a bend with R/W equal to 2 is not as significant as a bend with R/W equal to 1.

5.4.2 Influence of Abutment Location

When the bridge is located in the middle of the bend, the flow turns 45 degree from the inlet to the location of the abutment. The main flow direction does not change by as much as 45 degree because of the delay in the bend effect. The bed shear stress distribution around the inner and outer abutments is different since the flow field is not as symmetrical as in a straight channel. The magnitude of the bed shear stress is affected by many other factors, such as the R/W ratio , and the abutment shape. The bed shear stresses around the inner abutment always tend to be higher than the values around the outer abutment. This can be observed on all four simulations with the abutment in the middle of the channel bend. In a straight channel, the maximum bed shear stress usually appears at the upstream corner of the abutment, especially for abutments with sharp corners, such as a vertical wall or a wing-wall abutment. For an abutment in the middle of a channel bend, however, the maximum bed shear stress appears downstream on the inner main channel slope. This is closely related to the flow field distribution in the bend. When approaching the middle of the channel bend, the inner side of the main channel already exhibits a higher velocity than the outer side. The high velocity region then moves gradually from the inner to the outer part along the bend. The inner abutment further forces the flow towards the outer bank. However, the local acceleration around the upstream corner of the inner abutment is not as large as in the straight channel. The deflected higher velocity region does not reach the outer

over bank when passing the middle of the bend since the local flow is not highly accelerated yet. So, the outer abutment will have little influence on the deflected flow. This implies that abutments located in the middle of the bend tend to strenghten the deflection of the flow towards the outer bank. Hence, the downstream outer bank will be attacked by the flow more seriously.

When the bridge is located at the downstream end of the bend, the bend direction changes 90 degree before it reaches the abutment. In the approaching cross section in front of the abutment, the velocity in the main channel is increasing from the inner side to the outer side. The highest velocity appears on the outer side main channel slope and in part of the flood plain. The trend is opposite to the cases where the abutment is in the middle of the bend. This indicates that the outer over bank will experience the higher erosion even if there is no contraction due to the abutment. Actually, this is the reason for the development of a channel meander. This trend is further strengthened at the middle of the abutment. As shown in Figure 5.26, the velocity on the inner main channel slope is lower than the velocity on the main channel center. The existence of the outer abutment will further acclerate the flow on the outer side of the main channel and generate higher bed shear stress. However, the acceleration also tends to force the deflected flow back to the channel center. As shown in the figures, the magnitude of the bed shear stress downstream and on both sides of the main channel tends to be similar. Downstream also, the outer overbank will not be attacked directly by the flow. The flow downstream of the abutments recovers a uniform condition very quickly. Hence, the existing of the abutment at the end of the bend tends to weaken the non uniform flow caused by the channel bend and protect the outer bank from erosion.

5.4.3 Influence of Abutment Shape

In chapter IV, the correction factor for abutment shape was proposed to correct the result with respect to a vertical wall abutment. A constant number of 0.65 is recommended for wing-wall abutment; and a constant number of 0.59 is recommended for spill-through abutment. To study the influence of the shape of an abutment in a channel bend, two sets of simulations were performed and are compared. The ratio R/W and the abutment location are the same in both cases. It should be noted that the unit discharge ratio is not the same for both cases because of the abutment shape. The results are tabulated in Table 5.7. These results in Table 5.7 are the maximum values at the toe of the abutment. Overall, the spill-through abutment tends to cause lower bed shear stress. This is consistant with the study of abutment shape in chapter 4 for straighte channel. The shape effect is still observable in the channel bend. There is no simulation with vertical wall abutment. So the comparison can only be conducted based on the results of the spill-through and the wing-wall abutments. It should be noted that the bed shear stress ratio between these two shapes is lower than 0.59/0.65 for all four pairs. The contracton ratio difference between the spill-through abutment and the wing-wall abutment may be the reason for the lower ratio. Considering this reason, the shape effect factor is not changed for the case of a bend.

Table 5.7 - Influence of abutment shape on channel bend.

Case #	$C_{f\_max\_WW}$	Case #	$C_{f\_max\_ST}$	$C_{f\_max\_ST}/C_{f\_max\_WW}$
T3WW_Mid 1:1	0.0130	T3ST_Mid 1:1	0.0098	0.75
T3WW_Mid 2:1	0.0109	T3ST_Mid 2:1	0.0087	0.80
T3WW_End 1:1	0.0108	T3ST_End 1:1	0.0095	0.88
T3WW_End 2:1	0.0092	T3ST_End 2:1	0.0070	0.76

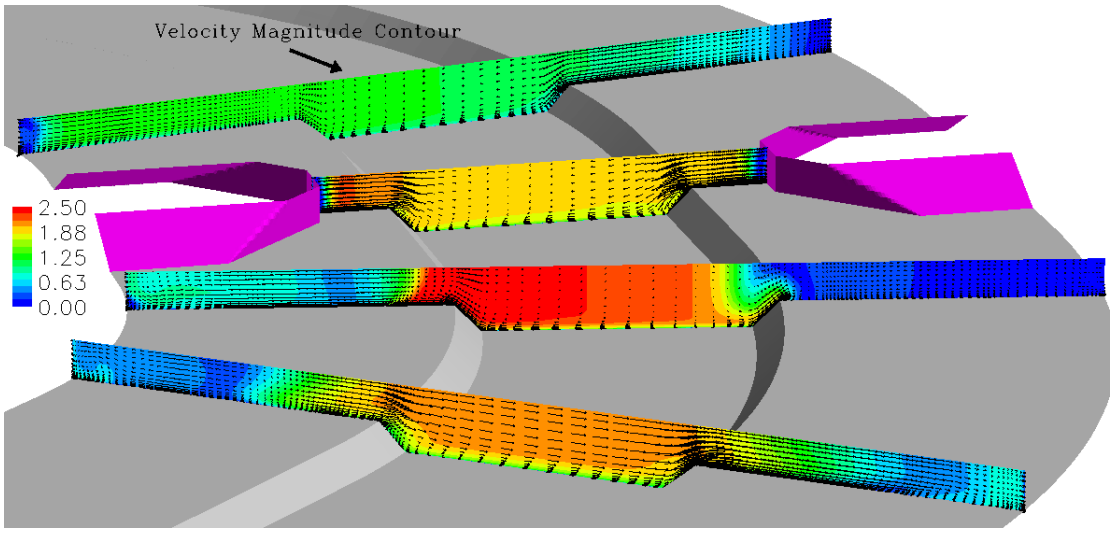

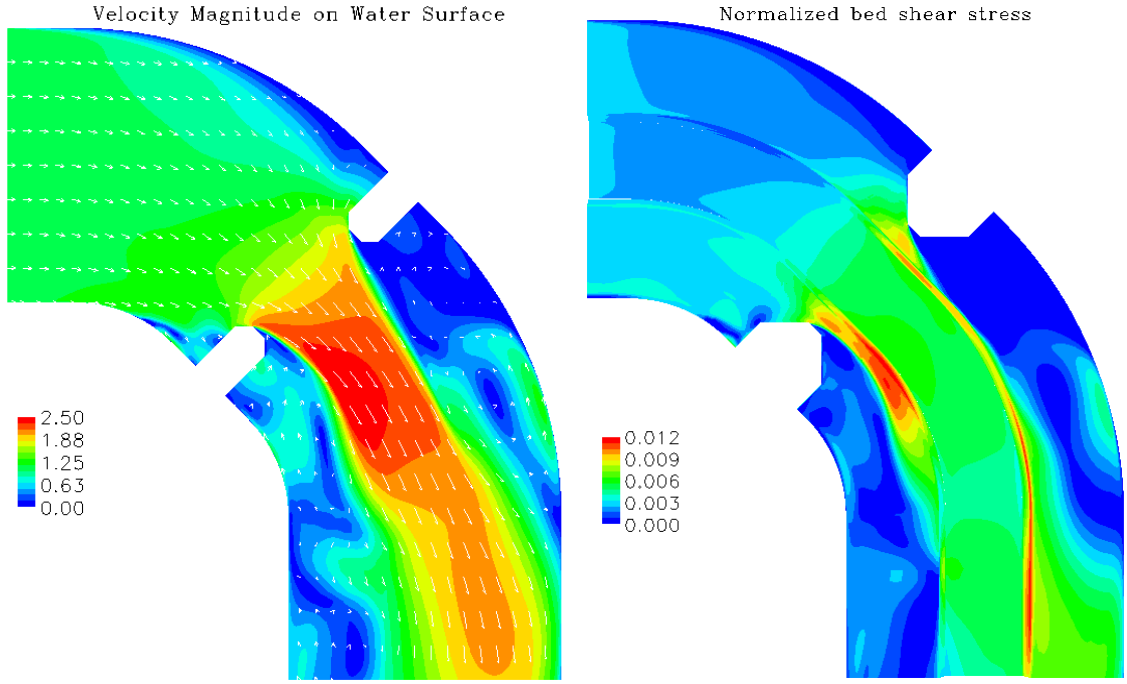

Figure 5.24 - Simulation results of case T3WW_Mid 1:1.

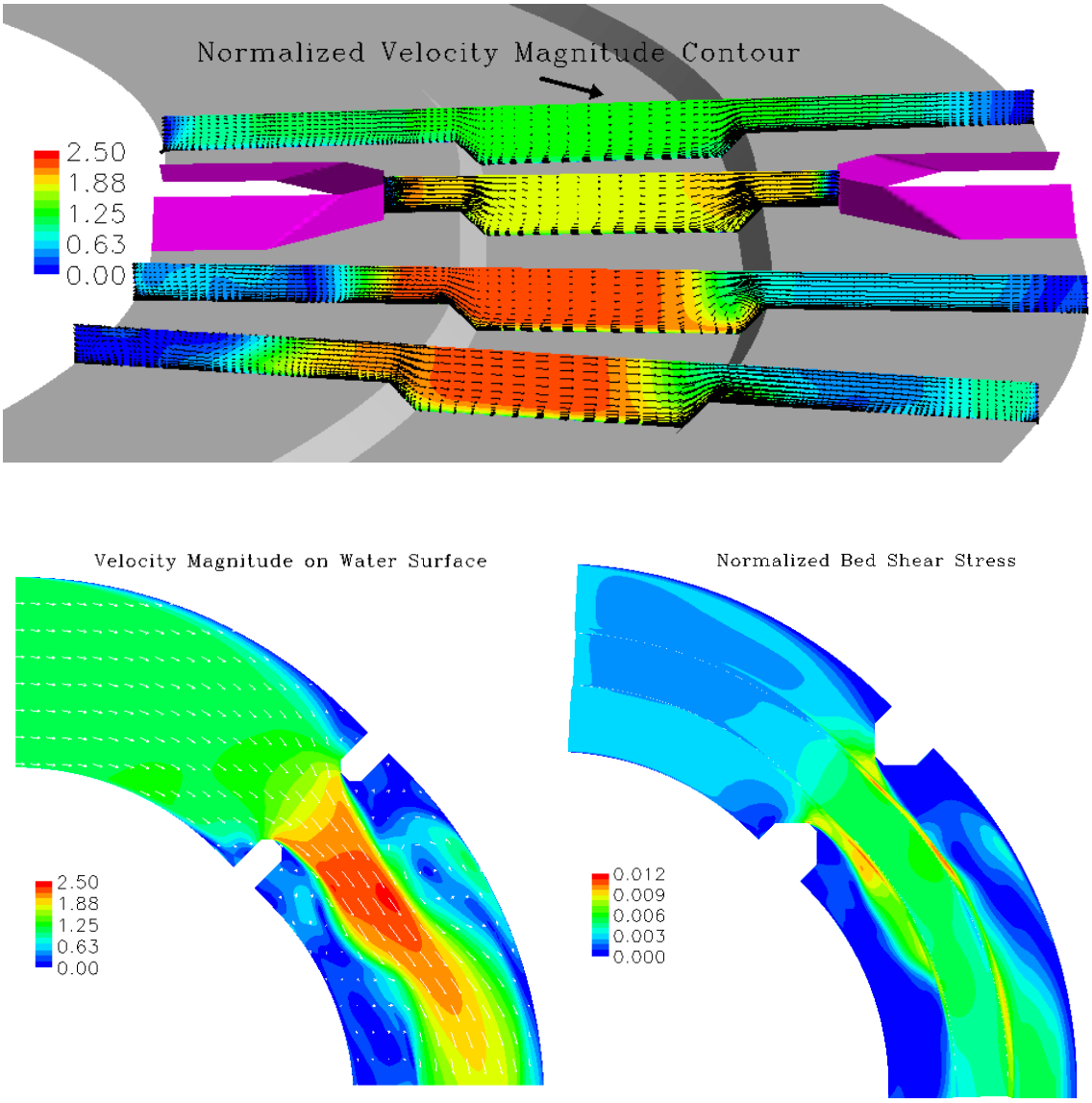

Figure 5.25 - Simulation results of case T3WW_Mid 2:1.

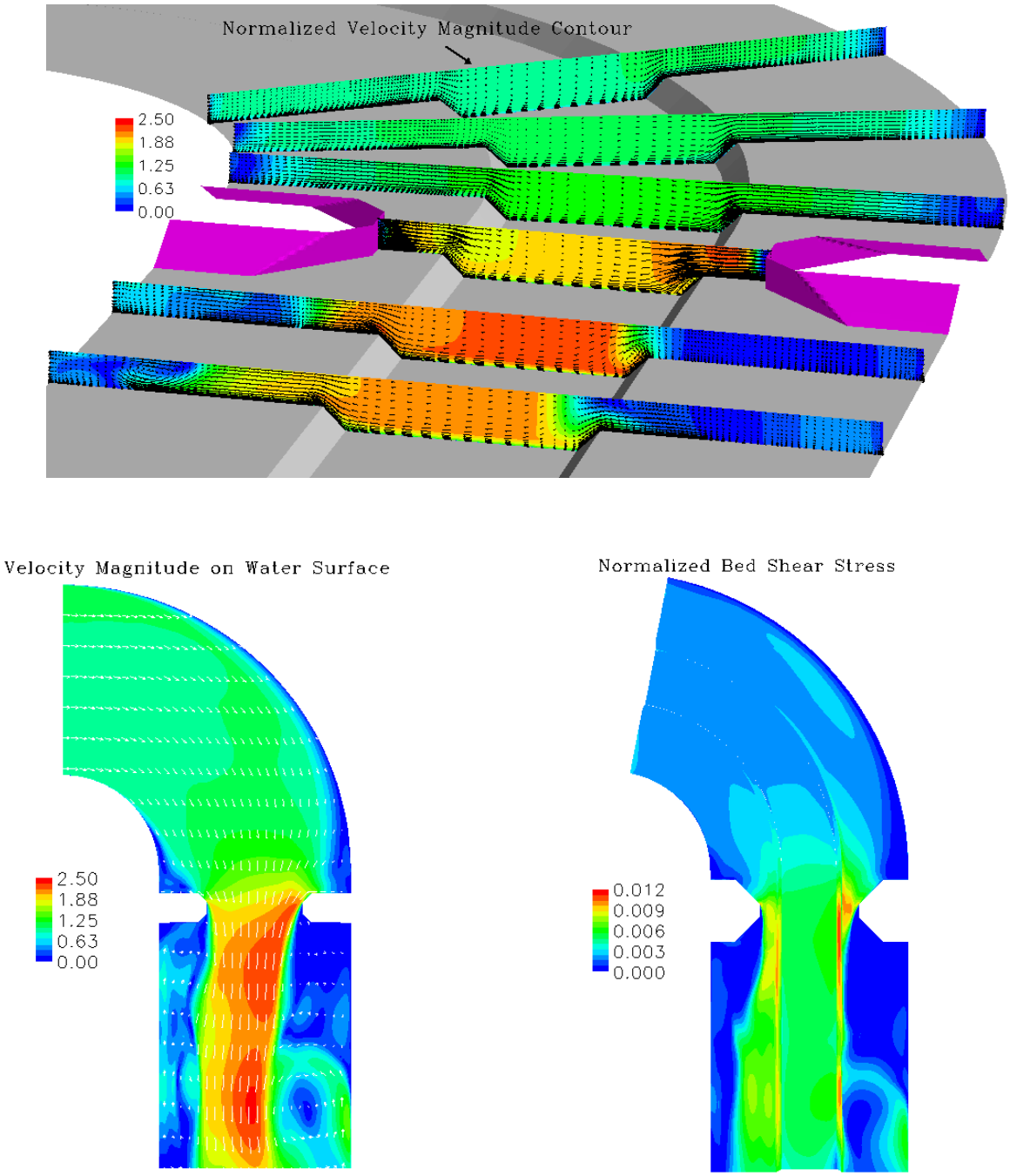

Figure 5.26 - Simulation results of case T3WW_End 1:1.

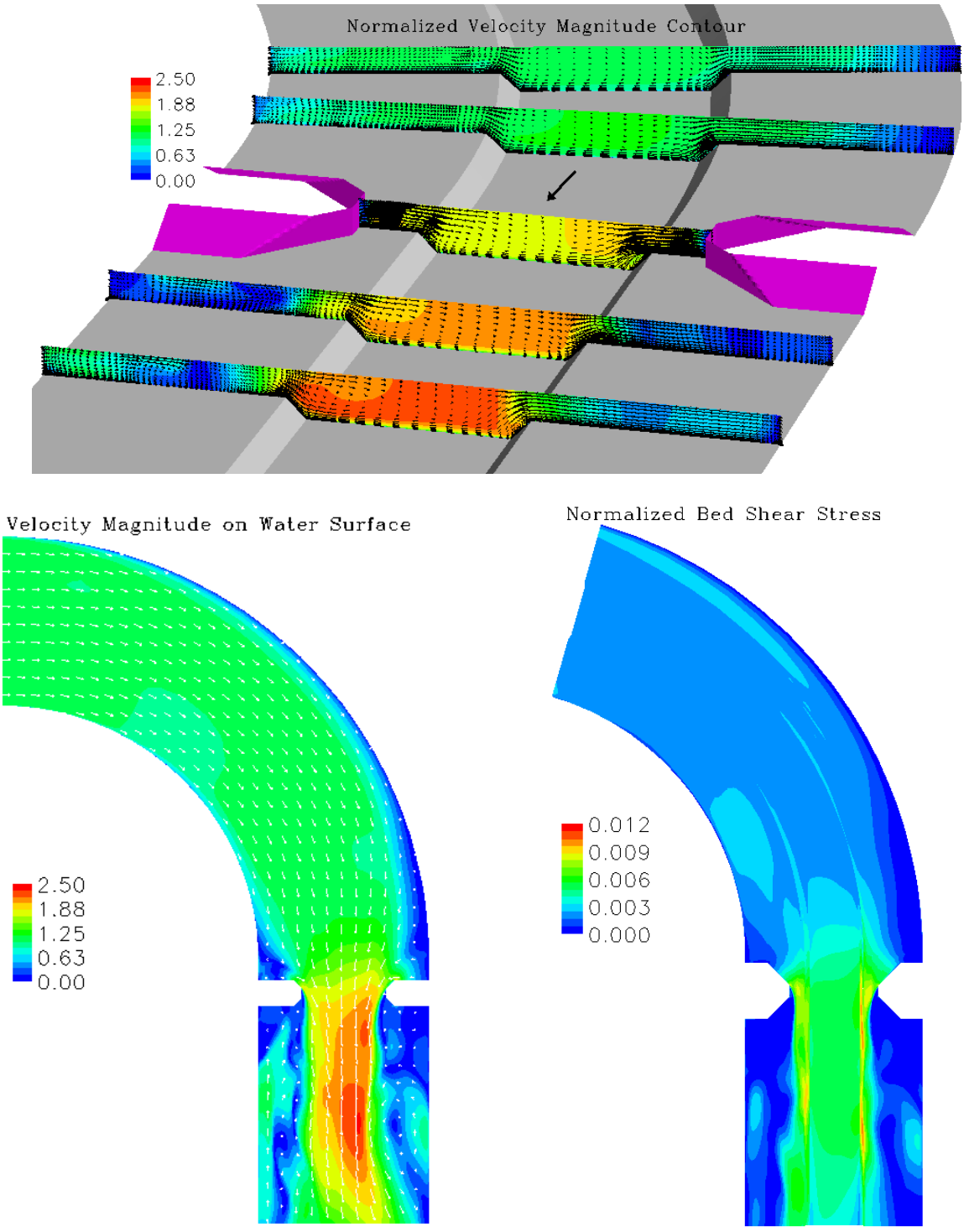

Figure 5.27 - Simulation results of T3WW_End 2:1.

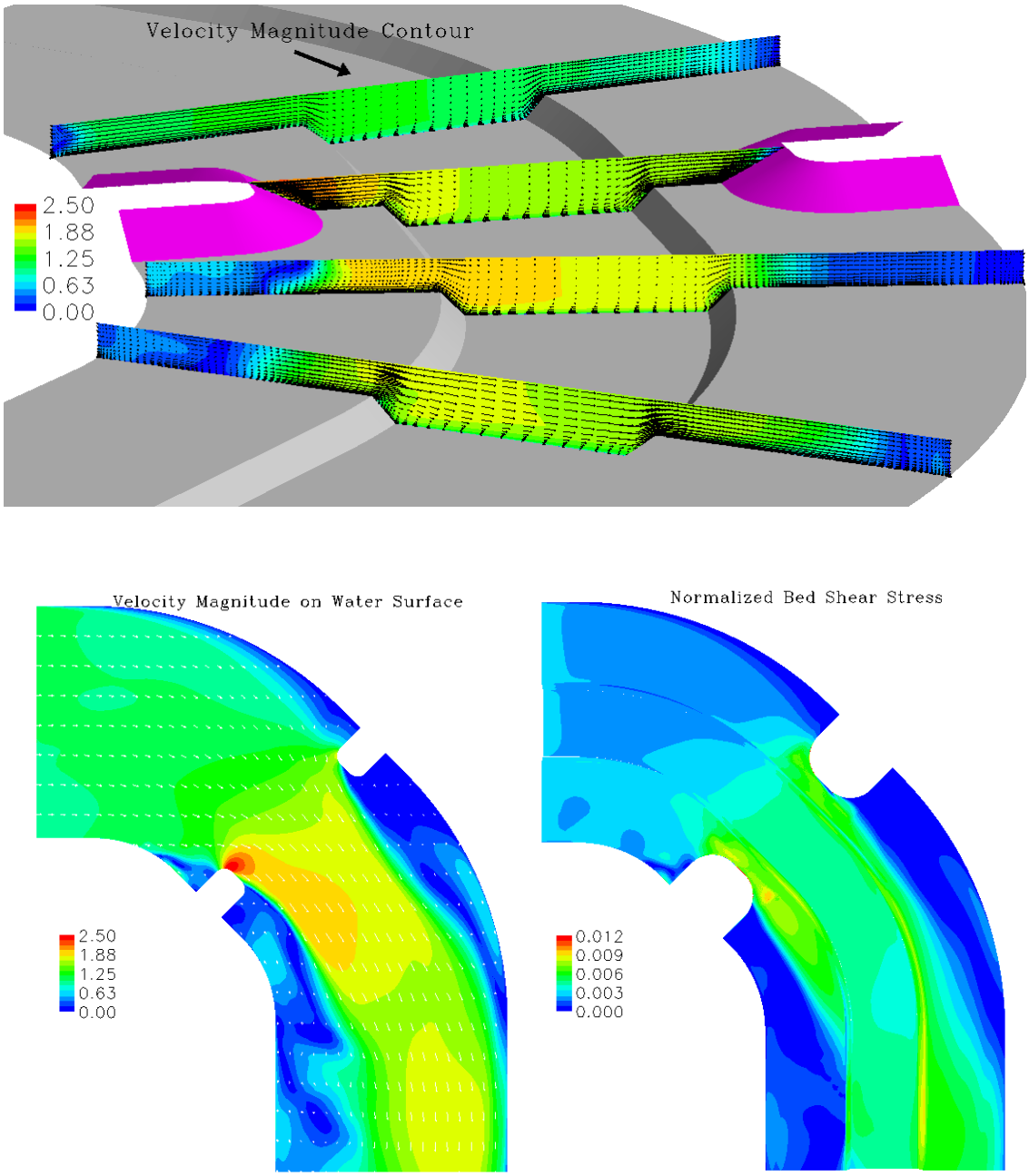

Figure 5.28 - Simulation results of T3ST_Mid 1:1.

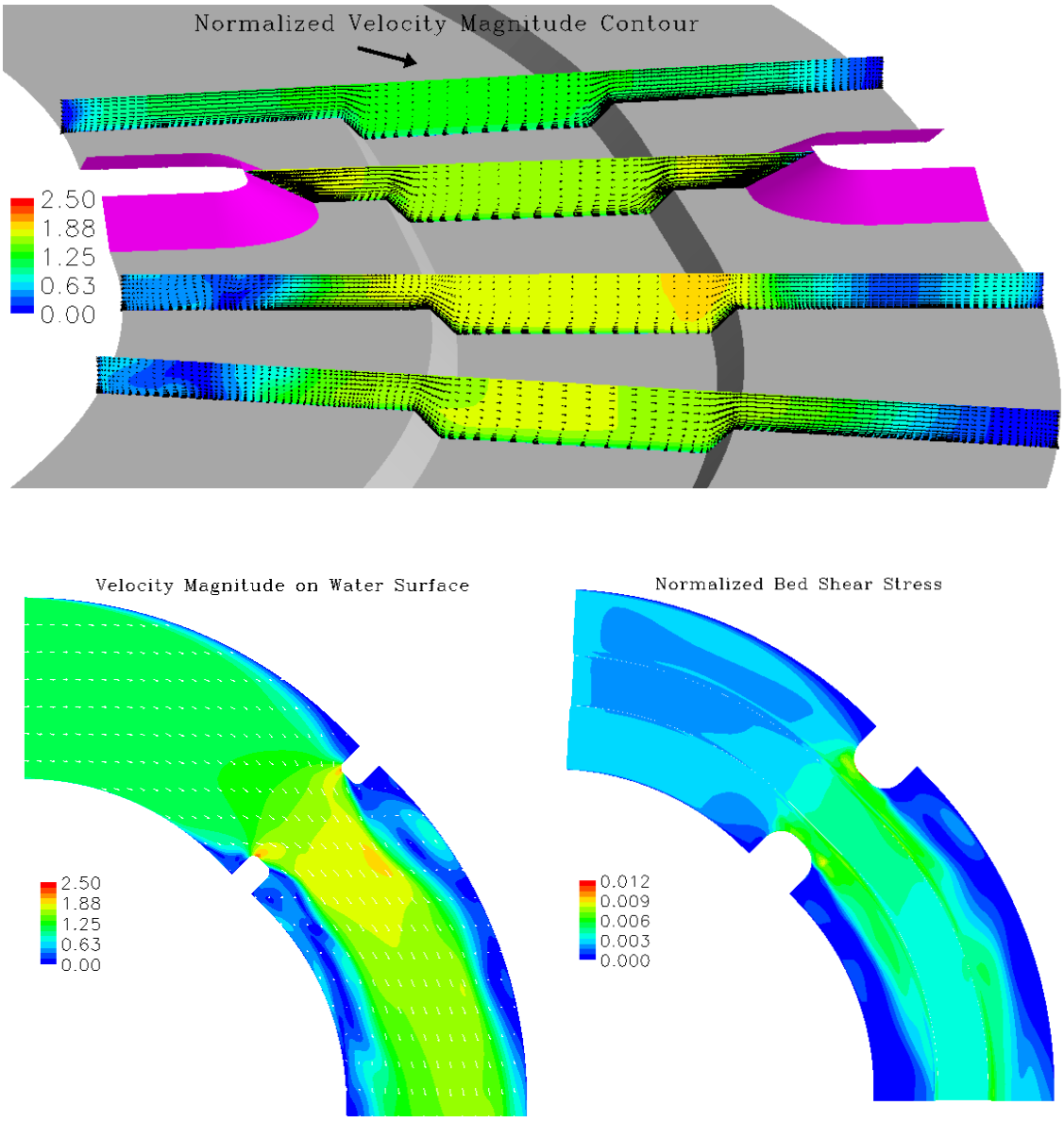

Figure 5.29 - Simulation results of T3ST_Mid 2:1.

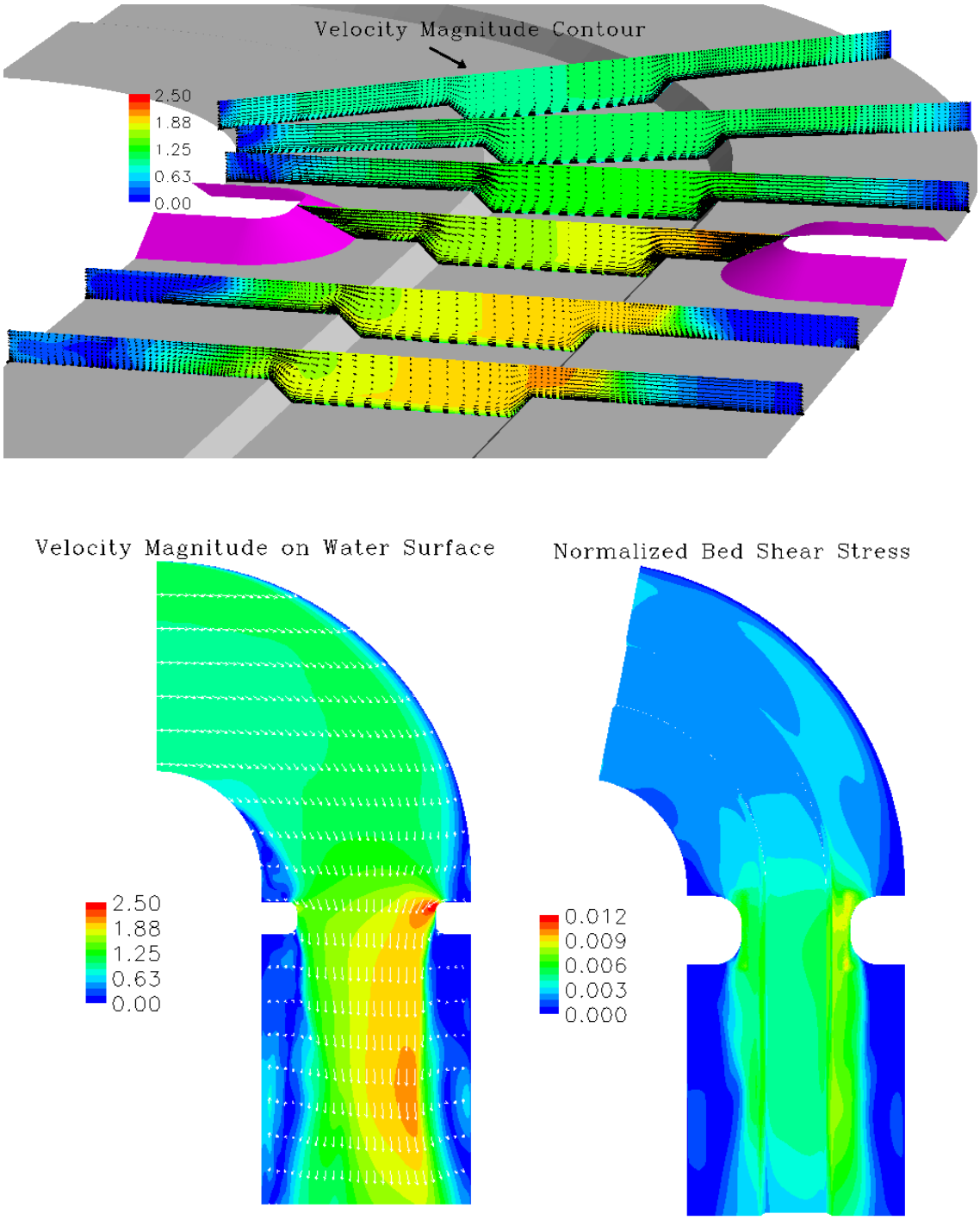

Figure 5.30 - Simulation results of T3ST_End 1:1.

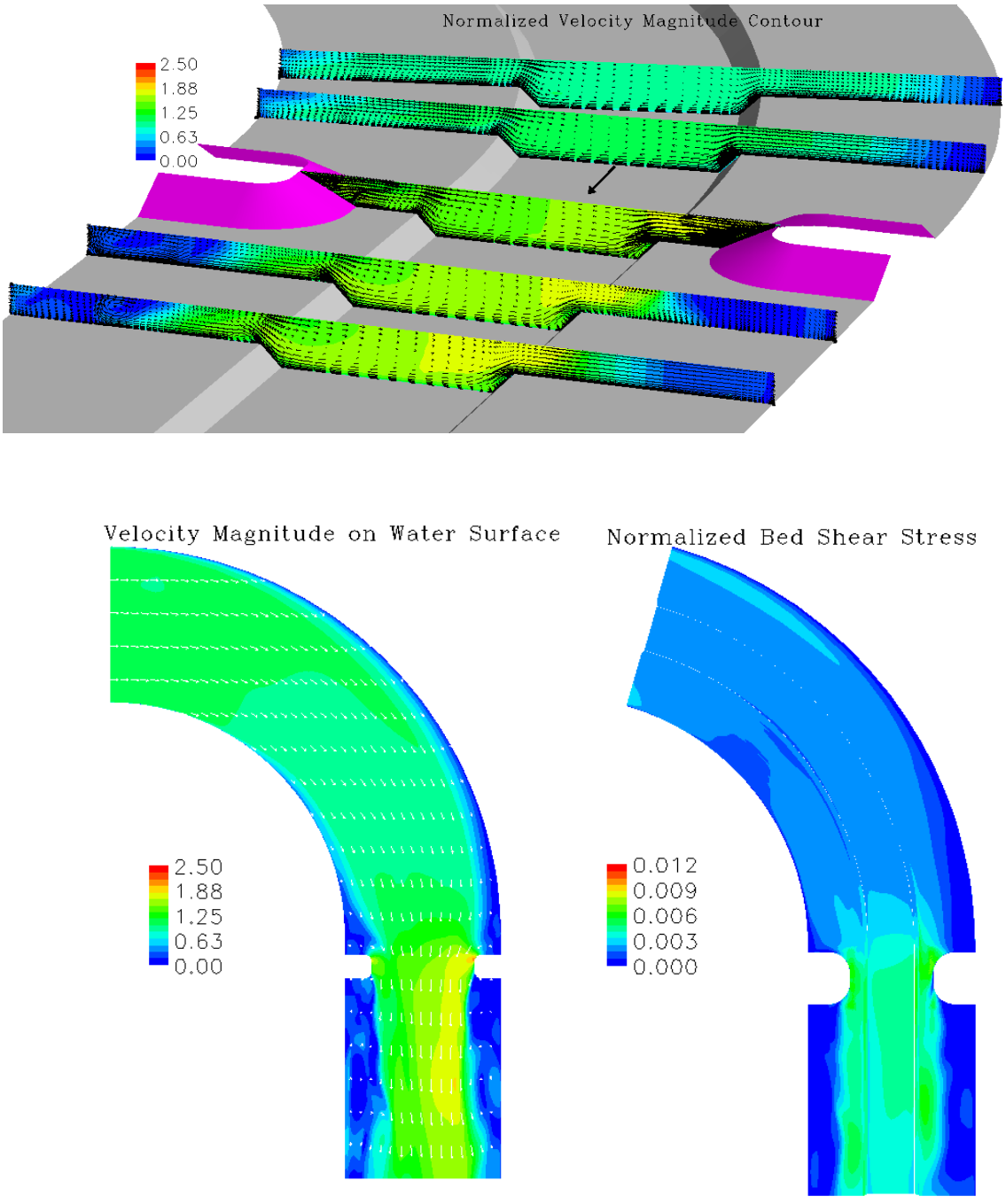

Figure 5.31 - Simulation results of T3ST_End 2:1.

5.5 OVERTOPPING FLOW ON CHANNEL BEND

Overtopping conditions have been discussed for straight channels with or without a floodplain. The bridge deck was found to make the flow more uniformly ditributed under the bridge. So the bed shear stress in the channel center will increase much faster than around the abutment when overtopping takes place. To study the influence of a bridge deck in a channel bend, the cases in section 5.4 have been modified to simulate overtopping conditions. The bridge is the same as the one used for the previous overtopping studies, including a 0.12m thick 0.46m wide deck. Figure 5.32 lists all the eight cases for the overtopping study. Figure 5.33 shows the cross section at the middle of the abutment.

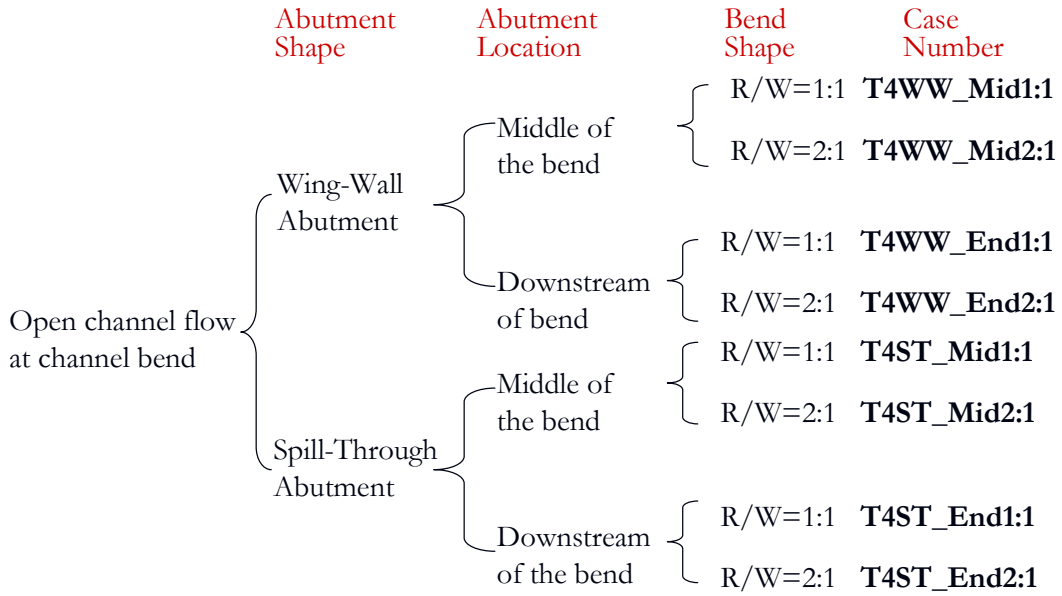

Figure 5.32 - Numerical cases for channel bend study in overtopping flow.

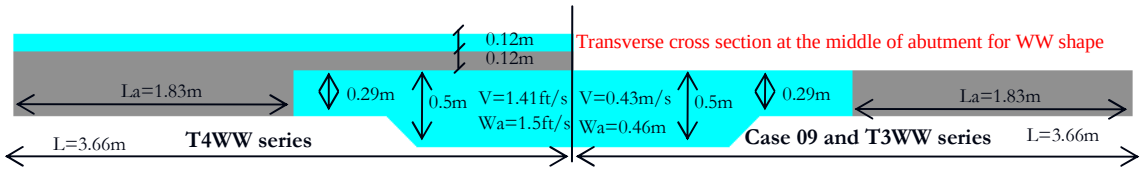

Figure 5.33 - Cross section of the wing-wall abutment cases in channel bend study.

5.5.1 Comparison of Open Channel Flow and Overtopping Flow in a Channel Bend

When comparing the two sets of simulations in a channel bend for the open channel flow and the overtopping flow, the bed shear stress is found to be significantly higher under overtopping conditions. The overtopping cases have a higher channel unit discharge ratio than the corresponding open channel cases due to the bridge deck blockage. The increase in unit discharge ratio is about 6.5% for the wing-wall abutment and 10.5% for the spill-through abutment. Table 5.8 shows a comparison of the maximum bed shear stresses. The increse are varies from 32% to 90%.

Table 5.8 - Results under overtopping and open channel conditions.

open channel flow	$C_{f\_max\_open}$	Overtopping flow	$C_{f\_max\_over}$	$C_{f\_max\_over}/ C_{f\_max\_open}$
T3WW_Mid 1:1	0.0130	T4WW_Mid 1:1	0.0187	1.44
T3WW_Mid 2:1	0.0109	T4WW_Mid 2:1	0.0167	1.53
T3WW_End 1:1	0.0108	T4WW_End 1:1	0.0178	1.65
T3WW_End 2:1	0.0092	T4WW_End 2:1	0.0175	1.90
T3ST_Mid 1:1	0.0098	T4ST_Mid 1:1	0.0129	1.32
T3ST_Mid 2:1	0.0087	T4ST_Mid 2:1	0.0134	1.54
T3ST_End 1:1	0.0095	T4ST_End 1:1	0.0132	1.39
T3ST_End 2:1	0.0070	T4ST_End 2:1	0.0130	1.86

Upstream of the bridge, the overtopping cases show lower bed shear stresses than the corresponding open channel flow cases in section 5.4. This is consistant with the influence of the water depth. Generally, the bed shear stress will decrease with an increase in water depth. Downstream of the bridge, the influence of the bridge deck can last for a long distance. This was observed in the straight channel study. Within the current computation domain, the downstream bed shear stress for the overtopping cases is still higher than the corresponding open channel flow cases.

5.5.2 Influence of R/W

The comparison is conducted between two cases with a wing-wall abutment at the middle of channel bend. Compared with the open channel flow cases, these two overtopping cases show a significant increase of the maximum bed shear stress. For R/W equal 1, the increase of water depth, C_{f_max} increases from 0.010 to 0.019 when the water depth on the flood plain increases from 0.29m to 0.54m. The location of C_{f_max} changes from the downstream main channel slope to the upstream corner of the abutment. For R/W equal to 2, C_{f_max} increases from 0.011 to 0.017 when the water depth on the flood plain increases from 0.29m to 0.54m. The location of the maximum bed shear stress also changes from the downstream main channel slope to the upstream corner of the abutment. The interesting finding is that the bed shear stress on both overbank areas under the bridge deck show a significant increase. The bed shear stress in this area is uniformly high. This is quite different from the open channel flow conditions. At the middle of the abutment, the difference between the inner and outer abutment is not large even for R/W equal to 1. For the case of R/W equal 2, the shear stress distribution is almost symmetrical.

The high bed shear stress found on the downstream inner overbank in case T3WW_Mid 1:1 is not found in the overtopping cases. Overall, the effect of the bridge deck is to decrease the influence of the channel bend and to make the flow more uniform. However, the influence of the channel bend can still be found downstream on the outer main channel slope. Both case T3WW_Mid 1:1 and case T4WW_Mid 1:1 have this feature. It is believed that the channel bend after the abutment is responsible for the highly asymmetric result.

For case T4WW_Mid 1:1, the flow has become asymmetric when approaching the abutment. The inner half channel has a higher velocity magnitude. However, at the middle of the abutment, the velocity contours are almost symmetrical. Even at the downstream side of the abutment, the velocity contours are still symmetrical for some distance. The asymmetric velocity contour begins from the end of the channel bend. This is consistent with the bed shear stress distribution. For case T4WW_Mid 2:1, the flow basically remains symmetrical when approaching the abutment. And this symmetric flow extends to the end of the channel bend. At the far downstream side, the asymmetric trend begins to show up. But it is not as significant as T4WW_Mid 1:1.

Cross section plots are also presented in Figure 5.34 and Figure 5.35. As for the straight channel, higher velocities appear on the bridge surface. Under the bridge deck, the velocity is stratified and remains relatively constant in the horizontal direction. The higher velocities appear in the bottom half channel. Downstream of the bridge deck, the surface velocity drops very quickly. The higher velocity region extends far downstream from the bridge.

5.5.3 Influence of abutment location

For the open channel flow, the higher bed shear stress is found to be around the inner abutment when the bridge is located in the middle of the channel bend. The inner abutment tends to force the flow further toward the outer bank. The influence of the outer abutment is not obvious. However, the trend is opposite when the bridge is located at the end of the channel bend. Higher bed shear stresses are observed around the outer abutment. The outer abutment tends to force the skewed flow back towards the main channel and to decrease the impact of the flow on the outer overbank. The effect of the inner abutment is not obvious.

For the over topping cases, the space under the deck is on closed by the abutments and the bridge deck. The flow passing through this closed space will be pressurized and redistributed. On the upstream side, there is no-slip boundary only on the river bottom. The velocity is highest at the free surface. Under the bridge deck, there is a no-slip boundary for both the top and bottom. So the flow will be squeezed towards the center. The adjustment of the flow will take place in both the vertical and horizontal direction. This adjustment will make the flow more uniformly distributed. This is reflected by the bed shear stress contours. For all the eight simulation results shown in Figure 5.34 to Figure 5.38, the difference on both sides of the overbank under the bridge deck is not as large as in the open channel flow cases. The influence of abutment location on the bed shear stress distribution under bridge deck can not be observed under overtopping conditions.

Far downstream, the influence of the bridge deck is not strong. The bend effect takes over and dominates the flow. For the cases where the abutment is in the middle of the channel bend,

the asymmetric bed shear stress contours appear again. This is very close to the distribution observed in open channel flow cases. It is believed that the second half of the channel bend after the bridge causes the disymmetry of the flow. However, this disymmetry is not found in the results where the abutment is at the end of the channel bend. This further proves that the bridge deck tends to make the bed shear stress uniformly distributed and the channel bend tends to cause asymmetry.

5.5.4 Influence of abutment shape

The unit discharge ratio for the overtopping geometry is higher than for the open channel conditions in section 5.4. According to the study in Chapter 4, the bed shear stress is linearly propotional to the channel unit discharge ratio. The correction factor for a wing-wall abutment is not sensitive to the change of unit discharge ratio. However, the correction factor for spill-through abutment will decrease with an increase in unit discharge ratio. The constant correction factor is proposed in Chapter 4 for convenience. Hence, the maximum bed shear stress difference between a wing-wall abutment and a spill-through abutment will be magnified when the unit discharge ratio increases. Table 5.9 shows a the comparison of the maximum bed shear stress for a wing-wall and a spill-through abutment for overtopping conditions. Obviouly, the difference is larger than in a open channel.

Table 5.9 - Results of wing-wall abutment and spill-through abutment.

Case #	$C_{f\_max\_WW}$	Case #	$C_{f\_max\_ST}$	$C_{f\_max\_ST}/ C_{f\_max\_WW}$
T4WW_Mid 1:1	0.0187	T4ST_Mid 1:1	0.0129	0.69
T4WW_Mid 2:1	0.0167	T4ST_Mid 2:1	0.0134	0.80
T4WW_End 1:1	0.0178	T4ST_End 1:1	0.0132	0.74
T4WW_End 2:1	0.0175	T4ST_End 2:1	0.0130	0.74

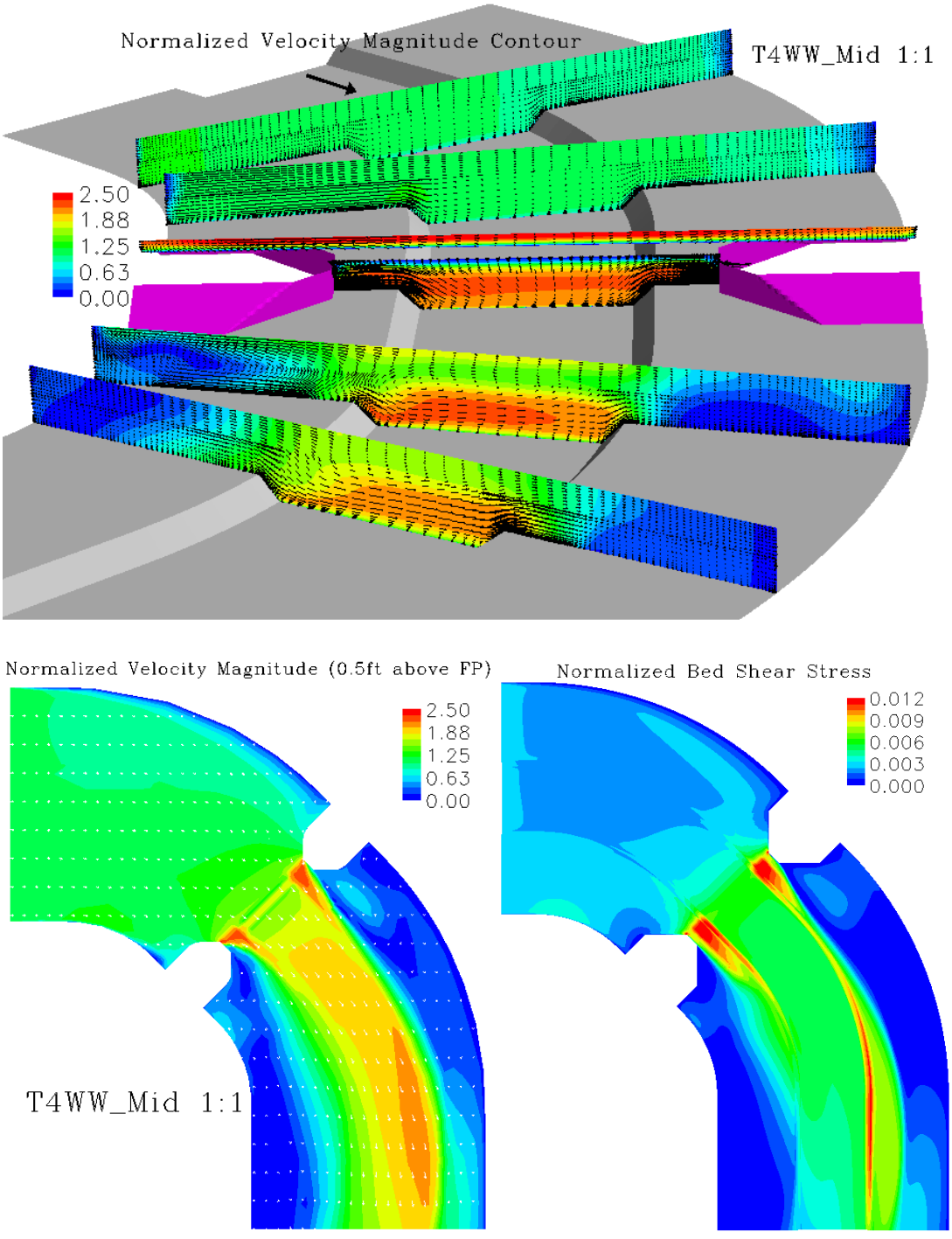

Figure 5.34 - Simulation results of T4WW_Mid 1:1.

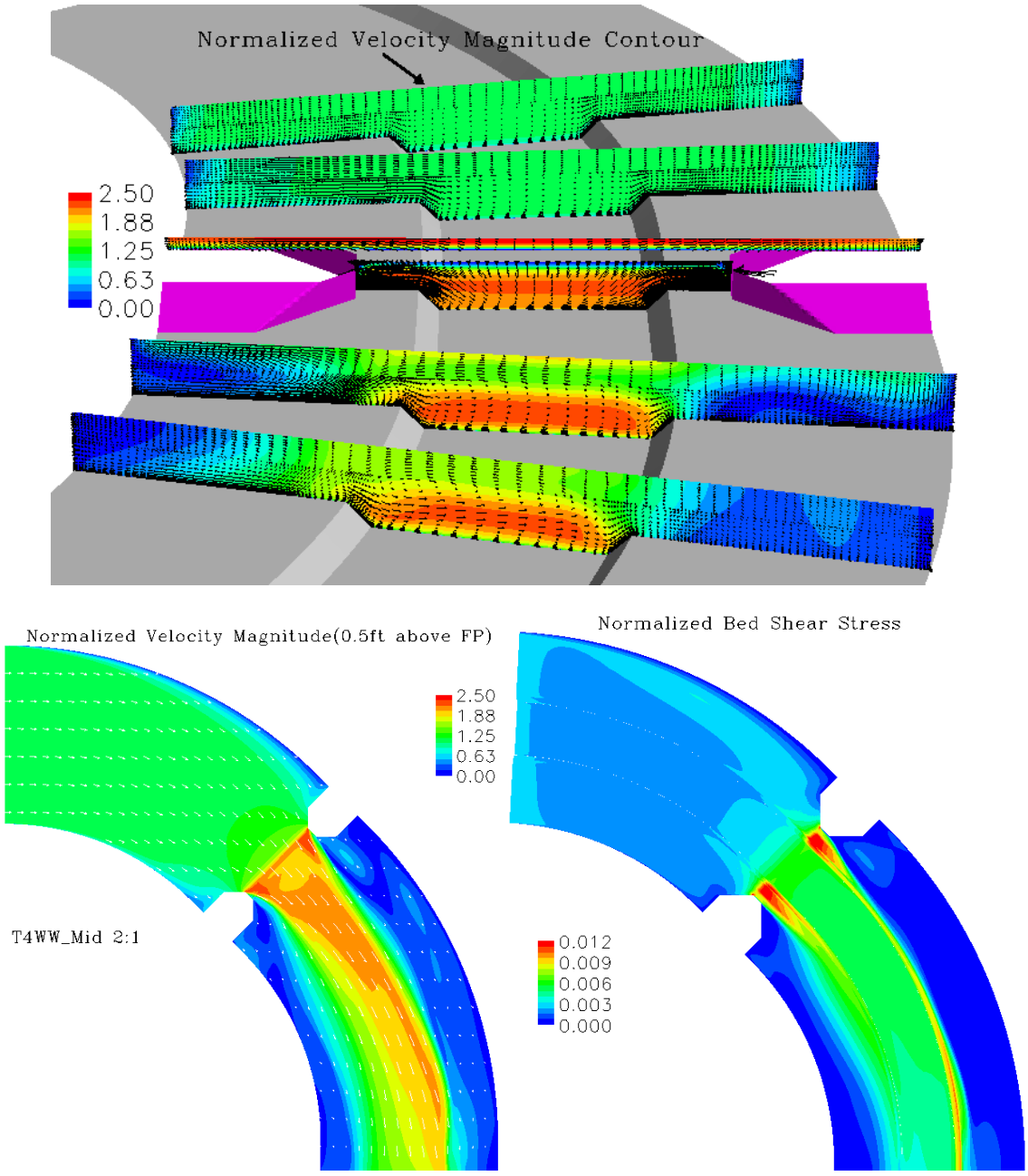

Figure 5.35 - Simulation results of T4WW_Mid 2:1.

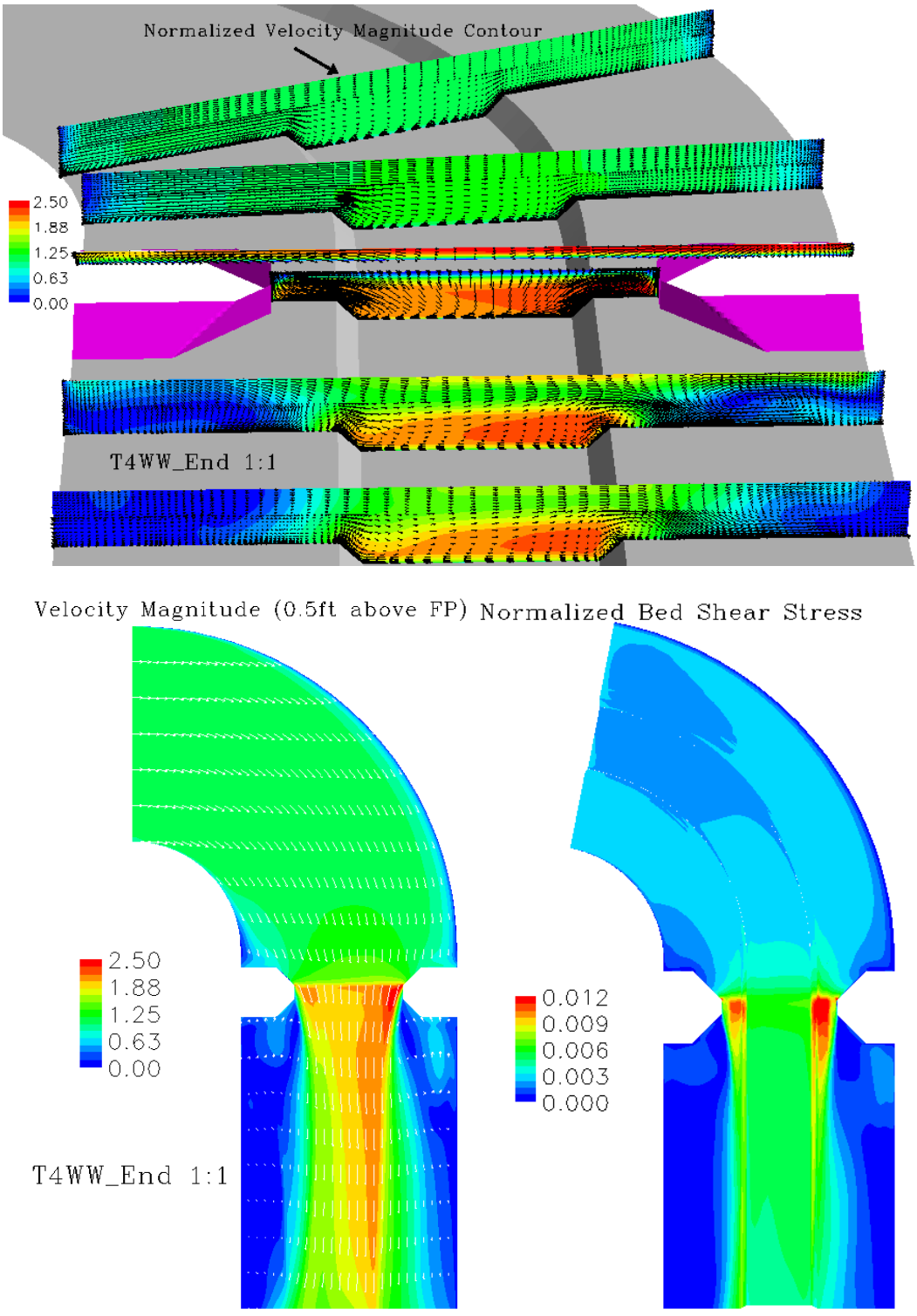

Figure 5.36 - Simulation results of T4WW_End 1:1.

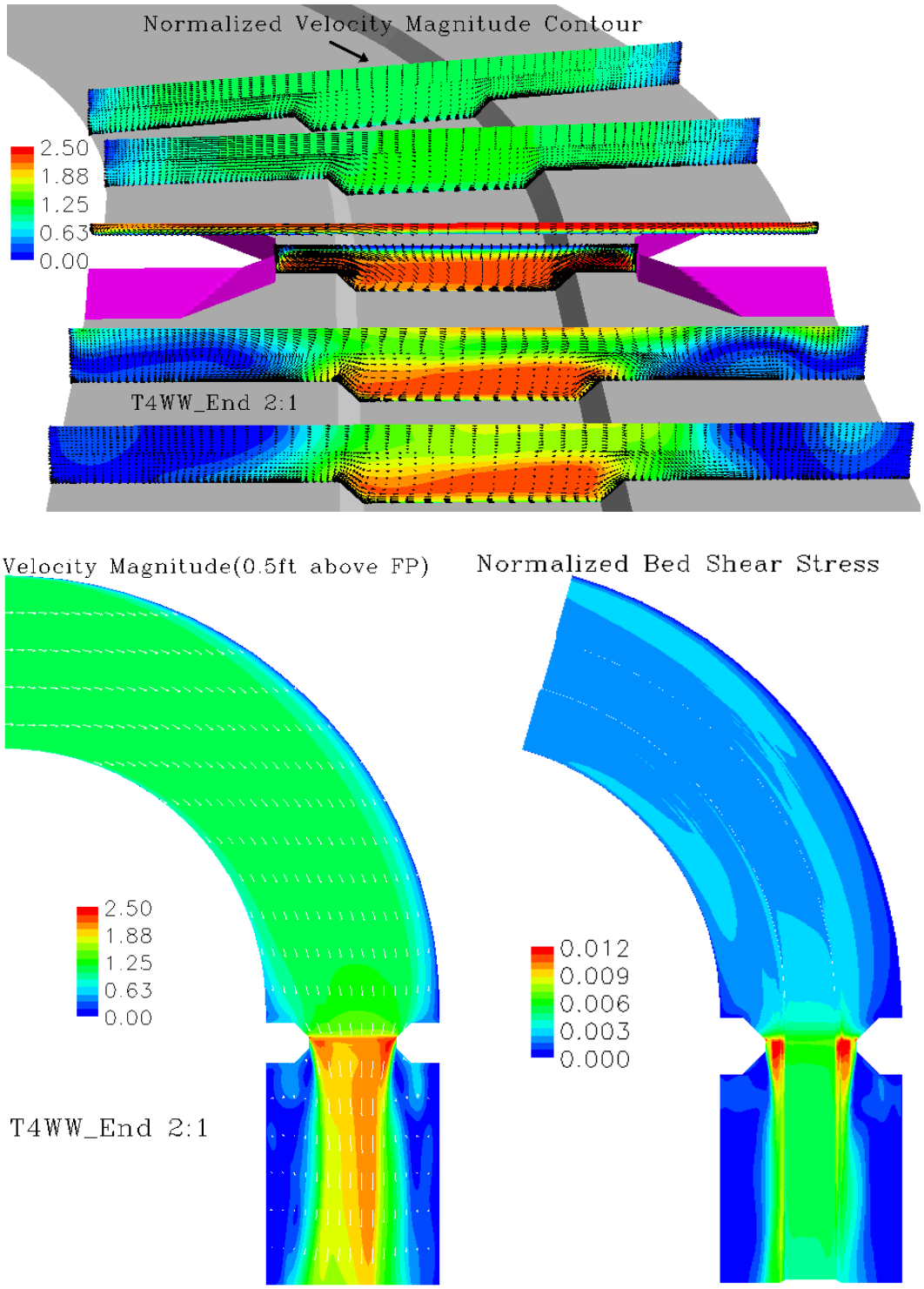

Figure 5.37 - Simulation results of T4WW_End 2:1.

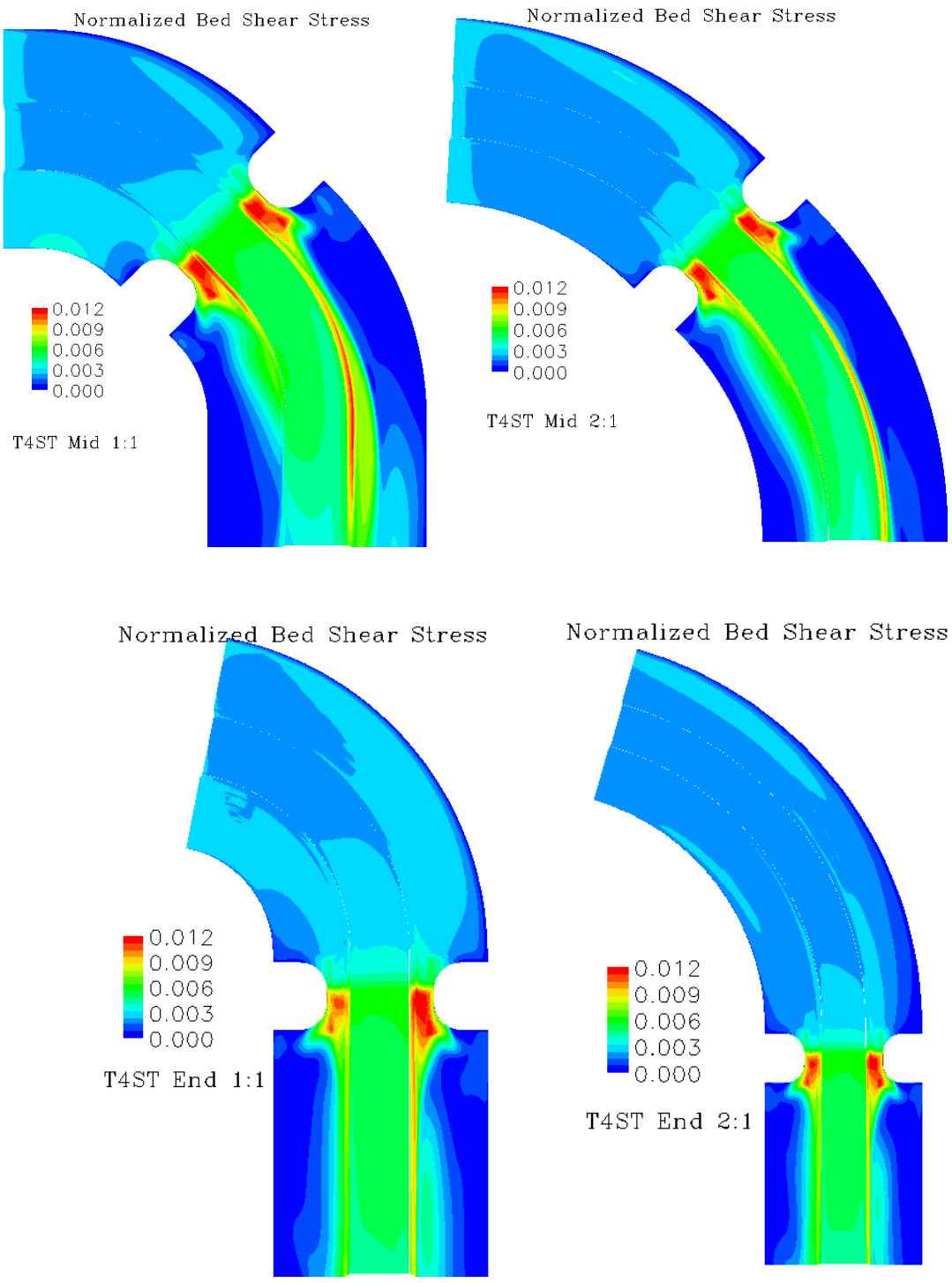

Figure 5.38 - Normalized bed shear stress contours of the spill-through abutment cases.

5.6 CONFLUENCE OF TRIBUTARY UPSTREAM OF A BRIDGE

Many situations can cause an asymmetric flow in a channel. The confluence of a tributary upstream of the bridge is one of those. It is simulated by modifing the flume test case 14 to include a tributary upstream of the bridge. Case 14 is a symmetric channel. To simplify the study, overtopping is not considered. The CHEN3D program is able to handle overtopping and confluence at the same time. In case 14, the channel is rectangular and 7.3m wide, the abutment is 1.32m long with a wing-wall shape, the water depth is 0.37m, the approach velocity is 0.33m/s. To study the non-symmetric flow, the full channel width is simulated instead of the half channel width. A tributary is added to the straight channel 7.3m ahead of the abutment. The width of the tributary is 3.66m. The water depth and velocity are the same as case 14. The tributary channel comes at an angle of 30 degree from the straight channel. A constant velocity is applied at the inlets of the straight channel and the tributary channel. The free surface is assumed to be a rigid lid.

Figure 5.39 shows the asymmetric velocity contours on the free surface. The shape of the contours depicts clearly the confluence of the flow from the two inlets. The flow rate from the tributary is only half of the flow rate in the straight channel. Obviously, the high flow rate component will dominate the direction of the confluence. The asymmetric flow starts from the confluence location and the high unit flow rate region gradually moves toward the channel center. When passing around the abutment, the highest unit flow rate is still on the tributary side. The contours show a smooth transition around the lower abutment. This indicates that the lower abutment has a smaller influence on the flow. On the other side, there is sharp transition from the upstream corner of the abutment to the channel center. This shows that the upper abutment impacts the skewness of the flow significantly. The highest velocity appears downstream of the abutment It is believed that the influence of the upstream confluence will decrease with an increase in the distance between the tributary and the abutment.

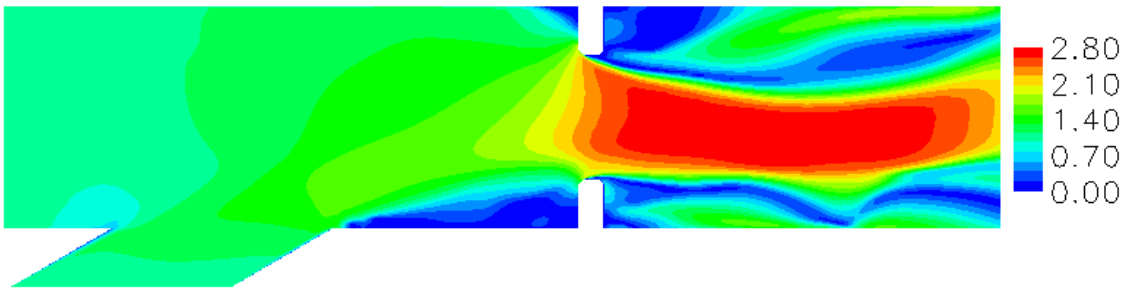

Figure 5.39 - Velocity magnitude contours on the water surface.

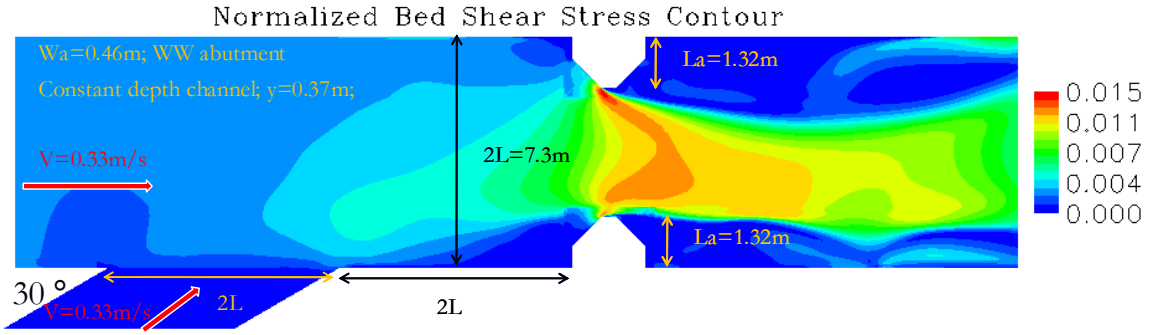

Figure 5.40 - Normalized bed shear stress contours.

Figure 5.40 shows the bed shear stress contours. The upstream pattern is very similar to the surface velocity. The bed shear stress is also asymmetric. At upstream side, the high bed shear stress region start from the confluence location and is skewed towards the opposite abutment. The maximum bed shear stress appears at the abutment opposite to the tributary channel. On the downstream side, the bed shear stress contour skews back to the side of the tributary channel.

5.7 MAXIMUM SHEAR STRESS FOR OVERTOPPING FLOW

Overtopping can cause the flow to be pressurized and forced under the bridge deck. This can make the flow more uniform and descrease the difference between the bed shear stress under the bridge deck near the abutment toe and the channel center. When overtopping occurs in a complicated channel geomery (channel bend or compound channel), the bed shear stress distribution can be quite different from the open channel case. The main concusions based on the studies in this chapter are summarized below:

1. When the water level reaches the bottom cord of the deck, the maximum bed shear stress around the abutment increases. This increase continues as the water depth rises until a highest value is reached with the water surface in flush with the top of the bridge deck. If the water depth continues to incease, the bed shear stress will begin to decrease.
2. The maximum bed shear stress in the case of pressure flow and ovretopping can be predicted by using the proposed maximum bed shear stress around an abutment by using a blockage effect of the bridge deck equal to a blockage effect of the abutment. The predicted value of τ_{max} in the case of rectangular chanels is within 10% of the numerical simulation values. For compound channel, this assumption can cause discrepancies as high as 50%.
3. When pressure flow and overtopping takes place in a channel bend, the bridge deck tends to diminish the non-symmetric nature of the flow caused by the bend. The maximum bed shear stress difference between the inner and outer side of the bend is not as significant as in an open channel flow. Also, overtopping decreases the channel curvature effect. However, the flow will recover the non-symmetric feature downstream if the channel bend continues after

the bridge. The influence of the abutment shape in a bend is about same as the influence of the abutment shape in a straight channel. The abutment location on the channel bend will affect the bed shear stress downstream of the abutment but not the maximum bed shear stress around the abutment.

Once the maximum bed shear stress is determined under overtopping conditions, the initial erosion rate of the river bottom can be estimated based on the erosion funciton of the soils, which can be derived from EFA (Erosion Function Apparatus) testing. Therefore, the SRICOS-EFA method can be applied for river overtopping problems. The procedure will be the same as the one for open channel flow calculation.

CHAPTER 6

VERIFICATION OF NUMERICAL SIMULATIONS

In this chapter, several scour rate models were proposed for the prediction of scour hole development around abutments in cohesive soils. The performances of these scour rate models were evaluated by comparing the numerical simulation results to the flume test cases in NCHRP 24-15(2). During the initial stage of the numerical simulations, the CHEN3D code was used without the scour rate model in order to establish the initial flow field for the abutment configurations on a fixed streambed. After the flow is fully established, various erosion rate models were then incorporated to predict the erosion of cohesive soil on the streambed. After successful simulation of abutment scour for flume test cases, the method was further extended to investigate the influence of pressure flow and overtopping conditions on abutment scour process in cohesive soils. Correction factors for overtopping flow have been proposed based on the numerical simulation results.

6.1 SOIL PROPERTIES

Porcelain clay was used in the flume tests of NCHRP 24-15(2). Geotechnical tests were performed according to ASTM standards. The results of two testing have been tabulated in Table 6.1. Erosion properties of the porcelain clay were tested using the Erosion Function Apparatus (EFA). Eleven EFA tests were performed using tap water. These samples were from different testing conditions. The first test was conducted with the fresh sample which should represent most of the clay used in the flume tests. The regression curve in Figure 6.1 is based on the first EFA test, which is used as the erosion function of the soils in all the numerical simulations of scour prediction. There were several samples taken from the clay stored for a long period of time or the leftover clays after the flume tests. These samples may have lower erosion rate because of moisture loss or some other ambient conditions. The EFA test results are shown in Figure 6.1 with the data scattering over a fairly wide range.

Table 6.1 - Soil properties of the clay used in NCHRP 24-15(2) (After Oh, 2009).

Property	Test 1	Test 2
Liquid Limit (%)	30.9	29.8
Plastic Limit (%)	16.9	17.24
Plasticity Index (%)	14.0	12.56
D_{50} (mm)	0.004	0.003
Shear Strength (kPa)	13.5	15.3

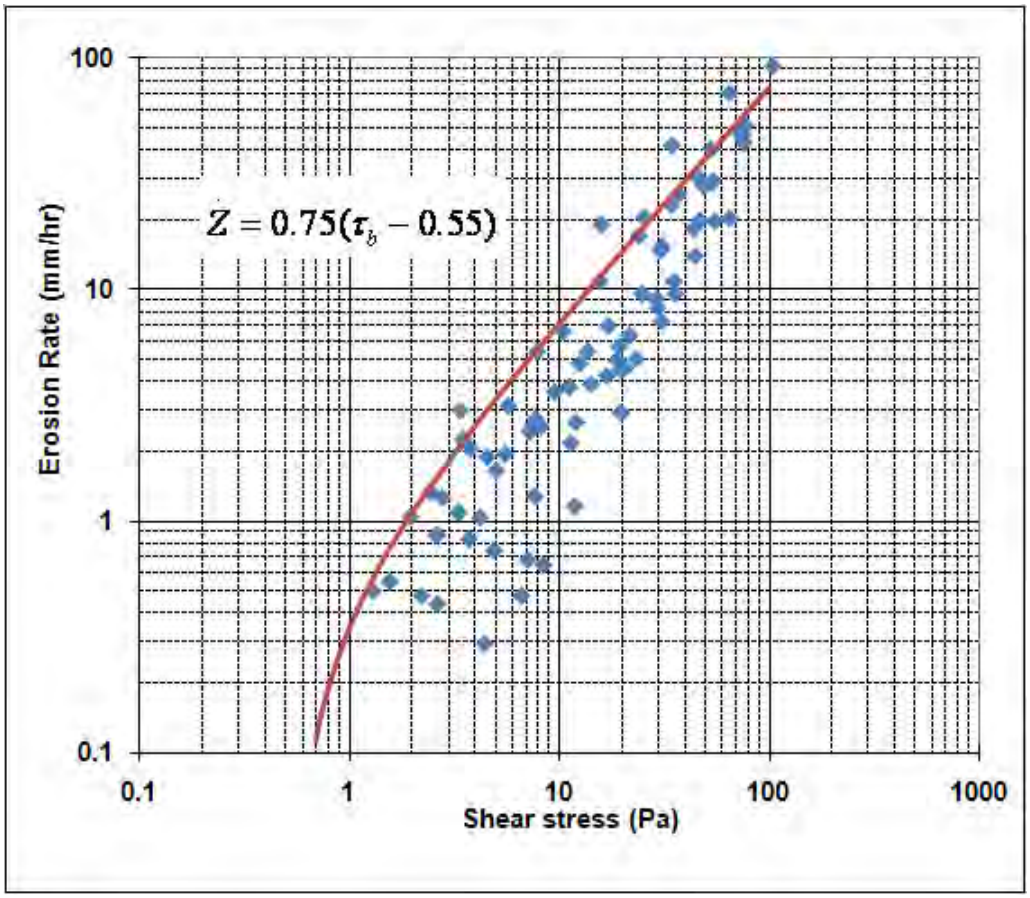

Figure 6.1 - Correlation between shear stresses and erosion rates (Oh, 2009).

The porcelain clay used in the present flume tests has also been used in several previous studies of bridge scour at Texas A&M University (Briaud et al., 1999a, 2001b, 2004). Figure 6.2 shows a comparison of the EFA results for the porcelain clay used in (a) simple pier scour, (b) complex pier scour and contraction scour, and (c) abutment scour. It is clearly seen that the erosion function may be quite different even for the same kind of well controlled commercial clay. The clay used in current study has the lowest erodibility when the bed shear stress is less than 10 Pa, but the erosion rate increases considerably faster than the other two clays when the bed shear stress is higher than 25 Pa. It should be noted that the shear stress is well below 25 Pa in the present flume tests.

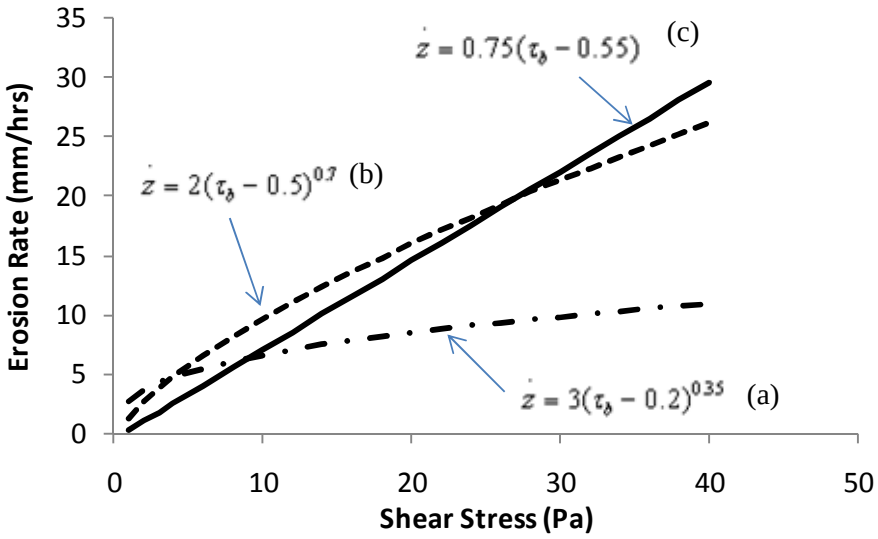

Figure 6.2 - Comparison of erosion functions for porcelain clay.

6.2 SCOUR RATE MODELS IN COHESIVE SOILS

The shear stress model mentioned in chapter II was employed by Nurtjahyo (2003) for the study of pier scour and contraction scour. Soil erosion rate is assumed to be a function of the shear stress applied on riverbed surface as well as the critical shear stress of the soils. The shear stress model used by Nurtjahyo (2003) provides reasonable prediction for the deepest scour depth. However, the predicted scour hole shapes are significantly different from those observed in the measurement. For example, the predicted maximum bed shear stress always occurs in the front section of the pier facing the flow where the strongest flow acceleration is observed. In the wake region behind the pier, the predicted scour hole is rather small since the bed shear stress is relatively low in the wake. On the other hand, the flume test results indicate that the scour depth behind the pier is of the same order as that in front of the piers for most pier scour tests in cohesive soils. This clearly suggested that the bed shear stress is not the sole mechanism responsible for the development of scour hole around hydraulic structure. A new scour rate model was proposed in Nurtjahyo (2003) to include the effect of turbulence kinetic energy in the scour rate equation:

$$\dot{z} = \dot{z}(\tau_b, \tau_c, k) = c(\tau_b - \tau_c) + b \cdot k \tag{6.1}$$

where, $\dot{z}$ is the erosion rate (mm/hour); τ_b is the bed shear stress (Pa); τ_c is the critical shear stress of the soils (Pa); c is the slope of erosion rate versus shear stress curve ($m^3/(N \cdot hr)$); k is turbulent kinetic energy $(m/s)^2$ and b is the constant (s/m). In Nurtjahyo (2003), the k value was chosen as the maximum value of turbulent kinetic energy in the vertical direction between the streambed and about 10% of water depth. The new model successfully predicted the scour pattern around a circular pier similar to that observed in the experiment. More specifically, the new

scour rate model produced a significantly deeper scour hole behind the pier since the turbulence intensity is quite high in the wake region.

All numerical results for pier scour presented in Nurtjahyo (2003) were obtained using the hydraulically smooth boundary condition for streambed. The influence of the surface roughness has been discussed in chapter V for the verification of overtopping flow experiments (Kerenyi, 2007). In the overtopping flow simulation, the equivalent sand grain roughness is constant and the streambed is fixed without scour development. Kerenyi's experiment clearly indicates that the bed shear stress in the roughened channel is significantly higher than that in the hydraulic smooth channel. For the porcelain clay used in the present flume tests, the soil particles are very fine and the channel bottom is flat before scour takes place. Therefore, it is appropriate to treat the streambed as a hydraulically smooth surface in the prediction of initial shear stresses for abutments on a fixed streambed. As the abutment scour develops, the streambed is no longer smooth and the bed form is similar to a sand bed with variable surface roughness. Since the roughness height is not constant, the surface roughness model in Chapter 5 cannot be directly employed to simulate the streambed roughness encountered in the scour process.
To account for the non-smooth bed form effects, the scour rate equation is modified to augment the bed shear stresses obtained from CHEN3D simulations under the hydraulically smooth surface boundary conditions:

$$\dot{z} = \dot{z}(\tau_b, \tau_c, k) = c(\beta\tau_{num} - \tau_c) + b \cdot k \tag{6.2}$$

where the correction factors β and b are determined from numerical optimization for the flume test cases. In the present investigations, the slope c (= 0.75 mm/hour) and critical shear stress τ_c (= 0.55 Pa) in equation (6.2) were determined from the EFA test results. For the baseline model (denoted as Model I) with β=1.0 and b = 0, the scour rate is assumed to be linearly proportional to the streambed shear stress ($\tau - \tau_c$) and the bed form roughness and turbulence effects are neglected. Comparisons of Model I results with the corresponding flume test data clearly show that the baseline scour rate model significantly underestimated the maximum scour depth around the abutment.

In order to improve the prediction of scour pattern, a systematic optimization was performed to determine the optimal correction factors β and b in equation (6.2). In Model II, the calculated streambed shear stress τ_{num} was scaled up by β to account for the effect of bed form roughness but the effect of turbulence was not incorporated (i.e., b = 0). The Model II test results indicate that the correction factors β should not be greater than 1.5 in order to avoid excessive scour in the main channel. However, the predicted scour depth with the highest correction factor β = 1.5 was still too shallow around the abutments for most flume test cases. This suggests that the flow turbulence also plays an important role in the scour process. After a systematic numerical optimization, it was found that b = 0.01 yields the best prediction of the maximum scour depth around the abutment. Therefore, the parameters in scour rate equation (6.2) were chosen as $c = 0.75 mm/hour$, $\tau_c = 0.55$ Pa, β = 1.5 and $b = 0.01$ for Model III. A detailed assessment of these three scour rate models abutment scour prediction is given in the following sections.

6.3 SCOUR PREDICTION OF THE FLUME TESTS IN NCHRP 24-15(2)

In this section, numerical simulations were performed for selected abutment configurations to evaluate the performance of the scour rate models proposed in Section 6.2. Five abutment configurations (Cases 1, 4, 9, 13, and 14) were chosen from the present flume test matrix to cover a wide range of abutment configurations including both wing-wall and spill-through abutments in rectangular as well as compound channels. The dimensional parameters of these five cases are tabulated in Table 6.2.

Table 6.2 - Dimensional parameters for the cases selected for scour prediction.

Flume tests	L (m)	L_m (m)	L_f (m)	L_a (m)	y_f (m)	V (m/s)	Abutment Shape	θ (°)
Case 1	3.66	1.22	2.44	1.83	0.29	0.43	ST	90
Case 4	3.66	1.22	2.44	1.83	0.29	0.34	ST	90
Case 9	3.66	1.22	2.44	1.83	0.29	0.43	WW	90
Case 13	3.66	0.00	3.66	1.01	0.37	0.34	WW	90
Case 14	3.66	0.00	3.66	1.62	0.37	0.34	WW	90

Figure 6.3 shows the five abutment configurations used in the CHEN3D simulation of abutment scour. Both Cases 13 and 14 involve wing-wall abutments in rectangular channel under the same water depth and approach velocity. The abutment in Case 14 is 0.61m longer than that in Case 13. These two cases were chosen to evaluate the influence of channel contraction on the scour pattern. The other three cases involves wing-wall and spill-through abutments in compound channel cases with the same abutment setback of $L_a/L_f = 0.75$. Cases 1 and 4 have identical abutment geometry and compound channel configuration, but different approach velocity. They were chosen to study the influence of the approach flow velocity on the scour depth. Case 9 has the same compound channel geometry, abutment length, water depth, and approach flow velocity as Case 1; the only difference is the abutment shape. It was chosen to investigate the effect of wing-wall and spill-through abutment shapes on the scour pattern.

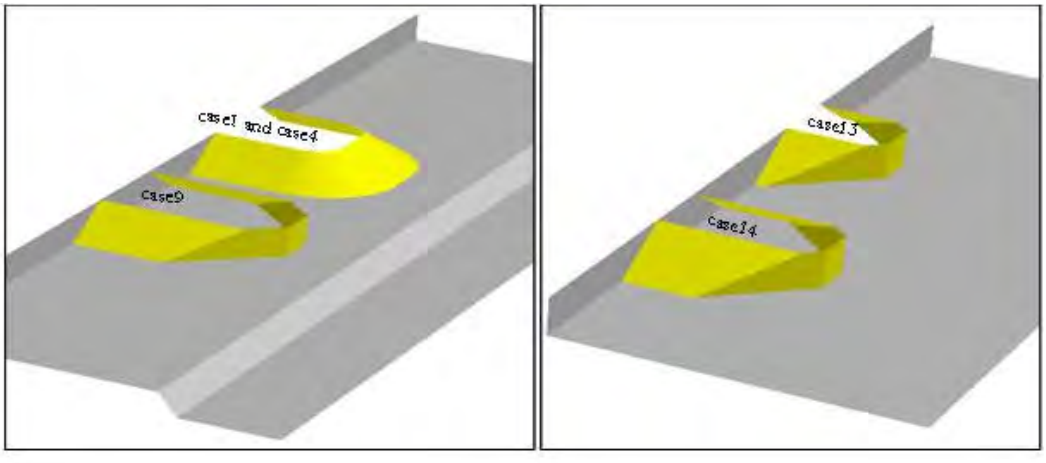

Figure 6.3 - Geometries of the flume test cases for CHEN3D scour prediction.

Numerical simulations were performed first for fixed streambed without scour development until the vortex shedding pattern is fully established. Various scour rate models were then used to calculate the erosion rate on the streambed and determine the new bed elevation after scour takes place. Since the scour rate is very small for porcelain clay, it is desirable to use a much large time increment of 150 sec to reduce the required CPU time for the simulation of scour hole development. Note that the change of streambed elevation and scour pattern are very small over one time step. In the present simulations, the numerical grids were adjusted each time step to conform with the new streambed elevation. As the scour hole deepens, the flow velocity decreases gradually due to increased channel cross-section area. This leads to a decrease of flow acceleration around the abutment and a reduction of shear stresses on the streambed. The final scour depth is reached when the bed shear stress is equal to the critical shear stress of the soil.

6.3.1 Scour Prediction on Compound Channel

6.3.1.1 Observations from the Flume Tests

Figure 6.4 shows the scour patterns for the three compound channel cases considered in the present numerical simulations. The observations from the flume tests are summarized in the following:

1. Deep scour hole can be observed at the abutment toe for all three cases. In Case 9 and Case 1, the scour hole in front of the abutment face extends from the toe all the way to the main channel and the flood plains together with the main channel slope in front of the abutment face are totally removed. In Case 4, however, the scour hole around the abutment toe is confined to the flood plain. The main channel slope and part of the flood plain remain standing after two weeks of continuous scour.
2. On the downstream side, the original main channel slope was completely washed away for Case 1 and Case 9 after the experiments. Moreover, the flood plain in Case 1 was eroded to the same level as the main channel or even lower. On the other hand, most of the main channel slope for Case 4 remained intact with only minor erosions on the slope. The scour hole started from the upstream corner of the abutment and extended toward downstream main channel slope, which shows the skewed flow streamlines forced by the abutment. However, this trend is not observed in Case 1 and Case 9 when the approach velocity is higher.
3. The surface of the channel bottom after scour is not as smooth as the initial conditions. The surface remains flat in the region without obvious erosion, such as the upstream section far from the abutment and the flood plain far downstream of the abutment. On the other hand, the streambed surface is highly uneven in regions with serious erosion.
4. The scour depth in the main channel is much smaller than that observed on the main channel slope and flood plain. The scour hole on the main channel slope can be as deep as the hole at the abutment toe.

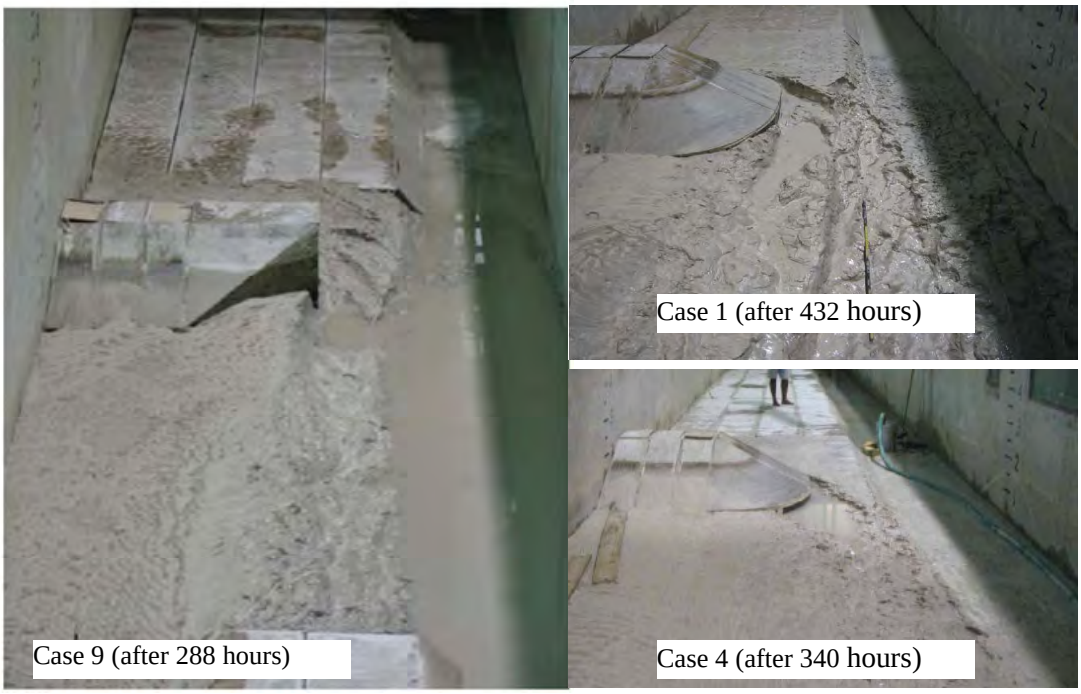

Figure 6.4- Scour patterns for flume test cases on compound channel (After Oh, 2009).

6.3.1.2 Simulation Result and Analysis of Case 9

Figure 6.5 shows a comparison of the measured and simulated scour patterns for Case 9 after 240 hours of scour process to facilitate a detailed assessment on the performance of three different scour rate models. It is seen that Model I (β = 1, b = 0) produced a fairly narrow eroded area and small scour depth. The deepest scour hole predicted by Model I is on the main channel slope with a depth of 0.12m, which is about half of the measured deepest scour depth. Furthermore, the location of the deepest scour hole was also incorrectly predicted. This indicates that the calculated bed shear stress is less than the actual bed shear stress applied by the flow. As noted earlier, the observed difference is most likely caused by the effect of bed form roughness. The effect of turbulence is typically confined to specific regions around the abutment where strong vortex shedding is observed. The scour depth in the main channel should not be strongly affected by the turbulence since the flow is fairly steady away from the abutment.
Model II (β = 1.5, b = 0) shows similar eroded area as that observed in the measurement. The predicted scour depth is also in good agreement with the measurement in most regions, especially for the contraction scour in main channel. This underscores the need to include the effect of bed form roughness in the scour model. However, it is also clear that the deepest scour depth, which is of primary concern in the bridge design, cannot be matched by scaling up the calculated bed shear stress uniformly with a constant correction factor β.

The simulation results for Model III (β = 1.5, b = 0.01) show deep scour holes in front of abutment face and on main channel slope similar to those observed in the experiment. Furthermore, the magnitude of the maximum abutment scour depth (abutment scour depth plus contraction scour depth) is very close to the corresponding measurement. However, the correction term

for turbulent kinetic energy also increased the scour depth in main channel. Further refinement in the scour rate model is still needed in order to more accurately predict the scour pattern for both the abutment and the main channel.

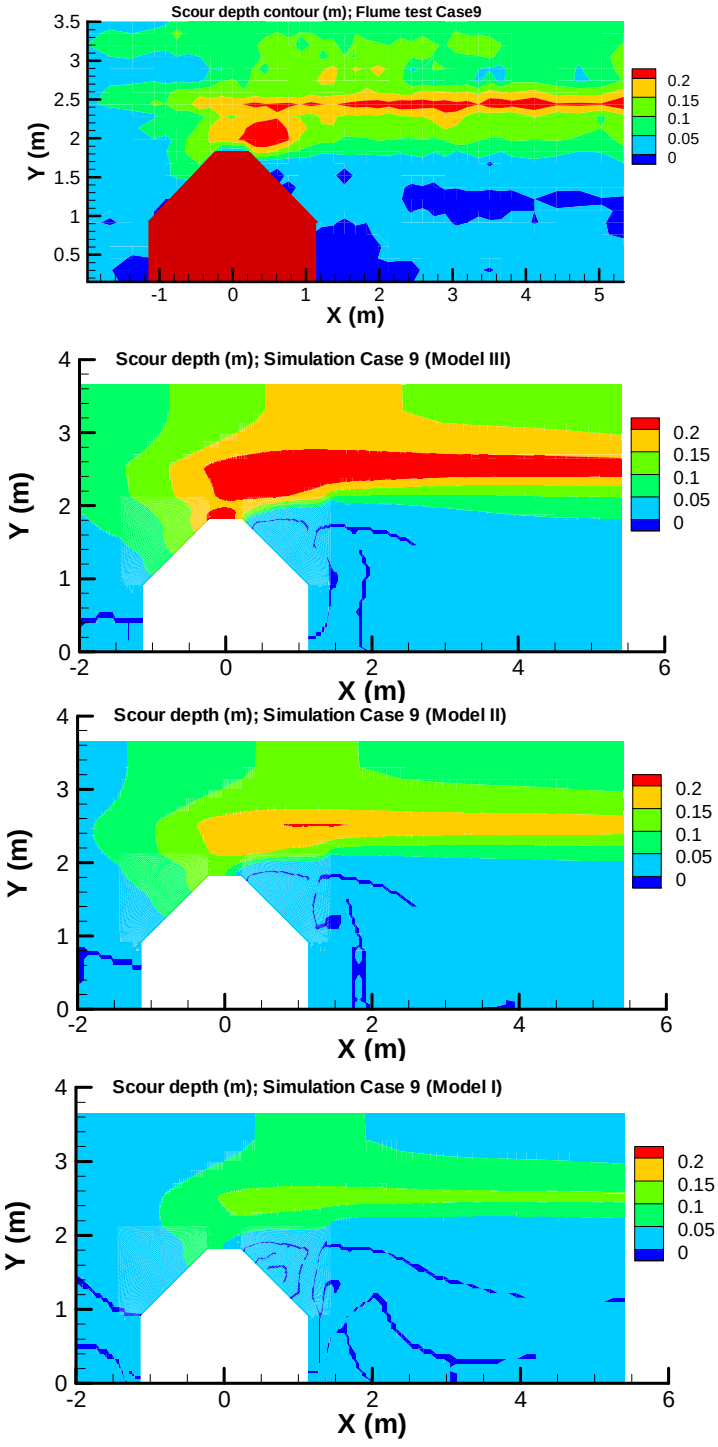

Figure 6.5- Comparison of measured and predicted scour depths after 10 days (Case 9).

Figure 6.6 shows a comparison of the predicted and measured scour profiles at three different cross sections located at upstream side, in the middle, and at downstream side of the abutment. The deepest scour may occur at other locations. However, the scour pattern around the abutment is of particular concern in the bridge design and scour monitoring.

On the upstream side of the abutment, the flow is accelerated around the abutment as the water is forced through the narrow opening between the abutment and the main channel centerline. The measured scour depth is very small in front of the abutment ($0 < y < 1.3$ m) since the flow is deflected by the abutment towards the channel centerline. The erosion begins at $y = 1.37$ m and the averaged scour depth is about 50 mm in the opening section between $y = 1.83$m and 3.66m. Model I underestimated the scour depth over the entire cross section. The predicted scour depth for Model II is in good agreement with the measurement. Model III predicted a similar profile as Model II and the measurement, but the scour depth is overestimated in most area.

In the middle of the abutment, the measured scour depth is about 200 mm at the abutment toe and about 80 mm in the main channel. It should be noted that the scour is deep on the main channel slope from transverse stations $y = 2.44$ m to $y = 2.64$ m, which is consistent with the bed shear stress distributions. Model I again underestimates the scour depth, while Model II yields good prediction in most regions except at abutment toe. For model III, the turbulent kinetic energy term significantly increased the scour depth at the abutment toe similar to that observed in the experiment. However, it is also obvious that the sour depth on the flood plain and main channel were significantly overpredicted.

At downstream side of the abutment, the measured scour depth behind the abutment from $y = 0$ m to 1.83 m is negligible. The deepest scour hole appears on the main channel slope with a scour depth of 200 mm. The contracted scour depth in the main channel is about 100 mm. All three scour rate models predicted the correct trend, but Model II gives the best overall agreement at this cross section.

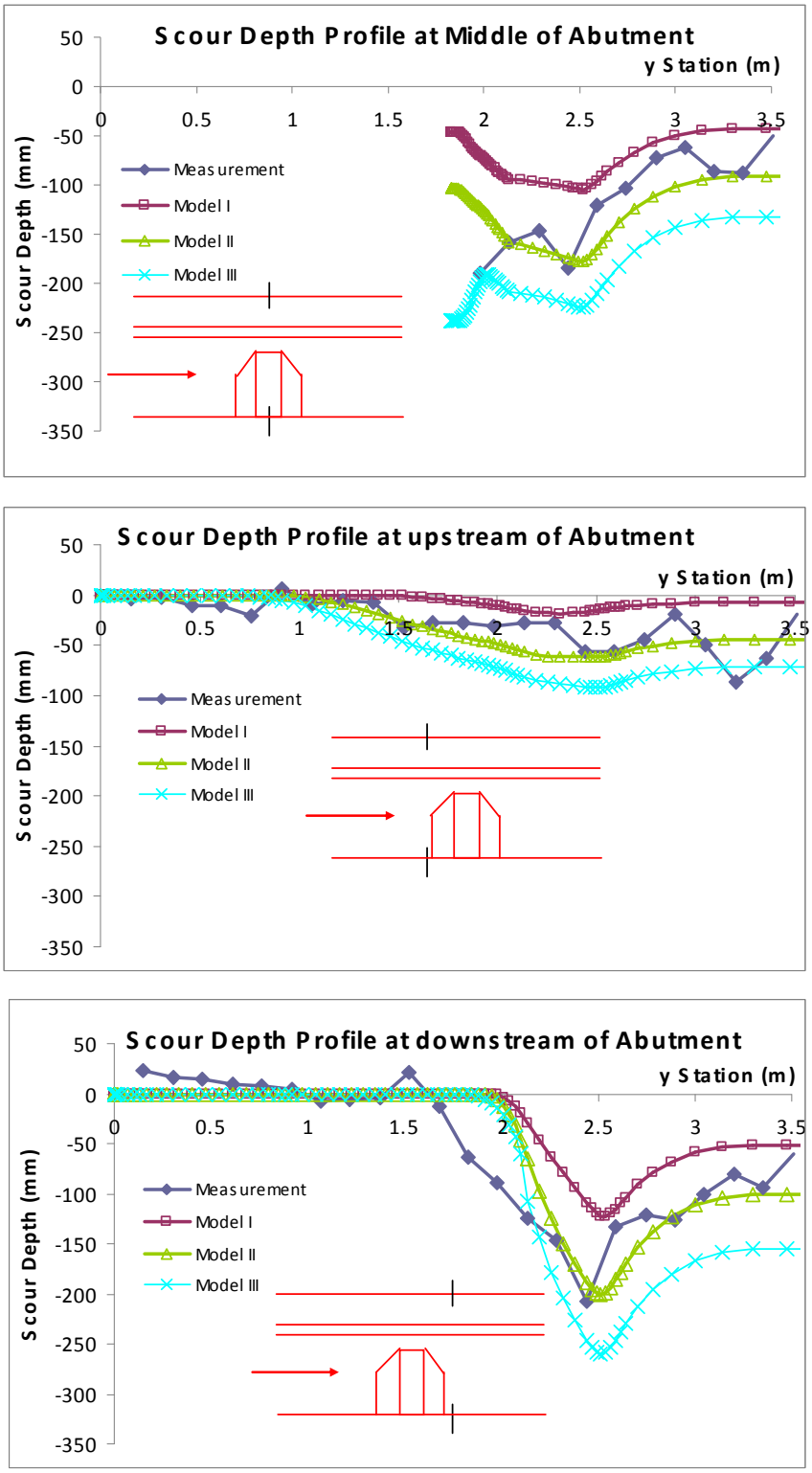

Figure 6.6 - Scour profiles for Case 9 after 10 days at different cross sections.

The maximum scour depth $y_{s(Abut)}$ over the lifespan of a bridge is one of the most critical parameters in the design and analysis of bridges. Note that all abutment scour equations in HEC-18 were aimed at predicting the maximum scour depth $y_{s(Abut)}$ without providing detailed scour patterns around the bridge abutment. In the present numerical simulations, it is also crucial to verify the predicted $y_{s(Abut)}$ with the experimental data in order to provide practical simulation results for abutment scour estimation. Figure 6.7 shows a comparison of the measured and predicted time histories of $y_{s(Abut)}$ for Case 9 obtained from three different scour rate models. It should be noted that the $y_{s(Abut)}$ in Figure 6.7 represents the deepest scour depth over the entire streambed at each time instant. The maximum scour depth increases with time as the scour hole develops around the abutments and eventually reaches an asymptotic value when the bed shear stress falls below the critical shear stress. It should also be noted that the location of $y_{s(Abut)}$ may vary over time since the maximum shear stress typically migrates to shallower areas as the scour hole deepens. The flume test result for Case 9 shows that the deepest scour hole is always in front of the abutment face, even though the scour on the main channel slope is also very deep. It is seen that Model III, which includes the correction factors for both bed form roughness and turbulence, provides the closest prediction of $y_{s(Abut)}$ for Case 9.

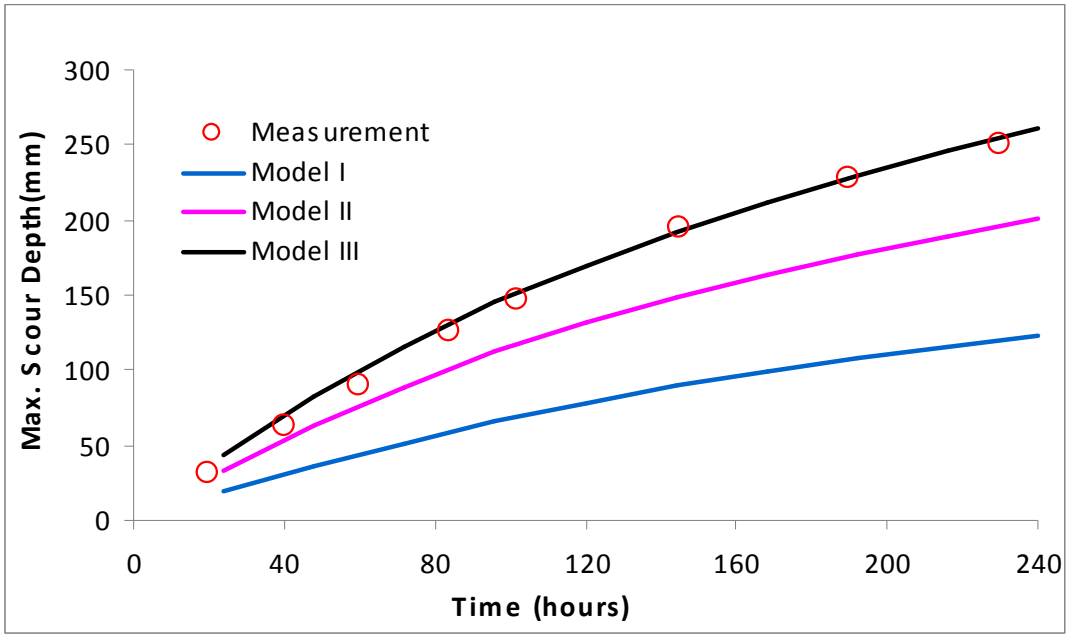

Figure 6.7- Time histories of maximum scour depths for Case 9.

6.3.1.3 Simulation Result and Analysis of Case 1

Figure 6.8 shows the scour profiles for Case 1 at the same three cross sections as Case 9. As noted earlier, the abutment length, water depth, compound channel geometry, and approach flow velocity are the same for Cases 1 and 9. The only difference between these two cases is the abutment shape. In general, the simulation results show that the scour depth around the spill-through abutment (Case 1) is somewhat smaller than that for the wing-wall abutment (Case 9). As expected, Model I underestimates the scour depth at all three cross sections. Model II provides reasonable prediction of scour profiles at the upstream section. At the middle section of the abutment, Model II also accurately predicted the deep scour hole observed at the abutment toe.

However, the deepest scour hole observed on the main channel slope was not captured by Model II. At the downstream side, Model II yields similar trend as the measurement, but the predicted scour depth is considerably lower than the corresponding measurement. On the other hand, Model III produced significantly deeper scour holes than Models I and II on all three cross sections but the predicted scour profiles do not match well with the measured scour pattern.

Comparing to the scour pattern for wing-wall abutment shown earlier in Case 9, the predicted scour depth for spill-through abutment (Case 1) is somewhat smaller. This is consistent with the widely accepted conclusion that wing-wall abutments produce deeper scour depth than spill-through abutments for the same abutment length. However, the present flume test result indicates that the maximum scour depth is larger for spill-thorough abutment even though it has a smaller blockage ratio. A detailed examination of the flume test results shows that the scour hole on the main channel slope is as deep as 330 mm while the deepest hole at abutment toe is only about 130mm. The deep hole observed in Case 1 may be caused by the variability of soil properties and the experimental setup. The porcelain clay used in the flume test Cases 1 and 9 may not come from the same batch, so the erosion properties may not be consistent with those shown earlier in the soil properties section. The soil compaction during the experimental setup may also cause problems. There is a possibility that the downstream main channel slope is not compacted as well as the other regions. The conditions will be quite different if there is void space between the clay blocks.

Figure 6.9 shows the measured plan view of the scour pattern and a comparison with the predicted scour pattern obtained from Model III. The flume test shows a large area of very deep scour hole on the main channel slope downstream of the abutment. This is highly usual and may be attributed to soil variability mentioned earlier. At the abutment toe, there is also a fairly deep scour hole but the scour depth is much shallower than that on the main channel slope. The numerical simulation results obtained using Model III shows the presence of two deep scour holes. The first hole is around the abutment toe on the flood plain while the second one is located on the main channel slope. It should be noted that massive erosions were observed on the main channel slope of compound channel for both Case 1 (spill-through abutment) and Case 9 (wing-wall abutment) because the abutments are close to the main channel with relatively short setback. This is consistent with the high shear stresses on the main channel slope as seen in the numerical predictions. Along the center of the main channel, the predicted scour depths at upstream and in the middle of the channel are larger than the corresponding measurements, but the agreement improves considerably in the far downstream area.

Figure 6.10 shows a comparison of the measured and predicted time histories of the maximum scour depth located on the main channel slope near the abutments. It is quite obvious that all three scour rate models significantly underestimated the maximum scour depth. As noted earlier, the numerical simulations predicted similar scour depth on the abutment toe and the main channel slope while the measurement show a much deeper scour hole on the main channel slope.

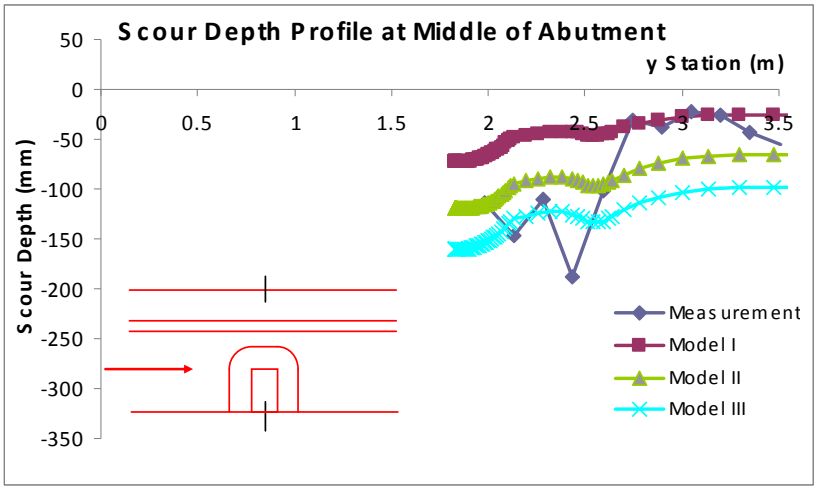

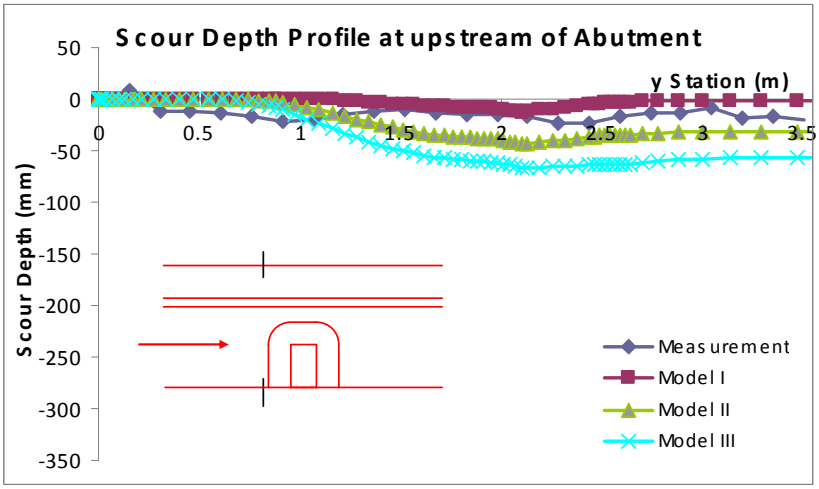

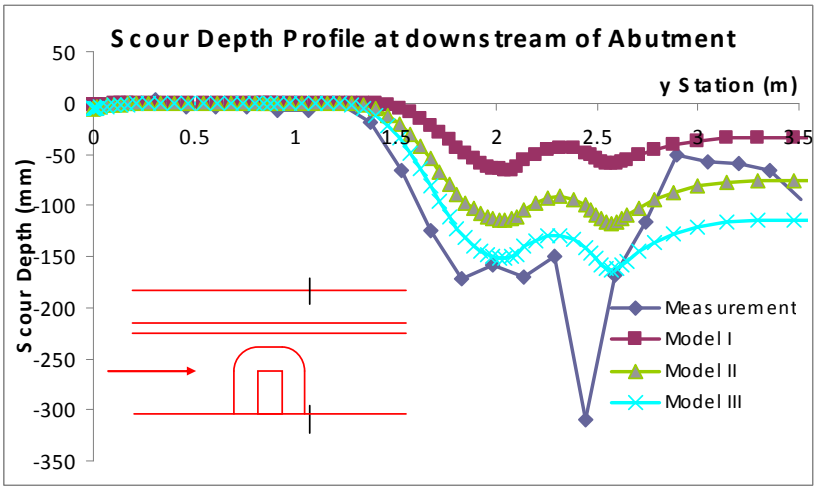

Figure 6.8- Scour profiles for Case 1 after 10 days at different cross sections.

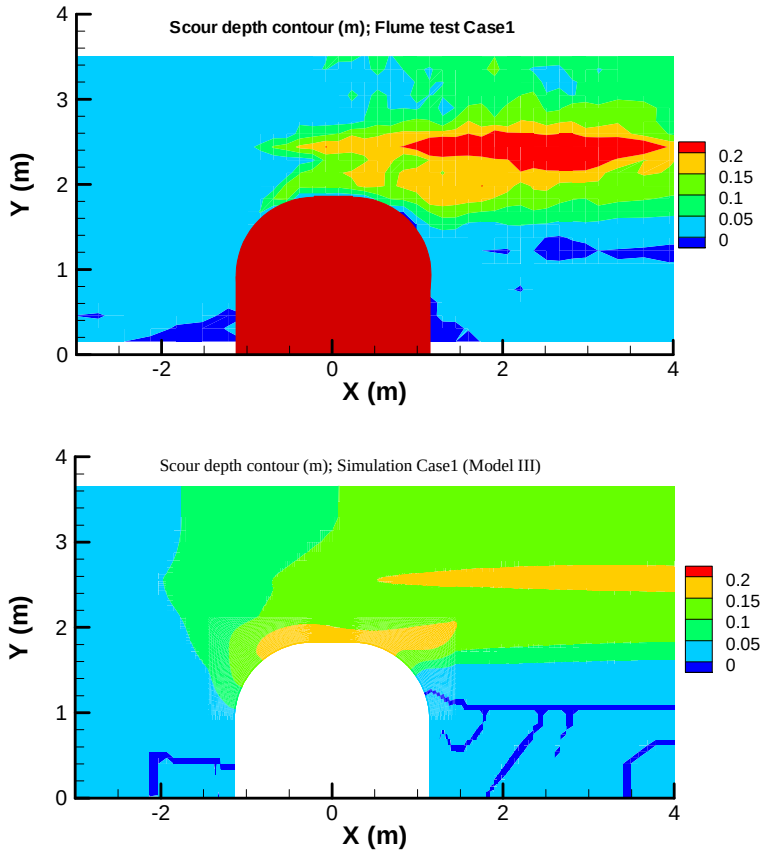

Figure 6.9 - Comparison of measured and predicted scour depths for Case 1 after 10 days.

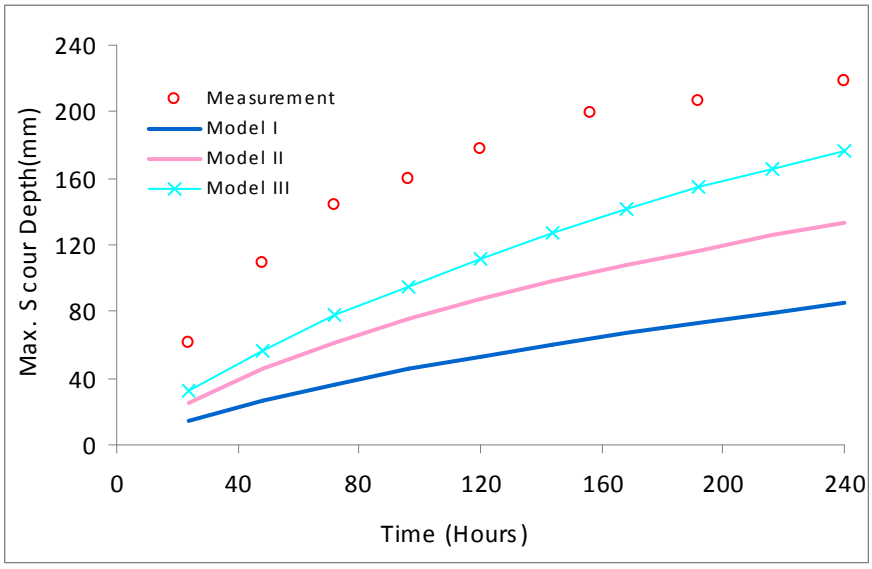

Figure 6.10 - Time histories of maximum scour depths for Case 1.

6.3.1.4 Simulation Result and Analysis of Case 4

Figure 6.11 shows the measured and predicted scour profiles for Case 4 which has a lower approach flow velocity than Cases 1 and 9 considered earlier. As expected, the scour depth for Case 4 is considerably smaller than that observed in Case 1 for the same spill-through abutment and compound channel configuration since the streambed shear stress is smaller when the approach velocity is reduced. At the upstream section, all three scour rate models underestimate the scour depth on the flood plain. This is contrary to the finding in Case 9 and Case 1. In the middle of the abutment, all three scour rate models predicted deep scour hole at the abutment toe. The measured scour depth at the middle of the abutment is similar to that observed at the upstream section, but the numerical simulations predicted much deeper scour depth in the middle of the abutment. At the downstream section, Models II gives reasonable prediction of the scour profiles across the channel but the maximum scour depth at the abutment toe is underpredicted. On the other hand, Model III overestimated the scour depth in the main channel but the predicted scour hole depth at the abutment toe matches very well with the corresponding flume test data.

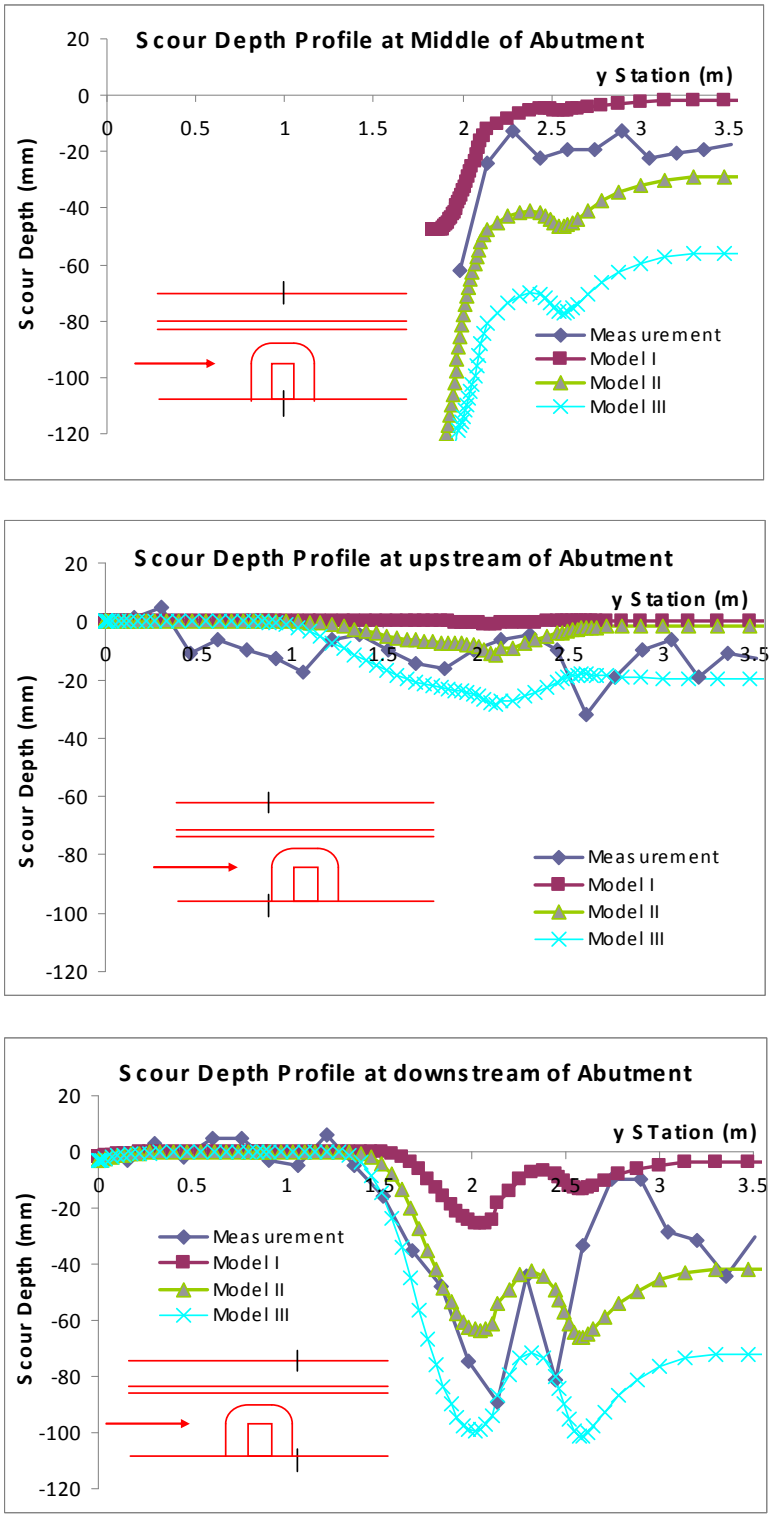

Figure 6.11 - Scour profiles for Case 4 after 9 days at different cross sections.

Figure 6.12 shows a comparison of the plan views of the measured and simulated scour patterns. The scour rate Model III predicted a deep scour hole at the abutment toe and another one on the main channel slope downstream of the abutment. Similar scour patterns were also observed in the flume test at the same locations. It is seen that the numerical simulation predicted a much wider eroded area than the corresponding measurements. However, the maximum scour depth predicted by Model III is in very good agreement with the measured time histories of $y_{s(Abut)}$ shown in Figure 6.13.

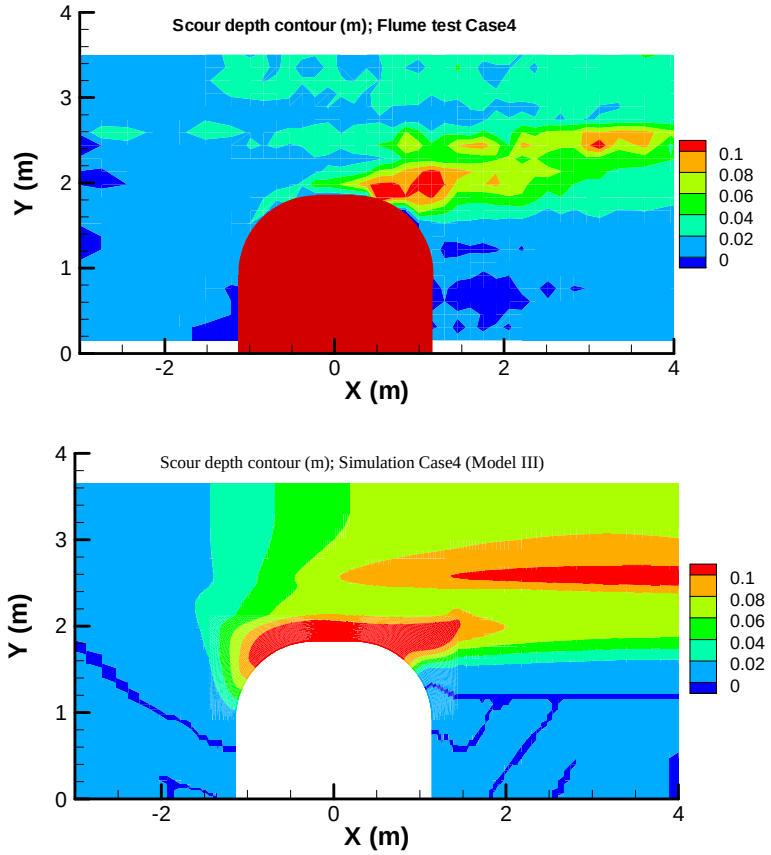

Figure 6.12 - Comparison of measured and predicted scour depths for Case 4 after 9 days.

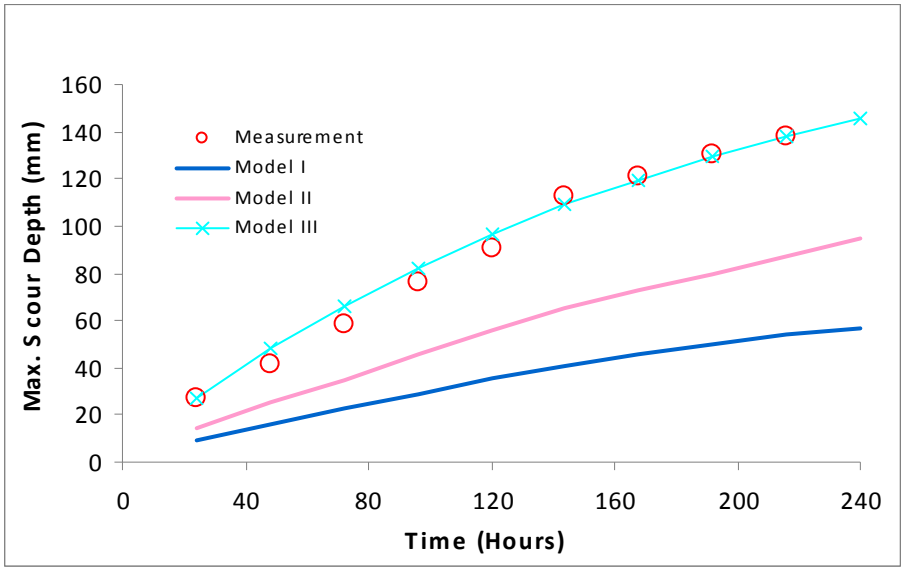

Figure 6.13 - Time histories of maximum scour depths for Case 4.

6.3.2 Scour Prediction on Rectangular Channel

Figure 6.14 - Scour patterns for the flume test cases on rectangular channel (After Oh, 2009).

6.3.2.1 Observations from the Flume Tests

Figure 6.14 shows the scour patterns of the two rectangular channel cases. The observations from the flume tests are summarized in the following:

1. For Case 14, deep scour hole can be observed at the abutment toe. The scour hole extends from the upstream corner of the abutment toward downstream over a long distance. The

scour depth along the channel center is smaller than that observed around the abutment. The streambed surface is uneven after scouring as shown in the picture.

2. For Case 13, the scour hole is shallower at the toe of the abutment than at the downstream section. This is rather unusual since the deepest scour hole in a rectangular channel typically occurs at the abutment toe as a result of local flow acceleration around the abutment. The deep scour hole away from the abutment may be caused by the variability of porcelain clay used in the flume test such as insufficient comparison or non-homogeneous soil properties. The unsteady vortex shedding around abutment may also produce higher turbulence intensity and deeper scour hole downstream of the abutment. Contrary to the other cases, the streambed surface of Case 13 is still very smooth after the completion of the flume test.

6.3.2.2 Simulation Result and Analysis of Case 14

Figure 6.15 shows the scour depth profiles for Case 14. At the upstream section, the scour is very uniform with a nearly constant depth of about 20 mm in the open area. In the middle of the abutment, the scour depth at the channel center is about 50 mm. The scour hole is as deep as 190 mm around the toe of the abutment. At the downstream section, the scour depth at channel center is about 64 mm and the deep hole extends downstream in line with the abutment toe. The blockage effect of abutment on the contraction scour is clearly observed according to the scour depth variation along the channel center. The deepest contraction scour depth typically occurs at the downstream section instead of in the middle of the abutment due to the convergence of streamlines downstream of the abutment. The contracted scour depth predicted by Model I agrees quite well with the experiment. However, the scour profiles around the abutment toe and in the wake region are significantly underestimated by the simple shear stress model. Models II and III improve the prediction of maximum scour depth around the abutment toe, but the contraction scour depth in the middle of the rectangular channel is drastically overestimated. It is quite clear that the correction factors for bed form roughness and turbulence effects need to be refined in order to provide accurate prediction of the scour pattern in different regions.

Figure 6.16 shows a comparison of the measured scour depth contours with the predicted contour pattern obtained by Model III. It is seen that the predicted scour depth at the abutment toe is close to that observed in the flume test. However, the location of the deepest scour hole predicted by Model III is somewhat different from that observed in the flume test. Also, the numerical simulation result shows the presence of a considerably wider and deeper scour hole than that observed in the experiment.

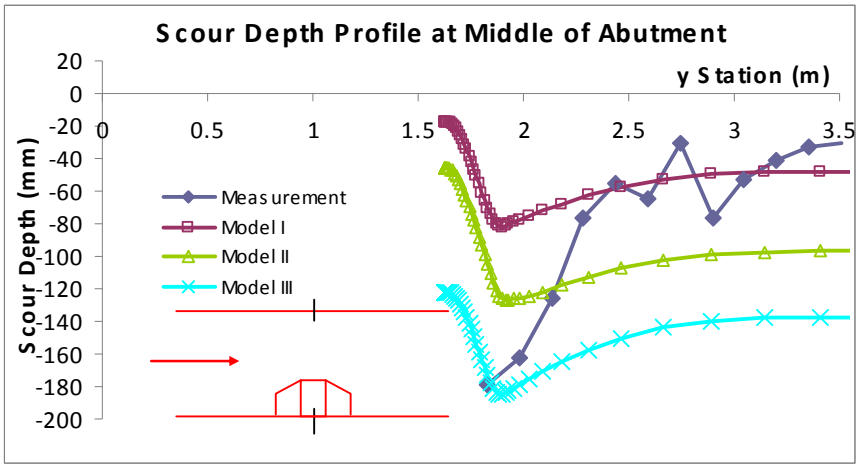

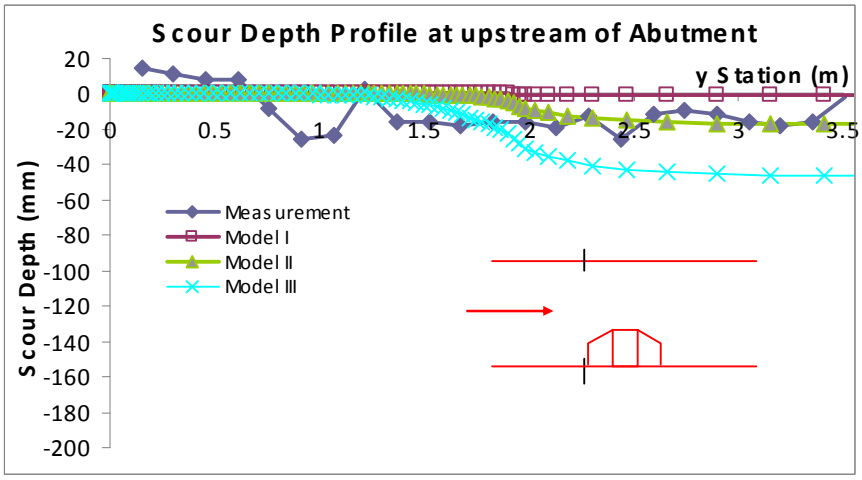

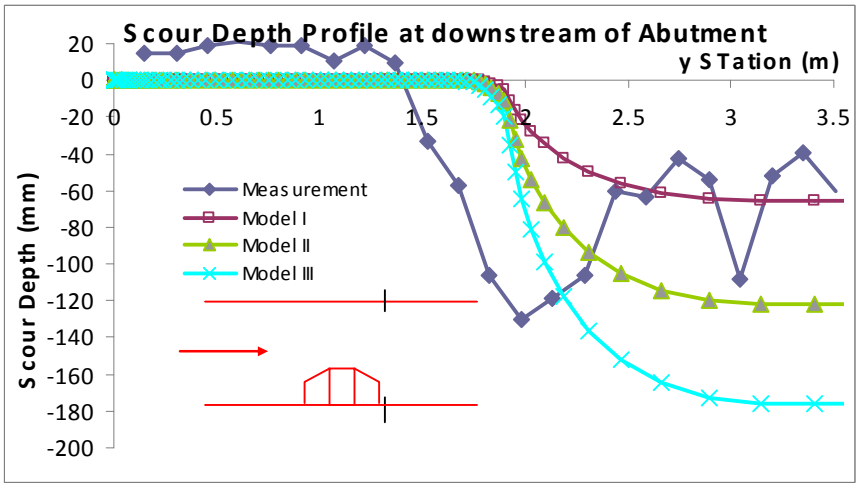

Figure 6.15- Scour profiles for Case 14 after 10 days at different cross sections.

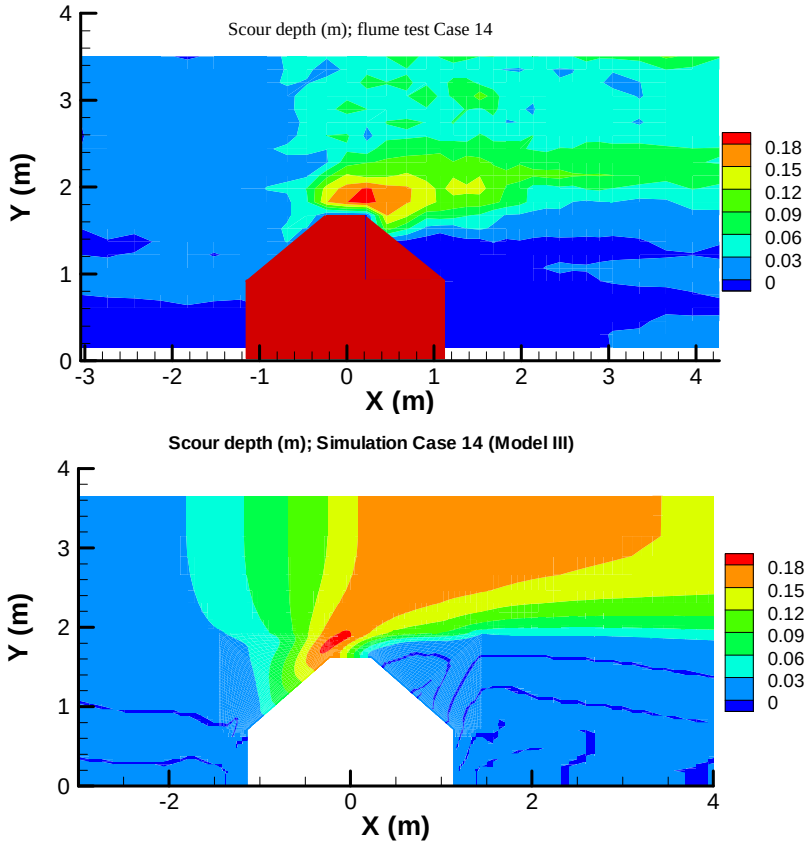

Figure 6.16 - Comparison of measured and predicted scour depths for Case 14 after 10 days.

Figure 6.17 shows a comparison of the measured and predicted time histories of the maximum abutment scour depth (abutment scour depth plus contraction scour depth) for Case 14. Similar to those reported earlier for the compound channel cases, Model III again provides the best prediction for the maximum scour depth by including the combined effects of bed form roughness and turbulence. However, it is also clear that the further improvements are still need in the present scour rate models in order to resolve the correct scour pattern over the entire streambed.

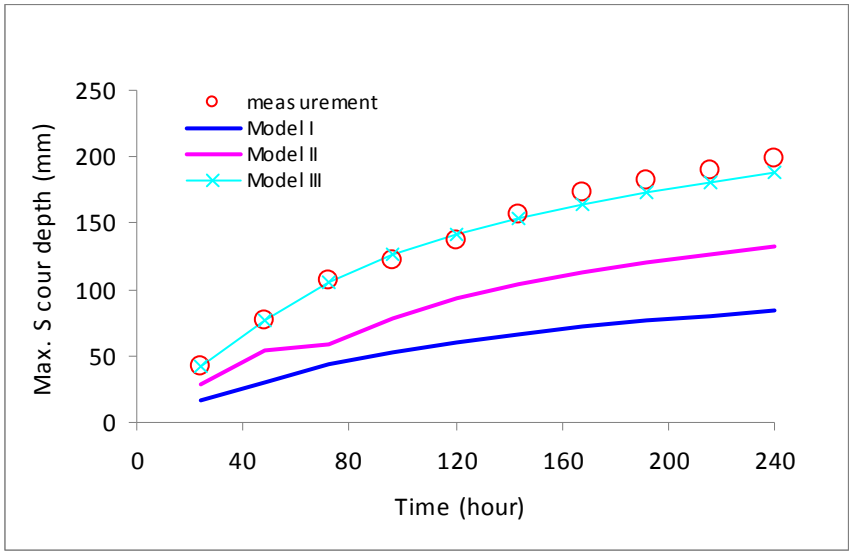

Figure 6.17 - Time histories of maximum scour depths for Case 14.

6.3.2.3 Simulation Result and Analysis of Case 13

Case 13 is a low contraction, low blockage, and low flow rate case with an approach velocity of 0.34 m/s. According to the EFA test results, the critical velocity of the porcelain clay used in the flume test is about 0.61 m/s. In the EFA test, the critical velocity is defined as the velocity which generates an erosion rate of 0.1 mm/hour. It is worthwhile to note that the deepest scour depth after 10 days of flume test is about 40 mm at the abutment toe which turns out to be only marginally higher than the erosion produced by the critical velocity. This suggests that the maximum bed shear stress around the abutment is only slightly higher than the critical shear stress. As shown in Figure 6.18, the scour depth profiles obtained by Model I are fairly close to the flume test data, while Model II produced a considerably larger scour hole than the corresponding measurement. This is to be expected since the river bed surface for Case 13 is still smooth after the flume test as shown in Figure 6.14. This implies that the correction factor β which accounts for the bed form roughness is not needed for Case 13. No attempt has been made to use Model III since the inclusion of turbulence will further increase the maximum scour depth in comparison with Model II.

Figure 6.19 shows a comparison of the measured scour depth contours with the Model I simulation results for Case 13. In general, the predicted maximum scour depth is in close agreement with the corresponding measurement as shown in Figure 6.20. This test case clearly illustrated the feasibility of using the simple shear stress model (i.e., Model I) in conjunction with the EFA test for the prediction of sour pattern when the influences of bed form roughness and turbulence are negligible. The correction factors β and b are needed only for higher contraction cases where the bed surface tends to be more irregular and the flow tends to be more turbulent.

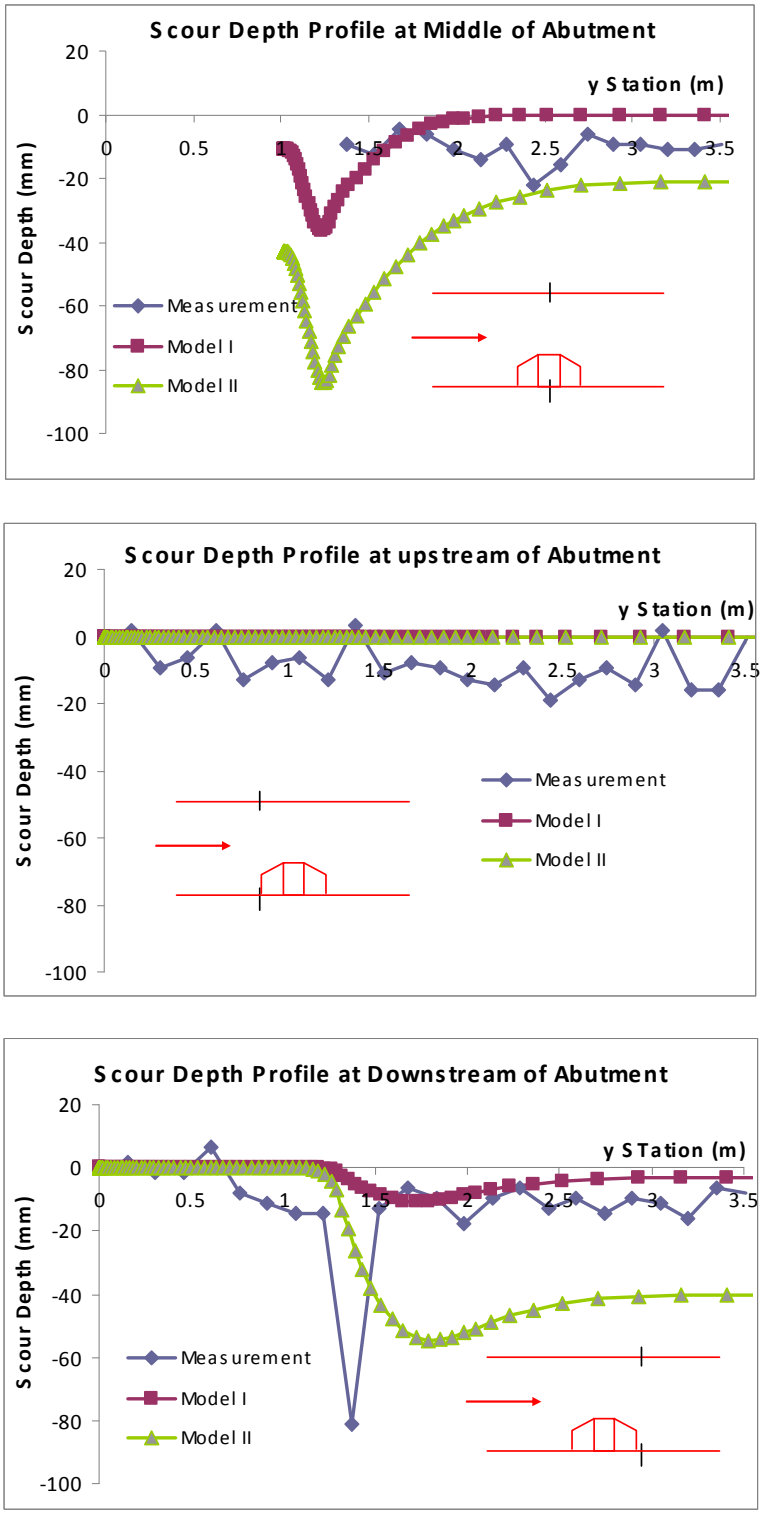

Figure 6.18- Scour profiles for Case 13 after 10 days at different cross sections.

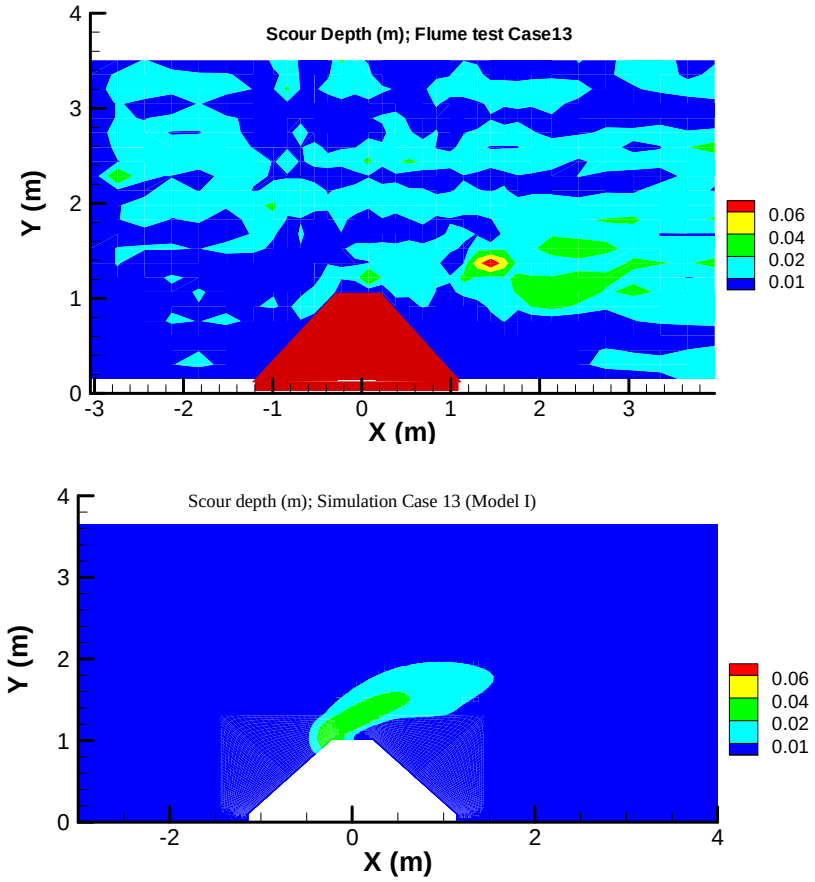

Figure 6.19 - Comparison of measured and predicted scour depths patterns for Case 13.

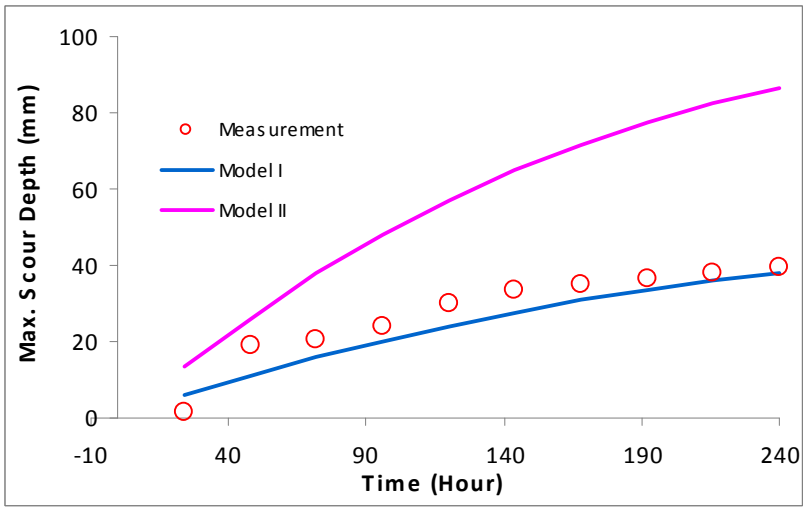

Figure 6.20 - Time histories of maximum scour depths for Case 13.

6.4 SCOUR PREDICTION WITH OVERTOPPING

Abutment scours under pressure flow and overtopping flow conditions are studied numerically in this section. The objective of this investigation is to establish a general understanding on the scour development when the flow is pressurized under the bridge deck. For simplicity, a model-scale vertical wall abutment is chosen for the overtopping flow study. The bridge deck is assumed to be 0.12 m thick and the clearance between the streambed and the low chord of the deck is 0.37m. The abutment is 1.01m long and the half width of the channel is 3.66m. The abutment is normal to the flow direction. An approach velocity of 0.33 m/s is chosen for the present simulations. For the same designed bridge and above mentioned parameters, seven test cases have been conducted with the upstream water depth varying from 0.37m to 0.85m. Figure 6.21 shows the cross sections and the velocity magnitude contours of four representative cases. Case (a) has open channel flow and water surface is almost touching the low chord; Case (b) is the case with water surface just touching the low chord; Case (c) has the water surface in flushed with the top surface of the deck, and Case (d) has water surface elevation 0.12m over the bridge deck surface. The other three cases are similar to Cases (c) and (d) with different upstream water depths of 0.43m, 0.73m, and 0.85m.

For simplicity, the rigid lid boundary condition is applied on the water surface. The simple shear stress model (i.e., model I) is employed for the prediction of scour pattern and the same erosion function given in Figure 6.1 is used to determine the erosion rate as a function of bed shear stress.

$$\dot{z} = c(\tau_{num} - \tau_c) \tag{6.3}$$

where $\dot{z}$ is the erosion rate (mm/hour), τ_{num} is the calculated bed shear stress (Pa); $\tau_c = 0.55Pa$ is the critical shear stress of the soils (Pa), and c = 0.75mm/(Pa*hour) is the slope of erosion rate versus shear stress curve. The numerical simulation procedures are also identical to those described earlier.

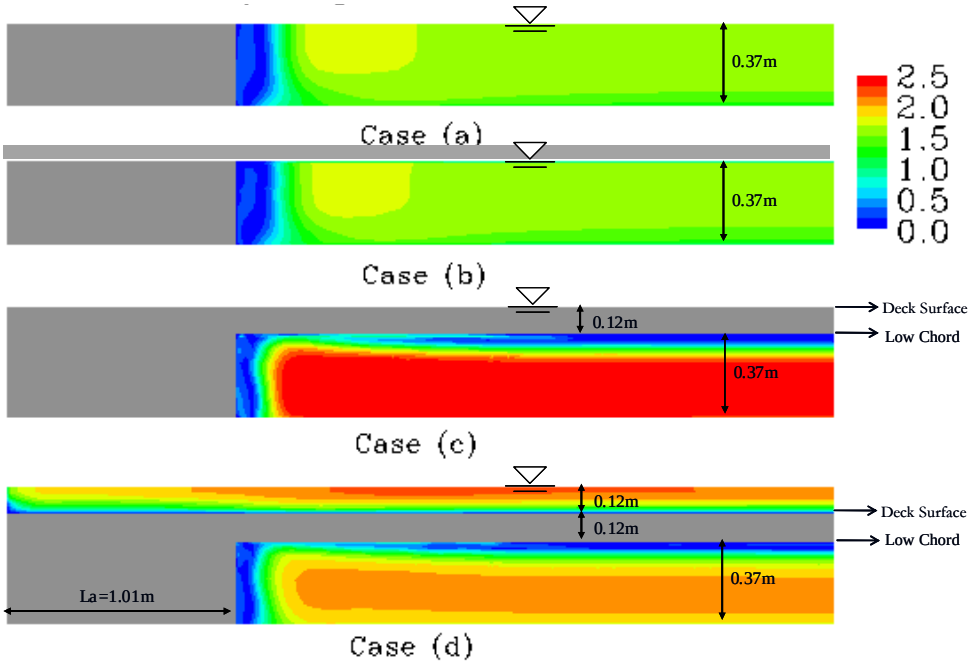

Figure 6.21 - Cross sections and the velocity magnitude contours.

Figure 6.22 shows the calculated scour depth contours after 10 days for the four representative cases shown in Figure 6.21. A constant time increment of 2.5 minutes was used in all simulations. The geometry, water depth, and flow conditions for Cases (a) and (b) are identical. The only difference between these two cases is the water surface boundary conditions. In Case (a), a symmetry boundary condition was used for the entire water surface since the free surface is slightly below the bridge deck. On the other hand, a no-slip boundary condition was used on the bottom surface of the bridge deck to resolve the boundary layer and shear force acting on the bridge deck. As expected, the change of boundary condition on the low chord of the bridge deck affects only the local boundary layer flow beneath the bridge deck and has little influence on the scour development. This is consistent with the finding in the bed shear stress study presented earlier in Chapter V. The scour depths of Case (a) and (b) are very shallow and the deepest scour holes are located around the upstream corner of the abutment. There is no scour at the center under the bridge, but the contraction scour can be clearly observed downstream of the bridge due to local flow acceleration in the middle section of the rectangular channel.

When the water level rises above the low chord of the bridge deck but below the deck top, the entire flow is forced to go through the narrow opening under the bridge deck and creates an undersirabe pressure flow situation. This leads to a sharp increase of streambed shear stress and scour depth as the flow is accelerated through the narrow opening bounded by the abutment, bridge deck, and the streambed. Case (c) is the pressure flow case with the highest blockage when the water level reaches the deck top but without flow overtopping. Under this condition, the river bed under the bridge deck is eroded seriously as shown in Figure 6.22(c). It should be noted that Case (c) is an extreme case since the bridge deck thickness (d_{deck} = 0.12 m) is very large in comparison with the clearance (h=0.37 m) between the streambed and the low chord of the bridge deck. Due to the large blockage ratio, the influence of the bridge deck is felt over the

entire channel cross section, not just around the abutment. This resulted in a nearly uniform scour depth under the bridge. The deepest scour hole in Case (c) is somewhat farther away from the abutment toe in comparison with those shown in Cases (a) and (b) since the bridge deck blockage effect is stronger than that caused by the abutment blockage.

When the water level rises above the bridge deck, some of the water will flow over the bridge deck as shown in Case (d). Under this overtopping flow condition, the water flow upstream of the bridge deck is allowed to move both above and beneath the bridge deck. This provides significant relief of the pressure flow under the bridge deck in comparison with Case (c) since a large portion of the water above the bridge low chord will flow over the bridge top where the resistance is much smaller than that in the narrow opening under the deck. It is seen from Figure 6.22 that the scour depth for Case (d) is shallower than Case (c) but still deeper than Cases (a) and (b). Similar to Case (c), the deepest scour hole in Case (d) is away from the abutment toe and the contraction scour under the bridge deck is also fairly uniform across the channel. As the water level further increased to 0.73 m and 0.85 m, the scour depth was continues to reduce since most of the water upstream of the bridge are allowed to flow over the bridge deck.

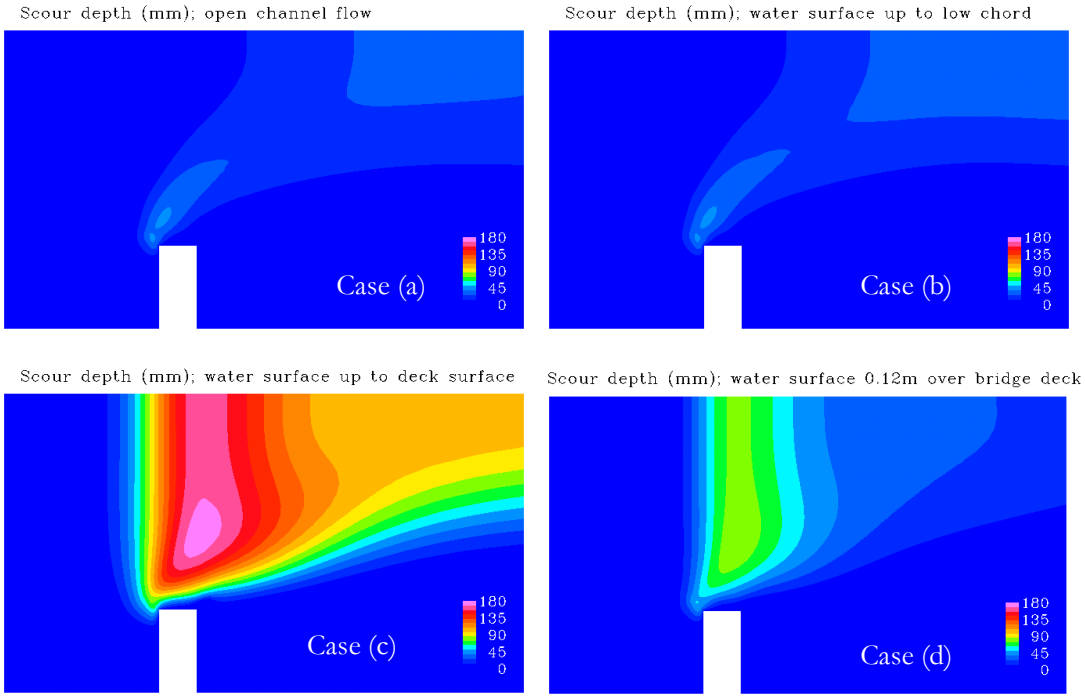

Figure 6.22 - Scour depth contours for overtopping cases.

Figure 6.23 shows the scour histories for six test cases with different water depths. These six cases can be divided into two groups, namely, pressure flow and overtopping flow. The flow is called pressure flow when the water surface is between the low chord and top surface of the bridge deck. As noted earlier, the flow is only slightly pressurized when the water surface just touches low chord with d_1 = 0 m. When the water surface is higher than the bridge deck surface (i.e., d_1 > 0.12 m), the flow is called overtopping flow. It should be noted that the flow under the bridge deck is still pressurized after overtopping occurs. For the three pressure flow cases, water

surface elevation varies from low chord, mid-chord, to the high chord with d_1 = 0 m, 0.06 m and 0.12 m, respectively. The channel contraction increases with the increasing water depth. It is seen from Figure 6.23 that the scour depth increases rapidly and reaches a maximum value which is about 4.5 times of that for the non-pressurized flow condition.

For the three overtopping cases, the channel contraction decreases with increasing water depth. This explains why the scour depth decreases with the increase of water depth under overtopping condition. In addition, a larger portion of the upstream flow tends to flow over the bridge deck because the flow resistance is much smaller in the open area above the bridge deck. This additional relief of pressure in the narrow opening beneath the bridge deck further reduces the shear stress and abutment and contraction scour on the streambed. It should be noted that the deepest scour depth occurs when the water surface is flushed with the top of the bridge deck. This is the limiting condition for maximum scour depth for a specific bridge. Under overtopping flow conditions, the influence of water depth on scour development diminishes gradually with increasing water depth. This is to be expected since the blockage effect due to the submerged bridge deck is relatively small under the deep water condition.

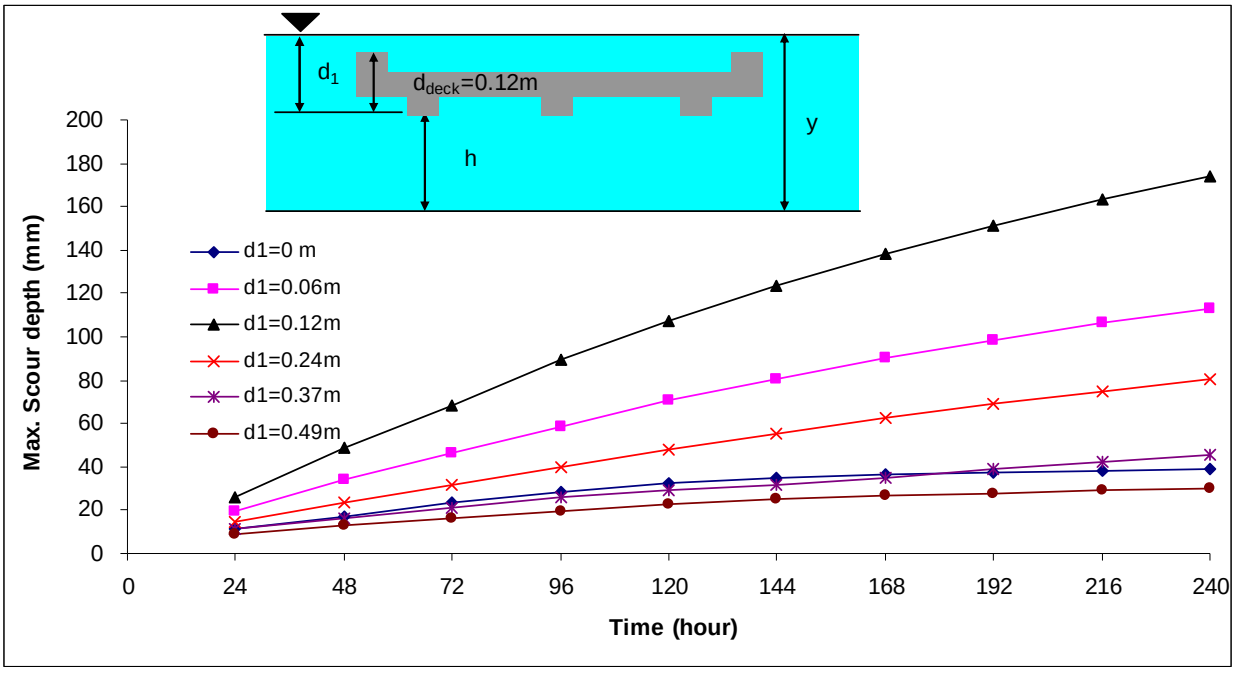

Figure 6.23 - Time histories of the maximum scour depths for overtopping flow.

Based on the present numerical simulation results for the idealized bridge deck shown in Figure 6.23, a correction factor is proposed to account for the effects of overtopping flow in the equation of maximum abutment scour depth (abutment scour depth plus contraction scour depth). The influence of pressure flow and overtopping flow is evaluated based on the condition of open channel flow with water surface elevation flushes with the low chord of the bridge deck. Scour is the interaction between flow and soils. All those parameters affecting shear stress in Chapter 4 and soil erosion property will impact the scour development in overtopping situations. The pri-

mary actions of flow on soils are the fluctuating stresses applied on the soil particles and the shear stress component is believed to be dominant. The maximum bed shear stress is commonly used to represent the erosion capacity of the flow, and the critical shear stress of the soil is used to represent the erosion resistance of the soil. Hence, the correction is proposed based on the difference between the maximum bed shear stress and the critical shear stress of soils. However, the location of the initial maximum bed shear stress may not be the same as that of the final deepest scour hole since the bed shear stress changes with the instantaneous streambed shape as the scour hole develops over time. Furthermore, the maximum shear stress also reduces quickly as the flow slows down around the scour hole. Therefore, it is necessary to correct the initial maximum bed shear stress in order to account for the decrease of shear stress during the scour process. In view of these, the following correction factor is proposed to account for the effect of overtopping flow on the abutment scour depth:

$$K_p = \frac{y_{s(Abut)}}{y_{s(Abut)\_low\,chord}} = \frac{\gamma\tau_{\max\_overtopping} - \tau_c}{\gamma\tau_{\max\_low\,\mathrm{chord}} - \tau_c} \tag{6.4}$$

where $y_{s(Abut)}$ value represents the final scour depth over the lifespan of a bridge.

However, the scour history shown in Figure 6.23 is only for 10 days which is much lower than the final scour depth. To obtain the final $y_{s(Abut)}$, it is necessary to extrapolate the calculated abutment scour depth (abutment scour depth plus contraction scour depth) using the hyperbolic model in the SRICOS method:

$$y_s(t) = \frac{t}{\frac{1}{\dot{z}_{ini}} + \frac{t}{y_{s(Abut)}}} \tag{6.5}$$

where $y_s(t)$ is the scour depth at time instant t, $\dot{z}_{ini}$ is the initial erosion rate, and $y_{s(Abut)}$ is the final maximum abutment scour depth.

The predicted final maximum scour depths for the six cases shown in Figure 6.23 are tabulated in Table 6.3. Based on these results, it is found that $\gamma = 0.342$ provides the best fit for the correction factor K_p. A critical shear stress of τ_c = 0.55 Pa is used in the analysis. It is worthwhile to note from Table 6.3 that a small increase of bed shear stress can result in a large increase in scour depth. For example, $\tau_{\max}$ in Case (c) is 3.49 Pa, which is about two times of the maximum bed shear stress in Case (a). However, the final $y_{s(Abut)}$ turns out to be as high as nine times of the deepest hole in Case (a). The reason that the increase in scour depth (500 mm vs. 55.25 mm) is much bigger than the corresponding changes in $\tau_{\max}$ (3.49 Pa vs. 1.82 Pa) is that the maximum shear stress is of the same order as the critical shear stress (τ_c = 0.55 Pa) of the soil in the model-scale simulations. For prototype simulations, the streambed shear stress $\tau_{\max}$ is much higher than the critical shear stress so the final scour depth should be proportional to the $\tau_{\max}$ ratio which is less than 2.0 according to the model-scale simulation results. Furthermore, the effect of deck blockage is also significantly overestimated in the present simulation since the thickness of the bridge deck (d_{deck} = 0.12 m) is about 32.5% of the clearance h = 0.37 m. This

implies that the proposed correction factor k_p for maximum abutment scour depth (abutment scour depth plus contraction scour depth) tends to be conservative for the estimation of overtopping effects on prototype bridges.

Table 6.3 - Simulation results for overtopping cases.

d_1 (m)	0.00	0.06	0.12	0.24	0.37	0.49
$y_{s(Abut)}$ (mm)	55.25	263.16	500.00	178.57	72.46	42.92
$y_{s(Abut)}$ (mm) @240hr	39.00	113.00	174.00	80.00	45.72	29.87
τ_{max} (Pa)	1.82	2.61	3.49	2.32	1.89	1.74
C_r	0.72	0.62	0.54	0.63	0.69	0.74
C_r/C_{r_Low}	1.00	0.86	0.75	0.88	0.96	1.02
$y_{s(Abut)}/y_{s(Abut)\_Low}$	1.00	4.76	9.05	3.23	1.31	0.78
$(r\tau_{max}-\tau_c)/(r\tau_{max\_low}-\tau_c)$	1.00	4.75	8.88	3.36	1.33	0.61
Note	r = 0.342; τ_c=0.55Pa					

The $\tau_{\max\_overtopping}$ in equation (6.4) can be evaluated directly using the proposed equation in Chapter 4. Another approach is to apply a correction factor to $\tau_{\max\_lowchord}$ based on the present simulation results. Figure 6.24 plots the ratio of $\tau_{\max\_overtopping} / \tau_{\max\_lowchord}$ as a function of d_1/d_{deck}, where d_1 is the water elevation above the low chord of the bridge deck and d_{deck} is the thickness of bridge deck. It is seen that the correction factor of maximum bed shear stress for overtopping flow $k_o = \tau_{\max\_overtopping} / \tau_{\max\_lowchord}$ reaches a maximum value of 1.91 when the water depth is flushed with the top surface of the bridge deck. A correction factor of $k_o = 1.0$ is recommended when d_1/h is greater than 3.

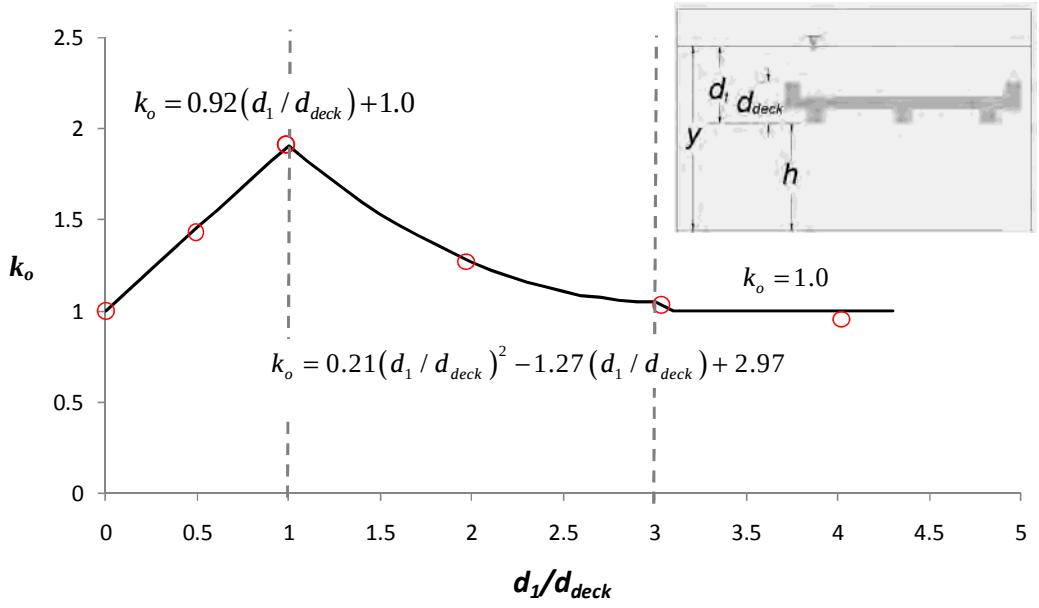

Figure 6.24 - Shear stress correction factor for overtopping flow.

CHAPTER 7

SRICOS EFA METHOD FOR MAXIMUM SCOUR DEPTH FOR ABUTMENT AND CONTRACTION

Bridge scour is the loss of soil by erosion due to flowing water around bridge supports. Bridge scour includes general scour and local scour. General scour is the aggradation or degradation of the riverbed not related to the presence of local obstacles. Aggradation is the gradual and general accumulation of sediments on the river bottom; one possible scenario is the existence of slope failures upstream leading to the formation of spoils in the river, the erosion of these spoils under higher velocities, followed by transport and deposition under lower velocities at the aggrading location. Degradation is the gradual and general removal of sediments from the riverbed; one possible scenario is the man-made straightening of a river course, a resulting increase in the water velocity and the associated increase in erosion. Local scour is the scour around obstacles to the water flow; it includes pier scour, abutment scour, and contraction scour. Pier scour is the removal of the soil around the foundation of the pier; abutment scour is the removal of the soil around the abutment at the junction between the bridge and the embankment; contraction scour is the removal of the soil from the bottom of the river due to narrowing of the river channel created by the approach embankments for the bridge. Figure 7.1 shows the definition of 3 types of local bridge scour.

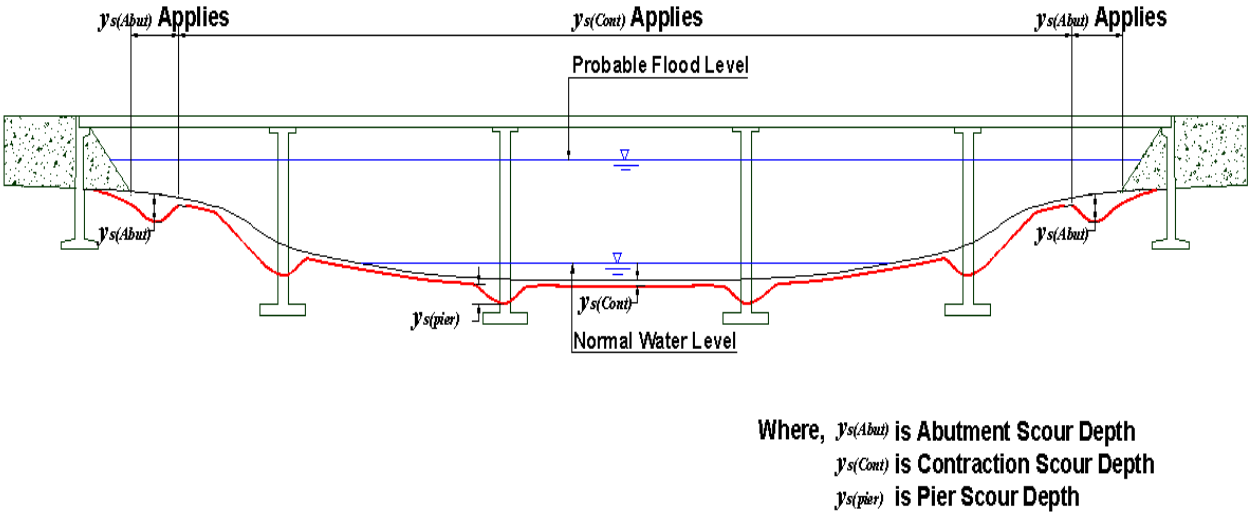

Figure 7.1 – Definitions of local bridge scour.

7.1 LITERATURE REVIEW

7.1.1 Abutment Scour in Sand

Laursen (1960) assumed that the depth of abutment scour is a multiple of the depth of long contraction scour. The depth of contraction scour was considered only as a function of the contraction ratio for live-bed scour. The width of the abutment scour hole was assumed to be 2.75 times the abutment scour depth. The relationship for live-bed abutment scour in sand was based on these assumptions and expressed as:

$$\frac{L'}{y_1} = 2.75 \frac{y_{s(Abut)}}{y_1} \left[\left(\frac{1}{11.5} \cdot \frac{y_{s(Abut)}}{y_1} + 1 \right)^{7/6} - 1 \right] \tag{7.1}$$

where L' is the projected length of abutment normal to the flow, y_1 is the water depth in the approach section, and $y_{s(Abut)}$ is the maximum abutment scour depth.

Laursen (1963) used the same approach and developed an equation to predict the depth of abutment scour for clear-water scour. The equation for abutment scour in sand was:

$$\frac{L'}{y_1} = 2.75 \frac{y_{s(Abut)}}{y_1} \left[\frac{\left(\frac{1}{11.5} \cdot \frac{y_{s(Abut)}}{y_1} + 1 \right)^{7/6}}{\left(\frac{\tau_1}{\tau_c} \right)^{1/2}} - 1 \right] \tag{7.2}$$

The scour depth equation (7.2) in the region of $1 \le L'/y_1 \le 10$ can be approximated by

$$\frac{y_{s(Abut)}}{y_1} = 0.8 \frac{L'}{y_1} \left(\frac{\tau_1}{\tau_c} \right)^{2/3} \tag{7.3}$$

where L' is the projected length of abutment normal to the flow, y_1 is the water depth in the approach section, and $y_{s(Abut)}$ is the maximum abutment scour depth, τ_1 is the shear stress on the channel bed at the approach section, and τ_c is the critical shear stress on the channel bed.

Garde and Nambudripad (1961) conducted a series of experiments in a rectangular channel with various contraction ratio, sediment size of sand, and discharge. The flume used in the experiments was 2 ft wide and 25 ft long. The maximum local scour occurred at the toe of the abutment and the shape of the abutment scour hole was conical. In their findings, the radius of the conical scour hole did not have any correlation with the depth of the abutment scour. This contradicts Laursen's (1960) finding that the radius is 2.75 times the scour depth. They also found that the median size of sediment, contraction ratio (L_2/L_1), and Froude number are crucial parameters that affect abutment scour depth. They suggested an equation for abutment scour in sand as follows:

$$\frac{y_{s(Abut)}}{y_1} = K\left(\frac{L_1}{L_2}\right)Fr_1^n - 1 \tag{7.4}$$

where K and n are coefficients that are function of the sediment size, L_1 is the width of the channel at the approach section, L_2 is the width of the channel at the contracted section, Fr_1 is the Froude number at the approach section, y_1 is the water depth in the approach section, and $y_{s(Abut)}$ is the maximum abutment scour depth.

Gill (1972) used Straub's (1940) model of long contraction scour to develop a maximum abutment scour model. He stated that the maximum scour occurred when the channel bed material is under the critical shear stress (i.e., $\tau_1 = \tau_c$). Both fine sand and coarse sand were used as channel material. The scour rate for the fine sand was observed to be much faster than that for the coarser sand. An equation for scour rate was proposed for both fine sand and coarse sand as:

$$\frac{y_{s(Abut)}(t)}{y_{s(Abut)}} = 0.206\log t + 0.310 \qquad \text{for coarse sand}$$

$$\frac{y_{s(Abut)}(t)}{y_{s(Abut)}} = 0.290\log t + 0.375 \qquad \text{for fine sand} \tag{7.5}$$

where $y_{s(Abut)}(t)$ is the abutment scour depth at time t, t is time in minute, and $y_{s(Abut)}$ is the maximum abutment scour depth. The empirical equation for predicting the maximum abutment scour depth in sand suggested by Gill is:

$$\frac{y_{s(Abut)}}{y_1} = 8.375\left(\frac{D_{50}}{y_1}\right)^{0.25}\left(\frac{L_1}{L_2}\right)^{6/7} - 1 \tag{7.6}$$

where D_{50} is the median size of soil particle, L_1 is the width of the channel at the approach section, L_2 is the width of the channel at the contracted section, y_1 is the water depth in the approach section, and $y_{s(Abut)}$ is the maximum abutment scour depth.

Froehlich (1989) performed data regression using a total of 164 clear-water and 170 live-bed abutment scour measurements in sand taken by other researchers in rectangular channels in different laboratories from 1953 to 1985. Froehlich applied multiple linear regression analysis to obtain the relation among the local scour (normalized by the initial water depth at the approach section) and several other dimensionless parameters. He proposed a live-bed scour and a clear-water scour equation for abutment scour in sand as follows:

Clear-water scour:

$$\frac{y_{s(Abut)}}{y_1} = 0.78 \cdot K_1 \cdot K_2 \cdot \left(\frac{L'}{y_1}\right)^{0.63} \left(\frac{y_1}{D_{50}}\right)^{0.43} Fr_1^{1.16} \sigma_g^{-1.87} \tag{7.7}$$

Live-bed scour

$$\frac{y_{s(Abut)}}{y_1} = 2.27 \cdot K_1 \cdot K_2 \cdot \left(\frac{L'}{y_1}\right)^{0.43} Fr_1^{0.61} \tag{7.8}$$

where $\sigma_g = \left(D_{84}/D_{16}\right)^{0.5}$ is the geometric standard deviation of the bed material, and D_{16}, D_{50}, and D_{84} are the particle size for 16, 50 and 84 percentile of weight, respectively, $Fr_1 = \left(V_1 / \sqrt{g \cdot y_1}\right)$ is Froude number based on approach water depth and approach velocity, K_1 is the correction factor for abutment shape that has a value of 1.0, 0.82 and 0.55 for vertical wall, wing-wall, and spill-through abutment, respectively. K_2 is the correction factor for the alignment of the abutment with respect to the flow direction $\left(K_2 = \left(\theta/90\right)^{0.13}\right)$ with θ being the angle of abutment alignment (the embankment is skewed downstream if $\theta < 90°$, and skewed upstream if $\theta > 90°$. *L'* is the average length of abutment ($L' = A_e / y_1$ with A_e being the flow area obstructed by the embankment), y_1 is the water depth in the approach section, and $y_{s(Abut)}$ is the maximum abutment scour depth.

HEC-18 uses equation (7.8) and a 1.0 safety factor for live-bed abutment scour prediction in sand, i.e.:

$$\frac{y_{s(Abut)}}{y_1} = 2.27 \cdot K_1 \cdot K_2 \cdot \left(\frac{L'}{y_1}\right)^{0.43} Fr_1^{0.61} + 1.0 \tag{7.9}$$

Melville (1992) developed a method to predict the abutment scour depth in sand in a rectangular channel using a large number of experimental results under the clear water scour condition. The ratio between the abutment length and the water depth was found to be very important for the prediction. The method is classified into three conditions: short abutment ($L'/y_1 \le 1.0$), intermediate abutment ($1.0 < L'/y_1 < 25$), and long abutment ($L'/y_1 \ge 25$). The effect of abutment shape becomes irrelevant as the length of abutment becomes longer. Similarly, the effect of the abutment alignment becomes irrelevant as the length of abutment becomes shorter. Melville proposed the following equations for the abutment scour depth in sand considering the three conditions as:

$$\begin{aligned} y_{s(Abut)} &= 2.0 \cdot K_I \cdot L' && \text{for } L'/y_1 \le 1.0 \\ y_{s(Abut)} &= 2.0 \cdot K_I \cdot K_1^* \cdot K_2^* \left(L' \cdot y_1\right)^{0.5} && \text{for } 1.0 < L'/y_1 < 25 \\ y_{s(Abut)} &= 10.0 \cdot K_2 \cdot y_1 && \text{for } L'/y_1 \ge 25 \end{aligned} \tag{7.10}$$

where L' is the projected length of abutment normal to the flow, $y_{s(Abut)}$ is the maximum abutment scour depth, K_I is a correction factor for flow intensity ($K_I = V_1/V_c$ for $V_1/V_c \le 1.0$ and $K_I = 1.0$ for $V_1/V_c > 1.0$), and K_1 and K_2 are correction factors for abutment shape and abutment alignment to the flow as shown in Table 7.1 and Figure 7.2, respectively. These two correction factors vary with the ratio between the abutment length and the water depth as expressed in the following:

$$K_1^* = K_1 \qquad \text{for } L'/y_1 \le 1.0$$

$$K_1^* = K_1 + (1-K_1)\left(0.1\,L'/y_1 - 1.5\right) \qquad \text{for } 1.0 < L'/y_1 < 25$$

$$K_1^* = 1.0 \qquad \text{for } L'/y_1 \ge 25$$

$$K_2^* = K_2 \qquad \text{for } L'/y_1 \ge 3.0$$

$$K_2^* = K_2 + (1-K_2)\left(1.5 - 0.5\,L'/y_1\right) \qquad \text{for } 1.0 < L'/y_1 < 3.0$$

$$K_2^* = 1.0 \qquad \text{for } L'/y_1 \le 1.0$$

Table 7.1 - Factor of abutment shape (K_1) (Melville, 1992).

Shape of Abutment		K_1
Vertical wall	narrow wall	1.0
	semicircular end	0.75
Wing-wall	45°	0.75
Spill-through (H:V)	0.5 : 1.0	0.6
	1.0 : 1.0	0.5
	1.5 : 1.0	0.45

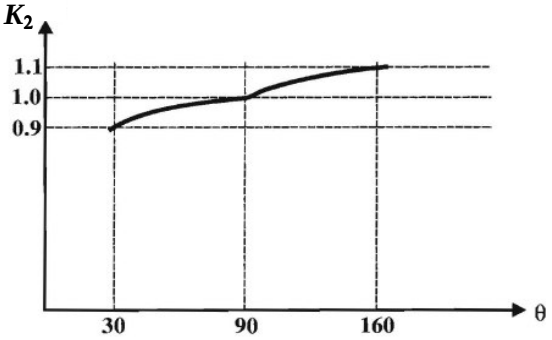

Figure 7.2 - Correction factor of abutment alignment (K_2) (Melville, 1992).

Melville (1995) verified the effect of compound channel using Dongol's (1994) experimental results. In his study, only the abutments terminating in the main channel were studied because abutments terminating on the floodplain were considered as being in rectangular channels. The correction factor for channel geometry was proposed as:

$$K_G = \frac{y_{s(Abut)}}{y^*_{s(Abut)}}$$

where $y^*_{s(Abut)}$ is the local scour depth at an abutment situated in a compound channel. The correction factor for channel geometry is:

$$K_G = \sqrt{L_e / L'}$$

where $L_e = L'\left\{1-\frac{L_f}{L'}\left(1-\frac{y_f}{y_m}\right)^{5/3}\frac{n_m}{n_f}\right\}$ in which L is the length, y is the depth, n is Manning's roughness coefficient, and the subscripts f and m indicate floodplain and main channel, respectively. Accordingly, Melville (1995) expressed the final form for abutment scour prediction in sand by considering all the conditions as:

$$\frac{y_{s(Abut)}}{\sqrt{L'\cdot y_1}} = 2.0\cdot K_I \cdot K_G \cdot K_1^* \cdot K_2^* \tag{7.11}$$

where y_1 is the approach water depth at the line of the toe of the abutment, $y_{s(Abut)}$ is the maximum abutment scour depth, L' is the projected length of abutment normal to the flow, K_I is a correction factor for flow intensity ($K_I = V_1/V_c$ for $V_1/V_c \le 1.0$ and $K_I = 1.0$ for $V_1/V_c > 1.0$), K_G is the correction factor for channel geometry, K_1^* is the correction factor for abutment shape, K_2^* is the correction factor for abutment alignment.

Sturm and Janjua (1994) conducted 37 experiments with sand in a compound channel using a vertical wall abutment for abutment scour prediction. The slope of the main channel was vertical and only half of the channel was modeled to maximize the scale. The channel thus was assumed to be symmetrical and the width of flume was one half of the channel width. They showed that the velocity at the approach section, the distribution of the discharge at the contracted section, and the critical velocity are the most important factors affecting the abutment scour depth. Although the ratio of the channel opening in the approach section to the channel opening in the contracted section were used in previous studies, the concept does not work in compound channels because of the difference in velocity distribution between the main channel and the floodplain. Both the contraction ratio in terms of discharge and the contraction ratio in terms of channel opening width were used in the data analysis and evaluated against the experimental results. They found that using the discharge contraction ratio results in a better comparison. Their abutment scour equation for sand obtained after data regression is as follows:

$$\frac{y_{s(Abut)}}{y_{f1}} = 7.7\left[\frac{V_{f1}}{M\cdot V_{fc}} - 0.35\right] \tag{7.12}$$

where V_{f1} is average approach velocity on the floodplain, V_{fc} is the critical velocity on the floodplain, $y_{s(Abut)}$ is the maximum abutment scour depth, y_{f1} is the approach water depth on the floodplain, and M is the discharge contraction ratio defined as $M = (Q_{total} - Q_{block})/Q_{total}$ with Q_{total} being the total discharge and Q_{block} being the discharge blocked by the approach embankment.

Sturm (1999, 2004) and Sturm and Janjua (1994) presents the results of flume tests for abutment scour in compound channels using 3 types of cross sections. Various contraction ratio, water depth, and soils were used but only a vertical wall abutment was used. The backwater problem found by some researchers was not found by Sturm and Janjua (1994). The flume used in their study is only 5.18 m long so it may be too short to observe the backwater effect. They

developed an equation for vertical abutment scour in sand using the test results without the influence of backwater caused by abutment. It is expressed as:

$$\frac{y_{s(Abut)}}{y_{f0}} = 8.14\left[\frac{q_{f1}}{C_r \cdot q_{fc0}} - 0.4\right] \tag{7.13}$$

where $q_{f1}(=V_{f1}\cdot y_{f1})$ is the unit flow rate at the approach section with the effect of backwater induced by the abutment, $q_{fc0}(=V_{fc0}\cdot y_{f0})$ is the critical unit flow rate on the floodplain without the effect of backwater, V_{f1} is the approach average velocity on the floodplain, $V_{fc0} = \left({}^{1}\!/_{k_n} \cdot \sqrt{(Gs-1)\tau_{*c}} D_{50}^{1/3} y_{f0}^{1/6} \right)$ is the critical velocity on the floodplain without backwater effect, Gs is the specific gravity of cohesionless soil, k_n is constant in Strickler-type relationship for Manning's n $\left(n = k_n D_{50}^{1/6}\right)$, τ_{*c} is the critical value of Shields' parameter, D_{50} is the median diameter of sediment, y_{f0} is water depth on floodplain without backwater effect, y_{f1} is the approach water depth on the floodplain and $y_{s(Abut)}$ is the maximum abutment scour depth.

Sturm (2004) found the effect of abutment shape to be negligible $(K_1 = 1.0)$ with the increase of the length of approach embankment. The correction factor associated with the abutment shape for spill-through abutments was calculated based on the ratio between the predicted scour depth using equation (7.13) and that using the vertical abutment. The correction factor for spill-through abutment was suggested as:

$$K_1 = 1.52\frac{\xi - 0.67}{\xi - 0.4} \qquad \text{for} \quad 0.67 \le \xi \le 1.2 \tag{7.14}$$

where $\xi = \dfrac{q_{f1}}{M \cdot q_{fc0}}$, $q_{f1}(=V_{f1}\cdot y_{f1})$ is the unit flow rate at the approach section with the effect of backwater induced by the abutment, $q_{fc0}(=V_{fc0}\cdot y_{f0})$ is the critical unit flow rate on the floodplain without the effect of backwater, and M is the discharge contraction ratio defined as $M = (Q_{total} - Q_{block})/Q_{total}$ with Q_{total} being the total discharge and Q_{block} being the discharge blocked by the approach embankment. Note that $K_1 = 1.0$ for $1.2 < \xi$ and $K_1 = 0$ for $\xi < 0.67$. The correction factor is the same for both wing wall abutment and spill-through abutment. Accordingly, the abutment scour depth considering abutment shape becomes:

$$\frac{y_{s(Abut)}}{y_{f0}} = K_1 \cdot 8.14\left[\frac{q_{f1}}{M \cdot q_{fc0}} - 0.4\right] \tag{7.15}$$

Kouchakzadeh and Townsend (1997) used a symmetrical compound channel with 2 types of sand to investigate the lateral momentum transfer on abutment scour. They used 4 types of abutments – vertical wall, wing wall, semi circular vertical wall, and spill-through. They found

the discharge ratio, Q_w / Q_a, is an important factor and developed the following dimensionless function:

$$\frac{y_{s(Abut)}}{y_{f1}} = f\left(\frac{Q_w}{Q_a}, Fr_{f1}, Fr_{fc}, Sh\right) \tag{7.16}$$

Based on multiple data regression, they obtained the following equation:

$$\frac{y_{s(Abut)}}{y_{f1}} = K_1 \cdot 13.5\left(\frac{Q_w}{Q_a}\right)^{3.9} Fr_{f1}^{1.17} \cdot Fr_{fc}^{-0.25} \tag{7.17}$$

where $Fr_{f1}\left(=\frac{V_{f1}}{\sqrt{gy_{f1}}}\right)$ is the Froude number in the approach section on the floodplain, $Fr_{fc}\left(=\frac{V_{fc}}{\sqrt{gy_{f1}}}\right)$ is the critical Froude number in the approach section on the floodplain, *Sh* is the shape of abutment, Q_w is the floodplain flow beyond the toe of the abutment which converges and accelerates towards the abutment toe, Q_a is the flow intercepted by the abutment, and K_1 is a shape correction factor of abutment with values of 1.25, 1.08, and 0.95, respectively, for vertical wall, wing wall, and spill-through abutment with a side slope of 0.85 (H): 1 (V) , y_{f1} is the approach water depth on the floodplain, and $y_{s(Abut)}$ is the maximum abutment scour depth.

Lim (1997) developed a maximum abutment scour equation for sand based on a semi-empirical analysis for clear water scour. He assumed that only the flow at the approach section with a width corresponding to the length of the abutment and the lateral length of local scour hole could develop the local scour at the toe of abutment. The shear velocity concept proposed by Rajaratnam and Nwachukwu (1983) was used to derive the equation. Lim's clear water abutment scour depth is given as:

$$\frac{y_{s(Abut)}}{y_1} = K_1 \cdot (0.9X - 2.0) \tag{7.18}$$

where y_1 is the approach water depth, $y_{s(Abut)}$ is the maximum abutment scour depth, K_1 is the correction factor for abutment shape that has a value of 1.0 for vertical wall abutments, and using Melville's (1992) correction factor for other shapes, *X* in the equation is given as:

$$X = \frac{F_0^{0.75}\left(D_{50} / y_1\right)^{0.25}}{\theta_c^{0.375} \cdot \left(0.9\sqrt{L' / y_1} + 1.0\right)}$$

where $F_0\left(=V_1 / \sqrt{(Gs-1)\cdot g \cdot D_{50}}\right)$ is the densimetric Froude number at the approach section, $\theta_c\left(=\tau_c / \left[\left(\rho_s - \rho\right) g D_{50}\right]\right)$ is Shields' parameter, *Gs* is the specific gravity of the soil solids, and

g is gravitational acceleration, τ_c is the critical shear stress, ρ_s is the density of soil particle, ρ is the density of water, and D_{50} is the median diameter of sediment. He suggested this equation should be used for the case of $X > 2.22$ because $y_{s(Abut)}/y_1 = 0$ for $X = 2.22$.

Lim and Cheng (1998) derived a maximum abutment scour equation for live bed condition using the same approach as in Lim (1997). The equation to predict abutment scour in sand is given as:

$$\left(1+\frac{y_{s(Abut)}}{2y_1}\right)^{4/3} = K_1 \cdot \frac{1+1.2\sqrt{L'/y_1}}{\sqrt{\left(\frac{u_{*c}}{u_{*1}}\right)^2 + \left(\frac{L'\cdot\tan\phi}{y_{s(Abut)}}+1\right)^{2/3}\cdot\left[1-\left(\frac{u_{*c}}{u_{*1}}\right)^2\right]}} \tag{7.19}$$

where y_1 is the approach water depth, $y_{s(Abut)}$ is the maximum abutment scour depth, K_1 is the correction factor for abutment shape, u_{*1} is the shear velocity at the approach section, u_{*c} is the critical shear velocity, L' is the length of abutment, and ϕ is the lateral side slope angle of scour hole.

In the clear water scour condition, the term $1-(u_{*c}/u_{*1})^2$ in equation (7.19) should be regarded as zero and the equation is reduced to the clear scour equation proposed by Lim (1997). The abutment scour depth equation for sand in the clear water condition is thus:

$$\left(1+\frac{y_{s(Abut)}}{2y_1}\right)^{4/3} = K_1 \cdot \frac{1+1.2\sqrt{L'/y_1}}{u_{*c}/u_{*1}} \tag{7.20}$$

Maryland SHA procedure was developed by Chang and Davis (1999a, 1999b), and has been updated. It a method to predict the abutment scour depth for non-cohesive soil by assuming that abutment scour is a function of contraction scour. Contraction scour was postulated to develop until the shear stress is in the critical state; it was expressed as:

$$V_c = q / y_{Cont} \tag{7.21}$$

where V_c is the critical velocity, q is the average unit discharge in the approach section, and y_{Cont} is the contraction scour flow depth. They transformed Neill's (1973) critical velocity curve, shown in Figure 7.3, in terms of median diameter of cohesionless soil and water depth into a set of equations to calculate the clear-water contraction scour flow depth. The clear-water contraction scour flow depth is given in equation (7.22).

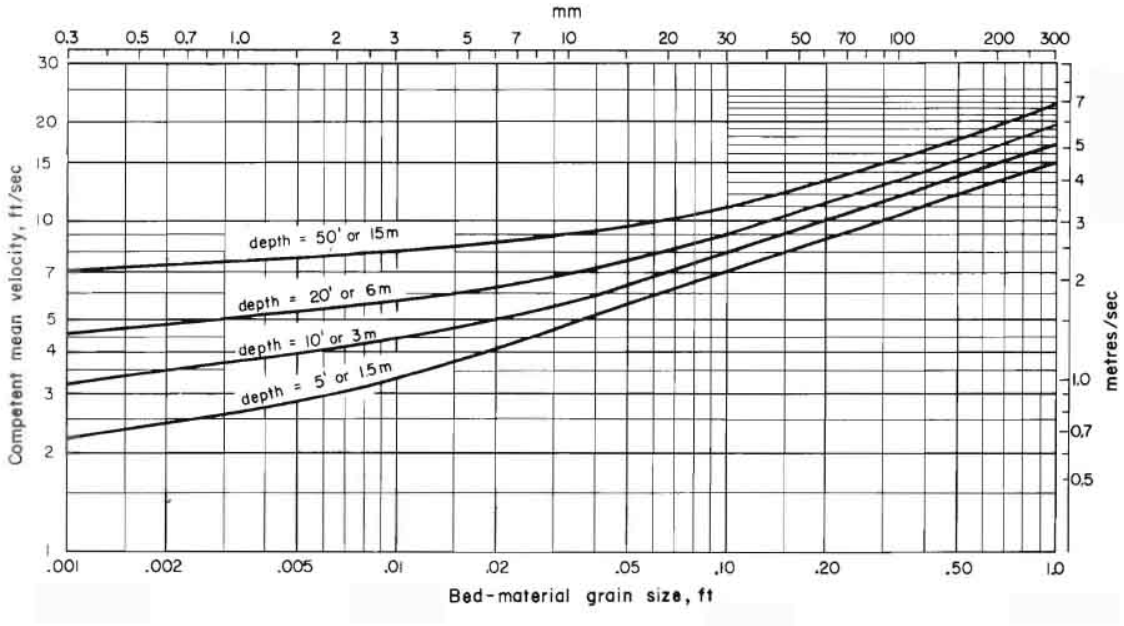

Figure 7.3– Neill's (1973) critical velocity curve in terms of median diameter of cohesionless soil and water depth.

$$y_{Cont} = \left(\frac{q_1}{6.35 \cdot D_{50}^{1/3}} \right)^{0.86} \qquad \text{for } D_{50} \geq 0.03\text{m}$$

$$y_{Cont} = \left(\frac{q_1}{4.16 \cdot D_{50}^{1/4}} \right)^{1/(1+0.125/D_{50}^{0.18})} \qquad \text{for } 0.03\text{m} > D_{50} \geq 0.0003\text{m}$$

$$y_{Cont} = 1.49 \cdot q_1^{0.67} \qquad \text{for } 0.0003\text{m} > D_{50} \qquad (7.22)$$

where y_{Cont} is the contraction scour flow depth, q_1 the average unit discharge in the approach section, and D_{50} is the median diameter of sediment. They recommended the use of Laursen's (1960) equation for the calculation of the live-bed contraction scour flow depth. The clear-water contraction scour depth ($y_{s(Cont)}$) is obtained by subtracting the initial flow depth at the contracted section from the contraction scour flow depth.

The abutment scour depth is always deeper than the contraction scour depth because of the high turbulence around the toe of the abutment. Chang and Davis (1999a, 1999b) proposed an abutment scour equation for vertical wall abutments which uses the flow around the end of abutment:

$$y_{s(Abut)} = K_p \cdot K_f \cdot K_v^{0.857} \cdot y_{Cont} - y_0 \qquad (7.23)$$

where $y_{s(Abut)}$ is the maximum abutment scour depth, y_0 is the initial flow depth at contracted section, y_{Cont} is the contraction scour flow depth, K_p is the correction factor for pressure flow ($K_p = 0.66 Fr_1^{-0.45}$), K_f is the correction factor for spiral flow at the abutment toe ($K_f = 0.13 + 5.85 Fr_1$ for clear water scour and $K_f = 0.46 + 4.16 Fr_1$ for live-bed scour), and K_v is

the ratio of velocity at the abutment toe to the mean velocity in the contracted section ($K_v = 0.8\left(q_1 / q_2\right)^{1.5} + 1$ with q_1 being the unit discharge in the approach section and q_2 the unit discharge in the bridge section) .

Subsequently, the effect of abutment shape was presented, and the correction factor for spiral flow was updated in Maryland SHA bridge scour program (ABSCOUR) (2007). The updated correction factor for spiral flow is $K_f = 0.13 + 5.85Fr_1$ for clear water scour and $K_f = 0.46 + 4.16Fr_1$ for live-bed scour. The value of K_f should be from 1.4 to 4.0. The effect of abutment shape diminishes with an increase of abutment length; the effect becomes negligible if the length of the abutment is ten times greater than the horizontal distance between the toe of abutment and the end of wetted part of abutment at the upstream section. The correction factor for abutment shape is proposed as:

$$K_1 = 0.55 + 0.05\left(X_2 / X_1 - 1\right) \quad \text{for spill-through abutment}$$

$$K_1 = 0.82 + 0.02\left(X_2 / X_1 - 1\right) \quad \text{for wing-wall abutment}$$

$$K_1 = 1.0 \quad \text{if } K_1 > 1.0 \qquad (7.24)$$

where X_1 is the horizontal distance between the toe of abutment and the end of the wetted part of the abutment at the upstream section and X_2 is the length of abutment as shown in Figure 7.4.

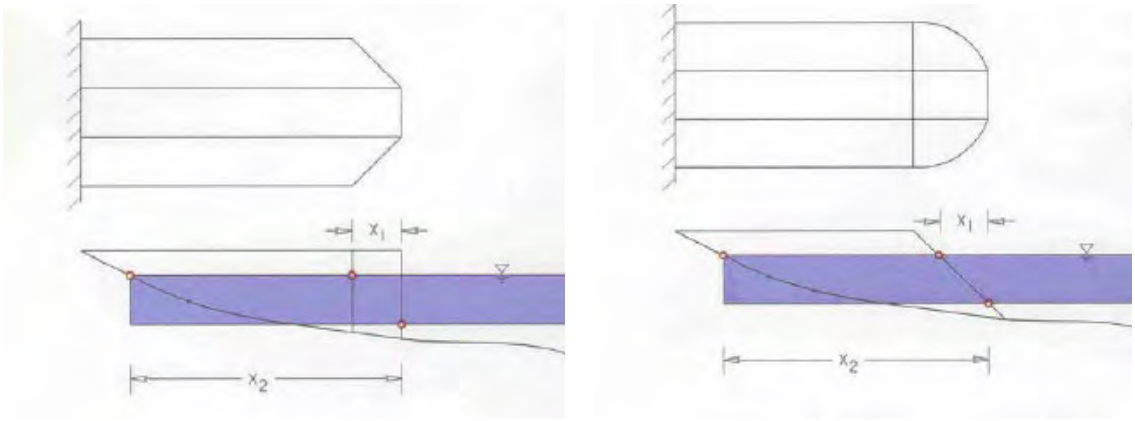

(a) Wing-wall abutment (b) Spill-through abutment

Figure 7.4 – Abutment shape factor measurement (Maryland SHA bridge scour program (ABSCOUR), 2007).

Finally the abutment scour equation is expressed in Maryland SHA bridge scour program (ABSCOUR) (2007) as:

$$y_{s(Abut)} = K_1 \cdot K_2 \left(K_p \cdot K_f \cdot K_v^{0.857} \cdot y_{Cont} - y_0\right) \qquad (7.25)$$

where $y_{s(Abut)}$ is the maximum abutment scour depth, y_0 is the initial flow depth at contracted sec-

tion, y_{Cont} is the contraction scour flow depth, K_p is the correction factor for pressure flow , K_f is the correction factor for spiral flow at the abutment toe, K_v is the ratio of velocity at the abutment toe to the mean velocity in the contracted section , K_1 is the correction factor of abutment shape, and K_2 is the correction factor for abutment alignment proposed by Froehlich (1989).

Ettema et al. (2008) categorized abutment scour into three conditions. In condition A ($L' \geq 0.75L_f$), the maximum local scour occurs in the main channel. In condition B ($L' < 0.75L_f$), the maximum local scour occurs on the floodplain. In condition C, the breach of embankment is fully developed and the abutment columns are exposed like a bridge pier. The maximum local scour flow depths ($y_{Abut} = y_{s(Abut)} + y_{f1}$ in condition B, $y_{Abut} = y_{s(Abut)} + y_{m1}$ in condition A) were compared to Laursen's long contraction scour flow depths ($y_{Cont} = y_{s(Cont)} + y_{f1}$ in condition B, $y_{Cont} = y_{s(Cont)} + y_{m1}$ in condition A). The scour condition A ($L' \geq 0.75L_f$) and B ($L' < 0.75L_f$) were classified as the ratio of the length of embankment projected normal to the flow (L') to the width of floodplain (L_f), as shown in Figure 7.5. The ratio (y_{Abut} / y_{cont}) was defined as an amplification factor: α_A, α_B α_A and α_C for the three scour conditions and discussed below.

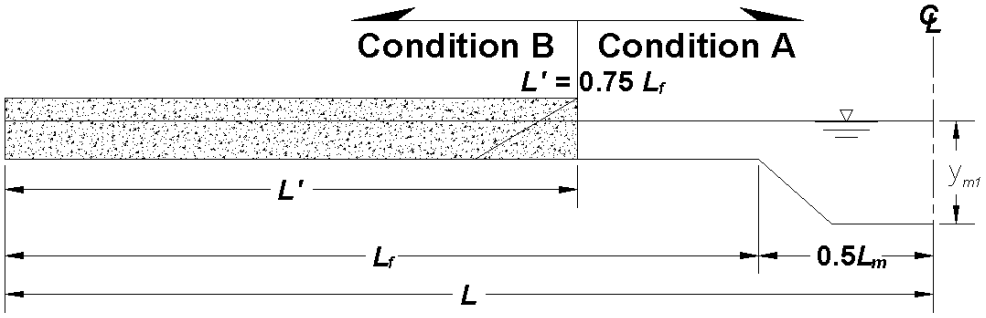

Figure 7.5 - Boundary of scour condition A and B with the ratio of abutment length to the width of floodplain (Ettema et. al, 2008).

Laursen's live bed contraction scour flow depth was used in condition A. Usually the floodplain is made of less erodible soils while the main channel is made with more erodible soils. Accordingly, live bed contraction scour occurs in the main channel and clear water scour occurs on the floodplain during a flood event. The amplification factor α_A depends on the unit discharge ratio and the abutment shape, as shown as Figure 7.6 (a). In the figure, q_1 is the average unit discharge at the approach section, q_2 is the average unit discharge at the bridge section, q_{f1} is the unit discharge in the floodplain at the approach section, and q_{f2} is the unit discharge in the floodplain at bridge section.

The maximum local scour occurs on the floodplain if the abutment has a long set back on the floodplain or exists in a rectangular channel (condition B). Laursen's clear water scour flow depth was used for condition B because scour on a floodplain is mainly clear water scour during

a flood event. The amplification factor α_B displays a relative higher peak than that for condition A. The highest value occurs when the length of abutment is very short as shown as Figure 7.6 (b).

In condition C, embankments were built with the same material as for the channel bottom so the embankments are vulnerable to erosion. Laursen's clear water scour flow depth was used to compare with the maximum local scour flow depth. The amplification factor α_C is less than 1.0 since embankments failed before local scour is fully developed. The foundation of the abutment is exposed to the flow like a pier.

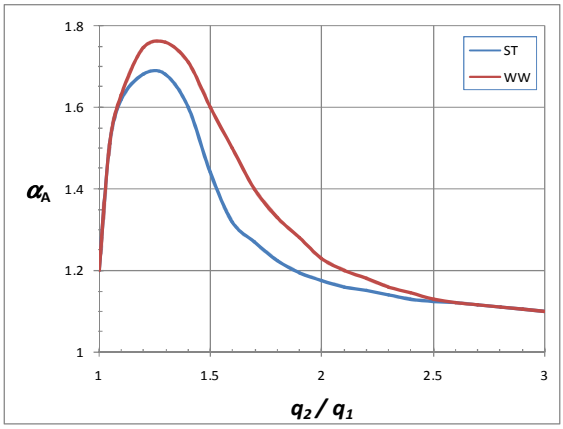

(a) Condition A

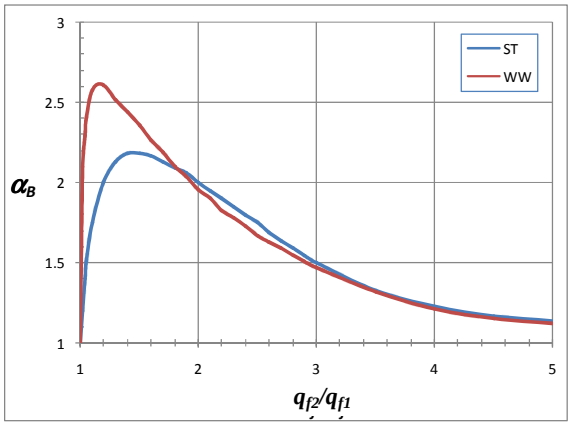

(b) Condition B

Figure 7.6 - Scour amplification factor versus unit discharge ratio (replotted using data from Ettema et al., 2008).

7.1.2 Abutment Scour in Clay

Yakoub (1995) varied *WC* (initial water content), *CC* (clay content), *C* (the degree of compaction related to the optimum compaction) and *CT* (clay type) for a series of tests on abutment scour in cohesive material. He compared abutment scour depth in cohesive material with that in sand. He used a constant water depth and the same abutment to examine the effect of clay. A vertical abutment that is 0.116 m (0.38 ft) long and 0.219 m (0.72 ft) wide was used. The medium size and the geometric standard deviation of the sand were 0.81 mm and 2.41, respectively. The experimental results in cohesive soil were directly compared with that in cohesionless soil with the same test condition. He found that the abutment scour depth in cohesive soil is related to *WC, CC, C,* and *CT* and can be expressed as:

For Montmorillonite clay

(1) 100 % of Montmorillonite clay

For unsaturated soil

$$\frac{d_{sc}}{d_{ss}} = (2.186 - 5.342 \cdot WC) \cdot \left(15.407 - 52.202 \cdot C + 60.873 \cdot C^2 - 23.512 \cdot C^3\right) \tag{7.26}$$

For saturated soil

$$\frac{d_{sc}}{d_{ss}} = (4.76 - 45.1 \cdot WC + 136.1 \cdot WC^2 - 126 \cdot WC^3) \cdot \left(-0.339 + 1.744 \cdot C\right) \tag{7.27}$$

(2) Effect of clay content

$$\frac{d_{sc}}{d_{ss}} = 1.0 - 0.608 \cdot CC - 4.286 \cdot CC^2 + 10.159 \cdot CC^3 \tag{7.28}$$

where d_{sc} is the abutment scour depth in cohesive material, d_{ss} is the abutment scour depth in sand based on a 0.81 mm D_{50}, *WC* is the initial water content, *CC* is clay content, *C* is the degree of compaction related to the optimum compaction, and *CT* is clay type

For Kaolinite clay

(1) 30 % of Kaolinite clay

The degree of compaction has no effect on the scour depth at the sandy soil with a 30% mixture of Kaolinite clay. The effect of initial water content was also found negligible.

(2) Effect of clay content

$$\frac{d_{sc}}{d_{ss}} = 0.988 - 2.788 \cdot CC - 52.56 \cdot CC^2 + 110 \cdot CC^3 \tag{7.29}$$

where d_{sc} is the abutment scour depth in cohesive material, d_{ss} is the abutment scour depth in sand based on a 0.81 mm D_{50}, and CC is clay content.

7.1.3 Contraction scour in sand and in clay

The most common cause of contraction scour is the encroachment of bridge approach embankments either into the main channel or into the floodplain. This causes an increase in velocity and in shear stress on the contracted channel bed. The major approach in previous studies was to predict the uniform contraction scour depth in a long contraction channel with a uniform rectangular cross-section in sand. This extensively studied situation is the simplest contraction case - a uniform flow can be assumed in the approach section far from the contraction opening and the associated unidirectional flow parameters can be easily calculated based on open channel theory. The live-bed and clear-water conditions for contraction scour were studied separately but both use a uniform flow in contracted and uncontracted channels. For the live-bed case, continuity equations of water and sediment are satisfied. The difference among the contraction scour equations is the selection of sediment transport models which are used to eliminate the velocity terms in the continuity equations. In the case of clear-water scour, Laursen (1963) stated that the limit of clear-water scour is reached when the boundary shear stress is equal to the critical shear stress of the streambed material. This means clear water scour equations could be derived based on this argument plus continuity equations. Laursen (1963) and Ivarson (1999) developed clear-water contraction scour equations for silica sand and clay, respectively. Laursen (1963) pointed out that higher scour rates were induced in the live-bed condition $(\tau_1 > \tau_c)$ while a deeper maximum scour depth was found in the threshold condition $(\tau_1 = \tau_c)$, which is the borderline between clear-water scour and live-bed scour. Some well-known equations for contraction scour depth for both live-bed and clear-water conditions are summarized in Tables 7.2 and 7.3.

Table 7.2- Equations for uniform contraction scour under live-bed condition.

Reference	Contraction Scour Equation	Notes	Soil Type
Laursen (1960)	$\frac{y_{(Cont)}}{y_1}=\left(\frac{Q_2}{Q_1}\right)^{\frac{6}{7}}\left(\frac{L_1}{L_2}\right)^{\frac{6}{7}\frac{2+a}{3+a}}\left(\frac{n_2}{n_1}\right)^{\frac{6}{7}\frac{a}{3+a}}$	a depends on the mode of sediment movement	Sand
Komura (1966)	$\frac{y_{(Cont)}}{y_1}=\left(\frac{\tau_{c1}}{\tau_{c2}}\right)^{\frac{2}{7}}\left(\frac{L_1}{L_2}\right)^{6/7}$	$\tau=\frac{\rho g n^2 V^2}{D_{50}^{1/3}}$	Sand
Gill (1981)	$\frac{y_{(Cont)}}{y_1}=C\left(\frac{L_1}{L_2}\right)^{6/7}\left[\left(\frac{L_2}{L_1}\right)^{1/m}\left(1-\frac{\tau_c}{\tau_1}\right)+\frac{\tau_c}{\tau_1}\right]^{-3/7}$	m is a function of sediment transport rate and varies between 1.5 and 3.0	Sand
Lim (1998)	$\frac{y_{(Cont)}}{y_1}=\left(\frac{L_2}{L_1}\right)^{0.75}$		Sand

Table 7.3- Equations for uniform contraction scour under clear-water condition.

Reference	Contraction Scour Equation	Notes	Soil Type
Lausen (1963)	$\frac{y_{(Cont)}}{y_1}=0.13\left(\frac{Q}{D_{50}^{1/3}y_1^{7/6}L_2}\right)^{6/7}$		Sand
Komura (1966)	$\frac{y_{(Cont)}}{y_1}=\left(\frac{\tau_{c1}}{\tau_{c2}}\right)^{\frac{2}{7}}\left(\frac{L_1}{L_2}\right)^{6/7}$	$\frac{\tau_c}{\rho}=ac\left[Gs-1\right]gD$	Sand
Ivarson (1999)	$\frac{y_{(Cont)}}{y_1}=\left(\frac{2.32q_2^3n^2}{y_1^{10/3}\left(\log S_u-2.367\right)}\right)^{3/10}-1$	$\tau_c=\frac{12.11\log S_u-28.67}{V_2}$ S_u is undrained shear stress of clay	Clay

7.2 EXPERIMENT SETUP

A concrete flume that is 45.7 m in length, 3.7 m in width and 3.4 m in depth was used to conduct the abutment scour tests. A sediment pit is located around the middle of the flume that has dimensions of 7.5 m in length, 3.7 m in width and 1.5 m in depth. Four recirculation pumps with a combined capacity of 2.21 m^3/s were used to generate the needed flow. A flow straightener was installed at the outlet of recirculation pumps to decrease the magnitude of flow irregularity. The water depth and velocity were controlled by varying the height of a tailgate and the output of the pumps since the slope of the flume is fixed. A false bottom was built and installed to form a compound channel. Figure 7.7 depicts the setup in the flume. Only one half of the channel was modeled in the tests to maximize the scale of the experiments.

Two types of channel were used in the experiments. One is a rectangular channel with a long setback abutment while the other is a compound channel with a short setback. Figure 7.8 shows the cross sectional view of the rectangular channel and compound channel. The rectangular channel was used directly without the installation of a false bottom, while a false bottom was used to induce a smooth flow to the test section and to form the compound channel. The width of floodplain (L_f) was fixed at L_f = 2.4 m for the compound channel, and the false bottom was installed between the approach section and the downstream section of the abutment. The upstream part is 18.3 m long and 2.4 m wide and the downstream part is 9 m long and 2.4 m wide. Three types of abutment made of plywood were used in the flume tests: the first one is of a wing wall shape, the second one is of a spill-through shape with a 2(H):1(V) slope, and the third one is of a spill-through shape with a 3(H):1(V) slope. They are shown in Figure 7.9. The projected length of abutment (L') was adjusted by changing the length of the embankment.

Porcelain clay was used to fill the sediment pit above an one-meter-thick layer so the quantity of clay could be minimized.

7.2.1 Soil and Soil Bed Preparation

The Porcelain clay used in the tests was prepared by a supplier. The mineral content, compaction degree, and water content were maintained in the clay. The clay was delivered in individual blocks of 150 mm x 150 mm x 230 mm in size. Each block was sealed in a plastic bag to minimize the change of water content.

Geotechnical tests were conducted according to ASTM (American Society for Testing and Materials) standards. The median grain size of the clay is 0.0035 mm and the plasticity index (PI) is 14.1%. The Porcelain clay is classified as CL (clay with low plasticity). The particle distribution is shown in Figure 7.10 and the results of Atterberg limit test for plasticity index are summarized in Table 7.3. Gudavalli (1997) and Li (2003) also used the Porcelain clay in their experiments. The geotechnical properties of the clay they used are summarized in Table 7.4 and Table 7.5, respectively. The erosion properties of the Porcelain clay were obtained after 11 EFA (Erosion Function Apparatus) tests (Briaud et al., 2001a). The results of the EFA tests are shown in Figure 7.11. Based on the tests, the critical shear stress of the Porcelain clay is 0.8 Pa and the erosion rate is $\dot{z}(\text{mm/hr}) = 0.135\tau^{1.325}(\text{Pa})$.

For the flume tests, the clay was installed block by block in the sediment pit and compacted with a 254 mm x 254 mm tamper to minimize voids and gaps between the clay blocks. Clay installation and compaction was repeated until the elevation of the clay surface was leveled with the channel bottom. The soil surface was then leveled and smoothened by using trowels. Figure 7.12 shows the clay installation. Figure 7.13 shows the test section after clay installation for the rectangular channel and the compound channel. After each test, the excessive water was pumped out of the test section, the layer of clay around the scour holes was removed until undisturbed clay was reached, and new clay was used to replace the excavated clay.

7.2.2 Measurement Equipment

Two side looking three-dimensional ADVs (Acoustic Doppler Velocimetry) were used for point velocity measurements. One ADV made by Nortek was capable of measuring velocities from 1 mm/s to 4 m/s with a 0.5% error of the measured value. The other ADV made by Sontek was capable of measuring velocity up to 2.5 m/s with a 1% error of the measured value. The sampling rate of the two ADVs was kept constant at 25 Hz. The depth-averaged velocities were approximated by taking measurements at the 60% water depth from the free surface. At each point the velocity was averaged over data taken 60 seconds or longer. The velocity measurement was performed to obtain the discharge and velocity pattern from the approach section to the downstream side. The locations of velocity measurement varied with the test condition. Figure Figure 7.14 shows the view of AVD probes used in flume tests. Figure 7.15 shows typical locations of velocity measurement in the tests.

A point gauge was used to measure the water depth and the maximum scour depth. The point gauge is designed based on the differences in electrical conductivity between two different materials: between clay and water and between water and air. The accuracy of the point gauge is 0.1 mm. Figure 7.16 shows the typical locations of water depth measurements in the tests.

A bed profiler was used to scan the channel bottom topography. It was necessary to use a profiler because the flow was very muddy during the tests. It is impossible to find the location of the deepest scour hole and the pattern of scour without using the profiler. The profiler consists of 23 sets of pipes. Each set consists of two plastic pipes with a different diameter and length. The bigger and shorter pipe guides the smaller and longer pipe to move only vertically. A ruler is attached to each of the smaller pipes. Each of the 23 sets measures the bed elevation at a given point. There is a 150 mm interval between two adjacent points. The accuracy of the measured profile is 3 mm. The point gauge was used to measure the maximum scour depth after finding the location of maximum scour using the bed profiler. Figure 7.17 shows eleven smaller pipes among the twenty-three smaller pipes of the profiler. Figure 7.18 shows typical points of scour measurement using the bed profiler in the experiments.

The ADVs, bed profiler, and point gauge were mounted on the carriage which is allowed to move forward and backward. Figure 7.19 shows the view of carriage and measurement scene.

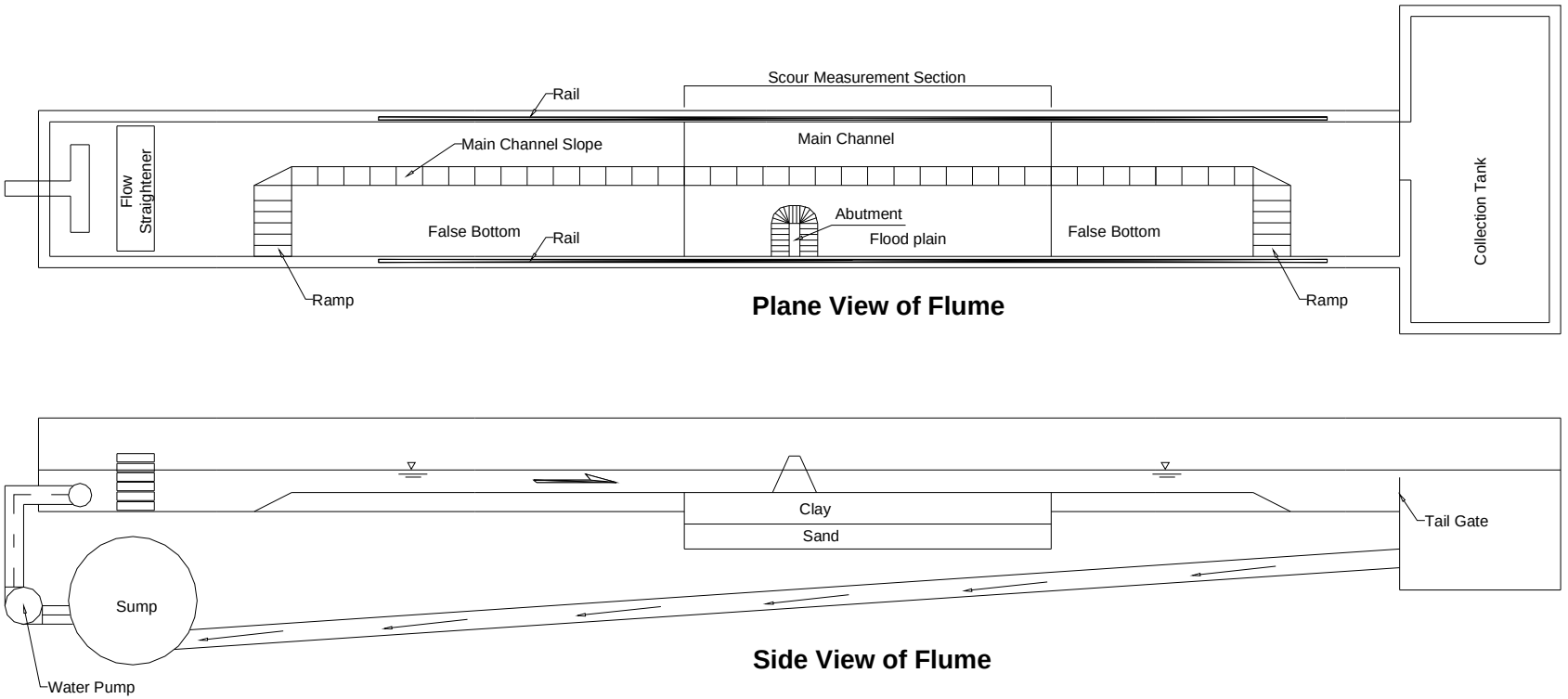

Figure 7.7 – Sketch of the flume and experimental setup (not to scale).

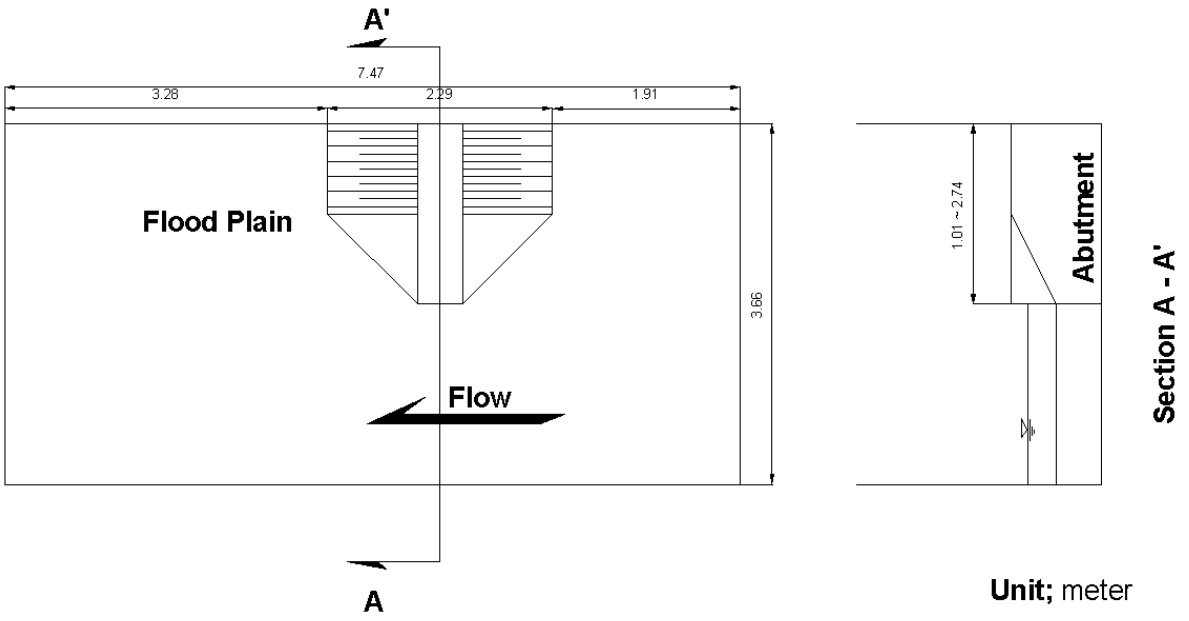

(a) Rectangular Channel

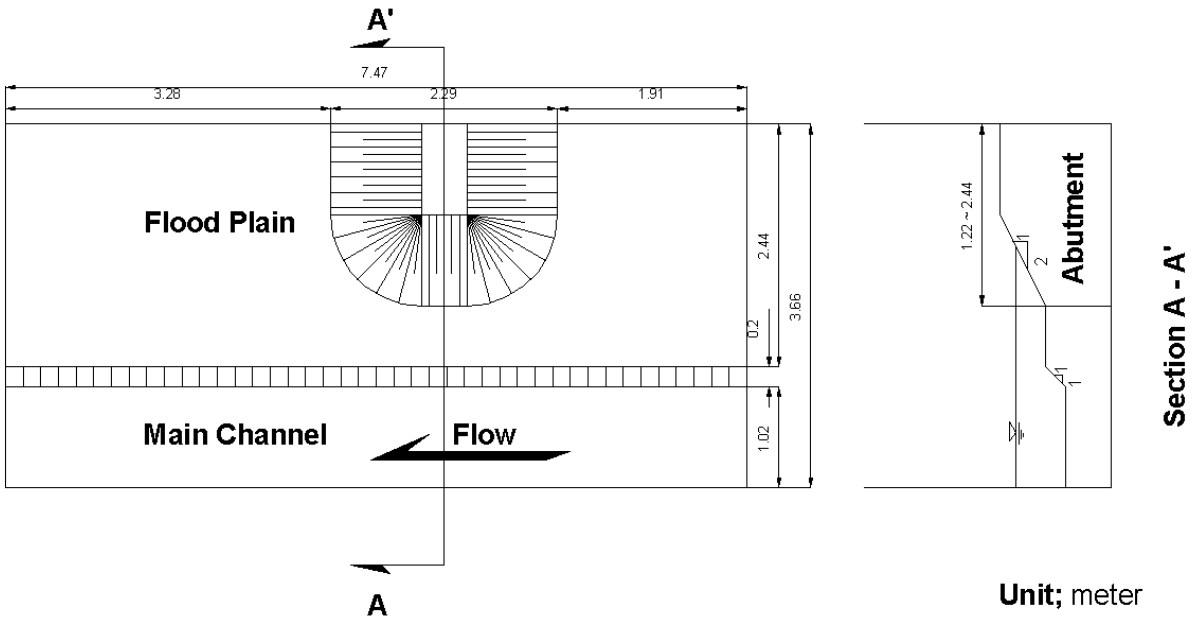

(b) Compound Channel

Figure 7.8 – Channel configurations.

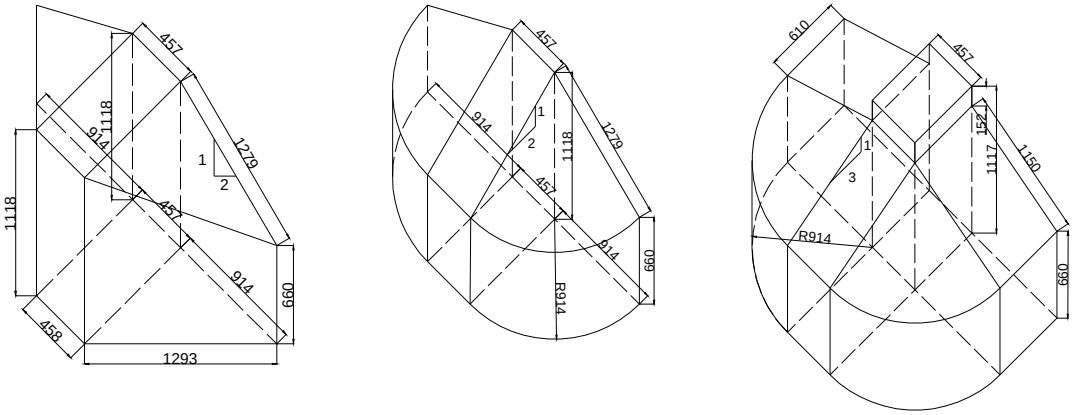

(a) Wing-Wall (b) Spill-Through (2(H):1(V)) (c) Spill-Through (3 (H): 1(V))

Figure 7.9 - Abutment shapes (all dimensions are in mm).

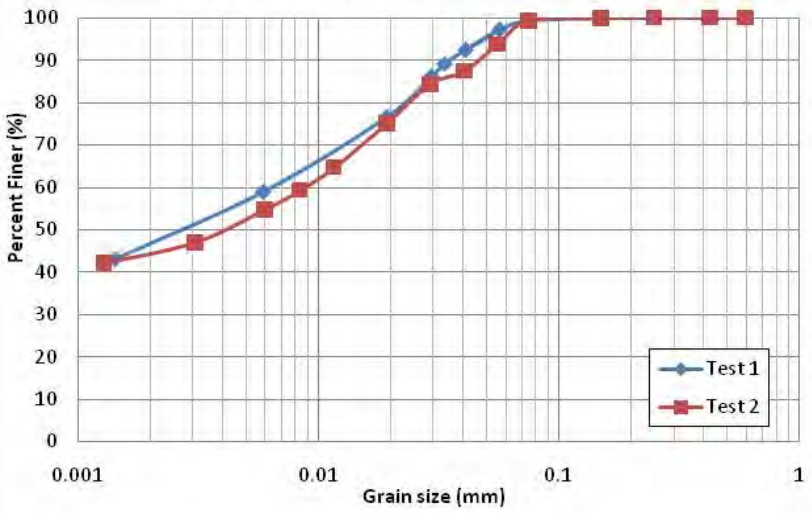

Figure 7.10 – Grain size distribution of the Porcelain clay.

Table 7.4 – Geotechnical properties of the Porcelain clay.

Property	Test 1	Test 2	Test 3	Test 4
Liquid Limit (LL) (%)	30.9	29.8	31.5	30.7
Plastic Limit (PL) (%)	16.9	17.2	16.0	16.3
Plasticity Index (PI) (%)	14.0	12.6	15.5	14.4
Water Content (%)	25.5	23.25	26.75	24.35
Undrained Shear Stress (kPa)	19.5	21.3	20.7	23.4

Table 7.5 – Geotechnical properties of the porcelain clay used in Li (2003).

Property	Test 1	Test 2
Liquid Limit (LL) (%)	40.23	37.7
Plastic Limit (PL) (%)	19.17	14.4
Plasticity Index (PI) (%)	21.06	23.3
Water Content (%)	27.35	30.5
Bulk Unit Weight (kN/m^3)	19.65	24.99
Undrained Shear Stress (kPa)	10.7	18.1

Table 7.6 – Geotechnical properties of the porcelain clay used in Gudavalli (1997).

Property	Porcelain clay
Liquid Limit (LL) (%)	34.40
Plastic Limit (PL) (%)	20.25
Plasticity Index (PI) (%)	14.15
Specific Gravity	2.61
Water Content (%)	28.51
Sand Content (%)	------
Clay Content (%)	100
Undrained Shear Strength (kPa)	12.51
CEC (meg/100g)	8.3
SAR	5.0
PH	6.0
Electrical Conductivity (mmhos/cm)	1.2
Bulk Unit Weight (kN/m^3)	18.0

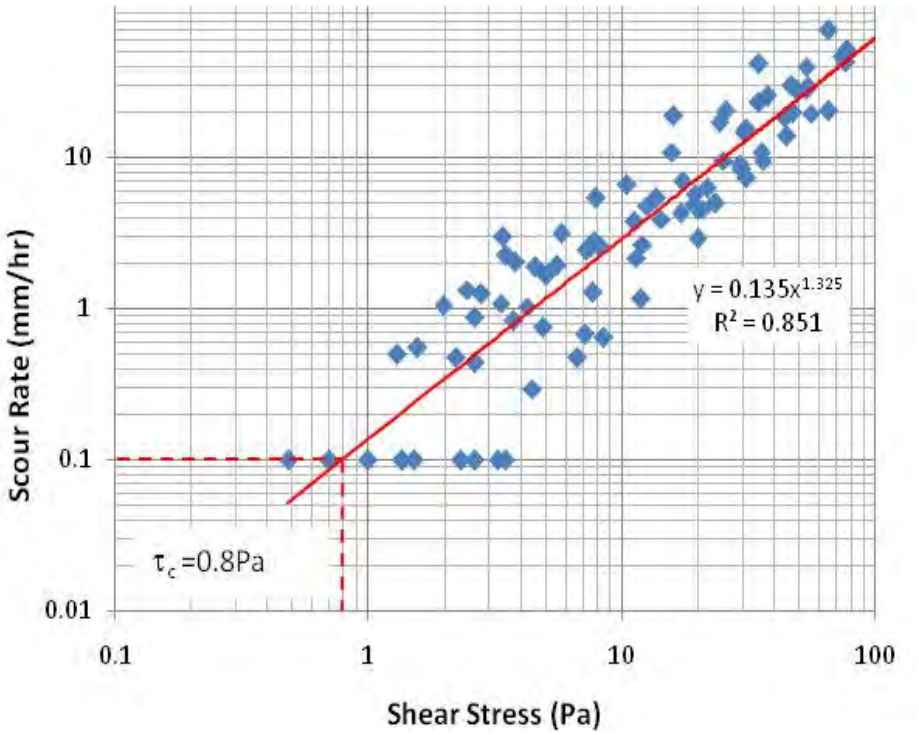

Figure 7.11 – Results of 11 EFA tests.

(a) Clay compaction (b) Plaster work

Figure 7.12 – Clay installation.

(a) Rectangular channel (b) Compound channel

Figure 7.13 – Test section after clay installation.

(a) Nortek side-looking 3D AVD

(b) Sontek side-looking 3D ADV

Figure 7.14 – View of ADVs.

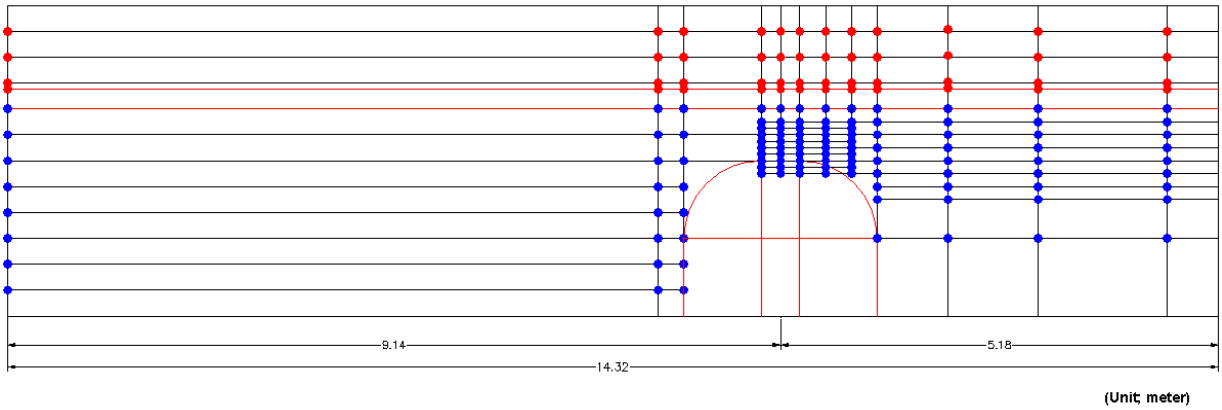

Figure 7.15 - Velocity measurement points.

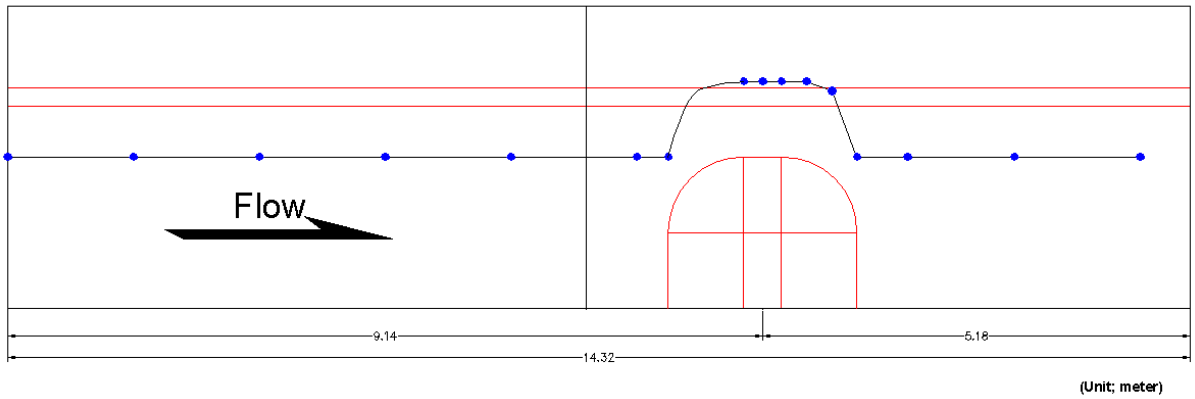

Figure 7.16 - Water depth measurement positions.

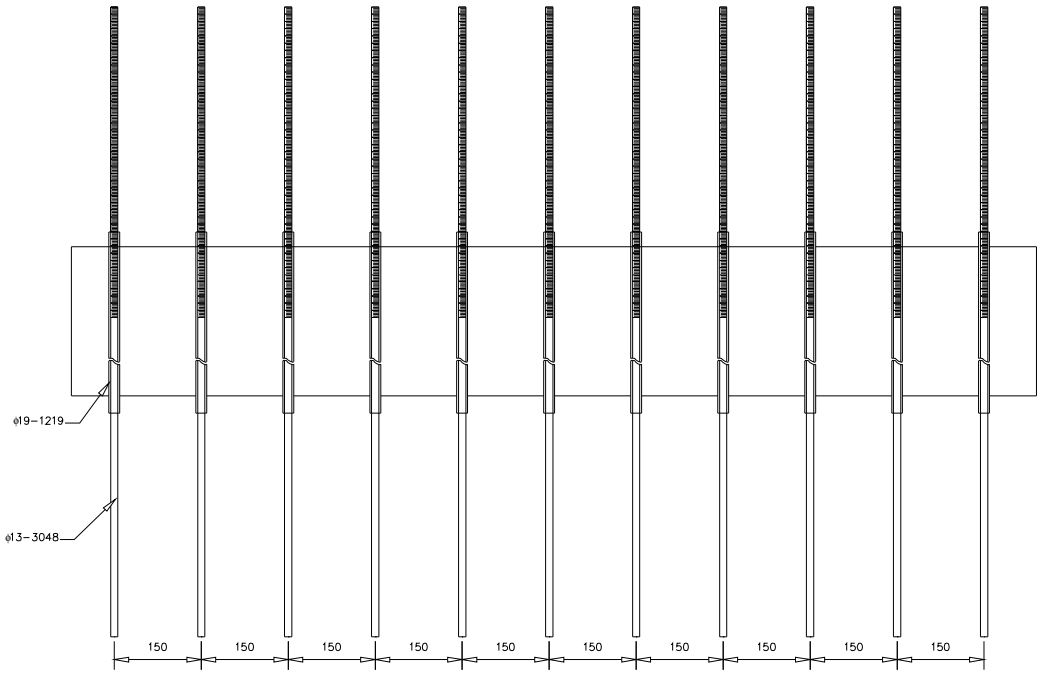

Figure 7.17 - Diagram of bed profiler (unit: mm).

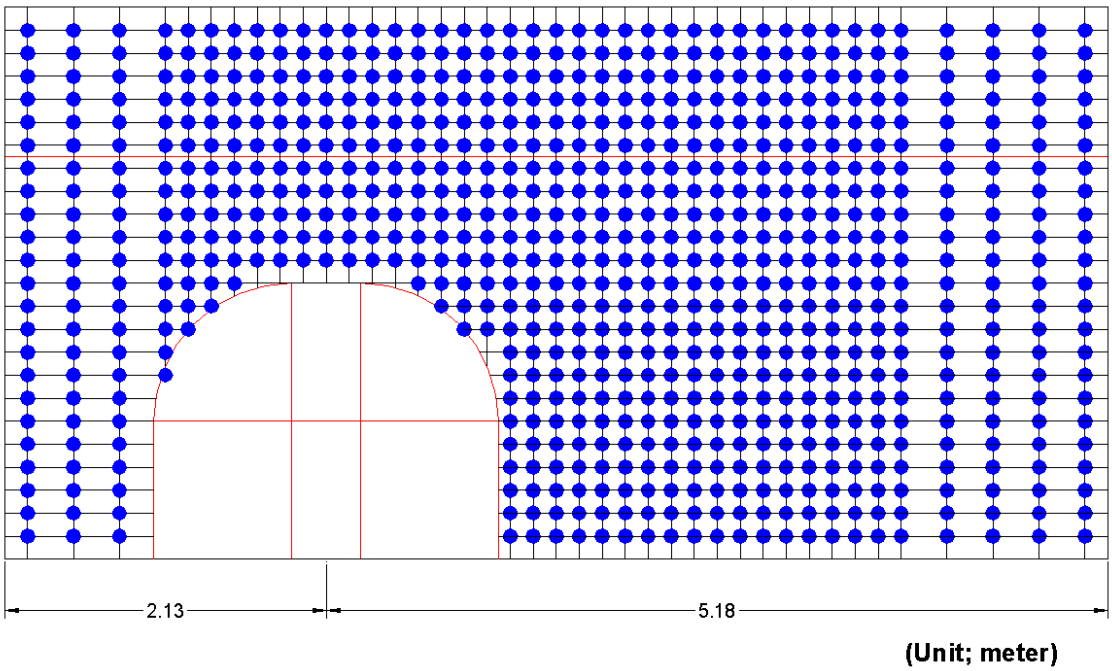

Figure 7.18– Points of scour measurement using the bed profiler.

Figure 7.19 - View of carriage and measurement scene.

7.2.3 Test Conditions

The test matrix for all the experiments is shown in Table 7.7 and Table 7.8 in dimensionless form and dimensional form, respectively. The definition of variables is illustrated in Figure 7.20. There are 17 experiments in the test matrix plus 2 additional experiments which are Case 12B and Case 1II. The test condition of Case 12B is identical to that of Case 12 except the velocity and Froude number. The velocity and Froude number in Case 12B at the approach section are 0.635 m/s and 0.31, respectively. Case 1II was performed as a repeatability test; the test condition is identical to that of Case 1. In Table 7.7, each dimensionless parameter was varied in the compound channel condition to examine the effect of the parameter. The cases with an even number have a lower value, while the cases with an odd number have a higher value in terms of the dimensionless parameter if compared with Case 1.

Table 7.7 - Test matrix in dimensionless form.

	Case	y_{f1}/L'	F_r	L'/L	$\tan(\beta_a)$	$\Theta(^o)$
Compound Channel	1	0.16	0.23	0.5	0.5	90
	2	0.1	0.23	0.5	0.5	90
	3	0.22	0.23	0.5	0.5	90
	4	0.16	0.18	0.5	0.5	90
	5	0.16	0.28	0.5	0.5	90
	6	0.16	0.23	0.333	0.5	90
	7	0.16	0.23	0.667	0.5	90
	8	0.16	0.23	0.5	0.3	90
	9	0.16	0.23	0.5	vertical	90
	10	0.16	0.23	0.5	0.5	60
	11	0.16	0.23	0.5	0.5	120
	12	0.16	0.18	0.5	vertical	90
Rectangular Channel	13	0.36	0.18	0.28	vertical	90
	14	0.23	0.18	0.44	vertical	90
	15	0.16	0.18	0.61	vertical	90
	16	0.13	0.18	0.75	vertical	90
	17	0.28	0.18	0.36	vertical	90

Table 7.8- Test conditions in dimensional form.

Test No.	Abutment Shape	Channel Type	V_1 (m/s)	y_{f1} (m)	y_{m1} (m)	L (m)	L_f (m)	L' (m)	θ (^{o})	$\tan(\beta_a)$	$0.5Q_{total}$ (m^3/s)
Case1	ST (2:1)	Comp.	0.464	0.291	0.494	3.658	2.438	1.829	90	0.5	0.573
Case 1II	ST (2:1)	Comp.	0.456	0.294	0.497	3.658	2.438	1.829	90	0.5	0.562
Case2	ST (2:1)	Comp.	0.377	0.184	0.387	3.658	2.438	1.829	90	0.5	0.320
Case3	ST (2:1)	Comp.	0.496	0.400	0.604	3.658	2.438	1.829	90	0.5	0.813
Case4	ST (2:1)	Comp.	0.358	0.278	0.482	3.658	2.438	1.829	90	0.5	0.442
Case5	ST (2:1)	Comp.	0.546	0.294	0.497	3.658	2.438	1.829	90	0.5	0.662
Case6	ST (2:1)	Comp.	0.432	0.294	0.497	3.658	2.438	1.219	90	0.5	0.561
Case7	ST (2:1)	Comp.	0.472	0.291	0.494	3.658	2.438	2.438	90	0.5	0.564
Case8	ST (3:1)	Comp.	0.456	0.291	0.494	3.658	2.438	1.829	90	0.33	0.570
Case9	WW	Comp.	0.453	0.294	0.497	3.658	2.438	1.829	90	vertical	0.568
Case10	ST (2:1)	Comp.	0.458	0.291	0.494	3.658	2.438	1.829	60	0.5	0.554
Case11	ST (2:1)	Comp.	0.457	0.291	0.494	3.658	2.438	1.829	120	0.5	0.565
Case12	WW	Comp.	0.347	0.294	0.497	3.658	2.438	1.829	90	vertical	0.433
Case12B	WW	Comp.	0.635	0.294	0.497	3.658	2.438	1.829	90	vertical	0.759
Case13	WW	Rect.	0.328	0.366	0.366	3.658	3.658	1.015	90	vertical	0.430
Case14	WW	Rect.	0.326	0.372	0.372	3.658	3.658	1.625	90	vertical	0.433
Case15	WW	Rect.	0.310	0.384	0.384	3.658	3.658	2.234	90	vertical	0.416
Case16	WW	Rect.	0.233	0.347	0.347	3.658	3.658	2.743	90	vertical	0.285
Case17	WW	Rect.	0.364	0.360	0.360	3.658	3.658	1.320	90	vertical	0.485

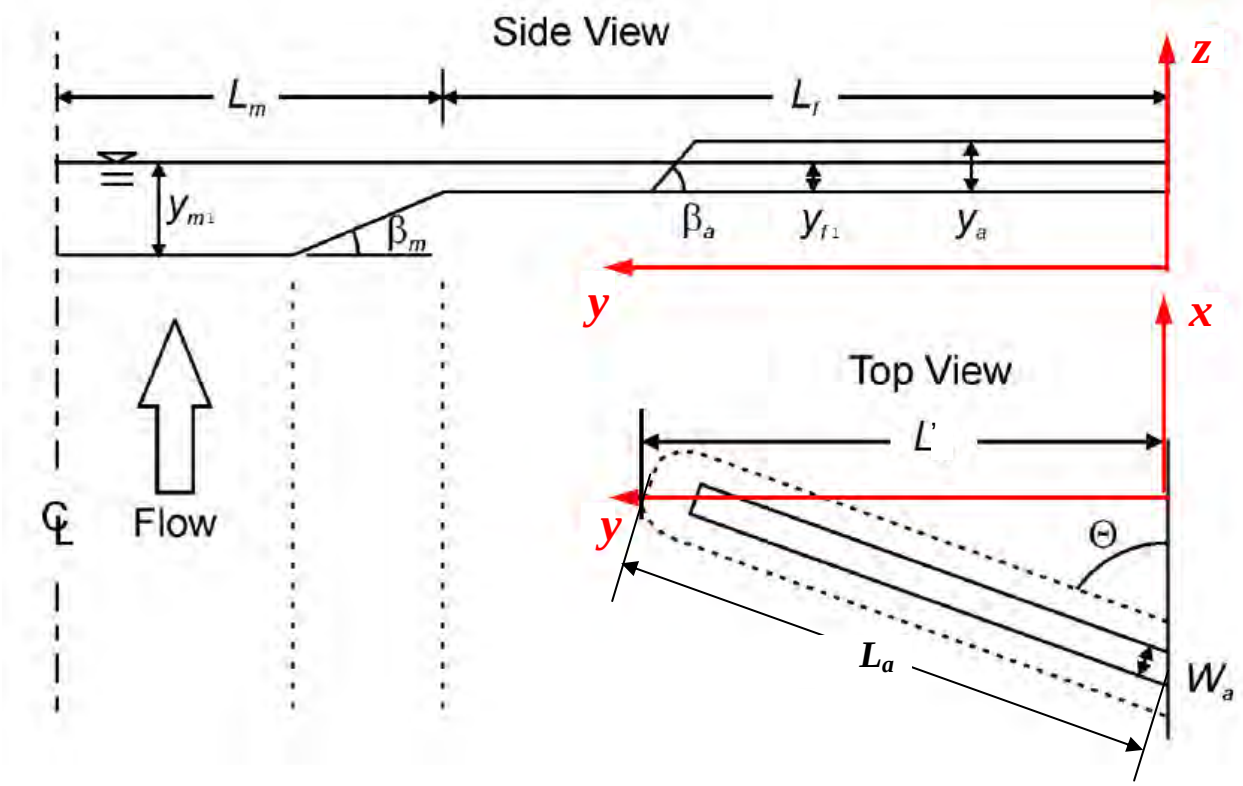

Notes: $\beta_a = 90^o$ for wing-wall shape abutment

Figure 7.20 - Definition of variables and coordinate system.

where L: half width of channel

L': length of embankment projected normal to flow

L_a: length of embankment

L_f: width of flood plain

L_m: half width of main channel

θ: skew angle of approach embankment

$\tan(\beta_a)$: slope of abutment (V:H)

V_1: approaching average velocity

y_{f1}: water depth at the toe of the abutment estimated as the water depth immediately upstream of the toe of the abutment

y_{m1}: approach water depth at main channel

7.3 WATER DEPTH AND VELOCITY MEASUREMENT RESULTS

7.3.1 Water Surface Profiles

The measured streamwise water surface profiles at the beginning of the experiments are shown in Figure 7.21 for all the tests cases in the present study with a compound channel. Note that the test matrix is shown in Table 7.7 and Table 7.8. Case 1 is the reference case while Case 1II is a repeat test of Case 1. All water surface measurement results in the compound channel are compared with that in Case 1 and Case 1II. In Figure 7.21, the variation of water surface profile at the approach section is negligible while the profile at the bridge section becomes more prominent with the increase of velocity and abutment length. The water level becomes stable after the bridge section in all the experiments.

In Figure 7.21(a), the length of abutment was held constant, while both the water depth and velocity were changed to maintain a constant Froude number to study the effect of water depth variation. In Figure 7.21 (b), the length of abutment and approach water depth were kept constant, while the approach velocity was varied to examine the effect of velocity variation. Figure 7.21 (c) shows the water depth profile for different abutment lengths. Figure 7.21(d) and (e) show that the abutment shape and abutment alignment do not have a remarkable effect on the water depth variation if the flow conditions are maintained constant.

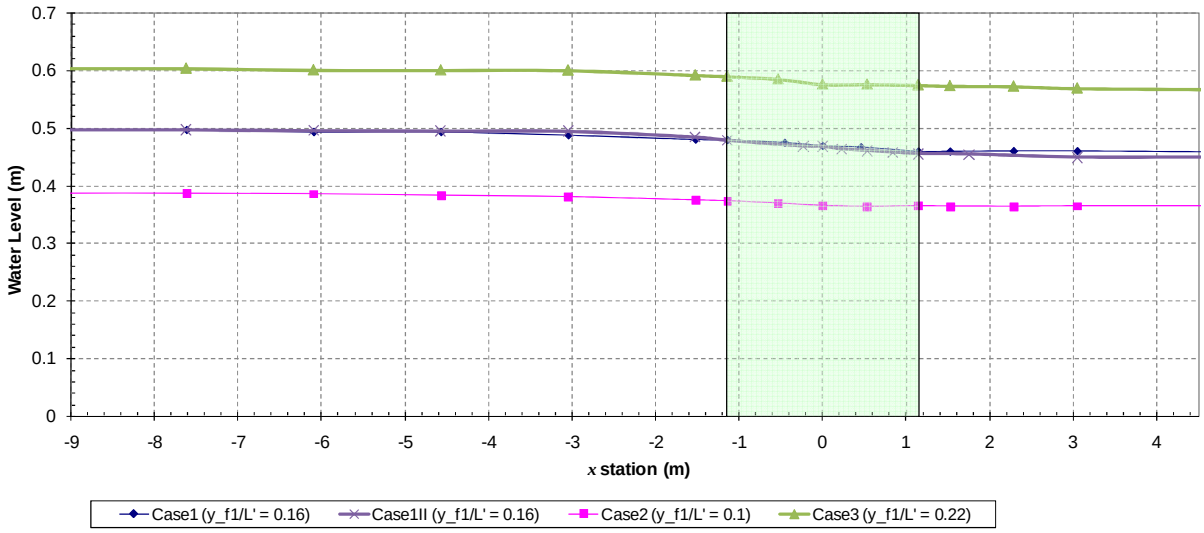

(a) Effect of water depth with the same Froude number and abutment length

Figure 7.21 – Water surface profile in compound channel.

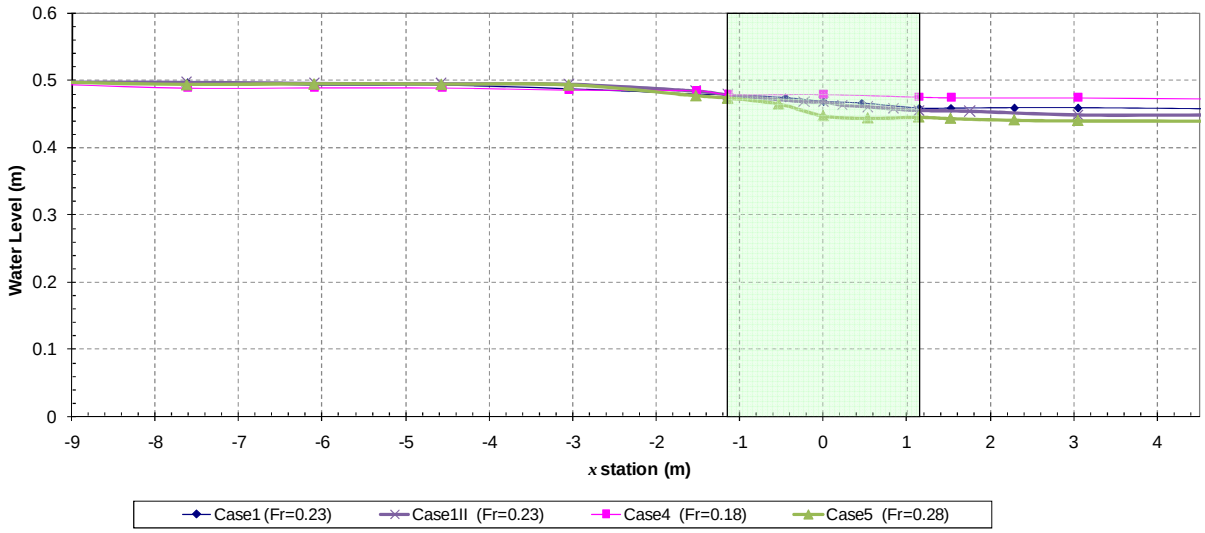

(b) Effect of velocity with the same approach water depth and abutment length

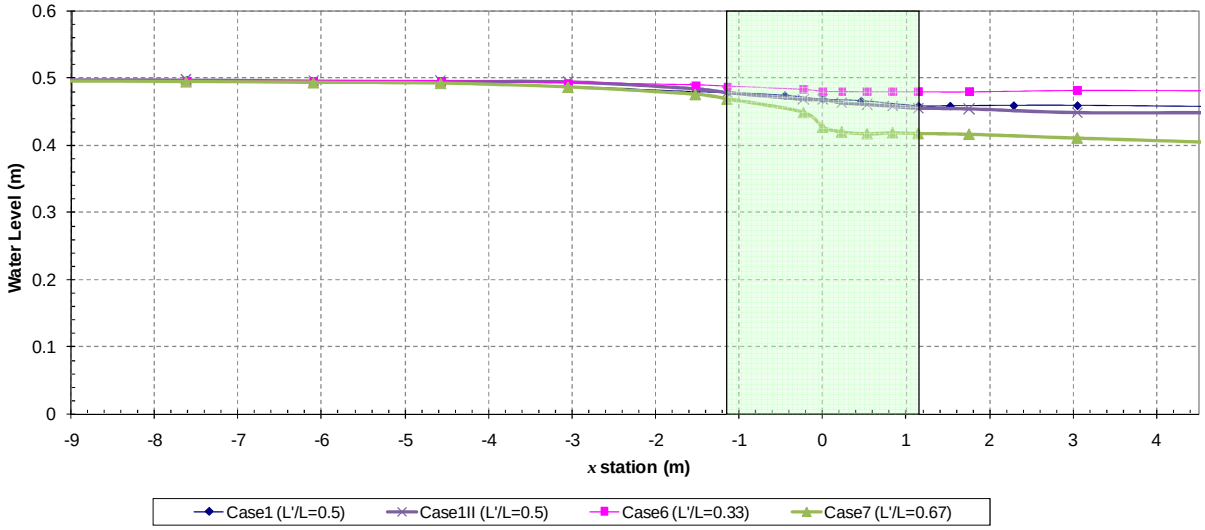

(c) Effect of abutment length with the same flow condition

Figure 7.21 (continued).

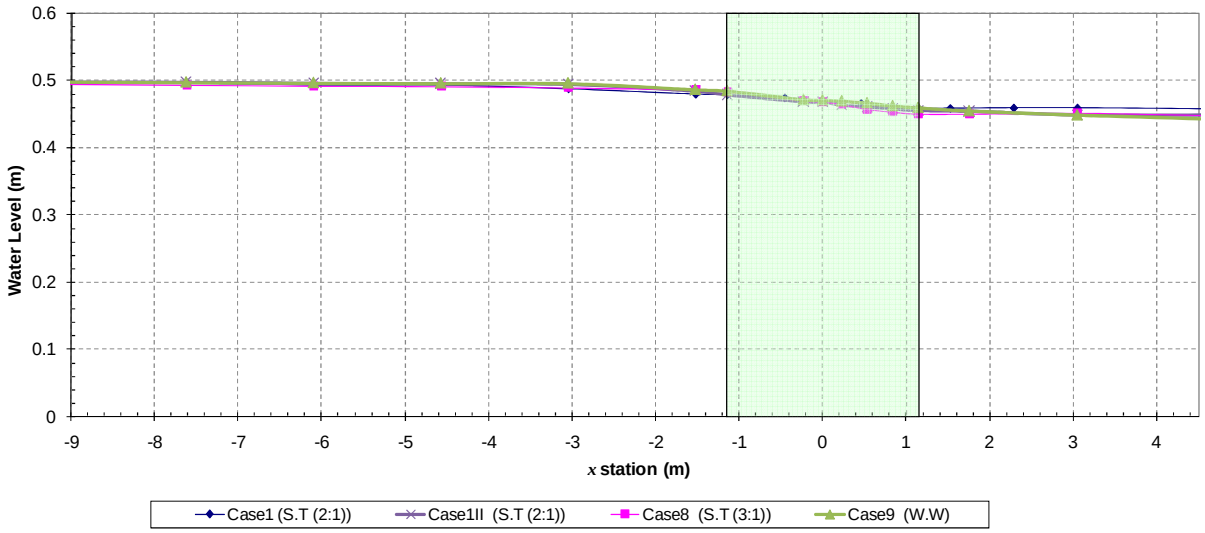

(d) Effect of abutment shape with the same flow condition and abutment length.

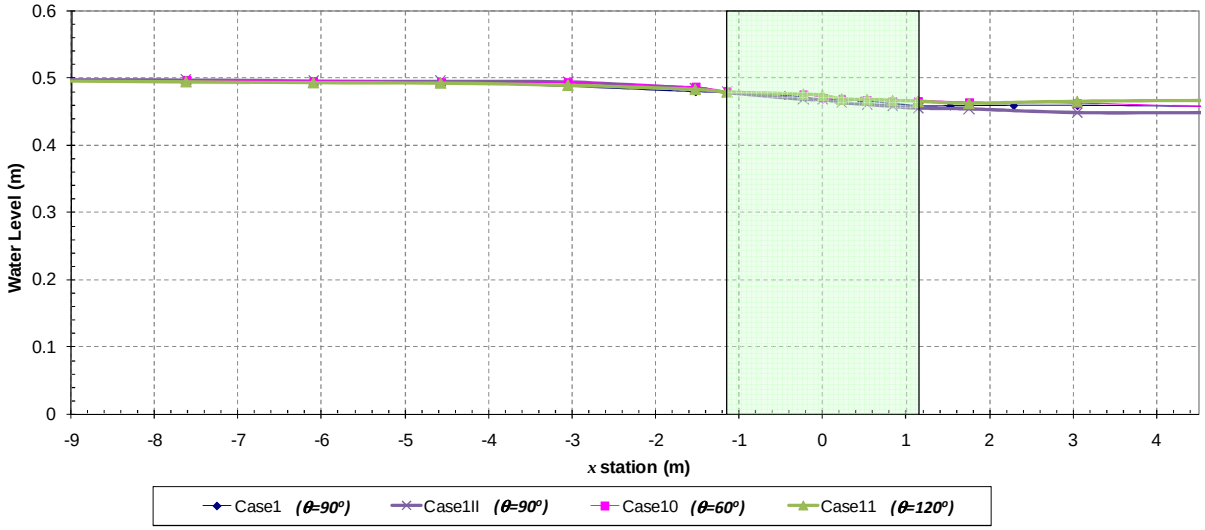

(e) Effect of abutment alignment with the same flow condition and abutment length

Figure 7.21 (continued).

The water surface profile changes as scour develops. The water surface at the approach section (up to x = -1.41 m) was almost constant while scour was progressing, but there were significant changes in the surface elevation after the approach section. The water level after the approach section increased as scour progressed. It finally reached the same level as that of the approach section and reached an equilibrium condition. Figure 7.22 shows the change of water surface profile for Case 1II and Case 7. The water depth at the approach section seems to be a dominant parameter in evaluating the scour depth. However, the approach water depth in a real channel is not constant through the flow direction while it is nearly constant in the flume test. Thus the water depth immediately upstream of the abutment is used to evaluate the clear water scour depth not only for the laboratory tests but also for the real channel.

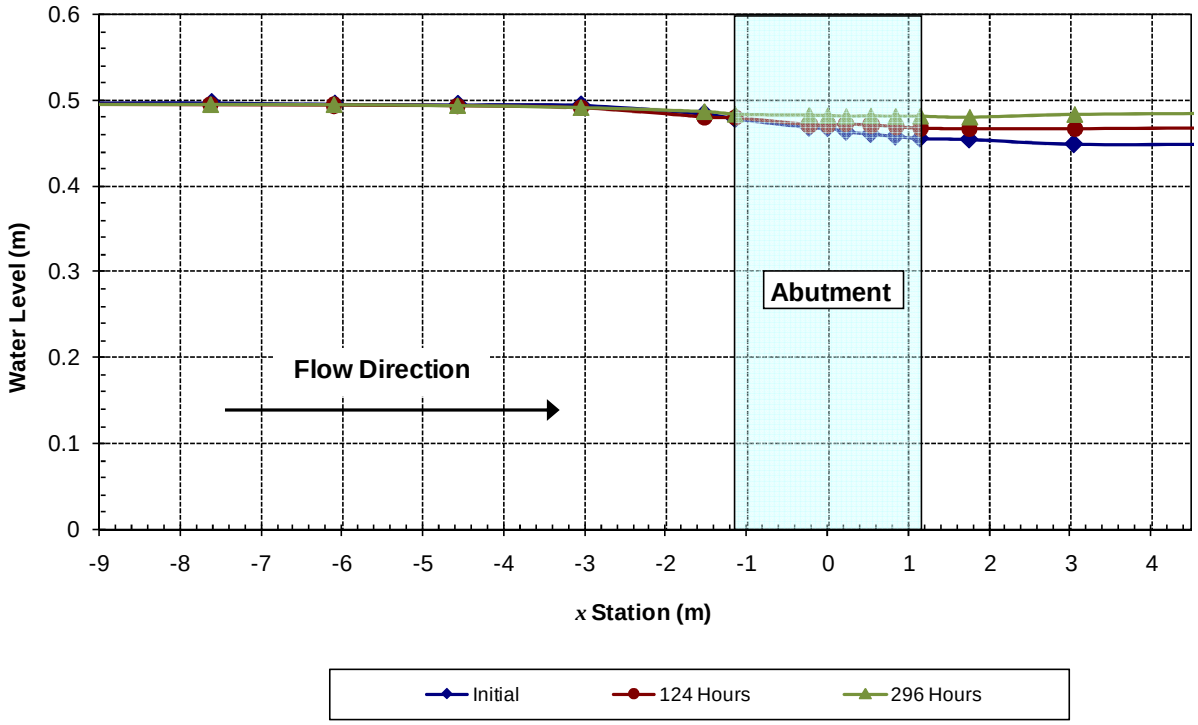

(a) Case 1II

Figure 7.22 – Change of water surface profile with scour development.

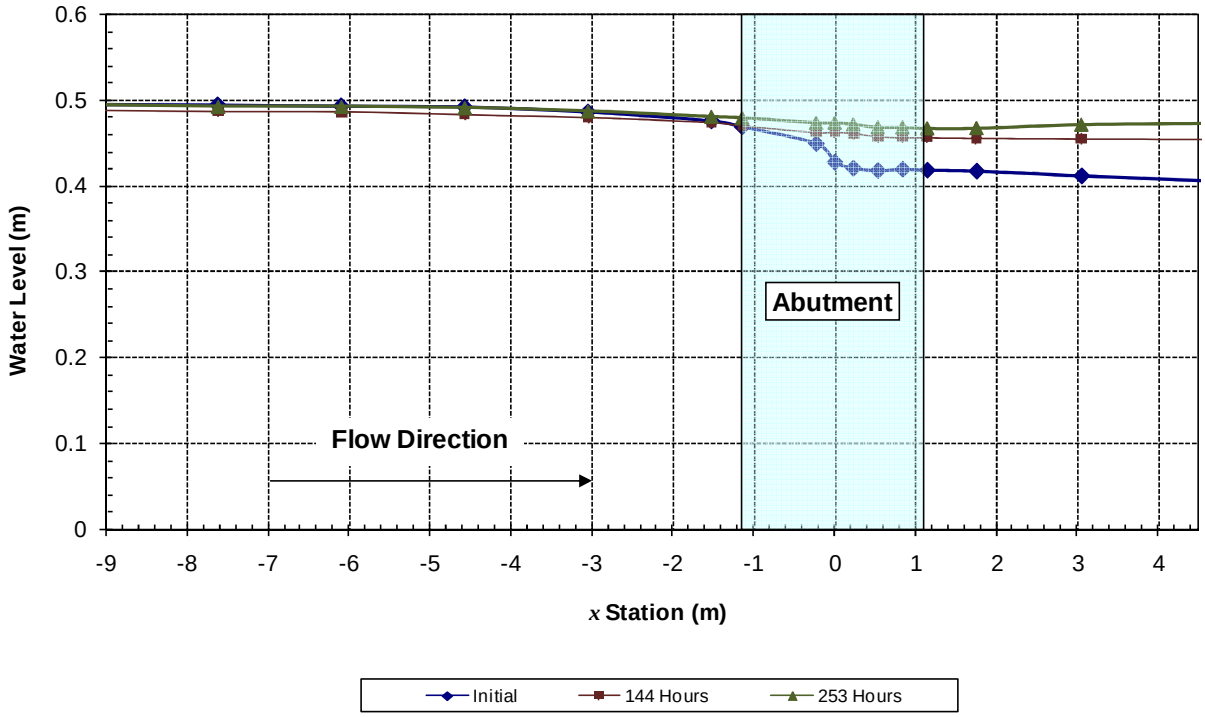

(b) Case 7

Figure 7.22 (continued).

7.3.2 Velocity Distribution

The streamwise velocity distribution in the approach section at the compound channel is shown in Figure 7.23. The main channel velocities are slightly higher than that on the floodplain, and the maximum difference of streamwise velocity between the floodplain and main channel is less than 10% throughout the experiments.

The streamwise velocity in the contracted section along the abutment centerline is shown in Figure 7.24. The maximum velocity is found to be around the toe of the abutment regardless of the shape, the alignment, and the length of the abutment. The ratio between the maximum streamwise velocity and the average velocity in the main channel is found in the range between 1.04 and 1.17 from the flume test results. Figure 7.25 shows the pattern of time averaged velocity distribution of Case 1II. The color indicates the magnitude of the velocity, and the arrows show the direction and magnitude of the velocity (V_x and V_y). The maximum velocity occurs downstream from the abutment and close to the flume wall near the center of the channel (only one-half of the channel is modeled). The downstream velocity decreases with the scour development.

TI (turbulence intensity) is calculated in this study and is expressed as:

$$TI = \sqrt{\sigma_x^2 + \sigma_y^2 + \sigma_z^2} \tag{7.30}$$

where σ is the standard deviation of the measured velocity and the subscripts *x*, *y* and *z* are the directions of flow. The coordination system is shown in Figure 7.20.

Figure 7.26 shows the corresponding pattern of turbulence intensity with scour development. The maximum turbulence intensity appears to be around the toe of abutment on the downstream side. The magnitudes of velocity and turbulence intensity decrease with the scour development. The patterns of velocity and turbulence intensity for other cases are displayed in Appendix A.

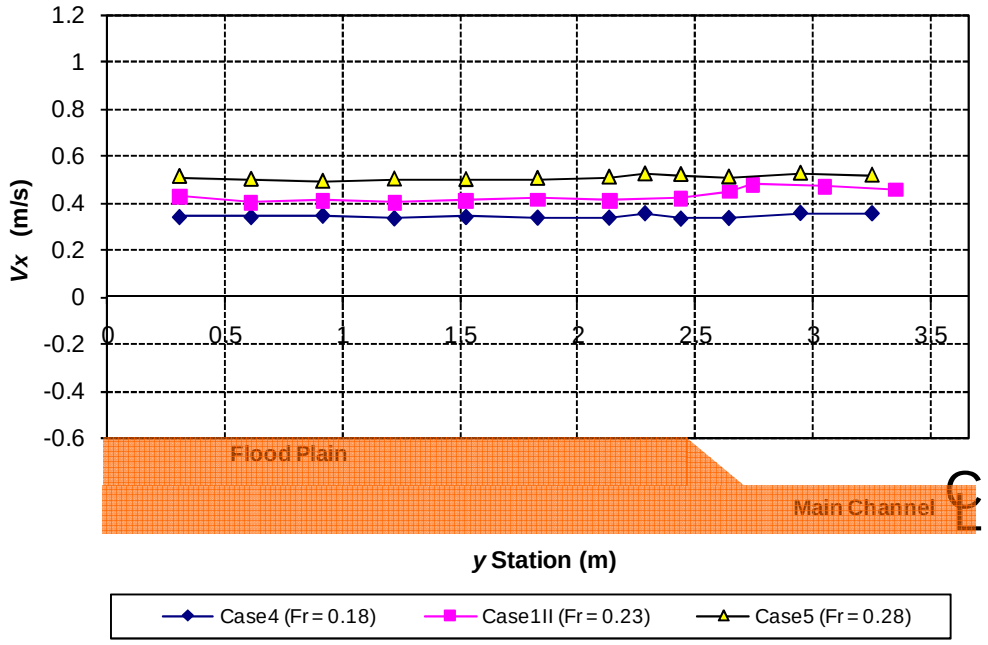

Figure 7.23 – Streamwise velocity distribution at approach section.

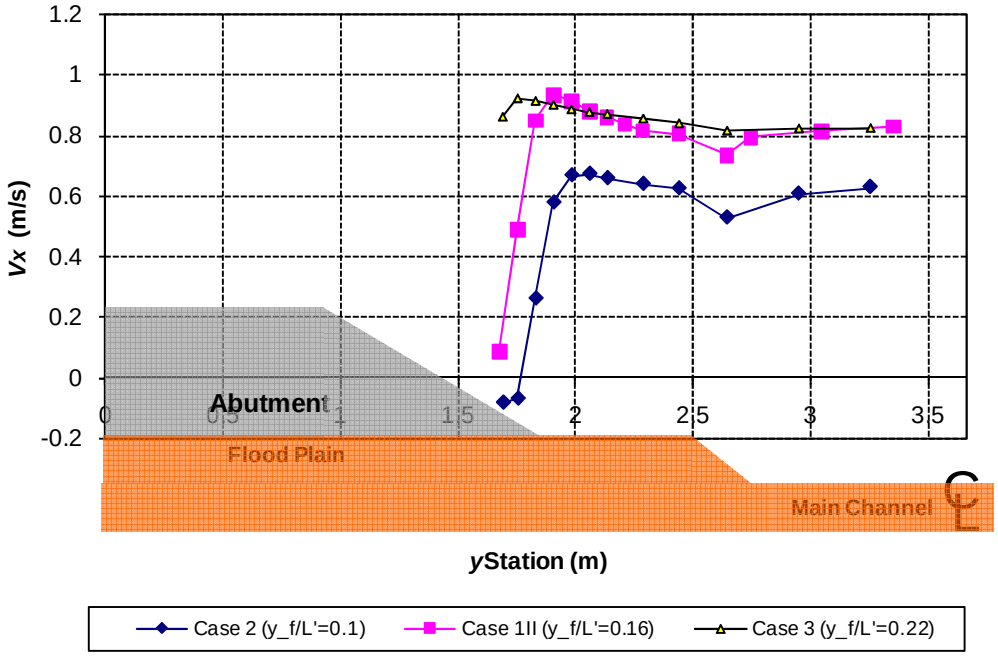

(a) Effect of water depth with the same Froude number and abutment length

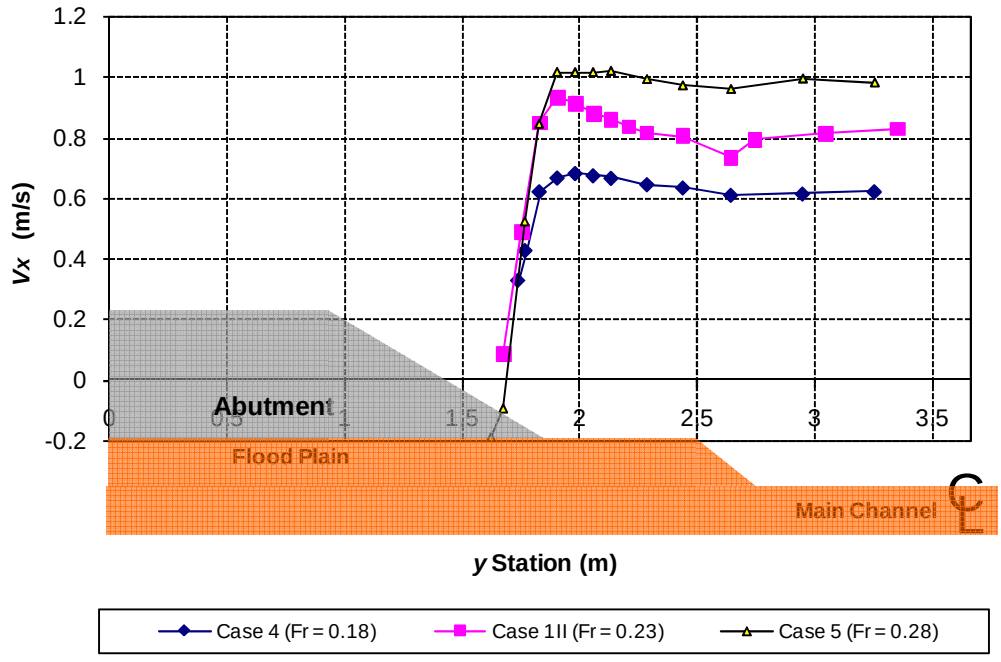

(b) Effect of velocity with the same approach water depth and abutment length

Figure 7.24 – Streamwise velocity distribution in the contracted section along the abutment centerline.

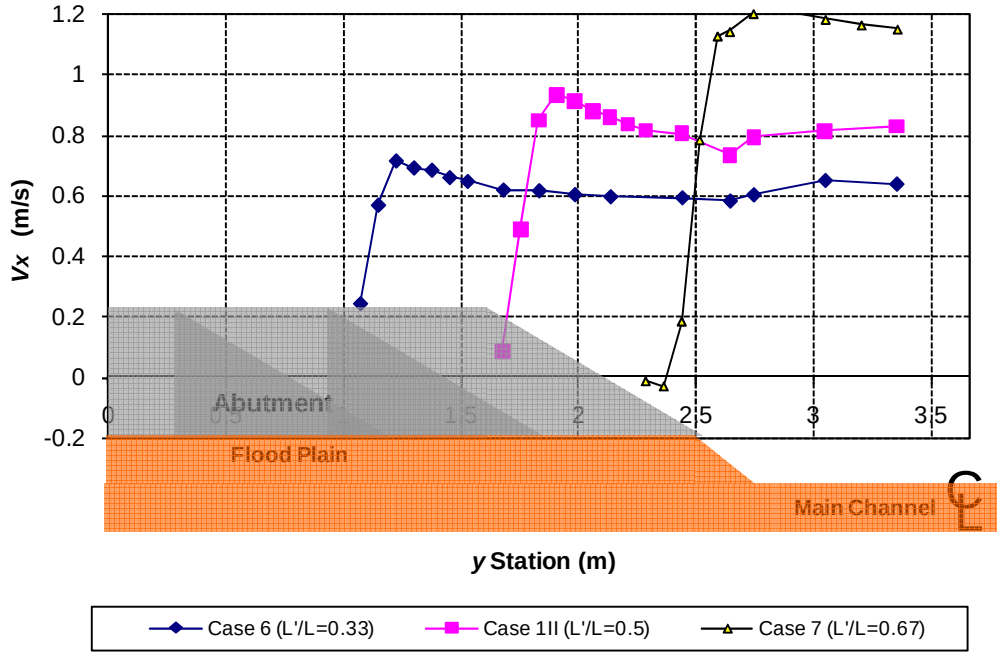

(a) Effect of abutment length with the same flow condition

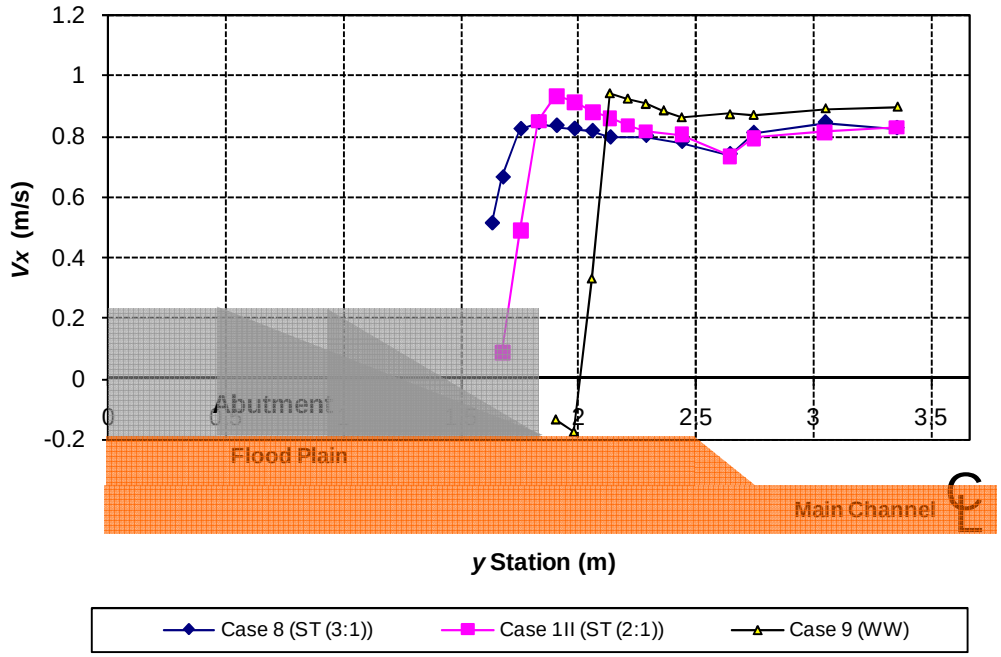

(b) Effect of abutment shape with the same abutment length and flow condition

Figure 7.24 (continued).

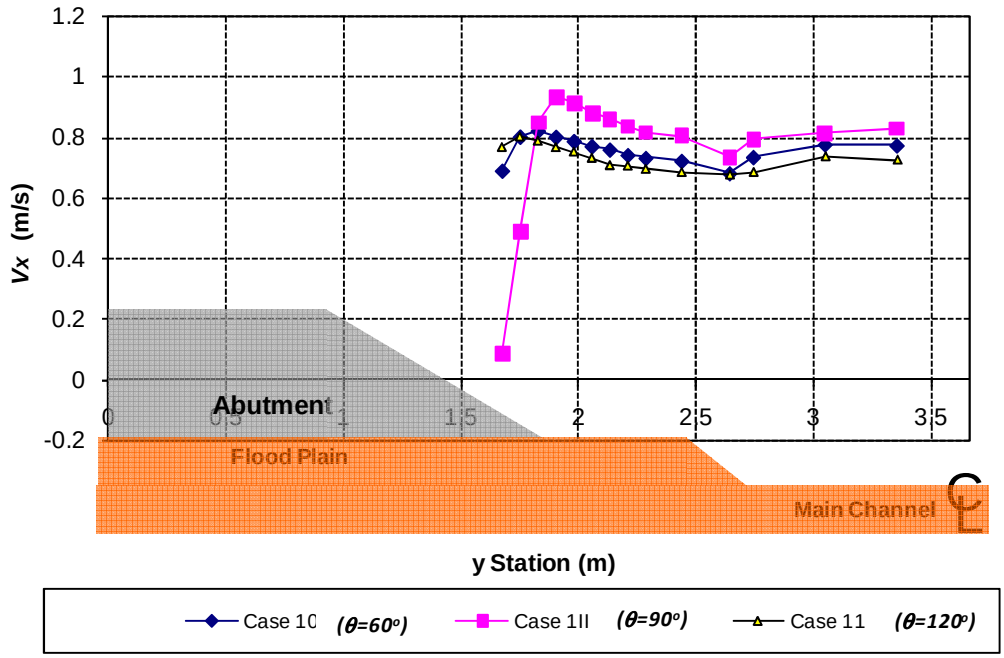

(c) Effect of abutment alignment with the same flow condition and abutment length

Figure 7.24 (continued).

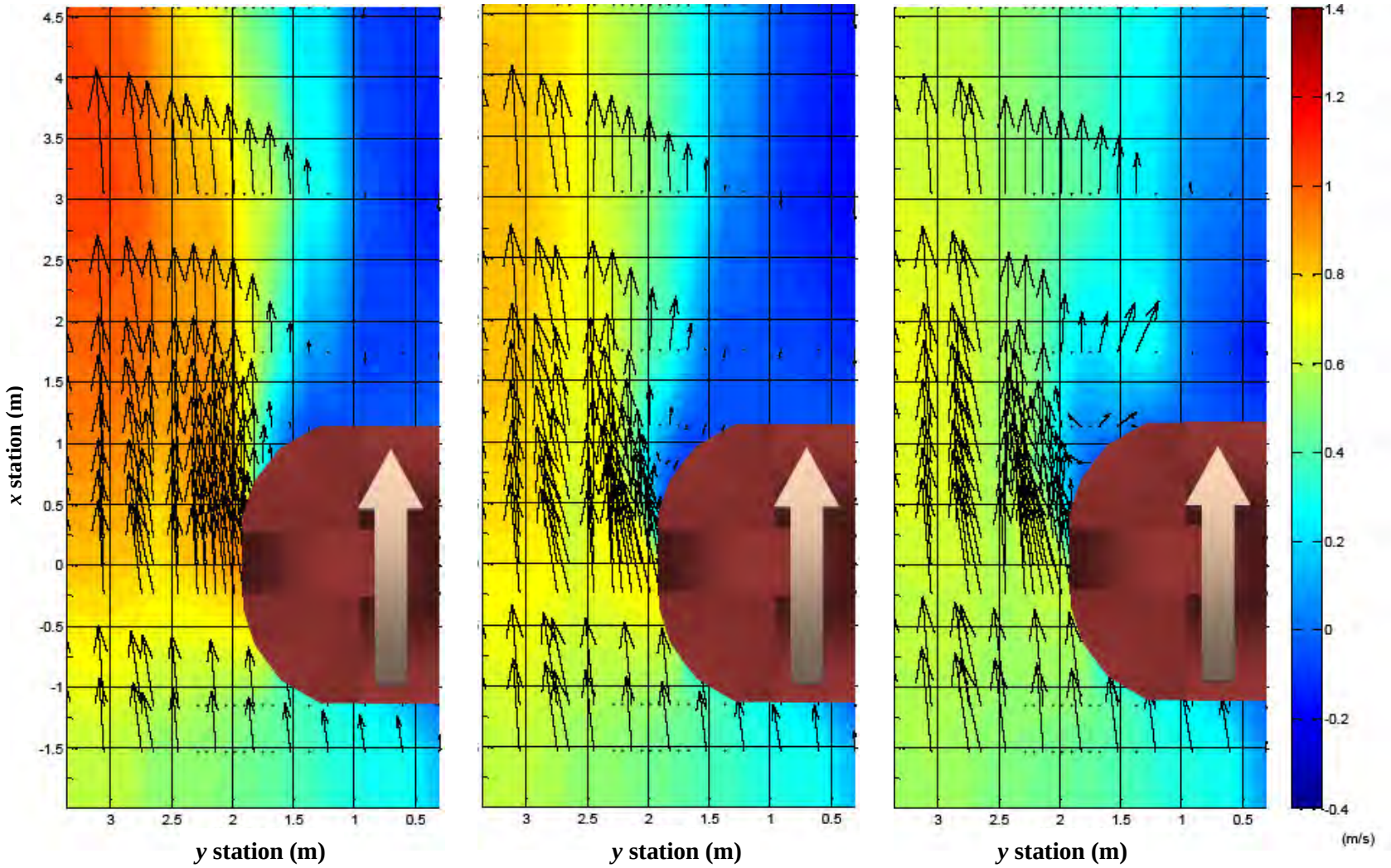

(a) Beginning of experiment (b) After 124 hours (c) After 296 hours

Figure 7.25– Pattern of velocity distribution (Case 1II).

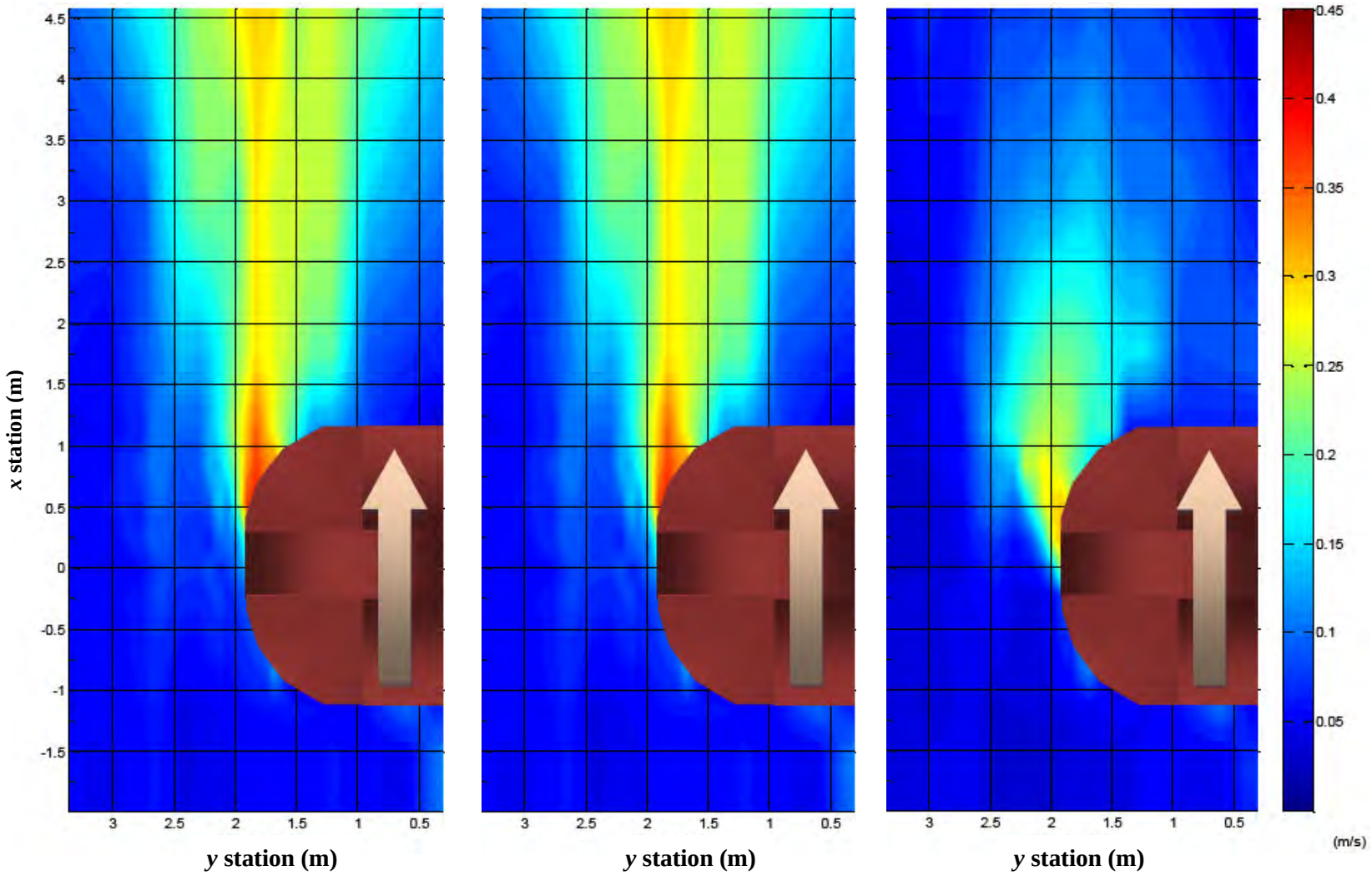

(a) Beginning of experiment (b) After 124 hours (c) After 296 hours

Figure 7.26 – Pattern of turbulence intensity distribution (Case 1II).

7.3.3 Comparison with HEC-RAS Results

Manning's n value is an important parameter in open channel flow, and many researchers have proposed different methods to find Manning's n value using soil particle size and water depth in cohesionless soil. However, those methods are inappropriate for cohesive soils due to its very small particle. For example, the mean diameter of Porcelain clay is 0.035×10^{-3}m and Strikler approximation $\left(n = 0.041 D_{50}^{1/6}\right)$ (after Richardson and Davis, 2001) results in n = 0.0074. This n value is much lower than the minimum value of HEC-RAS recommendation, which is 0.011.

To compare with HEC-RAS results, the Manning's n value was determined by matching the calculation with the flume test results after several trials. In order to find the best Manning's n value, the water depth was used for the comparison because the HEC-RAS velocity does not agree well with the measurement in the compound channel.
The followings are the steps to find the most appropriate Manning's n value.

(1) Input the geometry data identical to the flume test setup.

(2) Input an arbitrary Manning's n value.

(3) Input the flow data obtained from flume tests.

(4) Run HEC-RAS.

(5) Compare water depth results between the computation and the measurement for the approach section. There is no sudden change of water depth due to the bridge contraction. x = -5 m according to the flume tests.

(6) Change the Manning's n value but make sure it is in the reasonable range (referring HEC-RAS manual) and repeat steps (4) and (5).

(7) Repeat step (6) until the computed result matches the measurement.

The best Manning's n value is 0.011 after performing the steps above. This value is the minimum value recommended in the HEC-RAS manual for the trowel finished concrete channel. Figure 7.27 is a view of the flume after the setup of Case 7. Figure 7.28 is the channel geometry used in HEC-RAS calculation for Case 7. Figure 7.29 shows an example of the water depth change comparison between the measurement and the HEC-RAS calculation with different Manning's n values.

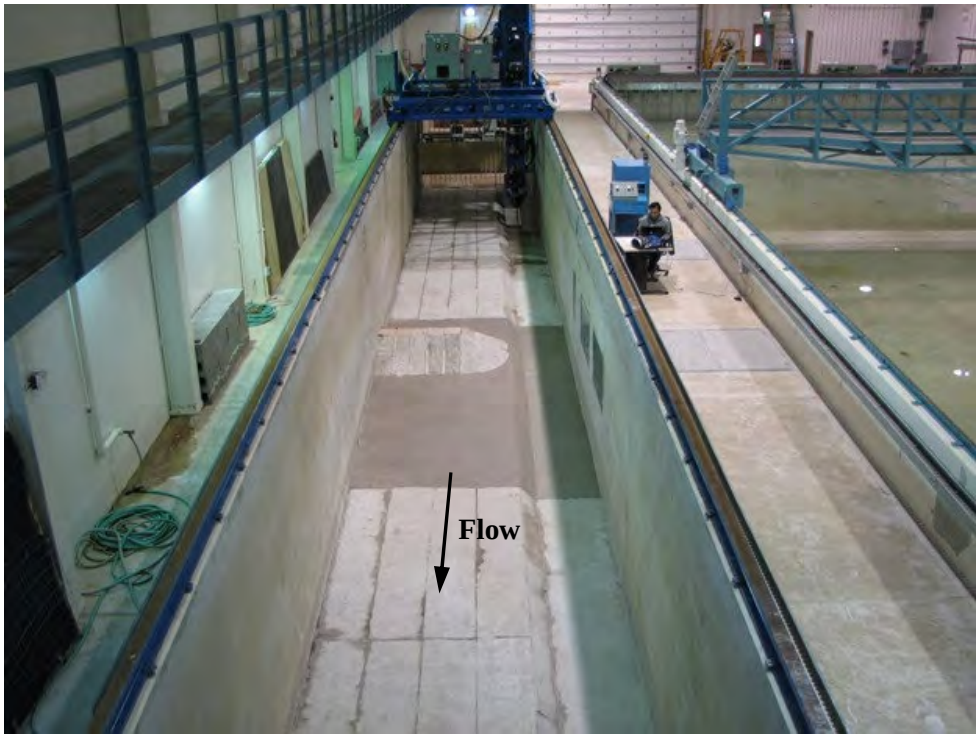

Figure 7.27– View of flume after setup (Case 7).

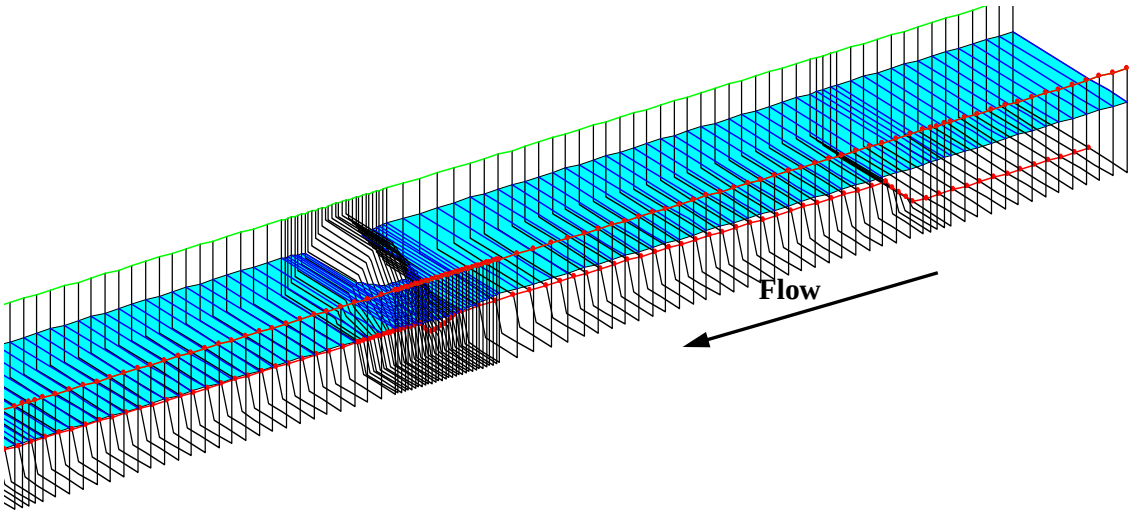

Figure 7.28– Channel geometry for HEC-RAS calculation (Case 7).

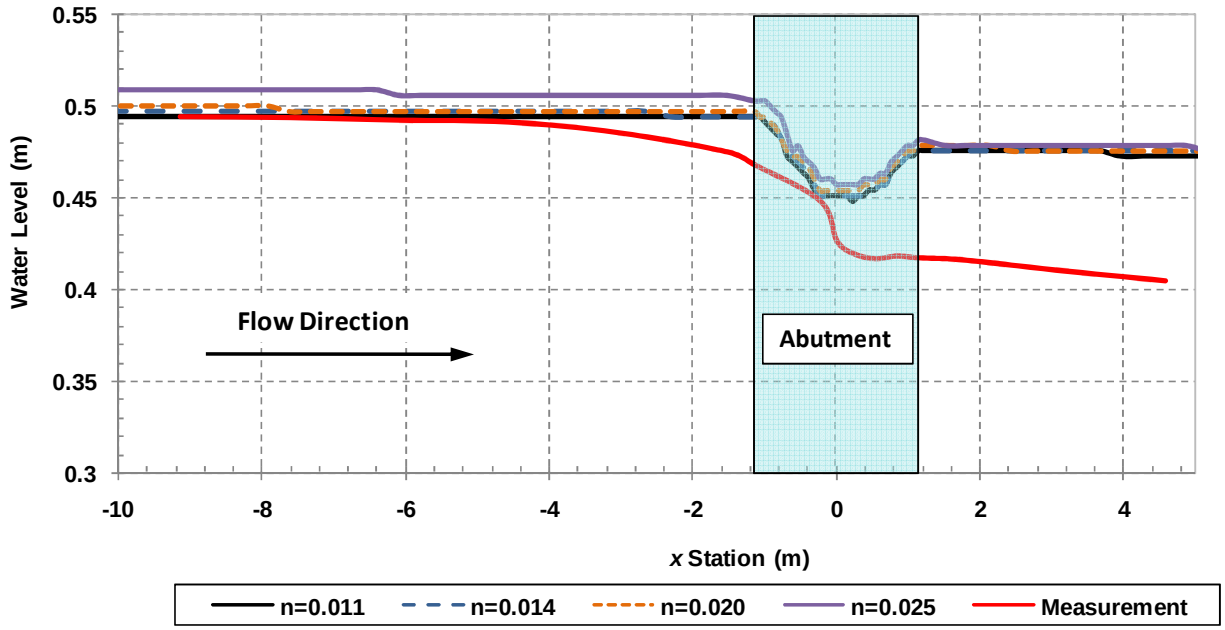

Figure 7.29– HEC-RAS water level comparison to measurement with different Manning's *n* values (Case 7).

The water surface profiles and velocity distributions calculated by HEC-RAS are compared with the laboratory test results. The calculated water surface profiles are compared with the measurement results for the same experimental conditions as shown in Figure 7.30. The profiles at the approach section (up to x = -1.43 m) calculated by HEC-RAS are almost constant in all test conditions, while smoothly decreasing water surface profiles were measured. The differences between the measurements and calculations increase with an increase in velocity and abutment (embankment) length. The maximum difference of water surface elevation between the HEC-RAS calculation and the measurement for all the test cases at x = -1.43 m (the section right before bridge contraction) is around 6%. The computed water surface decreases suddenly at the bridge section and then returns back to a level close to the approach water surface at the downstream side. On the contrary, the measured water level decrease does not recover after the bridge section.

The calculated and measured streamwise velocity distributions at the approach section (x = -9.1 m) and at the middle of the bridge section are also compared and shown in Figure 7.31 and Figure 7.32, respectively. The calculated velocity distribution at the approach section in the floodplain matches the measurement well but the agreement does not occur in the main channel. The calculated velocity in the main channel is consistently 20% to 25% higher than the calculated velocity on the floodplain. This differs from the fact that the measured velocity in the main channel is no more than 10% higher than that in the floodplain as shown in Figure 7.31. The averaged values of streamwise velocities at the approach section on the floodplain obtained by measurements and HEC-RAS calculation were compared and shown in Figure 7.33. Again, the HEC-RAS calculation under predicts the velocity on the floodplain and over predicts the velocity in the main channel at the approach section.

In Figure 7.33, the HEC-RAS calculated velocity at the bridge section agrees reasonably well with the measurement taken in the main channel. However, the calculated velocity on the floodplain where the maximum value was measured under predicts the measurements. The HEC-RAS velocity calculation in the main channel at the bridge section is consistently higher than that on the floodplain. The reverse is true for measurements.

In order to determine the Manning's coefficient which would best match the flume experiments, HEC-RAS simulation results were compared with the flume test results. After the trials mentioned before, the Manning's *n* value which gave the best agreement between the one dimensional calculations and the flume test results was 0.011. This *n* value will be used in the data analysis section to convert the critical shear stress to the critical velocity using the relationship suggested by Richardson et al. (1995).

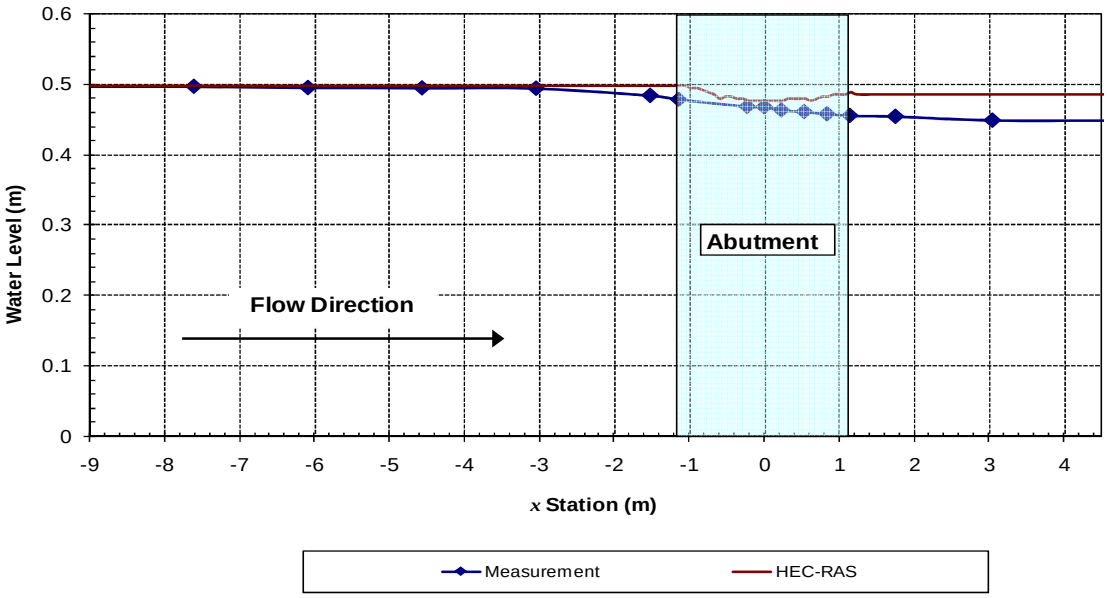

(a) Case 1II (ST abutment, $L'/L_f = 0.75$, $V_1 = 0.44$ m/s)

Figure 7.30 – Measured and HEC-RAS calculated water surface profiles. "ST" indicates spill-through abutment.

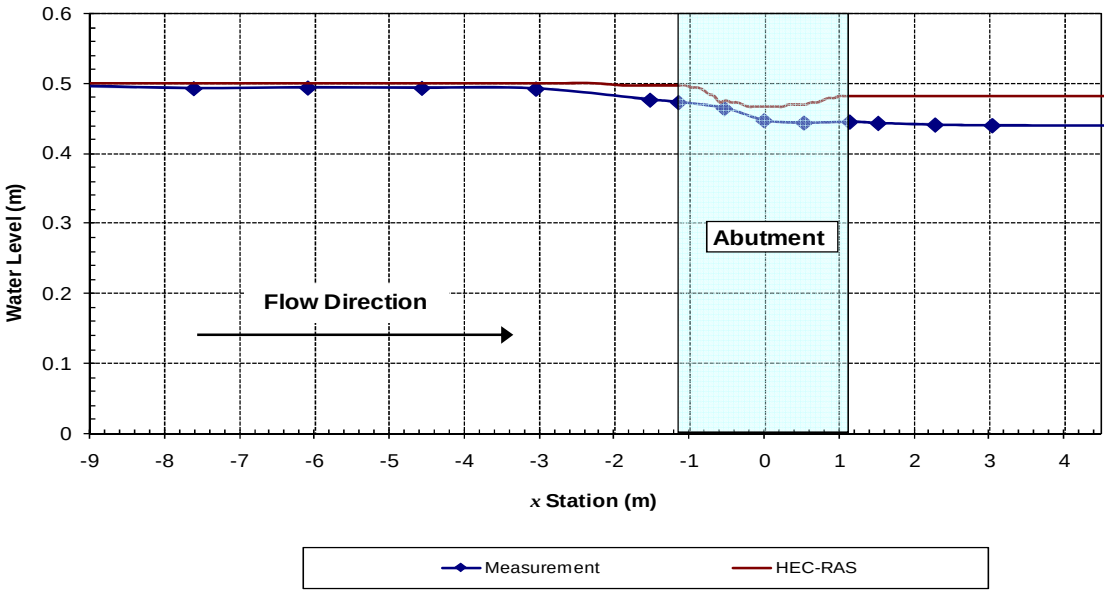

(b) Case 5 (ST abutment, $L'/L_f = 0.75$, $V_1 = 0.51$ m/s)

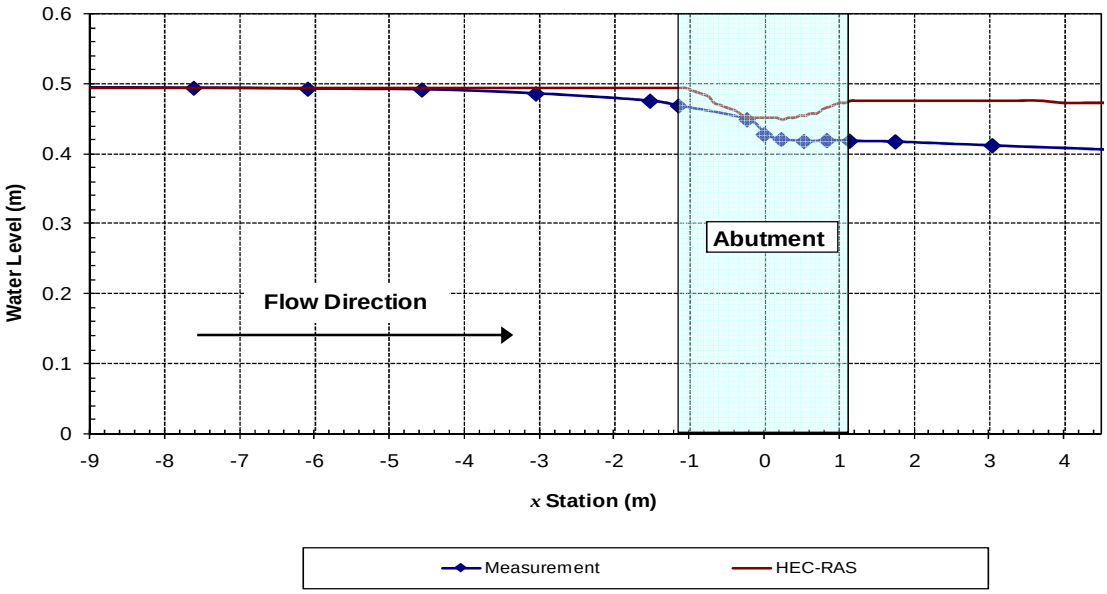

(c) Case 7 (ST abutment, L'/L_f=1.0, V_1=0.44m/s)

Figure 7.30 (continued).

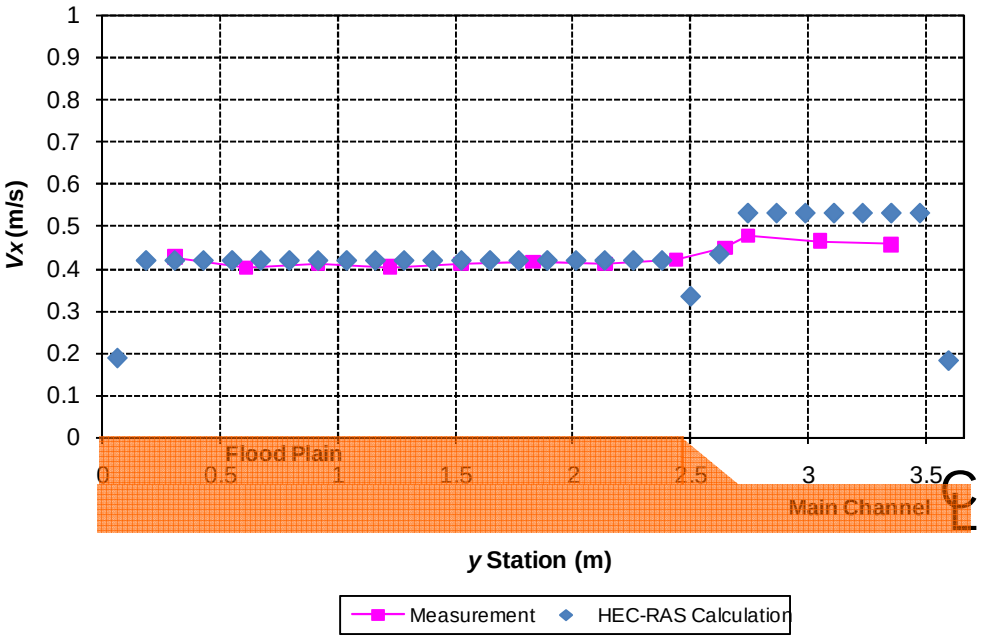

(a) Case 1II (ST abutment, L'/L_f=0.75, V_1=0.44m/s)

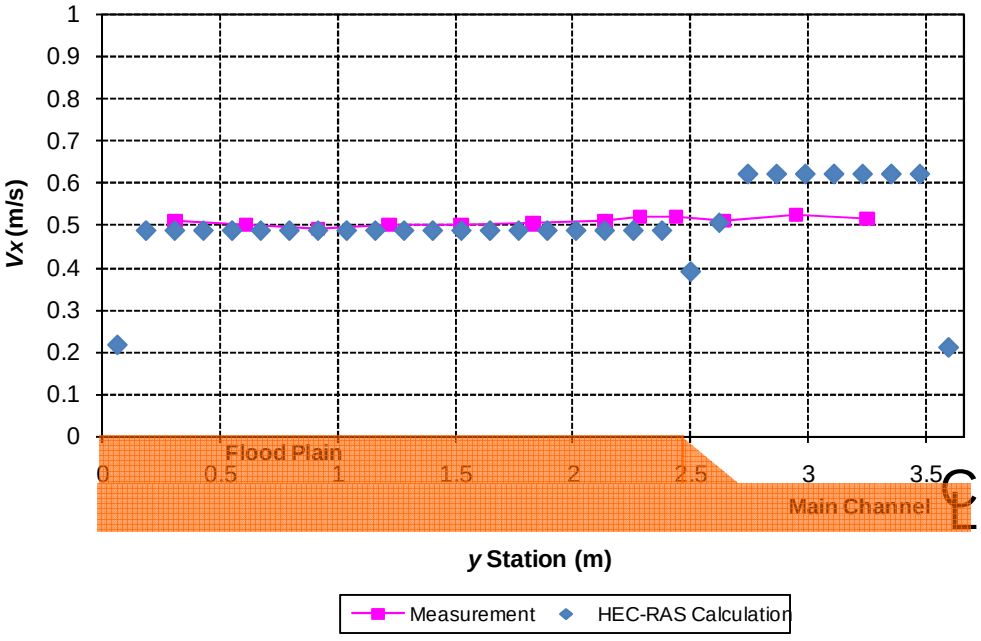

(b) Case5 (ST abutment, L'/L_f=0.75, V_1=0.51m/s)

Figure 7.31– Comparison of velocity distribution at approach section between measurement and HEC-RAS calculation.

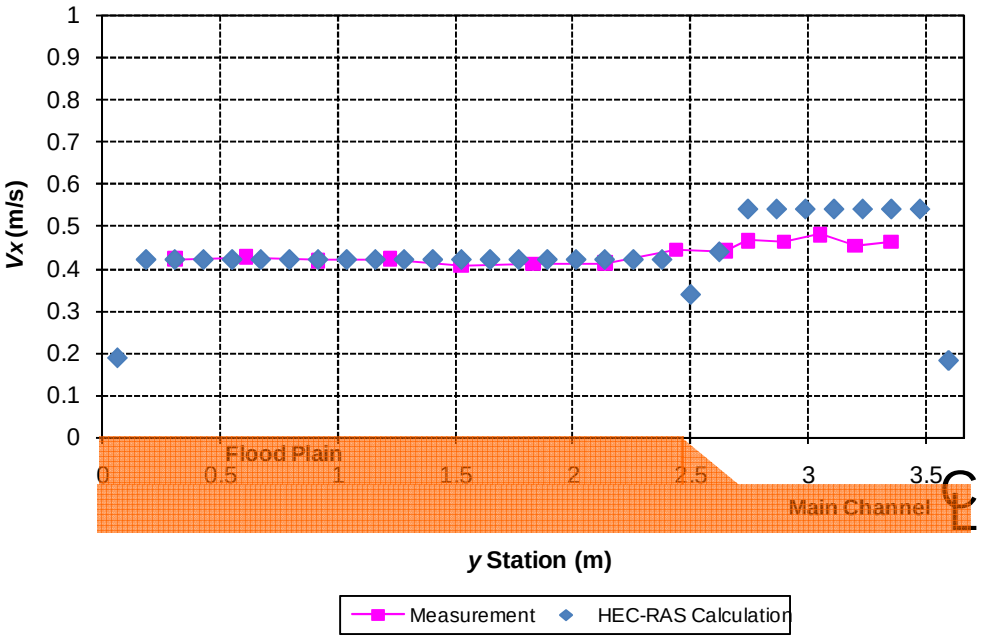

(c) Case7 (ST abutment, L'/L_f=1.0, V_1=0.44m/s)

Figure 7.31 (continued).

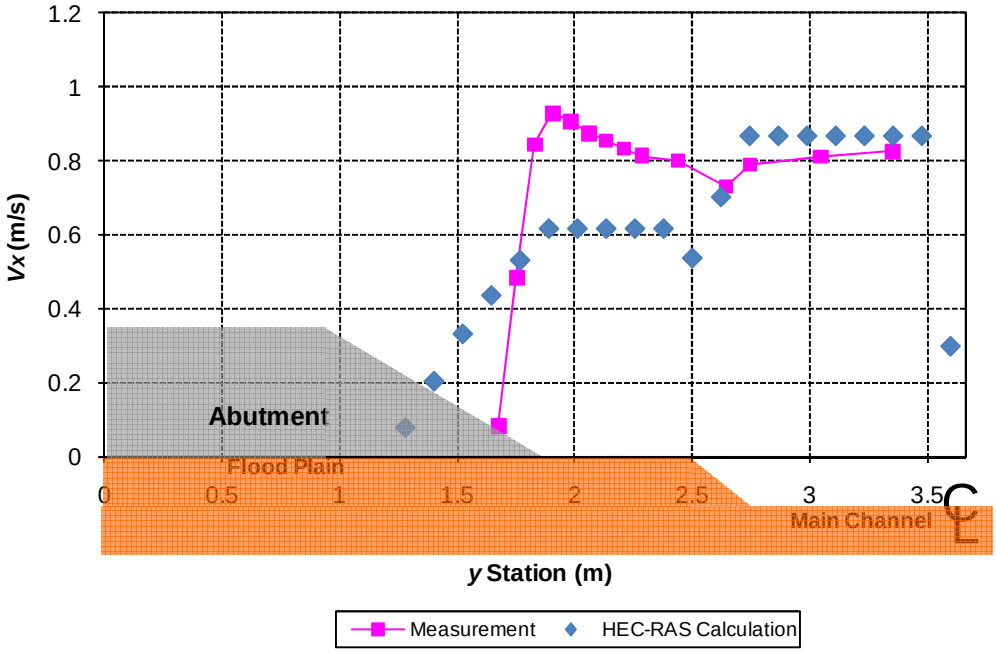

(a) Case1II (ST abutment, L'/L_f=0.75, V_1=0.44m/s)

Figure 7.32 – Comparison of velocity distribution at bridge section between measurement and HEC-RAS calculation.

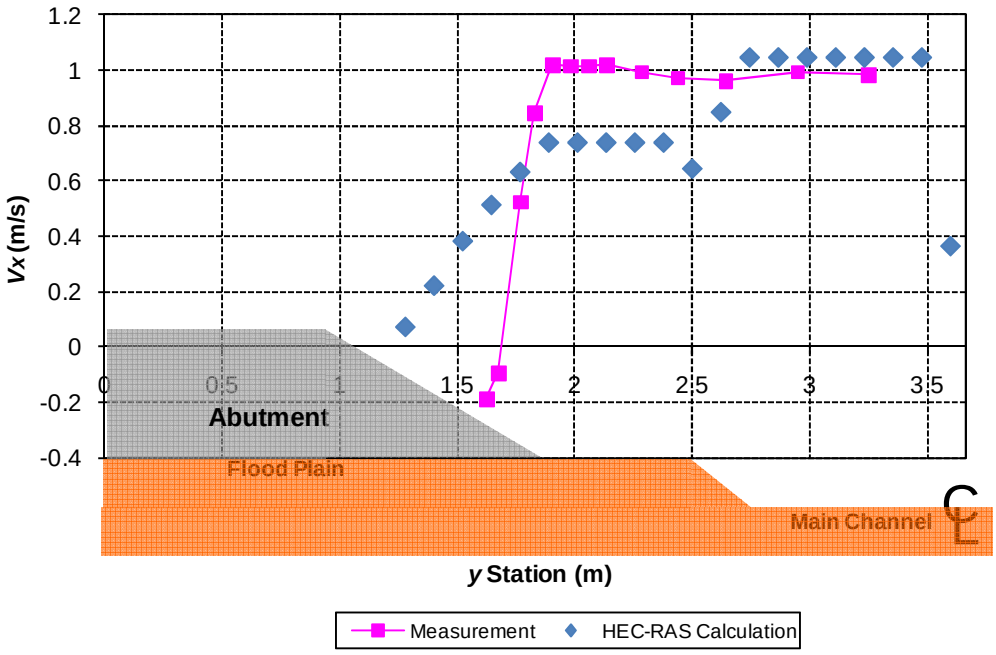

(b) Case5 (ST abutment, L'/L_f=0.75, V_1=0.51m/s)

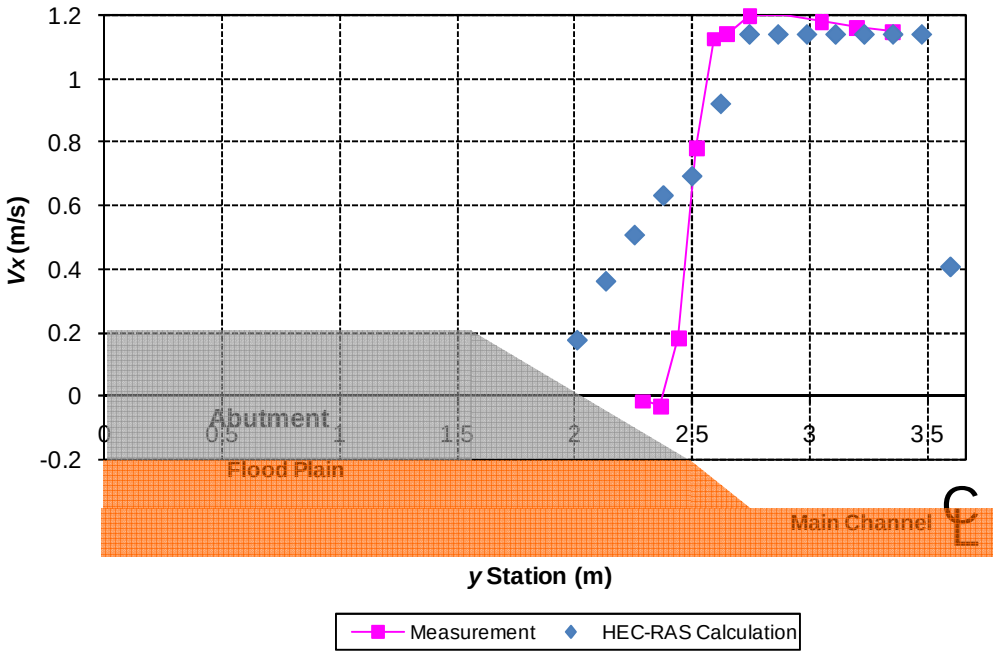

(c) Case7 (ST abutment, L'/L_f=1.0, V_1=0.44m/s)

Figure 7.32 (continued).

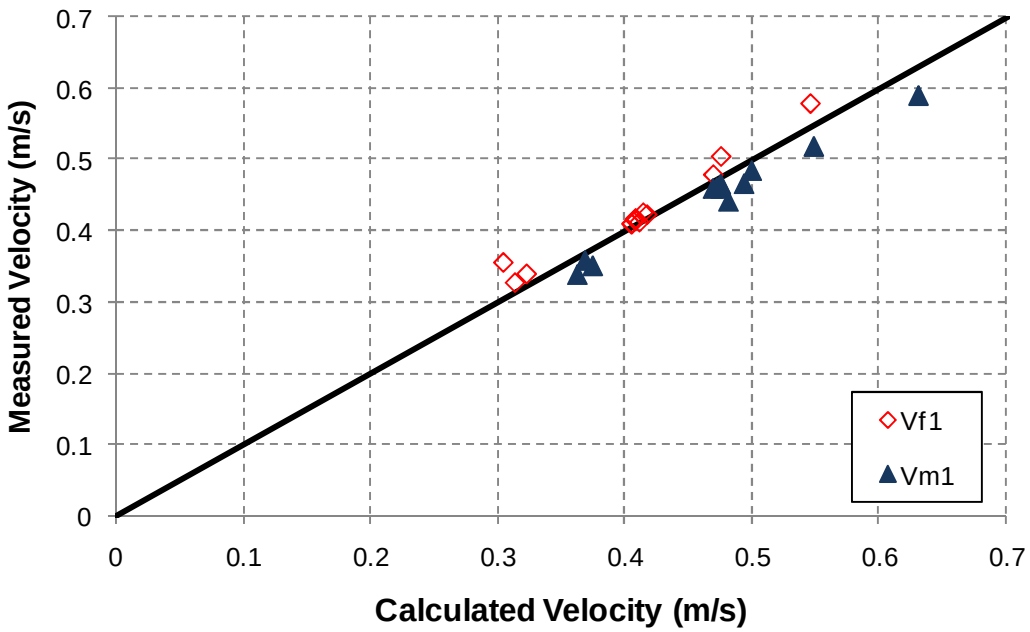

Figure 7.33 – Comparison of average streamwise velocity at approach section (at y = -9.1m) on the floodplain and in the main channel between measurement and HEC-RAS calculation (V_{f1} is the velocity on the floodplain and V_{m1} is the velocity in the main channel).

7.4 SCOUR DEVELOPMENT

7.4.1 Pattern of Scour

The erosion rate of cohesive soil is much lower than that of cohesionless soil. During the flume tests, the water was very muddy so it is impossible to see the eroded channel bottom. The bed profiler and point gauge (mentioned in Chapter 7.2) were used to scan the channel bottom and locate the deepest scour hole. Each test usually took several days. The interval of measurement in the first 5 days was every 20 hours and then approximately every 44 hours after that. This was done because the scour rate decreases with an increase in scour hole development. Figure 7.34, Figure 7.35 and Figure 7.36 show the channel bottom topography changes for Case 1II ($L'/L_f = 0.75$), Case 6 ($L'/L_f = 0.5$), and Case 7 ($L'/L_f = 1.0$), respectively. Case 7 was stopped after 257 hours of test run while the other cases were stopped after 320 hours because the maximum scour depth of Case 7 at 257 hour test run was almost close to the thickness of the clay layer. Detailed results for all the tests are presented in Appendix B. Figure 7.37, Figure 7.38 and Figure 7.39 show the views of test area before and after the test for Case 1II, Case 6 and Case 7, respectively. The pictures for all the tests are presented in Appendix C.

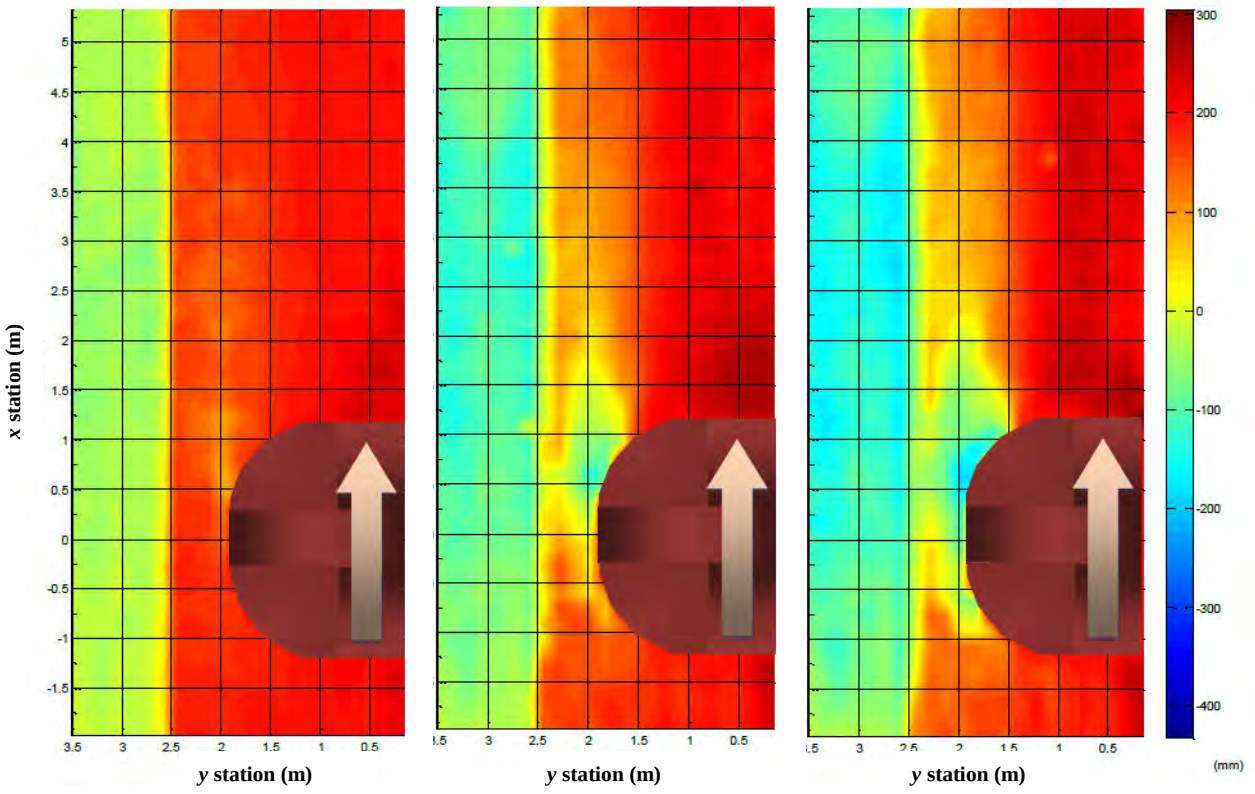

(a) After 60 hours (b) After 189 hours (c) After 320 hours

Figure 7.34 – Evolution of channel bottom topography (Case 1II).

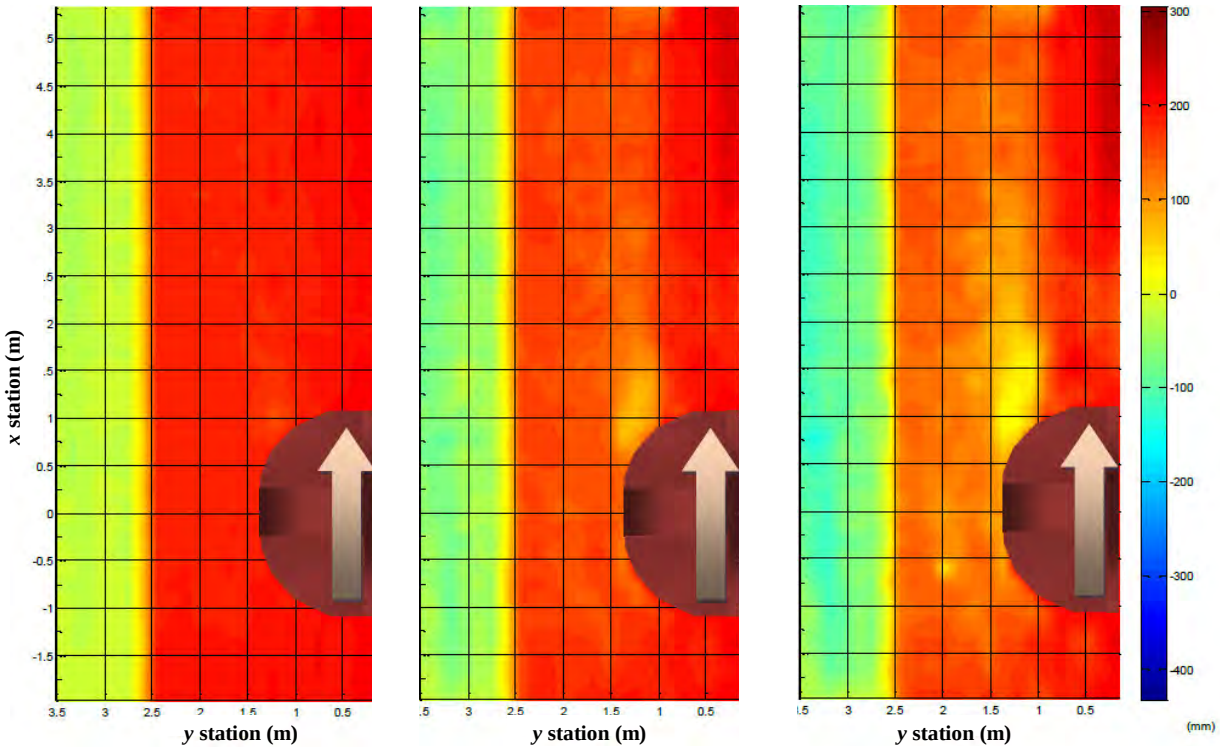

(a) After 60 hours (b) After 188 hours (c) After 320 hours

Figure 7.35– Evolution of channel bottom topography (Case 6).

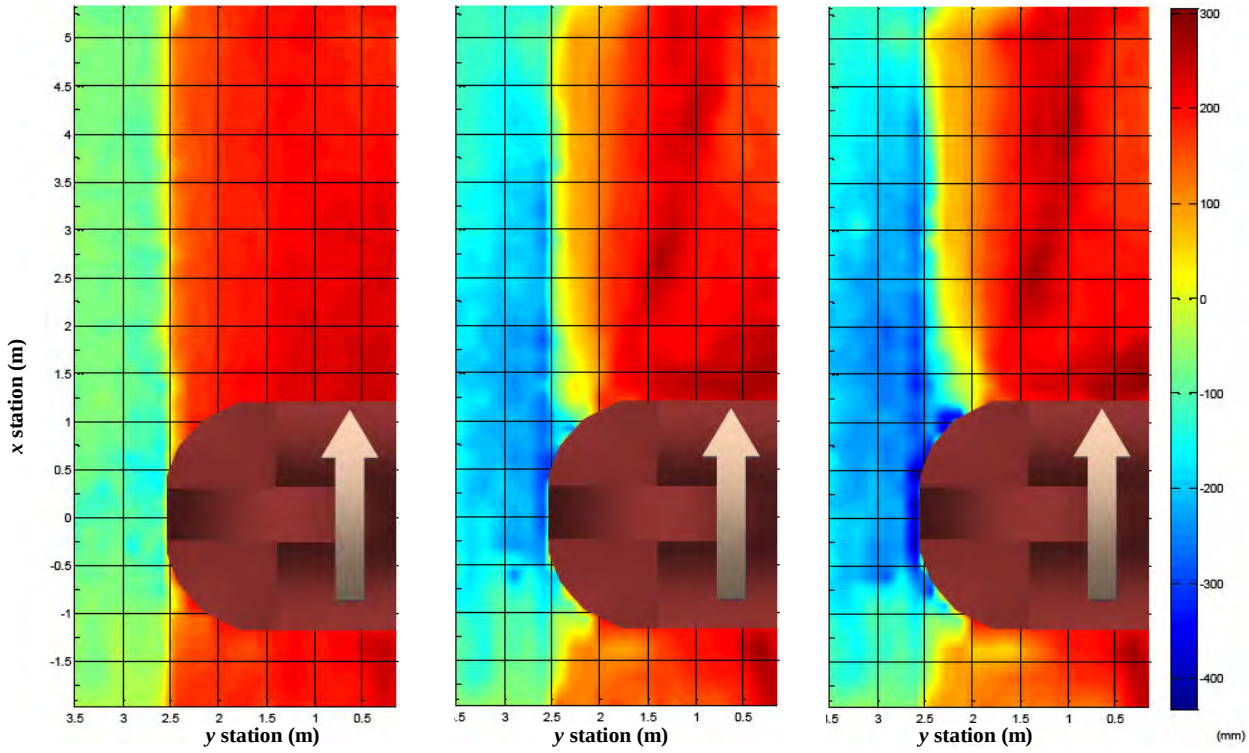

(a) After 60 hours (b) After 188 hours (c) After 257 hours

Figure 7.36– Evolution of channel bottom topography (Case 7).

(a) Before experiment

(b) After experiment (320 hours)

Figure 7.37 – View of test section (Case 1II, $L'/L_f = 0.75$).

(a) Before experiment

(b) After experiment (320 hours)

Figure 7.38 - View of test section (Case 6, $L'/L_f = 0.5$).

(a) Before experiment

(b) After experiment (257 hours)

Figure 7.39 - View of test section (Case 7, $L'/L_f = 1.0$).

The deepest abutment scour hole is usually located around the toe of the abutment but slightly downstream. The deepest contraction scour hole is usually located close to the wall away from the abutment and downstream of the abutment. This means that the deepest contraction scour hole occurred along the centerline of the river. This is consistent with the finding in Briaud et al. (2004) that the maximum contraction scour occurred at the centerline of the main channel if the channel is symmetrical.

Interestingly, the abutment scour pattern is similar to the pattern of *TI* (Turbulence Intensity) and the contraction scour pattern is similar to the time averaged velocity pattern as shown in Figure 7.40. The marked ellipses with dashed lines in that figure indicate the location where the maximum values were measured.

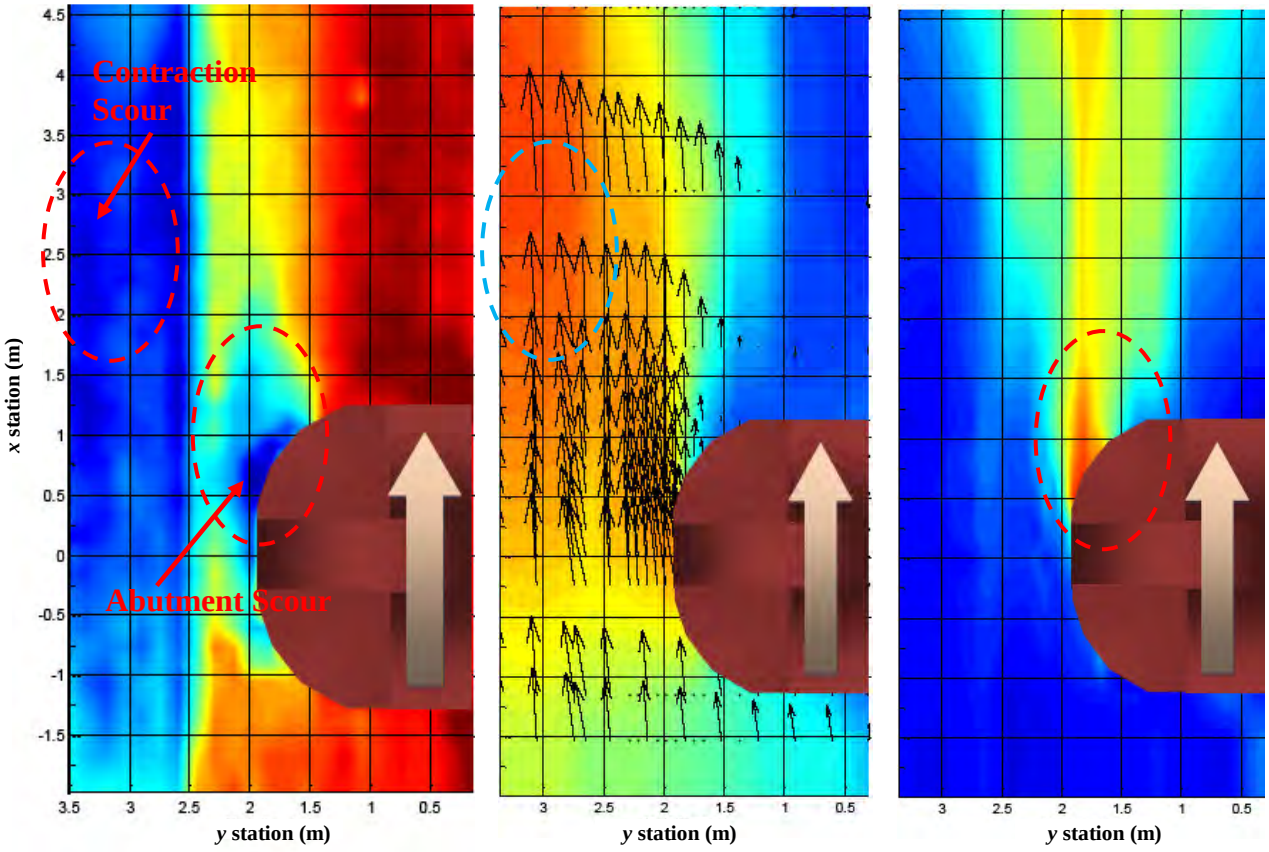

(a) Scour pattern after 320 hours

(b) Initial time averaged velocity

(c) Initial turbulence intensity

Figure 7.40 - Comparisons of scour pattern and velocity pattern (Case 1II).

It is known that a different geometry of abutment will result in a different flow pattern and abutment scour pattern. In the present study, 3 types of abutment, spill-through with a 3(H):1(V) slope, spill-through with a 2(H):1(V) slope, and wing-wall shape, were used to examine the abutment shape effect on the flow pattern and the abutment scour pattern. In addition, 3 types of different abutment alignments, θ=60^o, θ=90^o and θ=120^o, were used with the same discharge and embankment length (L'/L_f=0.75) for a spill-through abutment with a 2(H):1(V) slope.

The flow passing through the bridge section concentrates on the main channel. A steeper slope with a same embankment length induces a more concentration of flow to the main channel. The pattern of turbulence intensity shown in Figure 7.41 indicates that the high turbulence occurred on the floodplain for the spill-through abutment but on the main channel slope for the wing-wall abutment. Accordingly, a longer local scour pattern on the floodplain was observed for the spill-through abutment while a shorter local scour on the floodplain for the wing-wall abutment for the condition of L'/L_f=0.75. In Figure 7.41, the upper panels show the initial turbulence intensity and the lower panels show the channel bottom bathymetry of 3 types of abutments Note that the red dot lines are the slope of main channel. The test running time was 320 hours, 308 hours and 271 hours for Case 8, Case 1II and Case 9, respectively.

The skewed spill-through abutment induced a smoother flow than the abutment normally aligned to the flow. The finding consistent with previous research results for the abutment skewed toward downstream (θ=60^o), however the abutment skewed toward upstream (θ=120^o) the result contradicts to that in previous studies. The opposite result for the abutment skewed toward upstream may come from the shape of abutment because vertical wall abutments were used in previous studies while a spill-through abutment is used in the present study. As shown in Figure 7.42, the spill-through abutment skewed toward upstream induced a relatively smooth flow than the abutment perpendicularly aligned to the flow. The test running time for each case was 320 hours.

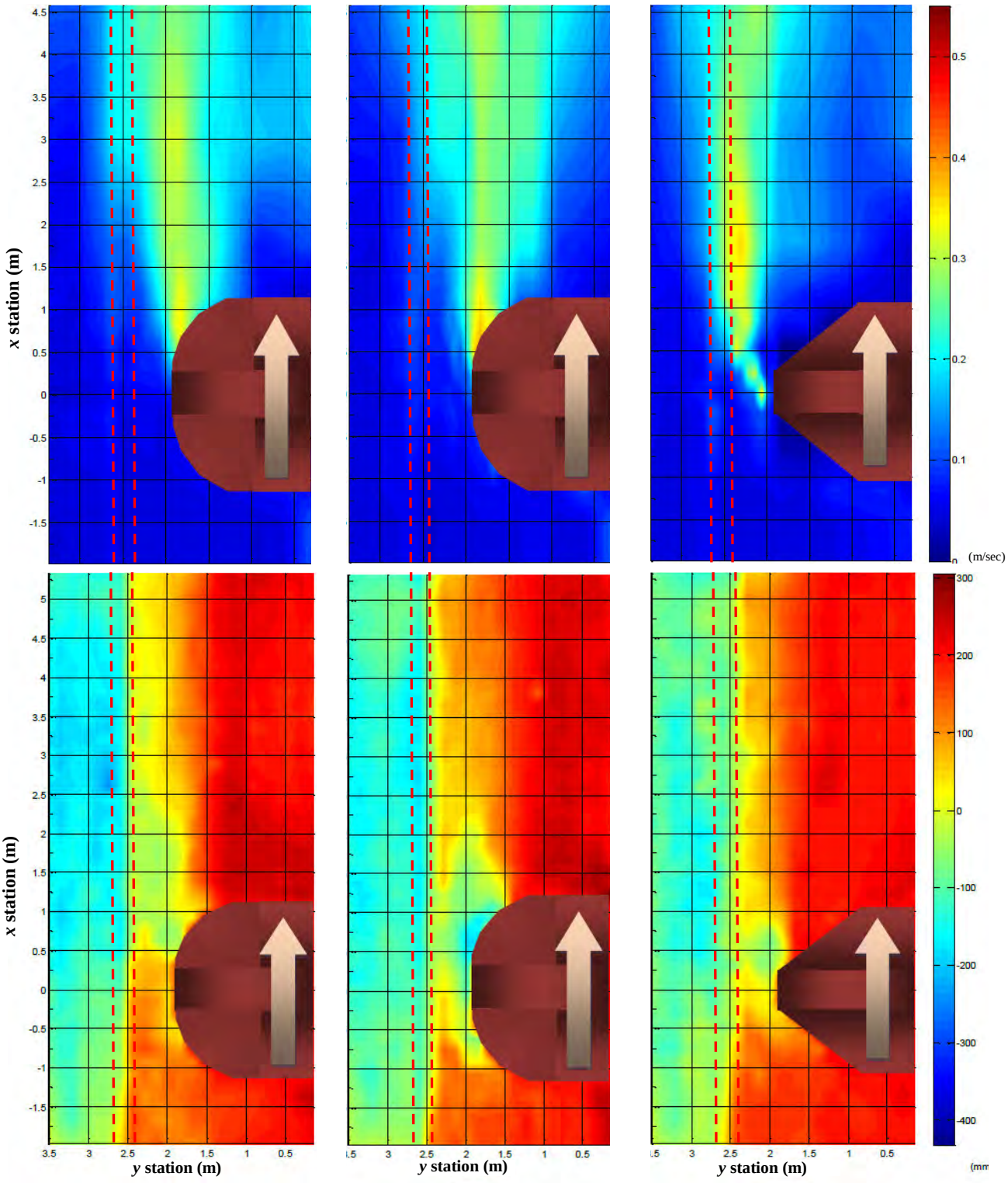

(a) Case 8 - ST (3(H):1(V)) (b) Case 1II – ST (2(H):1(V)) (c) Case 9 - WW

Figure 7.41 - Turbulence intensity (upper panels) and channel bottom bathymetry (lower panels) for different abutment shape.

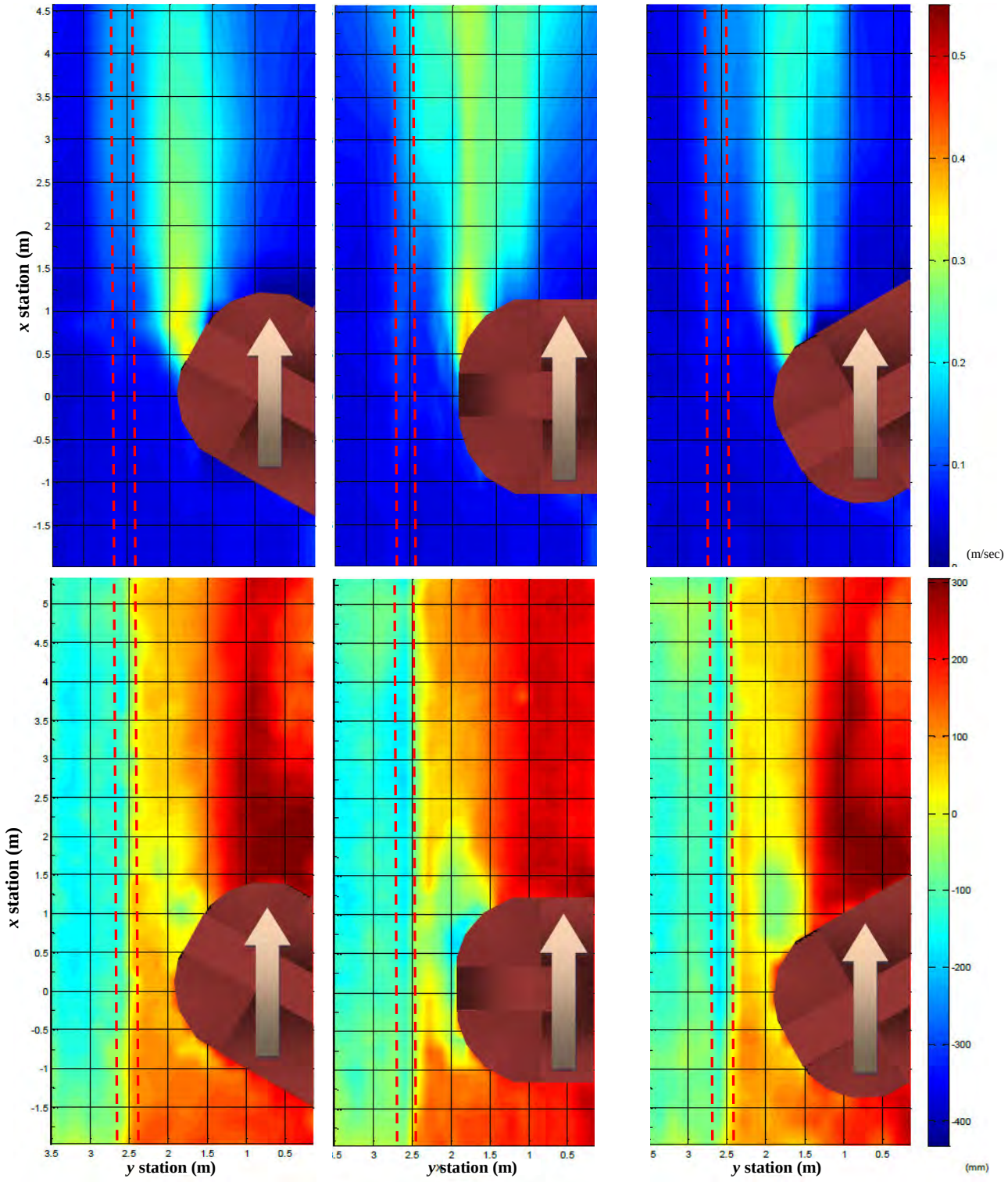

(a) Case 10 - θ=60^o (b) Case 1II - θ=90^o (c) Case 11 -θ=120^o

Figure 7.42 - Turbulence intensity (upper panels) and channel bottom bathymetry (lower panels) for different abutment alignment for spill-through abutment (2(H):1(V)).

The horizontal slope of local scour became steeper with scour development in the rectangular channel as shown in Figure 7.43. This phenomenon was also observed for short embankment in the compound channel as shown in Figure 7.44. However, the development of abutment scour hole became irregular if the local scour hole extended to the main channel slope. In the beginning of experiment the scour became gradually steeper and wider, but it became flatter if the abutment scour hole reached to the main channel slope as shown in Figure 7.45.

The slope of abutment scour hole in cohesive soil is usually steeper than the slope in cohesionless soil because of the existence of cohesion. For cohesionless soil, the slope of scour hole is milder to keep stable until it reaches the angle of repose. A rule of thumb is that the angle of repose is the internal friction angle of loose sand which is between 28^{o} and 30^{o} (Das, 1997). If the channel bottom is composed with loose sand and a symmetrical conical scour hole is assumed, the diameter of abutment scour hole is approximately

$$D = 2y_s / \tan\phi \approx 4y_s \tag{7.31}$$

where D is the diameter of abutment scour hole, y_s is the maximum abutment scour depth, and ϕ is the internal friction angle of soil.

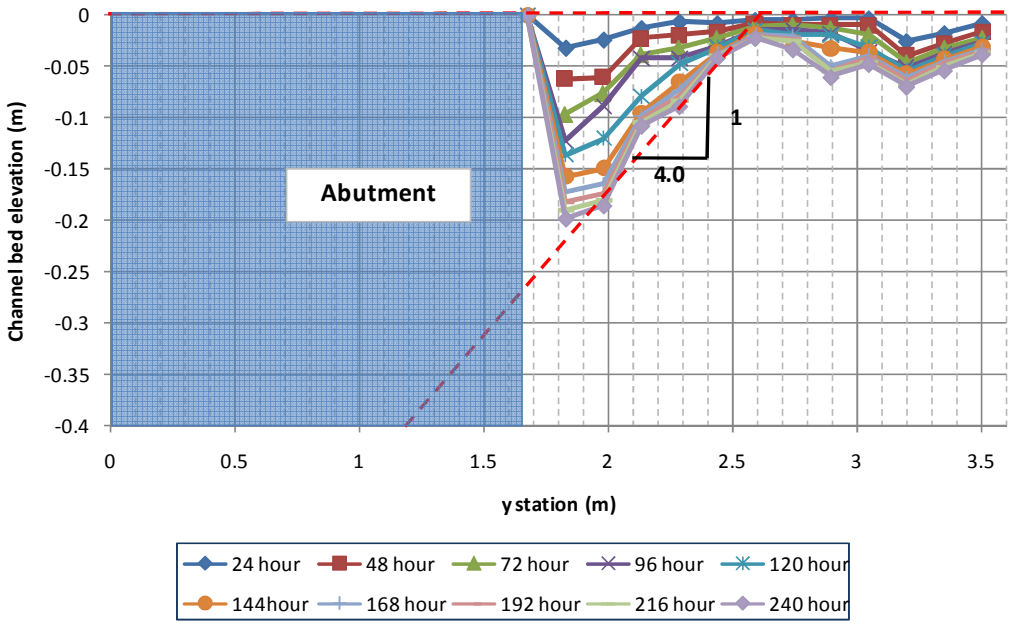

Figure 7.43 - Evolution of cross-sectional abutment scour hole profile in the rectangular channel (L'/L =0.45).

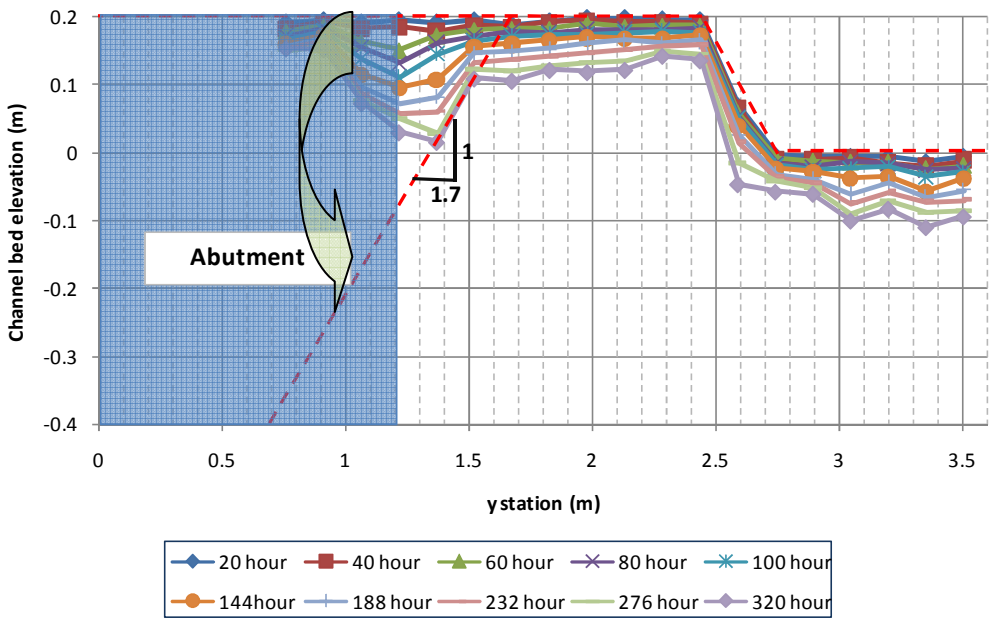

Figure 7.44 - Evolution of cross-sectional abutment scour hole profile in the compound channel ($L'/L_f = 0.5$).

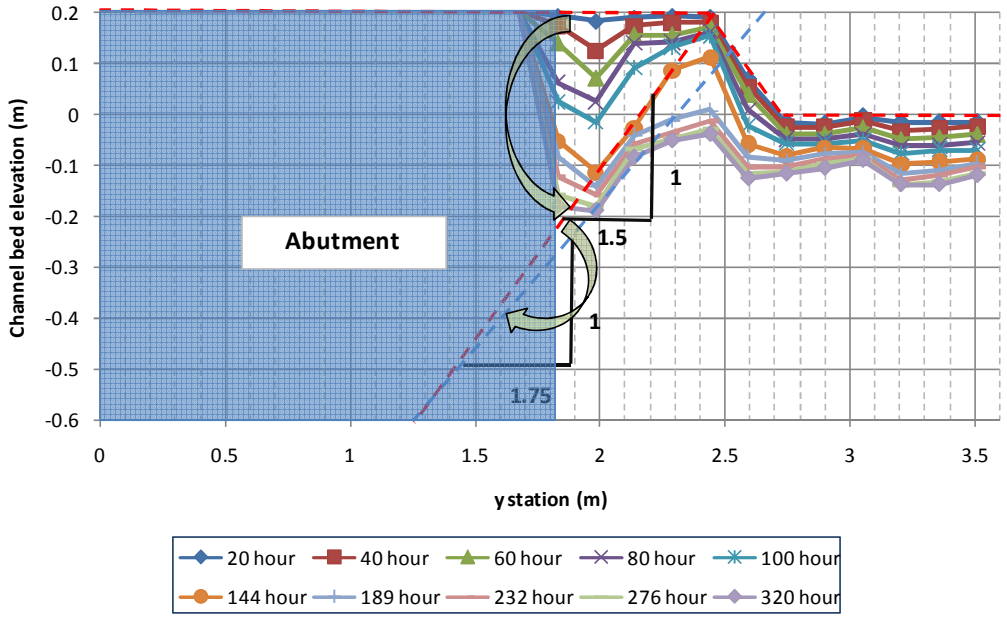

Figure 7.45 - Evolution of cross-sectional abutment scour hole profile in the compound channel ($L'/L_f = 0.75$).

7.4.2 Maximum Scour Depth

The depth of the deepest abutment scour hole and contraction scour hole were obtained from the measurements at every time step. Figure 7.46 shows the abutment scour depth (abutment scour depth plus contraction scour depth) developments for different abutment length and abutment alignment condition in the compound channel. The contraction scour depth developments for those two conditions show similar trends but not the same magnitude.

Although the duration for all the flume tests lasted more than 240 hours (10 days), the scour depth was still increasing at the end of each flume test. In the present study, the maximum scour depth was not directly measured but estimated by applying a hyperbolic model. This is due to the fact that the scour and erosion rates of cohesive soils are very low and much lower than that of cohesionless soils. The erosion rate of soils has been studied by Briaud et al. (1999a, 1999b, 2004). They found that the scour rate of cohesive soils can be 1000 times slower than that of cohesionless soils and a 10-day test may generate only a percentage of the maximum scour depth.

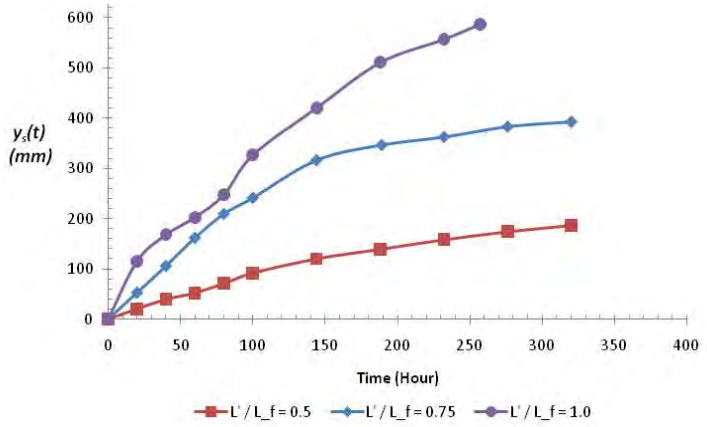

(a) Effect of abutment length (Case 6, Case 1II, Case 7)

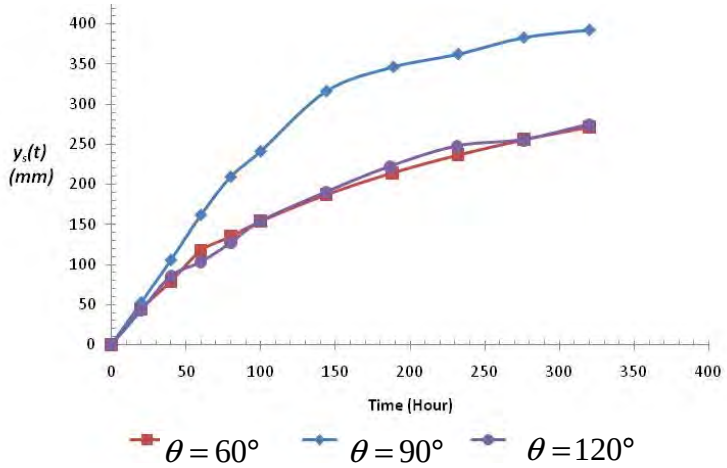

(b) Effect of abutment alignment (Case 10, Case 1II, Case 11)

Figure 7.46 – Development of abutment scour depth.

Using the measurement results in Figure 7.46, a hyperbolic model was applied to obtain the maximum scour depth for abutment scour and contraction scour. The form of the models used in the scour predictions for the abutment scour and contraction scour are

$$y_{s(Abut)} = \frac{t}{a_1 \cdot t + b_1} \tag{7.32}$$

$$y_{s(Cont)} = \frac{t}{a_2 \cdot t + b_2} \tag{7.33}$$

where $y_{s(Abut)}$ is the abutment scour depth, $y_{s(Cont)}$ is the contraction scour depth, t is time, a is the inverse of the asymptotive scour depth , and b is the inverse of the initial tangent to the scour depth versus time curve. The equations can be rewritten to the form of $(t/y) = at + b$ and fitted with a straight line.

Figure 7.47 shows the fitting of the hyperbolic model for both the abutment scour and contraction scour data for Case 17. The values of a and b for abutment scour are less than the a and b values for contraction scour in the test. This means that the initial scour rate and the maximum scour depth of abutment scour are higher and deeper than that of contraction scour. Figure 7.48 shows the comparison between the measurement and the hyperbolic model obtained by data fitting in Figure 7.47. The hyperbolic model seems to be in good agreement with the measurements. The maximum scour depths may be calculated as time reaches infinite ($t \to \infty$). These values are equal to $1/a_1$ and $1/a_2$ for abutment scour and contraction scour, respectively. Based on this approach, the values of a and b were calculated and presented in Table 7.9 for all the flume tests along with the calculated maximum scour depths.

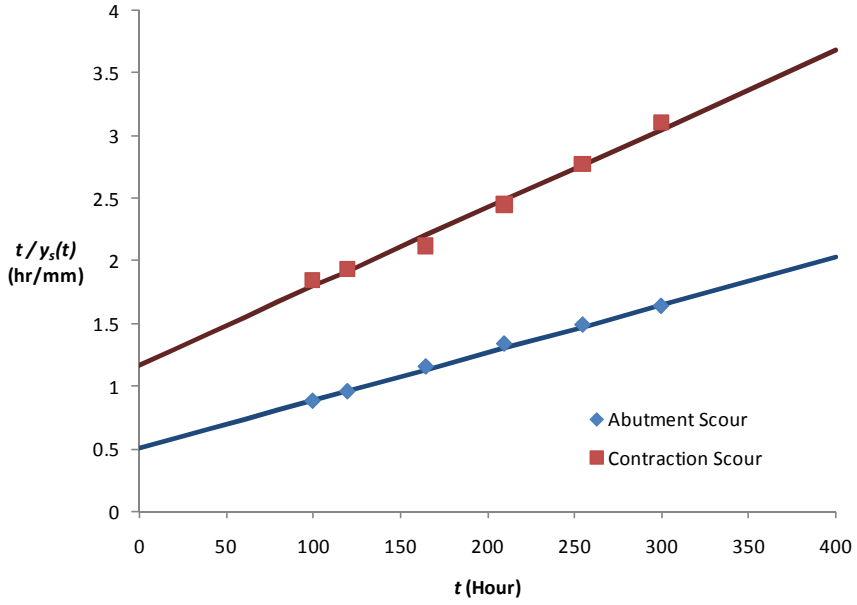

Figure 7.47 – Data fitting of hyperbolic model (Case 17).

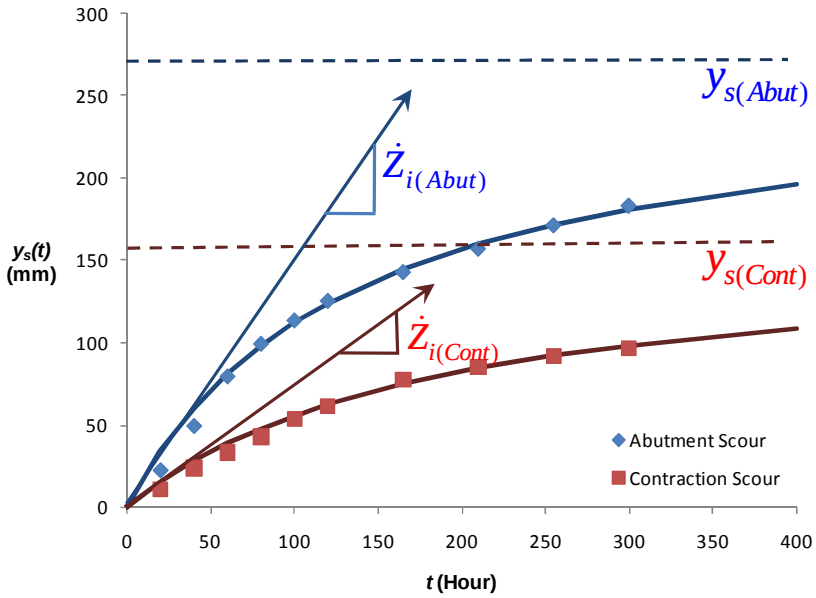

Figure 7.48 - Comparison between measurement and hyperbolic model (Case 17).

Table 7.9 – Summary of hyperbolic model and maximum scour depth.

	Abutment Scour			Contraction Scour		
	a_1 (mm^{-1})	b_1 (hour/mm)	$y_{s(Abut)}$ (mm)	a_2 (mm^{-1})	b_2 (hour/mm)	$y_{s(Cont)}$ (mm)
Case1	0.0023	0.1861	439	0.0048	0.7668	206
Case1II	0.0020	0.1623	490	0.0045	0.4049	224
Case2	0.0035	1.3509	282	0.0077	1.3868	130
Case3	0.0017	0.9482	589	0.0035	1.0177	282
Case4	0.0033	0.8745	300	0.0130	1.8744	77
Case5	0.0012	0.6025	808	0.0036	0.7867	277
Case6	0.0028	0.7976	351	0.0052	0.9581	191
Case7	0.0008	0.2198	1195	0.0029	0.2576	343
Case8	0.0024	0.4541	413	0.0040	0.3149	251
Case9	0.0015	0.5542	670	0.0038	0.7270	266
Case10	0.0024	0.4201	418	0.0045	0.4505	225
Case11	0.0023	0.4269	436	0.0042	0.6254	237
Case12B	0.0007	0.6804	1429	0.0040	0.6641	253
Case13	0.0151	2.3458	66	0.0214	4.3641	47
Case14	0.0033	0.4165	305	0.0069	0.5733	144
Case15	0.0030	0.5693	334	0.0045	0.3877	222
Case16	0.0022	0.3112	448	-	-	-
Case17	0.0038	0.5103	262	0.0063	1.1671	159

7.5 DATA ANALYSIS

7.5.1 Contraction Scour

Li (2002) studied contraction scour in rectangular channels using Porcelain clay as the channel bed material. A flume with symmetrical contraction was used (Figure 7.49). The maximum scour depth along the centerline of the channel was mentioned and used to determine the maximum contraction scour and uniform scour depths. In the present study, only half of the channel is simulated and the centerline is a wall. The maximum scour depth close to the wall but not at the wall on the other side of the abutment was measured for the determinations of the maximum contraction scour depth. This is to avoid the effect of the side wall.

7.5.1.1 Variables and Experiment Results of Contraction Scour

Li's (2002) contraction scour results were used in addition to the measurements conducted in the present study. The parameters and results in Li's study and the present study are listed in Table 7.10 and Table 7.11, respectively. In Li's study, the velocity at the contracted section (V_2) was obtained by HEC-RAS calculation.

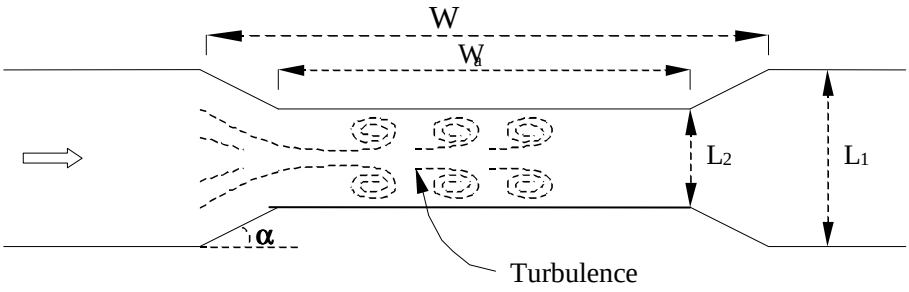

Figure 7.49 – Geometry of symmetrical channel in Li (2002).

Table 7.10 - Variables and results of contraction scour in Li (2002).

Test No.	Contraction Shape	Channel Type	L_1 (m)	y_{m1} (m)	y_{f1} (m)	L_2 (m)	W_a (m)	V_1 (m/s)	Q (m^3/s)	V_2 (m/s)	$y_{s(Cont)}$ (mm)
Ya-LI 1	VW (90°)	Rect.	0.450	0.165	0.165	0.113	1.319	0.267	0.020	1.070	**357**
Ya-LI 2	VW (90°)	Rect.	0.450	0.162	0.162	0.225	1.741	0.310	0.023	0.670	**116**
Ya-LI 3	VW (90°)	Rect.	0.450	0.106	0.106	0.338	1.521	0.459	0.022	0.710	**73**
Ya-LI 4	VW (90°)	Rect.	0.450	0.108	0.108	0.225	1.521	0.205	0.010	0.450	**29**
Ya-LI 5	VW (90°)	Rect.	0.450	0.251	0.251	0.225	1.521	0.207	0.023	0.410	**38**
Ya-LI 6	VW (90°)	Rect.	0.450	0.172	0.172	0.225	1.521	0.205	0.016	0.460	**36**
Ya-LI 7	VW (90°)	Rect.	0.450	0.174	0.174	0.225	1.521	0.390	0.031	0.840	**143**

Table 7.11 – Variables and results of contraction scour in the present study.

Test No.	Contraction Shape	Channel Type	$0.5L$ (m)	y_{m1} (m)	y_{f1} (m)	L' (m)	W_a (m)	V_1 (m/s)	$0.5Q$ (m^3/s)	V_2 (m/s)	$y_{s(Cont)}$ (mm)
Case 1	ST (2:1)	Comp.	3.658	0.494	0.291	1.829	0.457	0.444	0.573	0.722	**206.5**
Case 1II	ST (2:1)	Comp.	3.658	0.497	0.294	1.829	0.457	0.432	0.562	0.704	**224.2**
Case 2	ST (2:1)	Comp.	3.658	0.387	0.184	1.829	0.457	0.355	0.320	0.567	**130.0**
Case 3	ST (2:1)	Comp.	3.658	0.604	0.400	1.829	0.457	0.480	0.812	0.768	**282.3**
Case 4	ST (2:1)	Comp.	3.658	0.482	0.278	1.829	0.457	0.355	0.442	0.549	**76.7**
Case 5	ST (2:1)	Comp.	3.658	0.497	0.294	1.829	0.457	0.509	0.662	0.853	**277.5**
Case 6	ST (2:1)	Comp.	3.658	0.497	0.294	1.219	0.457	0.431	0.561	0.564	**191.2**
Case 7	ST (2:1)	Comp.	3.658	0.494	0.291	2.438	0.457	0.438	0.564	0.963	**342.5**
Case 8	ST (3:1)	Comp.	3.658	0.494	0.291	1.829	0.457	0.442	0.570	0.683	**251.3**
Case 9	WW	Comp.	3.658	0.497	0.294	1.829	0.457	0.437	0.568	0.811	**226.0**
Case 10	ST (2:1)	Comp.	3.658	0.494	0.291	1.829	0.457	0.438	0.565	0.710	**224.6**
Case 11	ST (2:1)	Comp.	3.658	0.494	0.291	1.829	0.457	0.438	0.564	0.713	**236.6**
Case 12B	WW	Rect.	3.658	0.497	0.294	1.829	0.457	0.583	0.759	1.167	**256.0**
Case 13	WW	Rect.	3.658	0.366	0.366	1.015	0.457	0.321	0.429	0.454	**47.5**
Case 14	WW	Rect.	3.658	0.372	0.372	1.625	0.457	0.318	0.432	0.594	**144.0**
Case 15	WW	Rect.	3.658	0.384	0.384	2.234	0.457	0.303	0.416	0.841	**222.2**
Case 17	WW	Rect.	3.658	0.360	0.364	1.320	0.457	0.368	0.484	0.579	**159.0**

In the tables, VW is a vertical wall abutment, ST is a spill-through abutment, WW is a wing-wall abutment, Rect. is a rectangular channel, L_1 is the width of channel at the approach section, L_2 is the width of channel at contracted section, W_a is the length of contraction channel, Q is total discharge, V_1 is the average approach velocity, V_2 is the average velocity at the contracted section, y_{m1} is water depth in the main channel immediately upstream of the bridge contraction, y_{f1} is the water depth at the toe of the abutment estimated as the water depth immediately upstream of the toe of the abutment, and $y_{s(Cont)}$ is the maximum contraction scour depth in the middle of channel

7.5.1.2 Dimensional Analysis

The variables affecting contraction scour can be listed as following

$$y_{s(Cont)} = f(y_{m1}, g, V_2, \rho_s, \rho, \mu, V_{mc}, sh) \tag{7.34}$$

Dimensional analysis yields the following dimensionless parameters:

$$\frac{y_{s(Cont)}}{y_{m1}} = f\left(\frac{\rho_s}{\rho}, Fr_{m2}, Fr_{mc}, \mathrm{Re}, sh\right) \tag{7.35}$$

$$Fr_{m2} = \frac{V_2}{\sqrt{gy_{m1}}};\ \mathrm{Re} = \frac{\rho y_{m1} V_1}{\mu};\ Fr_{mc} = \frac{V_{mc}}{\sqrt{gy_{m1}}} = \frac{\sqrt{\tau_c / \rho}}{gny_{m1}^{1/3}}$$

where $y_{s(Cont)}$ is the maximum contraction scour depth, y_{m1} is the main channel depth at the approach section, Fr_{m2} is the Froude number of the main-channel at the bridge section, Fr_{mc} is the critical Froude number for the main-channel, V_2 is the average velocity at the contracted section obtained by HEC-RAS, g is the gravitational acceleration, τ_c is the critical shear stress, n is Manning's roughness coefficient, ρ_s is the soil density, ρ is the water density, μ is the viscosity of water, sh is the shape of contraction, and V_{mc} is the critical velocity in the main channel. The

bed material used in the present study is a Porcelain clay so the value of ρ_s / ρ is fixed. Reynolds number in the experiments is very large (of the order of 10^5) so it may be reasonable to neglect the viscous effect. As mentioned in Chapter 7.3.1, the water depth at immediately upstream of the contraction section is used for dimensional analysis. Because the water surface at the approach section was almost constant while scour was progressing, but there were significant changes in the surface elevation after the approach section. The water level after the approach section increased as scour progressed. It finally reached the same level as that of the approach section and reached an equilibrium condition. However, the approach water depth in a real channel is not constant through the flow direction while it is nearly constant in the flume test. Thus the water depth immediately upstream of the abutment is used to evaluate the clear water scour depth for not only the laboratory tests but also in the real channel.

As a result, the relation is reduced to

$$\frac{y_{s(Cont)}}{y_{m1}} = f\left(Fr_{m2}, Fr_{mc}, sh\right) \tag{7.36}$$

7.5.1.3 Prediction of Contraction Scour

The maximum contraction scour equation for a given abutment shape may be expressed as

$$\frac{y_{s(Cont)}}{y_{m1}} = \alpha_1\left(\beta_1 Fr_{m2} - Fr_{mc}\right) \tag{7.37}$$

where α_1 and β_1 are correction factors to be determined experimentally, $Fr_{m2} = \frac{V_2}{\sqrt{gy_{m1}}}$, and $Fr_{mc} = \frac{V_{mc}}{\sqrt{gy_{m1}}} = \frac{\sqrt{\tau_c / \rho}}{gny_{m1}^{1/3}}$.

The values of τ_c and n were 0.7 Pa and 0.014 in Li's (2002) study. Nevertheless τ_c = 0.8 Pa and n = 0.011 are used in the present study. Manning's n value in the present study is decided from HEC-RAS results, using n = 0.011 agrees well with the measurements at the approach section as mentioned in chapter 7.3.3. Data regression was performed using Li's data with $\tau_c = 0.7\,\text{Pa}$ and n = 0.014 and using data in the 4 test cases in the present study for rectangular channel (Cases 13 to 15 and 17) with τ_c = 0.8 Pa and n = 0.011. The resulting prediction equation for contraction scour, as shown in Figure 7.50, is

$$\frac{y_{s(Cont)}}{y_{m1}} = 2.21\left(1.31 Fr_{m2} - Fr_{mc}\right) \tag{7.38}$$

where $y_{s(Cont)}$ is the maximum contraction scour depth, y_{m1} is the main channel depth at the approach section, $Fr_{m2}\left(=\frac{V_2}{\sqrt{gy_{m1}}}\right)$ is the Froude number of the main-channel at the bridge section,

$Fr_{mc}\left(=\frac{V_{mc}}{\sqrt{gy_{m1}}}=\frac{\sqrt{\tau_c/\rho}}{gny_{m1}^{1/3}}\right)$ is the critical Froude number of the main-channel, V_2 is the average velocity at the contracted section obtained by HEC-RAS, V_{mc} is the critical velocity in the main channel, τ_c is the critical shear stress, n is Manning's roughness coefficient, and ρ is the water density.

The prediction equation for contraction scour in Equation (7.38) was based on experimental data using rectangular channels. Interestingly, the equation predicts contraction scour well when applied to compound channels, as shown in Figure 7.51. The shape of abutment and the channel geometry seem to have no effect on the depth of maximum contraction scour.

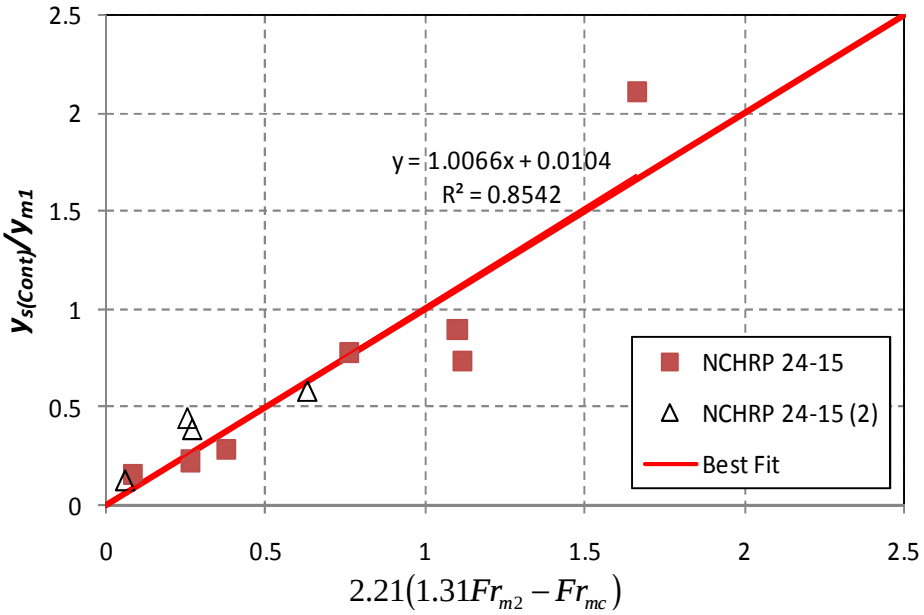

Figure 7.50 – Contraction Scour in Rectangular Channel: Measurement versus Prediction.

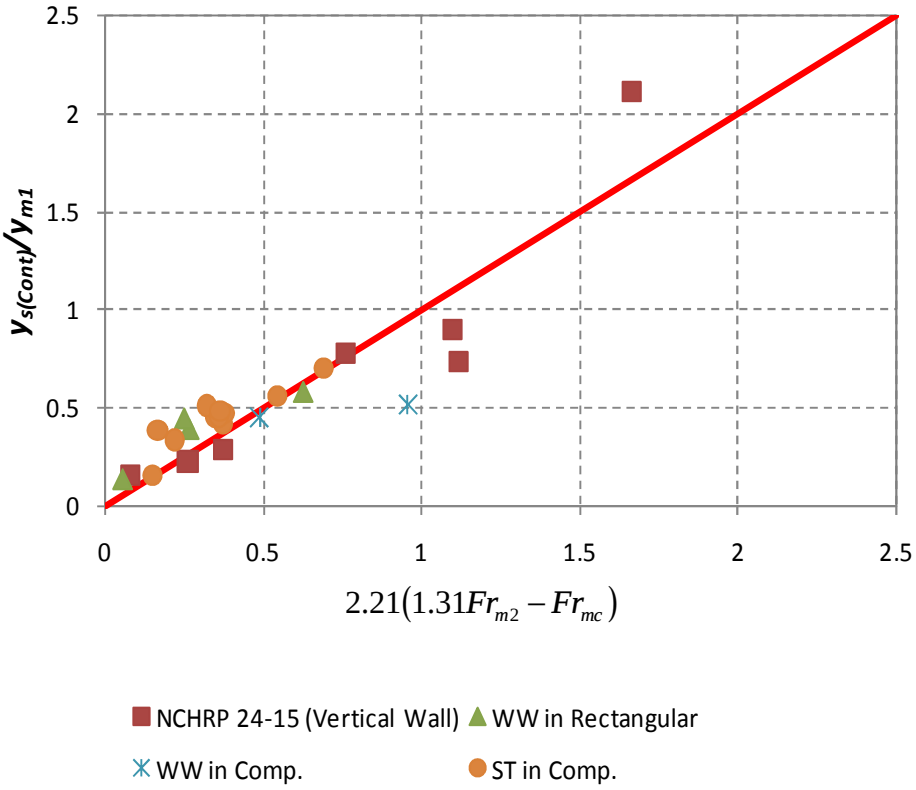

Figure 7.51 - Contraction scour in rectangular channel and compound channel: measurement versus prediction.

7.5.2 Abutment Scour

7.5.2.1 Variables and Experimental Results of Abutment Scour

The variables influencing local scour around an abutment are the soil properties, the geometry of channel, the length of abutment, the shape of abutment, the approach velocity, and the alignment of the abutment. They are discussed below with the variables and test results being summarized in Table 7.12.

(1) Soil properties. Porcelain clay was used as the channel bed material. The relation between the shear stress and erosion rate for the Porcelain clay was obtained from 11 EFA (Erosion Function Apparatus) tests (Figure 7.11). The critical shear stress was defined as the shear stress when the initiation of soil erosion occurs. In the tests, a 0.1 mm/hour erosion rate was used as the initiation of erosion and the corresponding value of shear stress was 0.8 Pa.

(2) Geometry of the channel. The flume used for the tests is 45.7 m (150 ft) long, 3.05 m (10 ft) deep, and 3.66 m (12ft) wide. For compound channels, the width of the floodplain was 2.44 m and the half width of main channel was 1.22 m, as shown in Figure 7.52.

(3) Shape of abutment. 3 types of abutment were tested in this study: The first one is of wing-wall shape, the second one is of spill-through with a 2(H):1(V) slope, and the third one is of spill-through with a 3(H):1(V) slope as depicted in Figure 7.53. Vertical wall with transition is another shape but it was not tested in this study.

(4) Water depth and approach velocity. 3 tests with different velocities in the same water depth and 3 tests with different water depths but a constant Froude number were conducted to examine the effect of these two variables.

(5) Alignment of abutment. 3 tests with different alignment angles with the spill-through abutment have been conducted. They are 60^o, 120^o, and 90^o, as shown in Figure 7.54. Note that the 90^o angle alignment indicates the abutment is normal to the flow direction, while for 60^o and 120^o the abutment is skewed towards downstream and upstream, respectively.

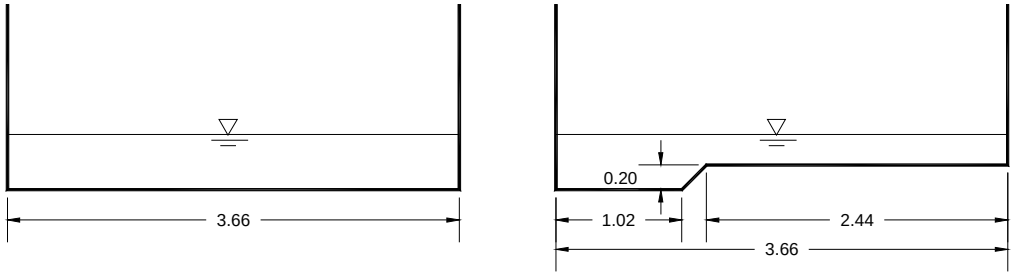

Figure 7.52 - Channel configurations (all dimensions are in meters).

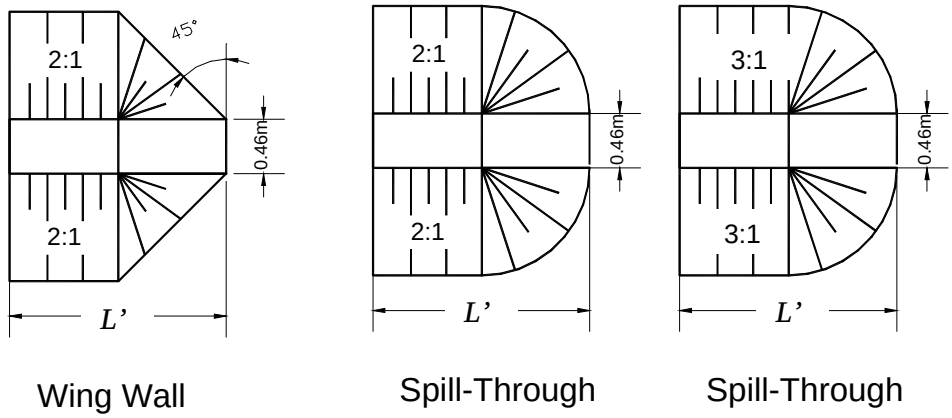

Figure 7.53 – Abutment shapes.

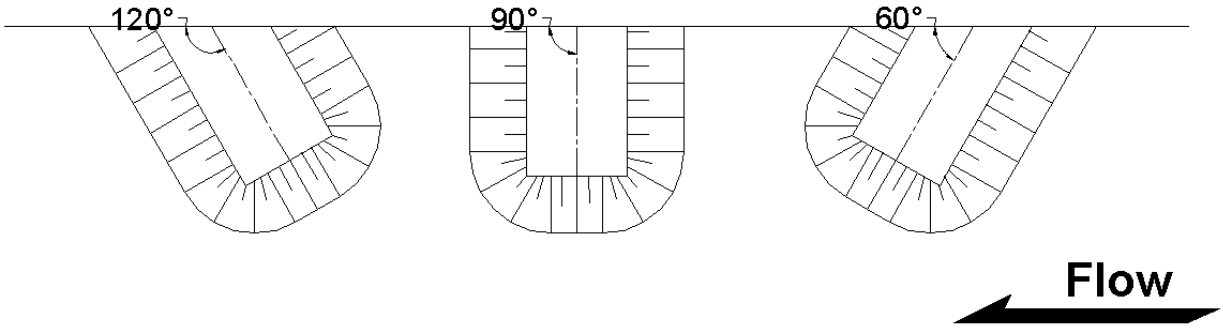

Figure 7.54 – Abutment alignment.

Table 7.12 - Variables and test results.

Test No.	Abutment Shape	Channel Type	V_1 (m/s)	y_{f1} (m)	y_{m1} (m)	L (m)	L_f (m)	L' (m)	θ (^{o})	$0.5Q_{total}$ (m^3/s)	V_2 (m/s)	Fr_{f2}	Fr_{fc}	$y_{s(Abut)}$ (mm)
Case1	ST (2:1)	Comp.	0.464	0.291	0.494	3.658	2.438	1.829	90	0.573	0.722	0.428	0.396	439
Case 1II	ST (2:1)	Comp.	0.456	0.294	0.497	3.658	2.438	1.829	90	0.562	0.711	0.419	0.394	490
Case2	ST (2:1)	Comp.	0.377	0.184	0.387	3.658	2.438	1.829	90	0.320	0.557	0.415	0.461	282
Case3	ST (2:1)	Comp.	0.496	0.400	0.604	3.658	2.438	1.829	90	0.813	0.806	0.407	0.356	589
Case4	ST (2:1)	Comp.	0.358	0.278	0.482	3.658	2.438	1.829	90	0.442	0.582	0.352	0.401	300
Case5	ST (2:1)	Comp.	0.546	0.294	0.497	3.658	2.438	1.829	90	0.662	0.837	0.493	0.394	808
Case6	ST (2:1)	Comp.	0.432	0.294	0.497	3.658	2.438	1.219	90	0.561	0.579	0.341	0.394	351
Case7	ST (2:1)	Comp.	0.472	0.291	0.494	3.658	2.438	2.438	90	0.564	0.930	0.551	0.396	1190
Case8	ST (3:1)	Comp.	0.456	0.291	0.494	3.658	2.438	1.829	90	0.570	0.715	0.423	0.396	413
Case9	WW	Comp.	0.453	0.294	0.497	3.658	2.438	1.829	90	0.568	0.743	0.438	0.394	667
Case10	ST (2:1)	Comp.	0.458	0.291	0.494	3.658	2.438	1.829	60	0.554	0.706	0.418	0.396	418
Case11	ST (2:1)	Comp.	0.457	0.291	0.494	3.658	2.438	1.829	120	0.565	0.720	0.426	0.396	436
Case12	WW	Comp.	0.347	0.294	0.497	3.658	2.438	1.829	90	0.433	0.566	0.334	0.394	155
Case12B	WW	Comp.	0.635	0.294	0.497	3.658	2.438	1.829	90	0.759	0.993	0.585	0.394	1429
Case13	WW	Rect.	0.328	0.366	0.366	3.658	3.658	1.015	90	0.430	0.445	0.235	0.367	66
Case14	WW	Rect.	0.326	0.372	0.372	3.658	3.658	1.625	90	0.433	0.573	0.300	0.364	304
Case15	WW	Rect.	0.310	0.384	0.384	3.658	3.658	2.234	90	0.416	0.761	0.392	0.361	334
Case16	WW	Rect.	0.233	0.347	0.347	3.658	3.658	2.743	90	0.285	0.896	0.485	0.373	448
Case17	WW	Rect.	0.364	0.360	0.360	3.658	3.658	1.320	90	0.485	0.576	0.307	0.369	262

In Table 7.12, ST is the spill-through abutment, WW is the wing-wall abutment, Comp. is the compound channel, Rect. is the rectangular channel, V_1 is the average velocity at the approach section, y_{m1} is the water depth of main-channel at the approach section, y_{f1} is the water depth of floodplain at the approach section, L is the half width of channel, L_f is the width of floodplain, L' is the projected length of abutment normal to the flow, θ is the alignment angle of abutment ($\theta = 90^o$ for normal to flow, $\theta > 90^o$ for skewed upstream, $\theta < 90^o$ for skewed to downstream), Q is the total discharge, V_2 is the average velocity at bridge section, $y_{s(Abut)}$ is the maximum abutment scour depth, $Fr_{f2(Abut)}$ is Froude number around the abutment (based on the average velocity at the contracted section and y_{f1}), Fr_{fc} is critical Froude number around the abutment (based on the critical velocity on the floodplain and y_{f1}), and $y_{s(Abut)}$ is the maximum abutment scour depth. Note that the water depths and velocities are obtained based on the HEC-RAS results.

7.5.2.2 Dimensional Analysis

In addition to the variables mentioned above, there are several more variables affecting abutment scour. The influential variables are listed as following

$$y_{s(Abut)} = f(y_{m1}, y_{f1}, L_m, L_f, L', \beta_m, \beta_a, \theta, g, V_{f2}, \rho_s, \rho, \mu, V_{fc}) \tag{7.39}$$

Dimensional analysis yields the following dimensionless parameters:

$$\frac{y_{s(Abut)}}{y_{f1}} = f\left(\frac{y_{f1}}{y_{m1}}, \frac{L_m}{y_{m1}}, \frac{L_f}{L_m}, \frac{L'}{L_f}, \frac{\rho_s}{\rho}, \beta_m, \beta_a, \theta, Fr_{f2}, Fr_{fc}, \mathrm{Re}_{f2}\right) \tag{7.40}$$

where L_m is the half-width of main channel, L_f is the width of floodplain, L' is the length of abutment, β_m is the slope of the main channel bank, β_a is the abutment slope, θ is the alignment angle of abutment, g is the gravitational acceleration, V_{f2} is the velocity around the toe of the abutment, ρ_s is the soil density, ρ is the water density, μ is the viscosity of water, and V_{fc} is the critical velocity in the floodplain, y_{f1} is the water depth of floodplain at the approach section, $y_{s(Abut)}$

is the maximum abutment scour depth, $Fr_{f2} = \frac{V_{f2}}{\sqrt{gy_{f1}}}$, $Fr_{fc} = \frac{V_{fc}}{\sqrt{gy_{f1}}} = \frac{\sqrt{\tau_c / \rho}}{gny_{f1}^{1/3}}$, and $\mathrm{Re}_{f2} = \frac{\rho y_f V_{f2}}{\mu}$.

Note that the value of ρ_s / ρ is fixed due to the fixed soil type. The velocity at the bridge section and the water depth based on the HEC-RAS results are used for data regression in the present study. Although HEC-RAS is capable of calculating velocity at the bridge section, the resulting velocity distribution does not match well with the measurements as mentioned in Chapter 7.3.3. In the present study the approach used in Maryland SHA Bridge Scour Program (ABSCOUR) (2007) was adopted to calculate the local velocity around the abutment. The method for converting the HEC-RAS results to the local velocity is as follows.

$$V_{f2} = \begin{cases} \frac{Q_{total}}{A_2}, \text{ for short setback } \left((L_f - L') \le 5y_{m1}\right) \\ \frac{Q_{fp1}}{A_{f2}}, \text{ for long setback } \left(L' \le 0.25L_f\right) \\ \text{otherwise use a linearly interpolated velocity between} \\ \frac{Q_{total}}{A_2} \text{ for } (L_f - L') = 5y_{m2} \text{ and } \frac{Q_{fp1}}{A_{f2}} \text{ for } L' = 0.25L_f \end{cases} \tag{7.41}$$

where Q_{total} is the total discharge, Q_{fp1} is the discharge on the floodplain at the approach section immediately upstream of the abutment, A_2 is total flow area at the contracted section, A_{f2} is the flow area on the floodplain at the contracted section, and $L_f - L'$ is the width of floodplain at the contracted section.

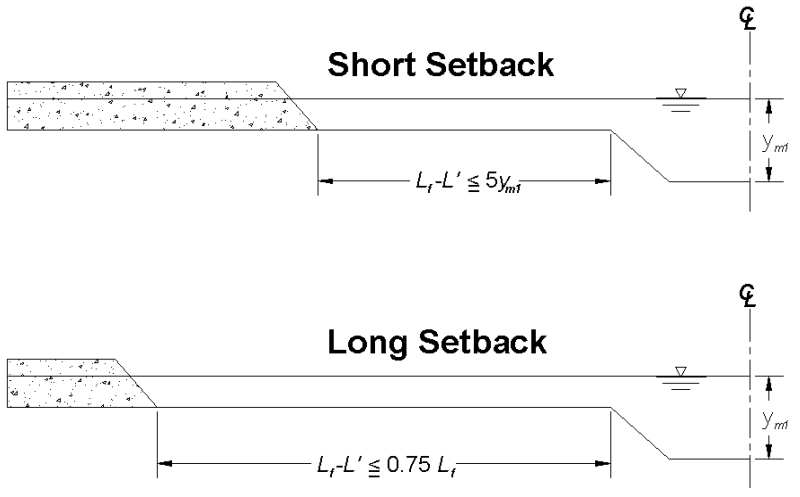

Figure 7.55 – Definition of degree of setback.

As a result of these observations, the relation is reduced to

$$\frac{y_{s(Abut)}}{y_{f1}} = f\left(\frac{L_f - L'}{y_{f1}}, \beta_a, \theta, Fr_{f2}, Fr_{fc}, \mathrm{Re}_{f2}\right) \tag{7.42}$$

where L_f is the width of floodplain, L' is the length of abutment, β_a is the abutment slope, θ is the alignment angle of abutment, $Fr_{f2} = \frac{V_{f2}}{\sqrt{gy_{f1}}}$, $Fr_{fc} = \frac{V_{fc}}{\sqrt{gy_{f1}}} = \frac{\sqrt{\tau_c / \rho}}{gny_{f1}^{1/3}}$, $\mathrm{Re}_{f2} = \frac{\rho y_f V_{f2}}{\mu}$, V_{f2} is the velocity around the toe of the abutment using equation (7.41), g is the gravitational acceleration, ρ_s is the soil density, ρ is the water density, μ is the viscosity of water, and V_{fc} is the critical velocity in the floodplain.

7.5.2.3 Prediction Equation

The abutment scour depths are likely to be proportional to the difference $\left(Fr_{f2} - Fr_{fc}\right)$. Thus the form of the equation sought for wing-wall abutment is:

$$\frac{y_{s(Abut)}}{y_{f1}} = \alpha\left(\beta \cdot Fr_{f2} - Fr_{fc}\right) \tag{7.43}$$

The factors α and β were obtained by optimizing the R^2 value in the regression on Figure 7.56, and the proposed equation is:

$$\frac{y_{s(Abut)}}{y_{f1}} = 7.94\left(1.65 \cdot Fr_{f2} - Fr_{fc}\right) \tag{7.44}$$

where $y_{s(Abut)}$ is the maximum abutment scour depth, y_{f1} is the water depth of floodplain at the approach section, $Fr_{f2} = \frac{V_{f2}}{\sqrt{gy_{f1}}}$, and $Fr_{fc} = \frac{V_{fc}}{\sqrt{gy_{f1}}} = \frac{\sqrt{\tau_c / \rho}}{gny_{f1}^{1/3}}$.

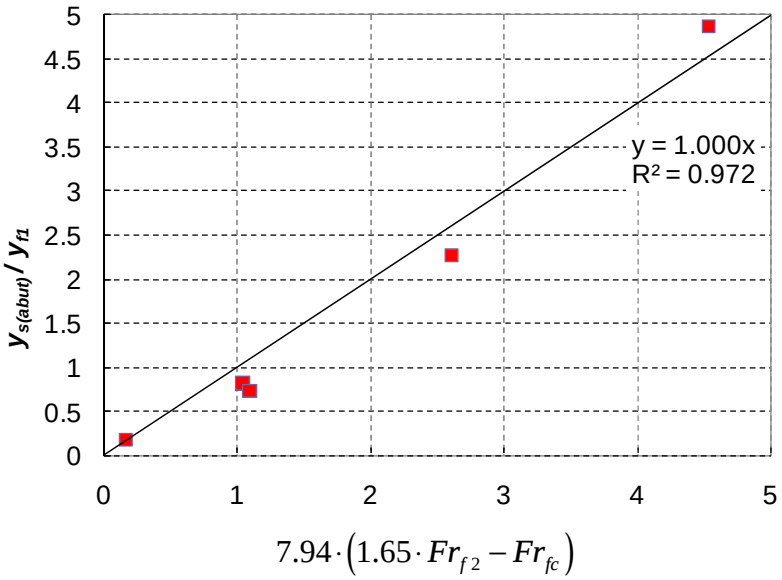

Figure 7.56 – Normalized abutment scour depth (abutment scour depth plus contraction scour depth) versus Froude number.

7.5.2.4 The Effect of Abutment Shape (K_1)

Three types of abutments were used in the compound channel. They are wing-wall abutment with a 2:1 slope at the upstream and downstream, spill-through abutment with a 2:1 slope, and spill-through abutment with a 3:1 slope. Equation (7.45) which is based on the wing-wall abutment was applied to the spill-through abutment to find the shape correction factor. The correction factor for abutment shape was calculated based on the slope shown in Figure 7.57 with values as follows:

$$K_1 = \begin{cases} 1.0 & \text{for Wing-wall abutment} \\ 0.73 & \text{for Spill-through abutment with 2:1 Slope} \\ 0.59 & \text{for Spill-through abutment with 3:1 Slope} \end{cases} \tag{7.45}$$

The correction factor for the abutment shape in Froehlich's study is 1.0, 0.82, and 0.55 for vertical wall, wing-wall and spill-through abutments, respectively. These numbers are the scour depth ratio to the scour depth for vertical wall abutment. If the correction factor in Froehlich's study was formularized with the wing-wall abutment as the reference abutment, it would be 1.22, 1.0, and 0.67 for vertical wall, wing-wall and spill-through abutments, respectively. The rearranged abutment shape correction factor for the spill-through abutment is consistent with the present study.

From the results of Froehlich's and the present study, it seems to be reasonable to use 1.22 as the abutment shape correction factor for the vertical wall, although the vertical wall abutment was not used in the present study. Thus the correction factor for abutment shape is:

$$K_1 = \begin{cases} 1.22 & \text{for Vertical-wall abutment} \\ 1.0 & \text{for Wing-wall abutment} \\ 0.73 & \text{for Spill-through abutment with 2:1 Slope} \\ 0.59 & \text{for Spill-through abutment with 3:1 Slope} \end{cases} \tag{7.46}$$

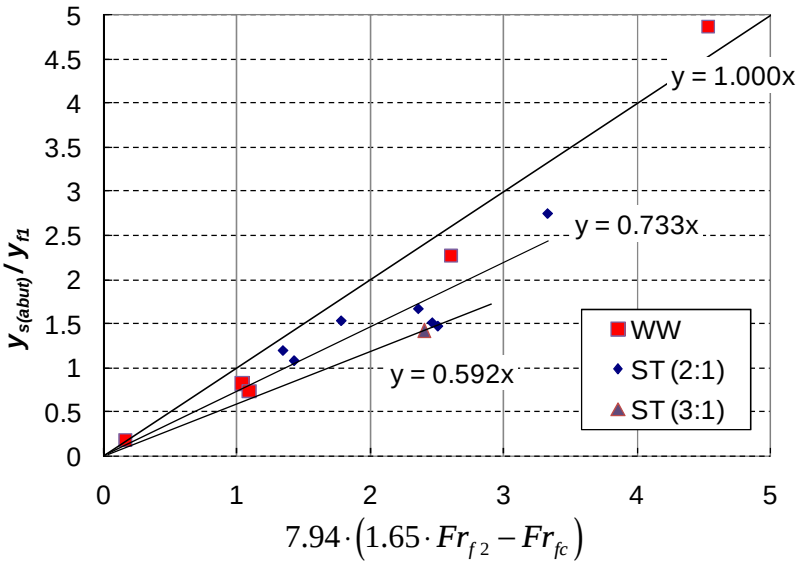

Figure 7.57 – Normalized maximum abutment scour depth (abutment scour depth plus contraction scour depth) with different abutment shape.

7.5.2.5 The Effect of Abutment Alignment (K_2) and Abutment Location (K_L)

Two tests were conducted to examine the effect of abutment alignment using the spill through abutment with a 2:1 slope. One has a 30° skewed angle (θ = 120°) toward the upstream flow while the other has a 30° skewed angle (θ = 60°) toward the downstream flow. The maximum abutment scour depth (abutment scour depth plus contraction scour depth) for skewed abutment was compared with the prediction equation including the effect of abutment shape. The comparison is shown in Figure 7.60. As expected the correction factor for θ = 60° is less than 1.0. However the value for θ = 120° is also less than 1.0 which is in contrary to previous research results. Since the abutment used in this study is a spill-through abutment, the abutment induced a relatively smooth flow during the transition even though the abutment is aligned toward upstream. This may be the reason for the lower correction factor. The turbulence level defined in equation (7.30) around the abutment is compared and shown in Figure 7.58. In Figure 7.58, the maximum turbulence level around the abutment was observed on the abutment normally aligned to the flow, whereas relatively lower turbulence level was observed on the skewed abutments. Note that the abutment scour pattern is similar to the pattern of *TI* (Turbulence Intensity) and the contraction scour pattern is similar to the time averaged velocity pattern as shown in Figure 7.40. In addition, the higher *TI* generates the deeper local scour depth.

Since the number of experiments to find the effect of the abutment alignment is very small, a linear decrease of the abutment scour depth (abutment scour depth plus contraction scour depth) with the abutment alignment variation is assumed. In addition, a 30° of skew angle is assumed as the maximum angle in design. The correction factor for abutment alignment is obtained from these two assumptions and from the experimental results, and can be expressed as follows:

$$K_2 = \begin{cases} 1.0 - 0.005\left|\theta - 90°\right| & \textit{for } 60° \le \theta \le 120° \\ 0.85 & \textit{otherwise} \end{cases} \tag{7.47}$$

As seen in Figure 7.59, when the toe of abutment is close to the end of main channel slope, the biggest turbulence which occurred at the channel slope eroded the channel bottom with high scour rate. Consequently, the maximum scour depth increased suddenly when the toe of the abutment was at the end of the floodplain (i.e., $L'/L_f = 1.0$), as shown in Figure 7.60. If a linear increase of the abutment scour depth (abutment scour depth plus contraction scour depth) with the decrease of distance between the toe of abutment and the end of floodplain is assumed, the correction factor for abutment location can be expressed as follows:

$$K_L = \begin{cases} -0.23\dfrac{L_f - L'}{y_{f1}} + 1.35 & \text{for } \dfrac{L_f - L'}{y_{f1}} < 1.5 \\ 1.0 & \text{otherwise} \end{cases} \tag{7.48}$$

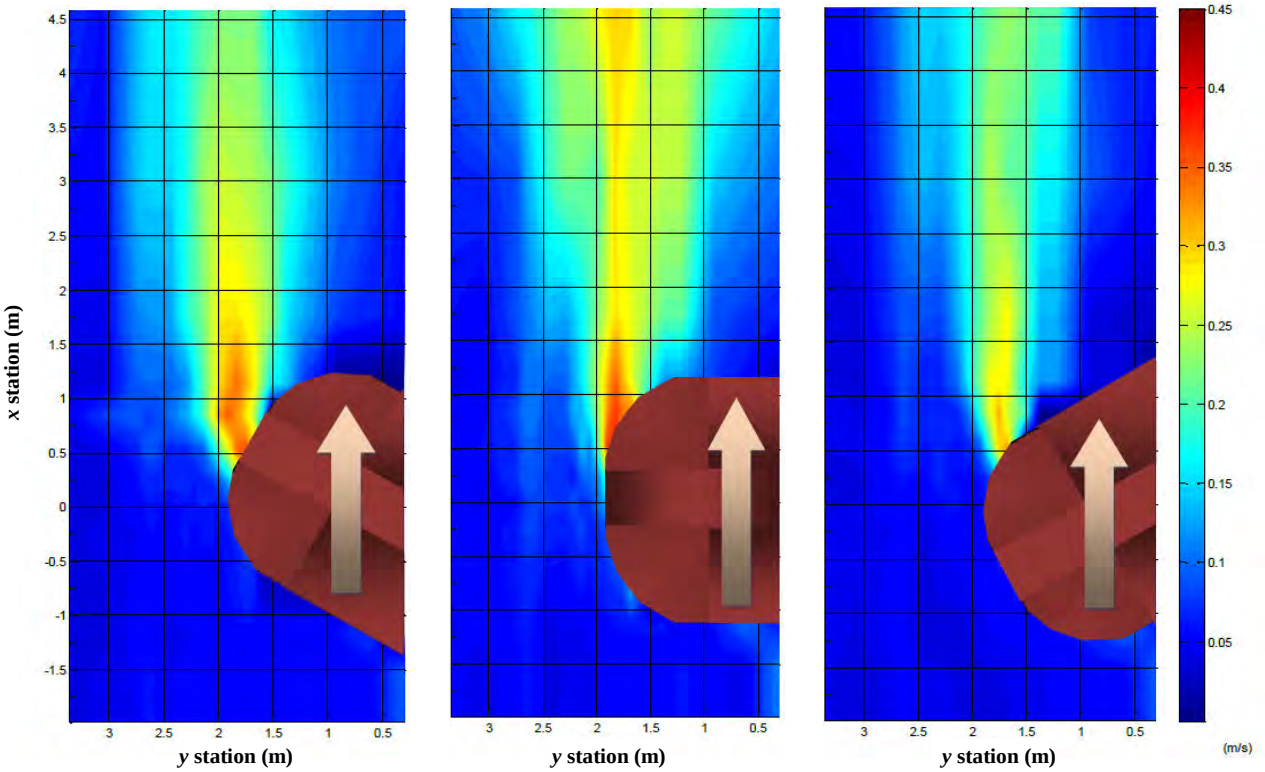

(a) $\theta = 60°$ (b) $\theta = 90°$ (c) $\theta = 120°$

Figure 7.58 – Variation of turbulence intensity with different attack angles at the initial test condition.

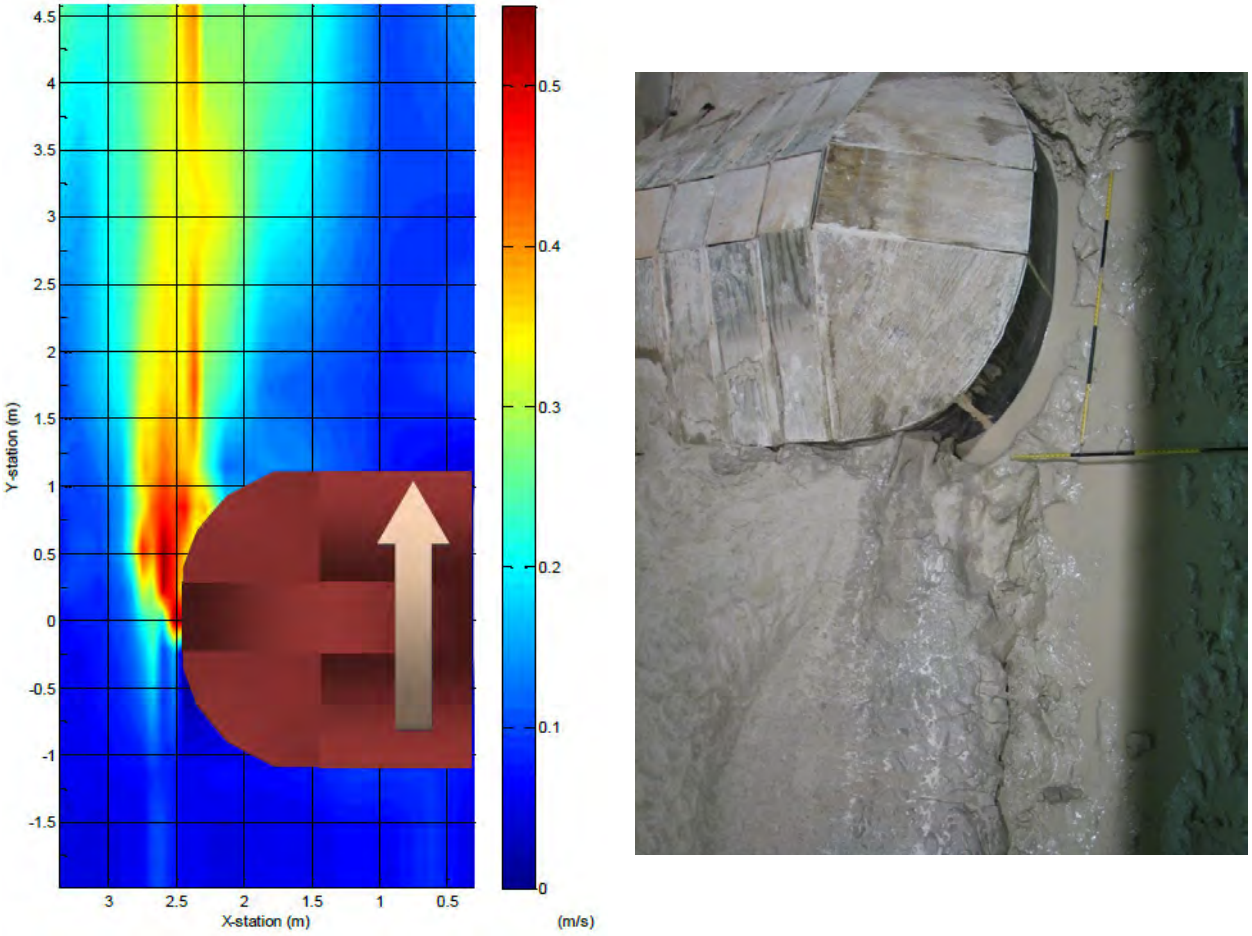

Figure 7.59 – Pattern of (a) turbulence, and (b) a downstream view of scour hole after 257 hours of experiment for $L'/L_f = 1.0$

Note that the color bars on Figure 7.58Figure 7.59 indicate the magnitude of *TI* (turbulence intensity) measured in the beginning of experiments. The unit of *TI* is meter per second, and the equation to obtain *TI* is:

$$TI = \sqrt{\sigma_x^2 + \sigma_y^2 + \sigma_z^2}$$

where σ is the standard deviation of the measured velocity and the subscripts *x*, *y* and *z* are the directions of flow.

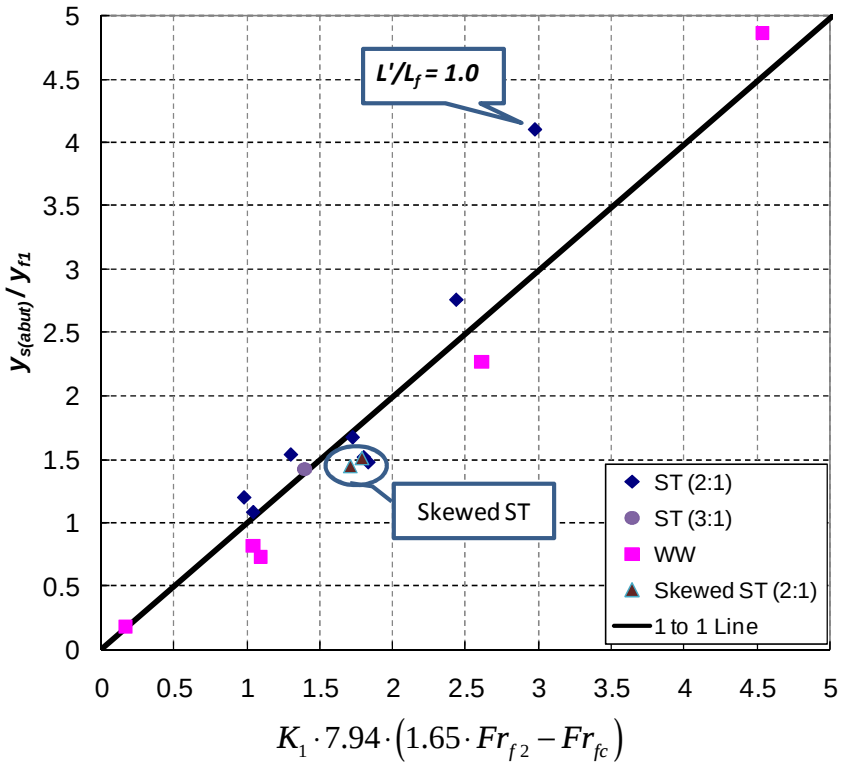

Figure 7.60 – Normalized maximum abutment scour depth (abutment scour depth plus contraction scour depth) versus prediction with abutment shape being accounted for.

7.5.2.6 The Effect of Channel Geometry (K_G)

The normalized abutment scour depths (abutment scour depth plus contraction scour depth) in the rectangular channel were shallower than the scour depths predicted by equation (7.44). In order to make the prediction satisfying all channel conditions, a correction factor for channel geometry is required. The measurement and prediction results for wing-wall abutments using equation (7.44) are compared in Figure 7.61. The slope of the best fit line for the rectangular channel is 0.42.

Thus the correction factor for channel geometry is:

$$K_G = \begin{cases} 1.0 & \text{for compound channel} \\ 0.42 & \text{for rectangular channel} \end{cases} \tag{7.49}$$

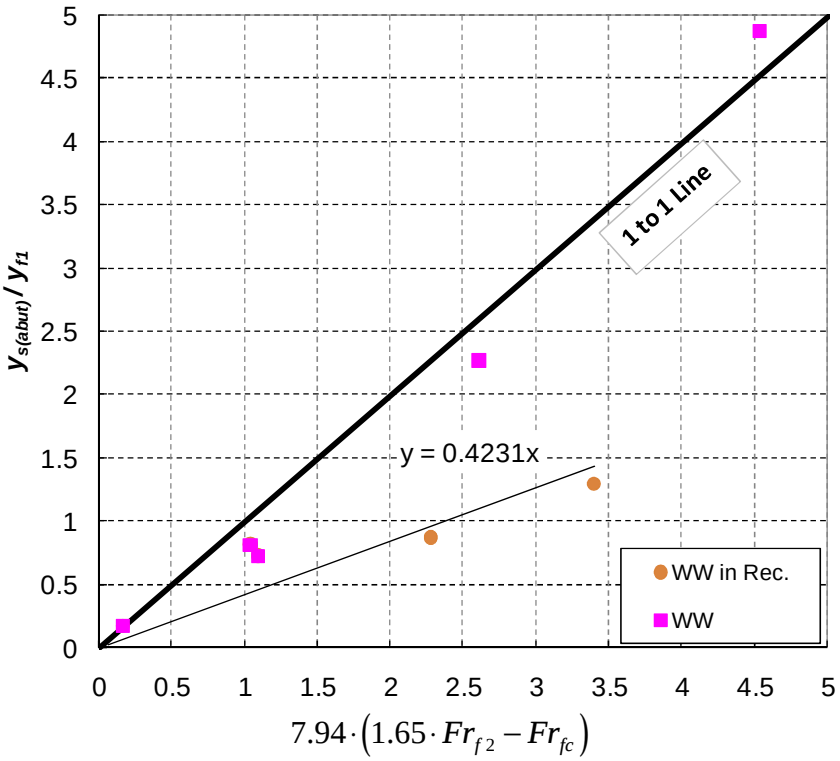

Figure 7.61 – The effect of channel geometry

7.5.2.7 Preliminary Prediction Equation for Abutment Scour and Reynolds number effect (K_{Re})

The prediction equation for the maximum abutment scour depth (abutment scour depth plus contraction scour depth) has thus been developed. There are four correction factors to account for the shape of abutment, the attack angle of the flow, the abutment location, and the different channel geometry condition. The preliminary abutment scour prediction equation is:

$$\frac{y_{s(Abut)}}{y_{f1}} = K_1 \cdot K_2 \cdot K_L \cdot K_G \cdot 7.94 \cdot \left(1.65 \cdot Fr_{f2} - Fr_{fc}\right) \tag{7.50}$$

In equation (7.50), $y_{s(Abut)}$ is the maximum abutment scour depth, y_{f1} is the water depth at the toe of the abutment estimated as the water depth immediately upstream of the toe of the abutment, $Fr_{f2} = \frac{V_{f2}}{\sqrt{gy_{f1}}}$, $Fr_{fc} = \frac{V_{fc}}{\sqrt{gy_{f1}}} = \frac{\sqrt{\tau_c / \rho}}{gny_{f1}^{1/3}}$, K_1 is the correction factor for the abutment shape, K_2 is the correction factor for the abutment skew angle, K_L is the correction factor for the abutment location, K_p is the correction factor for the pressure flow. Their values and formulas are as follows:

$$K_1 = \begin{cases} 1.22 & \text{for Vertical-wall abutment} \\ 1.0 & \text{for Wing-wall abutment} \\ 0.73 & \text{for Spill-through abutment with 2:1 Slope} \\ 0.59 & \text{for Spill-through abutment with 3:1 Slope} \end{cases}$$

$$K_2 = \begin{cases} 1.0 - 0.005\left|\theta - 90°\right| & \textit{for } 60° \le \theta \le 120° \\ 0.85 & \textit{otherwise} \end{cases}$$

$$K_G = \begin{cases} 1.0 & \text{for compound channel} \\ 0.42 & \text{for rectangular channel} \end{cases}$$

$$K_L = \begin{cases} -0.23\dfrac{L_f - L'}{y_{f1}} + 1.35 & \text{for } \dfrac{L_f - L'}{y_{f1}} < 1.5 \\ 1.0 & \text{otherwise} \end{cases}$$

Figure 7.62 shows prediction using the preliminary prediction equation versus the measurements for the flume test cases.

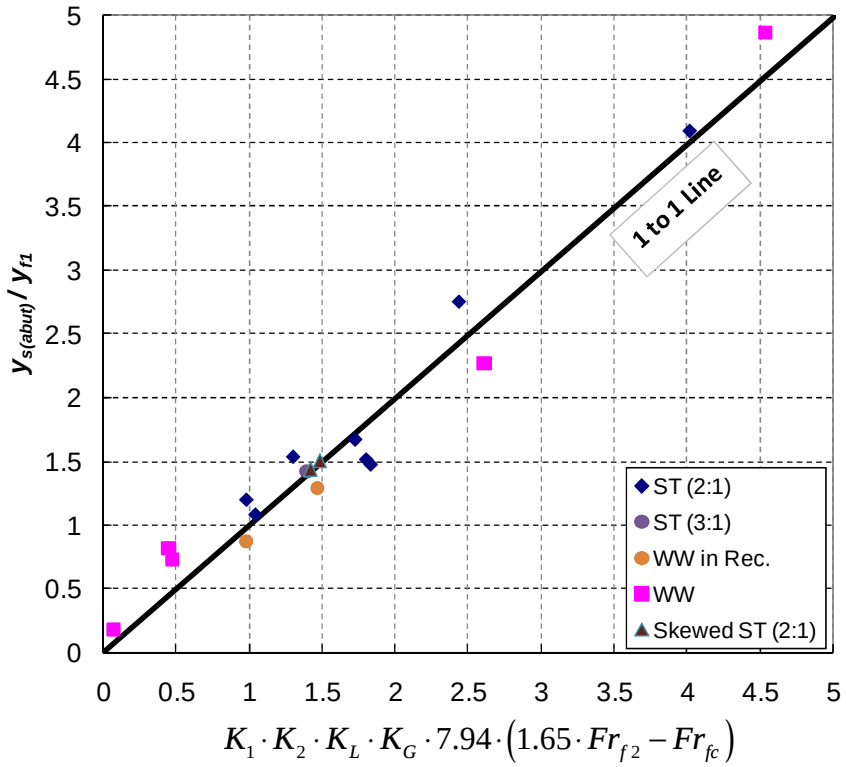

Figure 7.62 - Normalized maximum abutment scour depth: Test results versus prediction by preliminary equation.

Although the preliminary abutment scour equation (equation 7.50) is developed with laboratory test results for the cohesive soil, it is likely to be applicable to cohesionless soil because the property of the soil is included in the equation. The equation (7.50) is used to predict the maximum abutment scour depth (abutment scour depth plus contraction scour depth) for the comparison with other previous studies (Froehlich (1989), Sturm (2004), Benedict et al. (2006)). The detail about these databases will be mentioned in Chapter 8.

The comparisons between predictions based on the preliminary abutment scour prediction equation and that in databases of Froehlich, Sturm, and Benedict et al. are shown in Figure 7.63, Figure 7.64, and Figure 7.65, respectively. According to the figures, the equation (7.50) mostly yields underestimations for laboratory test, such as Froehlich's and Sturm's database, whereas it overestimates field measurement results by Benedict et al. The main difference among those databases is the range of Reynolds numbers. In Table 7.13, the range of Reynolds numbers for the three databases are listed. The range of Reynolds number in the databases of Froehlich and Sturm, which are underestimated by equation (7.50), is relatively lower than that of the present study, whereas in databases of Benedict et al., which are overestimated by equation (7.50), is higher than that of the present study.

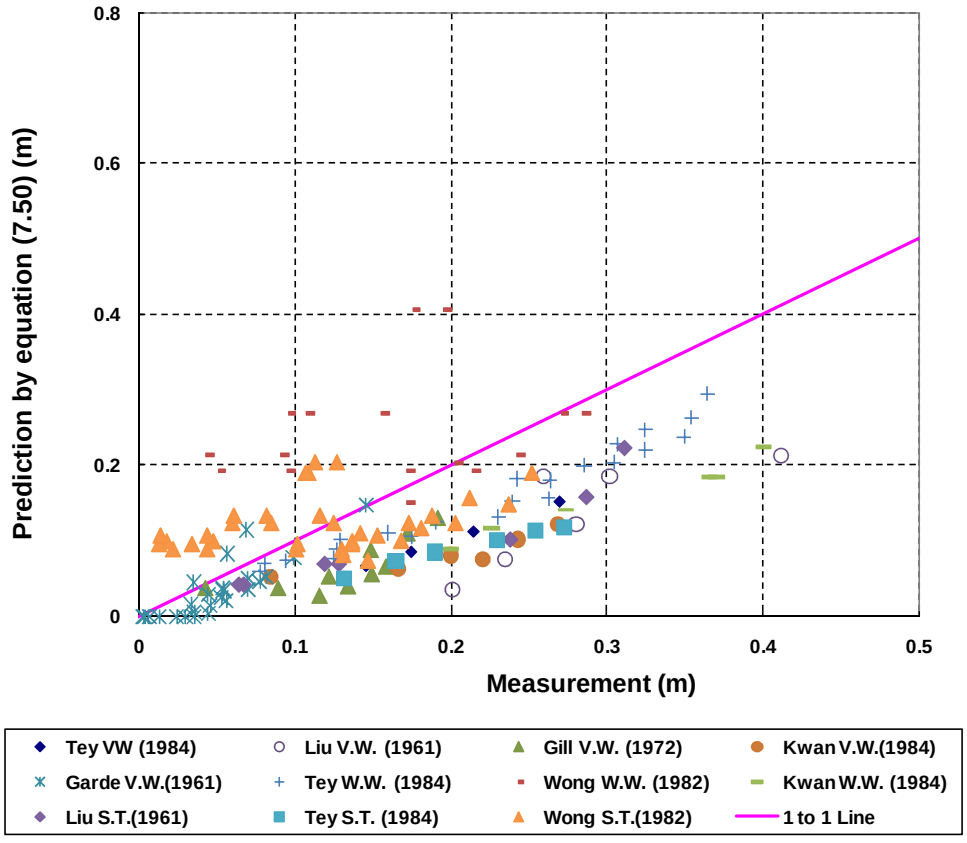

Figure 7.63 – Comparison between prediction by equation (7.50) and Froehlich's database (1989).

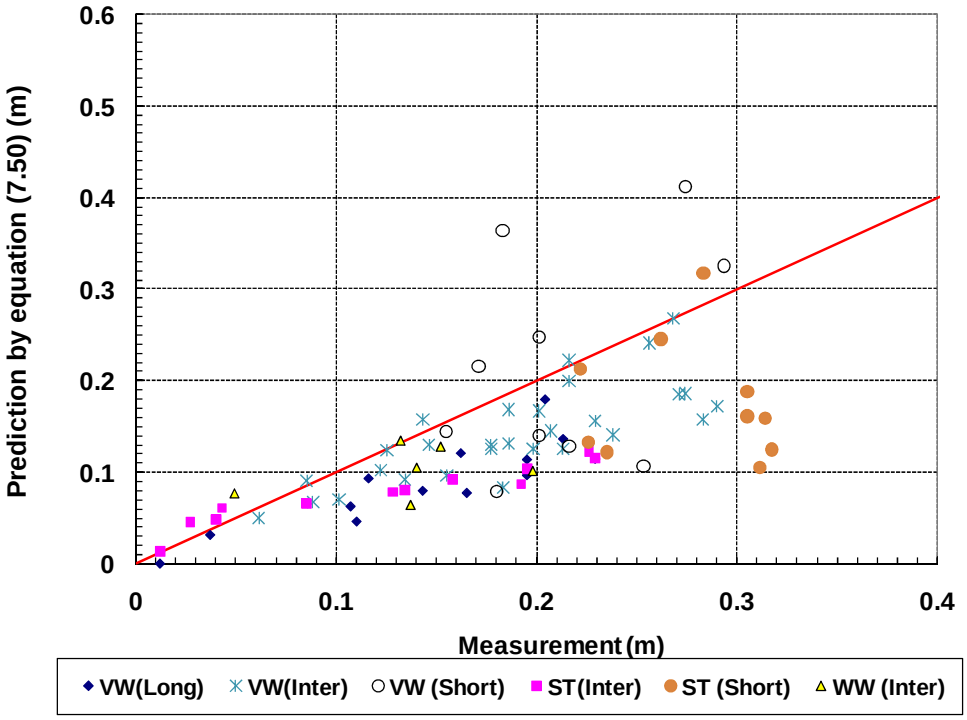

Figure 7.64 - Comparison between prediction by equation (7.50) and Sturm's database (2004).

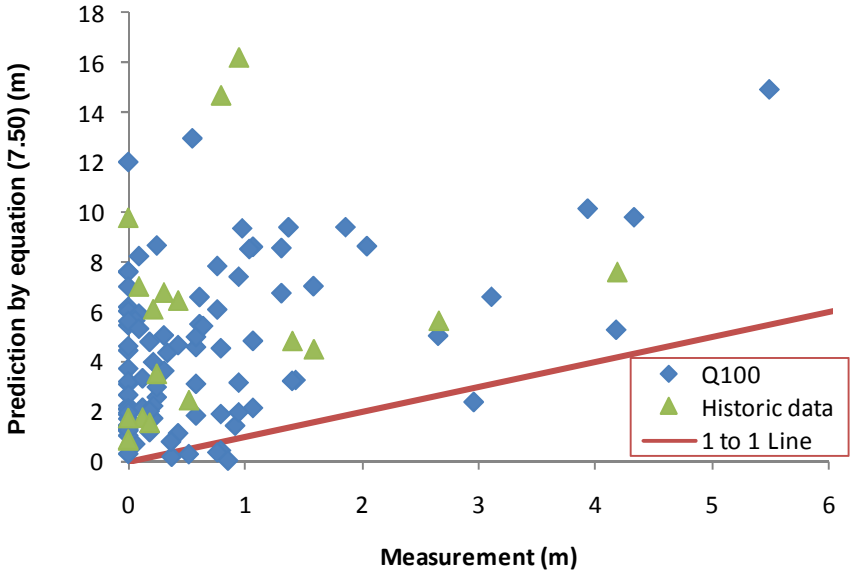

Figure 7.65 – Comparison between prediction by equation (7.50) and Benedict's database (2006).

Table 7.13 – Range of Reynolds numbers (Re_{f2}) in each study.

	Froehlich (1989)	Sturm (2004)	Present study	Benedict et al. (2006)
Min.	7,425	8,433	102,511	143,500
/Max.	71,133	55,451	322,681	11,436,281
Avg.	50,073	28,248	219,837	2,782,622

Figure 7.66 shows the effect of Reynolds number in maximum abutment scour depth. In order to find the Reynolds number effect, several points from laboratory test results, such as Froehlich (1989) and Strum (2004), were selected. Note that the database from Benedict et al. (2006) was not used because the accuracy of data from field measurements is much lower than that of laboratory test results. According to the relationship in Figure 7.66, the effect of Reynolds number is:

$$K_{\mathrm{Re}} = \frac{1}{0.0327 \cdot \mathrm{Re}_{f2}^{0.278}} \tag{7.51}$$

where, Re_{f2} is Reynolds number, defined as $\mathrm{Re}_{f2} = \dfrac{V_{f2} \cdot y_{f1}}{\nu}$

The maximum abutment scour prediction equation considering the effect of Reynolds number is:

$$\begin{aligned} \frac{y_{s(Abut)}}{y_{f1}} &= K_1 \cdot K_2 \cdot K_L \cdot K_G \cdot K_{\mathrm{Re}} \cdot 7.94 \cdot \left(1.65 \cdot Fr_{f2} - Fr_{fc}\right) \\ &= K_1 \cdot K_2 \cdot K_L \cdot K_G \cdot 243 \cdot \mathrm{Re}_{f2}^{-0.28} \cdot \left(1.65 \cdot Fr_{f2} - Fr_{fc}\right) \end{aligned} \tag{7.52}$$

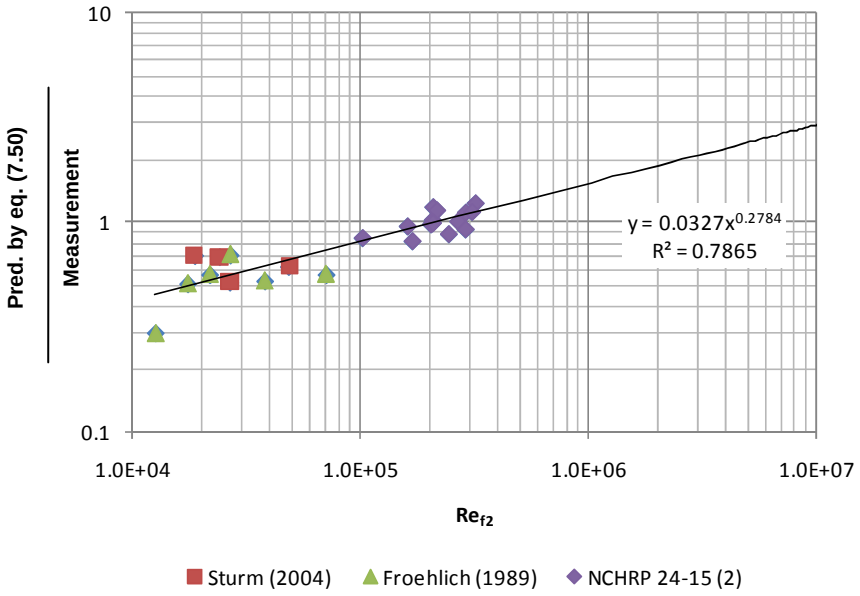

Figure 7.66 – The effect of Reynolds number in maximum abutment scour.

7.5.2.8 The Correction Factor for Pressure Flow (K_p)

According to the numerical results in the previous chapters, the maximum shear stress changes if the flow condition is changed to a pressure flow. Figure 7.67 shows the correction factor for the pressure flow condition. The correction factor varies with the ratio of the water depth above the lower chord of the bridge to the thickness of bridge deck (d_1/d_{deck}) as:

$$K_p = \begin{cases} 0.92 \cdot \left(d_1 / d_{deck}\right) + 1.0 & \text{for } d_1 / d_{deck} < 1.0 \\ 0.21\left(d_1 / d_{deck}\right)^2 - 1.27\left(d_1 / d_{deck}\right) + 2.97 & \text{for } 1.0 \le d_1 / d_{deck} \le 3.0 \\ 1.0 & \text{for } 3.0 < d_1 / d_{deck} \end{cases} \tag{7.53}$$

Note that the definitions of d_1 and d_{deck} are shown in Figure 7.67. The water depth which affects the scour depth is the depth between the lower chord of the bridge deck and the channel bottom because the flow above the bridge deck becomes irrelevant in scour development. Therefore the water depth y_{f1} in the prediction equation was replaced by h, which is the distance from the channel bottom to the lower chord of the bridge. These recommendations are based on the simulations where d_{deck}/h, is equal to 0.33. Full scale bridges are likely to have d_{deck}/h values smaller than that and therefore the use of K_p in general will be conservative.

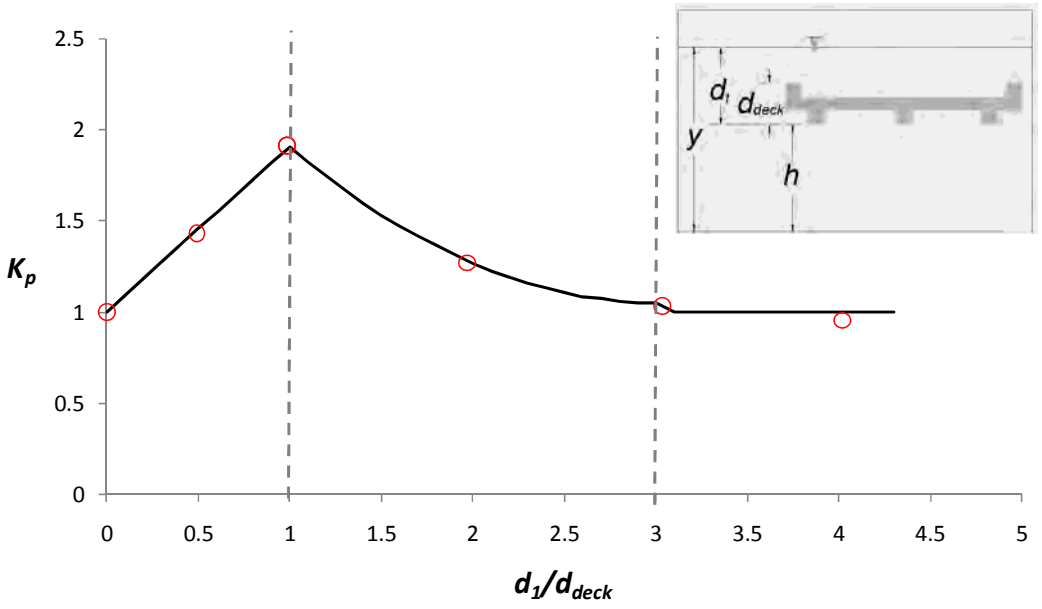

Figure 7.67 – Correction factor for pressure flow versus ratio of water depth (d_1/d_{deck}).

7.5.2.9 The Prediction Equation for Abutment Scour

The prediction equation for the maximum abutment scour depth (abutment scour depth plus contraction scour depth) has thus been developed. There are six correction factors to ac-

count for the shape of abutment, the attack angle of the flow, the abutment location, channel geometry, Reynolds number and the pressure flow condition. The final abutment scour prediction equation is

$$\frac{y_{s(Abut)}}{y_{f1}} = K_1 \cdot K_2 \cdot K_L \cdot K_G \cdot K_p \cdot 243 \cdot \mathrm{Re}_{f2}^{-0.28} \cdot \left(1.65 \cdot Fr_{f2} - Fr_{fc}\right) \tag{7.54}$$

Note that y_{f1} is replaced by h under the pressure flow condition (i.e., $y_{f1} > h$).

In equation (7.54), $y_{s(Abut)}$ is the maximum abutment scour depth, y_{f1} is the water depth at the toe of the abutment estimated as the water depth immediately upstream of the toe of the abutment, $Fr_{f2} = \frac{V_{f2}}{\sqrt{gy_{f1}}}$, $Fr_{fc} = \frac{V_{fc}}{\sqrt{gy_{f1}}} = \frac{\sqrt{\tau_c / \rho}}{gny_{f1}^{1/3}}$, $\mathrm{Re}_{f2} = \frac{V_{f2} \cdot y_{f1}}{\nu}$, K_1 is the correction factor for the abutment shape, K_2 is the correction factor for the abutment skew angle, K_L is the correction factor for the abutment location, K_p is the correction factor for the pressure flow. Their values and formulas are as follows:

$$K_1 = \begin{cases} 1.22 & \text{for Vertical-wall abutment} \\ 1.0 & \text{for Wing-wall abutment} \\ 0.73 & \text{for Spill-through abutment with 2:1 Slope} \\ 0.59 & \text{for Spill-through abutment with 3:1 Slope} \end{cases}$$

$$K_2 = \begin{cases} 1.0 - 0.005\left|\theta - 90°\right| & \textit{for } 60° \le \theta \le 120° \\ 0.85 & \textit{otherwise} \end{cases}$$

$$K_G = \begin{cases} 1.0 & \text{for compound channel} \\ 0.42 & \text{for rectangular channel} \end{cases}$$

$$K_L = \begin{cases} -0.23\dfrac{L_f - L'}{y_{f1}} + 1.35 & \text{for } \dfrac{L_f - L'}{y_{f1}} < 1.5 \\ 1.0 & \text{otherwise} \end{cases}$$

$$K_p = \begin{cases} 0.92 \cdot \left(d_1 / d_{deck}\right) + 1.0 & \text{for } d_1 / d_{deck} < 1.0 \\ 0.21\left(d_1 / d_{deck}\right)^2 - 1.27\left(d_1 / d_{deck}\right) + 2.97 & \text{for } 1.0 \le d_1 / d_{deck} \le 3.0 \\ 1.0 & \text{for } 3.0 < d_1 / d_{deck} \end{cases}$$

Figure 7.68 shows prediction using the prediction equation versus the measurements for the flume test cases.

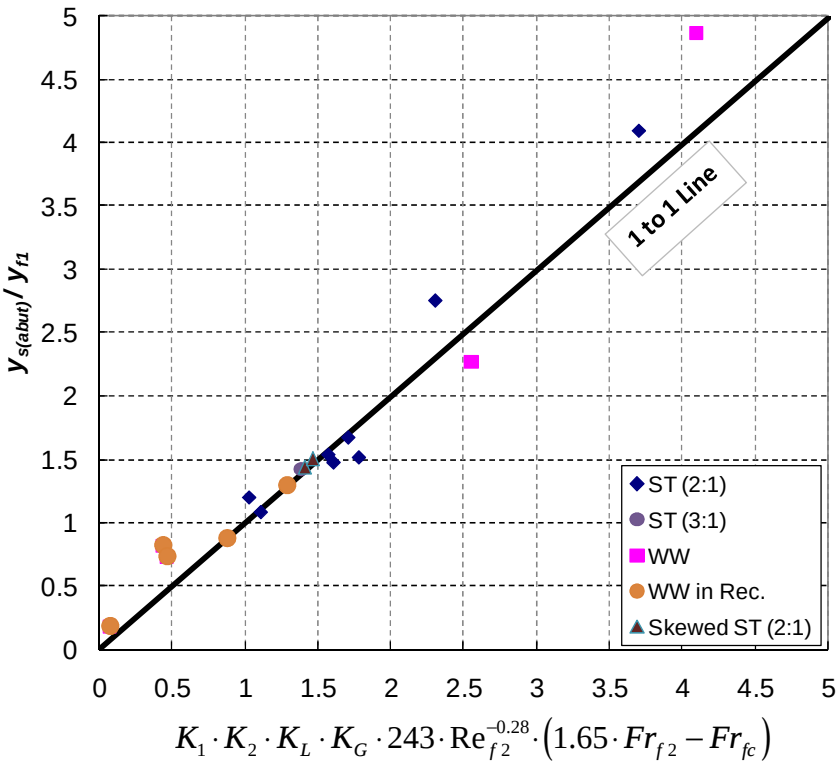

Figure 7.68 – Normalized Maximum Abutment Scour Depth: Test Results versus Prediction.

7.6 NEW APPROACH FOR ABUTMENT SCOUR DEPTH CALCULATION

The following definitions are used in this presentation for open channel flow near a bridge abutment (Figure 7.69) and for pressure flow near a bridge abutment (Figure 7.70).

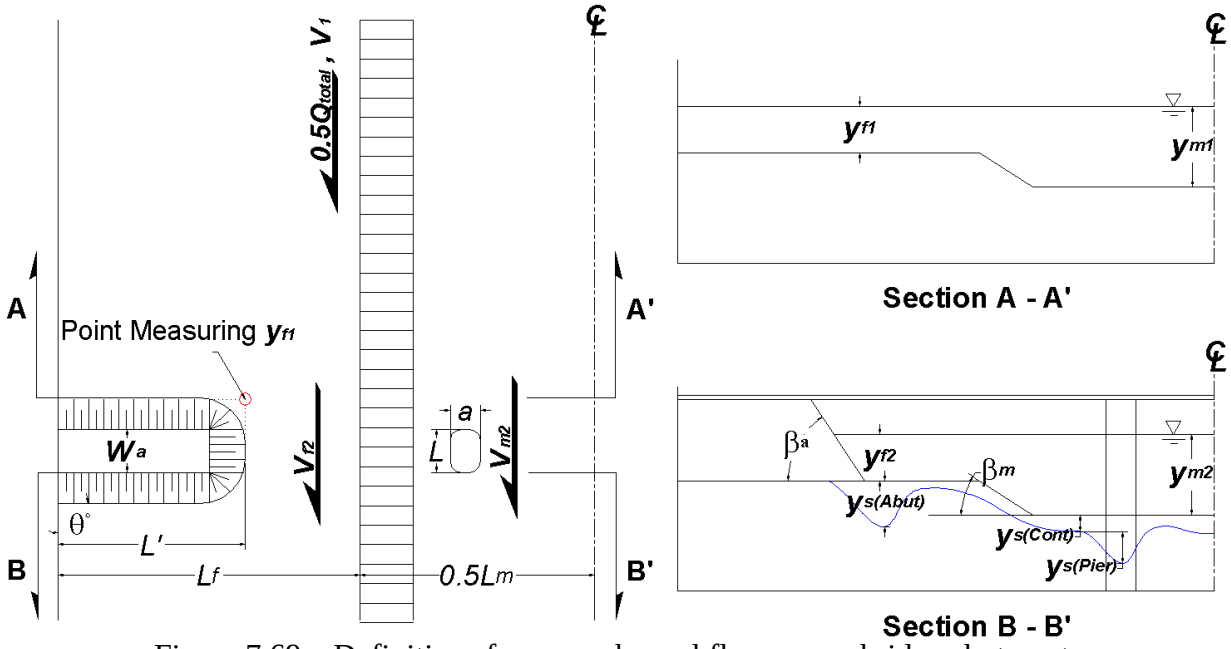

Figure 7.69 – Definitions for open channel flow near a bridge abutment.

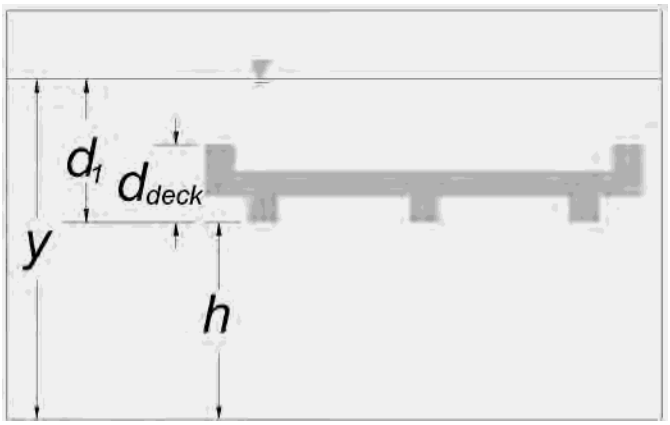

Figure 7.70 – Definitions for pressure flow near a bridge abutment.

The new approach is established for calculating the depth of the scour hole near an abutment (abutment scour depth plus contraction scour depth) constructed on a soil characterized by EFA curves or equivalent and subjected to a velocity hydrograph. This depth is called the final depth of scour (at the end of the hydrograph) not to be confused with the maximum depth of scour which is the depth reached for a chosen velocity sustained for an infinite time. This approach will be automated by a computer program (SRICOS-EFA). Note that the equations proposed are not limited to cohesive soils since they include a soil parameter able to represent any soil.

The proposed method makes use of samples collected at the site to obtain, as a minimum, the classification characteristics of the soil. One can either use the EFA to obtain the erodibility curves (preferred approach for final design) or the proposed charts (one for velocity and one for shear stress) below to obtain an estimate of the erodibility curve (acceptable for preliminary design). Note that with these recommended charts, the engineer can obtain the critical velocity of the soil by simply classifying the soil and reading the chart at an erosion rate of 0.1 mm/hr set as the threshold for erosion. Note also that some caution needs to be exercised as the velocity also depends on the water depth.

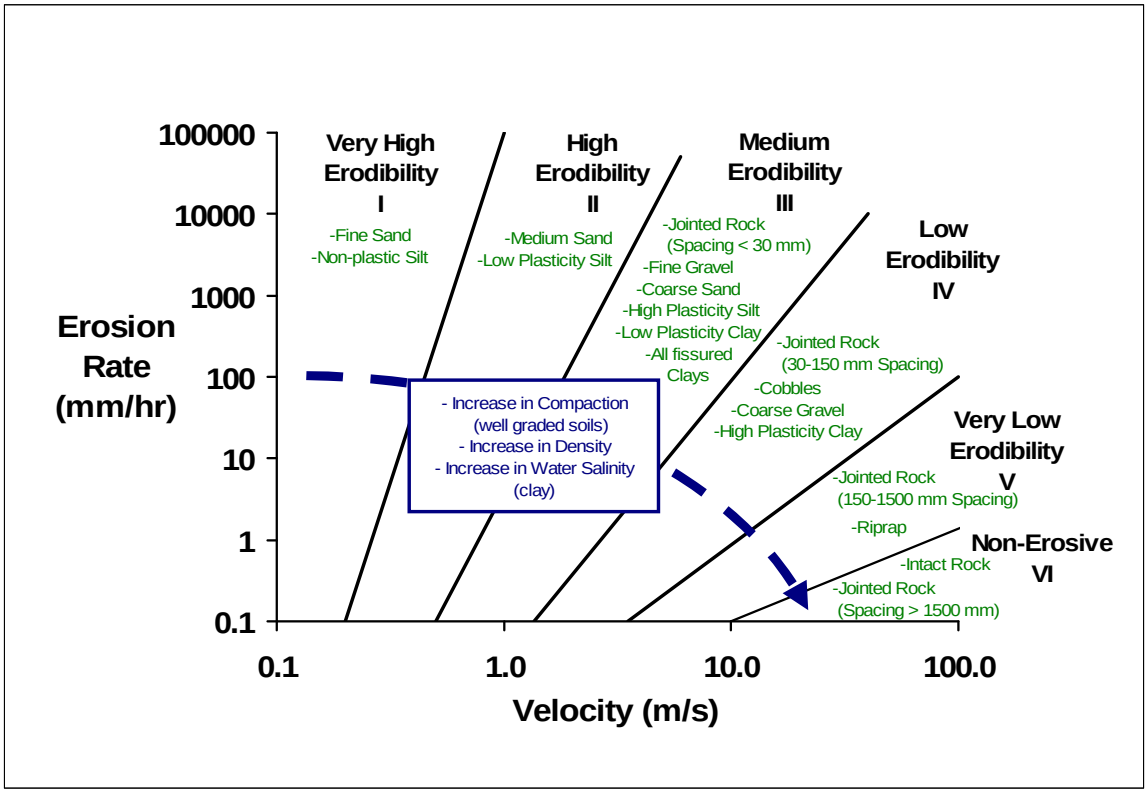

Figure 7.71 – Proposed erosion categories for soils and rocks based on velocity.

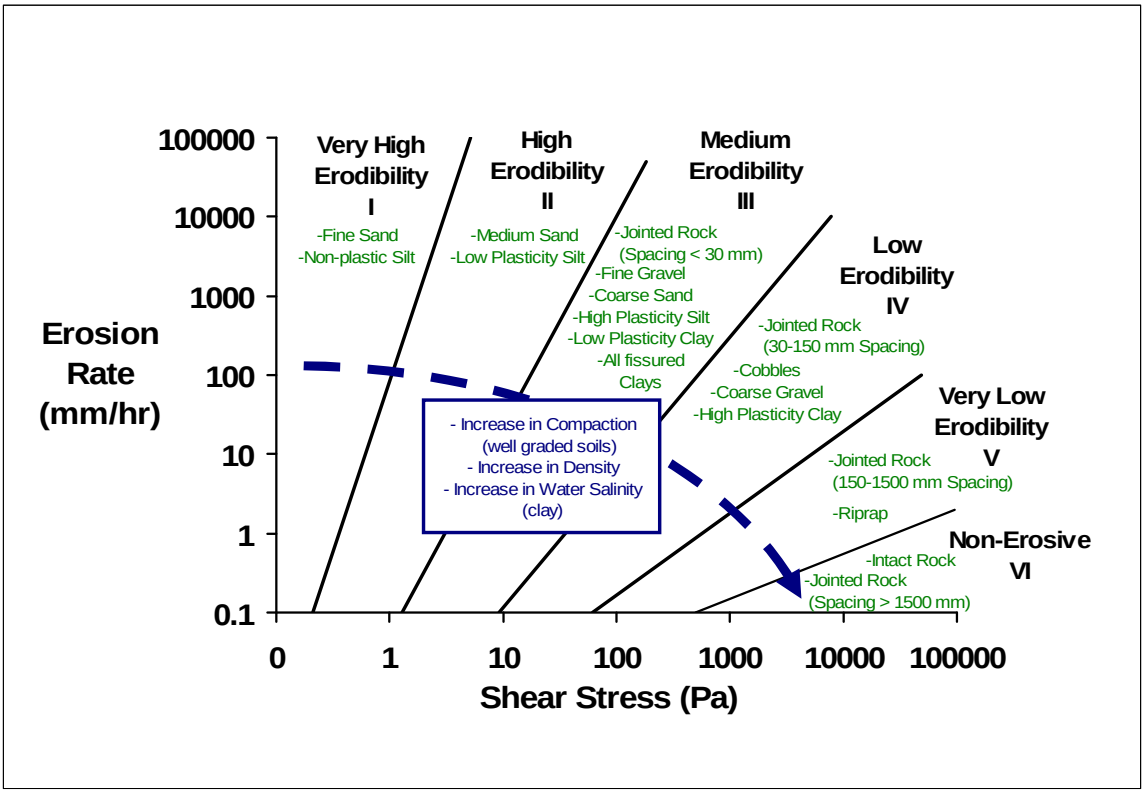

Figure 7.72 – Proposed erosion categories for soils and rocks based on shear stress.

Once the soil erodibility is classified, HEC-RAS is used to obtain hydraulic information including the unit discharge, the velocity, and the water depth near the abutment. Knowing the soil erosion function and the velocity, one can proceed with equations generated from the flume tests and the numerical simulations that we conducted. The equations give two parameters: the maximum depth of scour and the initial maximum shear stress. If only the maximum depth of scour is needed, one just uses the maximum depth of scour equation (Method A). To take advantage of the slow erosion process of an erosion resistant soil, one can use the time rate of erosion method proposed (HEC-18 Clay or Method B). This method consists of calculating the scour depth accumulated each day during the design life or remaining life of the bridge. This requires a hydrograph or the knowledge of Q100 and Q500, whichever is available at the site. A short cut to that method is to use a time compression concept to regroup the effect of the whole hydrograph into one time step called the final equivalent time (Method C). The final equivalent time is the time necessary for the highest velocity in the hydrograph to create the same scour depth as the entire hydrograph. In this case, the time rate calculations are significantly reduced and can be done on the back of an envelope.

The steps below explain the procedure carried out in the computer program which allows the calculations to be made for the case where a complete hydrograph is available (Method B). This computer program is the SRICOS-EFA program which is available free of charge on the web. It will be updated to include abutment scour.

Method A

1. Collect samples at the site
2. Test the samples in the EFA to get the erodibility curves or use the proposed soil erosion charts.
3. Describe the geometry of the abutment (length, width, shape, skew angle)
4. Describe the geometry of the river (main channel width, flood plain width left, flood plain width right, main channel to flood plain transition slope, flood plain bank slope, Manning coefficient, and longitudinal slope of the rive
5. Run HEC-RAS to obtain the velocity and water depth corresponding to the design flood.
6. Use the maximum abutment scour equation (Equation (7.55)) to calculate the maximum scour depth $y_{s(Abut)}$.

Method B

1. Collect samples at the site
2. Test the samples in the EFA to get the erodibility curves or use the proposed soil erosion charts.
3. Describe the geometry of the abutment (length, width, shape, skew angle)
4. Describe the geometry of the river (main channel width, flood plain width left, flood plain width right, main channel to flood plain transition slope, flood plain bank slope, Manning coefficient, and longitudinal slope of the river)
5. Input the flow hydrograph.
6. Run HEC-RAS to obtain the relationship between the flow and velocity, and the flow and water depth
7. Transform the flow hydrograph into a velocity hydrograph and a water depth hydrograph
8. Calculate the maximum scour depth $y_{s(Abut)}$ for the i^{th} velocity on the hydrograph (Equation (7.55))
9. Calculate the initial maximum shear stress τ_{max} around the abutment for the i^{th} velocity (before the scour hole develops) (Equation (7.56))
10. Read the initial scour rate corresponding to the initial maximum shear stress τ_{max} on the appropriate EFA curve
11. Use the results of steps 8 and 10 to construct the scour depth versus time curve for the i^{th} velocity
12. Calculate the equivalent time for the i^{th} velocity and the curve of step 11. The equivalent time for the i^{th} velocity is the time necessary for the highest velocity in the hydro-

graph up to the i^{th} time step to create the same scour depth as the hydrograph from start to the i^{th} time step.

13. Read the additional scour depth contributed by the i^{th} velocity during the i^{th} time step
14. Repeat steps 8 to 13 for the entire hydrograph
15. Output the scour depth versus time and read the final scour depth at the end of the hydrograph period.

Method C

1. Collect samples at the site
2. Test the samples in the EFA to get the erodibility curves or use the proposed soil erosion charts.
3. Describe the geometry of the abutment (length, width, shape, skew angle)
4. Describe the geometry of the river (main channel width, flood plain width left, flood plain width right, main channel to flood plain transition slope, flood plain bank slope, Manning coefficient, and longitudinal slope of the river.
5. Obtain the flow hydrograph.
6. Run HEC-RAS to determine the relationship between the flow and velocity, and the flow and water depth
7. Transform the flow hydrograph into a velocity hydrograph and a water depth hydrograph
8. Obtain the maximum velocity and corresponding water depth in the hydrograph
9. Calculate the initial maximum shear stress $\tau_{\max}$ around the abutment (before the scour hole develops) (Equation (7.56)) for the maximum velocity in the hydrograph
10. Read the initial scour rate corresponding to the initial maximum shear stress $\tau_{\max}$ on the EFA curve for the soil.
11. Calculate the maximum scour depth $y_{s(Abut)}$ around the abutment (Equation (7.55)) for the maximum velocity in the hydrograph
12. Use the results of steps 10 and 11 to construct the scour depth versus time curve for the maximum velocity in the hydrograph (Equation (7.57))
13. Calculate the final equivalent time for the entire hydrograph. The final equivalent time for the entire hydrograph is the time necessary for the highest velocity in the hydrograph to create the same scour depth as the entire hydrograph.
14. Read the final scour depth corresponding to the final equivalent time on the scour depth versus time curve of step12

Abutment maximum scour depth equation

The equation is presented below

$$\frac{y_{s(Abut)}}{y_{f1}} = K_1 \cdot K_2 \cdot K_L \cdot K_G \cdot K_p \cdot 243 \cdot \mathrm{Re}_{f2}^{-0.28} \cdot \left(1.65 \cdot Fr_{f2} - Fr_{fc}\right) \tag{7.55}$$

Note that y_{f1} is replaced by h under the pressure flow condition (i.e., $y_{f1} > h$).

where, $y_{s(Abut)}$ is the maximum abutment scour depth (abutment scour depth plus contraction scour depth), y_{f1} is the water depth at the toe of the abutment estimated as the water depth immediately upstream of the toe of the abutment, $Fr_{f2} = \frac{V_{f2}}{\sqrt{gy_{f1}}}$, $Fr_{fc} = \frac{V_{fc}}{\sqrt{gy_{f1}}} = \frac{\sqrt{\tau_c / \rho}}{gny_{f1}^{1/3}}$, $\mathrm{Re}_{f2} = \frac{V_{f2} \cdot y_{f1}}{\nu}$, K_1 is the correction factor for the abutment shape, K_2 is the correction factor for the abutment skew angle, K_L is the correction factor for the abutment location, K_p is the correction factor for the pressure flow. Their values and formulas are as follows:

$$K_1 = \begin{cases} 1.22 & \text{for Vertical-wall abutment} \\ 1.0 & \text{for Wing-wall abutment} \\ 0.73 & \text{for Spill-through abutment with 2:1 Slope} \\ 0.59 & \text{for Spill-through abutment with 3:1 Slope} \end{cases}$$

$$K_2 = \begin{cases} 1.0 - 0.005\left|\theta - 90°\right| & \textit{for } 60° \le \theta \le 120° \\ 0.85 & \textit{otherwise} \end{cases}$$

$$K_G = \begin{cases} 1.0 & \text{for compound channel} \\ 0.42 & \text{for rectangular channel} \end{cases}$$

$$K_L = \begin{cases} -0.23\dfrac{L_f - L'}{y_{f1}} + 1.35 & \text{for } \dfrac{L_f - L'}{y_{f1}} < 1.5 \\ 1.0 & \text{otherwise} \end{cases}$$

$$K_p = \begin{cases} 0.92 \cdot \left(d_1 / d_{deck}\right) + 1.0 & \text{for } d_1 / d_{deck} < 1.0 \\ 0.21\left(d_1 / d_{deck}\right)^2 - 1.27\left(d_1 / d_{deck}\right) + 2.97 & \text{for } 1.0 \le d_1 / d_{deck} \le 3.0 \\ 1.0 & \text{for } 3.0 < d_1 / d_{deck} \end{cases}$$

$$V_{f2} = \begin{cases} \dfrac{Q_{total}}{A_2} & \text{for short setback } \left((L_f - L') \le 5y_{m1}\right) \\ \dfrac{Q_{fp1}}{A_{f2}} & \text{for long setback } \left(L' \le 0.25L_f\right) \\ \text{otherwise use a linearly interpolated velocity between} & \\ \dfrac{Q_{total}}{A_2} & \text{for } (L_f - L') = 5y_{m2} \text{ and } \dfrac{Q_{fp1}}{A_{f2}} \text{ for } L' = 0.25L_f \end{cases}$$

Q_{total} = the total discharge,

Q_{fp1} = the discharge on the floodplain in the approach section immediately upstream of the abutment

A_2 = total flow area in the contracted section

A_{f2} = flow area on the floodplain in the contracted section

$L_f - L'$ = width of floodplain at contracted section (abutment setback from main channel)

V_{fc} = critical velocity for the material around the toe of the abutment, defined as

$$V_{fc} = \frac{\left(y_{f1}\right)^{1/6}}{n} \cdot \sqrt{\frac{\tau_c}{\rho \cdot g}}$$

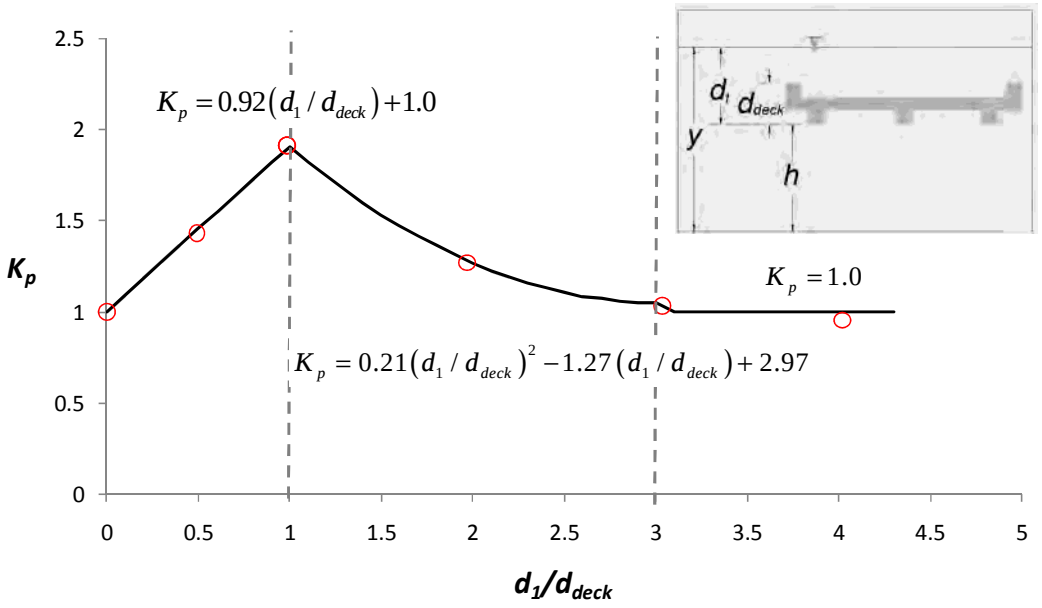

Figure 7.73 – Correction factor for pressure flow for abutment scour depth calculation.

Abutment maximum shear stress equation

The equation is presented below

$$\frac{\tau_{\max}}{\rho V_1^2} = k_c k_{sh} k_{Fr} k_s k_{sk} k_L k_o \cdot 12.45\,\mathrm{Re}^{-0.45} \tag{7.56}$$

where $\tau_{\max}$ = the maximum bed shear stress at the interface between the water and the river bottom near the abutment toe.

k_c = correction factor for channel conveyance ratio

k_{sh} = correction factor for the aspect ratio of the approach embankment

k_{Fr} = correction factor for Froude number

k_s = correction factor for abutment shape

k_{sk} = correction factor for skew angle

k_o = correction factor for overtopping

ρ = mass density of water

V_1 = upstream mean depth velocity in line with abutment edge

R_e = Reynolds number, defined as $R_e = VW_a / \nu$

ν = kinematic viscosity

W_a = top width of the abutment

F_r = Froude number, defined as $F_r = V / \sqrt{gy}$

g = acceleration due to gravity

y = upstream water depth in line with abutment edge

L' = projected abutment length normal to the flow direction

q_1 = unit discharge at approach section

q_2 = unit discharge around abutment

L_f = width of the flood plain

d_1 = distance from the water surface to the low chord of the bridge at upstream face of the bridge

d_{deck} = thickness of the bridge deck

$$k_c = 3.65\frac{q_2}{q_1} - 2.91$$

$$k_{sh} = 0.85 \times \left(\frac{L'}{W_a}\right)^{-0.24}$$

$$k_{Fr} = \begin{cases} 2.07Fr + 0.8 & \text{Fr} > 0.1 \\ 1.0 & \text{Fr} \le 0.1 \end{cases}$$

$$k_s = \begin{cases} 1.0 & \text{vertical-wall abutment} \\ 0.65 & \text{wing-wall abutment} \\ 0.58 & \text{spill-through abutment} \end{cases}$$

$$k_{sk} = 1.0$$

$$k_L = \begin{cases} 1.0 & \text{for } \left(L_f - L'\right)/y_f \le -2 \\ 0.6(L_f - L')/y_f + 1.2 & \text{for } -2 < (L_f - L')/y_f \le 0 \\ -1.2(L_f - L')/y_f + 1.2 & \text{for } 0 < (L_f - L')/y_f \le 1 \\ 1.0 & \text{for } 1 \le (L_f - L')/y_f \end{cases}$$

$$k_o = \begin{cases} 0.92 \cdot \left(d_1/d_{deck}\right) + 1.0 & \text{for } d_1/d_{deck} < 1.0 \\ 0.21\left(d_1/d_{deck}\right)^2 - 1.27\left(d_1/d_{deck}\right) + 2.97 & \text{for } 1.0 \le d_1/d_{deck} \le 3.0 \\ 1.0 & \text{for } 3.0 < d_1/d_{deck} \end{cases}$$

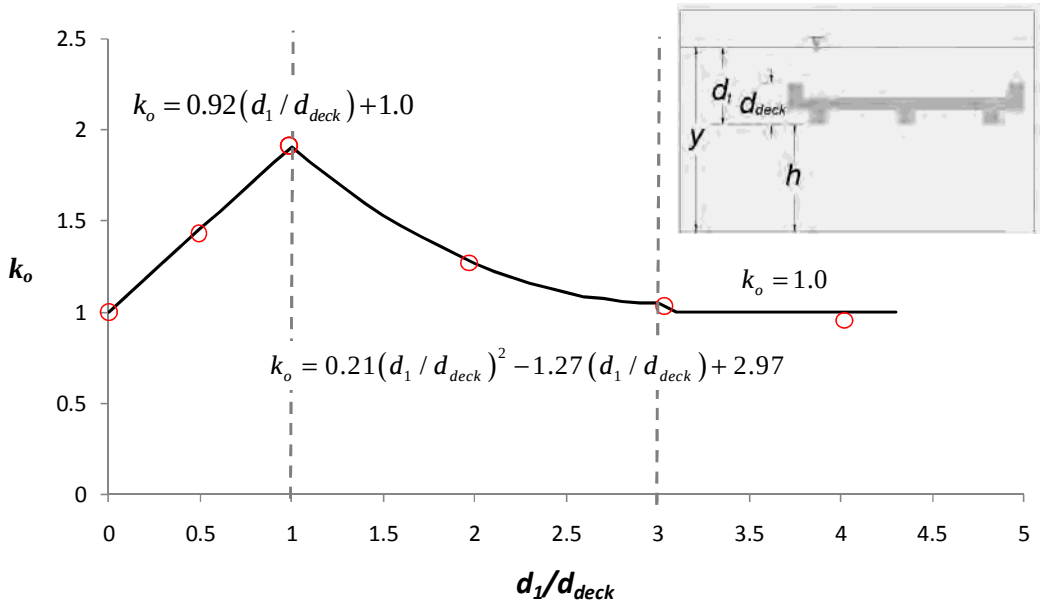

Figure 7.74 – Correction factor of overtopping flow for shear stress calculation.

Scour depth versus time curve equation

This equation describes the scour depth versus time curve:

$$y_{s(Abut)}(t) = \frac{t}{\frac{1}{\dot{z}_i} + \frac{t}{y_{s\ (Abut)}}} \tag{7.57}$$

where $y_{s(Abut)}(t)$ = abutment scour depth (abutment scour depth plus contraction scour depth) at time t

t = elapsed time after start of scour

$\dot{z}_i$ = initial rate of scour

$y_{s\ (Abut)}$ = maximum depth of scour near toe of abutment

7.7 NEW APPROACH FOR CONTRACTION SCOUR DEPTH CALCULATION

The following definitions are used in this presentation for open channel flow near a bridge abutment (Figure 7.75).

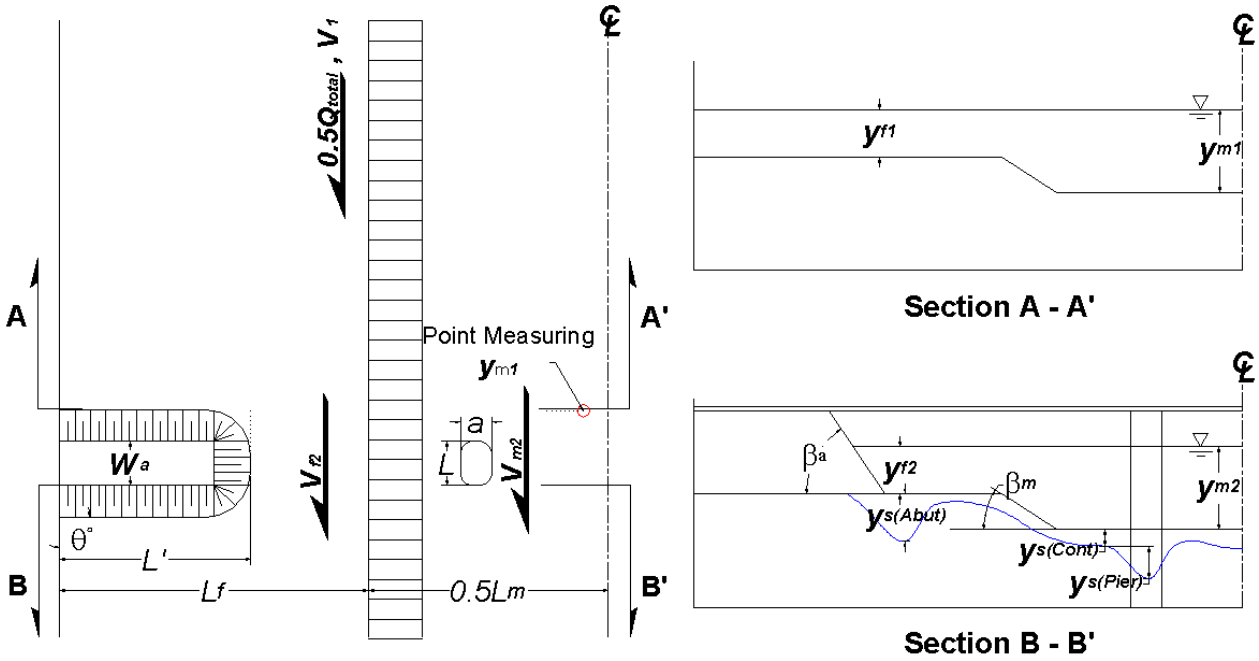

Figure 7.75 – Definition for the open channel flow at bridge section.

The new approach is established for calculating the depth of the contraction scour hole in the main channel constructed on a soil characterized by EFA curves or equivalent and subjected to a velocity hydrograph. This depth is called the final depth of scour (at the end of the hydrograph) not to be confused with the maximum depth of scour which is the depth reached for a chosen velocity sustained for an infinite time. This approach will be automated by a computer program (SRICOS-EFA). Note that the equations proposed are not limited to cohesive soils since they include a soil parameter able to represent any soil.

The proposed method makes use of samples collected at the site to obtain, as a minimum, the classification characteristics of the soil. One can either use the EFA to obtain the erodibility curves (preferred approach for final design) or the proposed charts (one for velocity and one for shear stress) below to obtain an estimate of the erodibility curve (acceptable for preliminary design). Note that with these recommended charts, the engineer can obtain the critical velocity of the soil by simply classifying the soil and reading the chart at an erosion rate of 0.1 mm/hr set as the threshold for erosion. Note also that some caution needs to be exercised as the velocity also depends on the water depth.

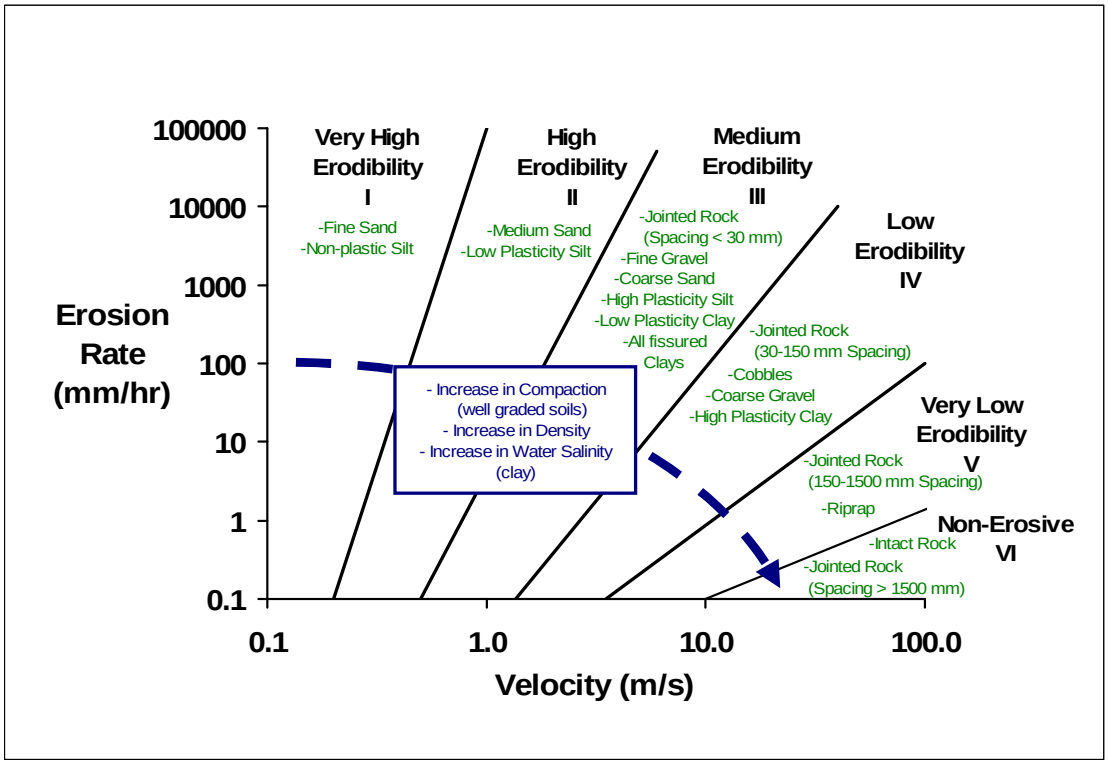

Figure 7.76 - Proposed erosion categories for soils and rocks based on velocity.

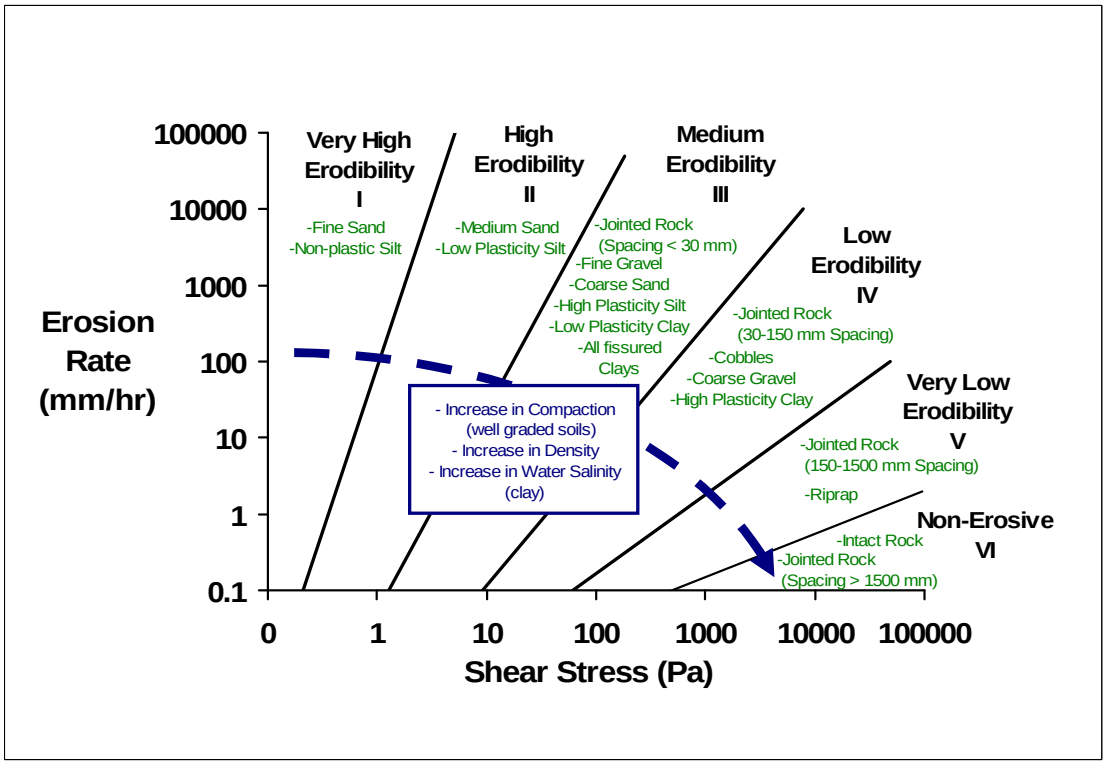

Figure 7.77 - Proposed erosion categories for soils and rocks based on shear stress.

Once the soil erodibility is classified, HEC-RAS is used to obtain hydraulic information including the unit discharge, the velocity, and the water depth near the abutment. Knowing the soil erosion function and the velocity, one can proceed with equations generated from the flume tests and the numerical simulations that we conducted. The equations give two parameters: the maximum depth of contraction scour and the initial maximum shear stress. If only the maximum depth of scour is needed, one just uses the maximum depth of scour equation (Method A). To take advantage of the slow erosion process of an erosion resistant soil, one can use the time rate of erosion method proposed (HEC-18 Clay or Method B). This method consists of calculating the scour depth accumulated each day during the design life or remaining life of the bridge. This requires a hydrograph or the knowledge of Q100 and Q500, whichever is available at the site. A short cut to that method is to use a time compression concept to regroup the effect of the whole hydrograph into one time step called the final equivalent time (Method C). The final equivalent time is the time necessary for the highest velocity in the hydrograph to create the same scour depth as the entire hydrograph. In this case, the time rate calculations are significantly reduced and can be done on the back of an envelope.

The steps below explain the procedure carried out in the computer program which allows the calculations to be made for the case where a complete hydrograph is available (Method B). This computer program is the SRICOS-EFA program which is available free of charge on the web.

Method A

1. Collect samples at the site
2. Test the samples in the EFA to get the erodibility curves or use the proposed soil erosion charts.
3. Describe the geometry of the abutment (length, width, shape, skew angle).
4. Describe the geometry of the river (main channel width, flood plain width left, flood plain width right, main channel to flood plain transition slope, flood plain bank slope, Manning coefficient, and longitudinal slope of the rive
5. Run HEC-RAS to obtain the velocity and water depth corresponding to the design flood.
6. Use the maximum abutment scour equation (Equation (7.58)) to calculate the maximum scour depth $y_{s(Cont)}$.

Method B

1. Collect samples at the site
2. Test the samples in the EFA to get the erodibility curves or use the proposed soil erosion charts.
3. Describe the geometry of the abutment (length, width, shape, skew angle).
4. Describe the geometry of the river (main channel width, flood plain width left, flood plain width right, main channel to flood plain transition slope, flood plain bank slope, Manning coefficient, and longitudinal slope of the river)

5. Input the flow hydrograph.
6. Run HEC-RAS to obtain the relationship between the flow and velocity, and the flow and water depth
7. Transform the flow hydrograph into a velocity hydrograph and a water depth hydrograph
8. Calculate the maximum scour depth $y_{s(Cont)}$ for the ith velocity on the hydrograph (Equation (7.58))
9. Calculate the initial maximum shear stress $\tau_{\max(Cont)}$ at the center line of channel for the ith velocity (before the scour hole develops) (Equation (7.59))
10. Read the initial scour rate corresponding to the initial maximum shear stress $\tau_{\max(Cont)}$ on the appropriate EFA curve
11. Use the results of steps 8 and 10 to construct the scour depth versus time curve for the ith velocity
12. Calculate the equivalent time for the ith velocity and the curve of step 11. The equivalent time for the ith velocity is the time necessary for the highest velocity in the hydrograph up to the ith time step to create the same scour depth as the hydrograph from start to the ith time step.
13. Read the additional scour depth contributed by the ith velocity during the ith time step
14. Repeat steps 8 to 13 for the entire hydrograph
15. Output the scour depth versus time and read the final scour depth at the end of the hydrograph period.

Method C

1. Collect samples at the site
2. Test the samples in the EFA to get the erodibility curves or use the proposed soil erosion charts.
3. Describe the geometry of the abutment (length, width, shape, skew angle)
4. Describe the geometry of the river (main channel width, flood plain width left, flood plain width right, main channel to flood plain transition slope, flood plain bank slope, Manning coefficient, and longitudinal slope of the river.
5. Obtain the flow hydrograph.
6. Run HEC-RAS to determine the relationship between the flow and velocity, and the flow and water depth
7. Transform the flow hydrograph into a velocity hydrograph and a water depth hydrograph
8. Obtain the maximum velocity and corresponding water depth in the hydrograph

9. Calculate the initial maximum shear stress $\tau_{\max(Cont)}$ at the center line of channel (before the scour hole develops) (Equation (7.59)) for the maximum velocity in the hydrograph
10. Read the initial scour rate corresponding to the initial maximum shear stress $\tau_{\max(Cont)}$ on the EFA curve for the soil.
11. Calculate the maximum contraction scour depth $y_{s(Cont)}$ in the main channel (Equation (7.58)) for the maximum velocity in the hydrograph.
12. Use the results of steps 10 and 11 to construct the scour depth versus time curve for the maximum velocity in the hydrograph (Equation (7.61))
13. Calculate the final equivalent time for the entire hydrograph. The final equivalent time for the entire hydrograph is the time necessary for the highest velocity in the hydrograph to create the same scour depth as the entire hydrograph (Equation (7.60).
14. Read the final scour depth corresponding to the final equivalent time on the scour depth versus time curve of step12

Contraction maximum scour depth equation

$$\frac{y_{s(Cont)}}{y_{m1}} = 2.21\left(1.31Fr_{m2} - Fr_{mc}\right) \tag{7.58}$$

where $y_{s(Cont)}$ is the maximum contraction scour depth, y_{m1} is the main channel depth at the approach section, $Fr_{m2}\left(=\frac{V_2}{\sqrt{gy_{m1}}}\right)$ is the Froude number of the main-channel at the bridge section, $Fr_{mc}\left(=\frac{V_{mc}}{\sqrt{gy_{m1}}}=\frac{\sqrt{\tau_c/\rho}}{gny_{m1}^{1/3}}\right)$ is the critical Froude number of the main-channel, V_2 is the average velocity at the contracted section obtained by HEC-RAS, V_{mc} is the critical velocity in the main channel, τ_c is the critical shear stress, n is Manning's roughness coefficient, and ρ is the water density.

Contraction maximum shear stress equation

Nurtjahyo (2003) numerically studied the maximum bed shear stress at the center of the channel under long contraction. The equation is generated by correcting the open channel flow equation. including the effect of the contraction ratio k_R, the effect of contraction transition angle k_θ, the effect of the contraction length k_L.

$$\tau_{\max(Cont)} = k_R k_\theta k_L \gamma n^2 V_1^2 R_h^{-\frac{1}{3}} \tag{7.59}$$

where $\tau_{\max(Cont)}$ =contraction maximum shear stress at the center line of channel

γ = unit weight of water

n = Manning's coefficient

R_h = hydraulic radius of approach section

V_1 = average approach velocity

A_1 = the approach channel area

A_2 = the channel area at the bridge section

W_a = top width of bridge abutment

α = the contraction transition angle

$$k_R = 0.62 + 0.38\left(\frac{A_1}{A_2}\right)^{1.75}$$

$$k_\theta = 1 + 0.9\left(\frac{\alpha}{90}\right)^{1.5}$$

$$k_L = \begin{cases} 1 & , for \quad k_L \geq 0.35 \\ 0.77 + 1.36\left(\frac{W_a}{L'_{(Left)} + L'_{(Right)}}\right) - 1.98\left(\frac{W_a}{L'_{(Left)} + L'_{(Right)}}\right)^2 & , for \quad k_L < 0.35 \end{cases}$$

Final equivalent time equation

The final equivalent time t_e refers to the entire hydrograph; it is the time necessary for the highest velocity in the hydrograph to create the same scour depth as the entire hydrograph.

Contraction Scour

$$t_e(\text{hrs}) = 644.32 \cdot \left(t_{hydr}(\text{years})\right)^{0.4242} \cdot \left(V_{\max}\left(\text{m}/\text{s}\right)\right)^{1.648} \cdot \left(\dot{z}_{i,mean}\left(\text{mm}/\text{hr}\right)\right)^{-0.605} \qquad (7.60)$$

where $t_e(\text{hrs})$ = equivalent time necessary for the highest velocity in the hydrograph to create the same scour depth as the entire hydrograph

$t_{hydro}(\text{years})$ = the duration of the hydrograph

$V_{\max}(\text{m/s})$ = maximum velocity in the hydrograph

$\dot{z}_i(\text{mm/hr})$ = initial rate of scour corresponding to the maximum velocity

$\dot{z}_{i,mean}(\text{mm/hr})$ = mean initial rate of scour corresponding to the maximum velocity

Scour depth versus time curve equation

This equation describes the scour depth versus time curve:

$$y_{s(Cont)}(t) = \frac{t}{\frac{1}{\dot{z}_i} + \frac{t}{y_{s\,(Cont)}}} \tag{7.61}$$

where $y_{s(Cont)}(t)$ = contraction scour depth at time t

t = elapsed time after start of scour

$\dot{z}_i$ = initial rate of scour

$y_{s\,(Cont)}$ = maximum depth of scour near toe of abutment

CHAPTER 8

VERIFICATION OF THE SRICOS-EFA METHOD

The SRICOS-EFA method for contraction and abutment scour in cohesive soils was developed on the basis of flume tests for the maximum scour depth equations and numerical simulations for the maximum initial shear stress equations. As with any new method, there is a need to verify the method against other measurements. The following databases were found in the literature review.

(1) Gill (1981) for contraction scour

(2) Sturm (2004) for abutment scour in compound channels

(3) Froehlich (1989) for abutment scour in rectangular channels (=short setback)

(4) NCHRP 24-20 (2008) for abutment scour depth, and the scour ratio between abutment scour and contraction scour

(5) Benedict et al. (2006) for the abutment scour with full scale measurement

These databases are for cohesionless soils but it is useful to compare the SRICOS-EFA method to the measurement for cohesionless soils. In addition, a comparison with previous equations for abutment scour depth using imaginary conditions is performed.

The Shields diagram was used to calculate the critical shear stress for cohesionless soils. The relationship between the critical shear stress and the critical velocity in open channels in Richardson et al. (1995) was used to obtain the critical velocity for the cohesionless soil.

8.1 CONTRACTION SCOUR

Experimental data in Gill (1981) were used for comparison of contraction scour depth. Gill conducted a series of contraction scour tests in the laboratory. The experiments were conducted in a rectangular channel which is 11.4 m long, 0.76 m wide and 0.46 m deep. Two contracted sections were used in the channel. In the first series of experiments, the effective length of the contraction is 1.83 m, excluding the 0.46 m long upstream (inlet) and 0.46 m long downstream (outlet) transitions. In the second series of experiments, the effective length of the contraction is 2.44 m with the transitions. The width of the contracted section is 0.5 m. Two types of nearly uniform sand were used in the experiments. The average size of the coarse sand, D_{50}, is 1.53 mm while D_{50} of the fine sand is 0.92 mm. The angle of transition at the contraction is approximately 15°.

The comparison between predictions by equation (7.58) and Gill's test results is shown in Figure 8.1. The comparison between predictions using the HEC-18 method and that in Gill's test results (conducted in NCHRP 24-15) is shown in Figure 8.2. According to the figures, the predictions based on the present study are in reasonable agreement with the database while the HEC-18 method severely under predicts the scour depths.

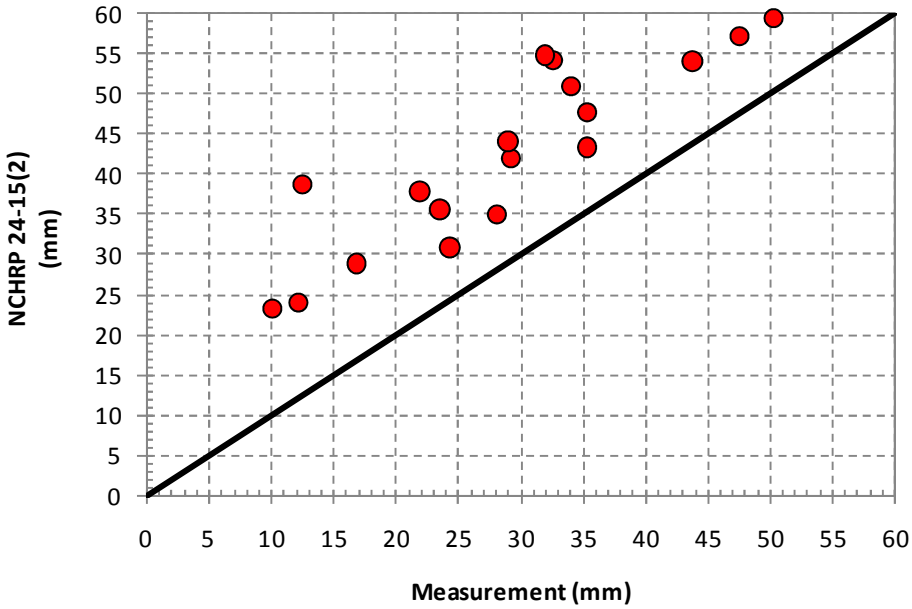

Figure 8.1 – NCHRP 24-15(2) predictions versus Gill (1981) database.

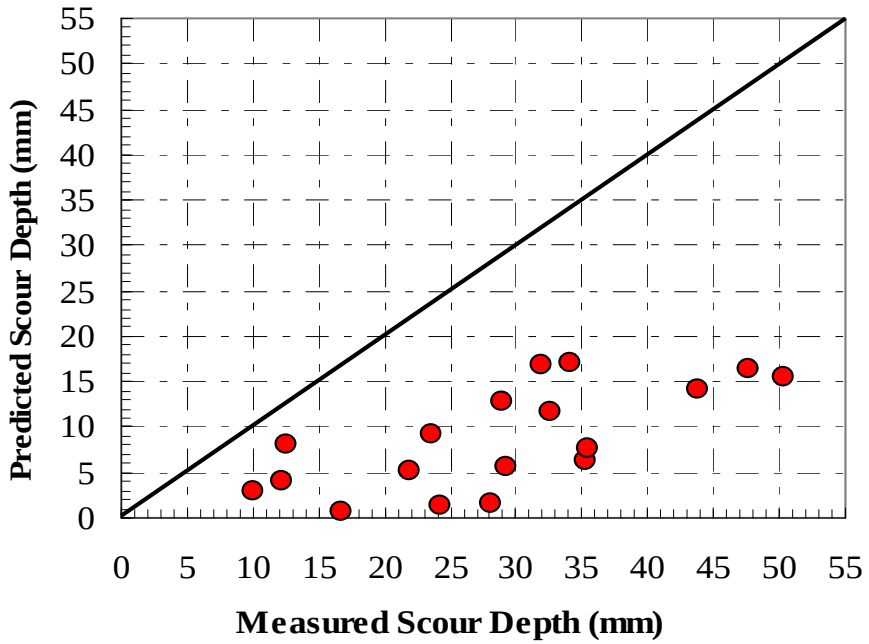

Figure 8.2 - HEC-18 method versus Gill (1981) database (cited from Briaud et al. (2004)).

8.2 ABUTMENT SCOUR

8.2.1 Comparison with Laboratory Test Results

The abutment scour prediction equation developed in the present study has also been applied to non-cohesive soil. Data from Sturm (2004) taken in compound channels and data from Froehlich (1989) (which was cited in Palaviccini's Ph.D. dissertation in 1993) taken in rectangular channels were used for the comparisons. Comparisons with the study of NCHRP 24-20 (2008) was also performed for the scour condition B (the long set back condition in NCHRP 24-20).

(1) Data in Sturm (Sturm, 2004)

Sturm (2004) used three types of abutments: vertical-wall, spill-through, and wing-wall. The length of abutments was varied and 3 different types of sands were used in a compound channel. The experiments were conducted in a 4.2 m wide and 24.4 m long flume. The ratio of the abutment length to the floodplain width (L'/L_f) was varied from 0.22 to 1.0. The median sizes of the 3 types of sand are 3.3 mm, 2.7 mm, and 1.1 mm. Figure 8.3 shows the comparison between Sturm's data and predictions using the prediction equation in the present study. Based on the figure, equation (7.55) yields both under estimations and over estimation. For the safe design, the factor of safety is required in this comparison, and it is 2.0. Note that in Figure 8.3 "VW" represents vertical wall abutments, "ST" represents spill-through abutments, "WW" represents wing-wall abutments, "Long" indicates long setback $\left(L_f - L' > 5y_m\right)$, "Short" indicates short setback $\left(L' \le 0.25L_f\right)$, and "Inter" indicates intermediate setback.

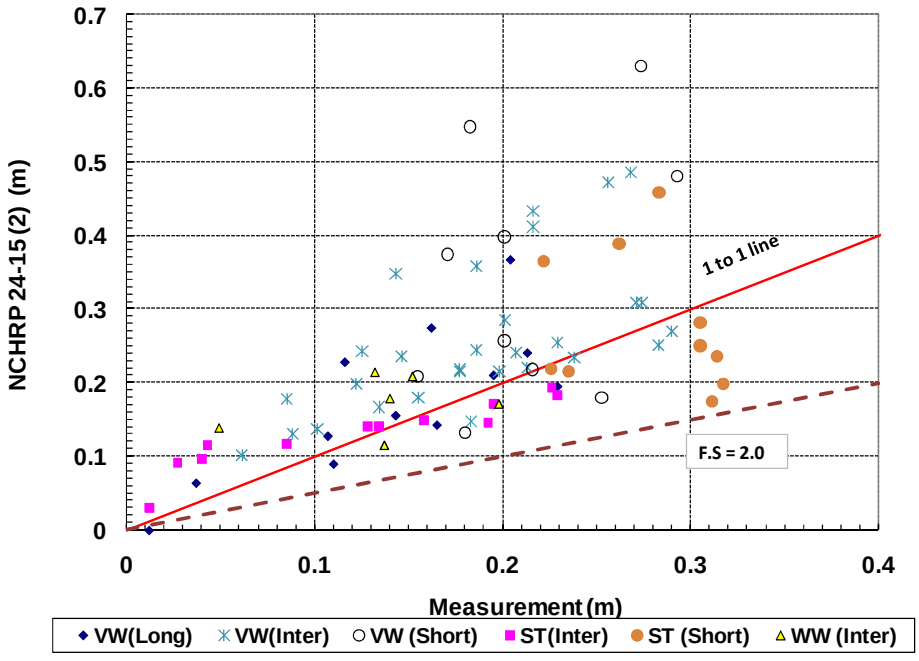

Figure 8.3 – Comparison with Sturm's (2004) data.

(2) Froehlich's database (Froehlich, 1989)

Froehlich analyzed 170 live-bed scour and 230 clear-water scour measurements taken by other researchers in rectangular channels in different laboratory flumes. Many types of abutments, such as vertical board, vertical wall, semicircular, triangular, wing-wall, and spill-through abutments were covered in the analysis. A total of 195 clear-water scour measurements (101 for vertical-wall, 45 for spill-through, and 45 for wing-wall) were selected from Froehlich's 230 clear-water scour cases for comparison. Figure 8.4 shows the comparison between Sturm's data and predictions using the prediction equation in the present study. Based on the figure, equation (7.55) yields both under estimations and over estimation. For the safe design, the factor of safety is required in this comparison, and it is 2.0.

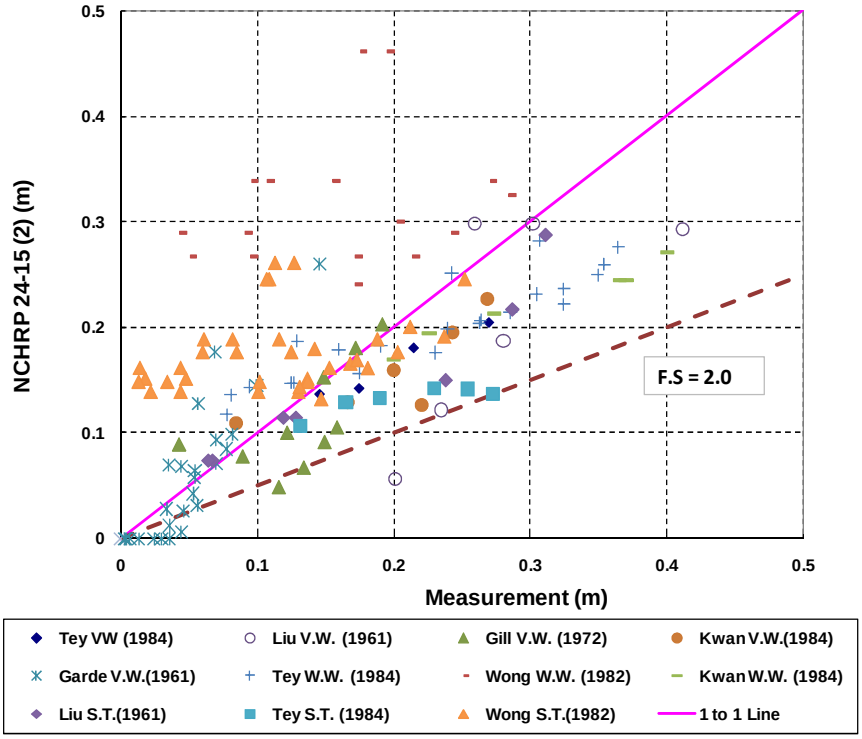

Figure 8.4 – Comparison with Froehlich's (1989) data.

(3) Comparison with NCHRP 24-20 (Ettema et al., 2008)

Three types of scour pattern were studied in NCHRP 24-20, and those are:

1. Condition A: the floodplain is made of less erodible soils while the main channel is made with more erodible soils.
2. Condition B: the maximum local scour occurs on the floodplain, if the abutment has a long set back on the floodplain or exists in a rectangular channel.
3. Condition C: embankments were built with the same material as for the channel bottom so the embankments are vulnerable to erosion.

In the present study, Porcelain clay was used at both floodplain and main channel, and nonerosive abutment was used. Thus condition A and C are totally different with the test condition of the present study. For the comparison with the study in NCHRP 24-20, the data for condition B were selected. Figure 8.5 shows the comparison between the prediction by equation (7.55) and measurement results obtained in NCHRP 24-20. Based on the figure, equation (7.55) yields good prediction to those data.

Using the contraction scour equation (Equation (7.38)) and the abutment scour equation (Equation (7.55)) in the present study, the predicted scour depth to flow depth ratio is compared with that in NCHRP 24-20. The simple rectangular channel condition (Condition B in NCHRP 24-20) was assumed and 3 velocity ratios (V_1/V_c = 1.0, 0.95, 0.75) were used in the comparison. Figure 8.5 shows the comparison. The scour depth ratio in NCHRP 24-20 increases rapidly for a small unit discharge ratio q_2/q_1 ($q_2/q_1 \le 1.2$ for wing-wall abutments and $q_2/q_1 \le 1.2$ for spill-through abutments) and then it decreases gradually. The predicted trend for the spill-through abutment agrees well with that in NCHRP 24-20 for a big unit discharge ratio of $q_2/q_1 > 3.5$, but does not for the discharge ratio of $q_2/q_1 < 3.5$. The predicted trend curve for the wing-wall abutment does not agree with the result of NCHRP 24-20. Note that in Figure 8.6 y_{max} is the abutment scour flow depth ($y_{max} = y_{s(Abut)} + y_{f1}$), y_c is the contraction scour flow depth ($y_c = y_{s(Cont)} + y_{f1}$), q_1 is the unit discharge at the approach section, and q_2 is the unit discharge at the bridge section.

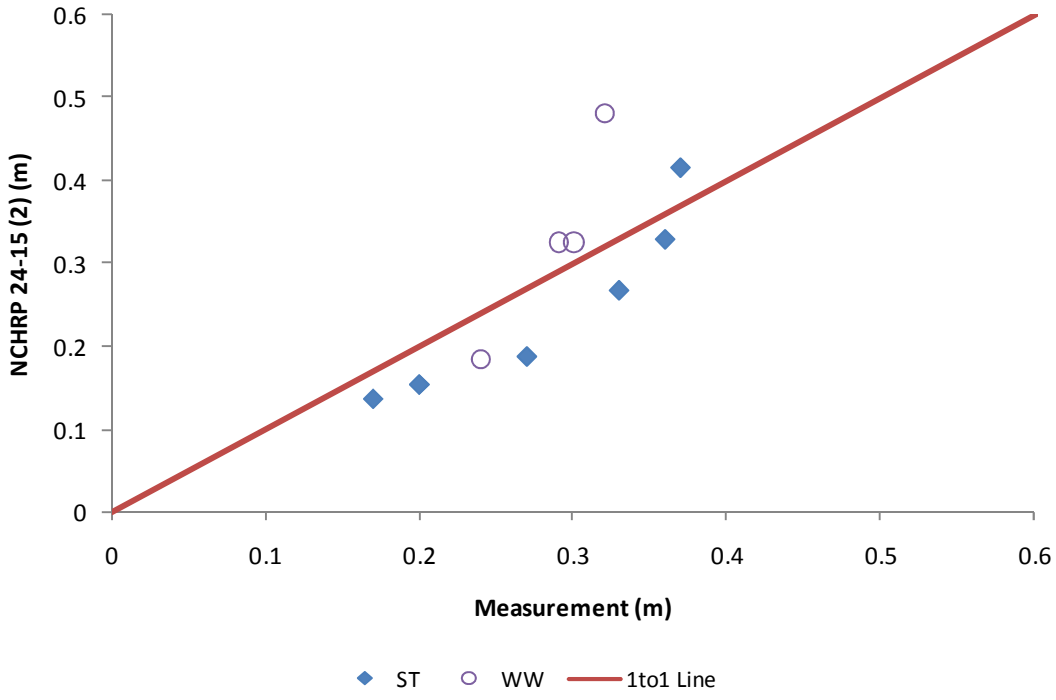

Figure 8.5 – Comparison between prediction by present study and measurement results in NCHRP 24-20 (2008)

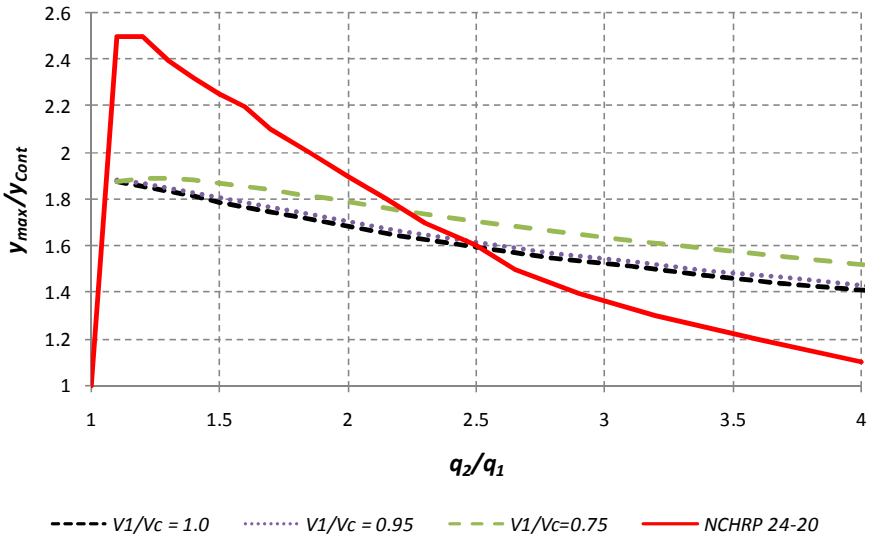

(a) Wing-Wall shape abutment

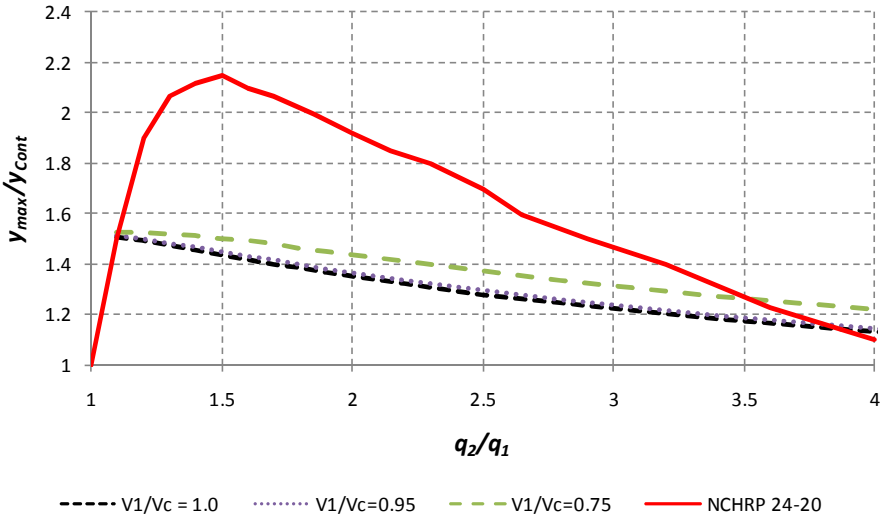

(b) Spill-Through abutment

Figure 8.6 - Comparison with NCHRP 24-20 (2008).

8.2.2 Comparison with Full Scale Measurement

Benedict et al. (2006) conducted field survey at 144 bridges in South Carolina for abutment scour depth. Their database is available for download at the USGS web site at http://pubs.usgs.gov/of/2003/ofr03-295/index.html (as of March 2009). The data for Q100 and historic data in the Piemont area were compared with the predictions based on the present study. All the soil materials were assumed as cohesionless in the calculation of critical shear stress and critical velocity. Figure 8.7 shows the comparison. Equation (7.55) mostly over predicts the field data based on the comparison, but the factor of safety as 2.0 is required for the safe design.

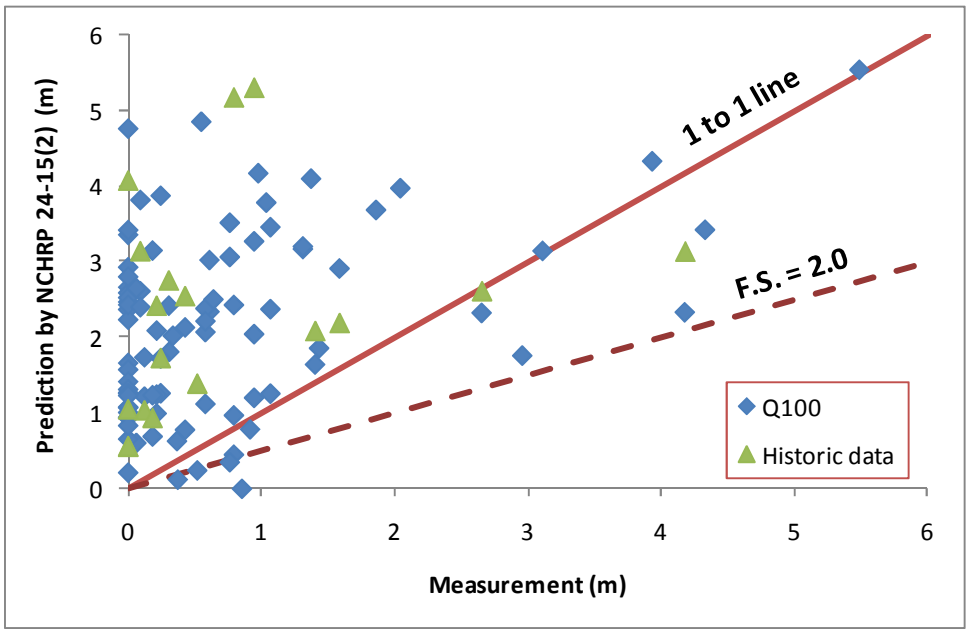

Figure 8.7 – Comparison with Benedict and et al.'s (2006) data.

8.2.3 Comparison with Previous Equations for Abutment Scour Depth Using Imaginary Condition

Due to the scarcity of field data and the unknown property of the soil, imaginary bridge conditions were made up to calculate the scour depth for full scale bridges. The proposed maximum abutment scour depth equation in the present study and equations in other reports were used for the prediction. The full scale imaginary bridge properties are summarized in Table 8.1. Three types of sand (D_{50} = 0.4 mm, 2.0 mm and 10 mm) were considered. The half width of the main channel was fixed as 77.1 m and the slope of main channel was assumed as 3(H):1(V). The spill-through abutment with a 2(H):1(V) abutment slope was assumed. The schematic diagram of the imaginary full scale channel is shown in Figure 8.8.

A series of HEC-RAS runs were performed to obtain the velocities and water depths. The back water effect was neglected in the predictions. The water depths and velocities at the approach section in Sturm's (2004) study were calculated with the presence of embankment in the HEC-RAS runs. The comparisons are presented in Figure 8.9.

According to Figure 8.8, most prediction methods yield overestimated scour abutment scour depths compared to the scour depth by present study. Especially, Sturm's (2004) and Melville's (1992) formula predict the deepest abutment scour depths. The calculated abutment scour depths based on Maryland SHA Bridge Scour Program (ABSCOUR) (2007), agree well with those based on the present study. The calculated abutment scour depths based on HEC-18 recommendation are deeper than those based on the present study. Note that the HEC-18 method is based on the HIRE (Richardson et al. (2001)) equation for $L' > 25y_{f1}$ and Froehlich's (1989) live bed scour equation for $L' \leq 25y_{f1}$.

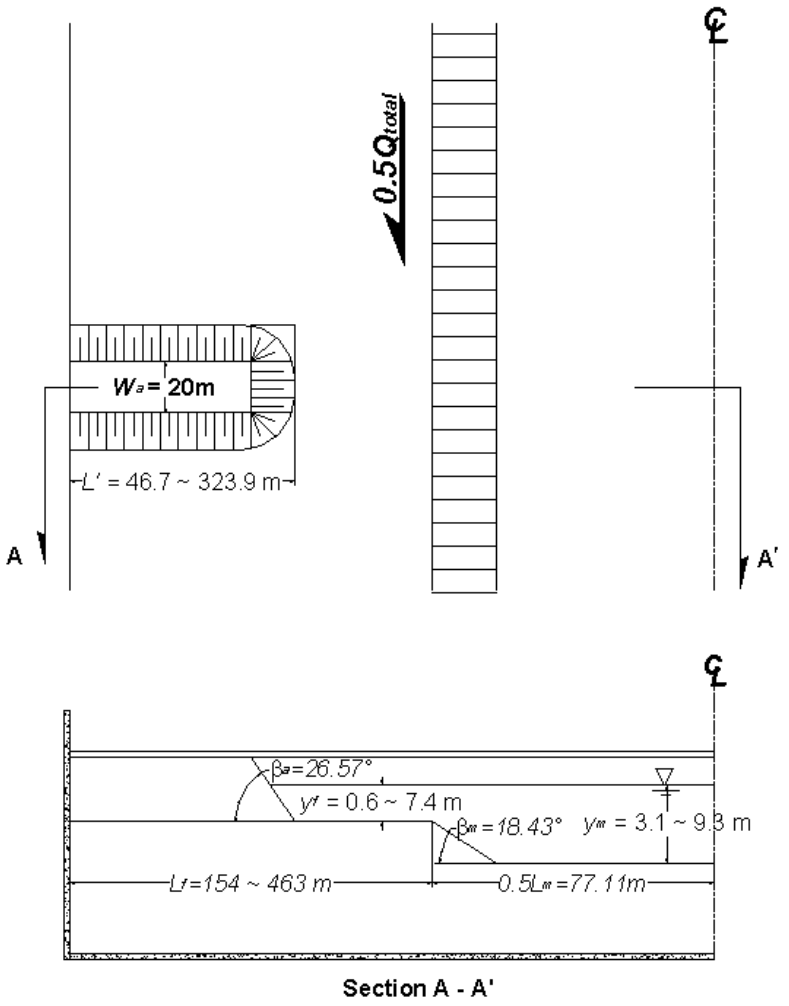

Figure 8.8 – Schematic diagram of imaginary full scale channel.

Table 8.1 – Summary of the imaginary test conditions for comparisons with different prediction equations.

Case No.	y_m (m)	y_f (m)	L_m (m)	L_f (m)	L' (m)	V_{fl} (m/s)	V_{ml} (m/s)	D_{50} (mm)	n	τ_c (Pa)	$0.5Q$ (m^3/s)	V_{fc} (m/s)	V_{max} (m/s)
1	3.08	0.62	77.11	154.23	46.69	0.17	0.46	0.4	0.011	0.364	122.29	0.51	0.48
2	3.08	0.62	77.11	154.23	46.69	0.21	0.58	2	0.015	1.006	155.51	0.65	0.61
3	3.08	0.62	77.11	154.23	46.69	0.41	1.10	10	0.019	6.164	294.42	1.22	1.15
4	9.25	1.85	77.11	154.23	46.69	0.23	0.56	0.4	0.011	0.364	415.74	0.60	0.59
5	9.25	1.85	77.11	154.23	46.69	0.29	0.71	2	0.015	1.006	528.67	0.77	0.75
6	9.25	1.85	77.11	154.23	46.69	0.54	1.35	10	0.019	6.164	1000.92	1.45	1.42
7	15.42	3.08	77.11	154.23	46.69	0.27	0.60	0.4	0.011	0.364	709.37	0.66	0.64
8	15.42	3.08	77.11	154.23	46.69	0.34	0.77	2	0.015	1.006	902.06	0.84	0.81
9	15.42	3.08	77.11	154.23	46.69	0.65	1.46	10	0.019	6.164	1707.86	1.58	1.55
10	3.08	0.62	77.11	154.23	107.96	0.17	0.47	0.4	0.011	0.364	122.29	0.50	0.51
11	3.08	0.62	77.11	154.23	107.96	0.21	0.58	2	0.015	1.006	155.51	0.64	0.64
12	3.08	0.62	77.11	154.23	107.96	0.40	1.13	10	0.019	6.164	294.42	1.21	1.25
13	9.25	1.85	77.11	154.23	107.96	0.23	0.56	0.4	0.011	0.364	415.74	0.60	0.63
14	9.25	1.85	77.11	154.23	107.96	0.29	0.71	2	0.015	1.006	528.67	0.77	0.8
15	9.25	1.85	77.11	154.23	107.96	0.54	1.35	10	0.019	6.164	1000.92	1.45	1.52
16	15.42	3.08	77.11	154.23	107.96	0.27	0.61	0.4	0.011	0.364	709.37	0.66	0.69
17	15.42	3.08	77.11	154.23	107.96	0.34	0.77	2	0.015	1.006	902.06	0.84	0.88
18	15.42	3.08	77.11	154.23	107.96	0.65	1.46	10	0.019	6.164	1707.86	1.58	1.67
19	9.25	1.85	77.11	154.23	154.23	0.23	0.56	0.4	0.011	0.364	415.74	0.60	0.66
20	9.25	1.85	77.11	154.23	154.23	0.29	0.71	2	0.015	1.006	528.67	0.77	0.84
21	9.25	1.85	77.11	154.23	154.23	0.54	1.35	10	0.019	6.164	1000.92	1.46	1.61
22	9.25	3.70	77.11	154.23	154.23	0.38	0.62	0.4	0.011	0.364	630.24	0.68	0.94
23	9.25	3.70	77.11	154.23	154.23	0.48	0.79	2	0.015	1.006	801.43	0.86	1.2
24	9.25	3.70	77.11	154.23	154.23	0.91	1.50	10	0.019	6.164	1517.34	1.63	2.31
25	9.25	7.40	77.11	154.23	154.23	0.55	0.61	0.4	0.011	0.364	1057.05	0.76	1.45
26	9.25	7.40	77.11	154.23	154.23	0.70	0.77	2	0.015	1.006	1344.18	0.97	1.85
27	9.25	7.40	77.11	154.23	154.23	1.32	1.46	10	0.019	6.164	2544.92	1.83	3.73
28	6.17	4.94	77.11	308.46	215.92	0.52	0.58	0.4	0.011	0.364	1065.71	0.71	1.21
29	6.17	4.94	77.11	308.46	215.92	0.66	0.74	2	0.015	1.006	1355.20	0.91	1.55
30	6.17	4.94	77.11	308.46	215.92	1.26	1.39	10	0.019	6.164	2565.77	1.71	3.11
31	9.25	7.40	77.11	462.69	323.88	0.56	0.61	0.4	0.011	0.364	2361.65	0.76	1.42
32	9.25	7.40	77.11	462.69	323.88	0.72	0.77	2	0.015	1.006	3003.16	0.97	1.82
33	9.25	7.40	77.11	462.69	323.88	1.36	1.46	10	0.019	6.164	5685.83	1.83	3.67

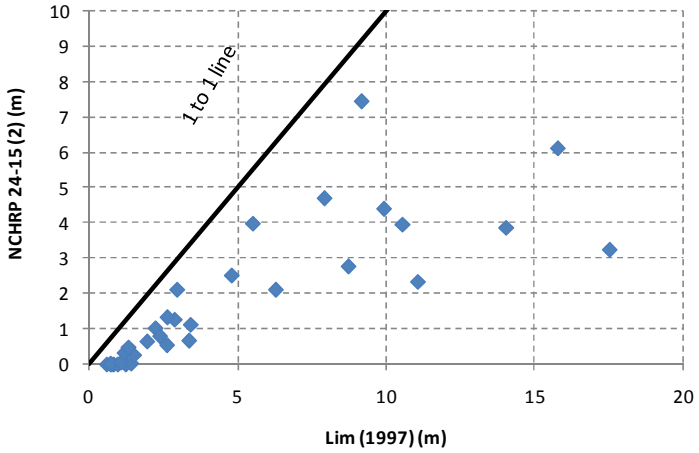

(a) Comparison with Lim's (1997) equation

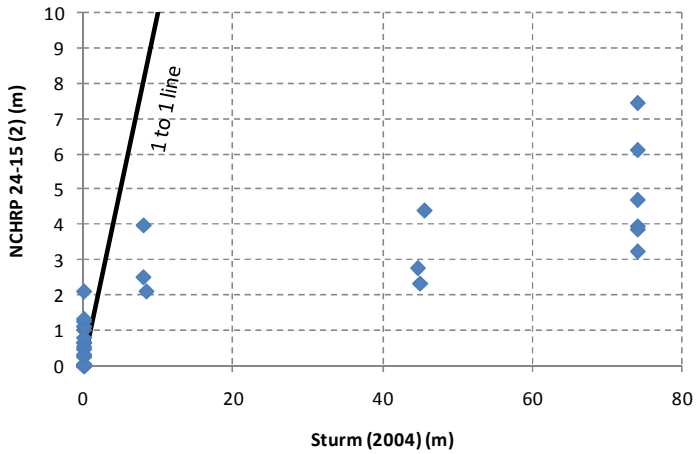

(b) Comparison with Sturm's (2004) equation

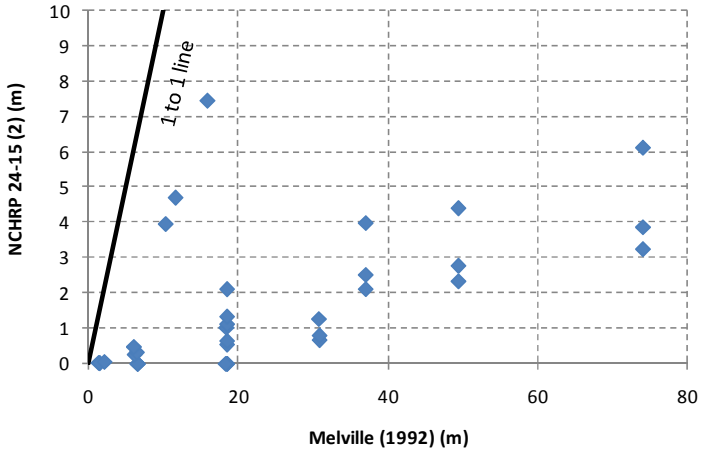

(c) Comparison with Melville's (1992) equation

Figure 8.9 – Comparisons with other prediction equations for full scale bridge.

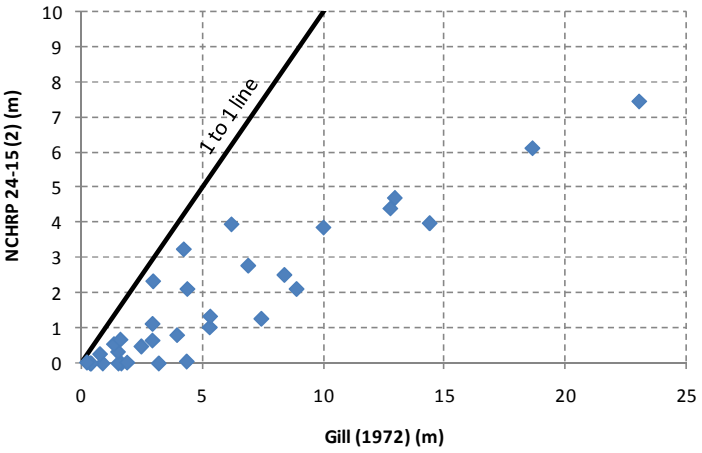

(d) Comparison with Gill's (1972) equation

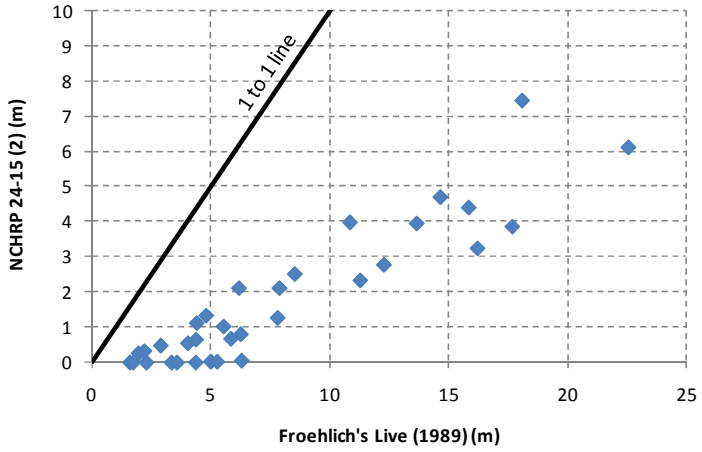

(e) Comparison with Froehlich's (1989) equation

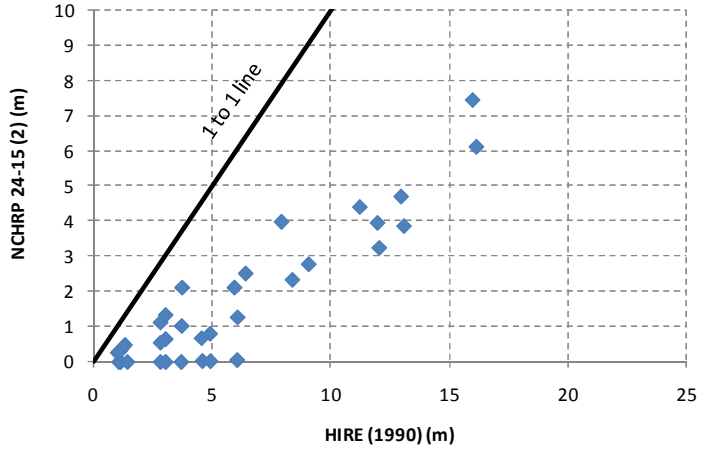

(f) Comparison with HIRE (2001) equation

Figure 8.9 (Continued).

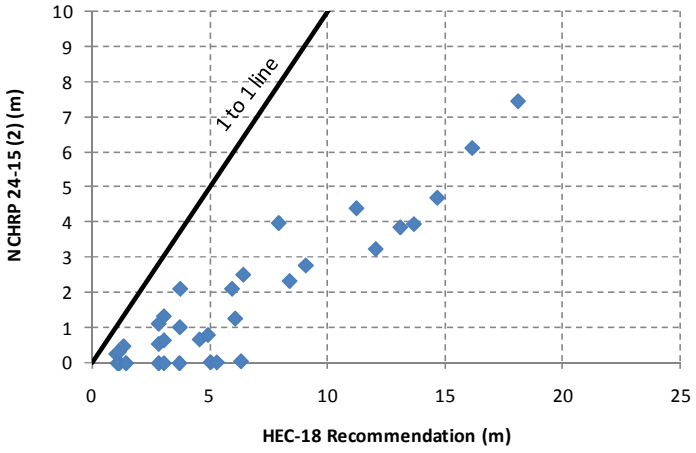

(g) Comparison with HEC-18 recommendation

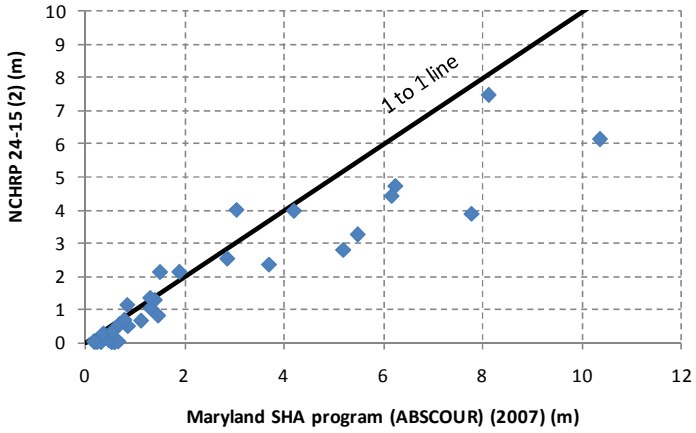

(h) Comparison with method in Maryland SHA program (ABSCOUR) (2007) equation

Figure 8.9 (Continued).

CHAPTER 9

SCOUR EXAMPLE PROBLEMS

Problem $0.5Q = 1{,}000 m^3/s,\ V_1 = 1.13 m/s, V_{f1} = 0.78 m/s, V_{m1} = 1.40 m/s,\ R_{h_1} = 3.65 m$

$y_{f1} = 2.55 m,\ y_{m1} = 7.89 m, V_2 = 1.75 m/s, \tau_c = 3.96 Pa,\ n = 0.018$

Flood duration = 48 hrs, Abutment length = 124m, What is the depth of scour after the flood?

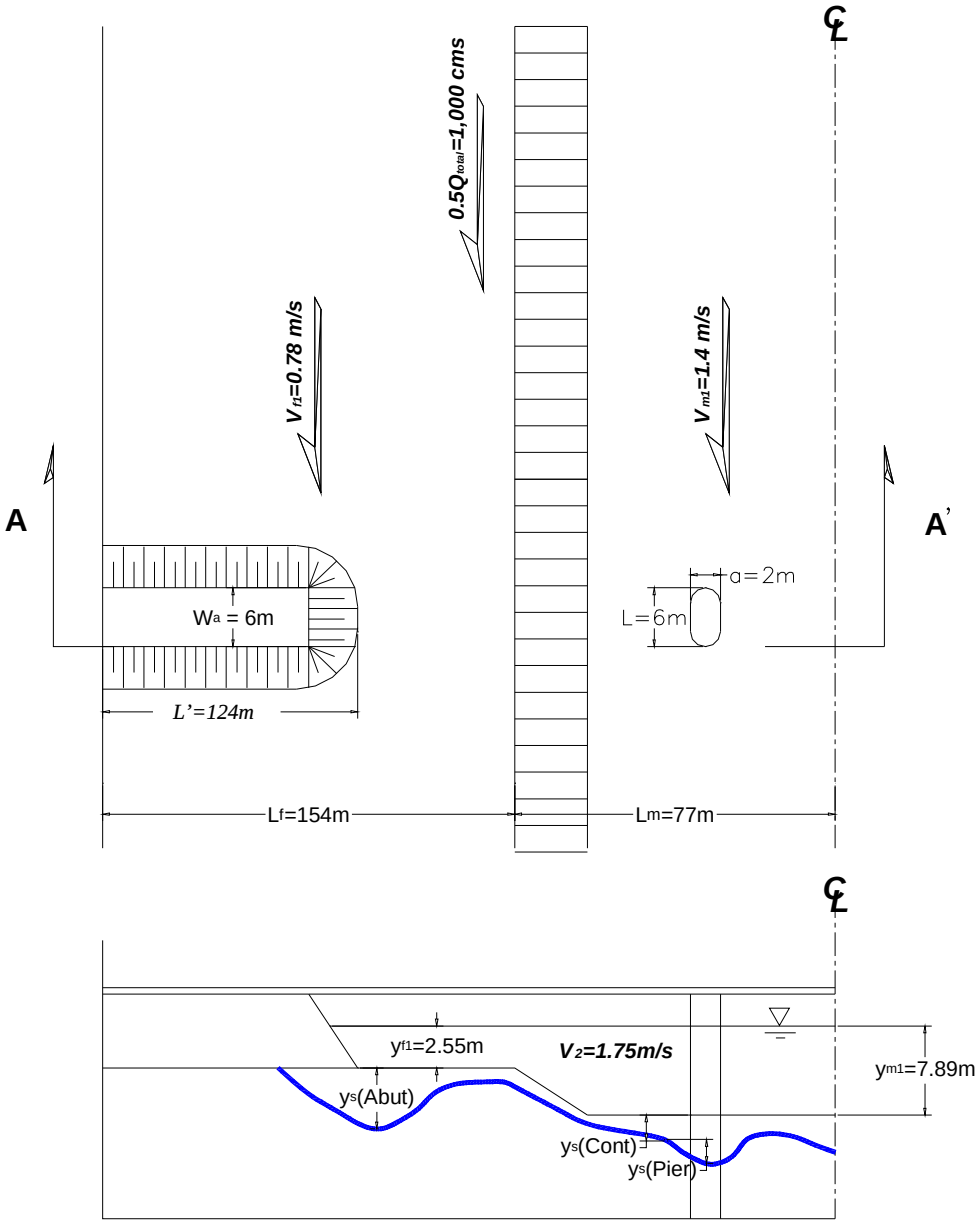

Section A - A'

Solution *S-SRICOS Method*

1. Results of EFA tests gave the $\dot{z}$ *vs* τ curve shown

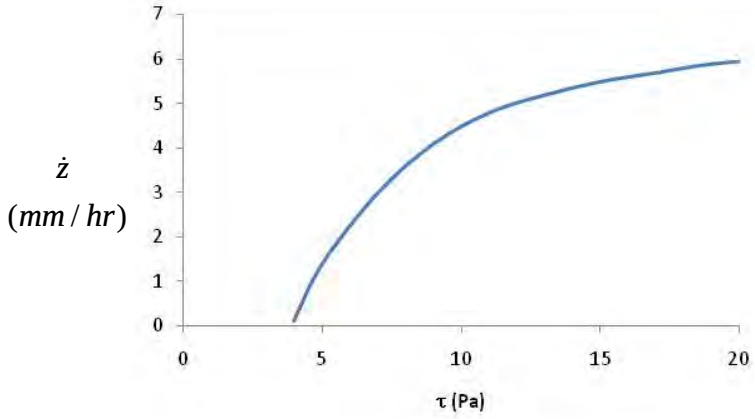

2. Maximum shear stress around abutment, and in the middle of channel are:

$$\tau_{\max(Abut)} = 12.45 \cdot K_c \cdot K_{sh} \cdot K_{Fr} \cdot K_s \cdot K_L \cdot \rho \cdot V_1^2 \, \mathrm{Re}^{-0.45}$$
$$= 12.45 \times 2.74 \times 0.41 \times 1.27 \times 0.65 \times 1000 \times 1.13^2 \times \left(6.78 \times 10^6\right)^{-0.45}$$
$$= 12.45 Pa$$

$$\tau_{\max(Cont)} = K_R \cdot K_L \cdot K_\theta \cdot K_W \cdot \gamma \cdot n^2 \cdot V_1^2 \, \mathrm{R}_h^{-1/3}$$
$$= 1.44 \times 0.83 \times 1.9 \times 1 \times 9810 \times 0.018^2 \times 1.4^2 \times 3.65^{-1/3}$$
$$= 5.98 Pa$$

3. The initial rate of scour $\dot{z}_i$ abutment and contraction scour are read on the EFA curve at $\tau = \tau_{\max}$:

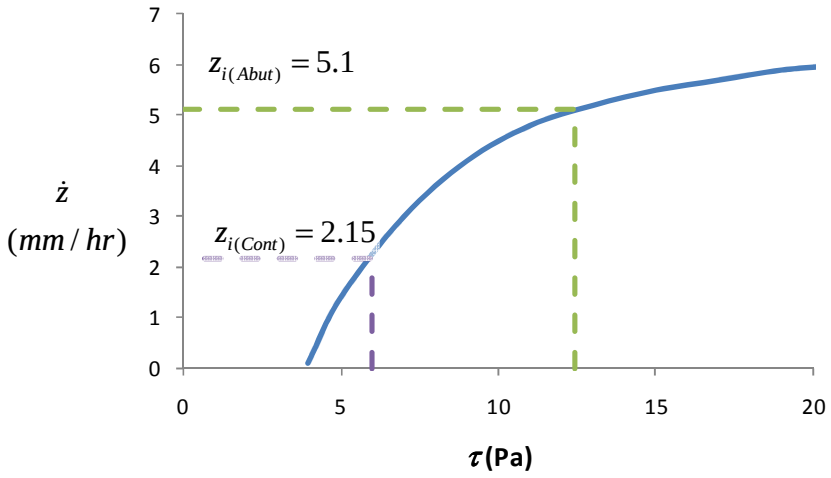

4. The velocity at the bridge section V_{f2} is

$$\frac{L_f - L'}{y_m} < 5 \text{, thus short setback condition}$$

$$\therefore V_{f2} = V_2 = 1.75 m/s$$

5. The maximum depths of scour $y_{s(Abutment)}$, $y_{s(Cont)}$ are

$$y_{s(Abut)} = K_1 \cdot K_2 \cdot K_L \cdot K_G \cdot K_P \cdot 243 \cdot \mathrm{Re}_{f2}^{-0.28} \left(1.65 \cdot Fr_{f2} - Fr_{fc}\right) \cdot y_{f1}$$

$$= 0.73 \times 1 \times 1 \times 1 \times 243 \times \left(\frac{1.75 \times 2.55}{10^{-6}}\right)^{-0.28} \times \left(1.65 \times \frac{1.75}{\sqrt{9.81 \times 2.55}} - \frac{1.30}{\sqrt{9.81 \times 2.55}}\right) \times 2.55$$

$$= 1.97 m$$

$$y_{s(Cont)} = 2.21\left(1.31 \cdot Fr_{(Cont)} - Fr_{c(Cont)}\right) \cdot y_{m1}$$

$$= 2.21 \times \left(1.31 \times \frac{1.75}{\sqrt{9.81 \times 7.89}} - \frac{1.57}{\sqrt{9.81 \times 7.89}}\right) \times 7.89$$

$$= 1.42 m$$

6. The equation for the y(t) curve is

$$y_s(t) = \frac{t(hrs)}{\frac{1}{\dot{z}_i} + \frac{t(hrs)}{y_s}}$$

$$y_{s(Abut)}(48) = \frac{48}{\frac{1}{5.1} + \frac{48}{1970}} = 218 mm,$$

$$y_{s(Cont)}(48) = \frac{48}{\frac{1}{2.15} + \frac{48}{1420}} = 96 mm$$

7. Maximum flood lasts 48 hours, therefore

11% of $y_{s(Abut)}$, and 6.8% of $y_{s(Cont)}$

Problem $Q_{100} = 861.4m^3/s, V_1 = 1.64m/s, V_{m1} = 2.83m/s, R_{h_1} = 3.39m, y_{f1(Left)} = 4.36m,$
$y_{f1(Right)} = 4.53m, y_{m1} = 6.89m, V_2 = 2.98m, \tau_{c(floodplain)} = 7.02Pa, \tau_{c(main\ channel)} = 11.63Pa,$
$n_{(floodplain)} = 0.019, n_{(main\ channel)} = 0.021, h = 2.65m, d_1 = 2.24m, d_{deck} = 0.9m,$
$L'_{(left)} = 30.6m, L'_{(Right)} = 77.3m, W_a = 13.4m$

The channel geometry and HEC-RAS results are shown in following 2 figures. Flood duration = 48 hrs. What is the depth of scour after the flood?

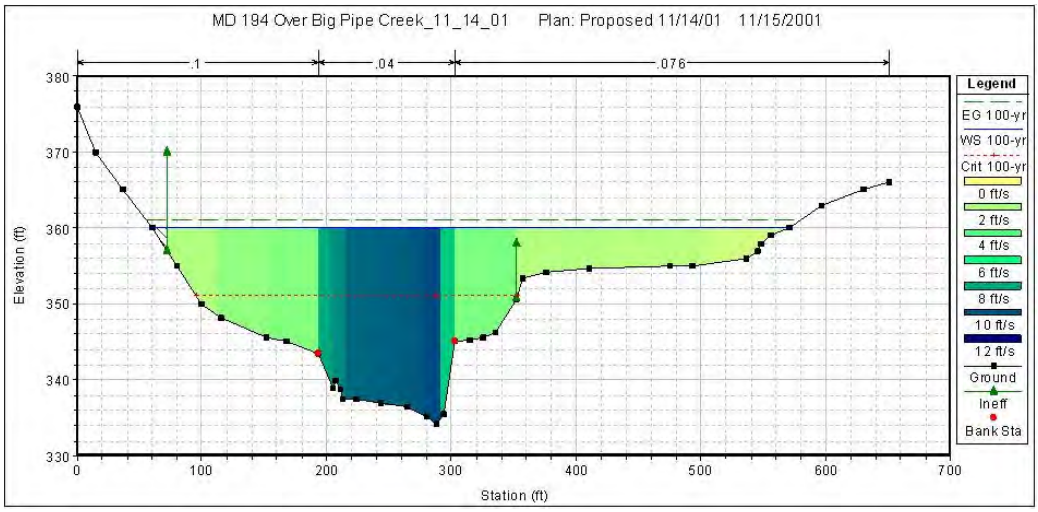

(a) Approach Section

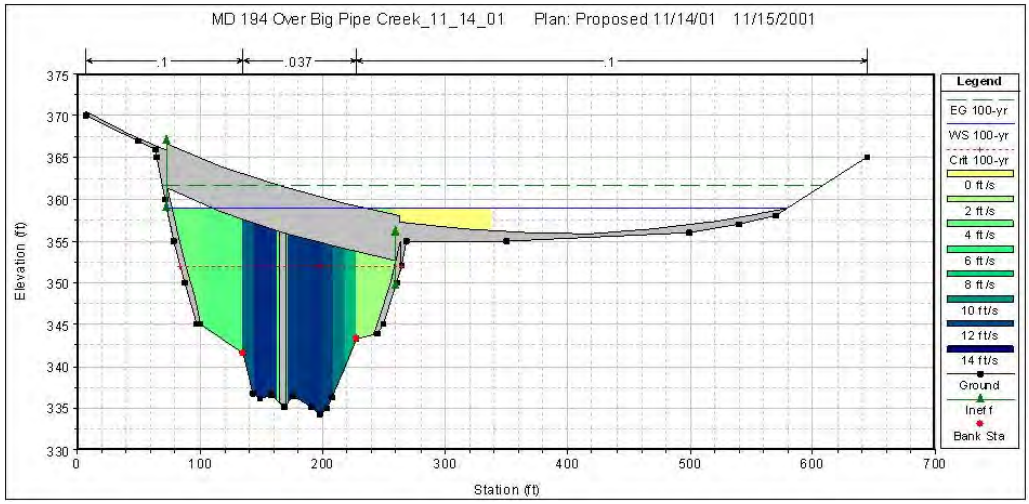

(b) Bridge Section

Solution *SRICOS Method C*

1. Results of EFA tests gave the $\dot{z}$ vs τ curve shown. These curves were obtained by using the critical shear stress from the D_{50} of the soil and then using the erodibility charts to generate the erosion function.

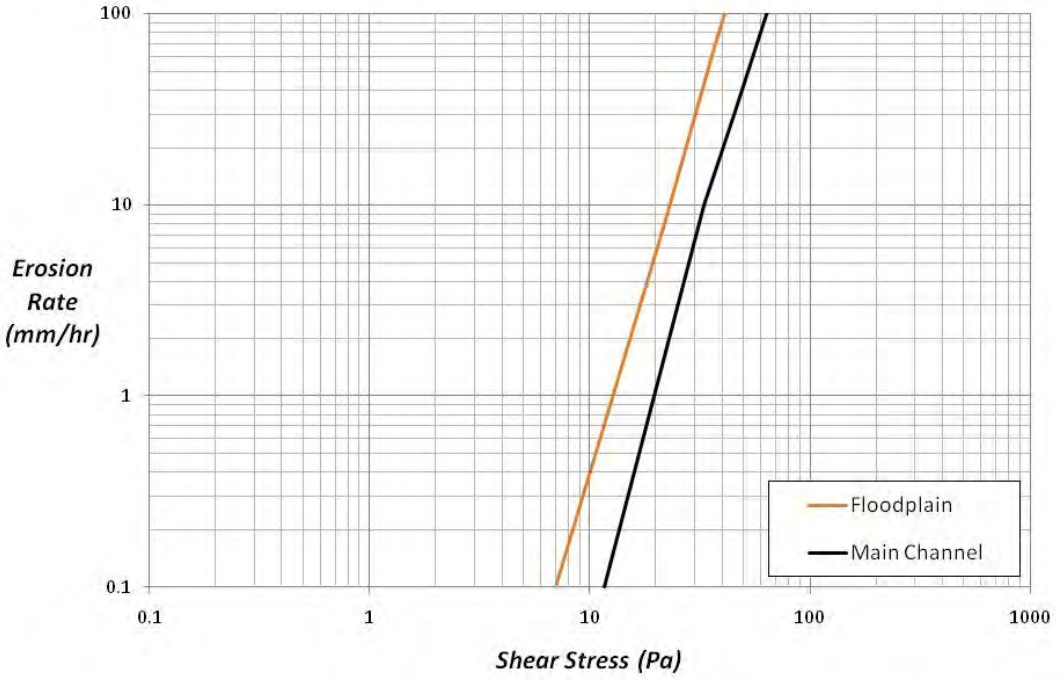

2. Maximum shear stress around abutment, and in the middle of channel are:

Contraction

$$\tau_{\max(Cont)} = k_R \cdot k_L \cdot k_\theta \cdot k_W \cdot \gamma \cdot n^2 \cdot V_1^2 \, R_h^{-1/3}$$
$$= 1.7 \times 0.99 \times 1.9 \times 1 \times 9810 \times 0.021^2 \times 1.64^2 \times 3.4^{-1/3}$$
$$= 23.84 Pa$$

Left abutment

$$\tau_{\max(Abut)} = 12.45 \cdot k_c \cdot k_{sh} \cdot k_{Fr} \cdot k_s \cdot k_L \cdot k_o \cdot \rho \cdot V_1^2 \, \mathrm{Re}^{-0.45}$$
$$= 12.45 \times 3.71 \times 0.7 \times 1.32 \times 0.65 \times 1.0 \times 1000 \times 1.64^2 \times \left(2.2 \times 10^7\right)^{-0.45}$$
$$= 37 Pa$$

Right abutment

$$\tau_{\max(Abut)} = 12.45 \cdot k_c \cdot k_{sh} \cdot k_{Fr} \cdot k_s \cdot k_L \cdot k_o \cdot \rho \cdot V_1^2 \, \mathrm{Re}^{-0.45}$$
$$= 12.45 \times 3.71 \times 0.56 \times 1.47 \times 0.65 \times 1.0 \times 1.1 \times 1000 \times 1.64^2 \times \left(2.2 \times 10^7\right)^{-0.45}$$
$$= 35.7 Pa$$

3. The initial rate of scour $\dot{z}_i$ for pier, abutment and contraction scour are read on the EFA curve at $\tau = \tau_{\max}$:

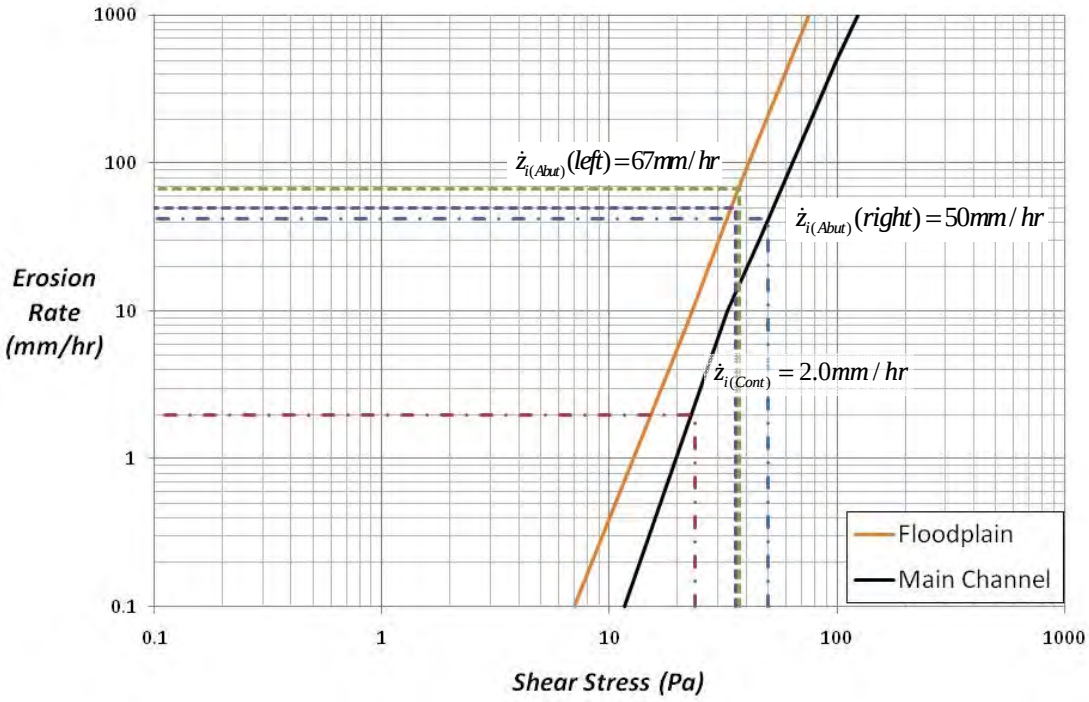

4. The maximum depths of scour $y_s(Cont)$, $y_s(Abutment)$ are

Contraction Scour

$$y_{s(Cont)} = 2.21\left(1.31 \cdot Fr_{(Cont)} - Fr_{c(Cont)}\right) \cdot y_{m1}$$

$$= 2.21 \times \left(1.31 \times \frac{2.98}{\sqrt{9.81 \times 6.89}} - \frac{2.3}{\sqrt{9.81 \times 6.89}}\right) \times 6.89$$

$$= 2.96m$$

Left Abutment

$$y_{s(Abut)} = K_1 \cdot K_2 \cdot K_L \cdot K_G \cdot K_P \cdot 243 \,\mathrm{Re}_{f2}^{-0.28} \left(1.65 \cdot Fr_{(Abut)} - Fr_{c(Abut)}\right) \cdot y_{f1}$$

$$= 0.73 \times 243 \times \left(\frac{2.98 \times 4.36}{10^{-6}}\right)^{-0.28} \times \left(1.65 \times \frac{2.98}{\sqrt{9.81 \times 4.36}} - \frac{1.79}{\sqrt{9.81 \times 4.36}}\right) \times 4.36$$

$$= 3.77m$$

Right Abutment (y_{f1} = h for pressure flow)

$$y_{s(Abut)} = K_1 \cdot K_2 \cdot K_L \cdot K_G \cdot K_P \cdot 243 \,\mathrm{Re}_{f2}^{-0.28} \left(1.65 \cdot Fr_{(Abut)} - Fr_{c(Abut)}\right) \cdot y_{f1}$$

$$= 0.73 \times 1.1 \times 243 \times \left(\frac{2.98 \times 2.65}{10^{-6}}\right)^{-0.28} \times \left(1.65 \times \frac{2.98}{\sqrt{9.81 \times 2.65}} - \frac{1.65}{\sqrt{9.81 \times 2.65}}\right) \times 2.65$$

$$= 3.88m$$

5. The equation for the *y(t)* curve is

$$y_s(t) = \frac{t(hrs)}{\frac{1}{\dot{z}_i} + \frac{t(hrs)}{y_s}}$$

Thus the scour depth after 48 hours for this flood event is

$$y_{s(Contt)}(48) = \frac{48}{\frac{1}{2} + \frac{48}{2960}} = 93mm$$

$$y_{s(Abut\_left)}(48) = \frac{48}{\frac{1}{67} + \frac{48}{3770}} = 1736mm$$

$$y_{s(Abut\_right)}(48) = \frac{48}{\frac{1}{50} + \frac{48}{3880}} = 1483mm$$

6. Maximum flood lasts 48 hours, therefore

3% of $y_{s(Cont)}$, 46% of $y_{s(Abut\_left)}$, and 38% of $y_{s(Abut\_right)}$

REFERENCES

Abed, L. M. (1991). "Local Scour around Bridge Piers in Pressure Flow," Department of Civil Engineering, Colorado State University, Fort Collins, CO.

Arneson, L. A. (1997). "The Effects of Pressure Flow on Local Scour in Bridge Openings," Department of Civil Engineering, Colorado State University, Fort Collins, CO.

Arulanandan, K. (1975). "Fundamental Aspects of Erosion in Cohesive Soils." *Journal of Hydraulic Division, ASCE*, 101, 635-639.

Arulanandan, K., Loganathan, P., and Krone, R.B. (1975). "Pore and Eroding Fluid Influences on Surface Erosion of Soil." *Journal of Geotechnical Engineering*, 101, 51-66.

ASTM D1587, American Society for Testing and Materials, Philadelphia, USA.

Awazu, S. (1967). "On Scour around Spur Dikes." *Proceeding of 12th Congress of the International Association for Hydraulic Research 3, C12*, Delft, The Netherlands.

Benedict, S.T., Despande, N., Aziz, N.M., and Conrads, P.A. (2006). "Trends of abutment-scour prediction equations applied to 144 fields sites in South Carolina" *Open-File Rep. 2003-295*, U.S. Geology Survey, Washington, DC.

Briaud, J.-L., Chen, H.-C., Li, Y., Nurtjahyo, P., and Wang, J. (2004). "Complex Pier Scour and Contraction Scour in Cohesive Soils." *NCHRP report 516*, Transportation Research Board, Washington, DC.

Briaud, J.-L., Ting, F., Chen, H.C., Cao, Y., Han, S.-W., and Kwak, K. (2001 (a)). "Erosion Function Apparatus for Scour Rate Predictions." *Journal of Geotechnical and Geoenvironmental Engineering*, ASCE, Vol.127, No. 2, pp.105-113.

Briaud, J.-L., Ting F., Chen, H.-C., Gudavalli, R., Kwak, K., Philogene B., Han, S.-W., Perugu, S., Wei, G.S., Nurtjahyo, P., and Cao, Y.W., Li, Y. (1999 (a)). "SRICOS: Prediction of Scour Rate at Bridge Piers." *TTI Report no. 2937-1 to the Texas DOT*, Texas A&M University, College Station, Texas, USA.

Briaud, J.-L., Ting, F., Chen, H.C., Gudavalli, S.R., Perugu, S., and Wei, G. (1999 (b)). "SRICOS: Prediction of Scour Rate in Cohesive Soils at Bridge Piers." *ASCE Journal of Geotechnical Engineering* Vol.125, pp. 237-246.

Briaud, J. L., Chen, H. C. Kwak K., Han S-W., and Ting F. (2001 (b)). "Multiflood and Multilayer Method for Scour Rate Prediction at Bridge Piers." *Journal of Geotechnical and Geoenvironmental Engineering, ASCE*, Vol.127, No. 2, pp.105-113.

Briaud, J. L. (2008), "Case Histories in Soil and Rock Erosion: Woodrow Wilson Bridge, Brazos River Meander, Normandy Cliffs, and New Orleans Levees", *The 9th Ralph B. Peck Lecture, Journal of Geotechnical and Geoenvironmental Engineering*, Vol 134, No.10, ASCE, Reston Virginia, USA.

Cao, Y. (2001). "The Influence of Certain Factors on the Erosion Functions of Cohesive Soil," Texas A&M University, College Station, Texas, USA.

Cebeci, T., and Bradshaw, P. (1977). *Momentum Transfer in Boundary Layers*, Hemisphere Publishing Corporation.

Chabert, J., and Chauvin, J.L. (1963). "Formation de Dunes et de Rides Dans Les Modeles Fluviaux. Bull." *Cen. Rech. Ess. Chatou*, No. 4.

Chang, F., and Davis, S. (1999 (a)). "Maryland SHA procedure for estimating scour at bridge abutments, Part 1 - Live Bed Scour." Stream Stability and Scour at Highway Bridges, E. V. a. F. L. Richardson, Peter, ed., ASCE, pp. 401-411.

Chang, F., and Davis, S. (1999 (b)). "Maryland SHA procedure for estimating scour at bridge abutments, Part 2 - Clear Water Scour." Stream Stability and Scour at Highway Bridges, E. V. a. F. L. Richardson, Peter, ed., ASCE, pp. 412-416.

Chen, C. J., and Chen, H.C. (1982). "The Finite Analytic Method." IIHR Report No. 232-IV, Iowa Institute of Hydraulic Research, University of Iowa, Iowa City, Iowa.

Chen, C. J., and Chen, H.C. (1984). "Finite Analytic Numerical Method for Unsteady Two-Dimensional Navier-Stokes Equation." *Journal of Computational Physics*, 53, 210-226.

Chen, H. C., and Patel, V.C. (1988). "Near-Wall Turbulence Models for Complex Flows Including Separation." *AIAA Journal*, 26, 641-648.

Chen, H. C., and Patel, V.C. (1989). "The Flow around Wing-Body Junctions." *Proceeding of 4th Symposium on Numerical and Physical Aspects of Aerodynamic Flows*, Long Beach, California, 1-15.

Chen, H. C., Patel, V.C., and Ju, S. (1990). "Solutions of Reynolds-Averaged Navier-Stokes Equations for Three-dimensional Incompressible Flows." *Journal of Computational Physics*, 88, 305-336.

Chen, H. C., and Korpus, R.A. (1993). "A Multi-Block Finite-Analytic Reynolds-Averaged Navier-Stokes Method for 3D Incompressible Flow." *Individual Papers in Fluids Engineering, ASME*, 150, 113-121.

Chen, H. C., and Chen, M. (1995). "Unsteady RANS/Free–Surface Method for Transient Flows, Induced by a Berthing Ship." COE Report No. 344, Texas Engineering Experiment Station, Texas A&M University System, College Station, Texas.

Chen, H. C., and Chen, M. (1996). "Time Domain Simulation of a Berthing DDG-51 Ship in Translational and Rotational Motions." COE Report No. 351, Texas Engineering Experiment Station, Texas A&M University System, College Station, Texas.

Chen, H. C., and Chen, M., Davis, D.A. (1997). "Numerical Simulation of Transient Flows Induced by a Berthing Ship." *International Journal of Offshore and Polar Engineering*, 7, 277-284.

Chen, H. C. (2002). "Numerical Simulation of Scour around Complex Piers in Cohesive Soil." *Proceeding of First International Conference on Scour of Foundation*, Texas A&M University, College Station, Texas, 14-33.

Chen, H. C. (2002). "Numerical Simulation of Scour around Complex Piers in Cohesive Soil." *Proceeding First Intl Conf. on Scour of Foundations*, ICSF-1, Texas A&M University, College Station, Texas, USA, Vol.1, 14-33.

Das, B. M. (1997). *Advanced Soil Mechanics, 2nd edition,* Taylor & Francis, Washington, D.C.

Dongol, D. M. S. (1994). "Local Scour at Bridge Abutments." *Report No. 544*, School of Engineering, University of Auckland, Auckland, New Zealand.

Dufresne, M., Vazquez, J., Terfous, A., Ghenaim, A., Poulet, J.-B (2007). "Prediction of Sedimentation in a Storm-Water Tank Pilot Using Computational Fluid Dynamics." *Ninth International Symposium on Fluid Control, Measurement and Visualization*, Tallahassee, Florida, USA.

Dunn, I. S. (1959). "Resistance of Cohesive Channels." *Journal of Soil Mechanics and Foundation Division, ASCE*, 85, 1-24.

Durbin, P. A., Medic, G., Seo, J.M., Eaton, J.K., Song, S. (2001). "Rough Wall Modification of Two-Layer $k-\varepsilon$" *Journal of Fluids Engineering*, 123, 16-21.

Ettema, R., Nakato, T., and Muste, M. (2008). "Estimation of Scour Depth at Bridge Abutment." NCHRP 24-20, Washington, D.C.

Froehlich, D. C. (1989). "Local Scour at Bridge Abutment." *Proceedings of National Conference on Hydraulic Engineering*, New York, pp. 13-18.

Garde, R. J., Nambudripad, K. D. (1961). "Study of Scour around Spur-Dikes." *Journal of Hydraulics Division*, 87(HY 6), pp. 23-37.

Gill, M. A. (1972). "Erosion of Sand Beds around Spur Dikes." *Journal of Hydraulics Division*, 98(HY9), pp. 1587 - 1602.

Gill, M. A. (1981). "Bed Erosion in Rectangular Long Contraction." *Journal of the Hydraulics Division*, 107(HY3), pp. 273 - 284.

Gudavalli, S. R. (1997). "Prediction Model for Scour Rate around Bridge Piers in Cohesive Soils on the Basis of Flume Tests," Ph.D Dissertation, Texas A&M Uninversity, College Station, TX.

HEC-RAS River Analysis System, *User's Manual, Version 3.1*, Hydrologic Engineering Center, 2002, U.S. Army Corps of Engineering, Davis, CA

Hjorth, P. (1975). "Studies on Nature of Local Scour." Bulletin Series A. No. 46, Department of Water Resources Engineering, Lund Institute of Technology/University of Lund, Sweden.

Hoffmans, G. J. C. M. and. Booij, R. (1993). "Two-dimensional Mathematical Modeling of Local Scour Holes." *Journal of Hydraulic Research*, Vol. 31, No.5.

Hosny, H. M. (1995). "Experimental Study of Local Scour around Circular Bridge Piers in Cohesive Soils," Colorado State University, Fort Collins, Colorado.

Ivarson, W. R. (1999). "Scour and erosion in clay soils." *Stream Stability and Scour at Highway Bridges, Compend. papers ASCE water resources eng. conf. 1991 to 1998*, E.V. Richardson and P.F. Lagasse, eds., Reston, VA, 104 -119.

Jiang, J., Ganju, N.K., and Menta, A.J. (2004). "Estimation of Contraction Scour in Riverbed Using SERF." *Journal of Waterway, Port, Coastal, and Ocean Engineering*, 130, No.4, 215-218.

Jones, J. S., Bertoldi, David, A., and Umbrell, E.R. (1993). "Preliminary Studies of Pressure Flow Scour." *Proceedings of the ASCE Hydraulic Engineering Conference*, San Francisco, CA, Reston, VA.

Johnson, P. A. (1998). "Scour at wide piers relative to flow depth." *ASCE Compendium of Conference Scour Papers (1991 to 1998)*, Reston, VA, pp. 280-287.

Johnson, P. A. and. Jones, J. S. (1992). "Shear Stress at Base of Bridge Pier." *Bridge and Hydrology Research, Transportation Research Board No 1350*, pp.14-18.

Knight, D. W., and Demetriou, J.D. (1983). "Flood Plain and Main Channel Flow Interaction." *Journal of Hydraulic Engineering*, 109, No.8 1073-1092.

Komura, S. (1966). "Equilibrium Depth of Scour in Long Constrictions." *Journal of the*

Hydraulics Division, 92(HY5), pp. 17-38.

Kouchakzadeh, S., and Townsend, R. D. (1997). "Maximum Scour Depth at Bridge Abutment Terminating in the Floodplain Zones." *Canadian Journal of Civil Engineering*, 24, No. 6, pp. 996-1006.

Kwak, K., Briaud, J.-L., Cao, Y., Chung M.-K., Hunt, B., and Davis, S., (2002). "Pier Scour at Woodrow Wilson Bridge and SRICOS Method." *First International Conference on Scour of Foundations*, College Station, Texas, USA.

Kwak K., B. J.-L., and Chen H.-C., (2001). "SRICOS: Computer Program for Bridge Pier Scour." *Proceedings of the 15th International Conference on Soil Mechanics and Geotechnical Engineering*, A.A. Balkema Publishers, Rotterdam, The Netherlands.

Laursen, E. M. (1958). "The Total Sediment Load of Streams." *Journal of the Hydraulics Division*, 84(1530), pp. 1-36.

Laursen, E. M. (1960). "Scour at Bridge Crossings." *Journal of the HYDRAULICS DIVISION*, 86(HY 2), pp. 39 - 54.

Laursen, E. M. (1963). "An Analysis of Relief Bridge Scour." *Journal of Hydraulics Division, ASCE*, 89(No. HY3), pp. 93-118.

Li, Y. (2002). "Bridge Pier Scour and Contraction Scour in Cohesive Soils on the Basis of Flume Tests," Ph. D Dissertation, Texas A&M University, College Station, TX.

Liu, H. K. (1957). "Mechanics of Sediment-Ripple Formation." *Journal of Hydraulic Division ASCE*, 183, No.HY2, 1-23.

Liu, T. J. (2002). Time-Domain Simulation of Large-Amplitude Ship Motions Including Capsizing. Ph.D. Dissertation, Department of Civil Engineering, Texas A&M University, College Station, Texas.

Lim, S.-Y. (1997). "Equilibrium Clear-Water Scour around an Abutment." *Journal of Hydraulic Engineering, ASCE*, 123, No. 3, pp. 237-243.

Lim, S.-Y., and Cheng, N.-S. (1998). "Scouring in Long Contractions." *Journal of Irrigation and Drainage Engineering*, Vol. 124, No. 5, pp. 258-261, Reston, VA.

Lim, S. Y., and Cheng, N. S. (1998). "Prediction of Live-Bed Scour at Bridge Abutments." *Journal of Hydraulic Engineering*, 124, No. 6, pp. 635-638.

Maryland SHA Bridge Scour Program (ABSCOUR) (2007), *Users Manual*, Maryland State Highway Administration.

Melville, B. W. (1992). "Local Scour at Bridge Abutment." *Journal of Hydraulic Engineering*, 118(No. 4), pp. 615-631.

Melville, B. W. (1995). "Bridge Abutment Scour in Compound Channels." *Journal of Hydraulic Engineering*, 121(No. 12), pp. 863 - 868.

Melville, B. W. (1997). "Pier and Abutment Scour: Integrated Approach." *Journal Hydraulic Division, ASCE*, Vol. 123, No. 2, pp. 125-136.

Melville, B. W. and Coleman, S.E. (1999). *Bridge Scour*, Water Resources Publications, LLC.

Mirtskhoulava. (1988). "Basic Physics and Mechanics of Channel Erosion." *Gidometeoizdat, Leningrad*.

Molinas, A., Kheireldin, K., and Wu, B. (1998). "Shear Stress around Vertical Wall Abutments." *Journal of Hydraulic Engineering*, 124, 822-830.

Moody, L. F. (1944). "Friction Factors for Pipe Flow." Transaction of the American Society of Civil Engineers, Vol. 66, Reston, Virginia, USA.

Muller, D. S., and Landers, M. (1996). "Channel Scour at Bridges in the United States." FHWA-RD-95-184, Federal Highway Administration, VA, USA.

Munson, B. R., Young, D. F., and Okiishi, T. H. (1990). *Fundamentals of fluid mechanics*, Wiley, New York.

Naot, D., Nezu, I., and Nakagawa, H. (1993). "Hydrodynamic Behavior of Compound Rectangular Open Channels." *Journal of Hydraulic Engineering*, 119, No.3, 390-408.

Neill, C. R. (1973). *Guide to Bridge Hydraulics*, Roads and Transportation Association of Canada by University of Toronto Press.

Nurtjahyo, P. (2003). "Chimera RNAS Simulations of Pier Scour and Contraction Scour in Cohesive Soils," Texas A&M University, College Station, Texas, USA.

Parchure, T. M., and Mehta, A.J. (1985). "Erosion of Soft Cohesive Sediment Deposit." *Journal of Hydraulic Division, ASCE*, 111, No.10, 1309-1326.

Patel, V. C., and Yoon, J.Y. (1995). "Application of Turbulence Models to Separated Flow over Rough Surfaces." *Journal of Hydraulic Division*, 105, No.HY5, 573-588.

Rajaratnam, N., and Nwachukwu, B. (1983). "Flow near Groin-like Structure." *J. of Hydraulic Engineering*, 109, 463-480.

Richardson, E. V., and Davis, S. M. (1995). "Evaluating Scour at Bridges." Publication No.

FWHA-IP-90-017, HEC No.18, US Department of Transportation, Washington, D. C. .

Salim, M., and Jones, J. S. (1998). "Scour Around Exposed Pile Foundations", ASCE Compendium of Conference Scour Papers (1991 to 1998)." Reston, VA, pp. 104-119.

Shaikh, A., Ruff, J. F.,, and Abt, S. R. (1988). "Erosion Rate of Compacted Na-Montmorillonite Soils." *Journal of Geotechnical Engineering, ASCE*, 114, No.3, 296–305.

Shirole, A. M., and Holt, R.C. (1991). "Planning for Comprehensive Bridge Safety Assurance Program." Transp. Res. Rec. 1290, Transportation Research Board, Washington, D.C., 137-142.

Simons, D. B., and Richardson, E.V. (1963). "Form of Bed Roughness in Alluvial Channels." *Trans. ASCE*, 128, 284-323.

Simons, D. B., and Richardson, E.V. (1966). *Resistance to Flow in Alluvial Channels*, United States Geological Survey Professional Paper 422-J.

Smerdon, D. B., Beasley, and M.L. (1959). "Tractive Force Theory Applied to Stability of Opens Channels in Cohesive Soils." *Research Bulletin No. 715*, Agricultural Experiment Station, The University of Missouri, Columbia.

Straub, L. G. (1940). "Approaches to the Study of the Mechanics of Bed Movement." *Proceeding of 1st Hydraulics Conference of Iowa Studies in Engineering*, Iowa City, Iowa.

Strum, T. W. (2004). "Enhanced Abutment Scour Studies for Compound Channels." *FHWA-RD-99-156*, Georgia Institute of Technology, School of Civil and Environmental Engineering, Atlanta, GA 30332.

Strum, T. W., and Janjua, N. S. (1994). "Clear-water Scour around Abutments in Floodplains." *Journal of Hydraulic Engineering, ASCE*, 120(8), pp. 956-972.

Sturm, T. W. (1999). "Abutment Scour in Compound Channels." Stream Stability and Scour at Highway Bridges, E. V. a. F. L. Richardson, Peter, ed., Reston, VA. : ASCE.

Suhs, N. E., and Tramel, R. W. (1991). "PEGSUS 4.0 Users Manual." Arnold Engineering Development Center Report, AEDC-TR-91-8, Arnold Air Force Station, Tennessee.

Tingsanchali, T., and Maheswaran, S. (1990). "2-D Depth Averaged Flow Computation near Groyne." *Journal of Hydraulic Engineering*, 116, 71-86.

Umbrell, E. R., Kenneth, Y.G., Stein, S.M., and Jones, J.S. (1998). "Clearwater Contraction Scour under Bridges in Pressure Flow." *Journal of Hydraulic Engineering, ASCE*, 124, No.2, 236-240.

Van Rijn, L. C. (1984a). "Sediment Transport: Part I." *Journal of Hydraulic Engineering*, 110, 1431-1456.

Van Rijn, L. C. (1984b). "Sediment Transport: Part II: Suspended Load Transport." *Journal of Hydraulic Engineering*, 110, 1613-1641.

Van Rijn, L. C. (1984c). "Sediment Transport: Part III: Bed Form and Alluvial Roughness." *Journal of Hydraulic Engineering*, 110, 1733-1754.

Wei, G., Chen, H.C., Ting, F, Briaud, J.-L, Gudavalli, S.R., and Perugu, S. (1997). "Numerical Simulation to Study Scour Rate in Cohesive Soils." *Research Report prepared for the Texas Department of Transportation*, Department of Civil Engineering, Texas A&M University, College Station, Texas.

Winterwerp, J. C. (1989). "Sediments, Flow Included Erosion of Cohesive Beds." Rijkswaterstaat / Delft Hydraulics, Delft.

Wolfstein, M. (1969). "The Velocity and Temperature Distribution in One-Dimensional Flow with Turbulence Augmentation and Pressure Gradient." *International Journal of Heat and Mass Transfer*, 12, 301-318.

Wormleaton, P. R., and Merrett, D.J. (1990). "An Improved Method of Calculation for Steady Uniform Flow in Prismatic Main Channel/Flood Plain Sections." *Journal of Hydraulic Research*, 28, No.2, 157-174.

Yalin, M. S. (1964). "Geometrical Properties of Sand Waves." *Journal of Hydraulic Division, ASCE*, 90, No.HY5, 105-119.

Yakoub, N. G. R. (1995). "Effect of Cohesion on Bridge Abutment Scour," Ph. D. Dissertation, Colorado State University, Fort Collins.

Zaghloul, N. A. (1974). "Analytical and Experimental Investigation of Flow around Spur Dikes," Ph.D. Dissertation, Department of Civil Engineering, University of Windsor, Ontario, Canada.

Zhang, H., Faghri, M., and White, F.M. (1996). "A New Low-Reynolds-Number $k-\varepsilon$ Model for Turbulent Flow over Smooth and Rough Surfaces." *Journal of Fluids Engineering*, 118, 255-259.

APPENDIX A

DISTRIBUTION OF VELOCITY AND TURBULENCE INTENSITY

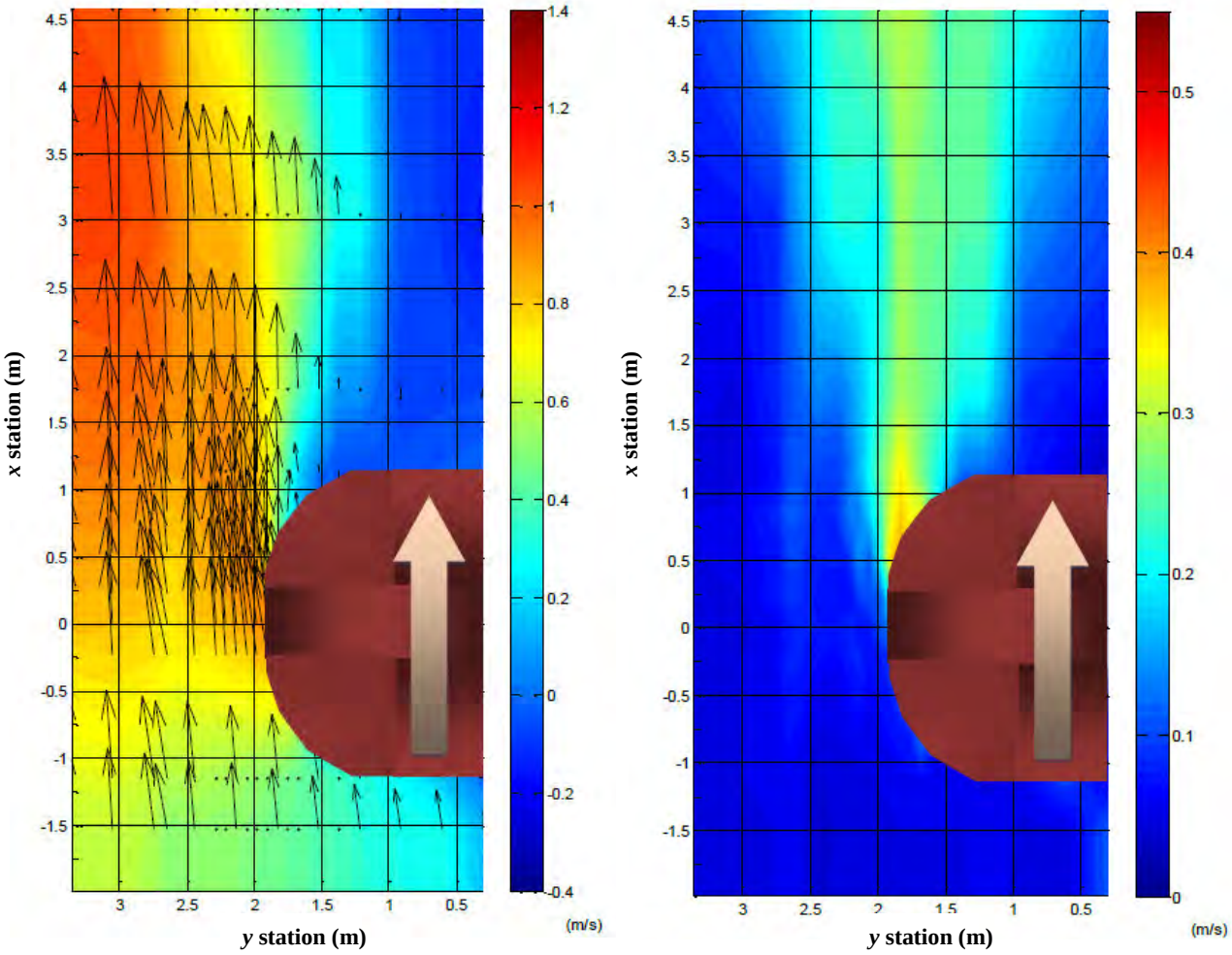

(a) Time Average Velocity (Initial) **(b) Turbulence Intensity (Initial)**

Figure A.1 – Case 1II

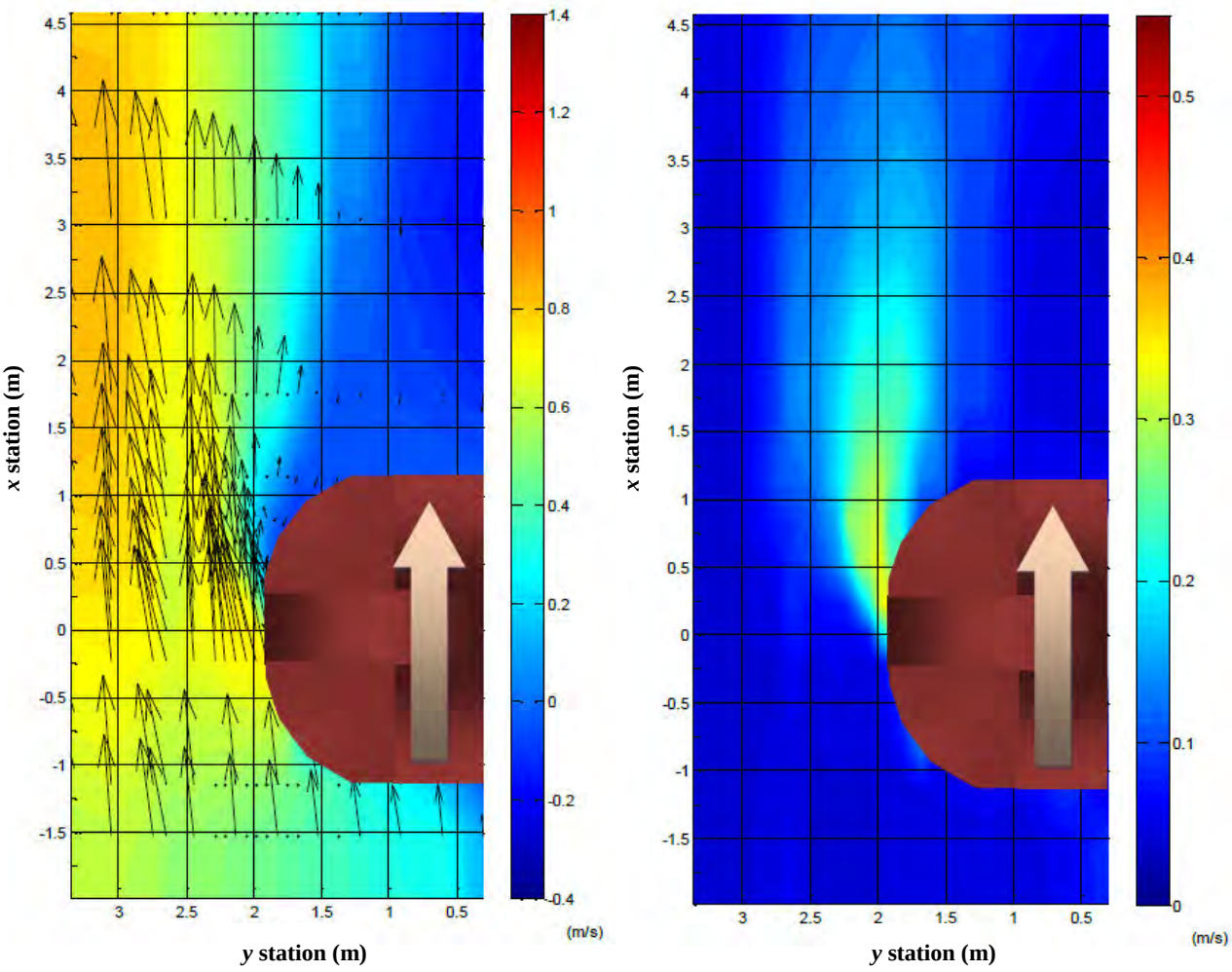

(c) Time Average Velocity (after 124hour run)

(d) Turbulence Intensity (after 124hour run)

Figure A.1(contd.) – Case 1II

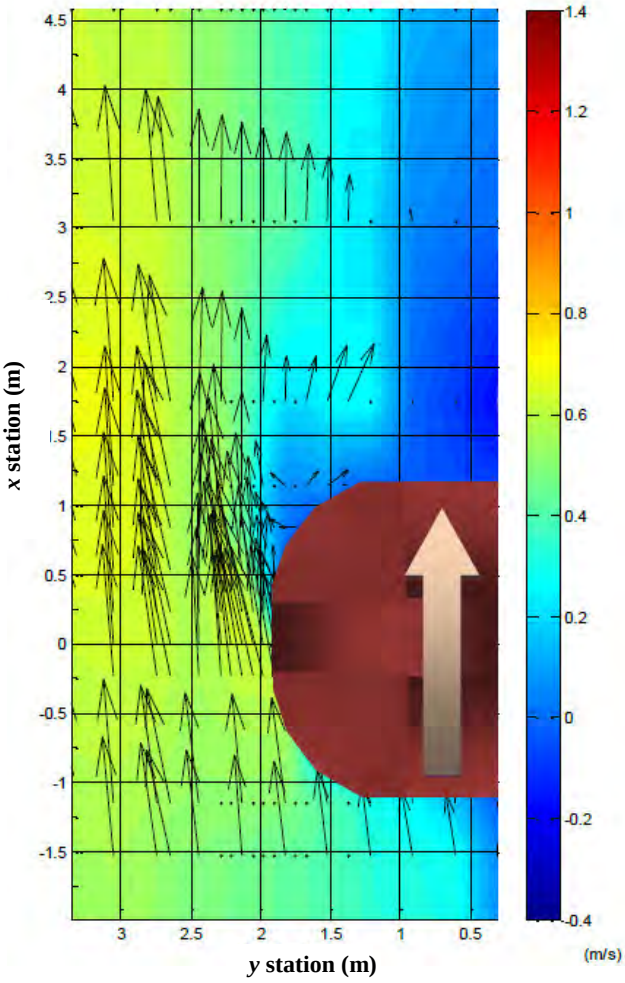

(e) Time Average Velocity (after 296hour run)

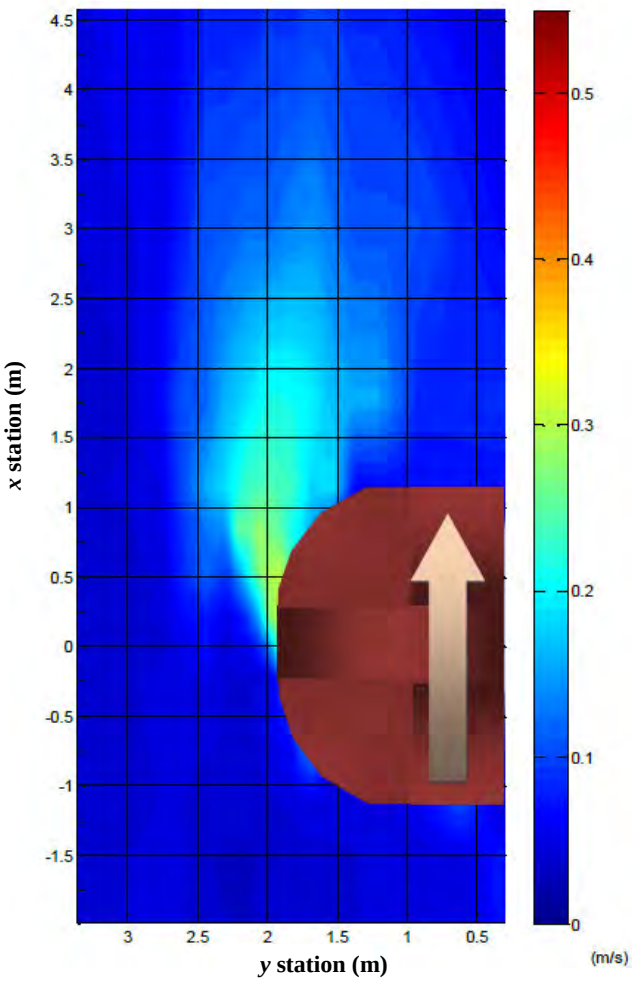

(f) Turbulence Intensity (after 296hour run)

Figure A.1(contd.) – Case 1II

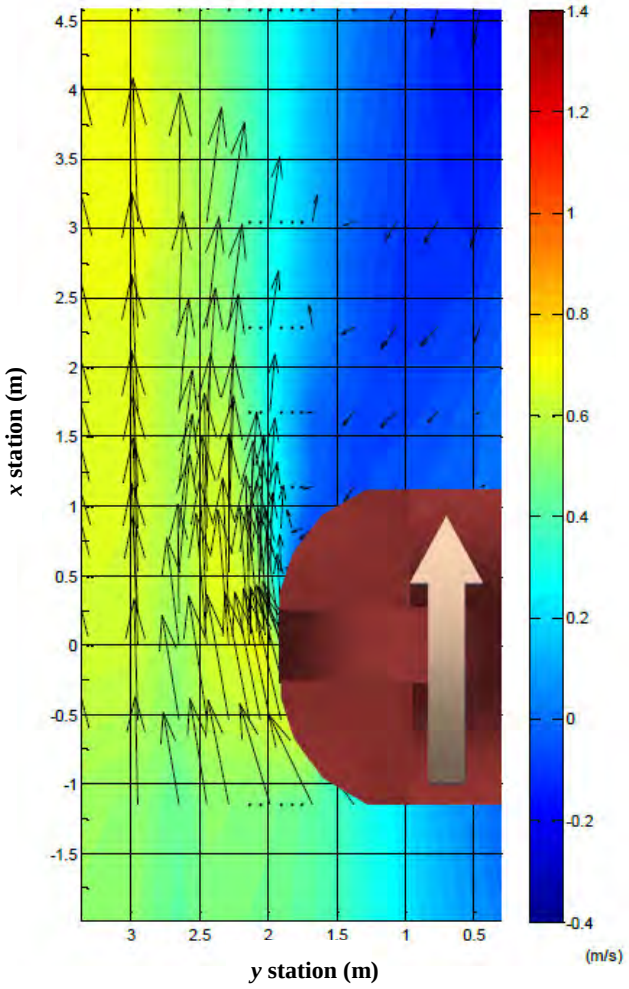

(a) Time Average Velocity (Initial)

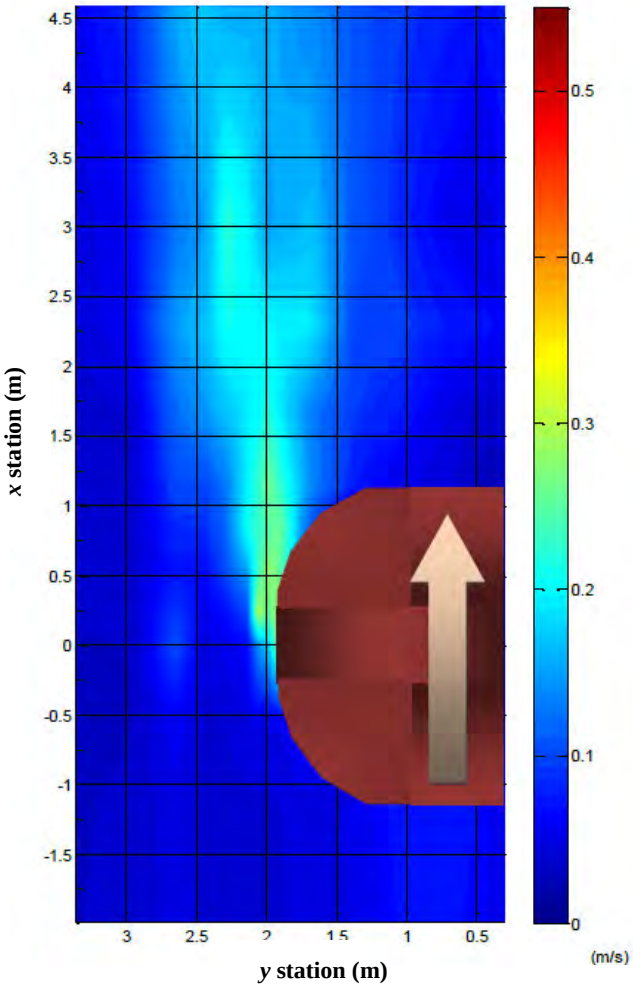

(b) Turbulence Intensity (Initial)

Figure A.2 – Case 2

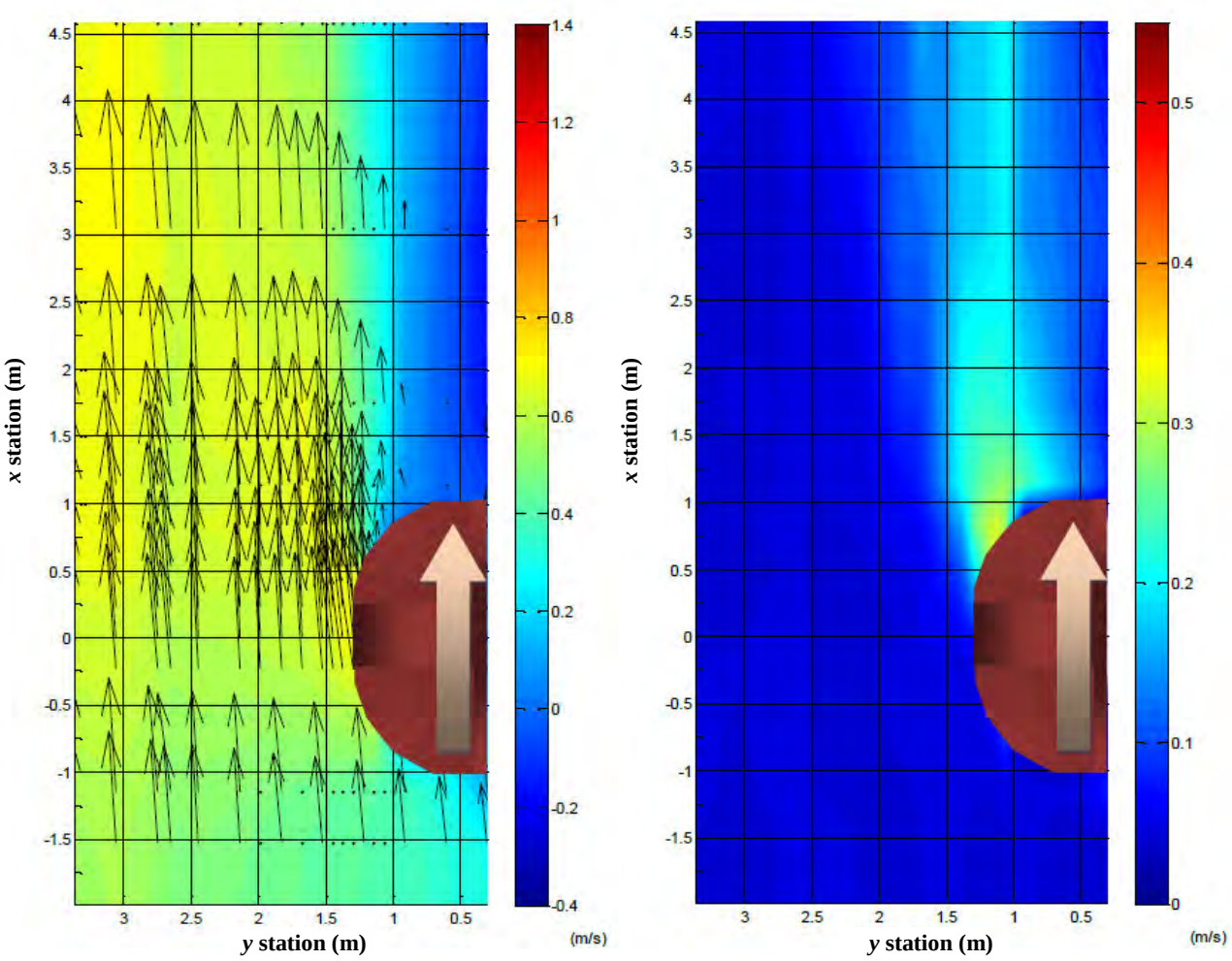

(a) Time Average Velocity (Initial)

(b) Turbulence Intensity (Initial)

Figure A.3 – Case 6

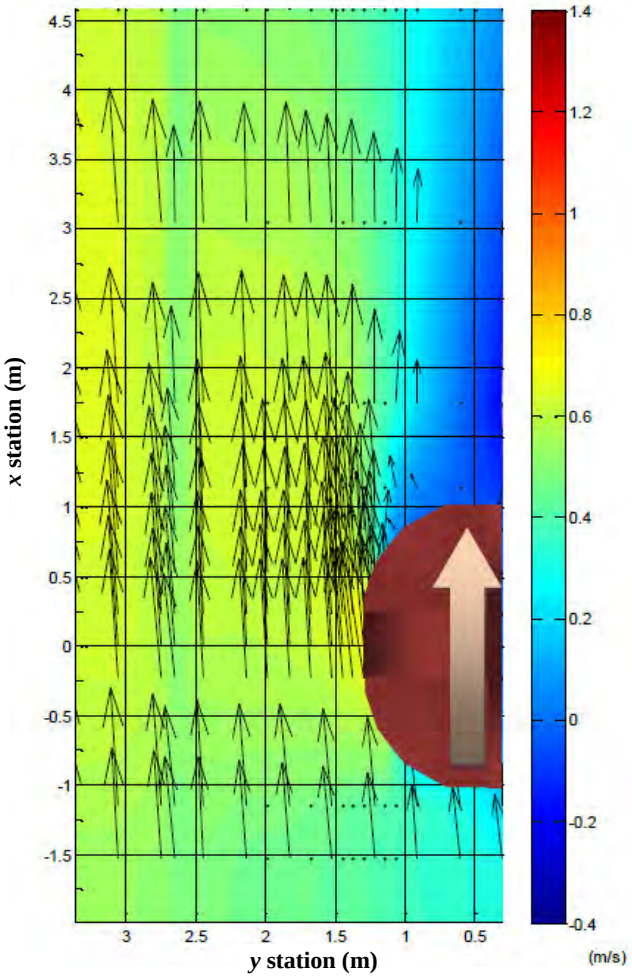

(c) Time Average Velocity (After 120 hour run)

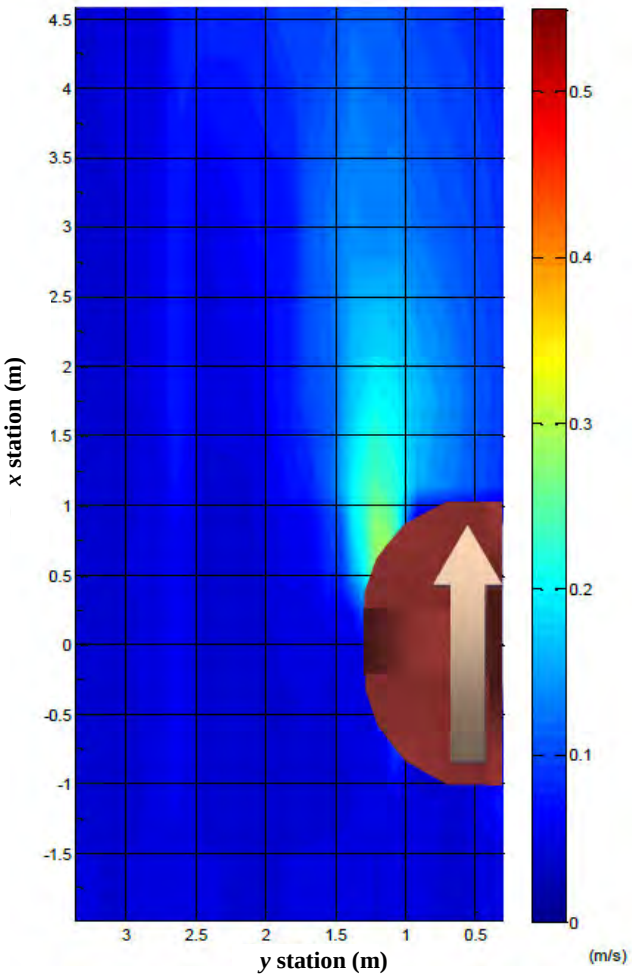

(d) Turbulence Intensity (After 120 hour run)

Figure A.3 (contd.) – Case 6

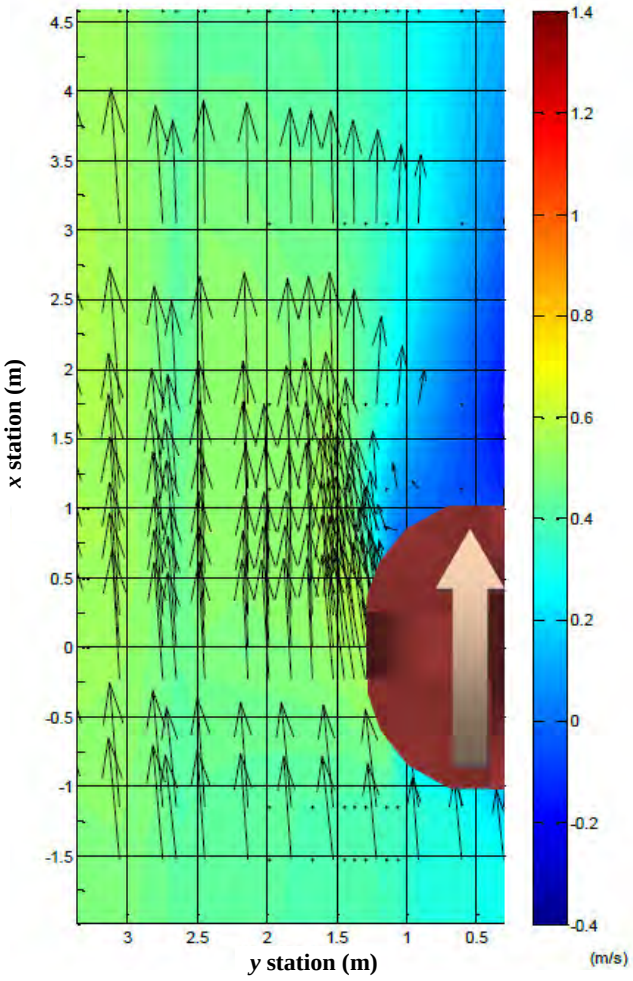

(e) Time Average Velocity (After 297 hour run)

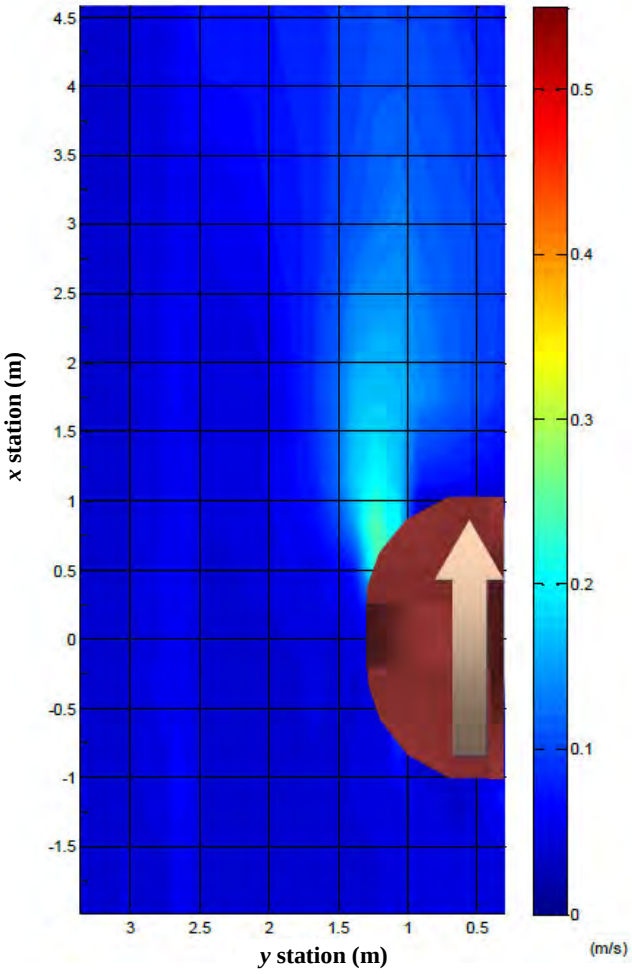

(f) Turbulence Intensity (After 297 hour run)

Figure A.3 (contd.) – Case 6

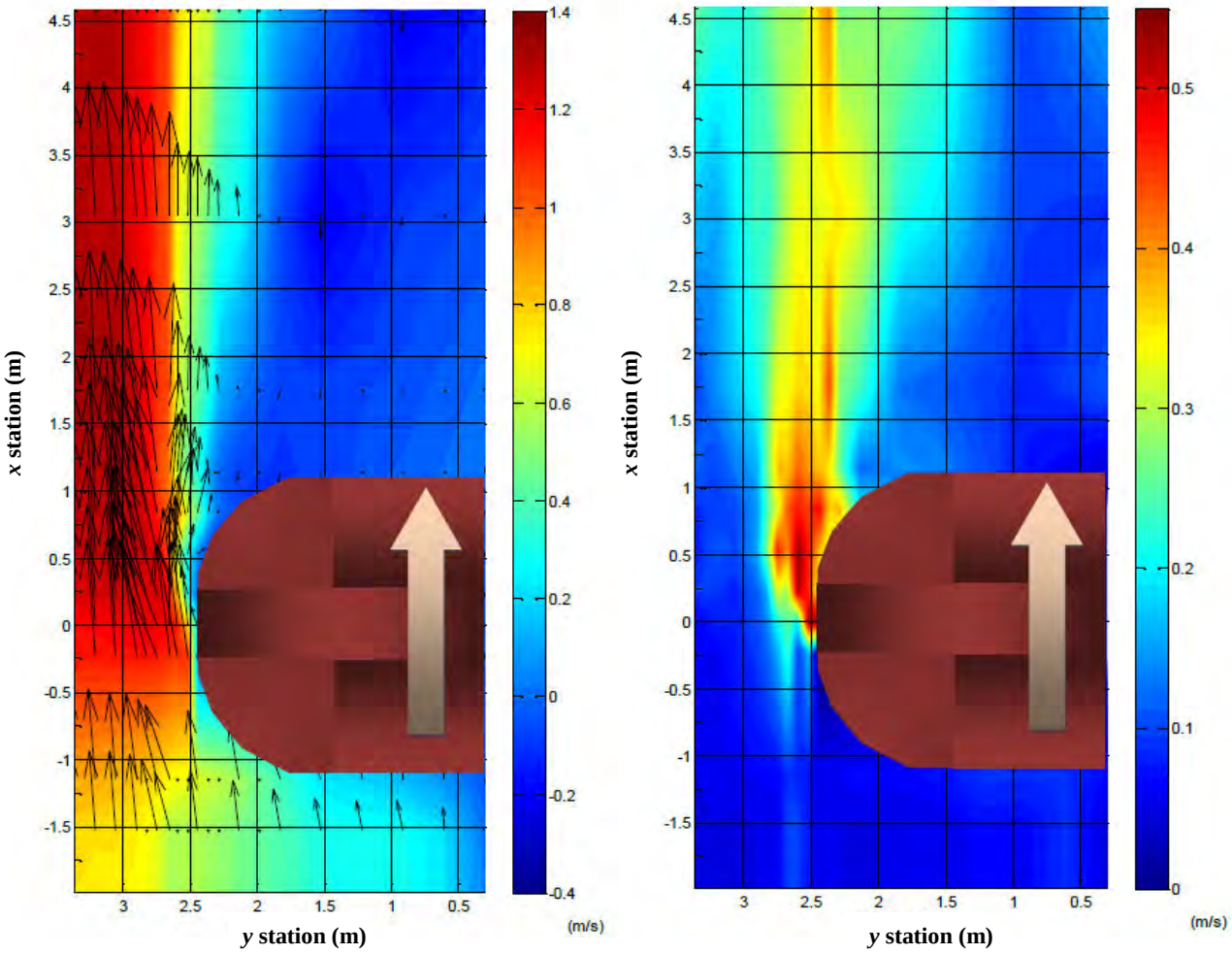

(a) Time Average Velocity (Initial)

(b) Turbulence Intensity (Initial)

Figure A.4 – Case 7

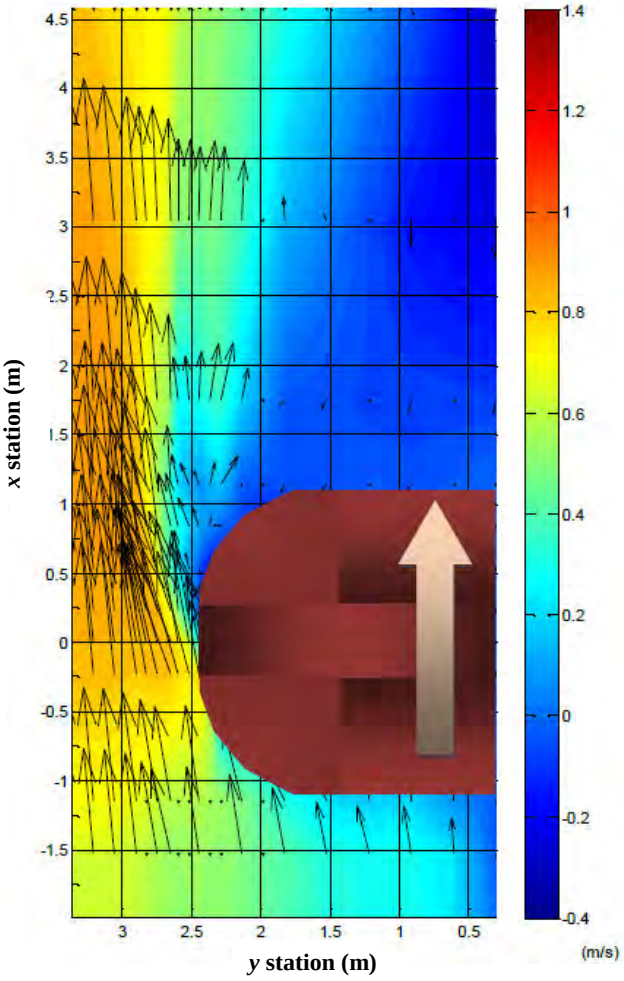

(c) Time Average Velocity (After 120 hour run)

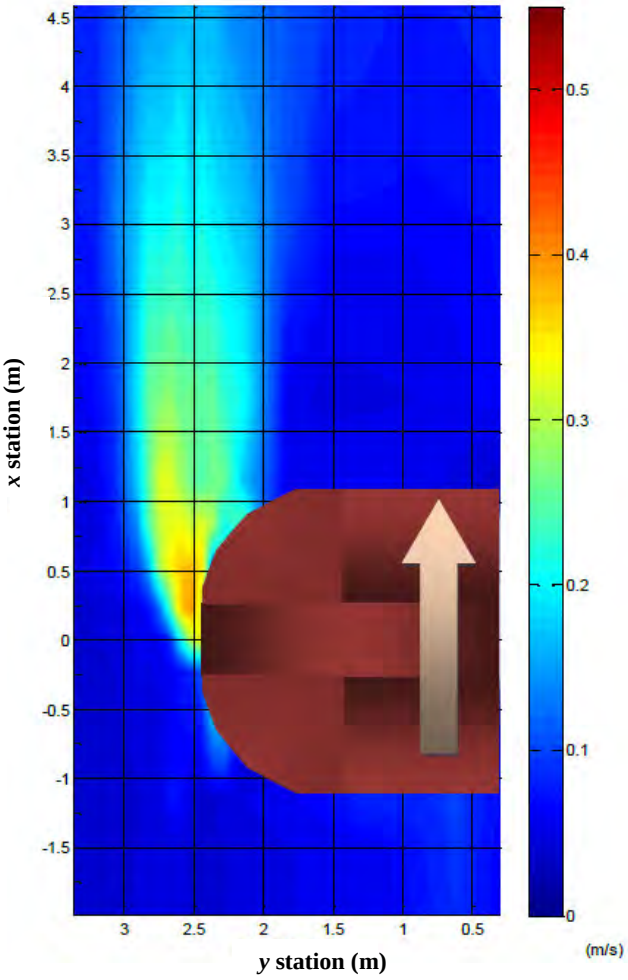

(d) Turbulence Intensity (After 120 hour run)

Figure A.4 (contd.) – Case 7

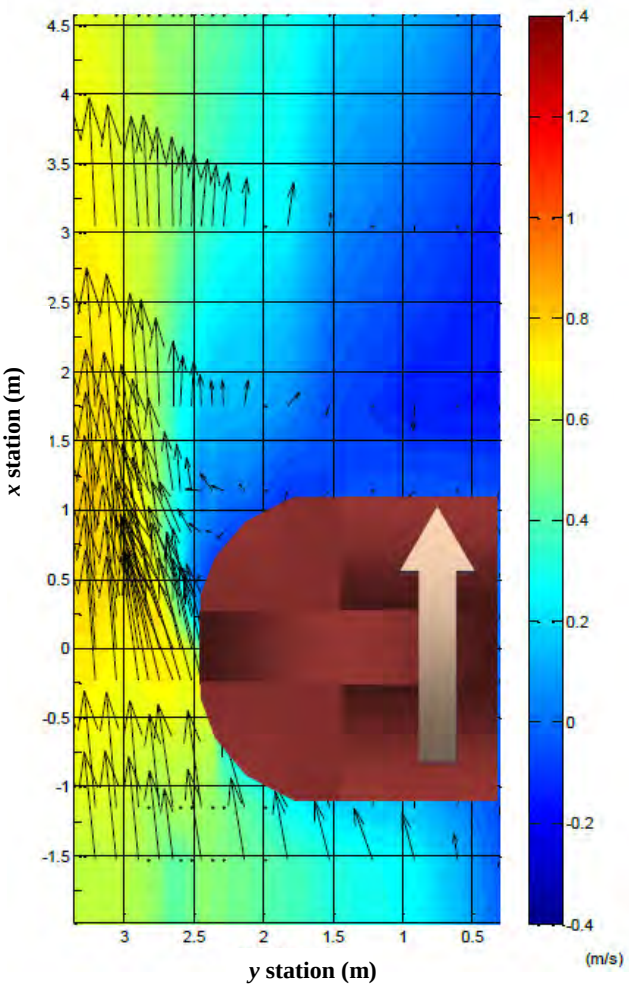

(e) Time Average Velocity (After 253 hour run)

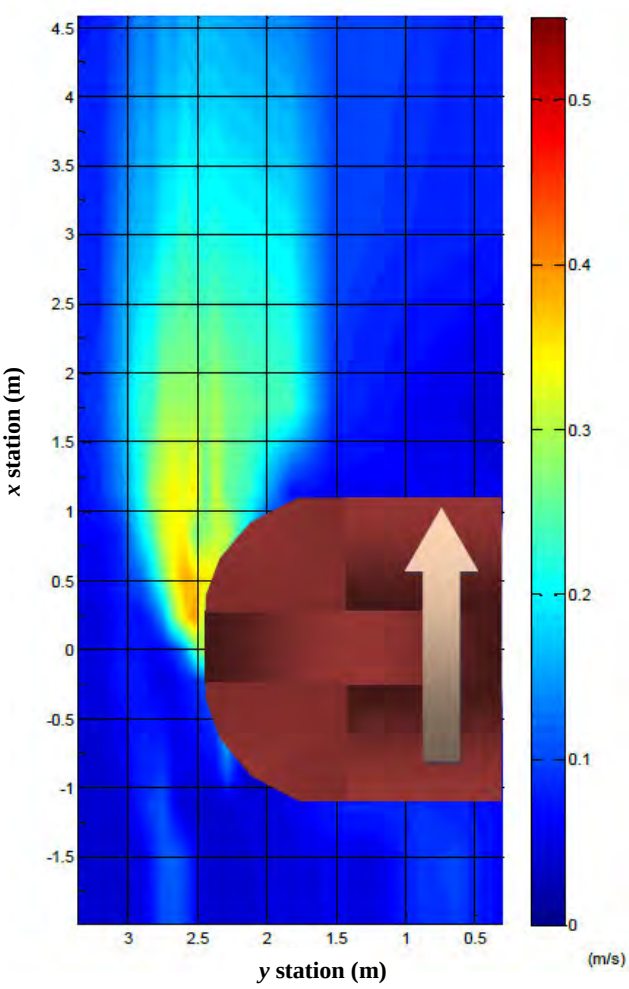

(f) Turbulence Intensity (After 253 hour run)

Figure A.4 (contd.) – Case 7

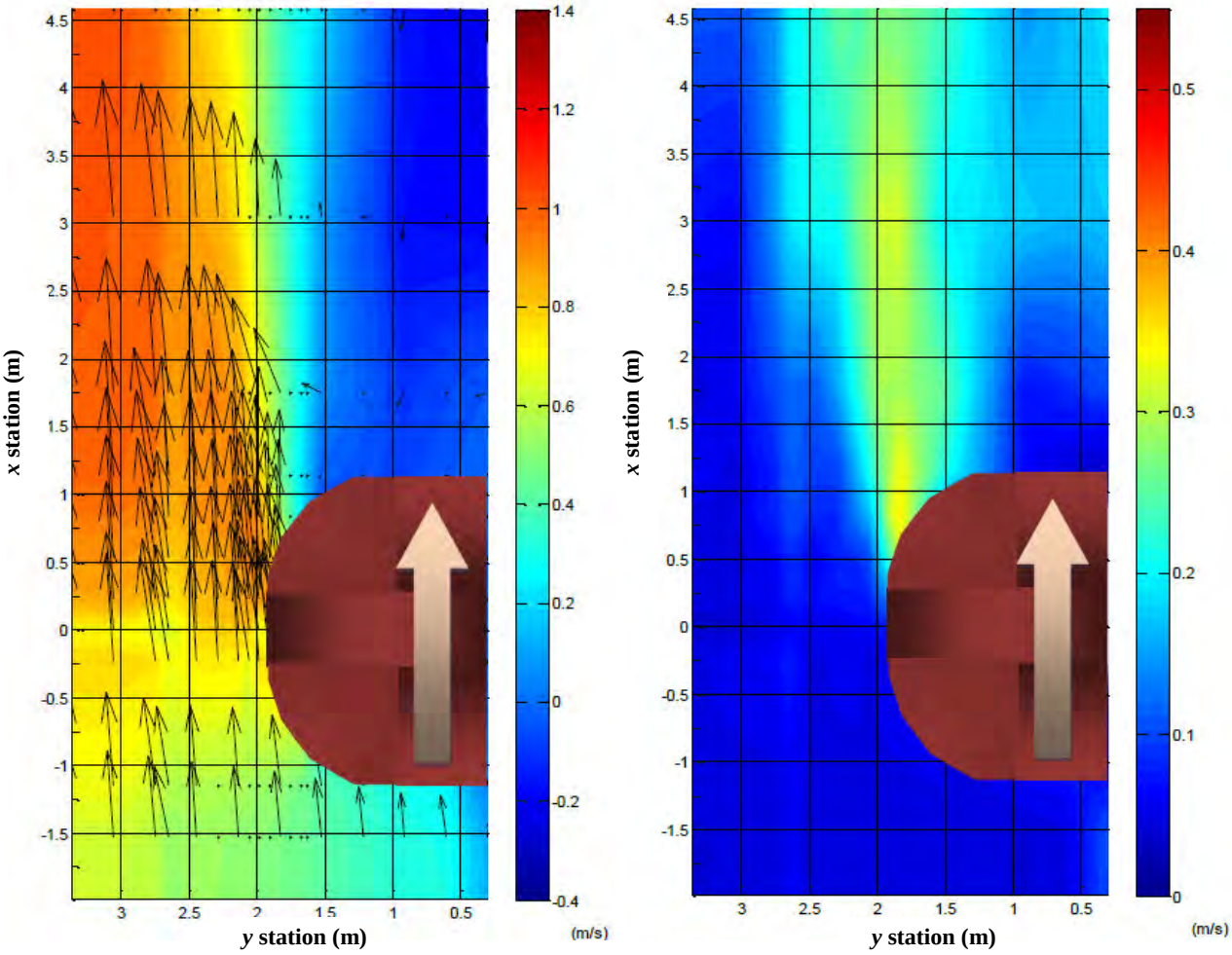

(a) Time Average Velocity (Initial)

(b) Turbulence Intensity (Initial)

Figure A.5 – Case 8

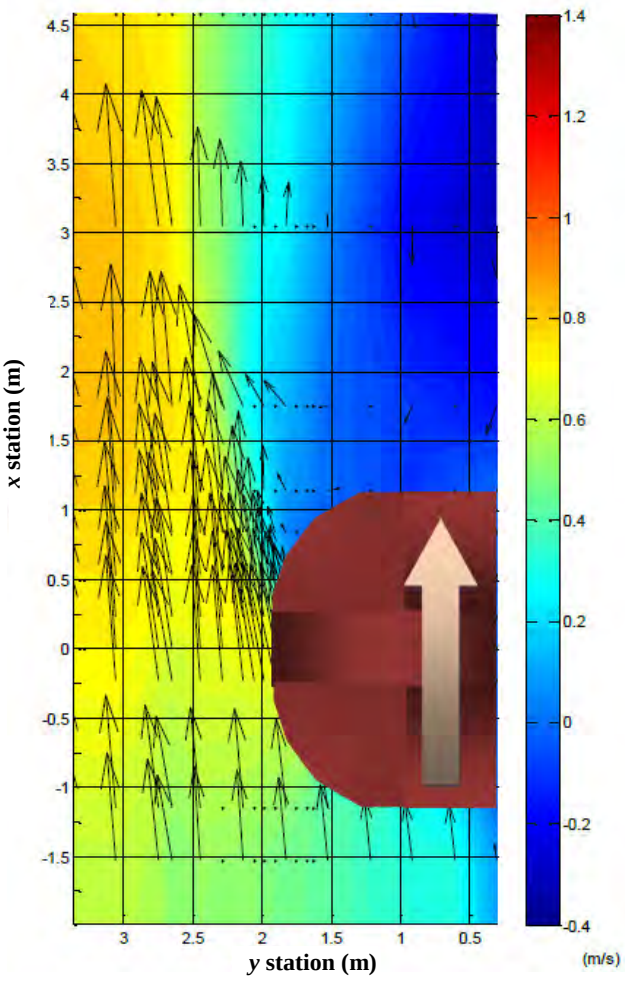

(c) Time Average Velocity (After 123 hour run)

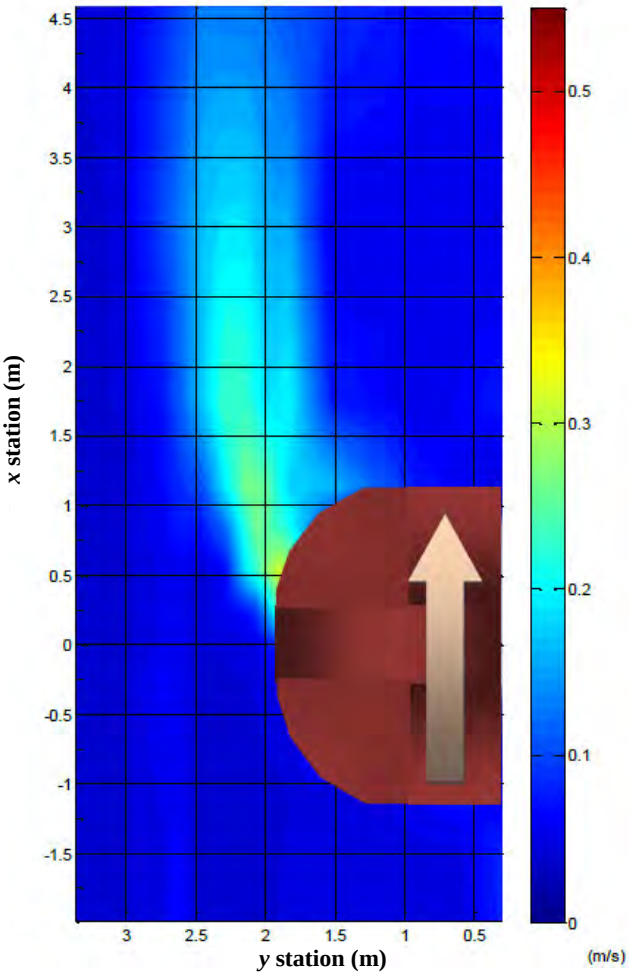

(d) Turbulence Intensity (After 123 hour run)

Figure A.5(contd.) – Case 8

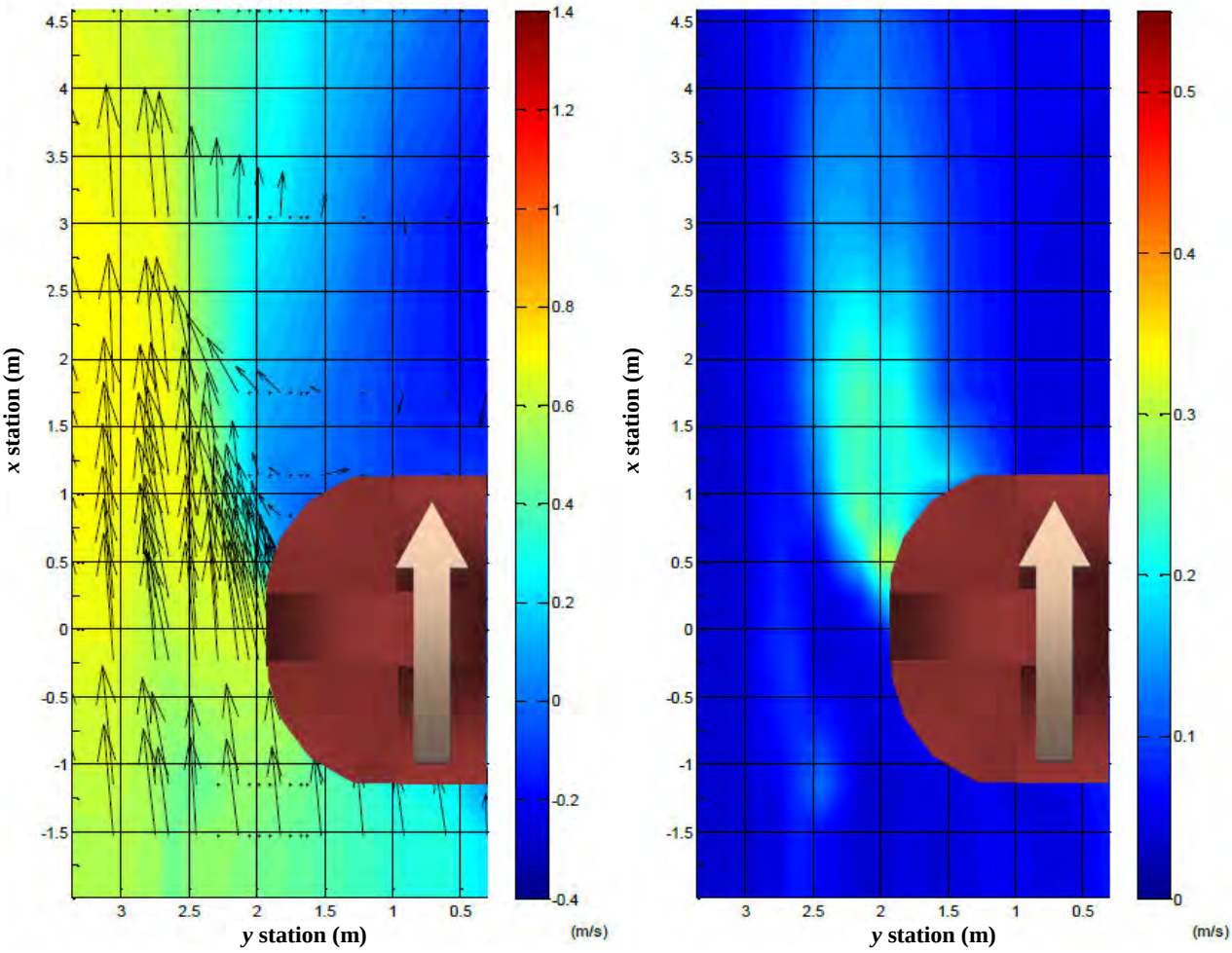

(e) Time Average Velocity (After 275 hour run)

(f) Turbulence Intensity (After 275 hour run)

Figure A.5(contd.) – Case 8

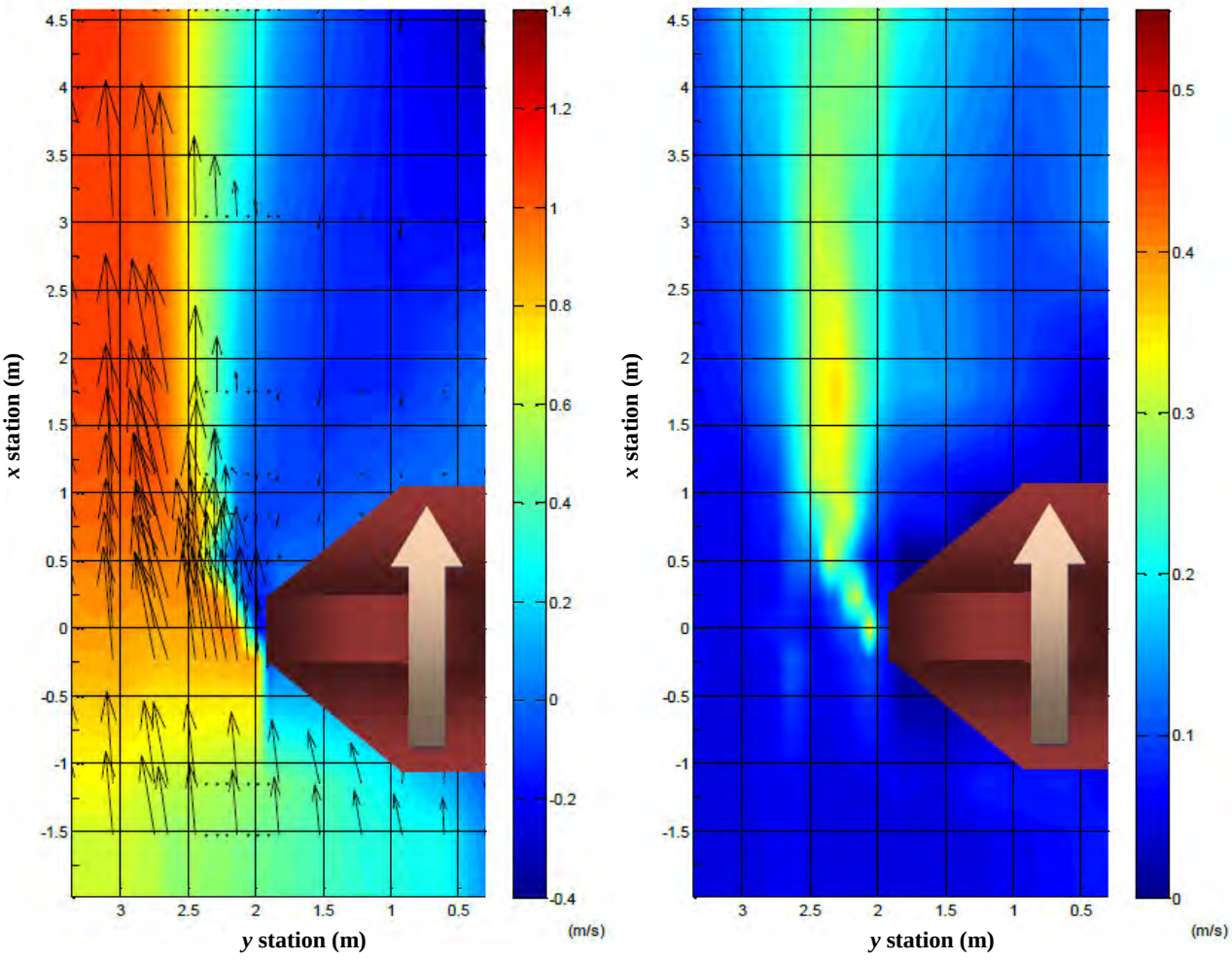

(a) Time Average Velocity (Initial)

(b) Turbulence Intensity (Initial)

Figure A.6 – Case 9

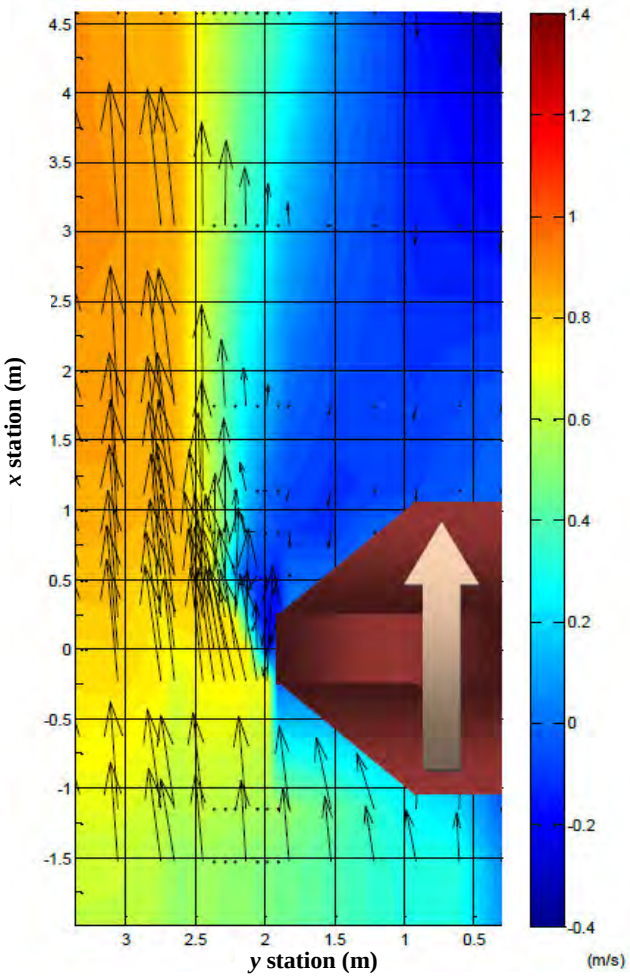

(c) Time Average Velocity (After 123 hour run)

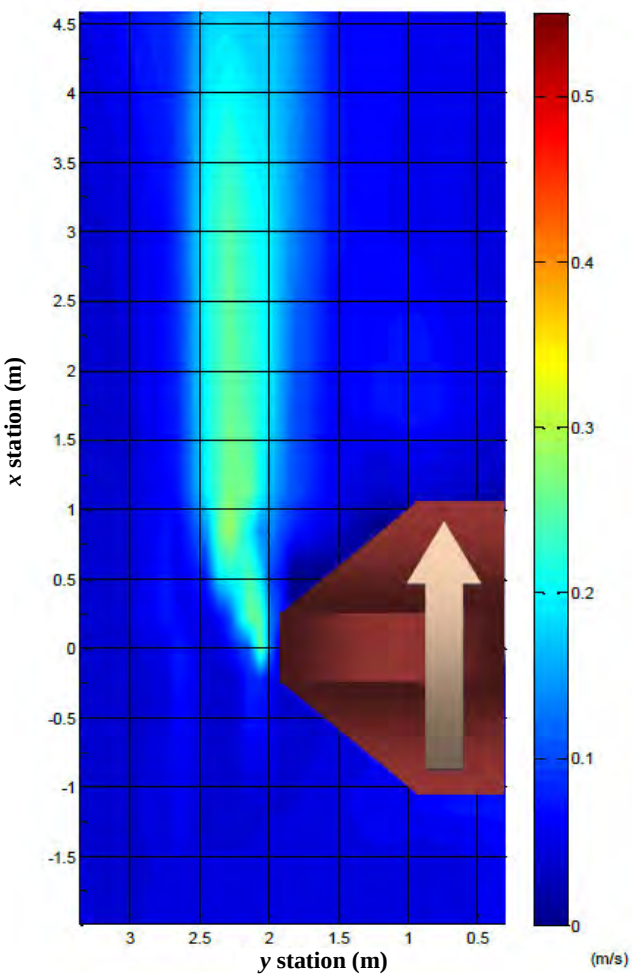

(d) Turbulence Intensity (After 123 hour run)

Figure A.6(contd.) – Case 9

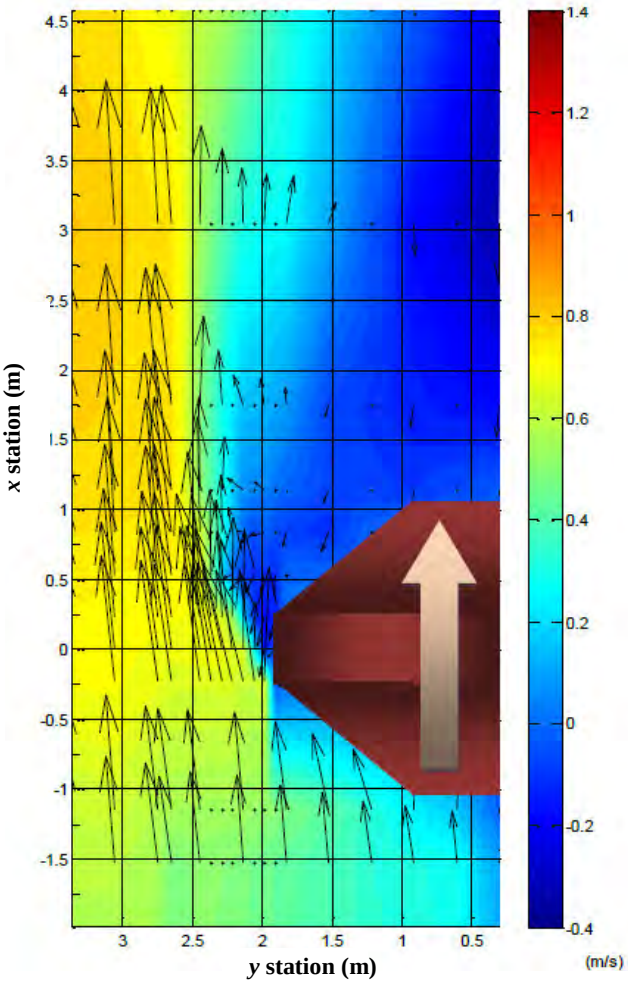

(e) Time Average Velocity (After 250 hour run)

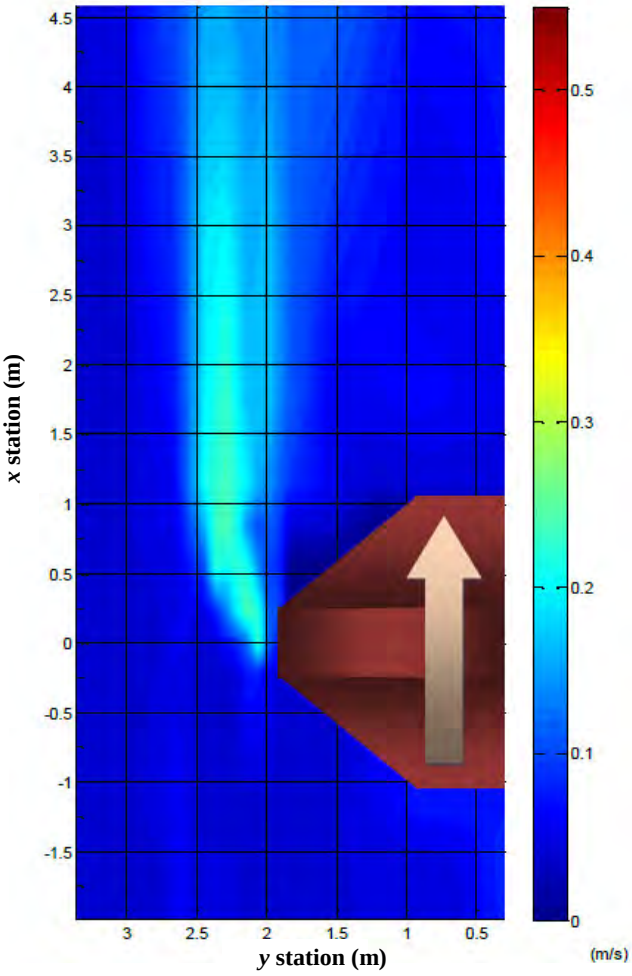

(f) Turbulence Intensity (After 250 hour run)

Figure A.6(contd.) – Case 9

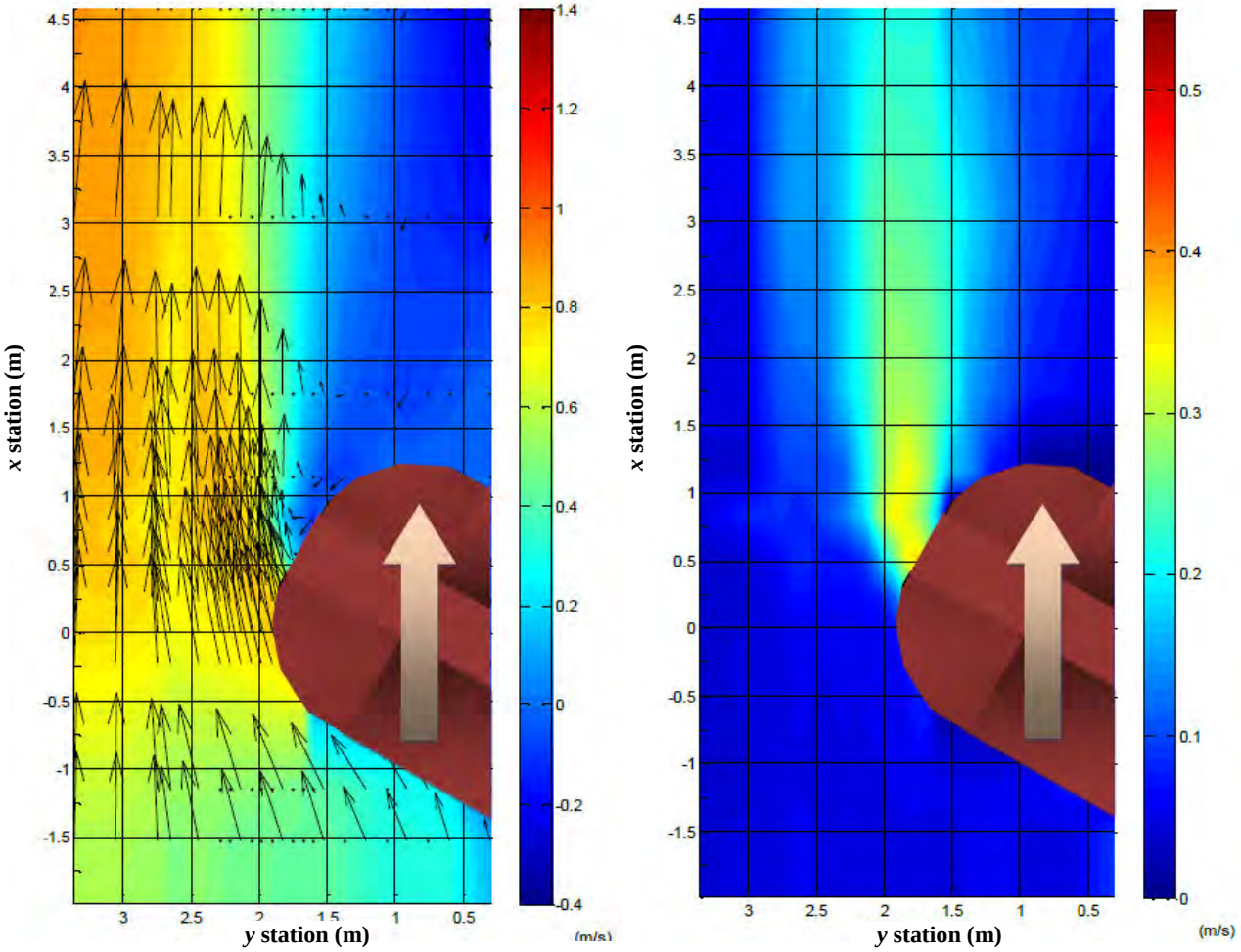

(a) Time Average Velocity (Initial)

(b) Turbulence Intensity (Initial)

Figure A.7 – Case 10

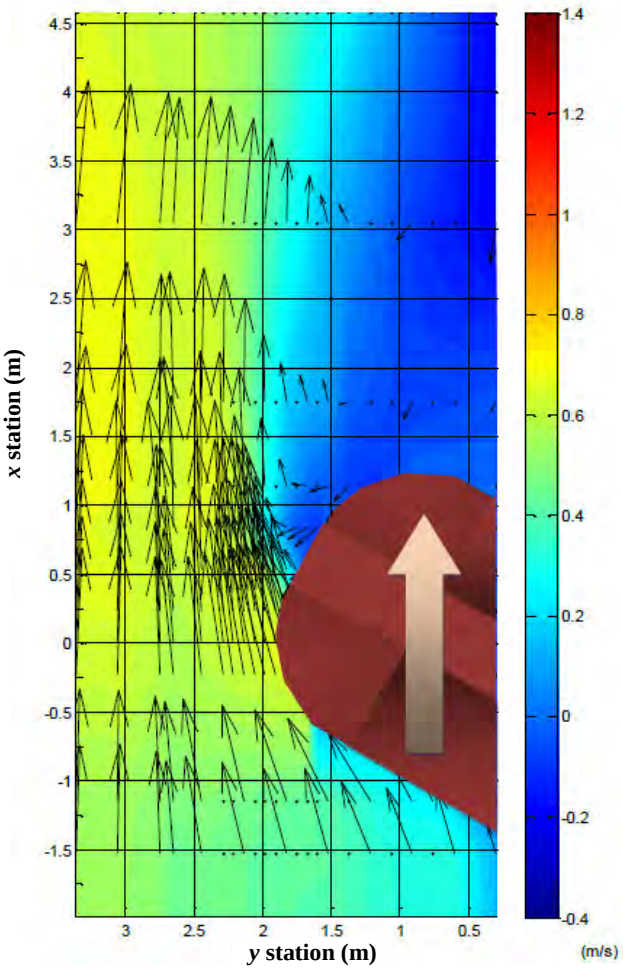

(c) Time Average Velocity (After 120 hour run)

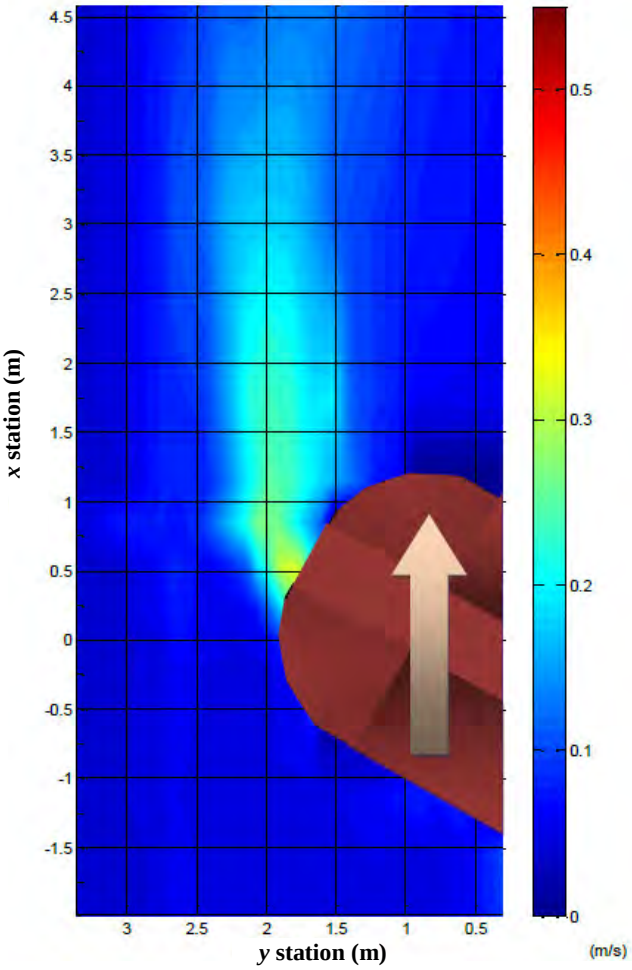

(d) Turbulence Intensity (After 120 hour run)

Figure A.7(contd.) – Case 10

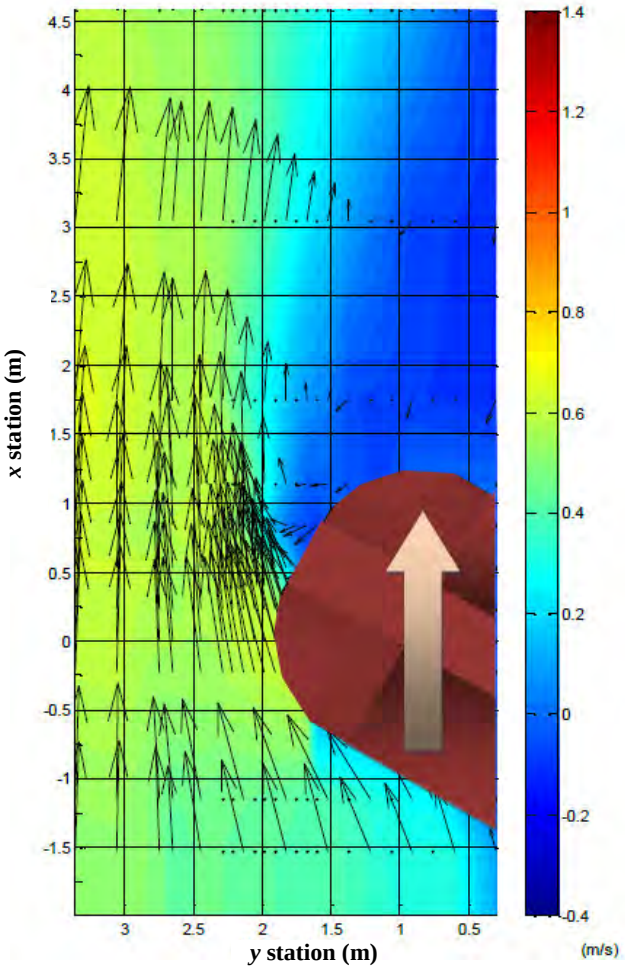

(e) Time Average Velocity (After 296 hour run)

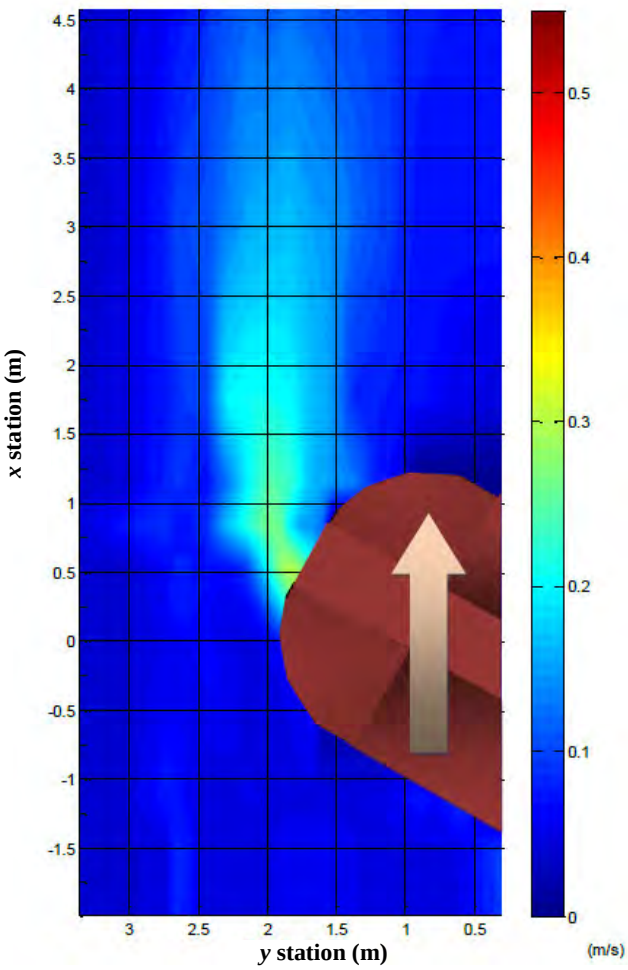

(f) Turbulence Intensity (After 296 hour run)

Figure A.7(contd.) – Case 10

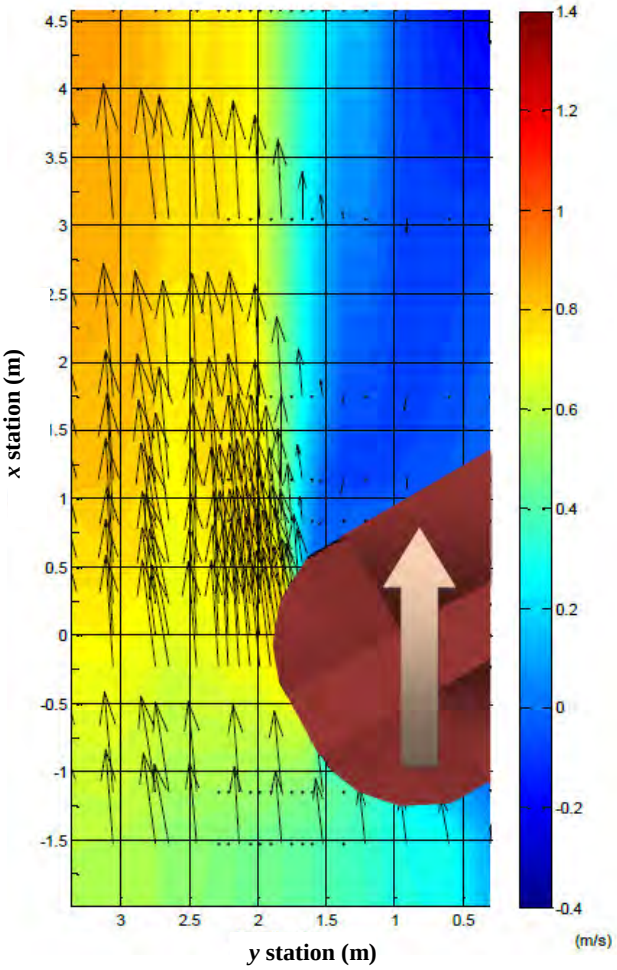

(a) Time Average Velocity (Initial)

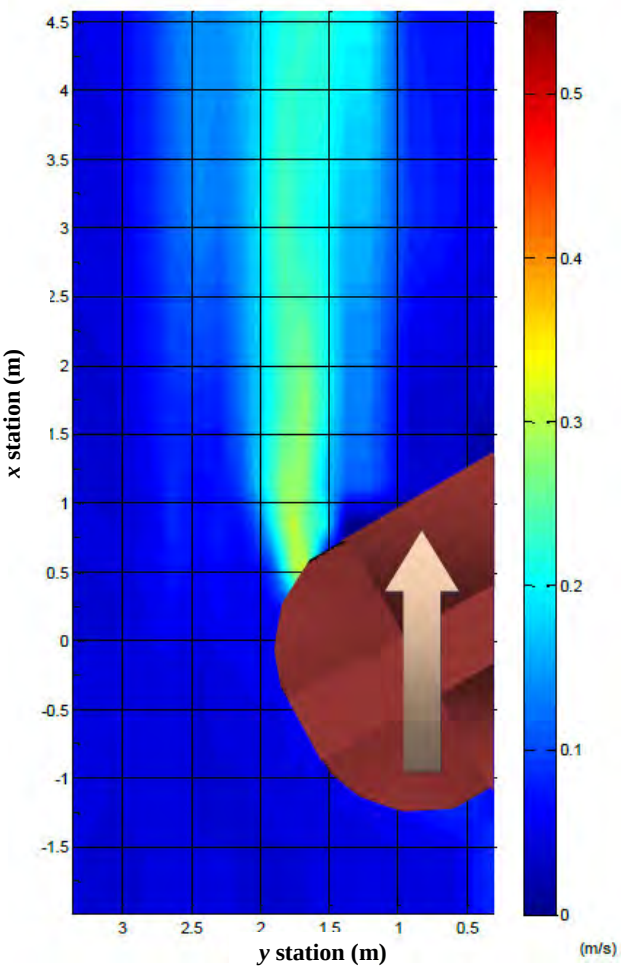

(b) Turbulence Intensity (Initial)

Figure A.8 – Case 11

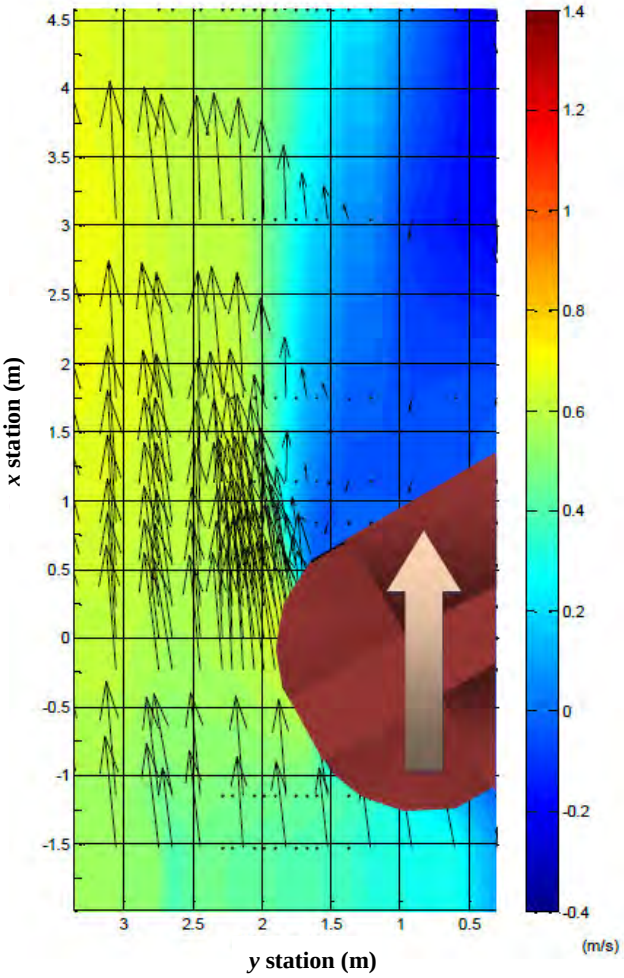

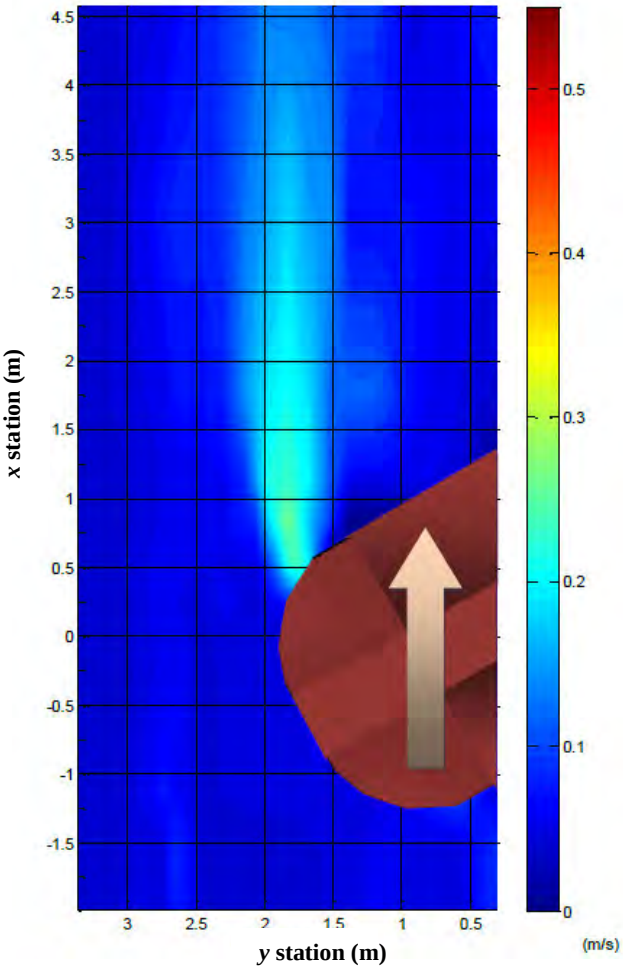

(c) Time Average Velocity (After 120 hour run)

(d) Turbulence Intensity (After 120 hour run)

Figure A.8(contd.) – Case 11

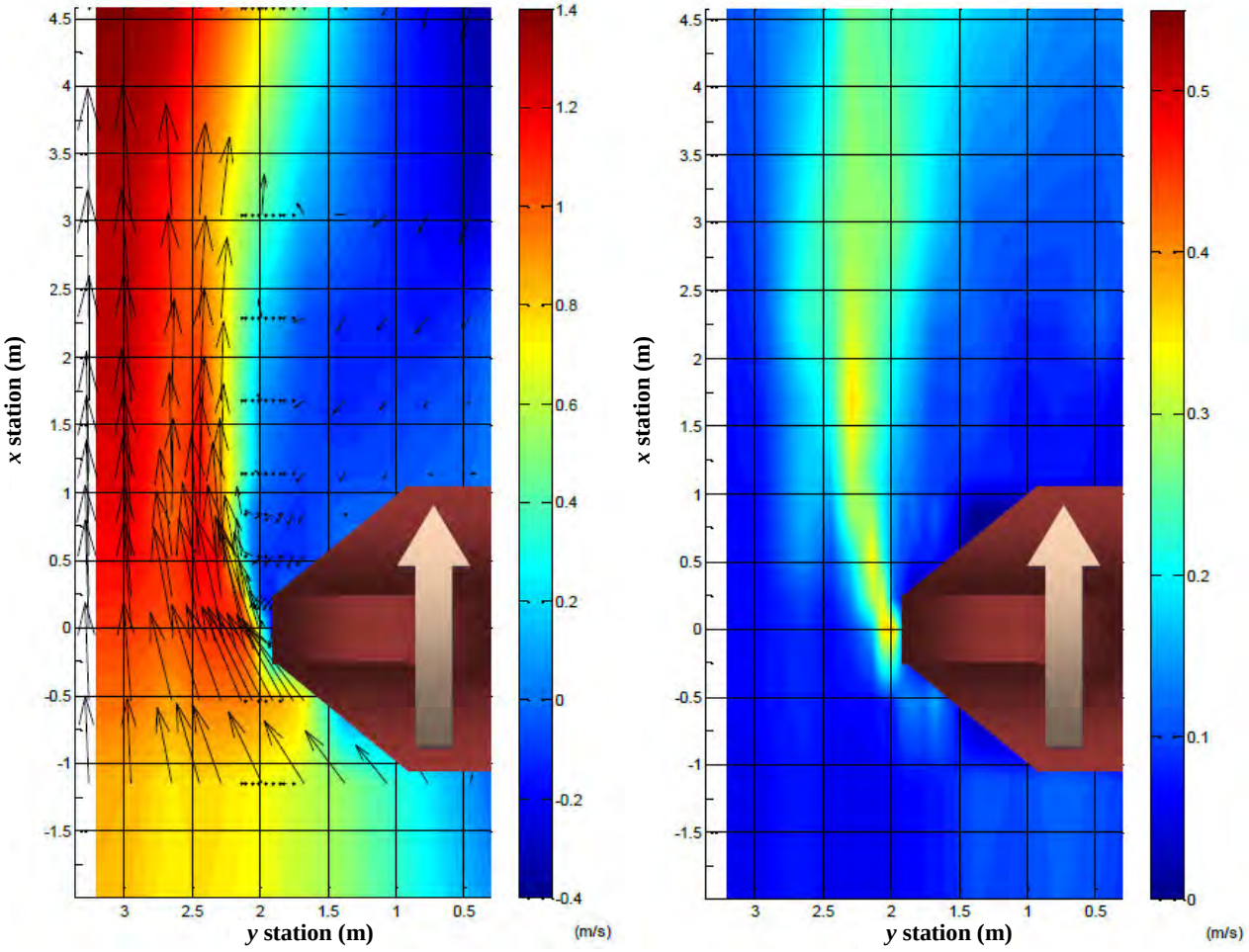

(a) Time Average Velocity (Initial)

(b) Turbulence Intensity (Initial)

Figure A.9 – Case 12B

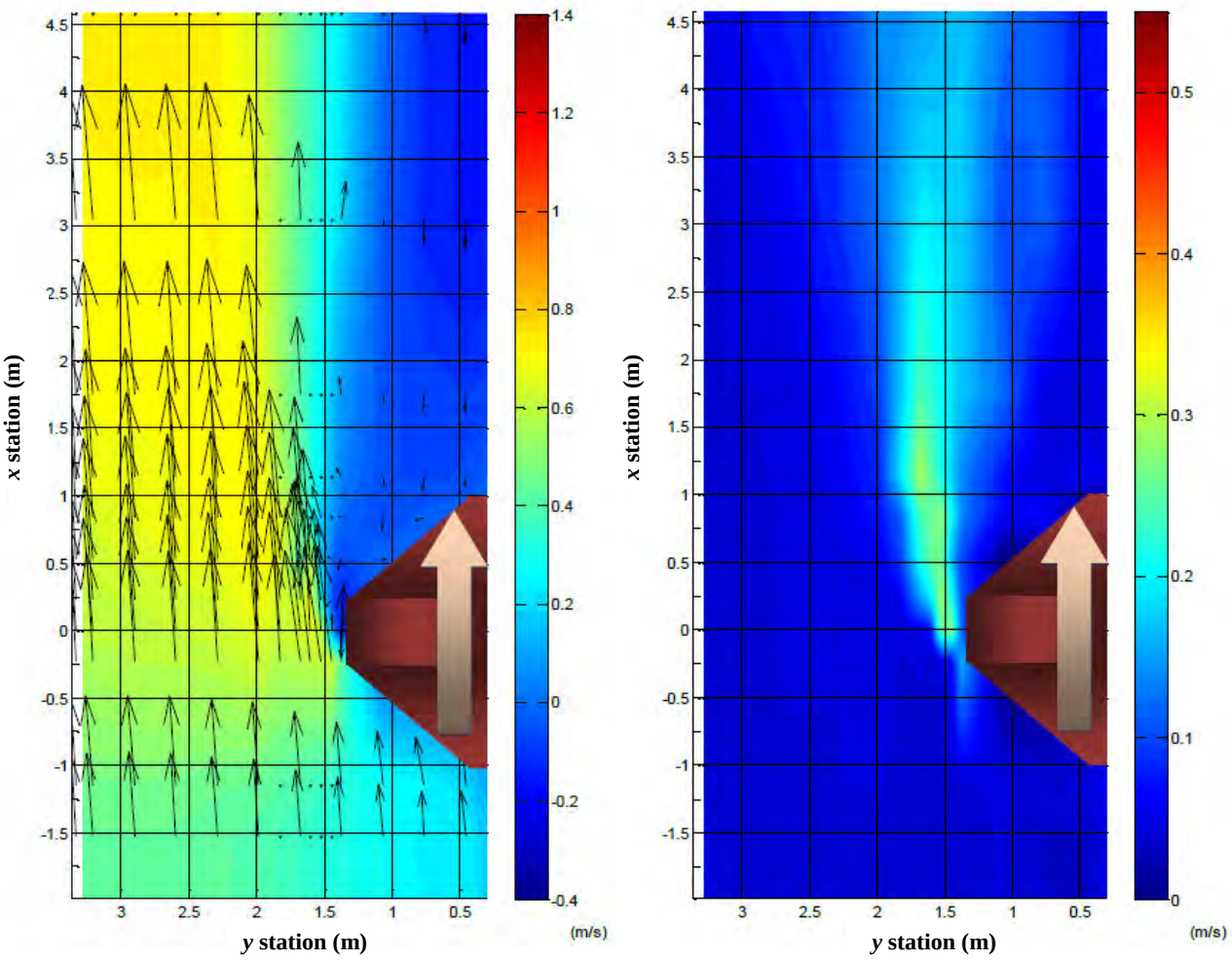

(a) Time Average Velocity (Initial)

(b) Turbulence Intensity (Initial)

Figure A.10– Case 17

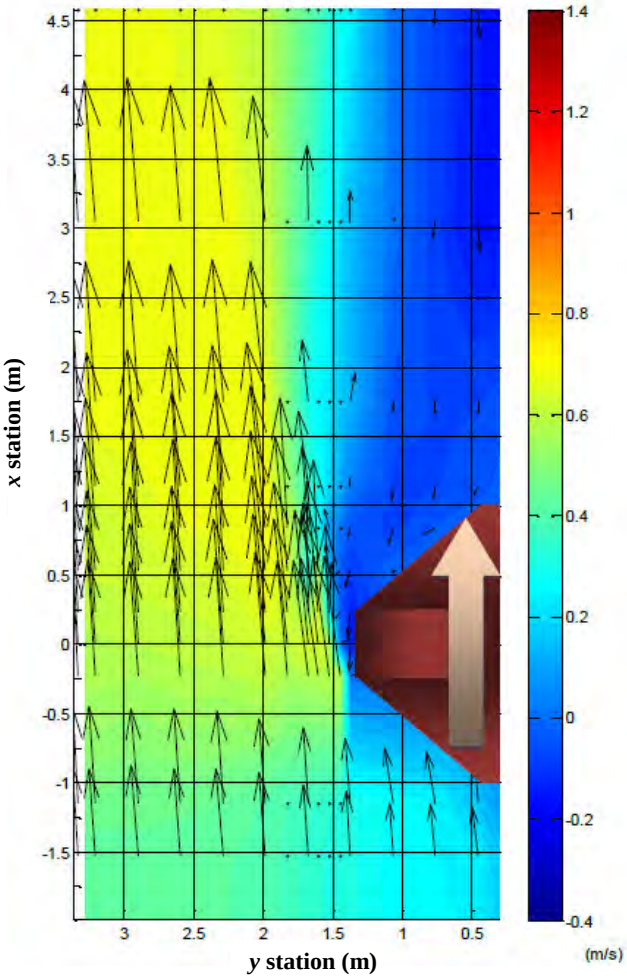

(c) Time Average Velocity (After 128 hour run)

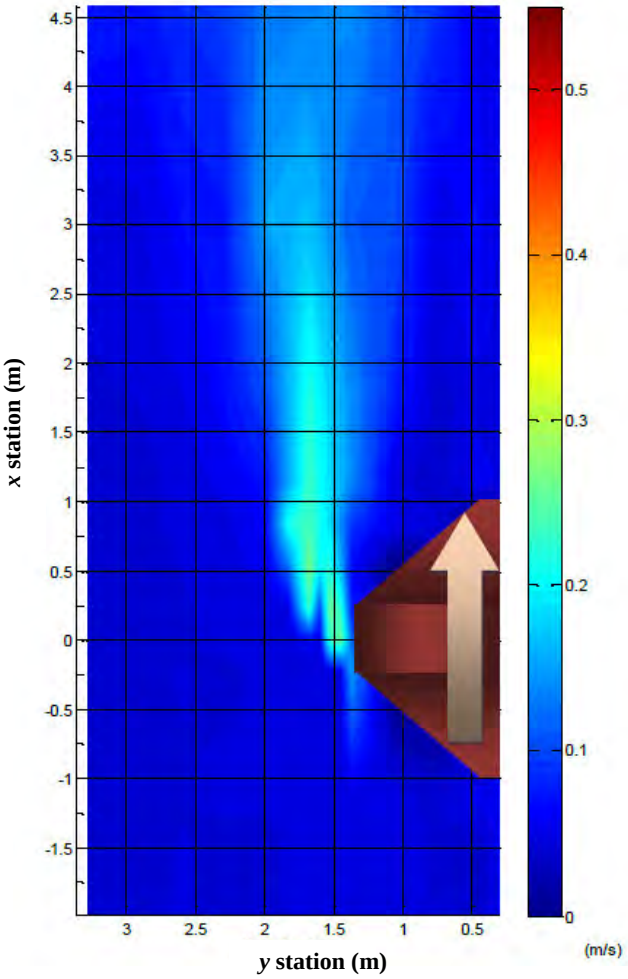

(d) Turbulence Intensity (After 128 hour run)

Figure A.10 (contd.) – Case 17

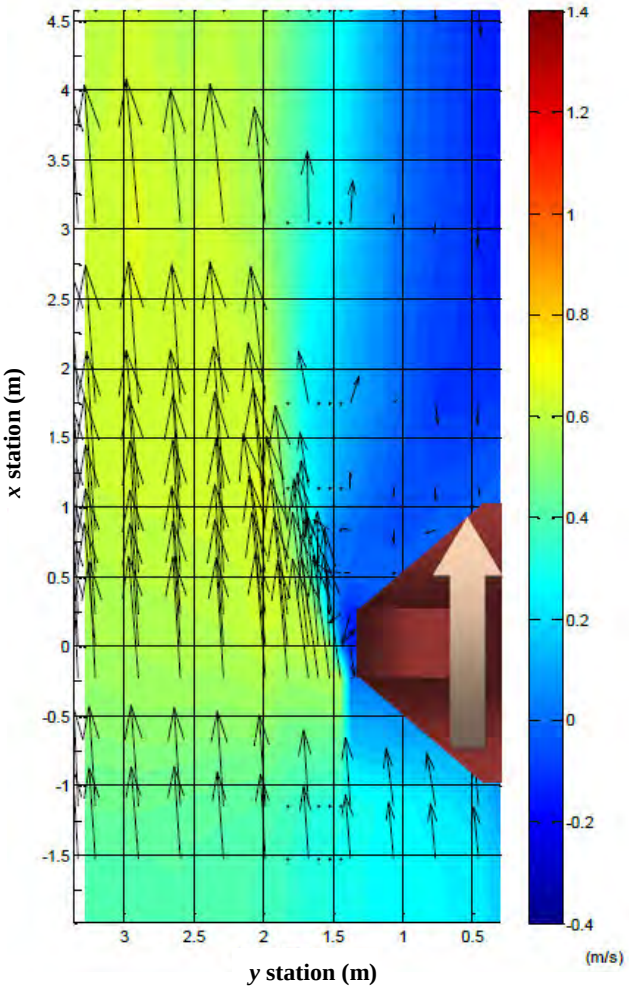

(e) Time Average Velocity (After 275 hour run)

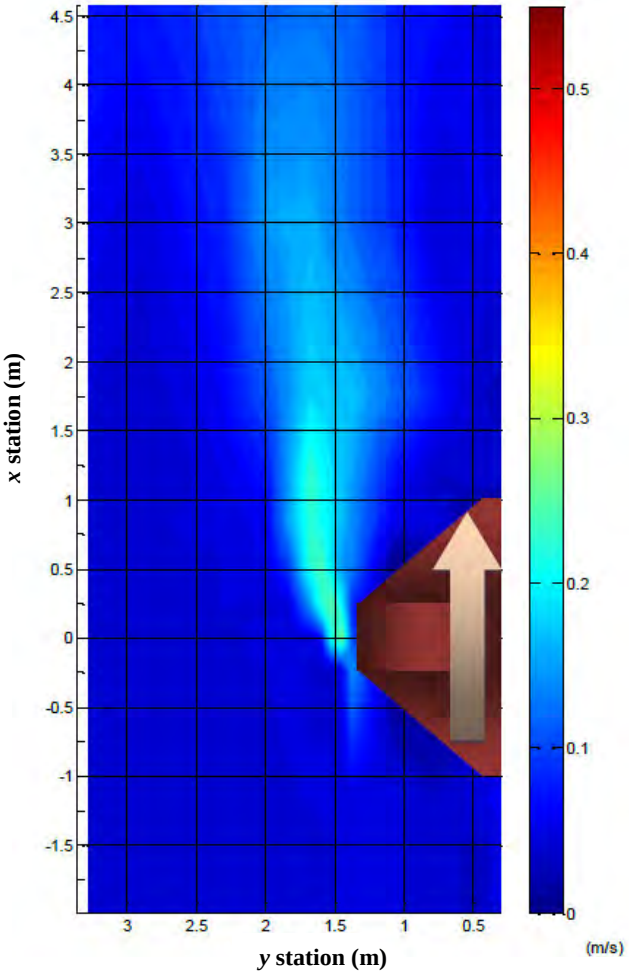

(f) Turbulence Intensity (After 275 hour run)

Figure A.10 (contd.) – Case 17

APPENDIX B

SCOUR DEVELOPMENT

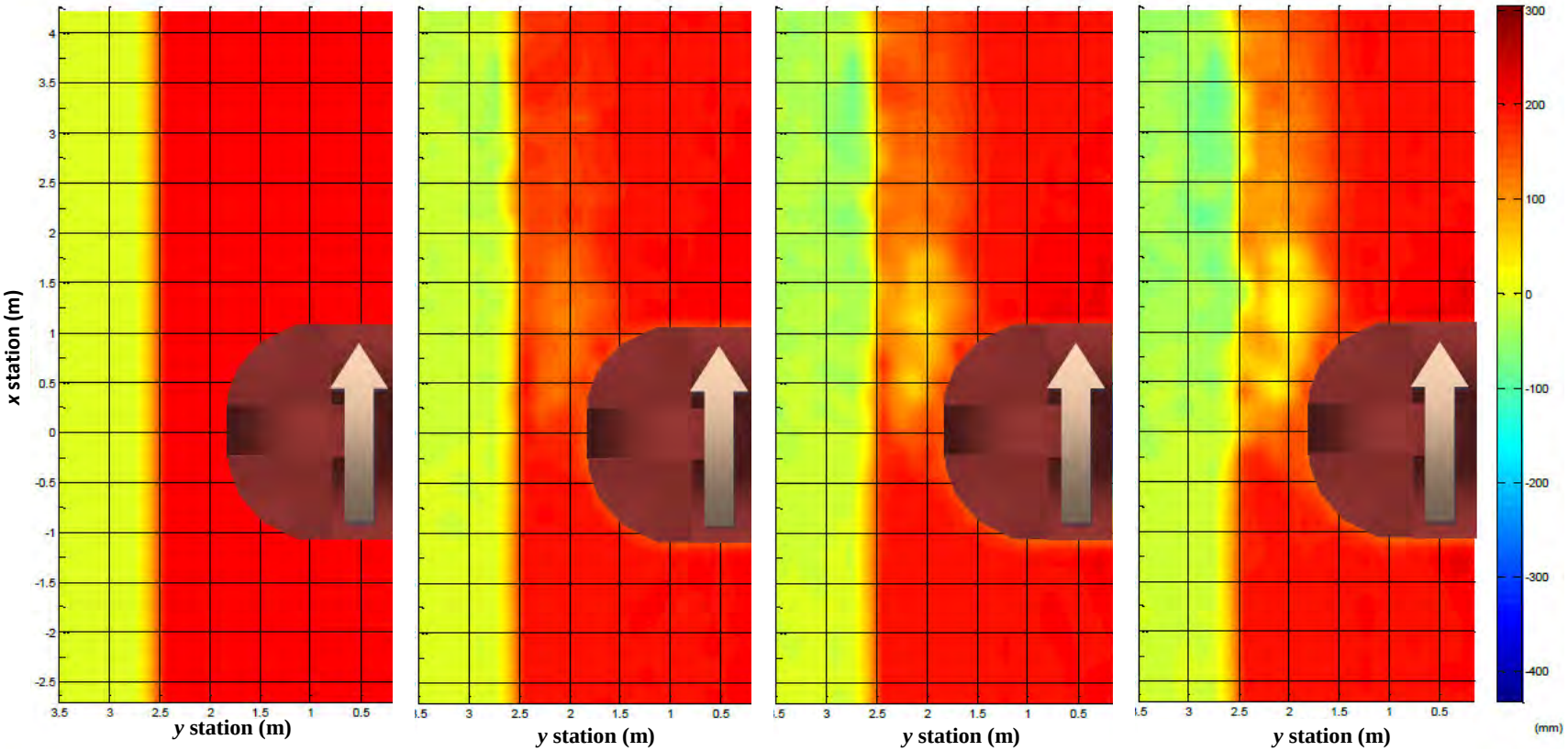

Initial **24 hours** **48 hous** **72 hours**

Figure B.1 – Case1

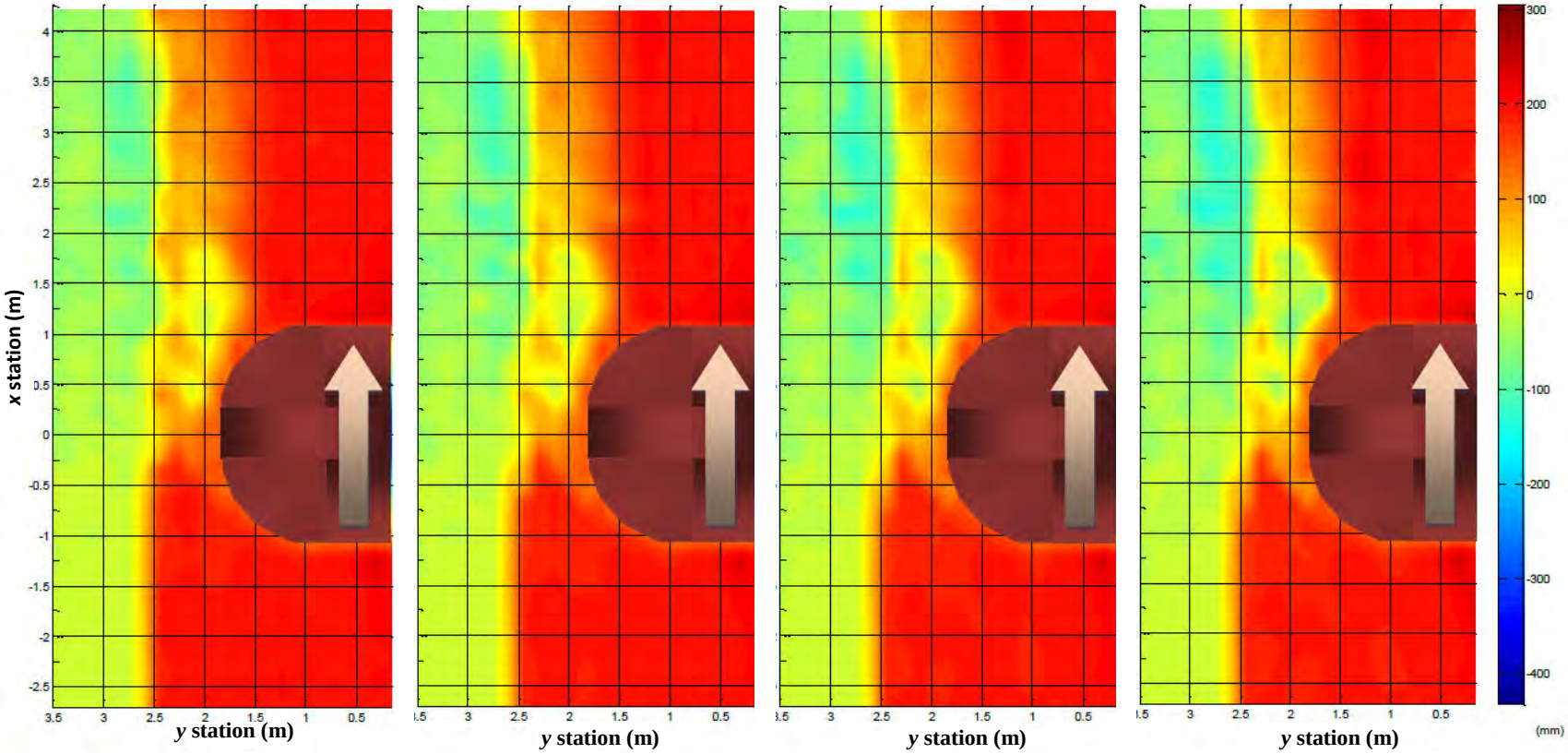

96 hours **120 hours** **156 hours** **182 hours**

Figure B.1 (contd.) – Case1

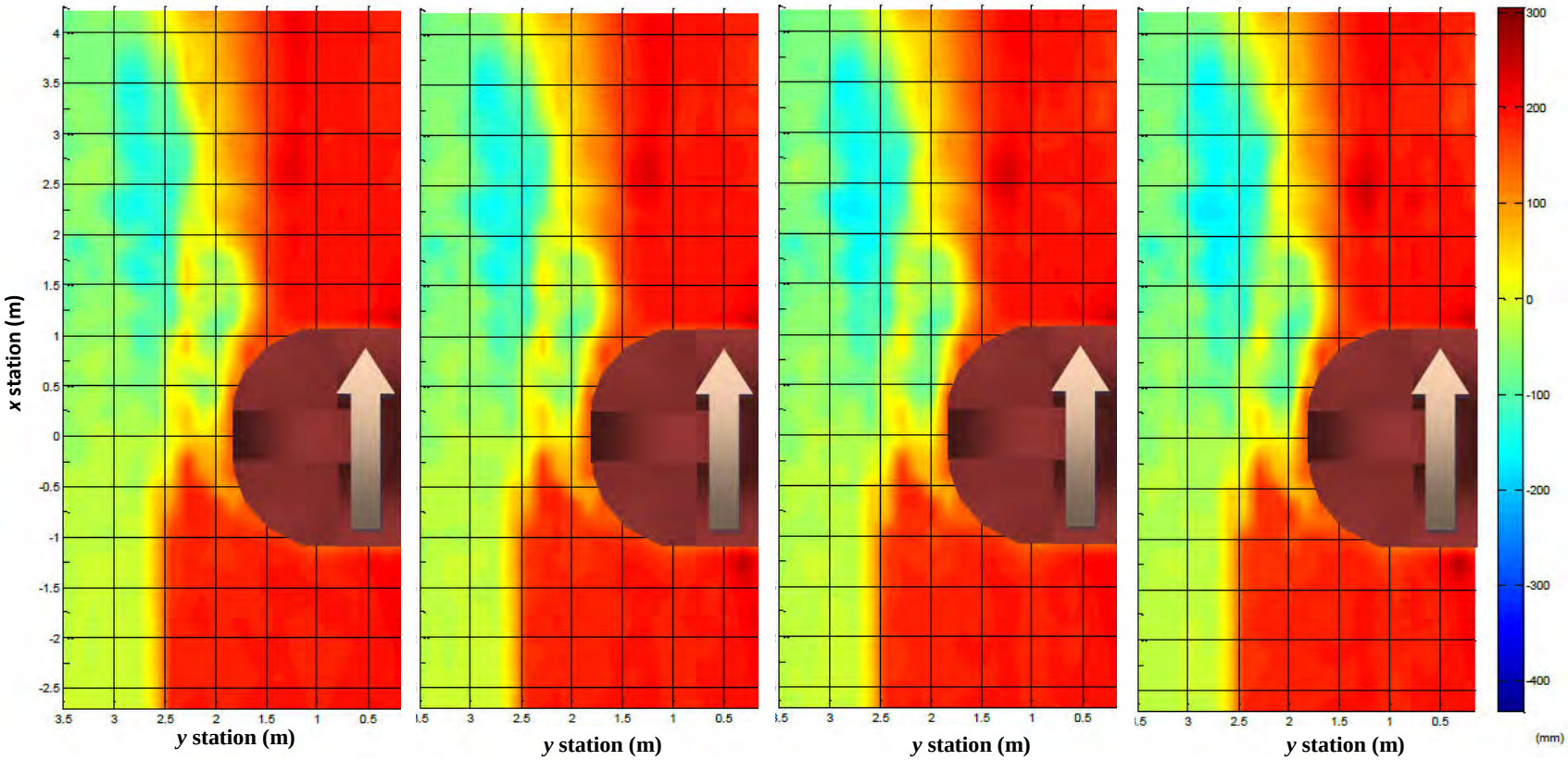

240 hours **288 hours** **336 hours** **384 hours**

Figure B.1 (contd.) – Case1

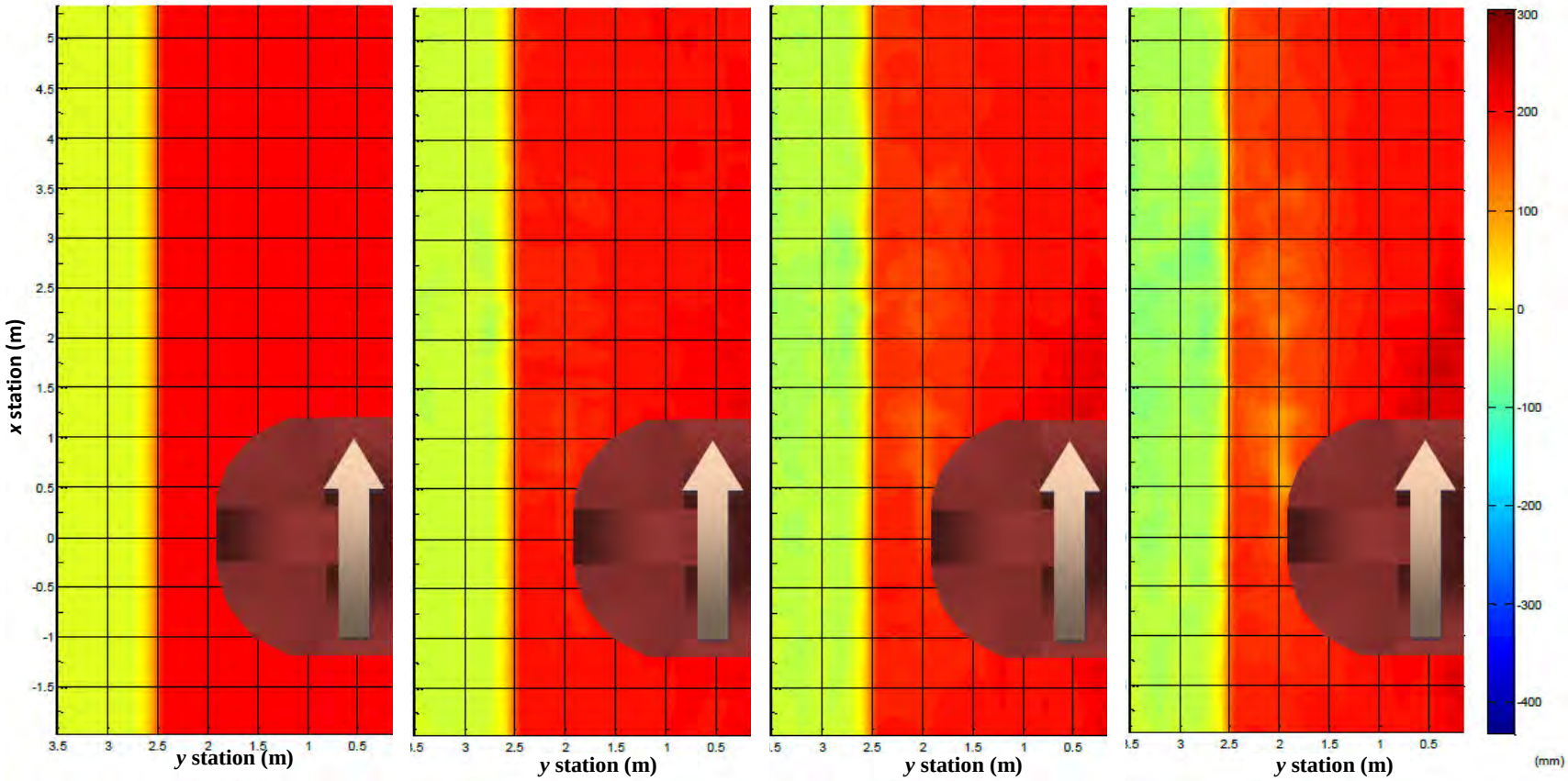

Initial **20 hours** **40 hours** **60 hours**

Figure B.2 – Case1II

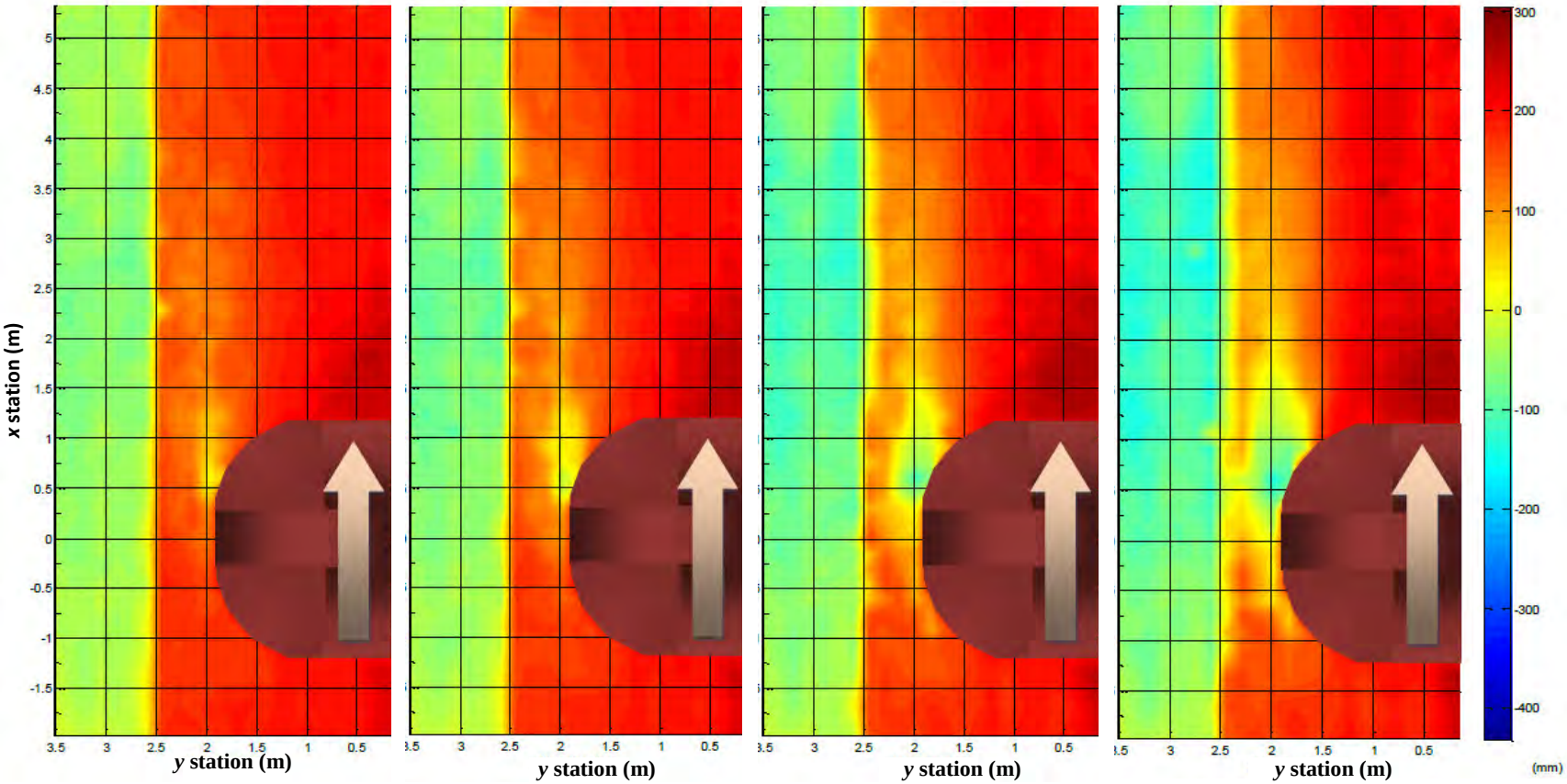

80 hours **100 hours** **144 hours** **189 hours**

Figure B.2 (contd.) – Case1II

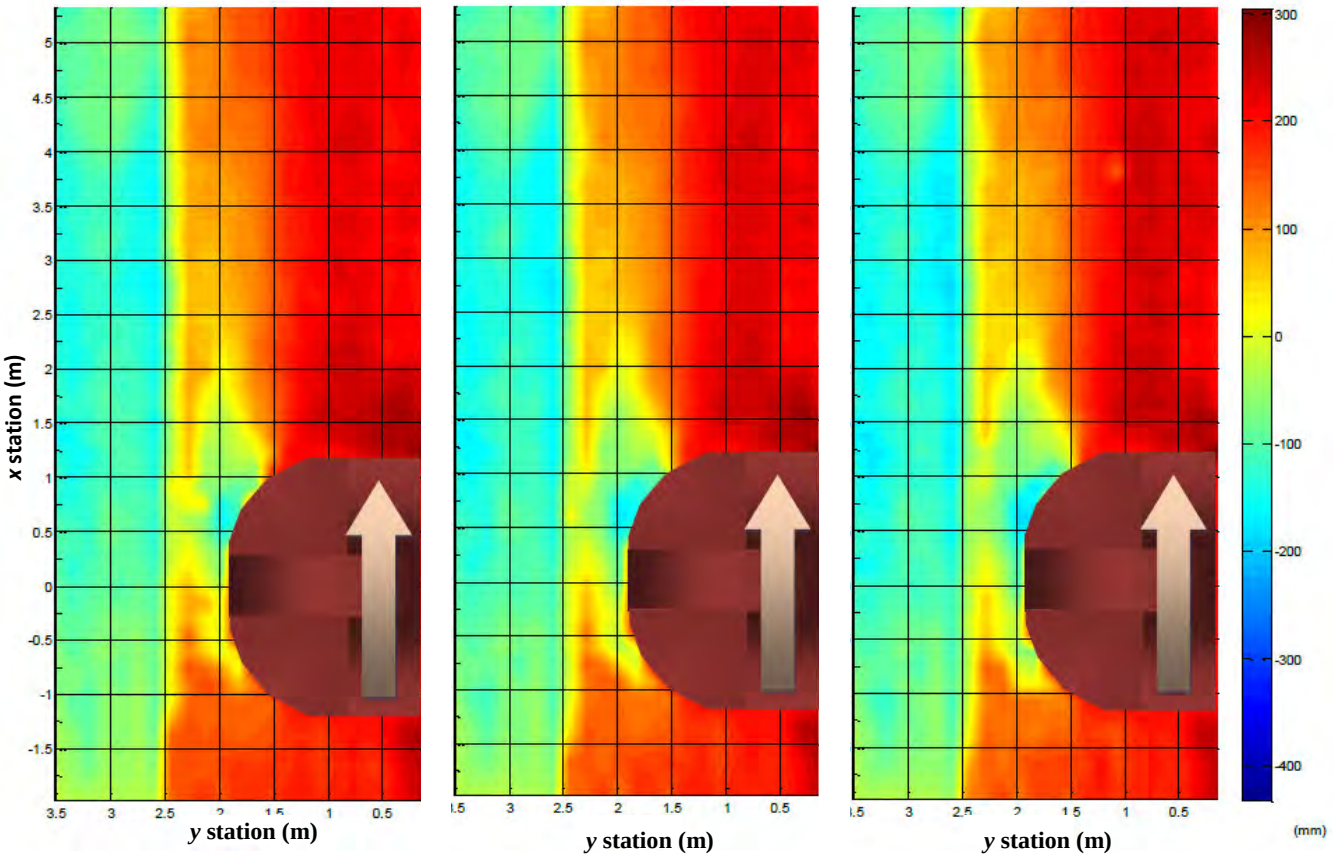

232 hours **276 hours** **320 hours**

Figure B.2 (contd.) – Case1II

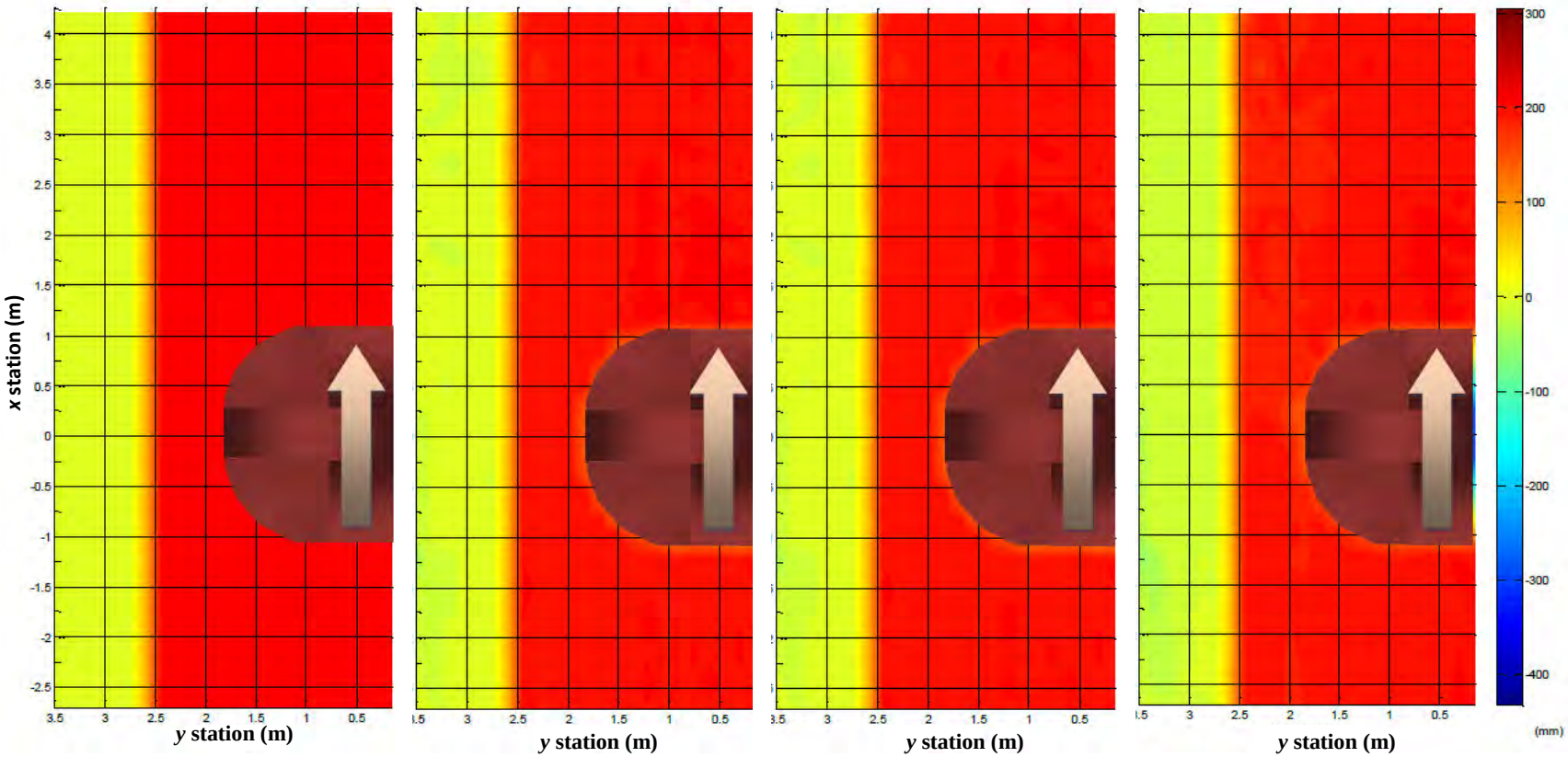

Initial **24 hours** **48 hours** **72 hours**

Figure B.3 – Case2

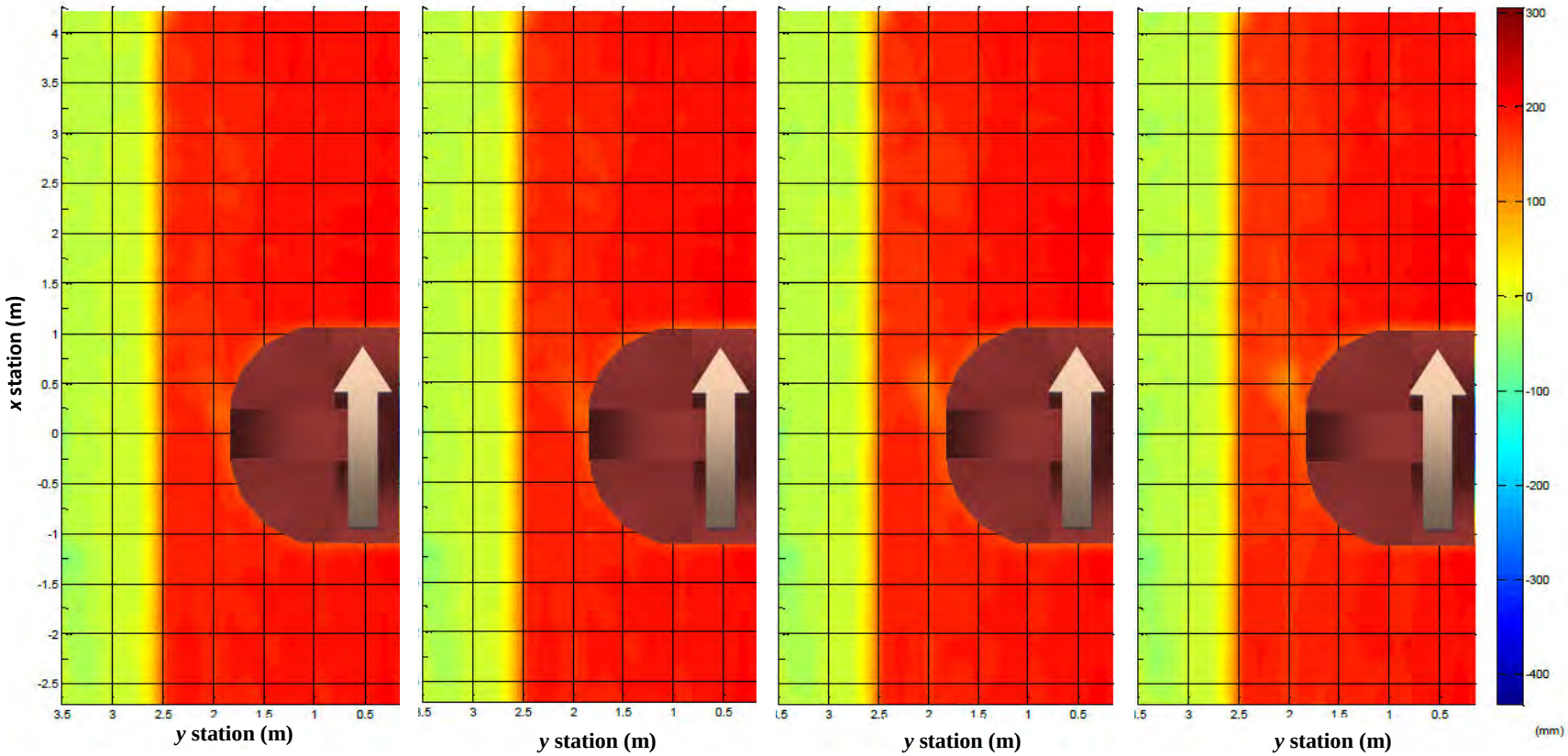

96 hours **120 hours** **156 hours** **192 hours**

Figure B.3(contd.) – Case2

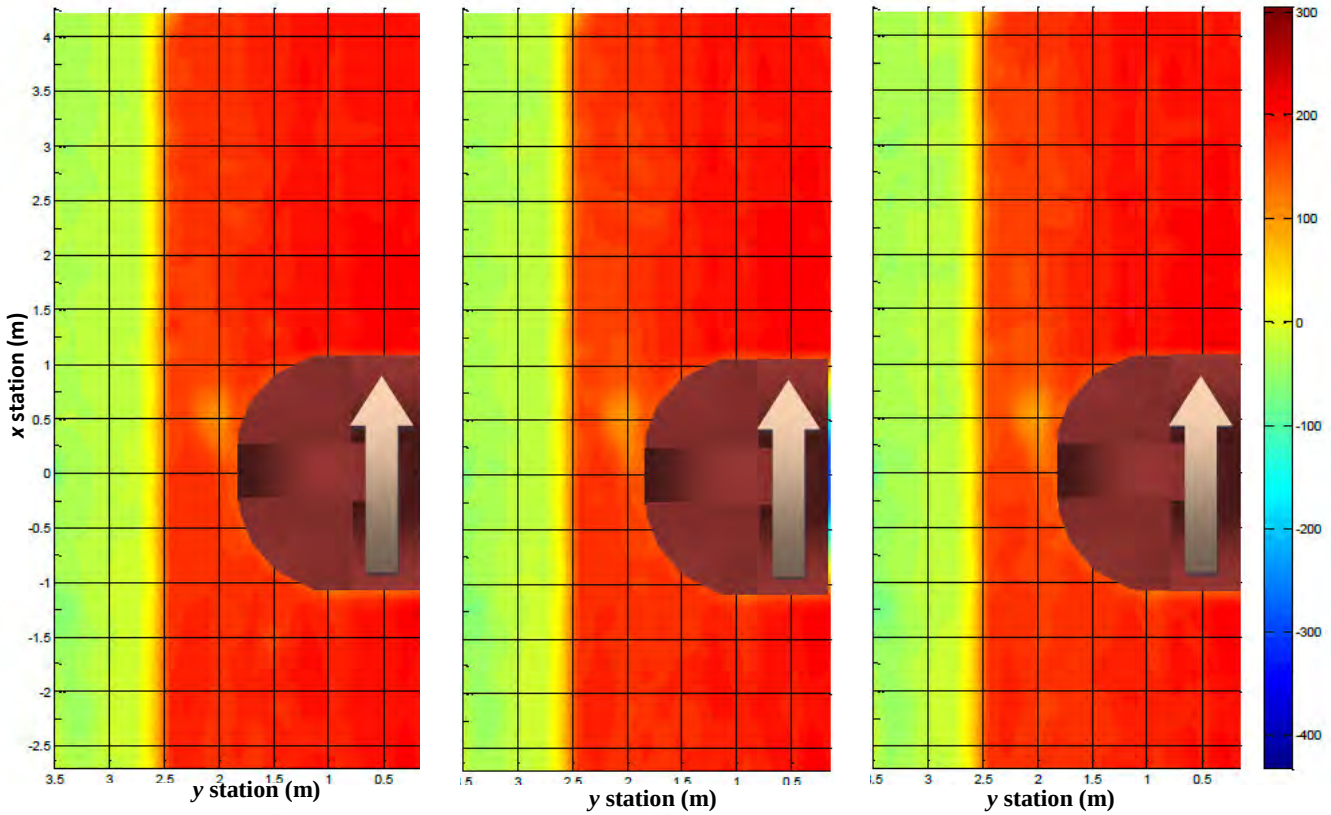

228 hours **264 hours** **300 hours**

Figure B.3 (contd.) – Case2

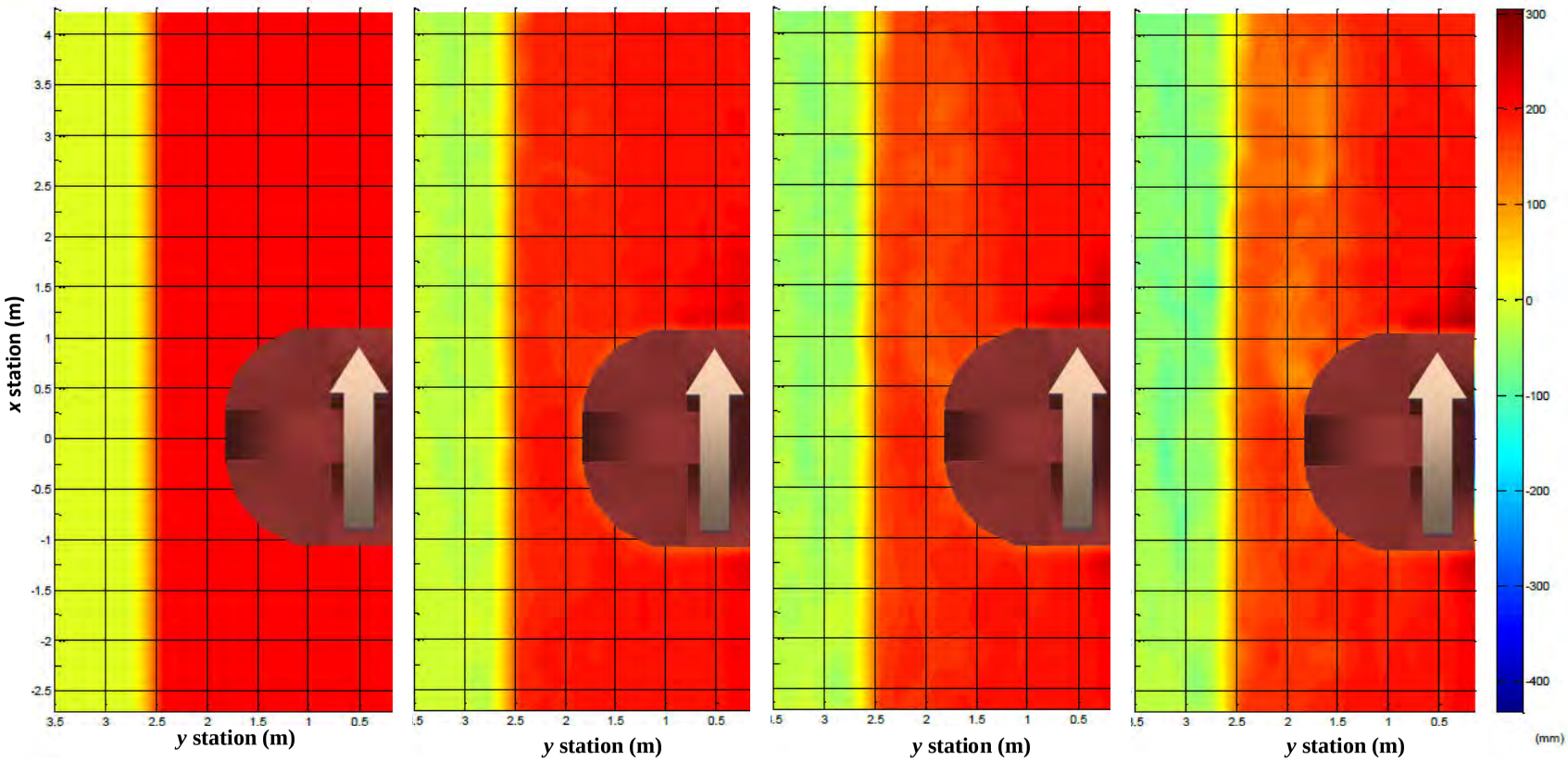

Initial **48 hours** **96 hours** **156 hours**

Figure B.4 – Case3

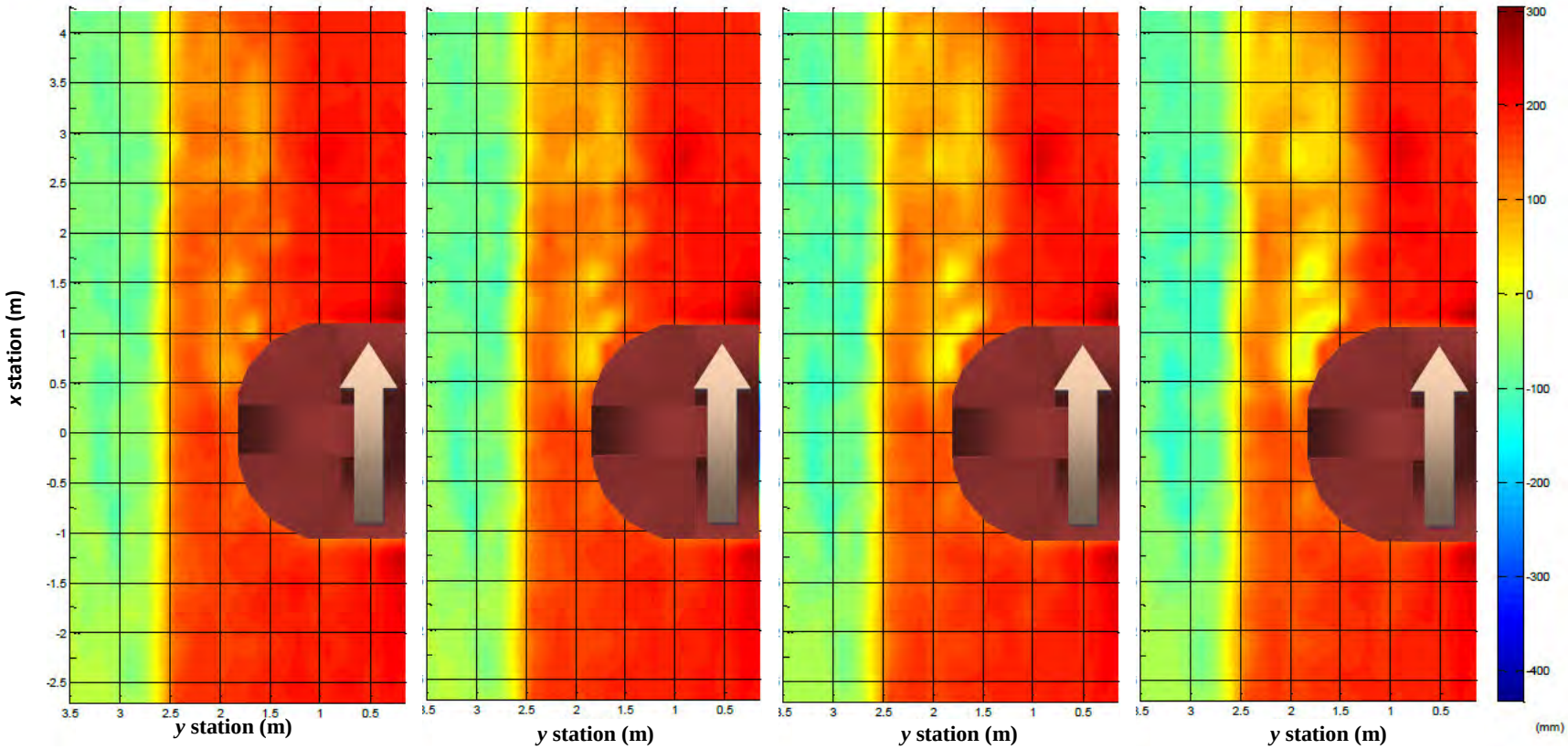

192 hours **228 hours** **264 hours** **300 hours**

Figure B.4 (contd.) – Case3

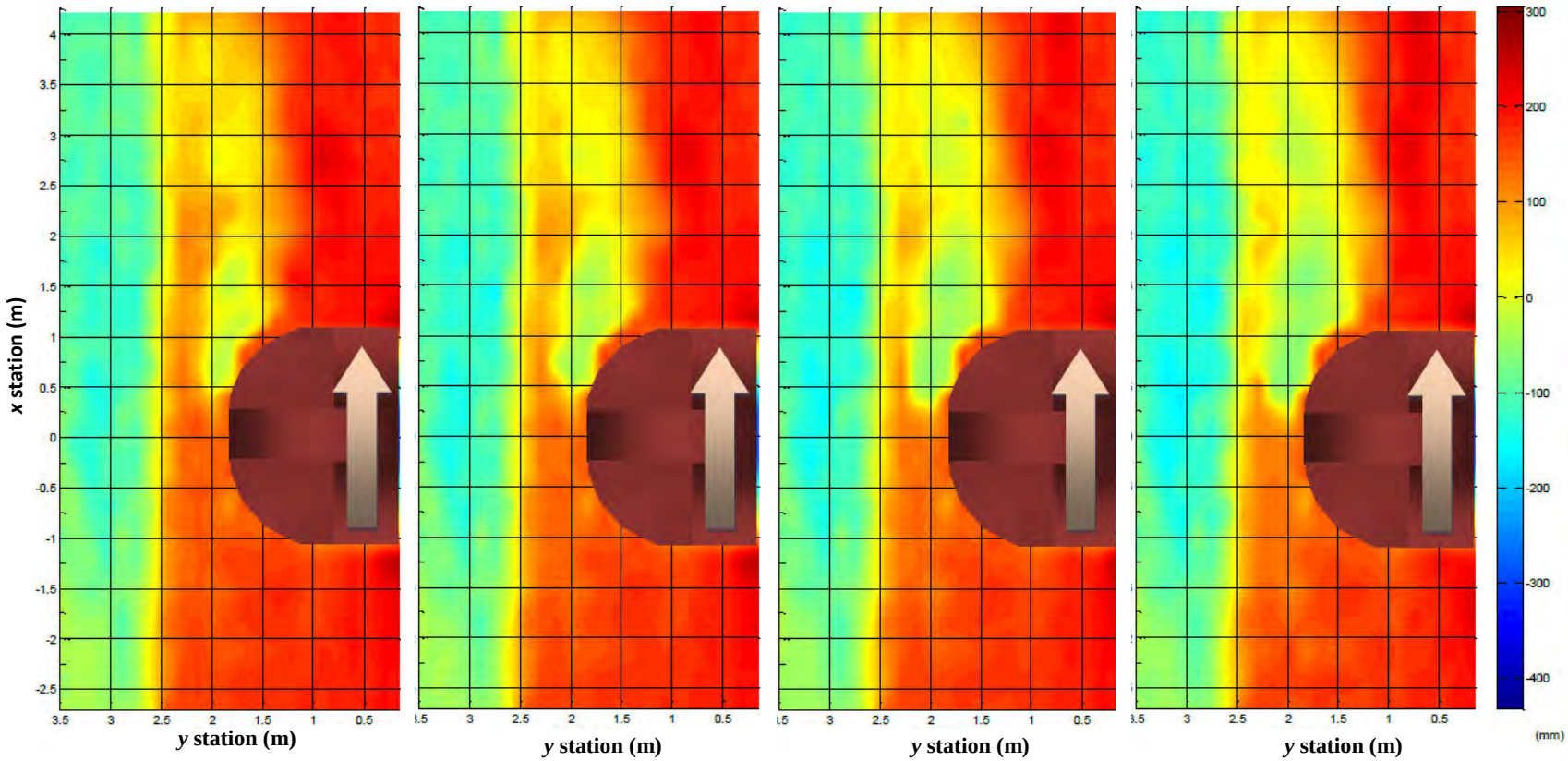

348 hours **396 hours** **456 hours** **504 hours**

Figure B.4 (contd.) – Case3

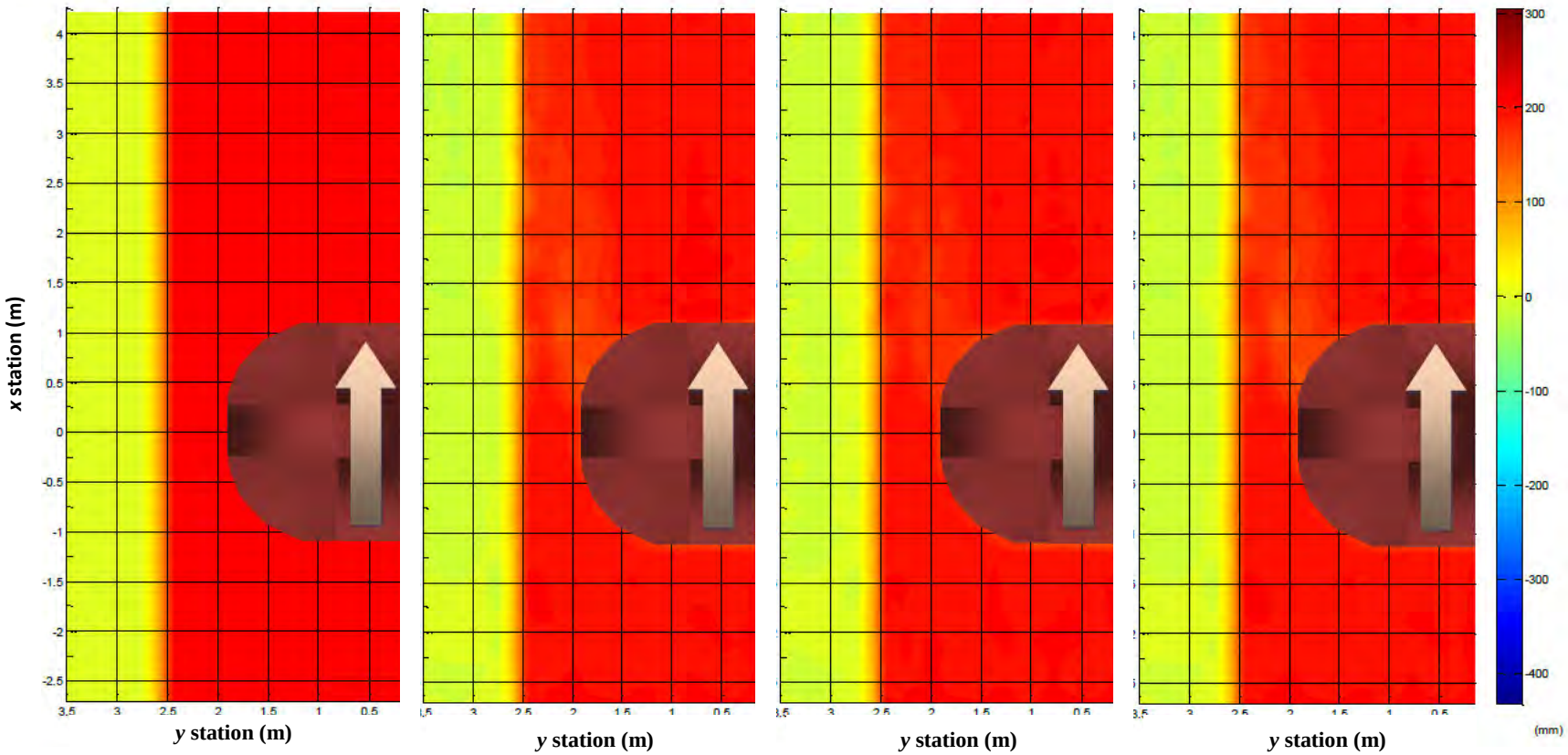

Figure B.5 – Case4

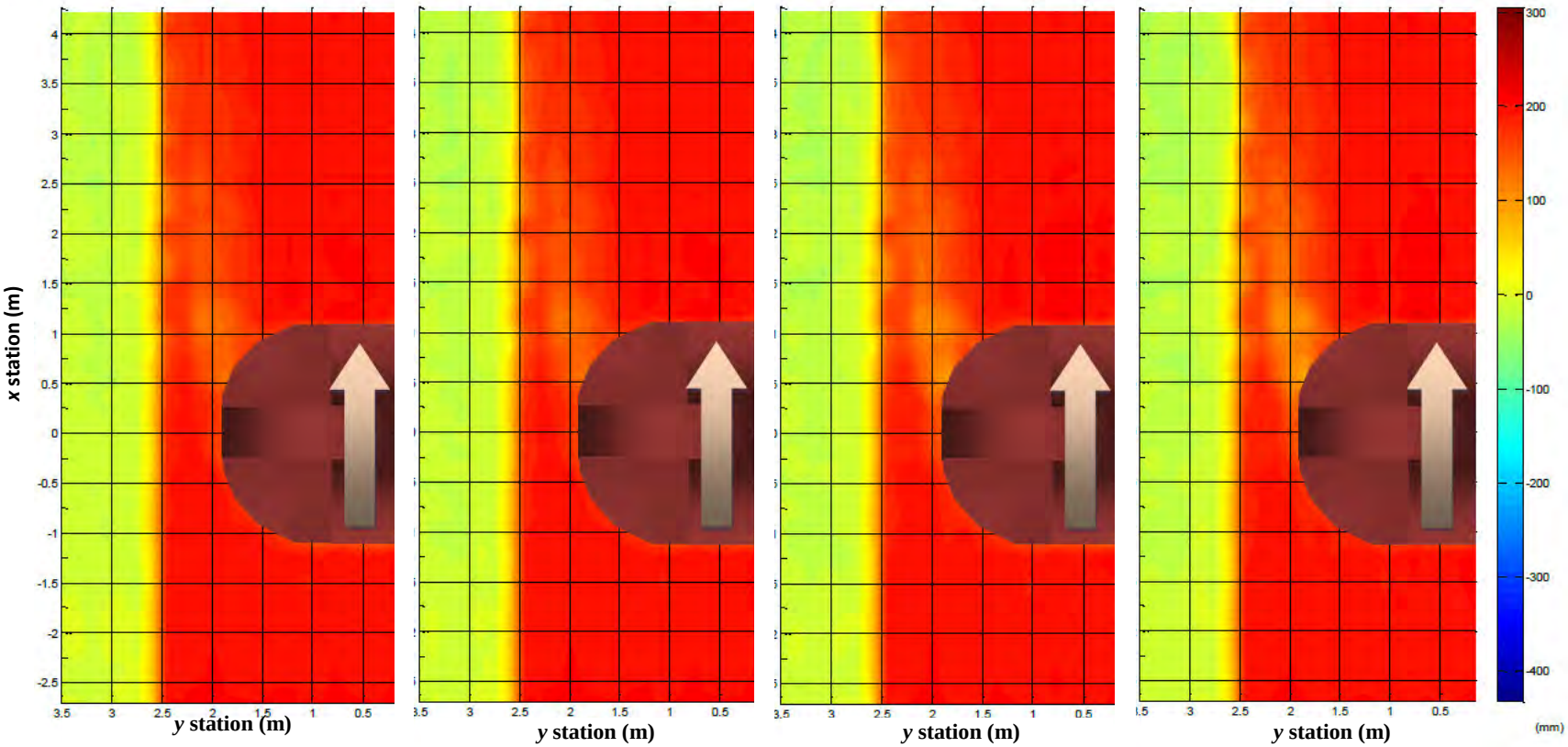

120 hours **144 hours** **168 hours** **192 hours**

Figure B.5 (contd.) – Case4

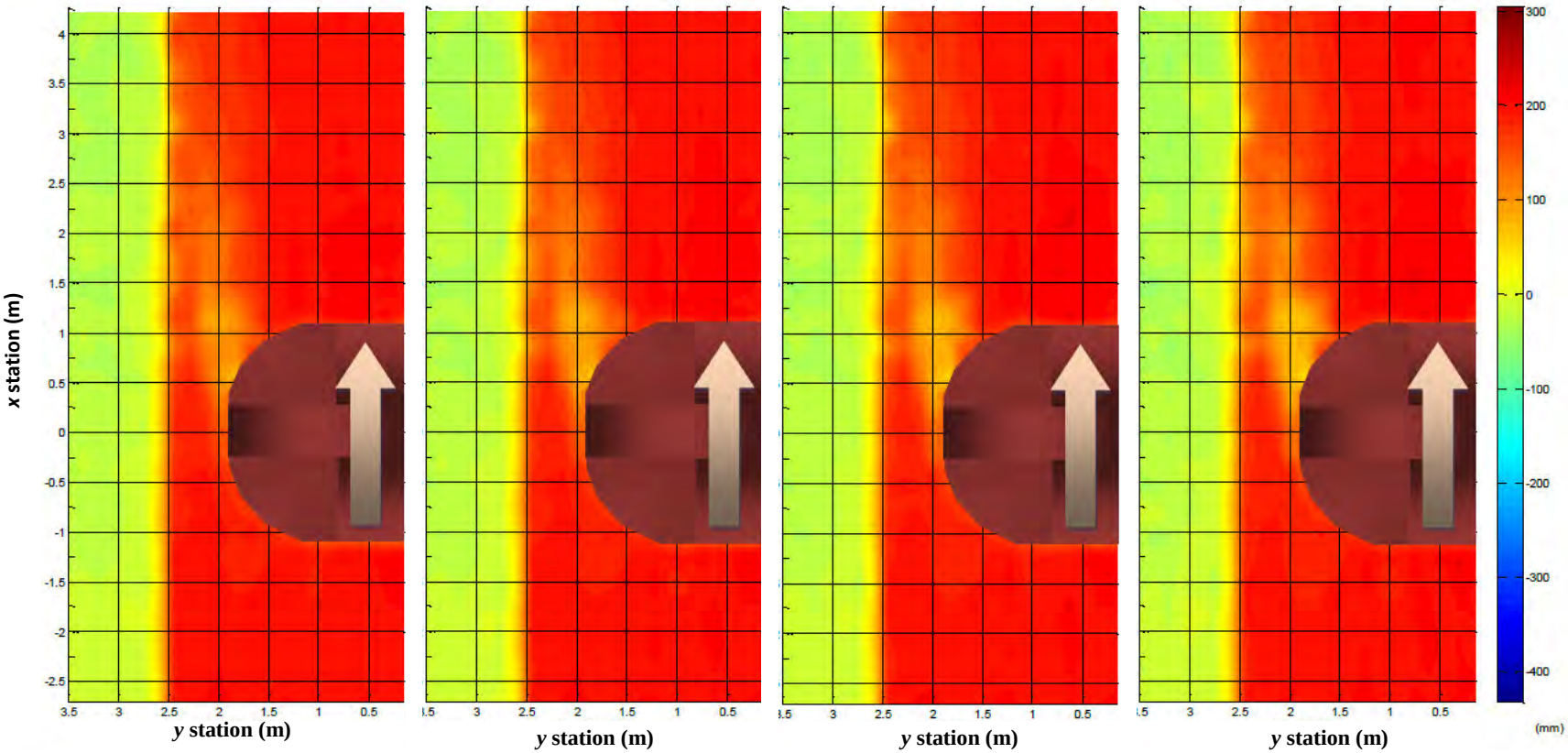

216 hours **252 hours** **298 hours** **340 hours**

Figure B.5 (contd.) – Case4

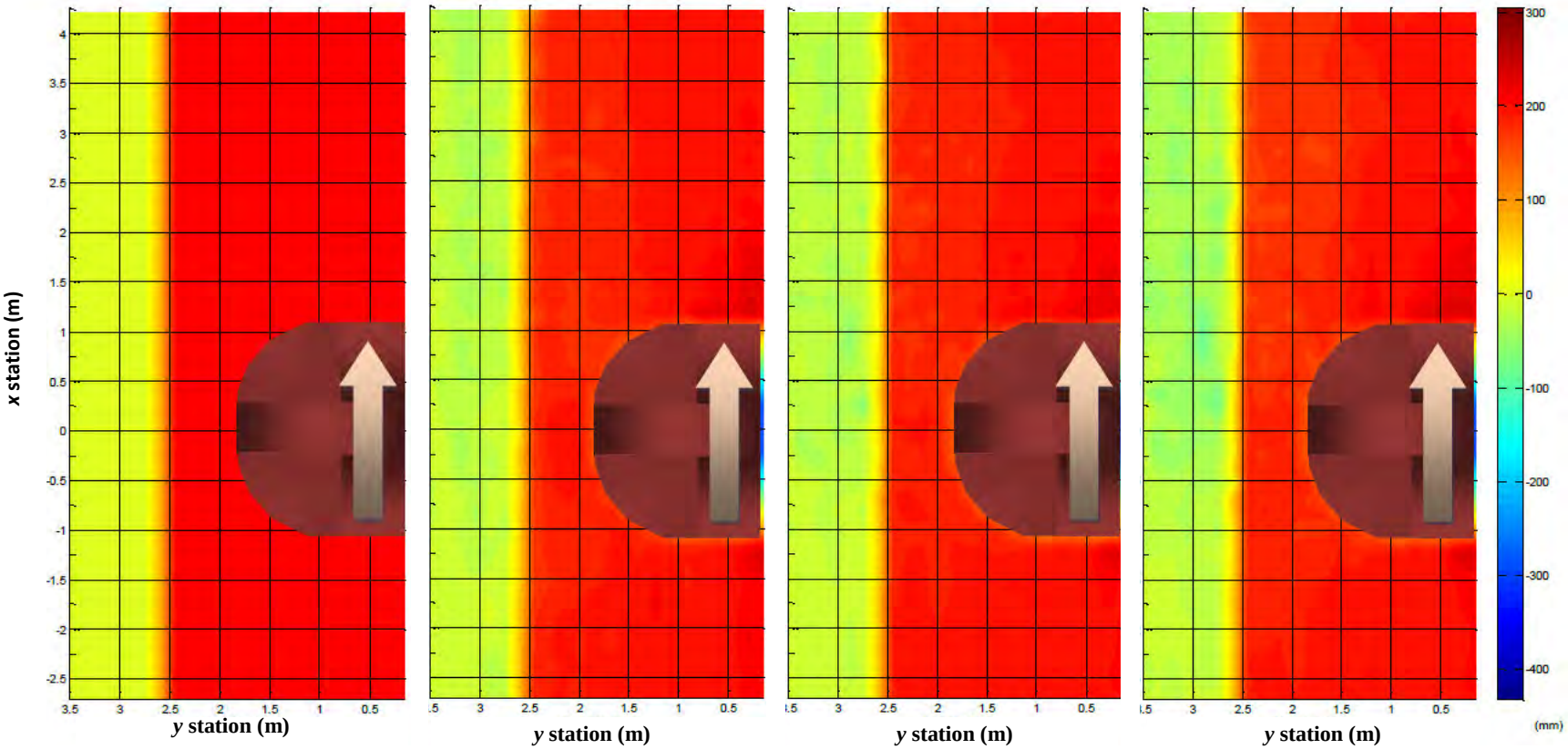

Initial **24 hours** **48 hours** **72 hours**

Figure B.6 – Case5

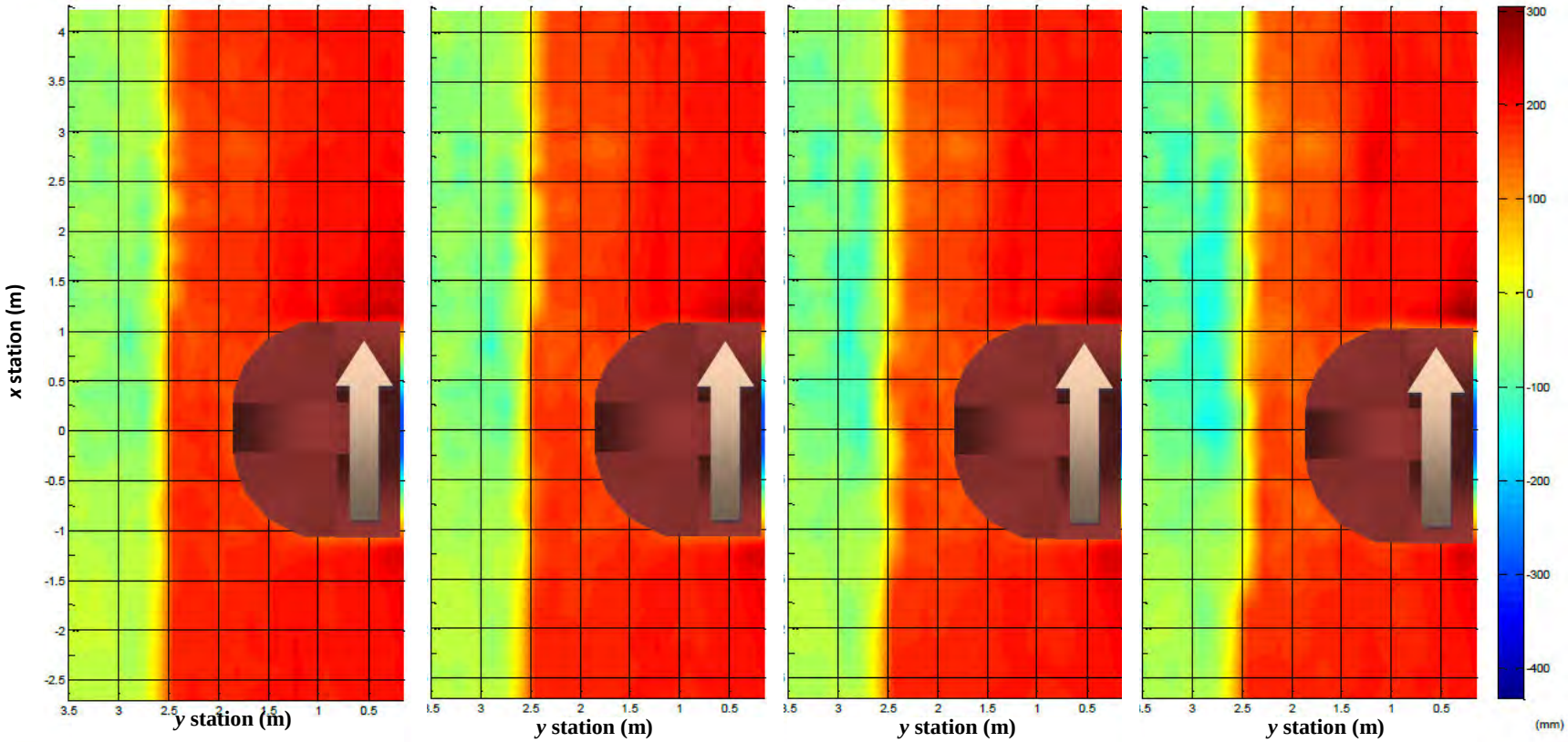

96 hours **120 hours** **168 hours** **216 hours**

Figure B.6 (contd.) – Case5

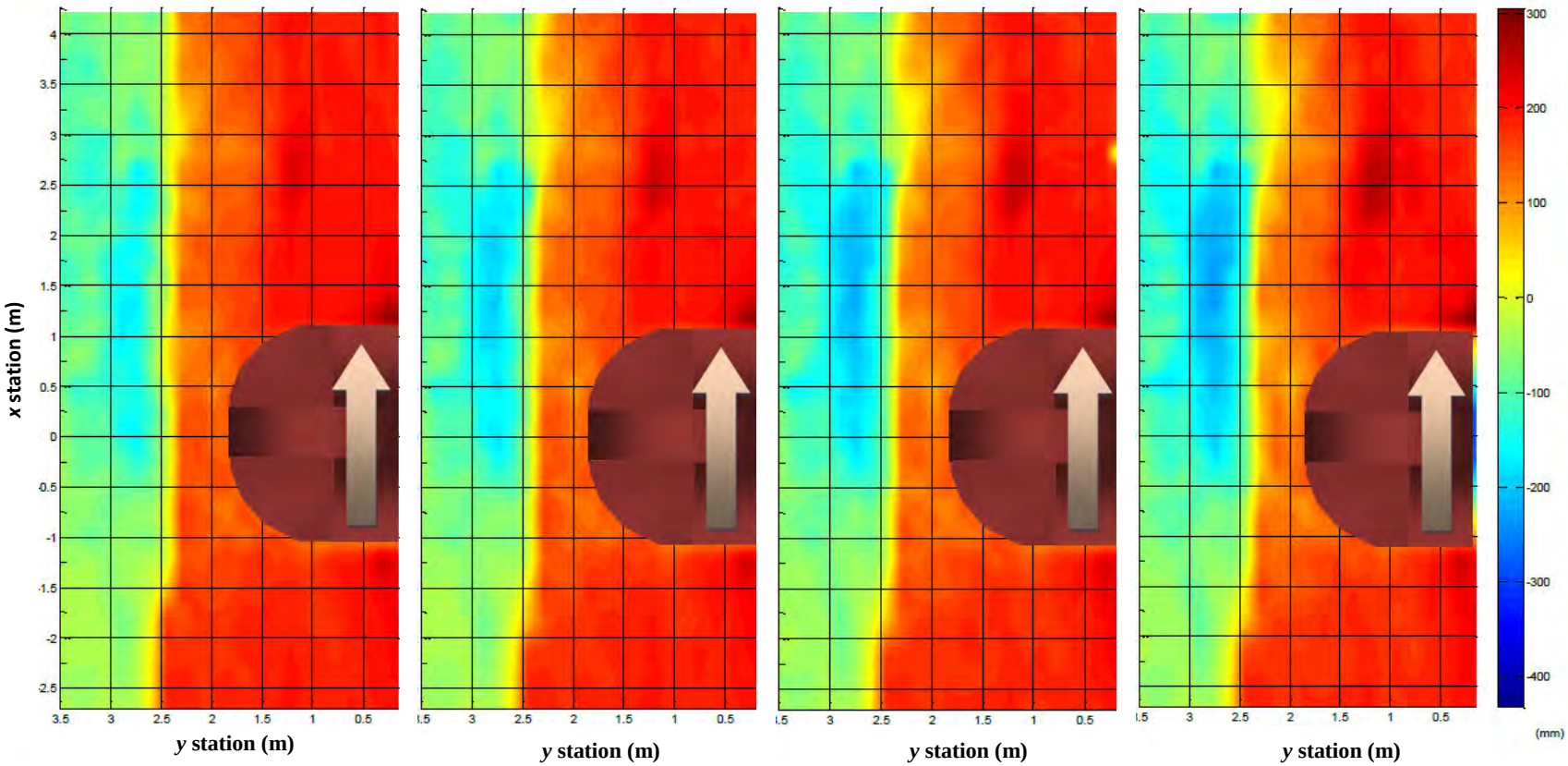

264 hours **312 hours** **360 hours** **408 hours**

Figure B.6 (contd.) – Case5

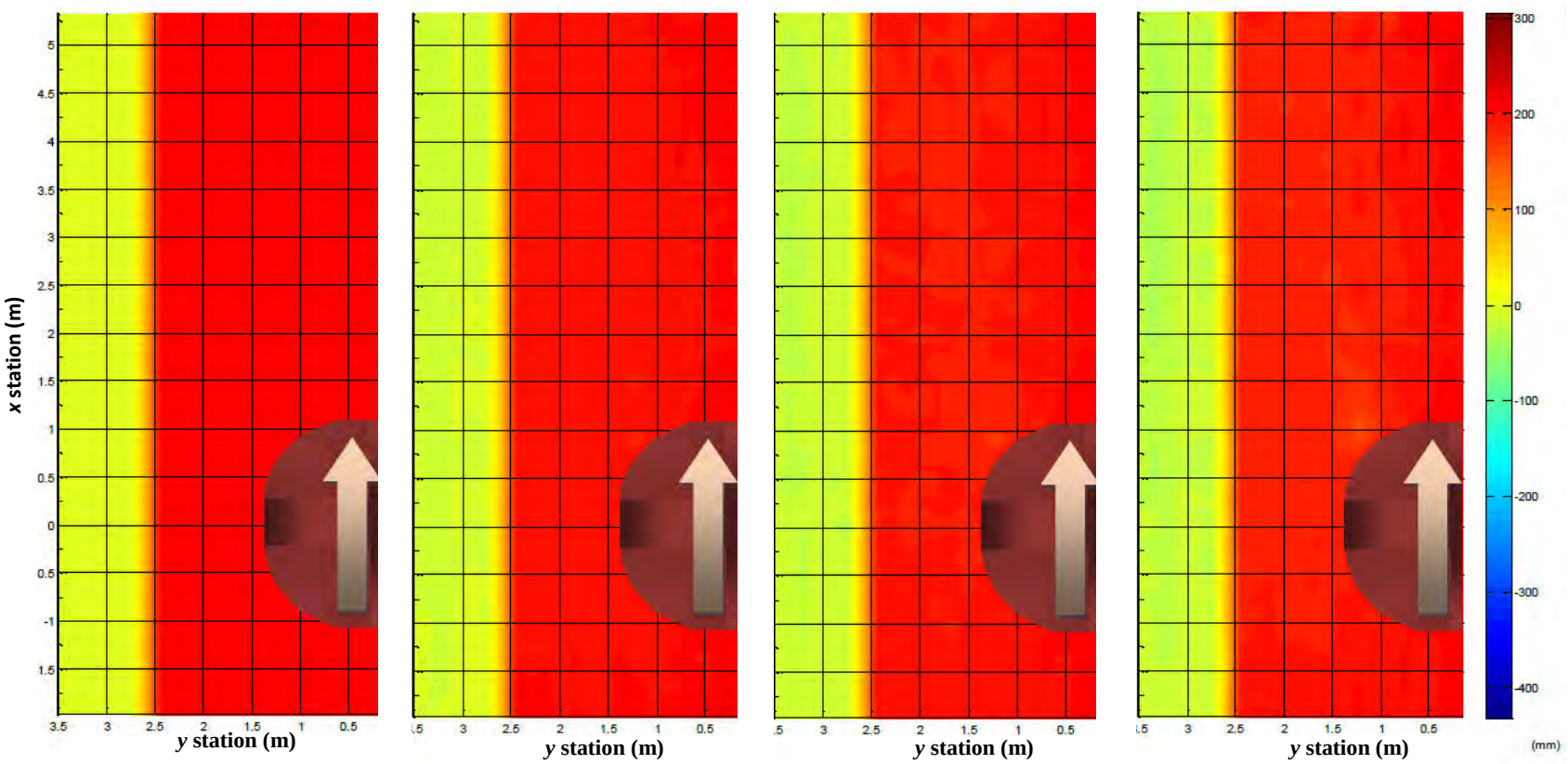

Initial **20 hours** **40 hours** **60 hours**

Figure B.7 – Case6

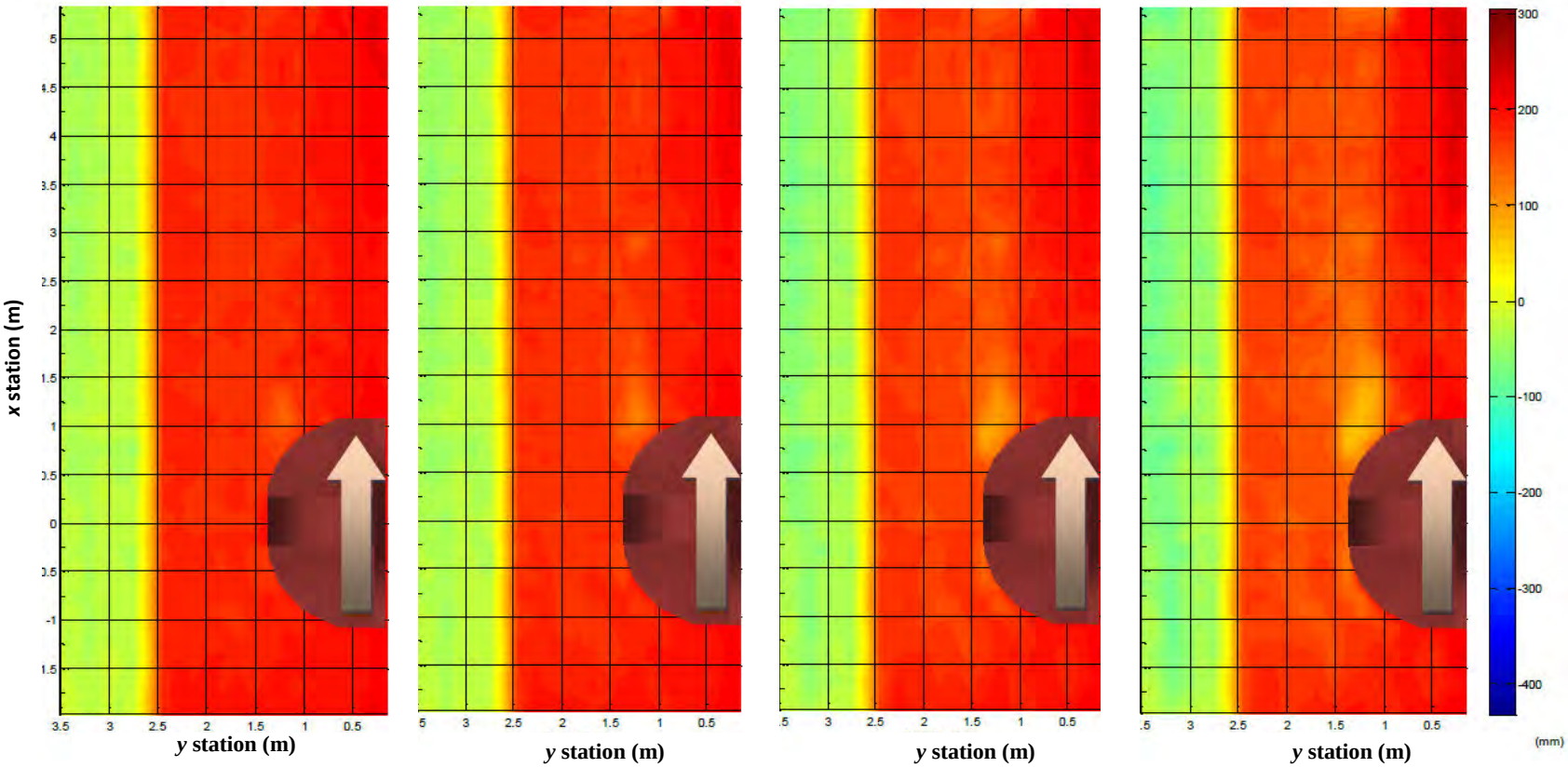

80 hours **100 hours** **144 hours** **188 hours**

Figure B.7 (contd.) – Case6

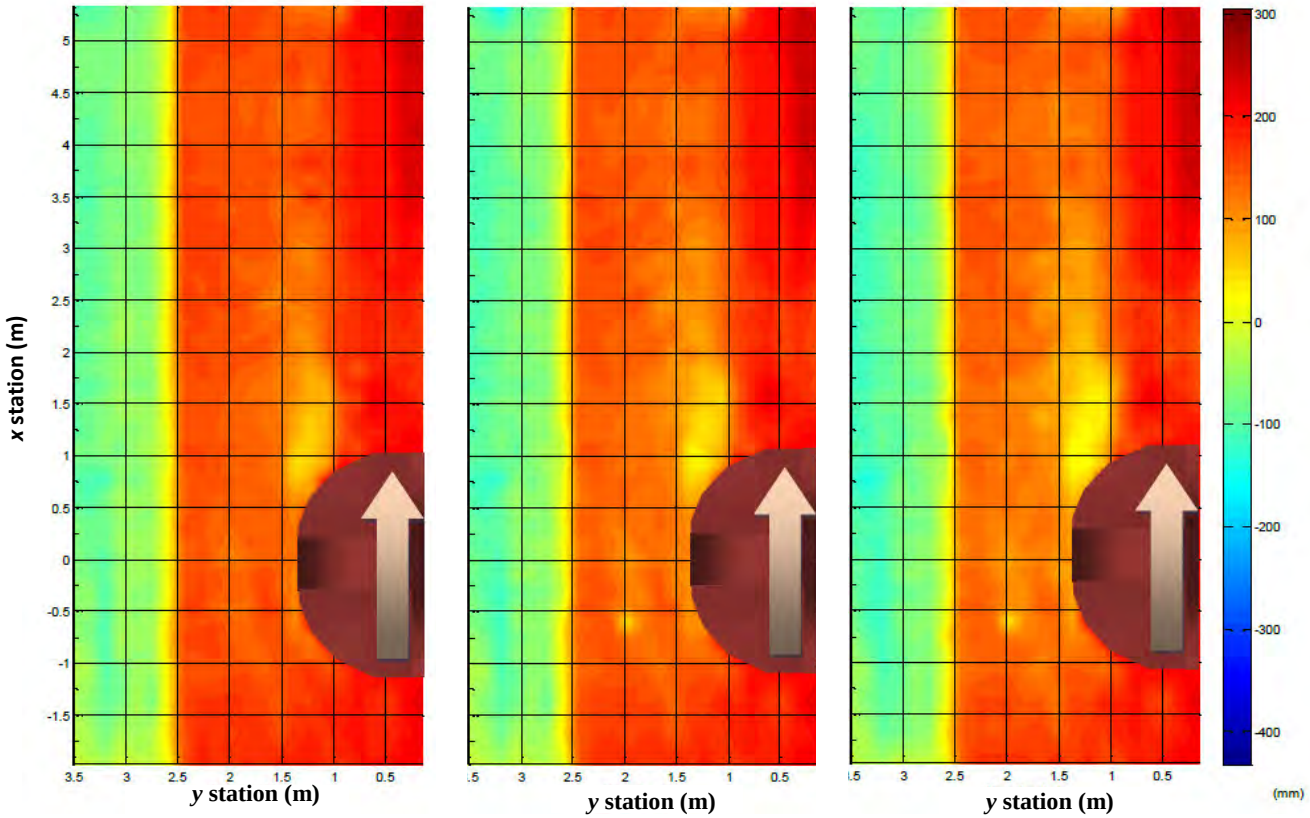

232 hours **276 hours** **320 hours**

Figure B.7 (contd.) – Case6

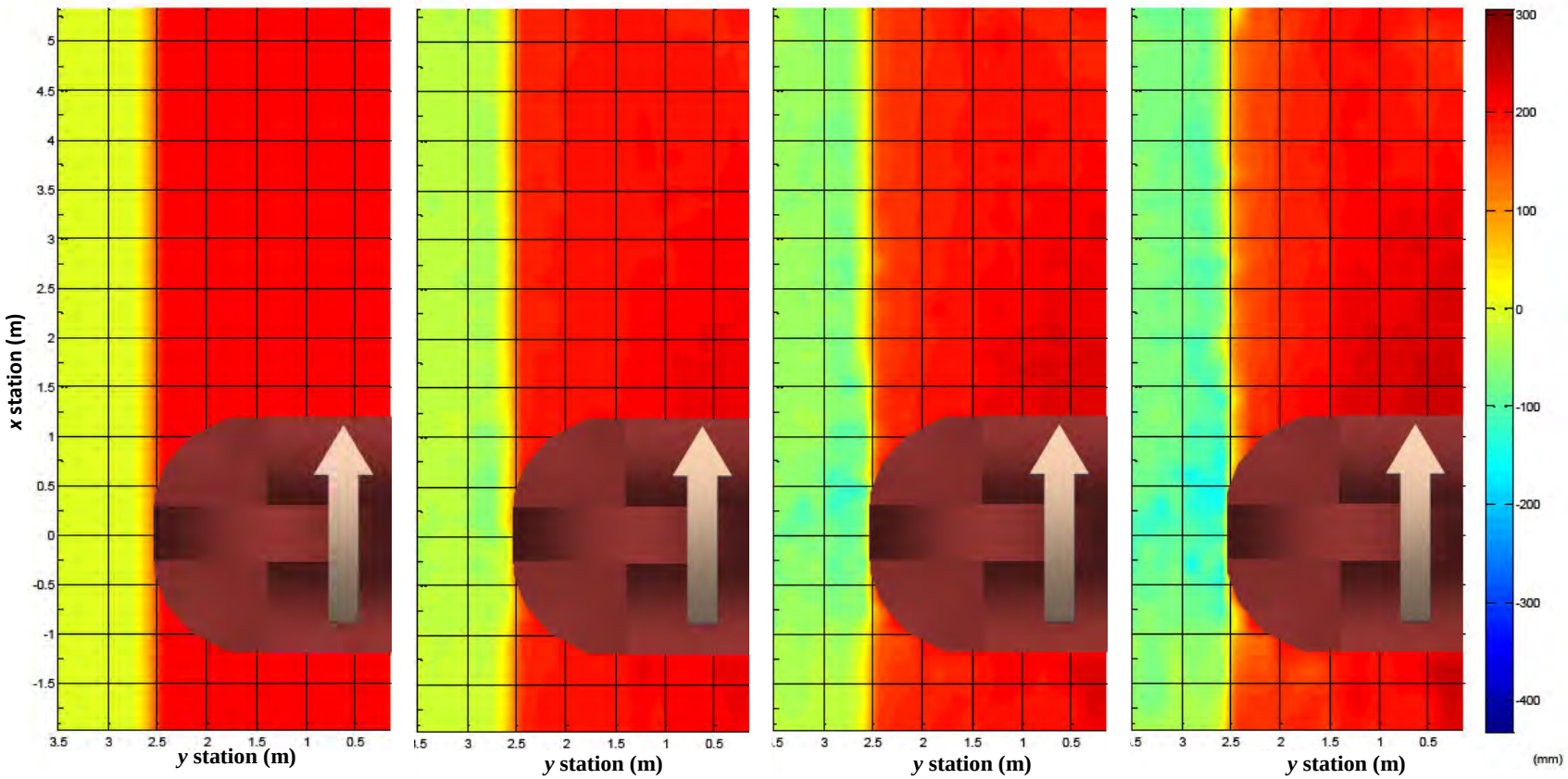

Initial **20 hours** **40 hours** **60 hours**

Figure B.8– Case7

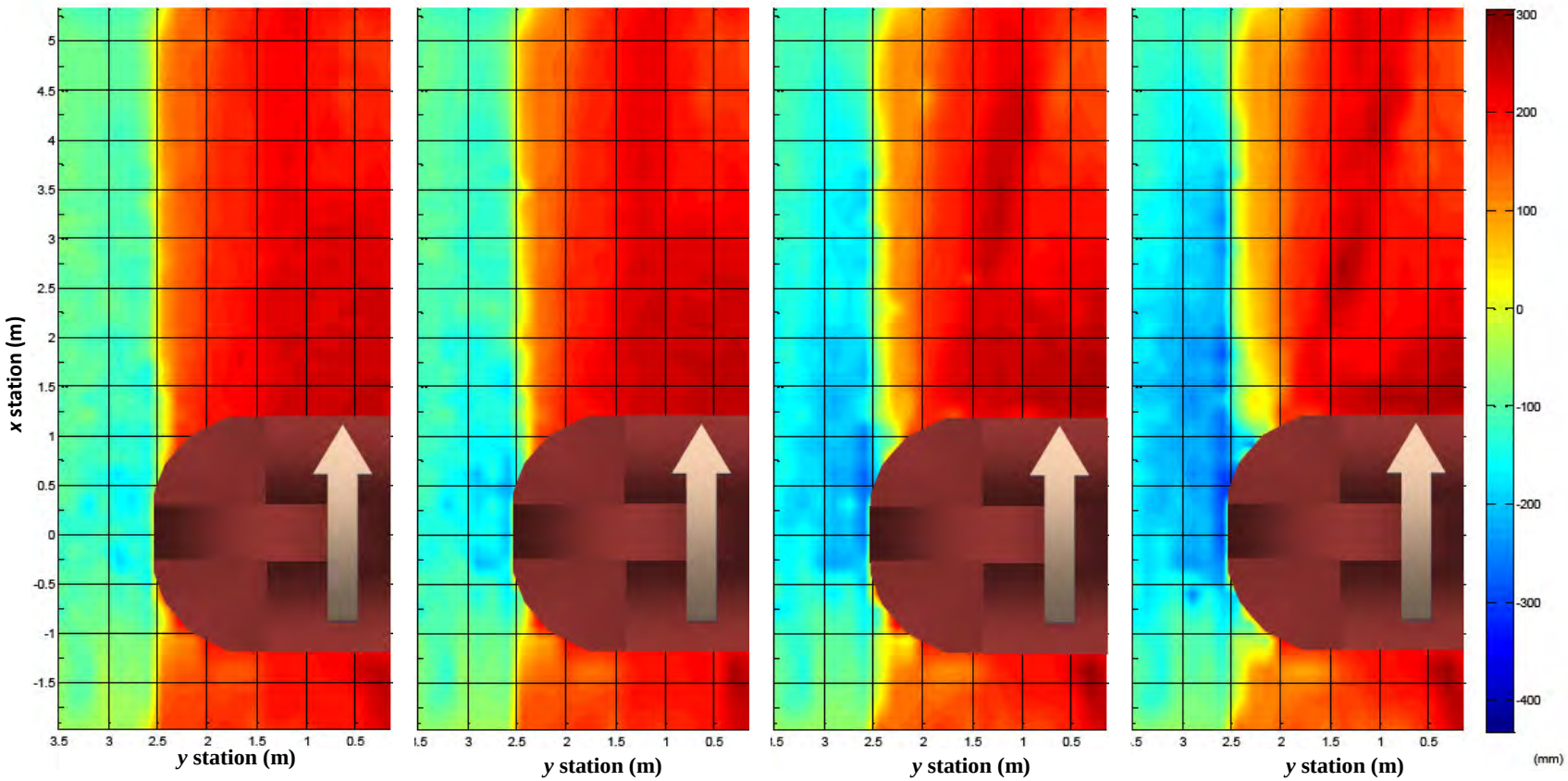

80 hours **100 hours** **144 hours** **188 hours**

Figure B.8 (contd.) – Case7

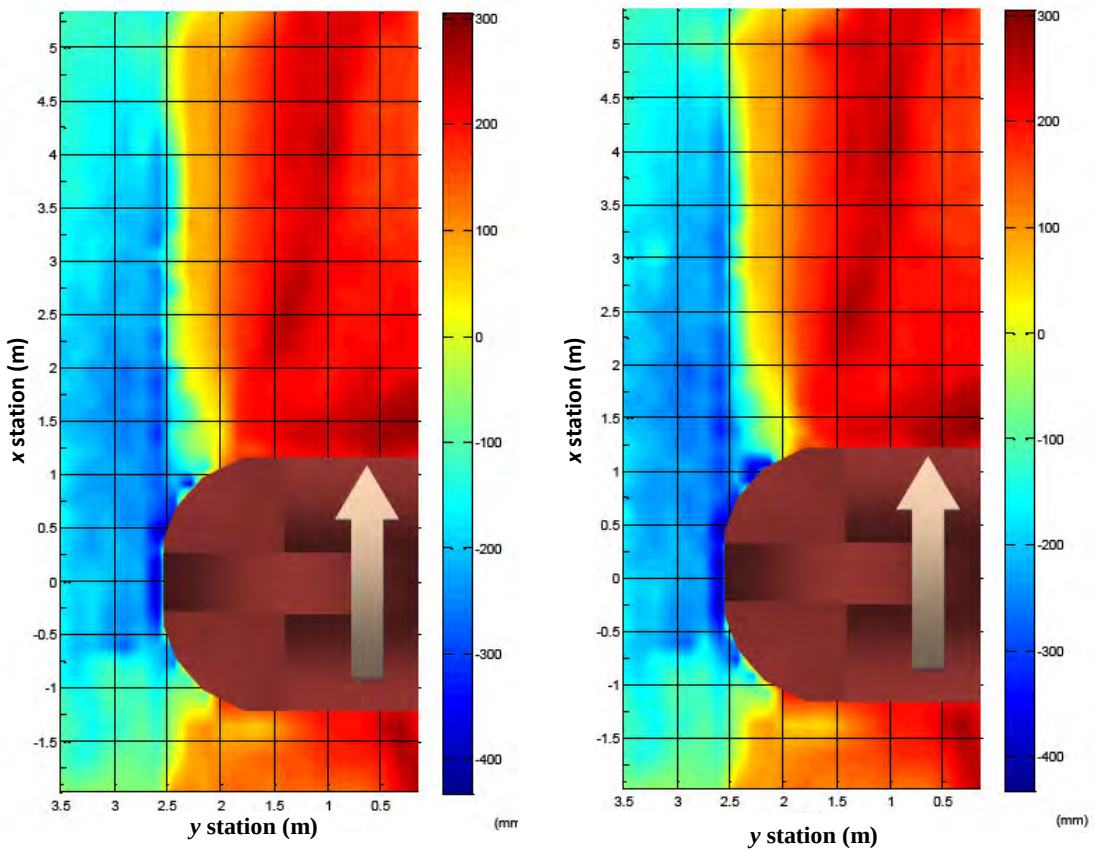

232 hours **257 hours**

Figure B.8 (contd.) – Case7

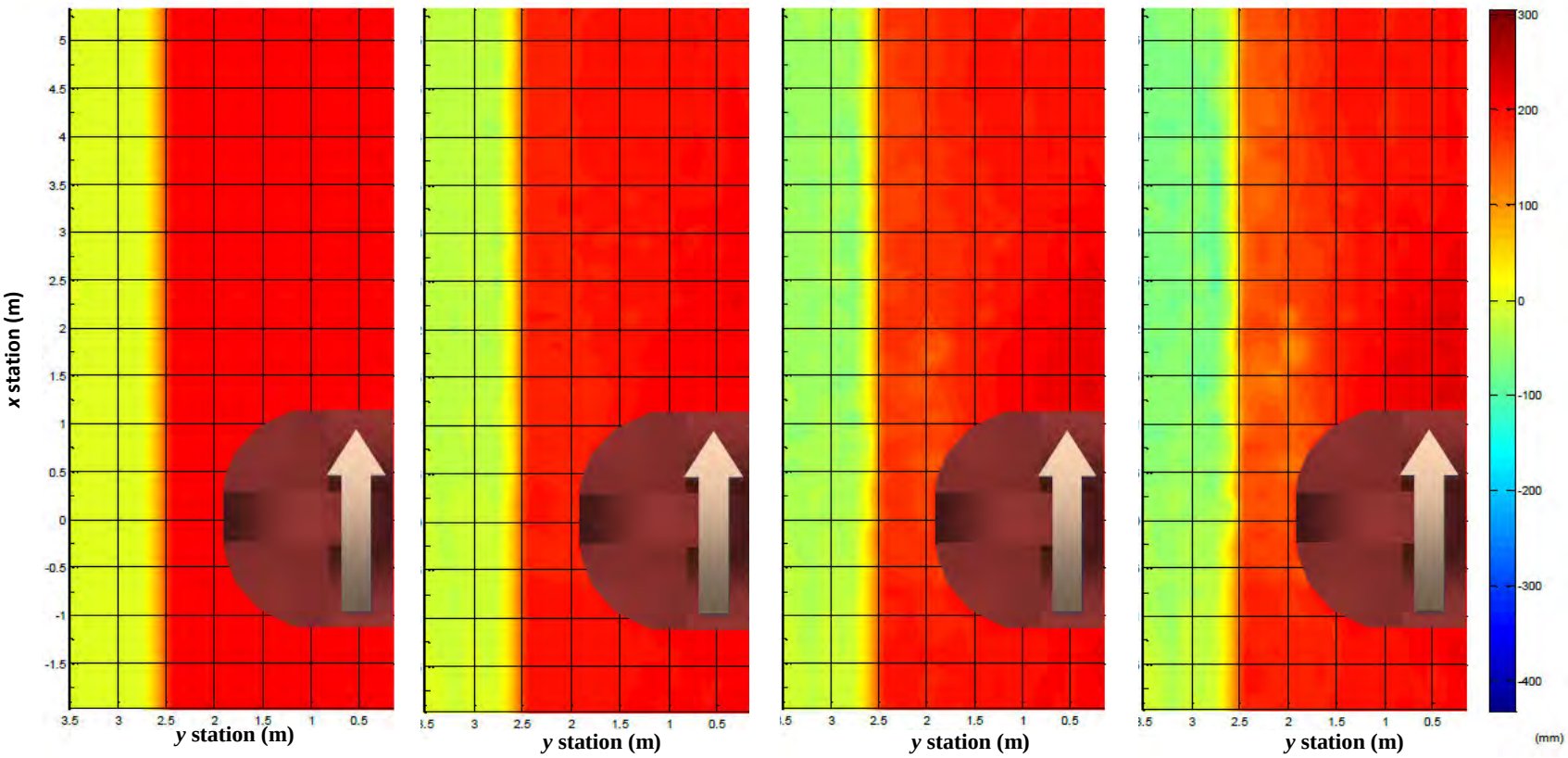

Initial **20 hours** **40 hours** **60 hours**

Figure B.9– Case8

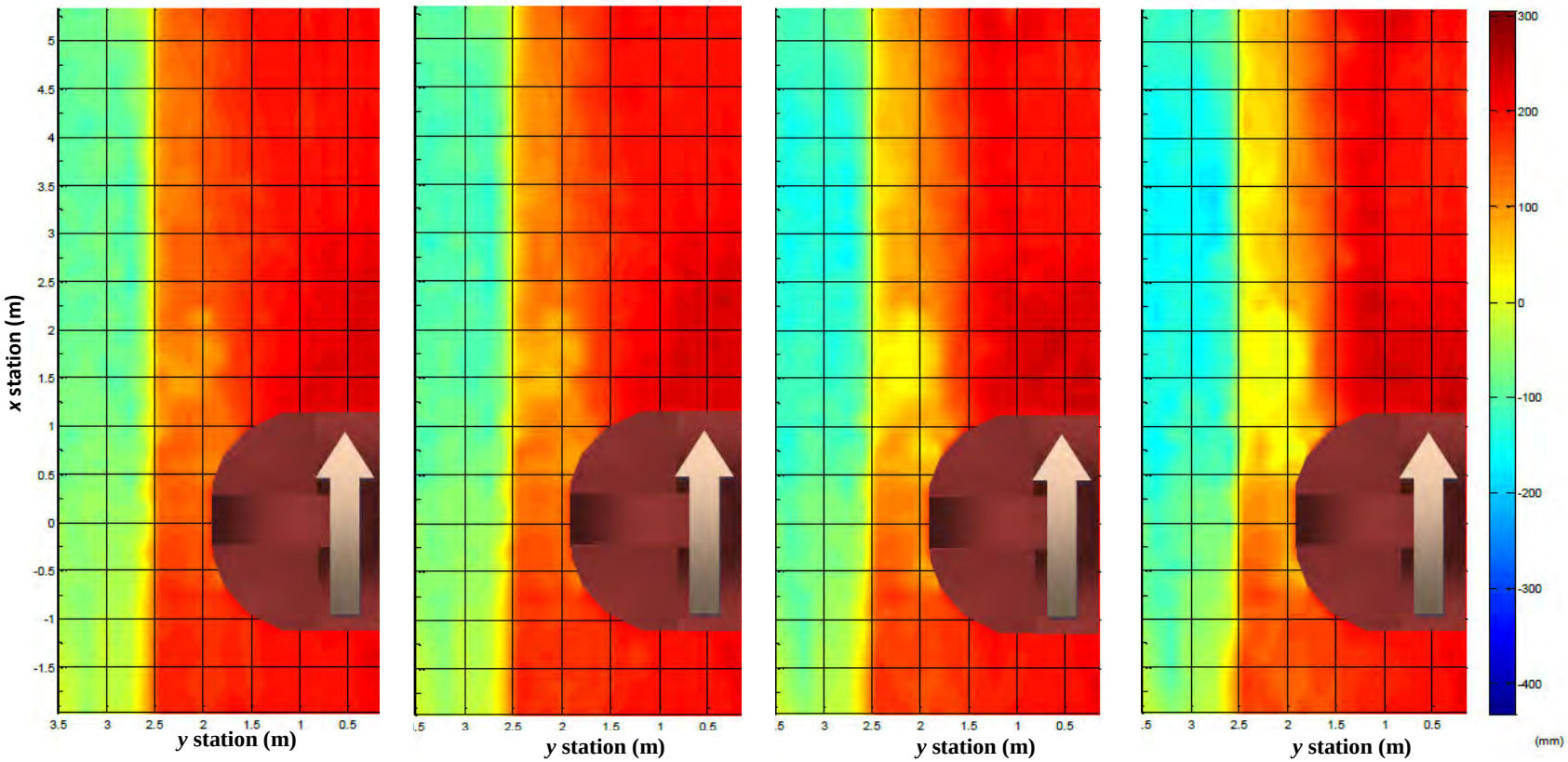

80 hours **100 hours** **140 hours** **180 hours**

Figure B.9 (contd.) – Case8

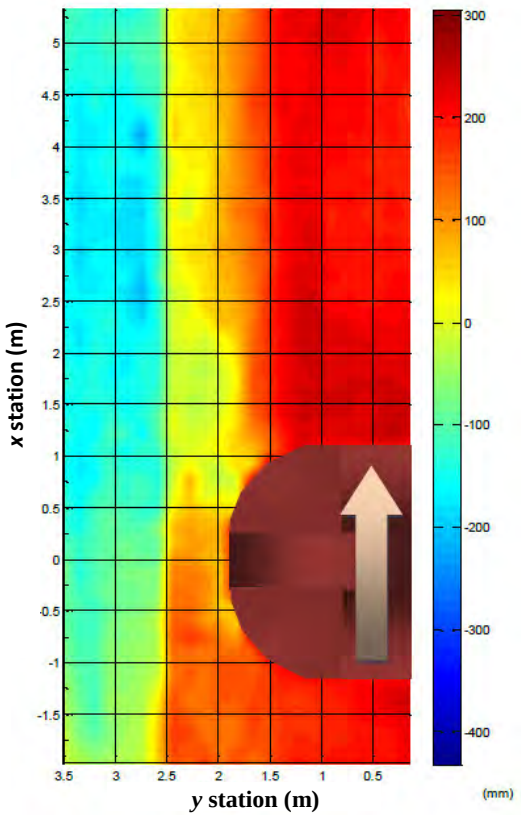

224 hours

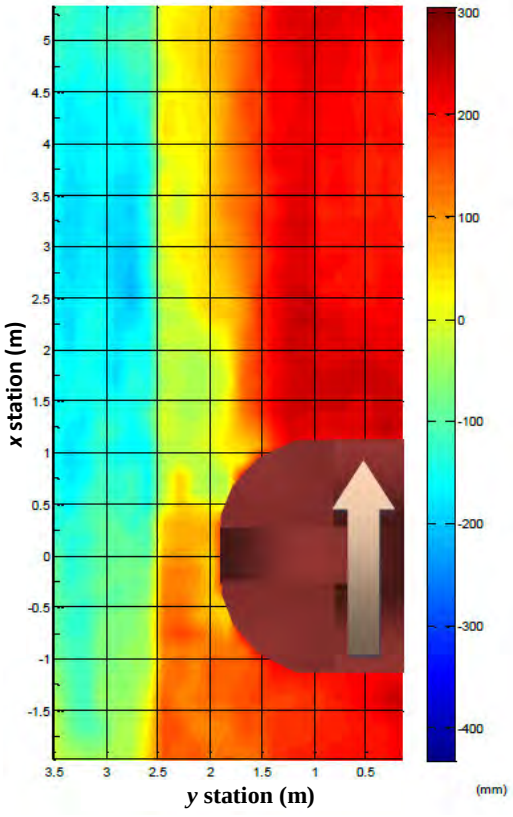

268 hours

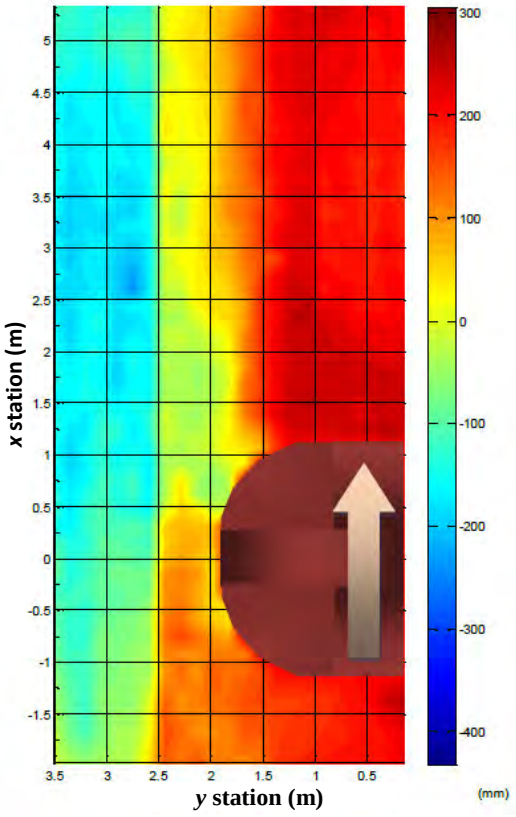

308 hours

Figure B.9 (contd.) – Case8

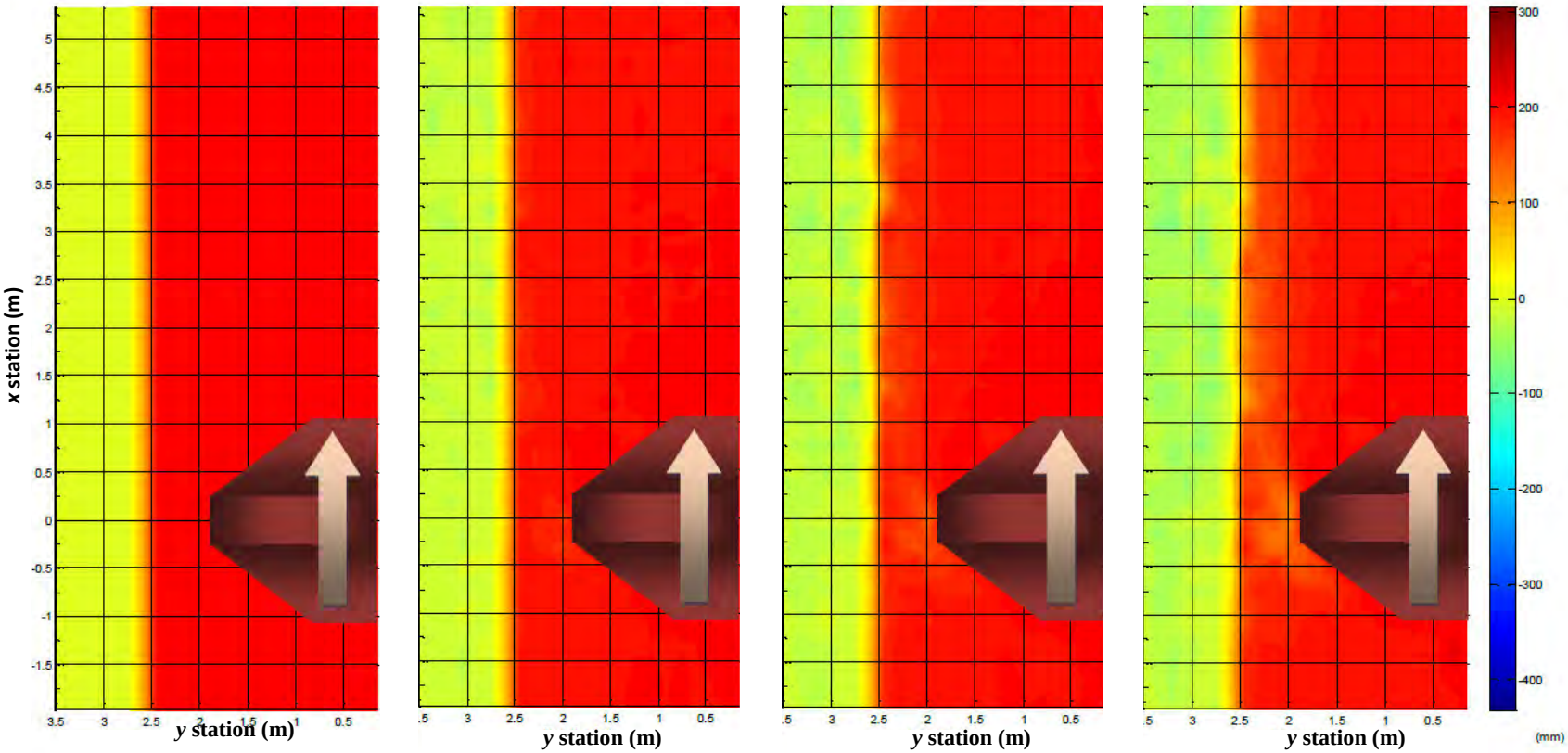

Initial **20 hours** **40 hours** **60 hours**

Figure B.10 – Case9

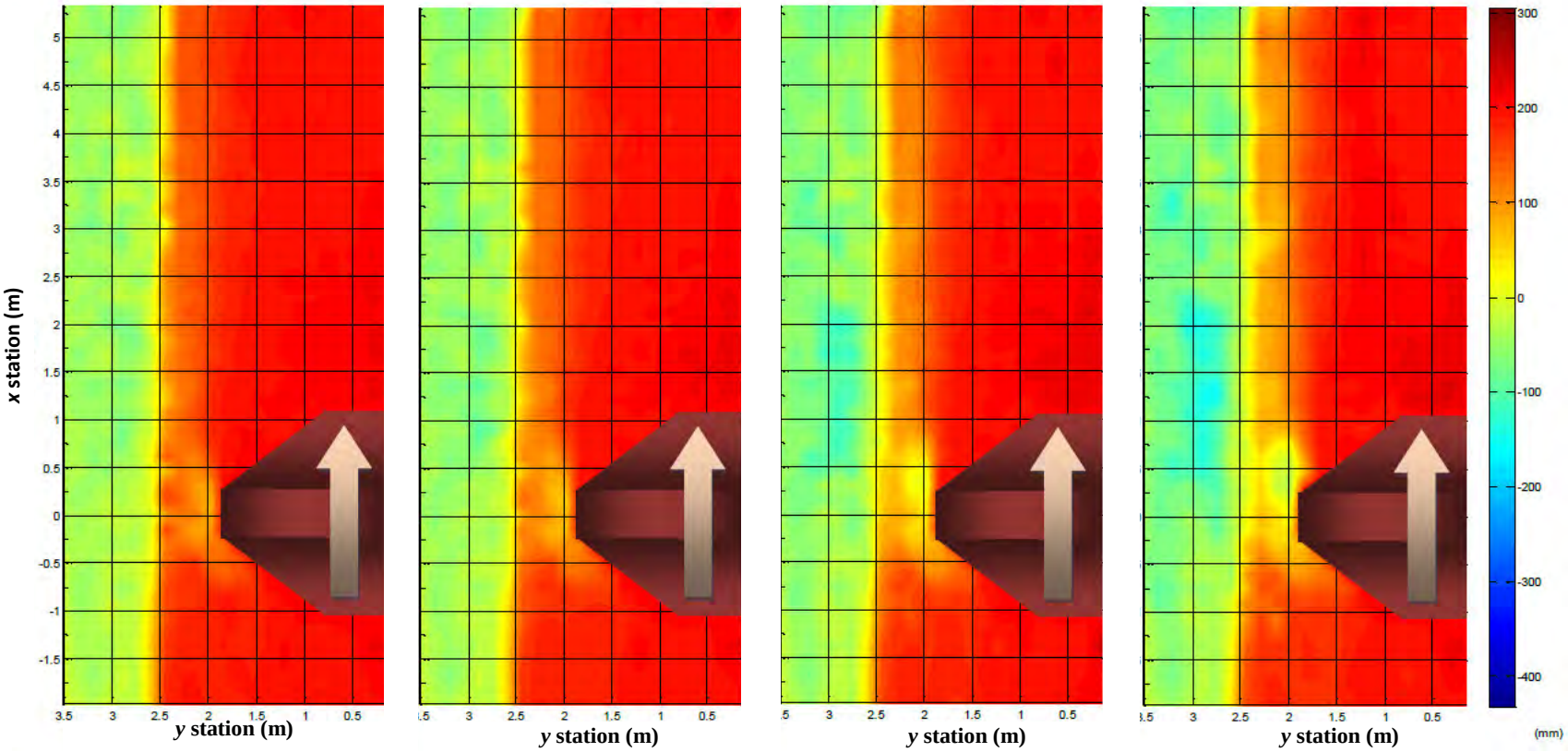

84 hours **102 hours** **145 hours** **190 hours**

Figure B.10 (contd.) – Case9

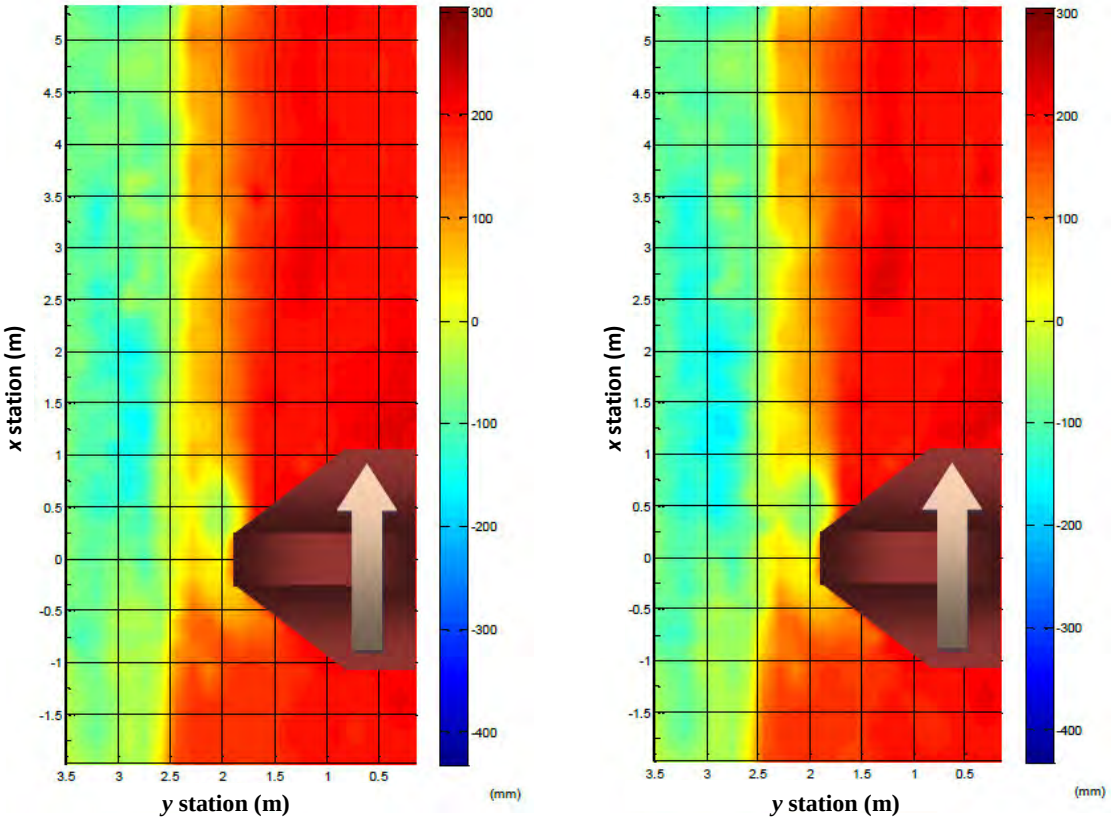

230 hours **271 hours**

Figure B.10 (contd.) – Case9

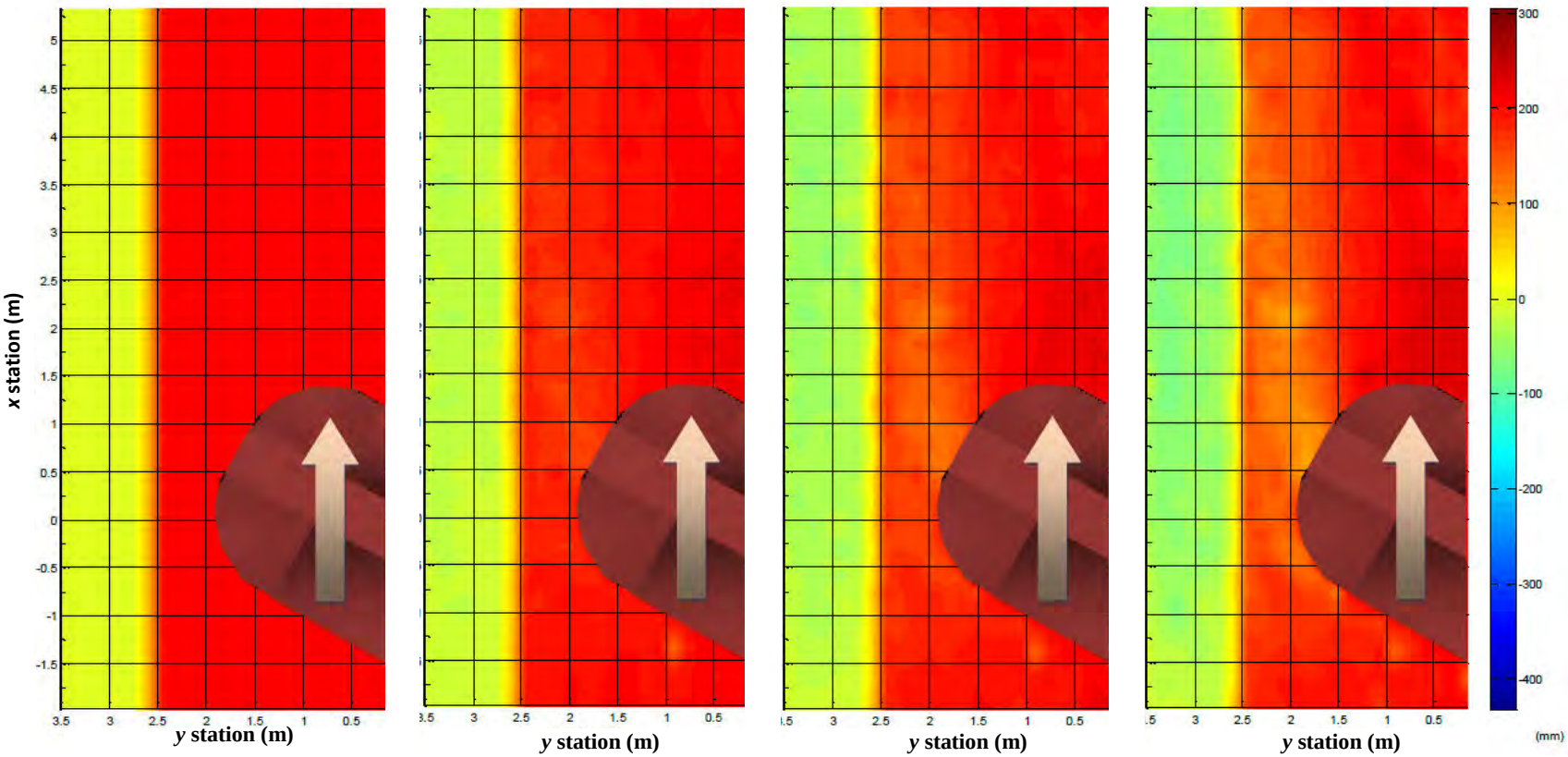

Initial **20 hours** **40 hours** **60 hours**

Figure B.11 – Case10

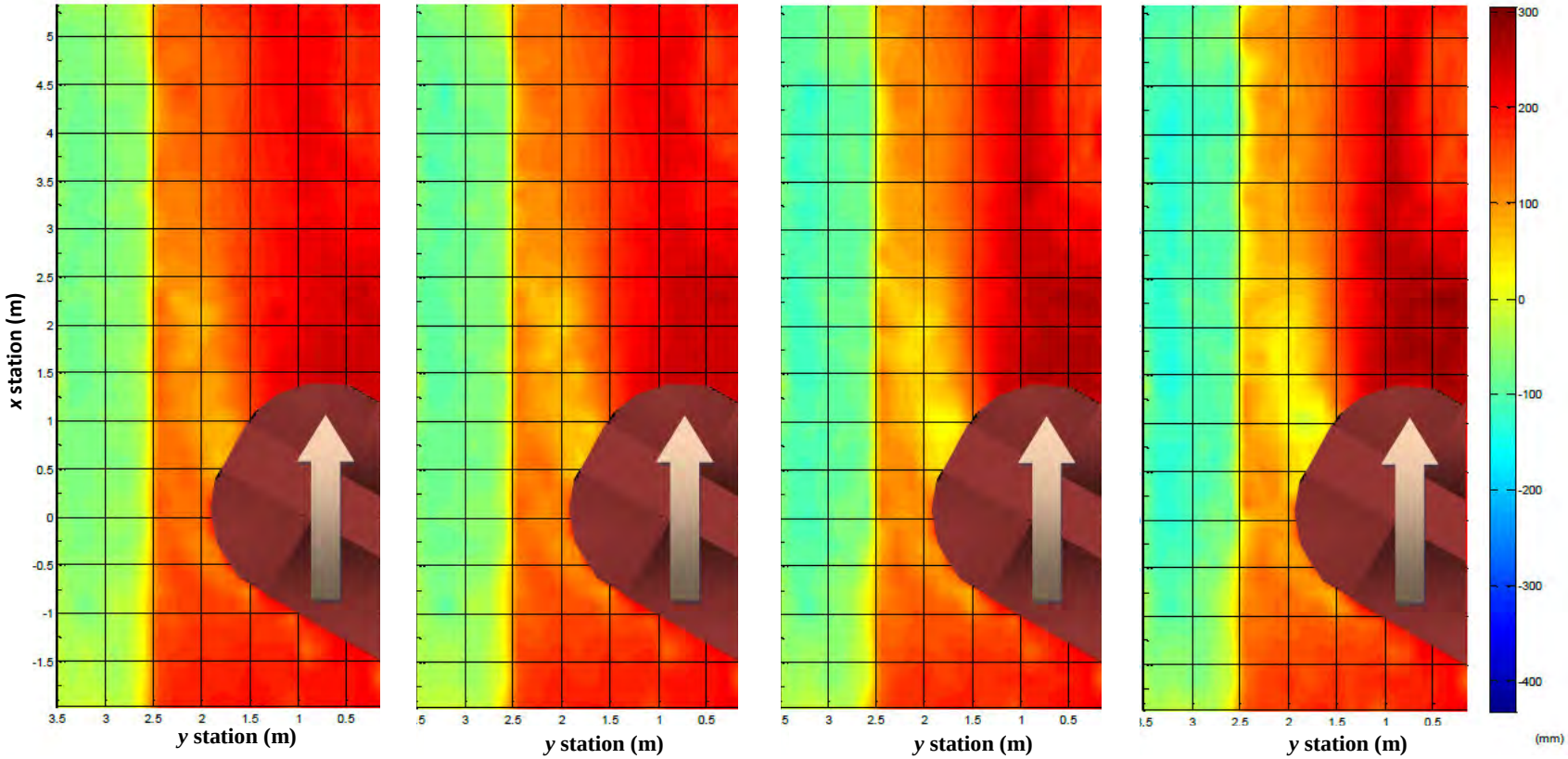

80 hours **100 hours** **144 hours** **188 hours**

Figure B.11 (contd.) – Case10

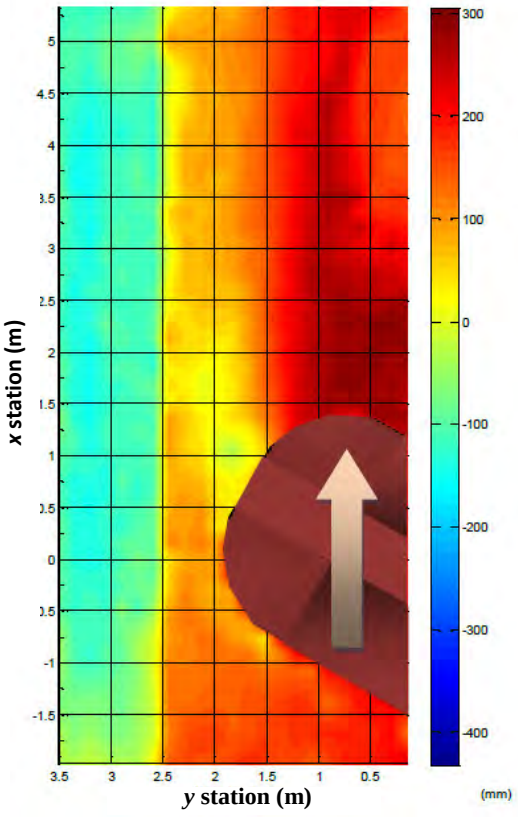

232 hours

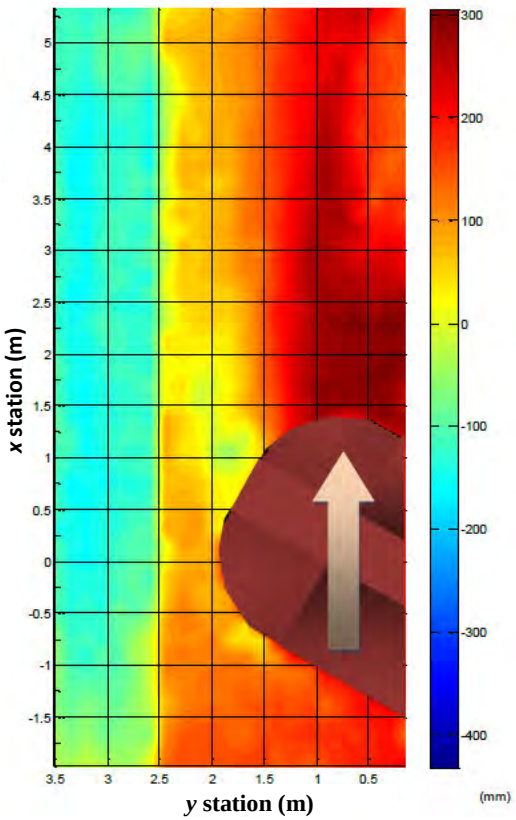

276 hours

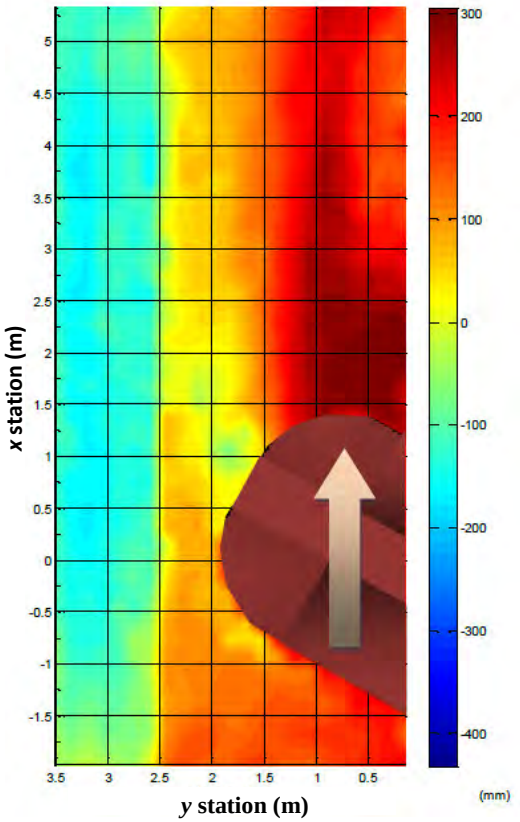

320 hours

Figure B.11 (contd.) – Case10

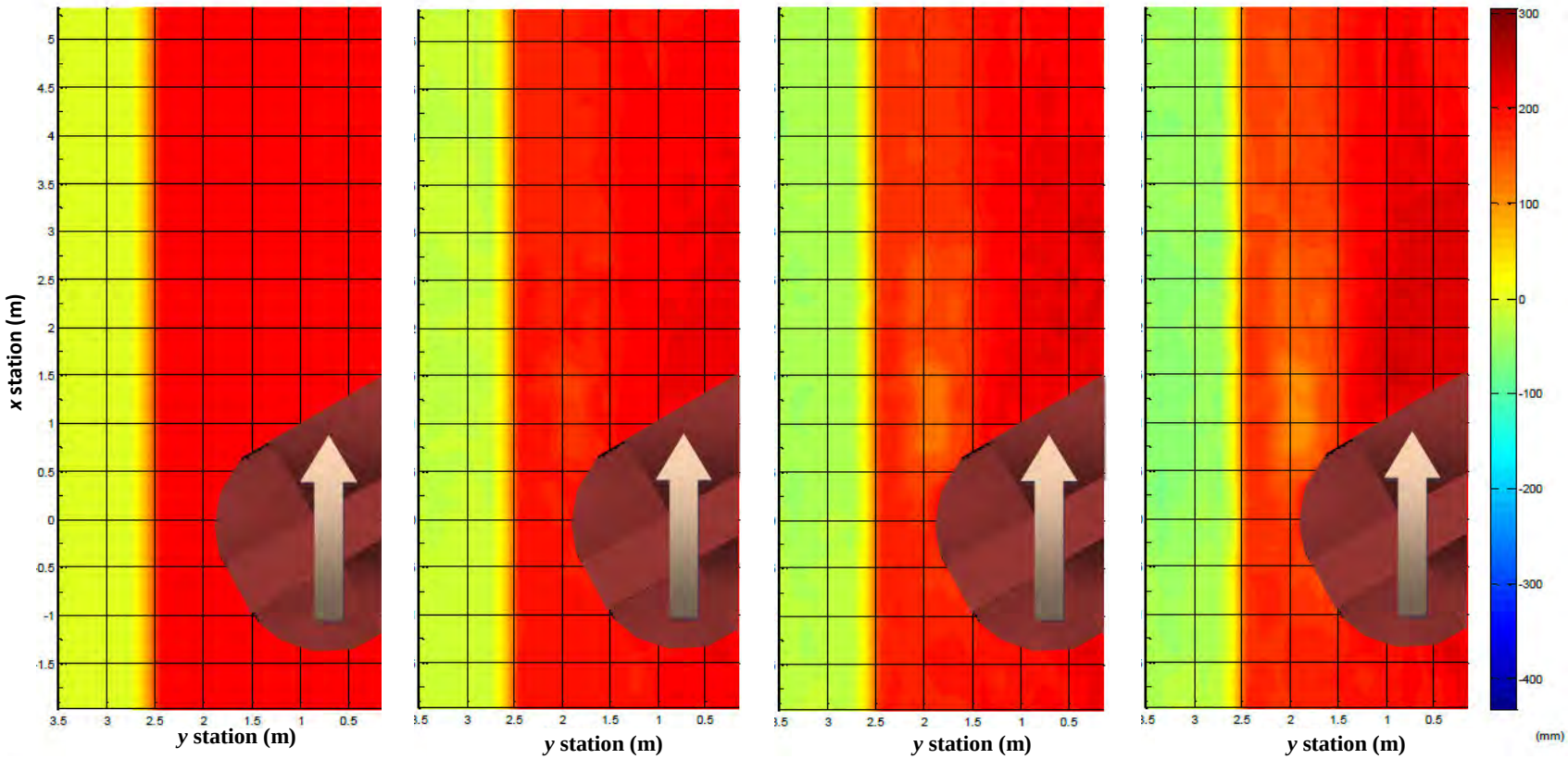

Initial **20 hours** **40 hours** **60 hours**

Figure B.12 – Case11

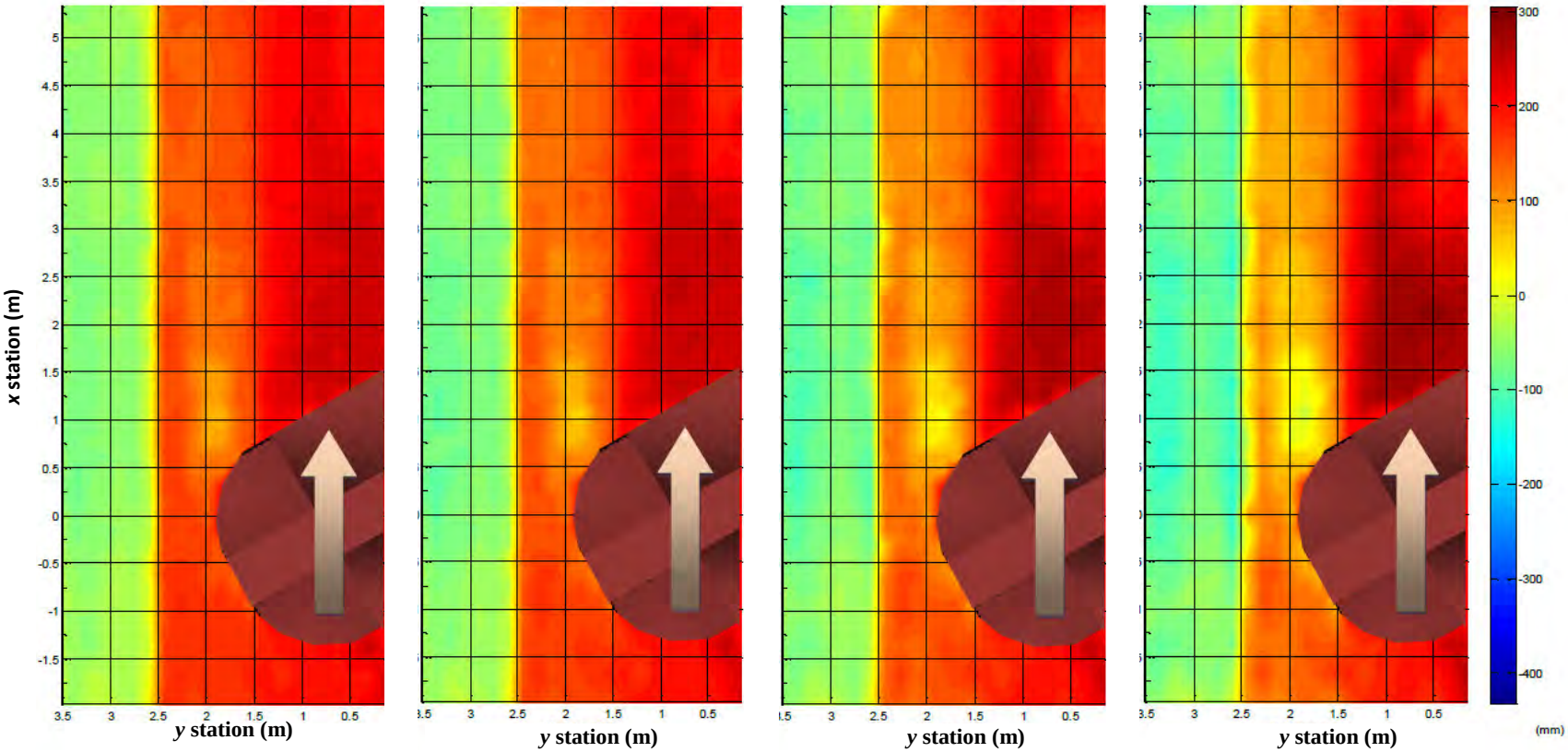

80 hours **100 hours** **144 hours** **186.5 hours**

Figure B.12 (contd.) – Case11

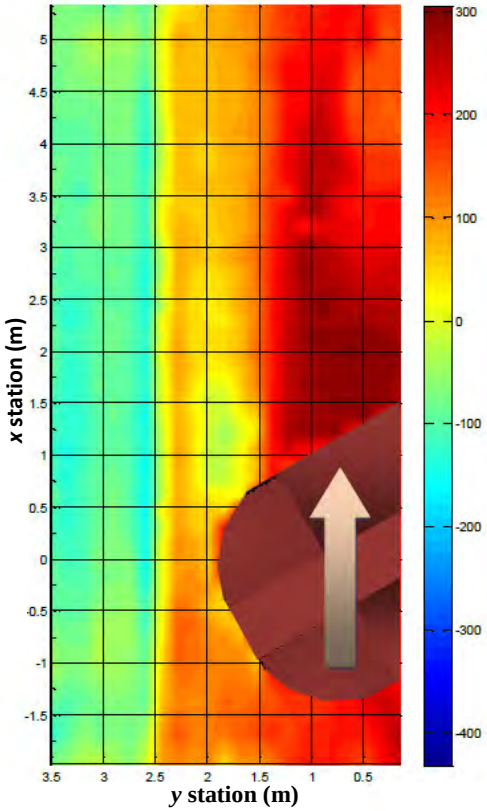

231.5 hours

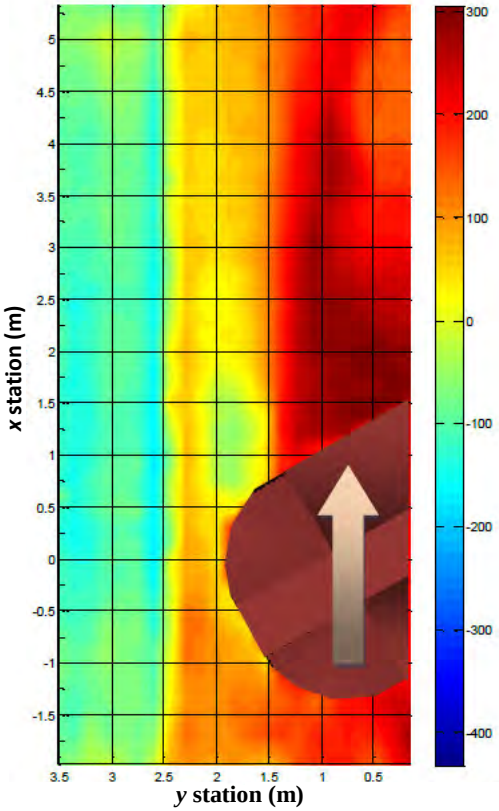

276 hours

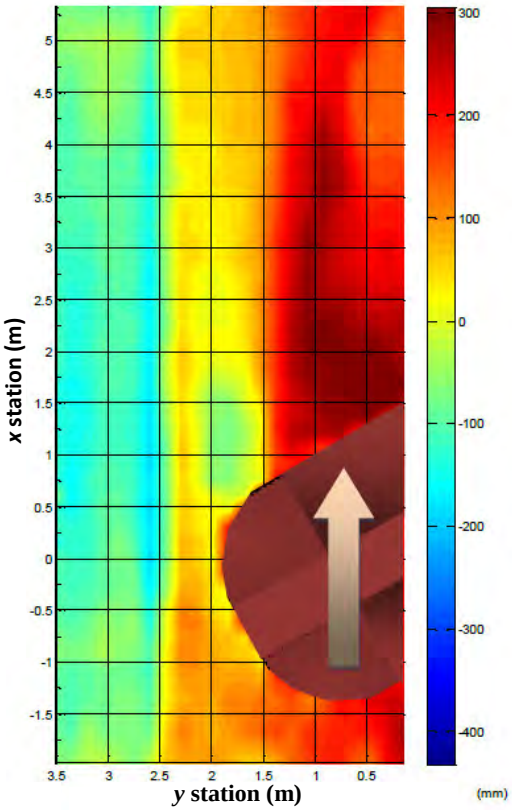

320 hours

Figure B.12 (contd.) – Case11

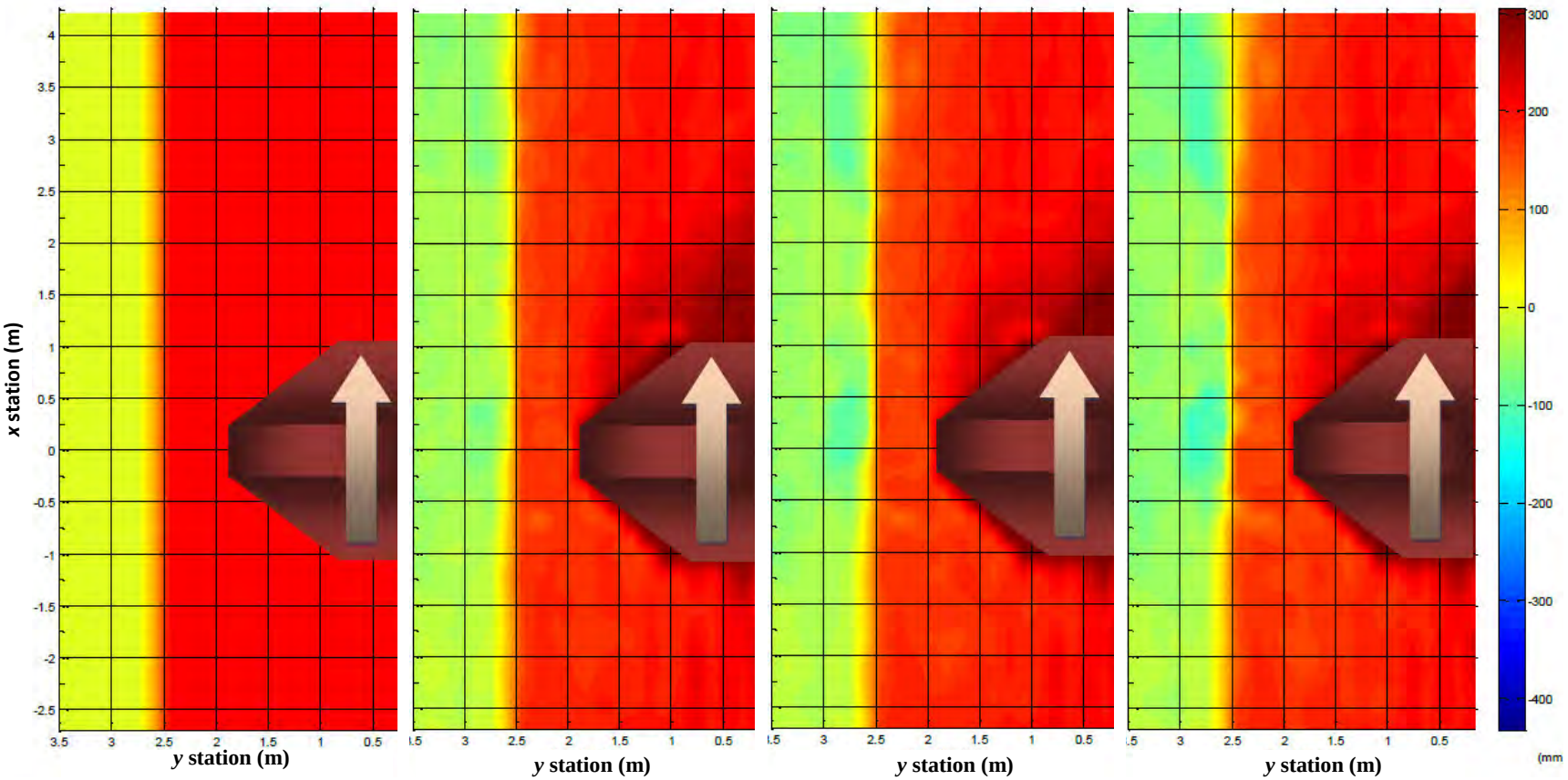

Initial **48 hours** **72 hours** **96 hours**

Figure B.13– Case12B

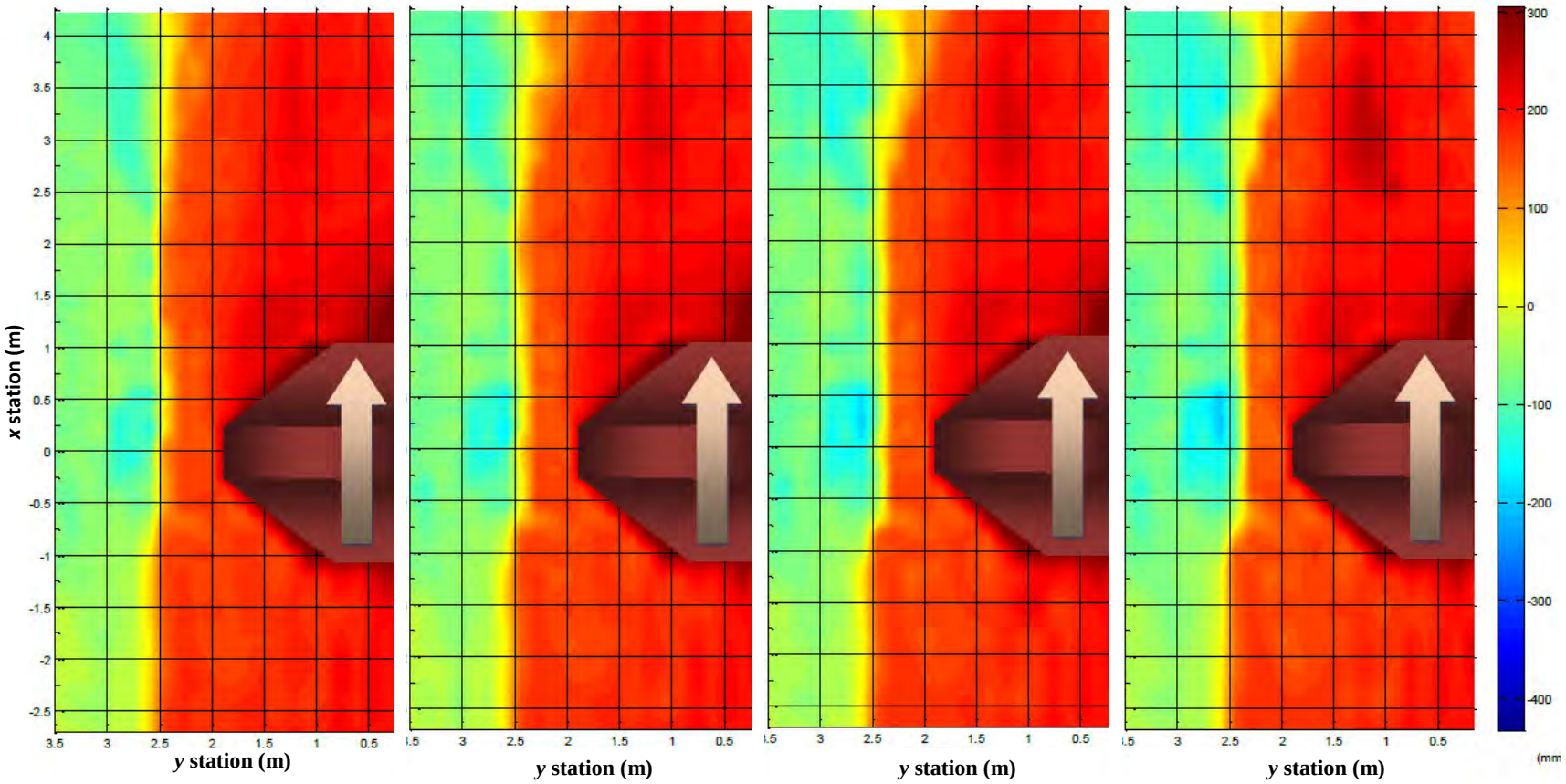

120 hours **144 hours** **168 hours** **192 hours**

Figure B.13 (contd.) – Case12B

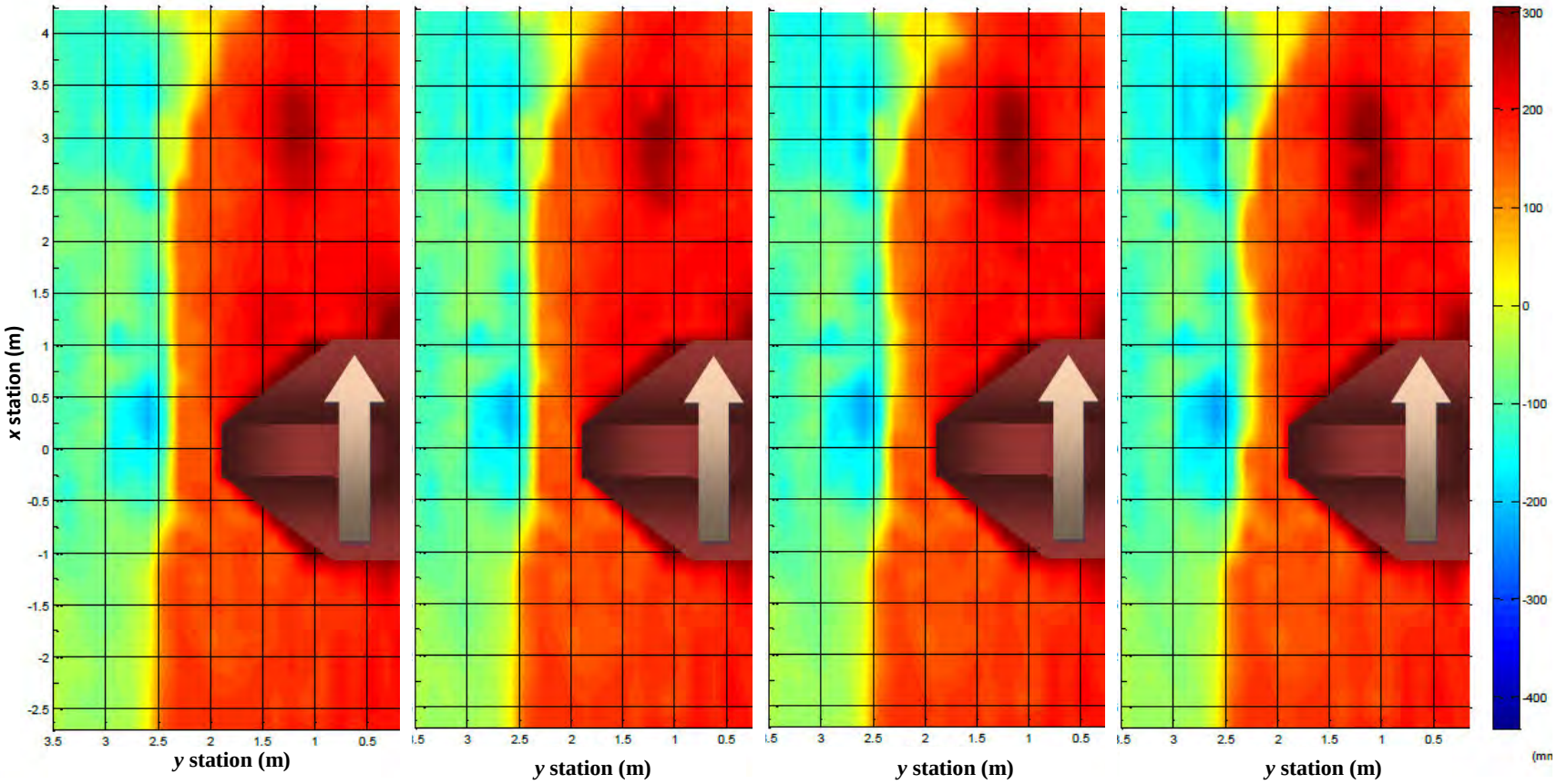

216 hours **240 hours** **264 hours** **288 hours**

Figure B.13 (contd.) – Case12B

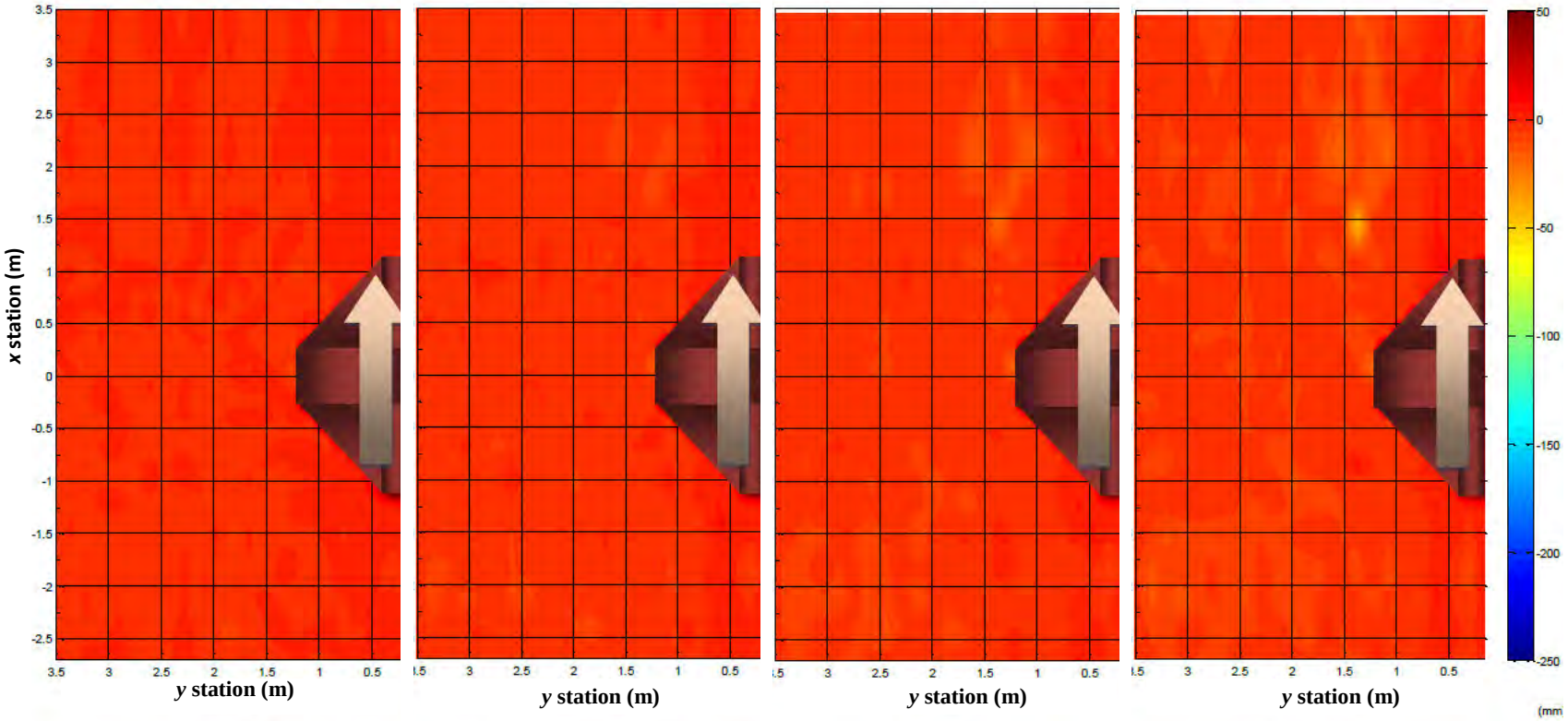

24 hours **48 hours** **72 hours** **96 hours**

Figure B.14– Case13

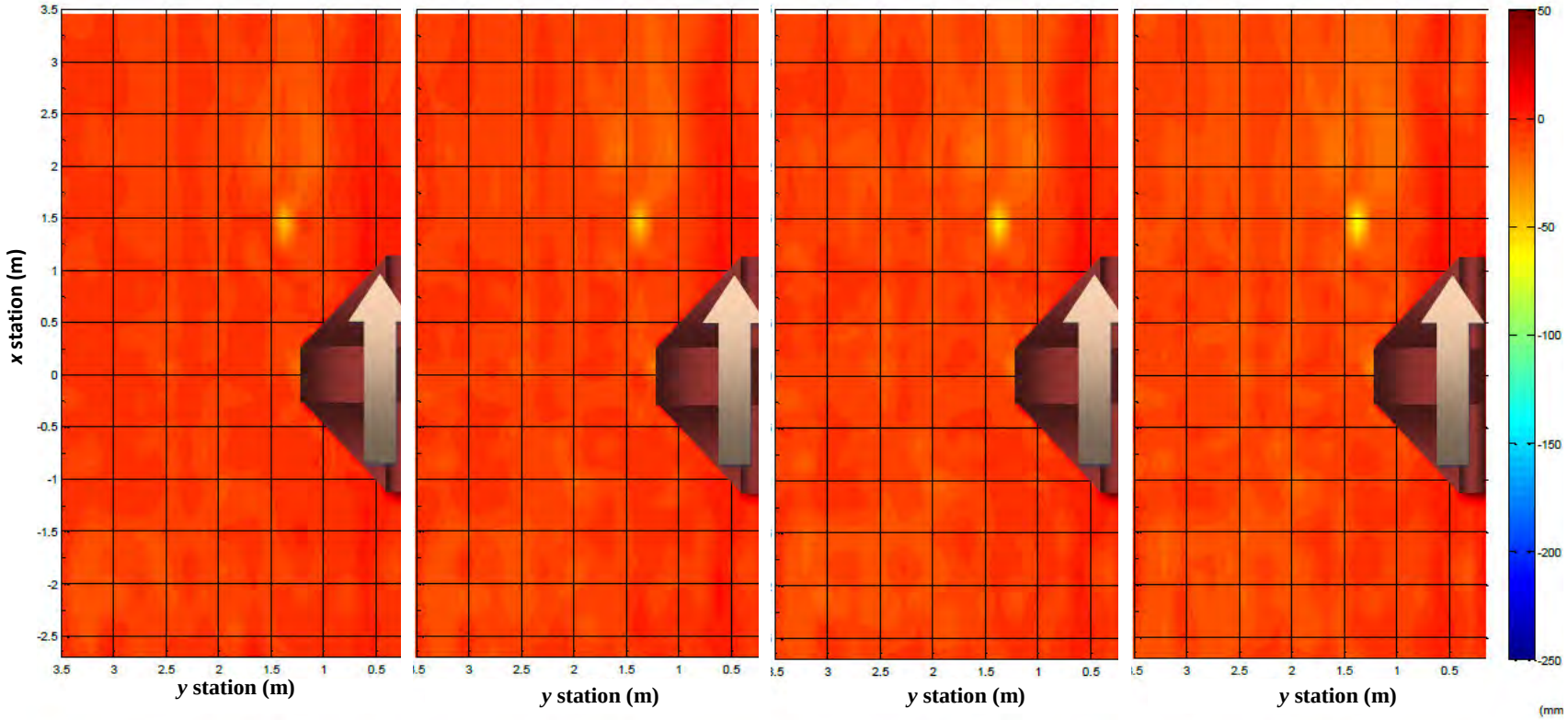

120 hours **144 hours** **168 hours** **192 hours**

Figure B.14 (contd.) – Case13

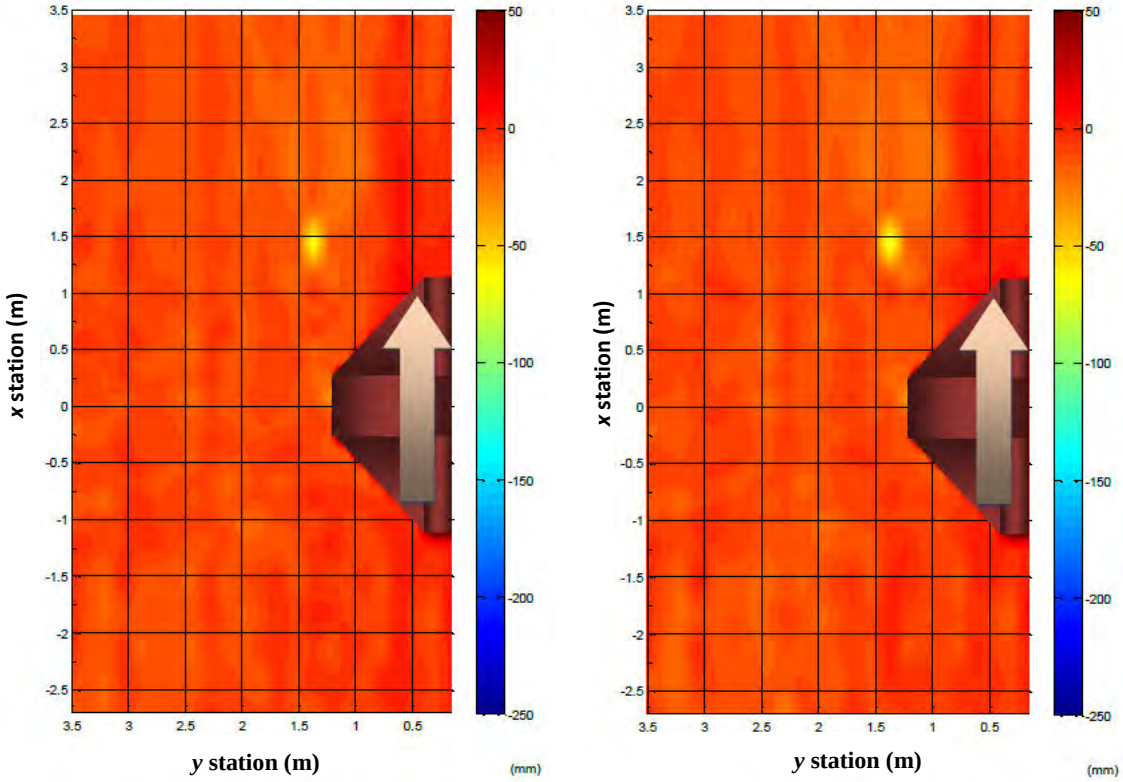

216 hours **240 hours**

Figure B.14 (contd.) – Case13

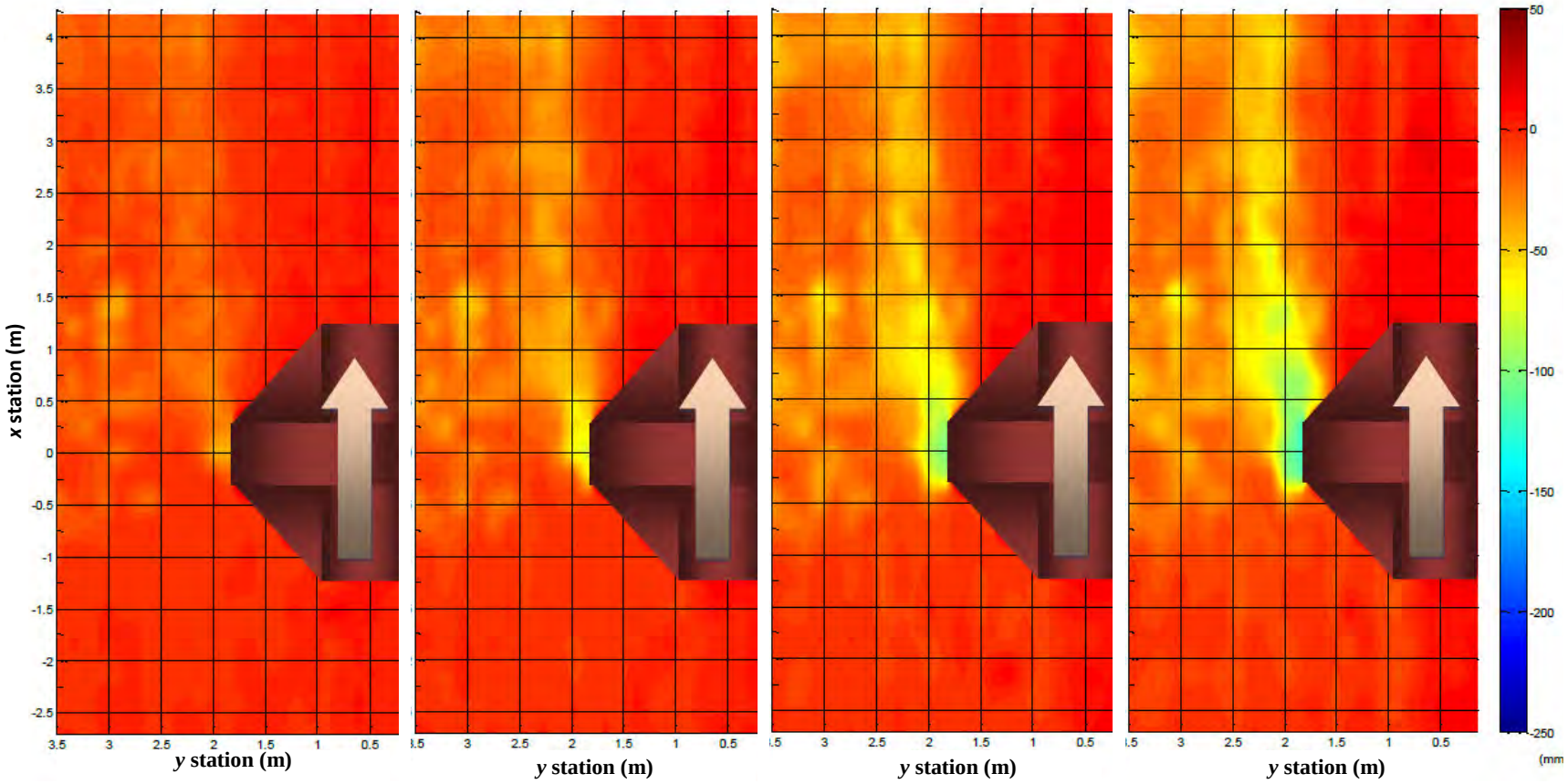

24 hours **48 hours** **72 hours** **96 hours**

Figure B.15– Case14

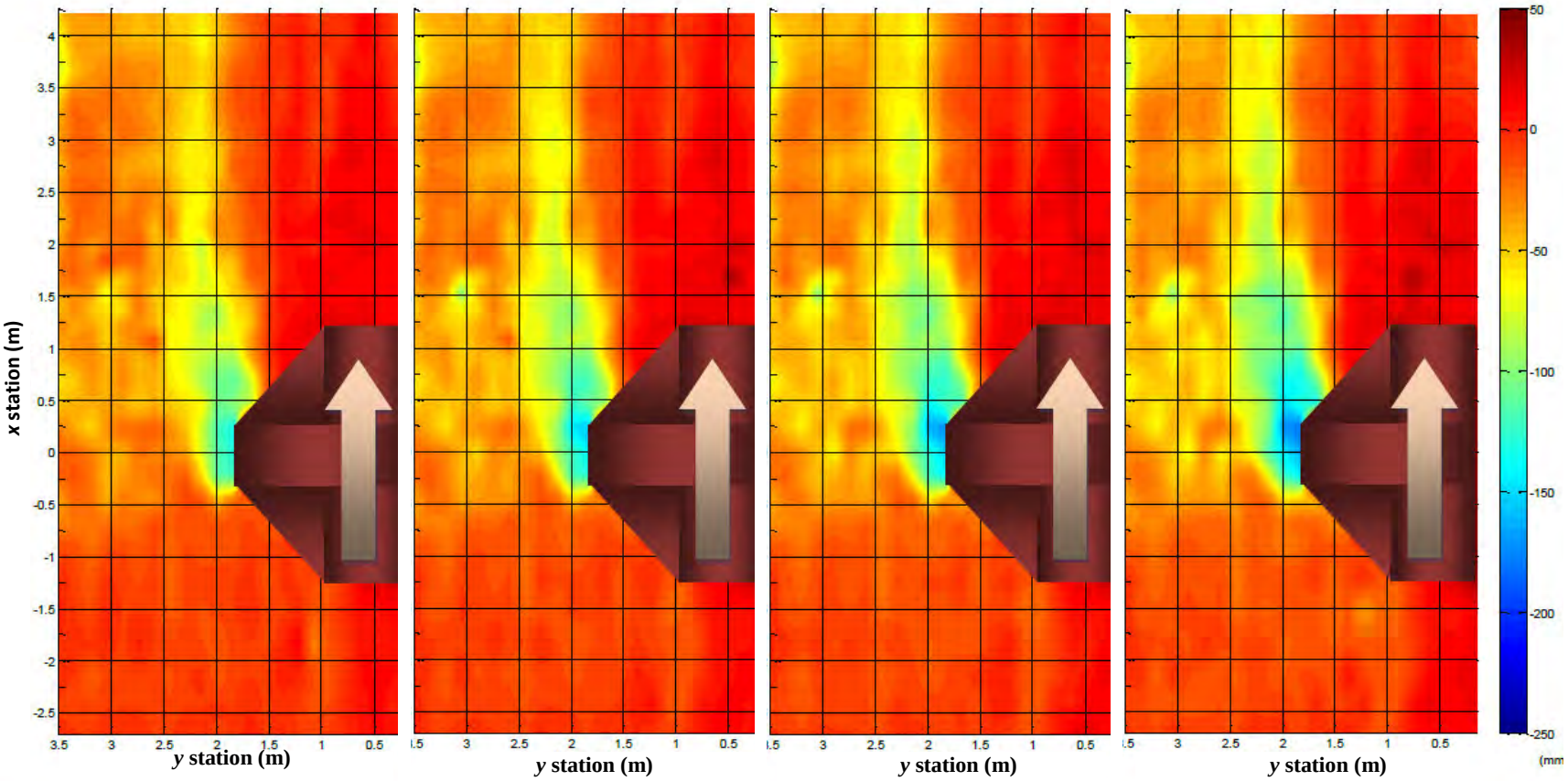

120 hours **144 hours** **168 hours** **192 hours**

Figure B.15(contd.) – Case14

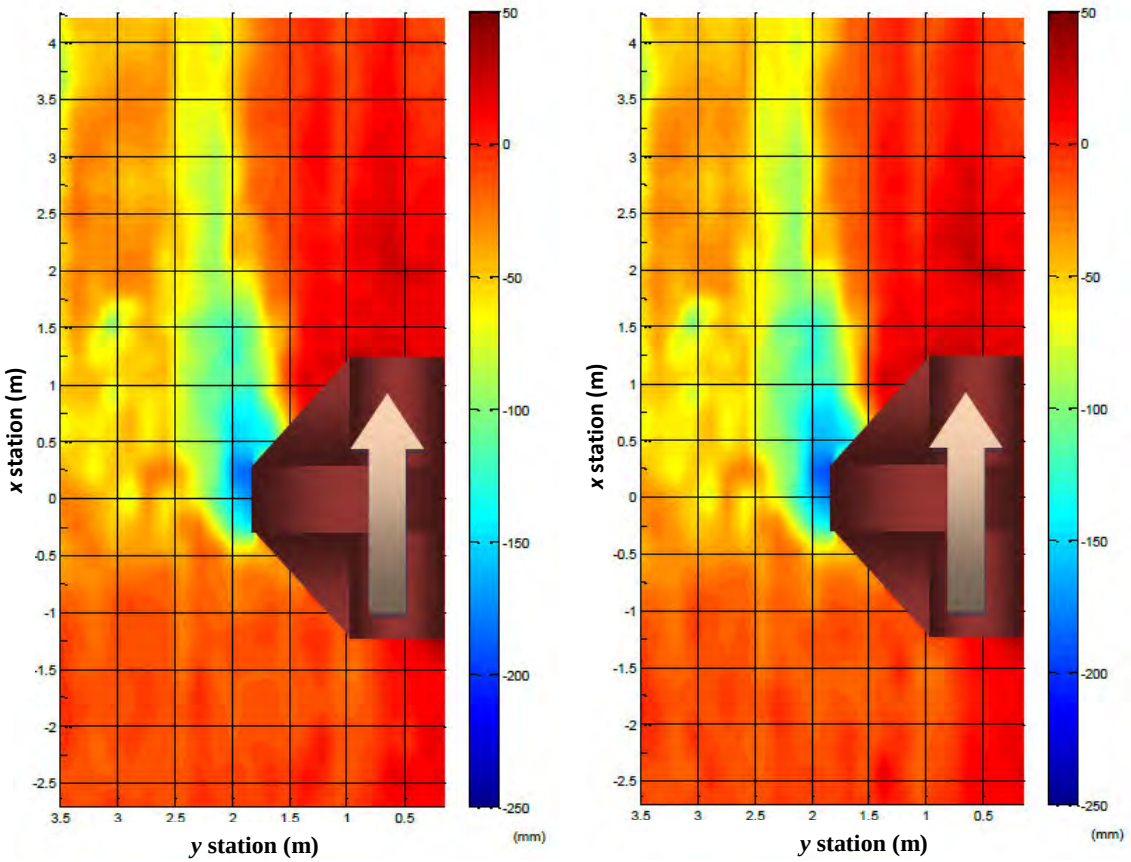

216 hours **240 hours**

Figure B.15 (contd.) – Case14

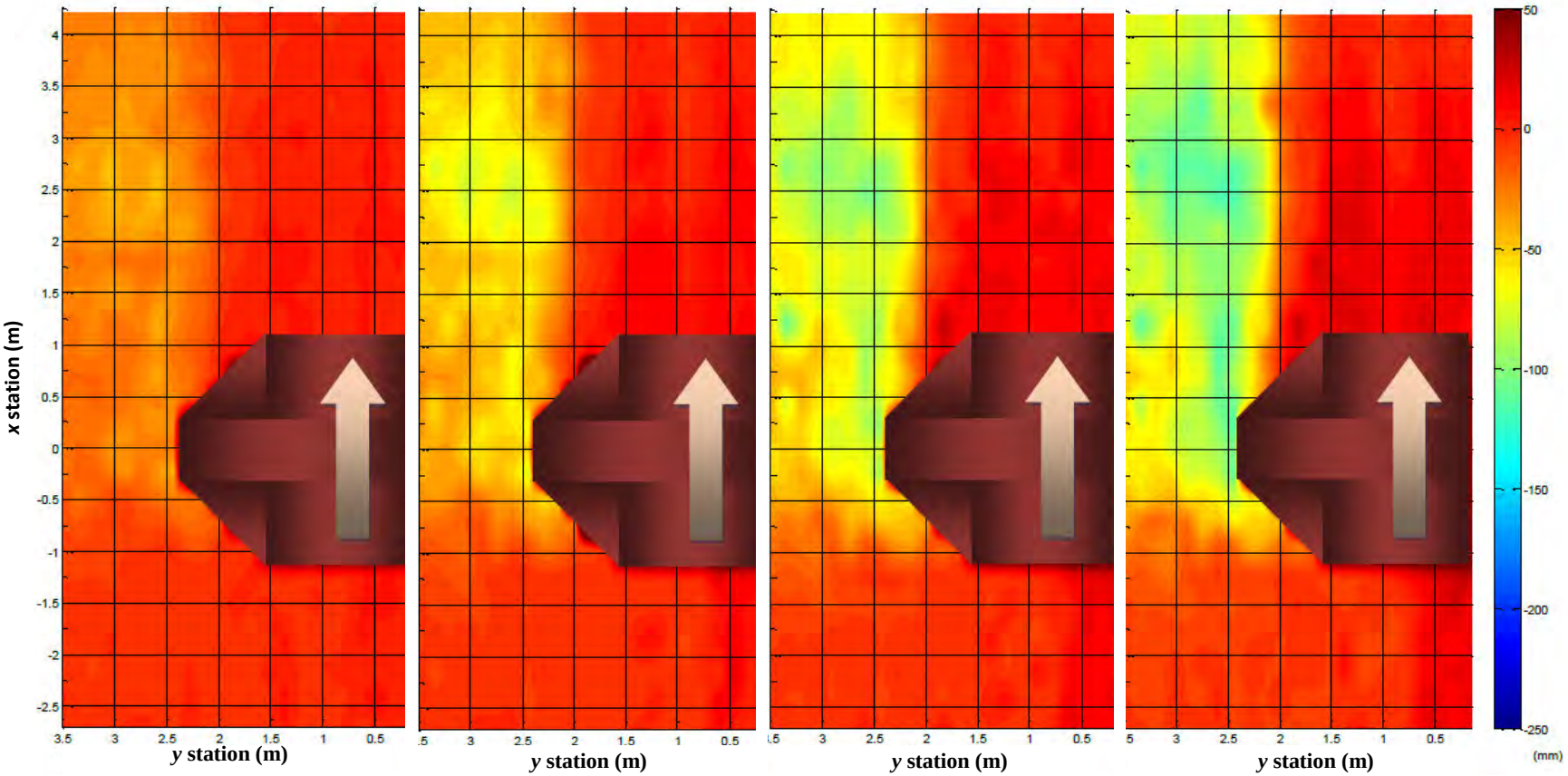

24 hours **48 hours** **72 hours** **96 hours**

Figure B.16 – Case15

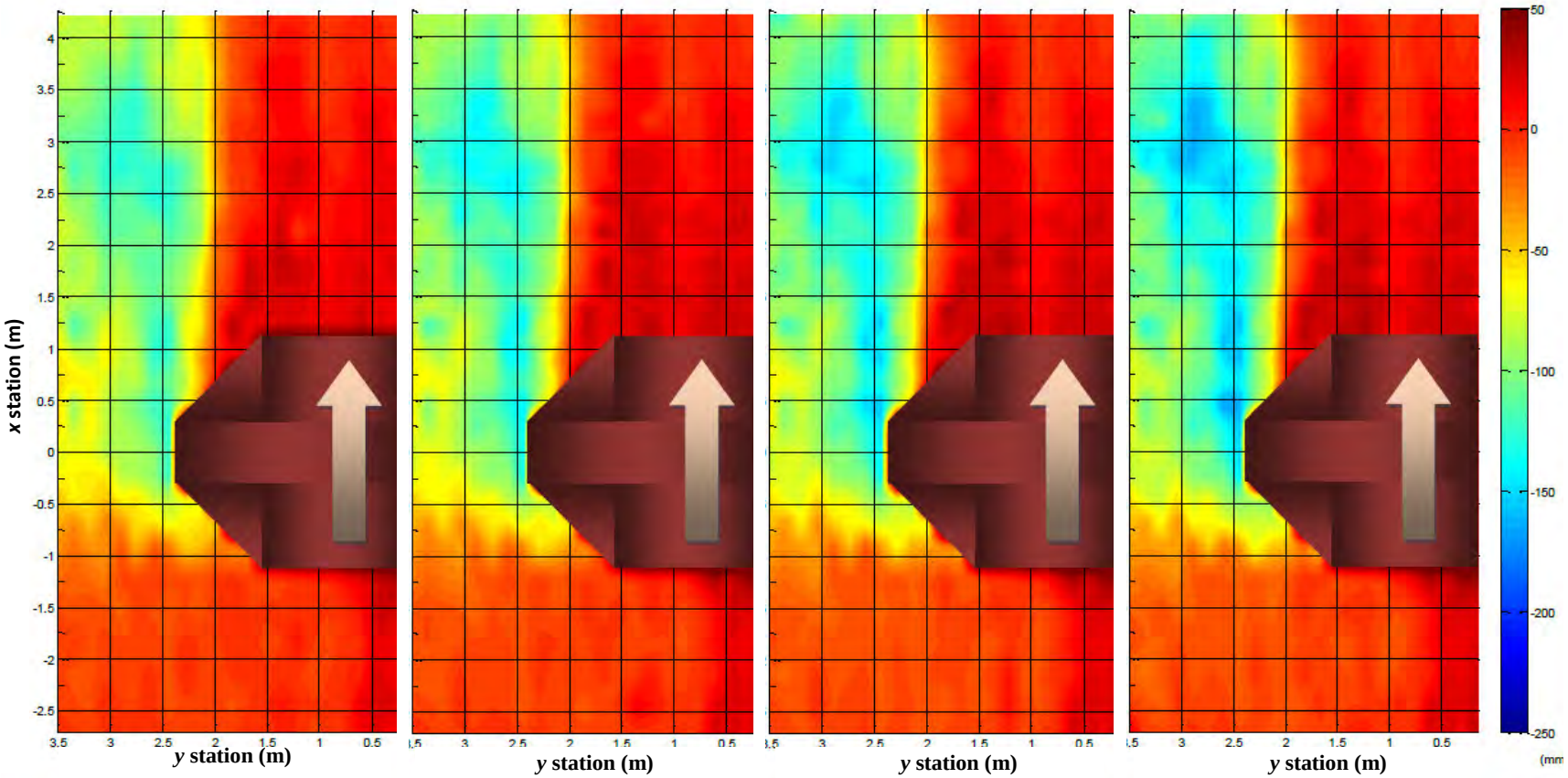

120 hours **144 hours** **168 hours** **192 hours**

Figure B.16 (contd.) – Case15

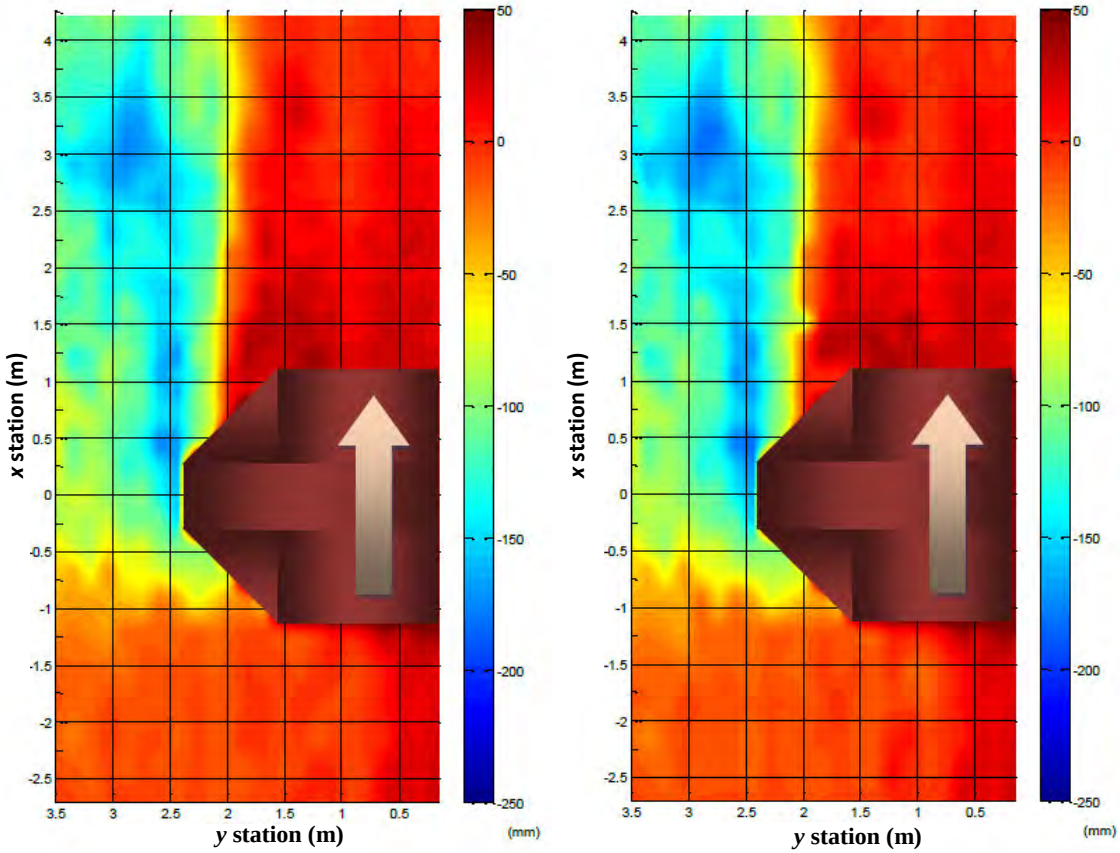

216 hours **240 hours**

Figure B.16 (contd.) – Case15

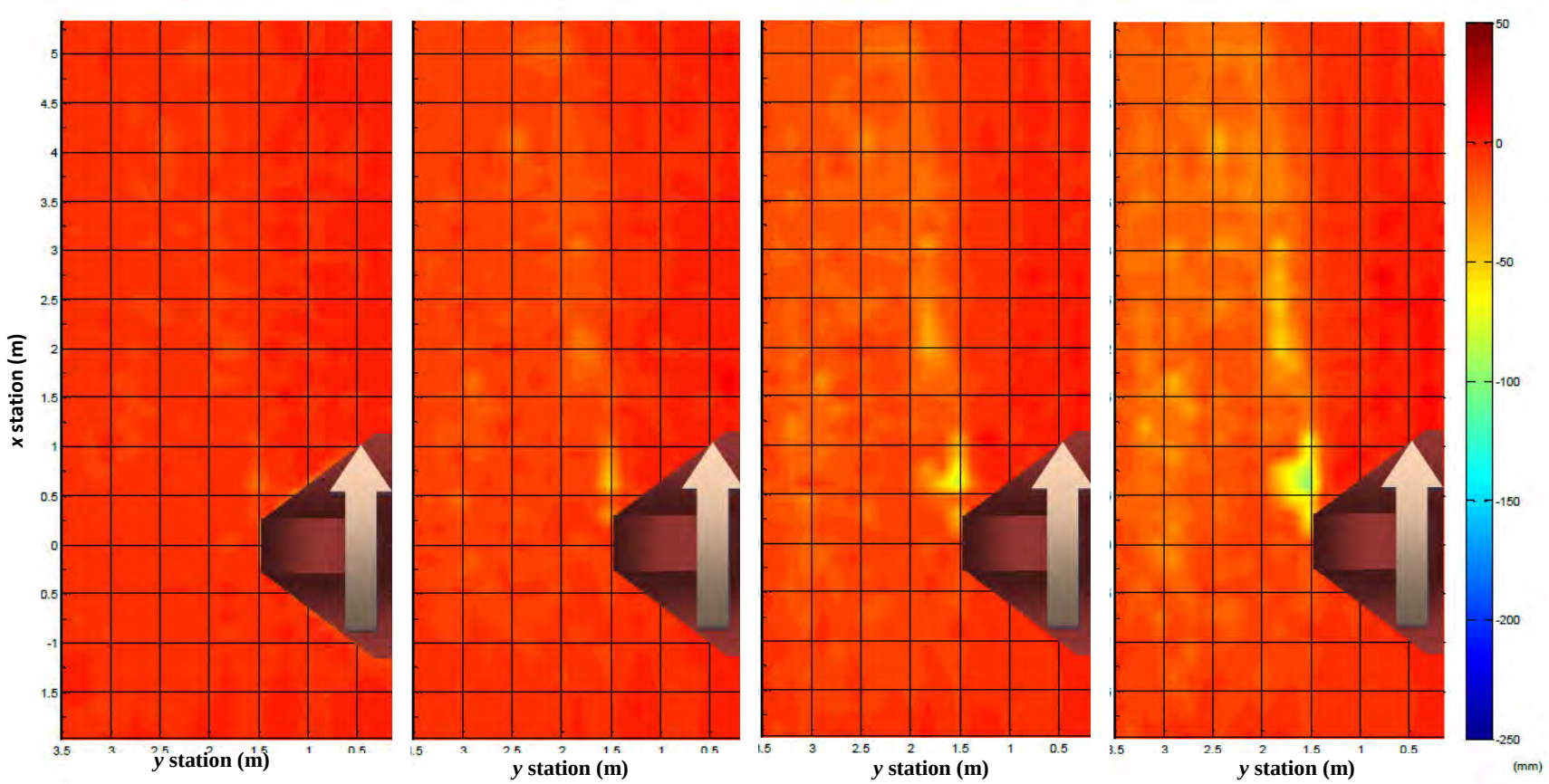

20 hours **40 hours** **60 hours** **80 hours**

Figure B.17– Case17

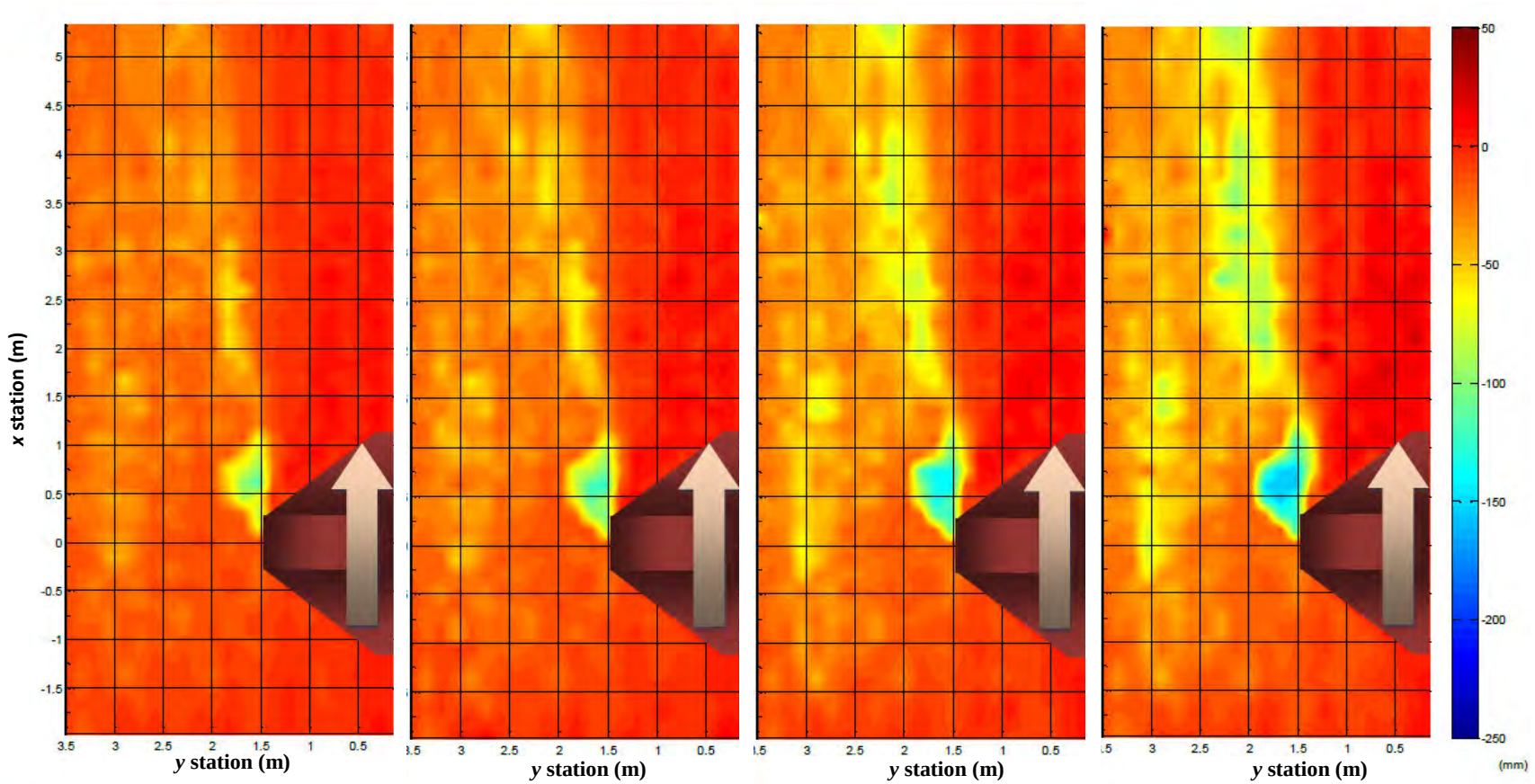

100 hours **120 hours** **165 hours** **210 hours**

Figure B.17 (contd.) – Case17

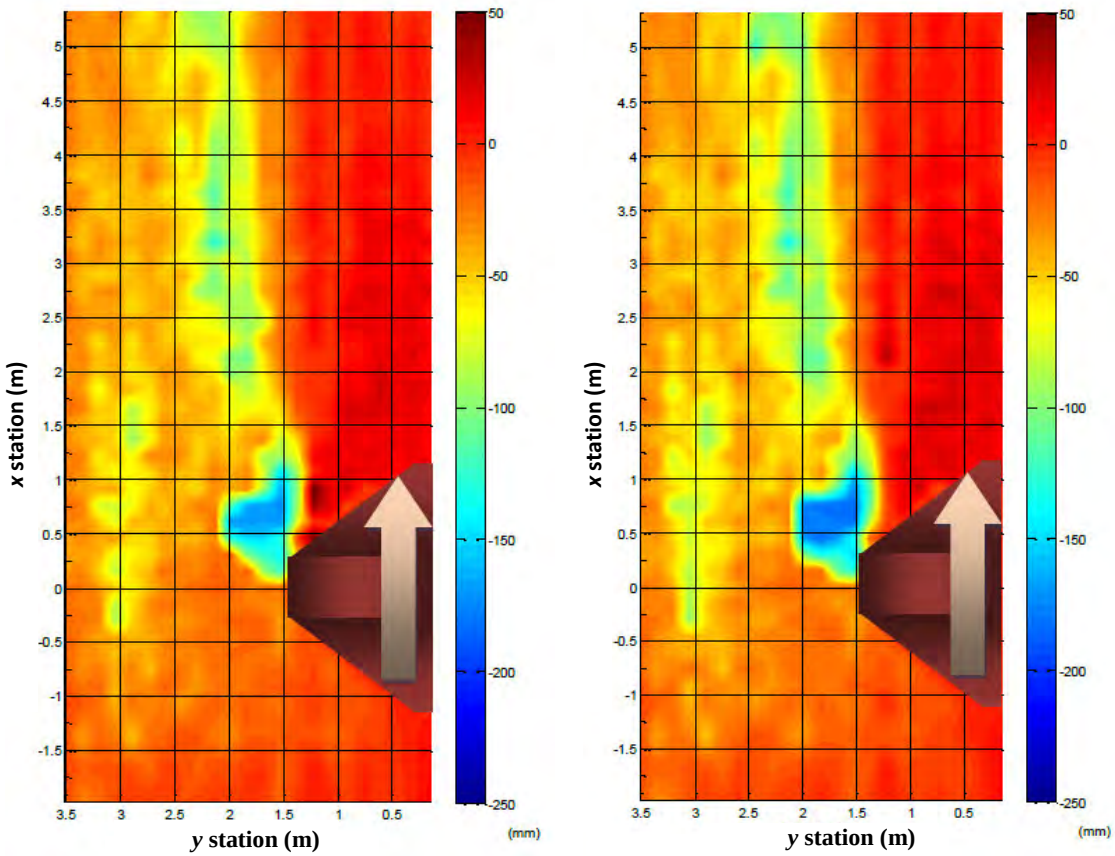

Figure B.17 (contd.) – Case17

APPENDIX C

PHOTOGRAPHS FROM THE FLUME TESTS

Figure C.1 - Flow Pattern around Abutment of Case 1 (Flow from right to left)

(a) Top View (Flow from left to right) **(b) Maximum Abutment Scour**

Figure C.2 – Scour Pattern of Case 1

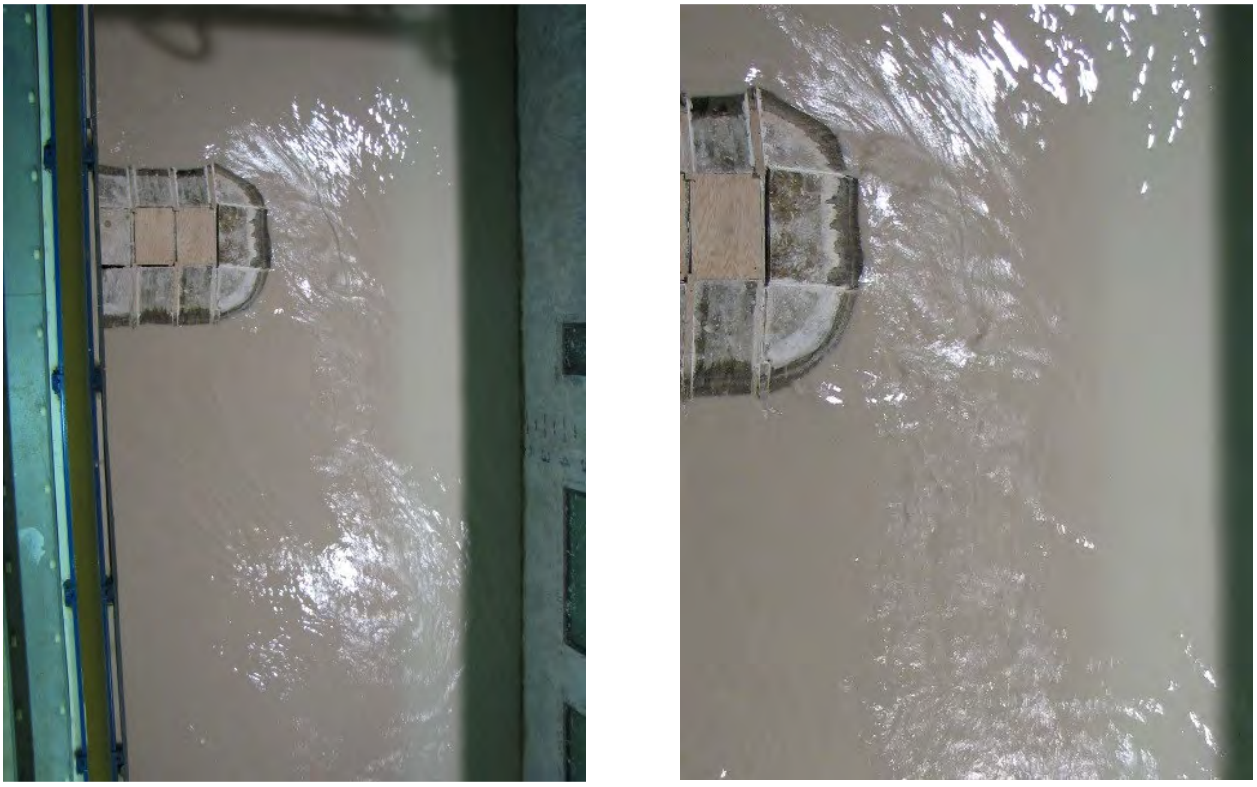

Figure C.3 - Flow Pattern around Abutment of Case 1II (Flow from top to bottom)

(a) Top View (Flow from left to right) **(b) Maximum Abutment Scour**

Figure C.4 – Scour Pattern of Case 1II

Figure C.5 - Flow Pattern around Abutment of Case 2 (Flow from left to right)

(a) Top View (Flow from left to right) **(b) Maximum Abutment Scour**

Figure C.6 – Scour Pattern of Case 2

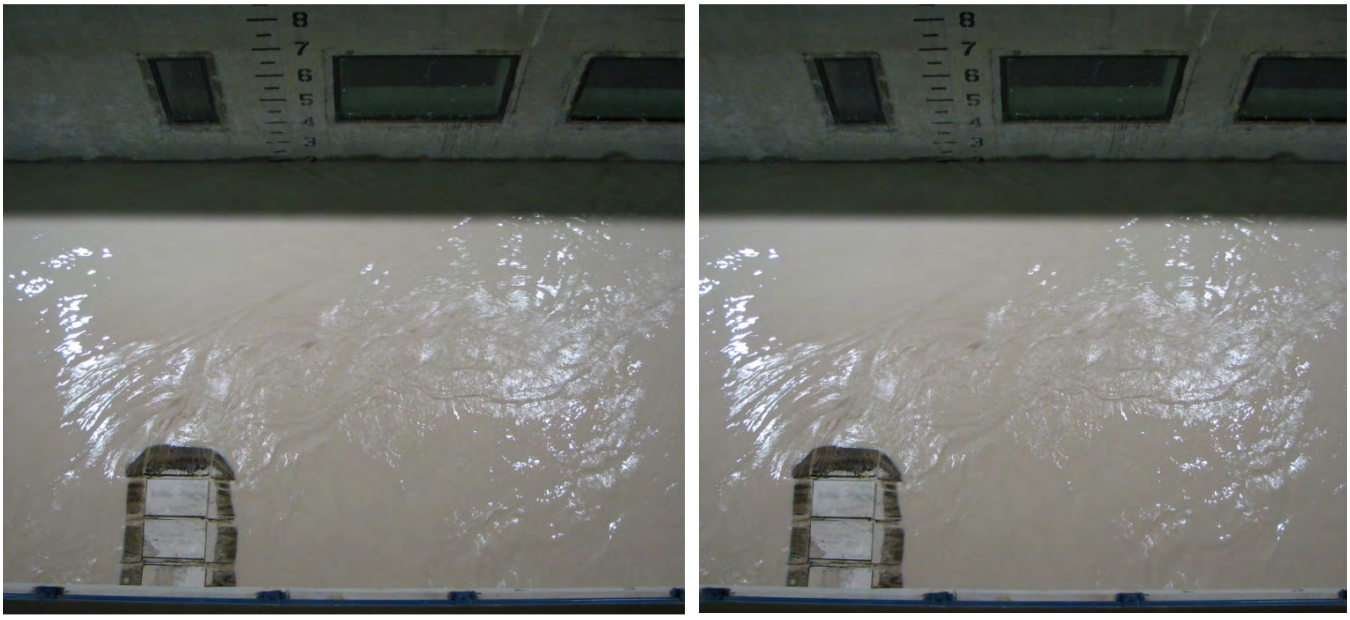

Figure C.7 - Flow Pattern around Abutment of Case 3 (Flow from left to right)

(a) Top View (Flow from left to right) **(b) Maximum Abutment Scour**

Figure C.8 – Scour Pattern of Case 3

Figure C.9 - Flow Pattern around Abutment of Case 4 (Flow from top to bottom)

(a) Top View (Flow from top to bottom) **(b) Maximum Abutment Scour**

Figure C.10 – Scour Pattern of Case 4

Figure C.11 - Flow Pattern around Abutment of Case 5 (Flow from top to bottom)

(a) Top View (Flow from top to bottom) **(b) Maximum Scour**

Figure C.12 – Scour Pattern of Case 5

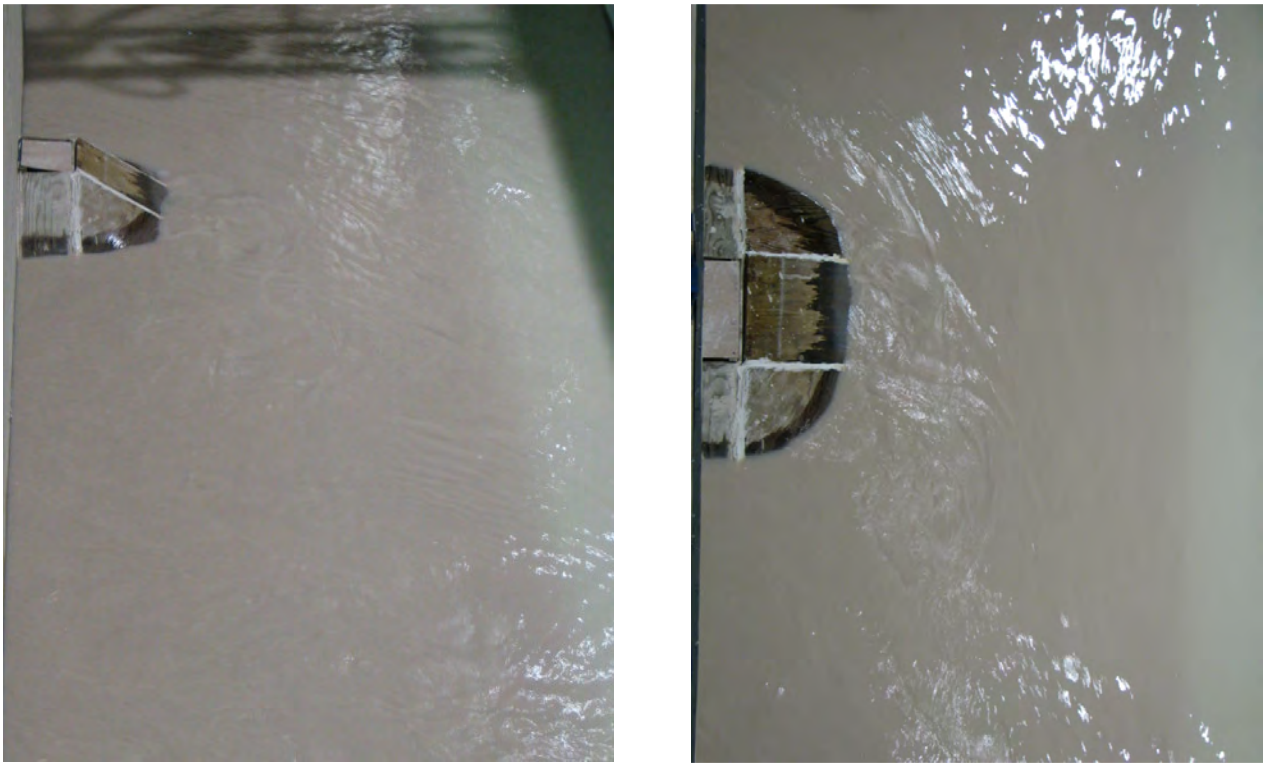

Figure C.13 - Flow Pattern around Abutment of Case 6 (Flow from top to bottom)

(a) Top View (Flow from top to bottom) **(b) Maximum Abutment Scour**

Figure C.14 – Scour Pattern of Case 6

Figure C.15 - Flow Pattern around Abutment of Case 7 (Flow from top to bottom)

(a) Top View (Flow from top to bottom) **(b) Maximum Abutment Scour**

Figure C16 – Scour Pattern of Case 7

Figure C.17 - Flow Pattern around Abutment of Case 8 (Flow from top to bottom)

(a) Top View (Flow from top to bottom) **(b) Maximum Abutment Scour**

Figure C.18 – Scour Pattern of Case 8

Figure C.19 - Flow Pattern around Abutment of Case 9 (Flow from top to bottom)

(a) Top View (Flow from top to bottom) **(b) Maximum Abutment Scour**

Figure C.20 – Scour Pattern of Case 9

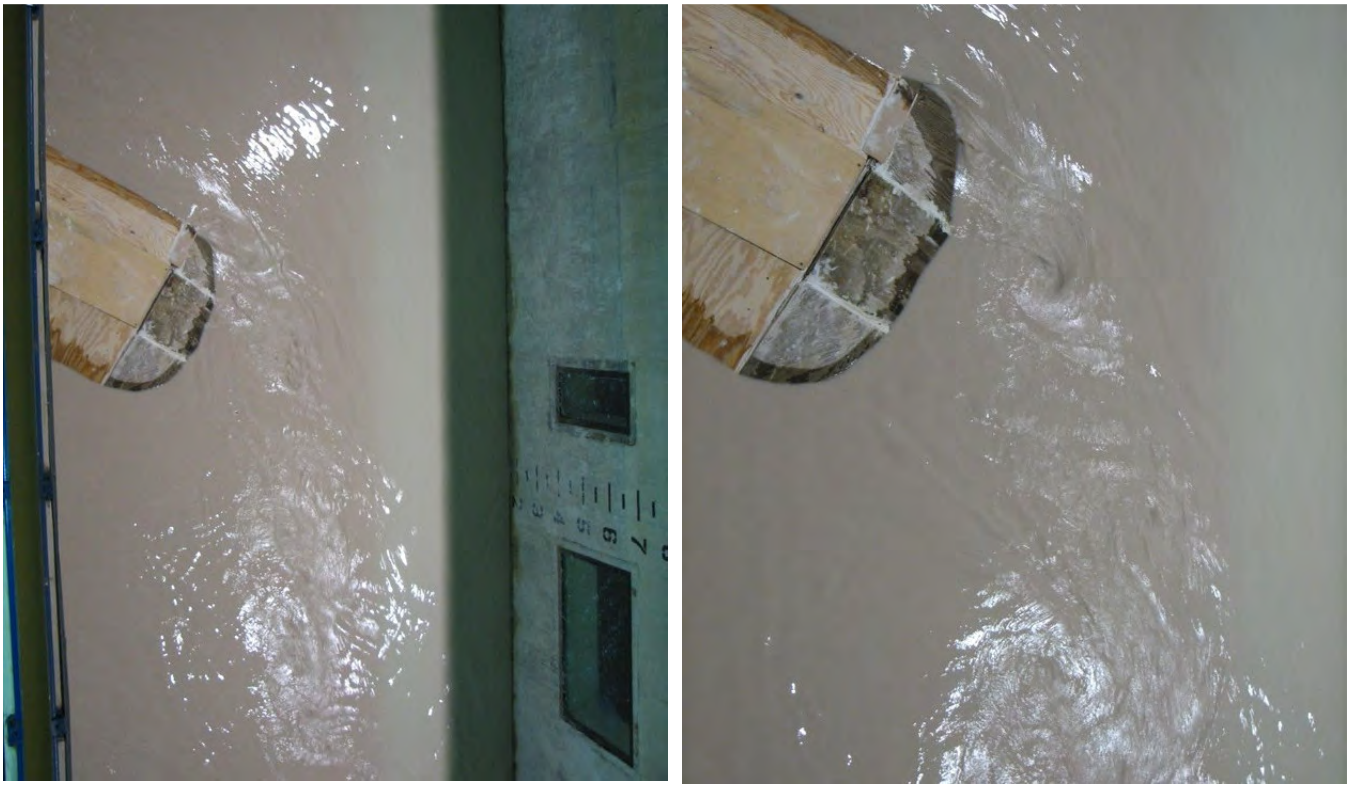

Figure C.21 - Flow Pattern around Abutment of Case 10 (Flow from top to bottom)

(a) Top View (Flow from top to bottom) **(b) Maximum Abutment Scour**

Figure C.22 – Scour Pattern of Case 10

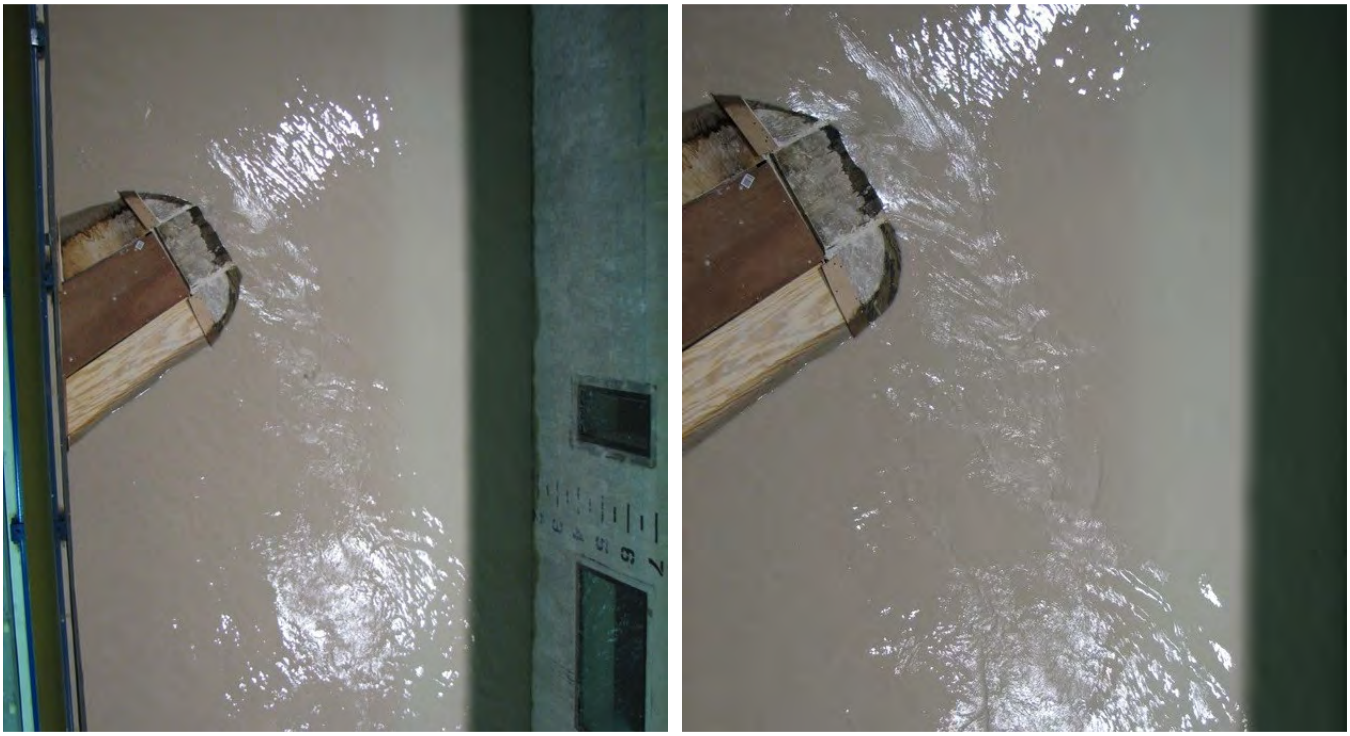

Figure C.23 - Flow Pattern around Abutment of Case 11 (Flow from top to bottom)

(a) Top View (Flow from top to bottom) **(b) Maximum Abutment Scour**

Figure C.24 – Scour Pattern of Case 11

Figure C.25 - Flow Pattern around Abutment of Case 12B (Flow from top to bottom)

(a) Top View (Flow from top to bottom) **(b) Maximum Abutment Scour**

Figure C.26 – Scour Pattern of Case 12B

Figure C27 – Before Test (Case 13)

Figure C28 - Flow Pattern around Abutment of Case 13

(a) At Down Stream (Flow from top to bottom)

(b) Maximum Scour

Figure C.29 – Scour Pattern of Case 13

Figure C.30 – Before Test (Case 14)

Figure C.31 - Flow Pattern around Abutment of Case 14

(a) At Down Stream (Flow from bottom to top)

(b) Maximum Abutment Scour

Figure C.32 – Scour Pattern of Case 14

Figure C.33 - Flow Pattern around Abutment of Case 15 (Flow from left to right)

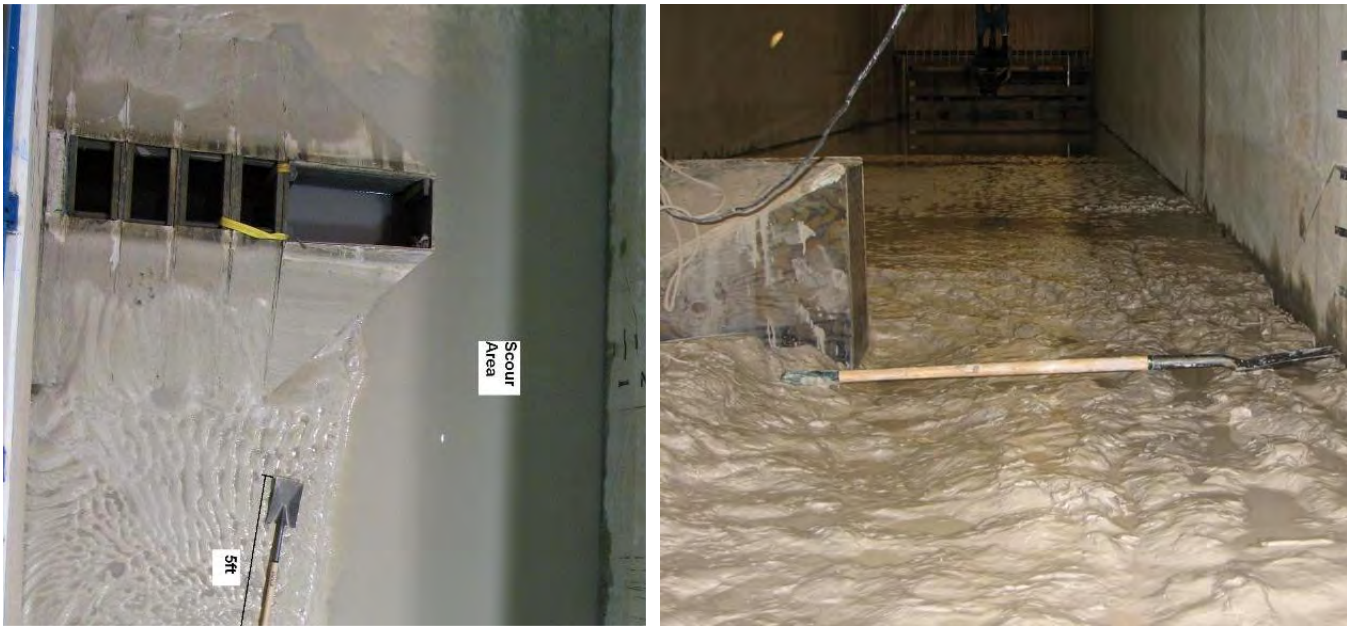

(a) Top View (Flow from top to bottom) **(b) Maximum Abutment Scour**

Figure C.34 – Scour Pattern of Case 15

Figure C.35 - Flow Pattern around Abutment of Case 16 (Flow from top to bottom)

(a) Top View (Flow from top to bottom) **(b) Maximum Abutment Scour**

Figure C.36 – Scour Pattern of Case 16

Figure C.37 - Flow Pattern around Abutment of Case 17 (Flow from top to bottom)

(a) Top View (Flow from top to bottom) **(b) Maximum Abutment Scour**

Figure C.38 – Scour Pattern of Case 17